

## Durham E-Theses

---

### *Developing a novel 3D model of the intestinal epithelium as a tool to study the pharmacokinetics of new chemical entities*

FREER, MATTHEW,ANDREW

#### How to cite:

---

FREER, MATTHEW,ANDREW (2020) *Developing a novel 3D model of the intestinal epithelium as a tool to study the pharmacokinetics of new chemical entities*, Durham theses, Durham University. Available at Durham E-Theses Online: <http://etheses.dur.ac.uk/13715/>

#### Use policy

---

The full-text may be used and/or reproduced, and given to third parties in any format or medium, without prior permission or charge, for personal research or study, educational, or not-for-profit purposes provided that:

- a full bibliographic reference is made to the original source
- a [link](#) is made to the metadata record in Durham E-Theses
- the full-text is not changed in any way

The full-text must not be sold in any format or medium without the formal permission of the copyright holders.

Please consult the [full Durham E-Theses policy](#) for further details.

---

Academic Support Office, Durham University, University Office, Old Elvet, Durham DH1 3HP  
e-mail: [e-theses.admin@dur.ac.uk](mailto:e-theses.admin@dur.ac.uk) Tel: +44 0191 334 6107  
<http://etheses.dur.ac.uk>



**Department of Biosciences**

**Developing a novel 3D model of the intestinal  
epithelium as a tool to study the  
pharmacokinetics of new chemical entities**

**Matthew Andrew Freer BSc (Hons) AFHEA**

**A Thesis submitted for the degree of Doctor of Philosophy**

**December 2019**

## **Declaration**

The work described herein was carried out in the department of Biosciences (Formally the School of Biological and Biomedical Sciences), University of Durham between October 2015 and September 2019. All of the work is my own, except where specifically stated otherwise. No part has previously been submitted for a degree at this or any other university.

## **Statement of Copyright**

The copyright of this thesis rests with the author. No quotations from it should be published without the prior written consent and information derived from it should be acknowledged.



## Abstract

New chemical entities (NCE) are in continuous development in pharmaceutical companies across the globe, in a never-ending arms race of human ingenuity against human disease. Methods for the testing of NCEs in the past have relied on the widespread use of basic cellular epithelial equivalents, generally made by culturing a single epithelial cell line on a 2D permeable plastic membrane, and animal models for the validation of NCEs. These techniques are utilised before progression onto animal and human trials and eventual commercial availability after thorough efficacy and safety testing.

The use of cell lines to create two-dimensional (2D) models of the intestinal epithelium have been the gold standard since the 1980's. These models benefit as both a cost saving exercise due to their simplicity and in reducing the need to use animals in research. which then, as today, is both ethically important and physiologically justified because animal models are often unreliable models of human anatomy, tissue and function. However, 2D models are unable to recreate complex structural variations present *in vivo*, usually incorporating a single cell phenotype in a non-physiologically based system. Whilst these simple models are cheap and mass producible, their use for NCEs analysis leads to progression of poor clinical candidates to later phases of development which fail due to *in vivo* functional irrelevance, toxicity or poor pharmacokinetics. Newer methods have been developed which improve the *in vivo* characteristics of 2D models, often through inclusion of additional cells lineages, such as goblet cells to make use of their distinct functions. Likewise, paracrine effects of fibroblasts or immune cells are increasingly shown to have critical functions in directing epithelial homeostasis and development. Three-dimensional (3D) tissue equivalents, are an emerging technology able to model a number of systems *in vitro*, bridging the gap between 2D models and human tissues. Ultimately however, conventional 2D monoculture models such as Caco-2 remain the gold standard for pharmacokinetic and toxicity analysis of NCE.

It was hypothesised that Caco-2 model phenotypes can be improved through the use of fibroblast conditioned medias and application of cell lines into a 3D model. The aim was to develop a more developed understanding of the effect of the paracrine microenvironment and 3D culture on epithelial, specifically Caco-2, phenotype.

Through utilisation of the Caco-2 cell line along with fibroblast cells of varying origin (Colon carcinoma, normal small intestine and skin) this study was able to create both 2D Transwell paracrine cultures and 3D models of both the intestinal epithelium and mucosae respectively. Colon derived fibroblast cells were shown to secrete significant concentrations of Keratinocyte Growth Factor (KGF) into media under normal 2D culture conditions. Moreover, the addition of paracrine factors released by fibroblast cells into culture and direct 3D co-culture allows for the creation of models with enhanced structural characteristics over Caco-2 monolayers with distinct epithelial and sub-epithelial compartmentalisation and similar structural morphologies as seen in *in vivo* tissues. Functionally, models were tested for their pharmacokinetic capability to a number of model compounds. Comparison of model functional between models and reported literature values for tissues and Caco-2 controls suggests that paracrine fibroblast secretome and 3D cells culture has a significant effect on Caco-2 function. Significant variation between models was observed in this study suggesting further research into the mechanistic actions behind the morphological changes seen is required.

## Acknowledgments

First of all I'd like to thank my supervisor Professor Stefan Przyborski and Dr Mathilde Roger for all the advice and guidance over the last four years that has helped me grow into the scientist I am today. It has been a real pleasure to have completed my doctoral research within your lab. I'd also like to thank Jim Cooper and the staff at ECACC for their generous provision of cells, and for the valuable industrial perspective and training given to me. Your positive comments after lunchtime seminars were great encouragement. Thanks also to my thesis committee, Prof. Jahoda, Dr Djoko and Dr Hole for your periodic contributions and care for the project. Additionally, I'd like to thank the staff of Reprocell, particularly Fred Tholozan for your contributions in my first year of study, getting me on the right path early on. Immense gratitude belongs to the staff of Durham Biosciences in general and to the imaging team of Joanne, Tim, Christine and Helen. With a special mention to the late Ian Cummings for his excellent work on the analysis of study samples. He will be missed by a great many.

As for the lab; Henry, your ideas make me realise I'm not the craziest person here. Ben, the morning crossword was possibly the most difficult part of this PhD. Lydia, housemate, friend and black-market peanut-puff supplier. Steve, for the trets (ughhh). Lucy and Nicole, the only people in lab 4 to have a reasonably sane conversation with. Claire, for funding the local taxi companies. Bek and Kirsty, for the laughs and guidance both in the lab and out. And to all others in the lab past and present, far too numerous to mention individually, mBiols, Masters and summer students who've made this experience amazing.

Caroline, thanks for putting up with me and guiding me through the years. Your steady presence helped more than you could know. Here's to future challenges faced together.

Finally, Mum and Dad, thank you for all the encouragement throughout all my education, from a tiny 4 year old at his first day at school to now, without your support this wouldn't have been possible. Love you both!

## Table of contents

<b>List of Tables .....</b>	<b>21</b>
<b>List of Figures.....</b>	<b>25</b>
<b>Abbreviations .....</b>	<b>40</b>
<b>1. General Introduction .....</b>	<b>43</b>
<b>1.1 Challenges of modern drug discovery .....</b>	<b>43</b>
<b>1.2 The general anatomy of the gastro-intestinal tract .....</b>	<b>48</b>
<b>1.3 Epithelial anatomy, the relation of structure and function. ....</b>	<b>54</b>
<b>1.4 Understanding the functional absorptive component of the intestine, the enterocyte. ....</b>	<b>57</b>
<b>1.5 Methods of epithelial permeability and epithelial junctional composition, development of a selective passive paracellular barrier. ....</b>	<b>60</b>
1.5.1 Methods of permeability through epithelial barriers .....	60
1.5.2 Occluding junctions .....	60
1.5.3 Anchoring junctions.....	62
1.5.4 Gap Junctions.....	64
<b>1.6 Quantitative techniques for monolayer integrity and tight junction formation measurement. ....</b>	<b>66</b>
<b>1.7 Paracellular permeability, measuring membrane integrity .....</b>	<b>67</b>
<b>1.8 Other cells of the intestinal epithelium and mucosa .....</b>	<b>68</b>
1.8.1 Goblet cells .....	68
1.8.2 Enteroendocrine cells.....	69

1.8.3 Paneth cells .....	69
1.8.4 Fibroblasts and myofibroblasts .....	70
<b>1.9 The Villus-crypt axis and the stem cell niche.....</b>	<b>71</b>
<b>1.10 <i>In Vitro</i> models of the intestinal epithelium .....</b>	<b>72</b>
1.10.1 Caco-2 Transwell models of the intestinal epithelium .....	72
1.10.2 Stem cells applied to the Transwell system .....	75
1.10.3 Utilising HT29-MTX as a goblet cell component of the epithelial layer .....	76
1.11 Understanding the growing use of CCD-18co cells in intestinal model cell culture. ....	78
<b>1.12 The growing use of advanced 2D and 3D models of the intestine over the current 2D standards. ....</b>	<b>79</b>
<b>1.13 Regulatory alignment and the challenges of applying new, more complex models to the drug development process.....</b>	<b>83</b>
<b>1.12 Project Hypothesis.....</b>	<b>85</b>
<b>1.13 Project Aims.....</b>	<b>85</b>
<b>1.14 Project Objectives.....</b>	<b>86</b>
<b>2. Materials and methods .....</b>	<b>87</b>
<b>2.1 Materials.....</b>	<b>87</b>
2.1.1 Chemicals and miscellaneous lab reagents .....	87
2.1.2 Cells and cell culture media components .....	87
2.1.3 Plastic ware .....	88
2.1.4 Antibodies.....	89
2.1.5 qPCR primers and PCR reagents .....	90
<b>2.2 General methods.....</b>	<b>91</b>

2.2.1 General cell culture .....	91
2.2.2 Passaging .....	92
2.2.3 Trypan Blue cell counting.....	92
2.2.4 Cryopreservation.....	93
2.2.5 Cell revival.....	93
<b>2.3 Embedding techniques for study samples .....</b>	<b>94</b>
2.3.1 Paraffin embedding.....	94
2.3.2 OCT embedding.....	95
<b>2.4 Immunocytochemistry .....</b>	<b>95</b>
2.4.1 Paraffin embedded samples .....	95
2.4.2 OCT embedded samples .....	96
2.4.3 Wholemount cell coverslips, wells and Transwell inserts. ....	96
<b>2.5 Histological staining techniques of paraffin embedded samples.....</b>	<b>97</b>
2.5.1 Haematoxylin and eosin.....	97
2.5.2 Periodic acid Schiff stain .....	97
2.5.3 Masson trichrome stain with methyl blue.....	98
<b>2.6 Scanning electron microscopy (SEM).....</b>	<b>98</b>
<b>2.7 Transmission electron microscope (TEM) .....</b>	<b>99</b>
<b>2.8 Drug permeability transport assays. ....</b>	<b>99</b>
<b>2.9 qPCR analysis of cell models and tissues .....</b>	<b>100</b>
2.9.1 mRNA purification and extraction from whole cell and tissue lysates. ....	100
2.9.2 mRNA quantification of purified cell model lysates. ....	101
2.9.3 mRNA reverse transcription into single strand complementary DNA .....	101
2.9.4 cDNA quantification and comparative analysis to controls. ....	102
<b>2.10 Bradford assay assessment of protein abundance.....</b>	<b>103</b>

2.11 Quantification of aminopeptidase activity .....	103
2.12 Standard Caco-2 Transwell experimental set up and conditioned media creation and application. ....	104
2.13 Human tissue processing and staining.....	105
2.14 Outgrowth of myofibroblast primary cell cultures from human tissue sections .....	106
2.15 Generation of a 3D intestinal model .....	107
2.16 Epithelial electrophysical resistance measurements of Transwell models of the intestine. ....	108
2.17 Statistical analysis of study data .....	108
<b>3. Development Transwell co-culture models.....</b>	<b>109</b>
<b>3.1 Introduction .....</b>	<b>109</b>
3.1.1 Caco-2 Transwell, the gold standard for intestinal pharmacokinetics.....	109
3.1.2 Understanding the role of sub-epithelial fibroblasts on the homeostasis of the intestinal epithelium.....	109
3.1.3 Methods for the advancement of model <i>in vivo</i> relevancy. ....	110
3.1.4 Understanding the importance of 3D architecture on model development. .	111
<b>3.2 Hypothesis, aims and objectives.....</b>	<b>113</b>
3.2.1 Hypothesis .....	113
3.2.2 Aims.....	113
3.2.3 Objectives .....	114
<b>3.3 Methods .....</b>	<b>115</b>
3.3.1 Immunohistochemical characterisation of intermediate filament expression in CCD-18co, HDFn and HIC cells. ....	115

3.3.2 Characterisation of Caco-2 and HT29-MTX in pre and post confluency states through immunohistochemistry. ....	115
3.3.3 Co-culture model formation.....	115
3.3.4 Trans-Epithelial Electrical Resistance (TEER) measurement of epithelial layers.....	116
3.3.5 MTT assay for the assessment of metabolic function.....	116
3.3.6 Assessment of conditioned media and KGF on the metabolic activity of Caco-2 epithelial cells. ....	117
3.3.7 Assessment of tight junction formation in conditioned media treated cellular layers through immunostaining of the tight junction protein Occludin.....	117
3.2.8 Immunostaining of wholemount Transwell models .....	118
3.3.9 qPCR analysis of Transwell model lysates.....	118
3.3.10 Aminopeptidase quantification of Transwell models compared to 3D cultures.....	118
3.3.11 Keratinocyte growth factor (KGF) conditioned media experiments in Snapwell format inserts. ....	119
3.3.12 MTT assessment of KGF treated Caco-2 layers.....	119
3.3.13 Assessment of tight junction formation in KGF treated cell layers through immunostaining of the tight junction protein Occludin.....	119
3.3.14 ELISA quantification of KGF abundance in conditioned media samples..	120
3.3.15 DNA concentration quantification for KGF ELISA normalisation.....	121
3.3.16 Transport assays utilising the Ussing chamber system for Transwell and Alvetex Lucifer Yellow permeability assays.....	121
3.3.17 qPCR analysis of conditioned media and KGF spiked Caco-2 2D layers..	123
<b>3.4 Results.....</b>	<b>125</b>
3.4.1 Morphological characterisation of stromal and epithelial cell lines. ....	125
3.4.2 Immunostaining characterisation of myofibroblasts for characteristic cytoskeletal markers. ....	125



3.4.3 Analysis of the changing characteristics of Caco-2 cells in pre and post confluency states.....	130
3.4.4 Understanding the effects of confluency on the differentiation of HT29-MTX cells in 2D culture. ....	133
3.4.5 Paracrine conditioned media has differential effects on epithelium development dependant on the origin of the fibroblasts.....	137
3.4.6 Trans-epithelial resistance is shown to decrease in the presence of conditioned media from all origins with a variable degree of response. ....	139
3.4.7 MTT metabolic measurements of Caco-2 2D paracrine co-culture models shows CCD-18co conditioned media increases the metabolic activity of Caco-2 cells at later timepoints by delaying lag phase onset. ....	140
3.4.8 Understanding the differential development of tight junction formation in Caco-2 cells treated with fibroblast conditioned media.....	143
3.4.9 Immunostaining of cells grown in Snapwell Transwell and CCD-18co effects on functional differentiation of Caco-2 cells with regards to P-gp expression and brush border formation. ....	145
3.4.10 qPCR analysis of the development of Caco-2 layers in relation to key targets of function and the effects of CCD-18co paracrine media on Caco-2 layer development.....	149
3.4.11 Co-culture of Caco-2 cells increases the aminopeptidase activity within intestinal models. ....	153
3.4.12 KGF changes the structural physiology of Caco-2 monolayers and decreases membrane TEER levels in a dose-dependent manner. ....	155
3.4.13 Immunostaining characterisation of KGF treated Caco-2 layers shows increased Villin expression with higher KGF concentrations. ....	159
3.4.14 KGF in Caco-2 culture media increases the metabolic activity of Caco-2 cells in a dose-dependent manner. ....	160
3.4.15 Understanding the development of tight junction expression in Caco-2 cells grown in control and KGF spiked media conditions. ....	164
3.4.16 Differential aminopeptidase activity of KGF conditioned layers.....	166

3.4.17 Quantification of the levels of KGF present in paracrine conditioned media samples.....	167
3.4.18 The effects of conditioned and KGF spiked media on the passive paracellular transport of Lucifer yellow. ....	173
3.4.19 qPCR analysis of conditioned and KGF spiked media samples for the relative abundance of mRNA for key tight junctional components. ....	174
3.5.20 qPCR analysis of conditioned and KGF spiked media samples for the relative abundance of mRNA for efflux transporter protein important in the function of Caco-2 cells.....	176
<b>3.5 Discussion .....</b>	<b>178</b>
3.5.1 Chapter overview .....	178
3.5.2 Fibroblast characterisation through phase contrast and immunohistological microscopy.....	179
3.5.3 Paracrine influences on structural morphology and Trans-Epithelial Electrical Resistance (TEER).....	181
3.5.4 Tight junctional formation in Caco-2 control and paracrine treated layers and its effect on epithelial layer TEER and permeability.....	184
3.5.5 Understanding the effects of conditioned media and KGF spiked media on the relative expression of key junctional and transporter proteins as assessed through qPCR analysis of 2D Caco-2 layers.....	190
<b>3.6 Conclusion.....</b>	<b>191</b>
<b>4. Epithelial - Goblet cell co-culture and its effect on model function. ....</b>	<b>193</b>
<b>4.1 Introduction .....</b>	<b>193</b>
4.1.1 Understanding the structure of the mucus layer and its importance on the functional aspects of the human intestine. ....	193
4.1.2 Limitations of the Caco-2 system to model the effects of mucus on the drug pharmacokinetics and methods to more accurately mimic the intestinal epithelium. ....	194

<b>4.2 Hypothesis, Aims and Objectives.....</b>	<b>197</b>
4.2.1 Hypothesis .....	197
4.2.2 Aims.....	197
4.2.3 Objectives .....	197
<b>4.3 Materials and Methods .....</b>	<b>198</b>
4.3.1 Generation of epithelial co-culture models consisting of Caco-2 and HT29-MTX cells. ....	198
4.3.2 H&E, PAS staining of sectioned and wholemount Caco-2/ HT29-MTX co-culture models.....	199
4.3.3 Toluidine blue staining of epithelial co-culture models. ....	199
4.3.4 TEM analysis of Caco-2/ HT29-MTX co-culture constructs. ....	200
4.3.5 qPCR analysis of Snapwell Transwell epithelial co-culture constructs. ....	200
4.3.6 Rhodamine 123 transport analysis of epithelial co-culture constructs. ....	200
<b>4.4 Results.....</b>	<b>202</b>
4.4.1 Trans-epithelial resistance measurements of Caco-2:HT29-MTX co-cultures and the effects of CCD-18co conditioned media on resultant co-culture layers. ..	202
4.4.2 Histological investigation of Caco-2:HT29-MTX 2D co-culture on Snapwell Transwell membranes. ....	207
4.4.3 Understanding the effects of CCD-18co paracrine culture on the development of Caco-2/HT29-MTX co-culture Snapwell® membranes. ....	211
4.4.4 Analysis of Co-culture model cellular phenotype under CCD-18co conditioned media by Toluidine blue staining of resin embedded sections. ....	215
4.4.5 Analysis of Caco-2:HT29-MTX co-cultures structural phenotype through high resolution transmission electron microscopy (TEM). ....	217
4.4.6 E-cadherin staining of Caco-2/ HT29-MTX layers highlights the changes in structural morphology when HT29-MTX cells are exposed to CCD-18co paracrine media.....	221

4.4.7 qPCR analysis of the development of Caco-2:HT29-MTX co-culture layers in relation to key targets of function. ....	223
4.4.8 Functional characterisation of Caco-2/ HT29-MTX co-culture Rhodamine 123 transport in Snapwell culture. ....	226
<b>4.5 Discussion .....</b>	<b>228</b>
4.5.1 Epithelial co-culture and the effects of differing seeding ratio on the Trans-Epithelial Electrical Resistance (TEER) of the tissue construct. ....	228
4.5.2 Functional transport characteristics of epithelial co-culture layers. ....	230
4.5.3 Understanding the effects of CCD-18co conditioned media on the development of the epithelial construct layers. ....	231
<b>4.6 Conclusion .....</b>	<b>233</b>
<b>5. Optimisation &amp; characterisation of an <i>in vitro</i> model of the intestinal mucosa and development of associated technology.....</b>	<b>235</b>
<b>5.1 Introduction .....</b>	<b>235</b>
5.1.1 The biological relevance of 3D culture.....	235
5.1.2 Different applications of the Caco-2 cell line to 3D systems of the intestinal epithelium. ....	236
<b>5.2 Hypothesis, Aims and Objectives.....</b>	<b>241</b>
5.2.1 Hypothesis .....	241
5.2.2 Aims.....	241
5.2.3 Objectives .....	242
<b>5.3 Materials and methods.....</b>	<b>243</b>
5.3.1 Seeding Caco-2 cells onto Alvetex® of varying format.....	243
5.3.2 Basement membrane addition to Alvetex Scaffold®. ....	243
5.3.3 Differential CCD-18co seeding density on model development. ....	243
5.3.4 The effect of culture time on model development. ....	244

5.3.5 MTT assay analysis of CCD-18co cells grown in Alvetex® Scaffold.....	245
5.3.6 SEM processing of differential seeded CCD-18co Alvetex® layers. ....	245
5.3.7 3D model processing for TEM analysis .....	246
5.3.8 Toluene Blue stained samples.....	246
5.3.9 Clearing of Alvetex Scaffold for high resolution lightsheet imaging of 3D intestinal models. ....	246
5.3.10 Immunostaining of 3D models and human intestinal tissue. ....	247
5.3.11 Developing a 24 and 96 well Ussing chamber design for the efficient functional analysis of Alvetex intestinal models. ....	247
<b>5.4 Results.....</b>	<b>248</b>
5.4.1 Caco-2 growth characteristics in different Alvetex® configurations. ....	248
5.4.2 Addition of a basement membrane protein to the surface of Alvetex Scaffold®.....	250
5.4.3 CCD-18co conditioned media effects on Caco-2 development on Collagen I Basement membranes in Alvetex Scaffold®.....	253
5.4.5 Optimisation of CCD-18co cells seeding density within Alvetex Scaffold® to create a surface layer to support the culture of Caco-2 epithelial cells. ....	255
5.4.6 Metabolic activity assessment of CCD-18co seeding optimisation experiments. ....	258
5.4.7 SEM analysis of the surface topography of CCD-18co seeding density layers. .....	261
5.4.8 The effects of extended culture time on the population of Alvetex Scaffold® with CCD-18co cells.....	261
5.4.9 SEM analysis of stromal fibroblast cell layers. ....	263
5.4.10 Structural analysis of optimised multiphasic seeded Caco-2/ CCD-18co Alvetex Scaffold® intestinal models. ....	264
5.4.11 Optimisation and structural analysis of Caco-2/ HDFn Alvetex Scaffold® intestinal models. ....	271

5.4.12 Histological analysis of the structure of Caco-2/ HIC Alvetex Scaffold® intestinal models. ....	277
5.4.13 Human colonic and small intestinal characterisation for comparison to 3D co-culture models.....	277
5.4.14 Human small intestine characterisation for comparison to 3D co-culture intestinal models. ....	282
5.4.15 3D CCD-18co intestinal model immunostaining characterisation. ....	286
5.4.16 3D HDFn intestinal model immunostaining characterisation.....	288
5.4.17 3D HIC intestinal model immunostaining characterisation.....	290
5.4.18 Lightsheet analysis of 3D model immunostaining morphology. ....	292
.....	294
5.4.19 Development of an Ussing chamber for the incorporation of the 24-well format Alvetex Scaffold®. ....	295
5.4.20 Creating a high throughput solution for the culture of 96-well format 3D Alvetex ®models. ....	298
5.4.17 Development of an Ussing chamber suitable for the analysis of 3D cultured 96 well format models. ....	301
<b>5.5 Discussion .....</b>	<b>305</b>
5.5.1 The properties of Alvetex® and its potential uses as a substrate for 3D culture systems.....	305
5.5.2 Optimisation of a 3D model of the intestinal epithelia utilising Alvetex Scaffold®.....	308
5.5.3 What does 3D tissue engineering tell us about the biology of tissues, understanding the limitation of 3D models.....	310
5.5.3 Overcoming the technical limitation of 3D models by designing a method of high throughput culture and analysis.....	311
<b>5.6 Conclusions .....</b>	<b>313</b>

<b>6. 3D Alvetex® and paracrine Transwell model transport dynamics of CCD-18co, HDFn and HIC/ Caco-2 co-culture models.....</b>	<b>315</b>
<b>6.1 Introduction .....</b>	<b>315</b>
6.1.1 Chapter goals .....	315
6.1.2 Understanding the disadvantages of 2D culture and methods for improved model in vivo physiology. ....	315
6.1.3 Model drugs, their mechanisms of action and relevance to this study. ....	319
6.1.3.1 Rhodamine 123 .....	319
6.1.3.2 Atenolol.....	322
6.1.3.3 Propranolol.....	324
6.1.3.4 Etoposide.....	326
6.1.3.5 Methotrexate .....	328
6.1.3.6 Lucifer Yellow .....	330
<b>6.2 Hypothesis, Aims and Objectives.....</b>	<b>332</b>
6.2.1 Hypothesis .....	332
6.2.2 Aims.....	332
6.2.3 Objectives .....	332
<b>6.3 Materials and methods.....</b>	<b>334</b>
6.3.1 Ussing chamber permeability assessment of Transwell and 3D intestinal tissue models.....	334
6.3.2 Efflux Co-efficient calculation from Papp permeability values .....	334
6.3.3 Electrophysiological measurements of Transwell Snapwell and 96 well Alvetex models. ....	335
<b>6.4 Results.....</b>	<b>340</b>
6.4.1 Transepithelial resistance measurements of 3D models compared to conventional Caco-2 standards and Human small intestinal sections. ....	340
6.4.2 Rhodamine 123 transport and Verapamil Hydrochloride MDR1/P-gp inhibition in Caco-2 Snapwell conditioned media models. ....	343

6.4.3 Rhodamine 123 transport and Verapamil Hydrochloride MDR1/ P-gp inhibition in 3D Caco-2/ Fibroblast bioengineered intestinal equivalents. ....	348
6.4.4 Timecourse analysis of Rhodamine permeability across conventionally and conditioned cultured Transwell models and 3D bioengineered co-culture systems. ....	354
6.4.5 Efflux co-efficient value calculation and analysis to show directional bias in Rhodamine 123 transport within 2D Transwell and 3D Alvetex ® intestinal models. ....	357
6.4.6 KGF treatment of Caco-2 Transwell models reduces its models capability to actively transport Rhodamine 123. ....	362
6.4.7 Atenolol Transport in Co-culture Transwell model layers. ....	365
6.4.8 Atenolol Transport in 3D bioengineered Alvetex models. ....	369
6.4.9 Efflux co-efficient of Caco-2 Transwell and 3D bio-engineered Caco-2 Alvetex models for Atenolol.....	373
6.4.10 Propranolol Transport of 2D Transwell co-cultures and 3D Alvetex based intestinal models. ....	376
6.4.11 Efflux co-efficient analysis of Propranolol permeability in 2D Transwell Snapwell and 3D Alvetex models.....	381
6.4.12 Etoposide transport of 2D Transwell co-cultures and 3D Alvetex based intestinal models. ....	382
6.4.13 Efflux co-efficient analysis of Etoposide permeability in 2D Transwell Snapwell and 3D Alvetex models demonstrate the differential effects of 3D culture on the permeability of tissue constructs.....	387
6.4.14 Methotrexate Transport for 2D Transwell paracrine co-cultures. ....	389
6.4.15 Methotrexate Transport for 3D Alvetex based intestinal models. ....	390
6.4.16 Efflux co-efficient values for 2D paracrine Transwell and 3D Alvetex methotrexate model transport. ....	395
6.4.17 Lucifer yellow transport of 2D Transwell co-cultures and 3D Alvetex based intestinal models. ....	396



6.4.18 Efflux co-efficient of lucifer yellow in 2D and 3D models .....	401
<b>6.5 Discussion .....</b>	<b>403</b>
6.5.1 Transport dynamics of model systems and the context for this chapter .....	403
6.5.2 2D paracrine Transwell and 3D intestinal equivalents both show significantly decreased membrane resistance compared to conventionally cultured Caco-2 models.....	403
6.5.3 Analysis of the functional capabilities of epithelial intestinal equivalents through the passive paracellular transport assessment of model drug compounds. ....	407
6.5.4 Actively transported compound analysis .....	410
<b>6.6 Conclusion .....</b>	<b>414</b>
<b>7. General discussion, project conclusions and future directions.....</b>	<b>416</b>
7.1 Introduction .....	416
7.2 Understanding the needs for an improved <i>in vitro</i> model of the intestinal epithelium.....	417
7.3 Understanding the paracrine microenvironment is key to developing systems with improved <i>in vivo</i> mimicry. ....	417
7.4 Stromal epithelial interactions result in loss of function of HT29-MTX cells when co-cultured <i>in vitro</i> . ....	422
7.5 3D fibroblast culture allows for the development of a complex ECM microenvironment within cell substrates. ....	424
7.6 Functional analysis of paracrine and 3D models shows significant changes in the function of Caco-2 epithelial layers. ....	425
7.7 Future work.....	433
7.8 Final remarks.....	434

<b>8. References .....</b>	<b>435</b>
<b>9. Appendix and supplementary information.....</b>	<b>464</b>
9.1 Negative control images .....	464
9.1.1 Fibroblast negative controls for 2D immunostained samples.....	464
9.1.2 Epithelial lineage negative controls for 2D immunostained samples.....	465
9.1.3 Caco-2 Transwell negative controls .....	466
9.1.4 Caco-2 and HT29-MTX Transwell controls.....	467
9.1.5 3D model negative controls .....	468
9.1.6 Human tissue negative controls .....	469
9.2 Intrinsic permeability of different Alvetex formats.....	470
9.3 PCR Primer optimisation .....	470
9.4 Project poster presentations .....	478
9.5 Project poster presentations .....	488

## List of Tables

<b>Table 2.1: Summary of plastic materials consumed during the course of this project including cell culture grade and general lab reagents. ....</b>	<b>89</b>
<b>Table 2.2: List of antibodies used in this project including secondary Alexa Fluor conjugated secondaries. ....</b>	<b>90</b>
<b>Table 2.3: qPCR primers including reference of origin. ....</b>	<b>91</b>
<b>Table 2.4: qPCR reagents for the isolation of RNA, reverse transcription into cDNA and expansion SYBR based detection methods.....</b>	<b>91</b>
<b>Table 3.1 Statistical analysis of Transwell model TEER measurements .....</b>	<b>138</b>
<b>Table 3.2: Significances of conditioned media MTT data .....</b>	<b>142</b>
<b>Table 3.3: Significances for comparative Villin expression in time course samples .....</b>	<b>151</b>
<b>Table 3.4: Significances for comparative Occludin expression in time course samples .....</b>	<b>151</b>
<b>Table 3.5: Significances for comparative OATP-B expression in time course samples .....</b>	<b>151</b>
<b>Table 3.6: Significances for comparative MRP2 expression in time course samples .....</b>	<b>152</b>
<b>Table 3.7: Significances for comparative BCRP expression in time course samples .....</b>	<b>152</b>

<b>Table 3.8: Significances for comparative MDR1 expression in time course samples</b>	<b>152</b>
<b>Table 3.9 Statistical analysis of Transwell model TEER measurements</b>	<b>154</b>
<b>Table 3.10: Time-point comparison of Conditioned media and KGF spiked conditions</b>	<b>163</b>
<b>Table 3.11: KGF levels in conditioned media normalised to DNA concentration of 2D cellular layers</b>	<b>170</b>
<b>Table 3.12: Absolute KGF levels in conditioned media statistical analysis</b>	<b>171</b>
<b>Table 3.13: DNA concentration of 2D fibroblast cellular layers statistical analysis</b>	<b>172</b>
<b>Table 4.1: Significance calculation between TEER values measured in epithelial co-culture Transwell models of the intestinal epithelium</b>	<b>206</b>
<b>Table 6.1: TEER expression comparison between Transwell and 3D intestinal models</b>	<b>342</b>
<b>Table 6.2: Significance values from Rhodamine 123 <math>\pm</math> Verapamil Hydrochloride permeability studies of Transwell conditioned media models – B-A and A-B data sets were analysed for significance separately</b>	<b>347</b>
<b>Table 6.3: Significance values from Rhodamine 123 <math>\pm</math> Verapamil Hydrochloride permeability studies of Transwell control compared with Alvetex<sup>®</sup> based intestinal models – B-A and A-B data sets were analysed for significance separately</b>	<b>353</b>
<b>Table 6.4: Efflux co-efficient analysis of Rhodamine 123 in 2D and 3D intestinal models both with and without Verapamil Hydrochloride and at both 60 and 120 minutes assay lengths</b>	<b>361</b>

<b>Table 6.5: Significancy values for Rhodamine 123 permeability between models of differing KGF concentration both with and without the addition of Verapamil Hydrochloride.....</b>	<b>364</b>
<b>Table 6.6: Significancy values for Atenolol permeability experiments.....</b>	<b>369</b>
<b>Table 6.7: Significancy values for Atenolol permeability in 3D intestinal models</b>	<b>373</b>
<b>Table 6.8: Significancy values for Atenolol Efflux Co-efficient for both 2D and 3D intestinal models.....</b>	<b>375</b>
<b>Table 6.9: Significancy values for Propranolol in 2D conditioned media Transwell models.....</b>	<b>380</b>
<b>Table 6.10: Significancy values for Propranolol in 3D Alvetex® models .....</b>	<b>380</b>
<b>Table 6.11: Significancy values for Etoposide in 2D conditioned media Transwell models.....</b>	<b>386</b>
<b>Table 6.12: Significancy values for Etoposide in 3D Alvetex® models.....</b>	<b>386</b>
<b>Table 6.13: Significancy values for Etoposide efflux co-efficient for both 2D and 3D intestinal models.....</b>	<b>388</b>
<b>Table 6.15: Significancy values for Methotrexate permeability in 3D Alvetex® based intestinal models.....</b>	<b>394</b>
<b>Table 6.14: Significancy values for Methotrexate permeability in 2D Transwell based intestinal models .....</b>	<b>394</b>
<b>Table 6.17: Significancy values for Lucifer yellow permeability in 3D intestinal models.....</b>	<b>400</b>
<b>Table 6.16: Significancy values for Lucifer yellow permeability in 2D intestinal models.....</b>	<b>400</b>

<b>Table 6.18: Comparative Papp values of models created in this study compared to values gained from the literature for both Caco-2 standards and intestinal tissues (Human and animal) .....</b>	<b>402</b>
--	------------

## List of Figures

<b>Figure 1.1: Understanding the costs for the development and testing of novel drug compounds .....</b>	<b>47</b>
<b>Figure 1.2: The gross anatomy of the digestive system with specific focus on the structure of the intestine – .....</b>	<b>50</b>
<b>Figure 1.3: The structural layers of the intestine .....</b>	<b>52</b>
<b>Figure 1.4: Structural characteristics of simple epithelial layers in the human body .....</b>	<b>55</b>
<b>Figure 1.5: Complex squamous epithelial show gradients of differentiation across the thickness of the epithelial layer .....</b>	<b>56</b>
<b>Figure 1.6: General methods of permeability through epithelial barriers .....</b>	<b>59</b>
<b>Figure 1.7: General organisation of a tight junction complex .....</b>	<b>62</b>
<b>Figure 1.8: Basic structural anatomy of the adherens junction complex .....</b>	<b>63</b>
<b>Figure 1.9: Basic anatomy of gap junction physiology .....</b>	<b>64</b>
<b>Figure 1.10: Basic anatomy of human small and large intestine - .....</b>	<b>65</b>
<b>Figure 1.11: Transepithelial resistance chopstick equipment and calculations .....</b>	<b>66</b>
<b>Figure 1.12: Expression of key proteins by Caco-2 cells in Transwell .....</b>	<b>73</b>
<b>Figure 2.1: Schematic representation of the embedding and sectioning process for both Transwell and Alvetex® based intestinal models – .....</b>	<b>94</b>
<b>Figure 2.2: Schematic representation of the process for setting up and culturing Transwell based intestinal models in control and conditioned media systems .....</b>	<b>105</b>

<b>Figure 2.3: Schematic representation of the process for setting up and culturing Alvetex® based intestinal models. ....</b>	<b>107</b>
<b>Figure 3.1: Fibroblasts from differing origins are indistinguishable morphologically by phase contrast microscopy – ....</b>	<b>127</b>
<b>Figure 3.2: Epithelial cells grow in densely packed “cobble stone” colony formations .....</b>	<b>128</b>
<b>Figure 3.3: Lineage specific intermediate filament expression analysis in 2D shows similar expression patterns between the three cell lineages. ....</b>	<b>129</b>
<b>Figure 3.4: Post-confluent Caco-2 cells express heightened levels of junctional marker, Occludin and surface efflux protein, MDR1.....</b>	<b>131</b>
<b>Figure 3.5: Caco-2 cells are negative for Vimentin and E-cadherin staining remains proportional in pre and post-confluency states .....</b>	<b>132</b>
<b>Figure 3.6: Immunofluorescent characterisation of 2D epithelial cells Pre and Post-confluency shows increasing differentiation expression with time in culture .....</b>	<b>134</b>
<b>Figure 3.7: Immunofluorescent characterisation of 2D epithelial cells Pre and Post-confluency .....</b>	<b>135</b>
<b>Figure 3.8: H&amp;E stained comparison of Caco-2 conditioned media co-culture models shows consistent monolayer formation in each of the model conditions. Cells are clearly able to differentiate and polarise in conditioned media at differential rates than in Control conditions.....</b>	<b>136</b>
<b>Figure 3.9: 7, 14 &amp; 21 day TEER measurements of Caco-2 cells on Transwell Snapwell in control and conditioned media experiments shows that addition of</b>	



conditioned media to the Caco-2 cellular layers results in a variable decrease in TEER values compared to control layers .....	138
Figure 3.10: The effects of fibroblast conditioned media on the MTT values of 2D cultured Caco-2 cells shows that CCD-18co paracrine influences have the most effect on Caco-2 cells with a continuation of growth up to 10 days in culture .....	141
Figure 3.11: Time-point comparison of all conditioned media conditions .....	142
Figure 3.12: Tight junction expression between conditioned media conditions shows increased cellular packing in conditioned media samples.....	144
Figure 3.13: Caco-2 control models appear to be well differentiated through expression of key proteins for model differentiation and function .....	147
Figure 3.14: Caco-2 cells grown in CCD-18co conditioned paracrine media shows differences in the cellular organisation as analysed through expression of key proteins for model function .....	148
Figure 3.15: Transwell time course models PCR for Villin, Occludin and OATP-B .....	151
Figure 3.16: Transwell time course models qPCR of MRP2, BCRP and MDR1..	152
Figure 3.17: Aminopeptidase activity levels increase in both paracrine and 3D CCD-18co cultures .....	153
Figure 3.18: 7, 14 & 21 day TEER measurements of Caco-2 cells on Transwell Snapwell in control and KGF spiked media conditions shows that addition of KGF to the Caco-2 models results in highly significant decreases in epithelial construct TEER values .....	154

<b>Figure 3.19: H+E of KGF spiked media Caco-2 Transwell models shows similar histology to the addition of paracrine media with increased cellular height and cytoplasmic staining .....</b>	<b>156</b>
<b>Figure 3.20: Immunofluorescence staining of Control Caco-2 Snapwell models .</b>	<b>157</b>
<b>Figure 3.21: Immunofluorescence staining of 0.5ng/ml KGF spikes Caco-2 Snapwell models.....</b>	<b>157</b>
<b>Figure 3.22: Immunofluorescence staining of 5ng/ml KGF spikes Caco-2 Snapwell models.....</b>	<b>158</b>
<b>Figure 3.23: Immunofluorescence staining of 25ng/ml KGF spikes Caco-2 Snapwell models.....</b>	<b>158</b>
<b>Figure 3.24: MTT assessment of cellular viability over 10 days culture period (2D) with and without KGF spiked media. ....</b>	<b>161</b>
<b>Figure 3.25: Time-point comparison of all conditions.....</b>	<b>162</b>
<b>Figure 3.26: Tight junction expression of Caco-2 cells treated with different KGF concentrations over 10 days .....</b>	<b>165</b>
<b>Figure 3.27: Aminopeptidase activity of KGF treated Caco-2 layers .....</b>	<b>166</b>
<b>Figure 3.28: DNA normalised KGF ELISA.....</b>	<b>169</b>
<b>Figure 3.29: Total KGF concentration of conditioned media .....</b>	<b>171</b>
<b>Figure 3.30: Total DNA abundance of fibroblasts utilised for the generation of conditioned media shows no significant differences between like-samples .....</b>	<b>172</b>
<b>Figure 3.31: Lucifer yellow paracrine transport across treated epithelial layers.</b>	<b>173</b>
<b>Figure 3.32: qPCR analysis of relative tight junctional component expression in 2D conditioned media studies.....</b>	<b>175</b>

<b>Figure 3.33: qPCR analysis of relative functional efflux protein component and Villin expression in 2D conditioned media studies.....</b>	<b>177</b>
<b>Figure 4.1: Schematic diagram of the process for the set up and culture of Caco-2/ HT29-MTX co-culture mucus models of the intestinal epithelium .....</b>	<b>198</b>
<b>Figure 4.2: Schematic diagram of the process for the set-up of Caco-2 co-culture models within an Ussing chamber system.....</b>	<b>201</b>
<b>Figure 4.3: Caco-2/ HT29-MTX co-culture decreases the TEER values of resultant epithelial constructs .....</b>	<b>204</b>
<b>Figure 4.4: CCD-18co paracrine co-culture with Caco-2/ HT29-MTX epithelial constructs increases TEER values compared to non-treated controls.....</b>	<b>205</b>
<b>Figure 4.5: Caco-2:HT29-MTX epithelial co-cultures shows significant differences in cellular morphology between models .....</b>	<b>209</b>
<b>Figure 4.6: Mucous staining in Caco-2:HT29-MTX epithelial co-cultures .....</b>	<b>210</b>
<b>Figure 4.7: CCD-18co effects on Caco-2:HT29-MTX epithelial co-cultures.....</b>	<b>213</b>
<b>Figure 4.8: Caco-2:HT29-MTX epithelial co-cultures with CCD-18co paracrine media .....</b>	<b>214</b>
<b>Figure 4.9: Toluidine blue stained sections of Caco-2/ HT29-MTX co-cultures with and without CCD-18co conditioned media on Transwell membranes.....</b>	<b>216</b>
<b>Figure 4.10: TEM images of Caco-2/ HT29-MTX co-cultures .....</b>	<b>219</b>
<b>Figure 4.11: TEM images of Caco-2 and HT29-MTX cultures in the presence of CCD-18co conditioned media .....</b>	<b>220</b>
<b>Figure 4.12: E-cadherin stained Caco-2/ HT29-MTX co-cultures in the presence and absence of CCD-18co conditioned media.....</b>	<b>222</b>

<b>Figure 4.13: qPCR analysis of Caco-2/ HT29-MTX co-culture Transwell models shows differential expression between Caco-2 and HT29-MTX cells lines .....</b>	<b>225</b>
<b>Figure 4.14: B-A Rhodamine 123 transport dynamics of Caco-2/ HT29-MTX co-cultures in control and CCD-18co paracrine treated Snapwell layers .....</b>	<b>227</b>
<b>Figure 5.1: Understanding the growth characteristics of Caco-2 cells in different formats of Alvetex® polystyrene supports.....</b>	<b>249</b>
<b>Figure 5.2: Application of basement membrane proteins to Alvetex Scaffold .....</b>	<b>252</b>
<b>Figure 5.3: Optimising the volume and concentration of Collagen I gels to add to the surface of the Scaffold to limit cellular invasion. ....</b>	<b>253</b>
<b>Figure 5.4: CCD-18co paracrine treatment of Caco-2 cells cultured on 2mg/ml Collagen I gel layers shows an enhanced Caco-2 phenotype over control layers..</b>	<b>254</b>
<b>Figure 5.5: Optimisation of fibroblast seeding density to limit the invasive characteristics of Caco-2 cells .....</b>	<b>256</b>
<b>Figure 5.6: Creating a quantifiable technique for the analysis of model sections for the percentage invasion of Caco-2 cells within the Alvetex scaffold .....</b>	<b>257</b>
<b>Figure 5.7: Metabolic activity of the models shows that seeding higher densities of CCD-18co cells at the beginning of model culture has little effect on the number of surviving fibroblasts at the time of analysis .....</b>	<b>259</b>
<b>Figure 5.8: SEM topographical analysis of optimisation CCD-18co layers shows significant gaps in the surface support for the culture of Caco-2 cells .....</b>	<b>260</b>
<b>Figure 5.10: Understanding the effects of time on the growth of CCD-18co population in 3D Alvetex models .....</b>	<b>262</b>

<b>Figure 5.9: The effects of time on the growth of CCD-18co population in 3D Alvetex models shows little active proliferation when cultured in 3D .....</b>	<b>262</b>
<b>Figure 5.11: Caco-2 invasion characteristics show that CCD-18co culture time has no significant effects on reducing the levels of Caco-2 invasion in Alvetex models .....</b>	<b>263</b>
<b>Figure 5.12: SEM Images of CCD-18co cells cultured in Alvetex Scaffold for a period of 21 days.....</b>	<b>264</b>
<b>Figure 5.13: 14 day multi-phasic culture design using young intestinal CCD-18co fibroblasts results in the formation of an intestinal model with little observable Caco-2 infiltration .....</b>	<b>267</b>
<b>Figure 5.14: Toluidine blue stained samples provides enhanced resolution over H&amp;E stained images allowing for closer analysis of the structural morphology of Caco-2 layers on the surface of CCD-18co models .....</b>	<b>268</b>
<b>Figure 5.15: High magnification analysis of Caco-2/ CCD-18co 3D models reveals differentiated enterocytes with clear microvilli formation and associated glycocalyx .....</b>	<b>269</b>
<b>Figure 5.16: TEM ultra-thin cross sections of CCD-18co 3D co-culture model showing microvilli, intercellular junctions and basement membrane formation .</b>	<b>270</b>
<b>Figure 5.17: H+E staining of 7, 14 and 21 day cultures of Caco-2 on 28 day matured dermal equivalents show a changing fibroblast morphology over time.....</b>	<b>273</b>
<b>Figure 5.18: Methyl Blue stained Collagen staining of the 7, 14 and 21 day cultured Caco-2 models shows how Collagen deposition decreases after 21 days in culture .....</b>	<b>274</b>

<b>Figure 5.19: 14 day multi-phasic culture design using low passage HDFn fibroblasts results in the formation of an intestinal model with little observable Caco-2 infiltration .....</b>	<b>275</b>
<b>Figure 5.20: 14-day multi-phasic culture design using low passage HIC fibroblasts results in the formation of an intestinal model with poor Caco-2 structure when compared to CCD-18co and HDFn optimised models.....</b>	<b>276</b>
<b>Figure 5.21: Histological analysis of normal human colonic tissue sections.....</b>	<b>279</b>
<b>Figure 5.22: Immunofluorescence analysis of normal Human Colonic tissue sections shows significant Collagen I, III and IV staining located at the sub-epithelial compartment of the tissues .....</b>	<b>280</b>
<b>Figure 5.23: Immunofluorescence analysis of normal human colonic tissue sections highlights the two distinct cellular populations between epithelial and stromal lineages .....</b>	<b>281</b>
<b>Figure 5.24: Histological analysis of normal Human Small intestinal tissue sections .....</b>	<b>283</b>
<b>Figure 5.25: Immunofluorescence study of normal Human Small intestinal tissue sections for the analysis of ECM deposition in the stromal intestinal tissues.....</b>	<b>284</b>
<b>Figure 5.26: immunofluorescence analysis of normal Human Small intestinal tissue sections shows distinct population of cells within the epithelial and stromal compartments .....</b>	<b>285</b>
<b>Figure 5.27: Immunofluorescence analysis of normal Human Small intestinal tissue sections .....</b>	<b>285</b>

<b>Figure 5.28: Immunofluorescence analysis of CCD-18co/ Caco-2 Alvetex 3D models shows significant ECM deposition within the substrate in addition to well defined epithelial layers.....</b>	<b>287</b>
<b>Figure 5.29: HDFn/ Caco-2 Alvetex models show well defined epithelial layers without the significant Collagen deposition within the substrate as seen in CCD-18co models.....</b>	<b>289</b>
<b>Figure 5.30: HIC/ Caco-2 3D models are shown to secrete significant levels of Collagen IV with only minor amounts of other ECM components, epithelial layering is significantly diminished compared to other model systems .....</b>	<b>291</b>
<b>Figure 5.31: 3D cellular organization of CCD-18co fibroblasts and Caco-2 cells.</b>	<b>293</b>
<b>Figure 5.32: 3D cellular organization of CCD-18co fibroblasts and Caco-2 cells.</b>	<b>294</b>
<b>Figure 5.33: Wireframe schematic diagram of the 24-well Alvetex Scaffold Ussing chamber design.....</b>	<b>296</b>
<b>Figure 5.34: Photographic images of the 24-Well format manufactured Ussing chamber.....</b>	<b>297</b>
<b>Figure 5.35: Creating a Deep well culture dish for the maintenance of the ideal conditions to allow for 3D intestinal model growth in 96 well formats.....</b>	<b>299</b>
<b>Figure 5.36: Photographic analysis of 96 well deep well format .....</b>	<b>300</b>
<b>Figure 5.37: Wireframe schematic of the 96 well Ussing chamber system, designed for the incorporation and functional testing of 96 well format Alvetex intestinal models.....</b>	<b>302</b>
<b>Figure 5.38: Photographic images of the 96 well format Ussing chamber with added 96 well Alvetex insert .....</b>	<b>303</b>

<b>Figure 5.39: Schematic diagram of the process require for addition of 96 well format inserts into the custom designed 96 well Ussing chamber .....</b>	<b>304</b>
<b>Figure 6.1: Theoretical Rhodamine 123 permeability routes – .....</b>	<b>321</b>
<b>Figure 6.2: Theoretical Atenolol permeability routes.....</b>	<b>323</b>
<b>Figure 6.3: Theoretical Propranolol permeability routes .....</b>	<b>325</b>
<b>Figure 6.4: Theoretical Etoposide permeability routes .....</b>	<b>327</b>
<b>Figure 6.5: Theoretical Methotrexate permeability routes .....</b>	<b>329</b>
<b>Figure 6.6: Theoretical Lucifer yellow permeability routes.....</b>	<b>331</b>
<b>Figure 6.7: Schematic representation of directional transport within the cells ....</b>	<b>334</b>
<b>Figure 6.8: Representative images of Ag/Cl electrodes used in electrophysiological studies .....</b>	<b>336</b>
<b>Figure 6.9: Representative images of Ussing equipment utilised in this study.....</b>	<b>339</b>
<b>Figure 6.10: TEER Values of 3D intestinal models shows a significant physiological decrease in TEER compared to conventional 2D Caco-2 Transwell models.....</b>	<b>341</b>
<b>Figure 6.11: Schematic representation of the transport processes being studied in this experiment .....</b>	<b>343</b>
<b>Figure 6.12: Comparative analysis of Rhodamine 123 transport across Control and paracrine media treated Caco-2 membranes shows a significant increase in Rhodamine 123 transport in HDFn treated Caco-2 layers .....</b>	<b>346</b>
<b>Figure 6.13: Schematic representation of the transport processes of 3D Alvetex systems being studied in this experiment .....</b>	<b>350</b>



<b>Figure 6.14: Comparative analysis of Rhodamine 123 transport across Control and 3D Alvetex Caco-2/ Fibroblast intestinal tissue equivalents shows a large increase in Rhodamine 123 membrane permeability in CCD-18co and HIC 3D models.....</b>	<b>352</b>
<b>Figure 6.15: Time course analysis of Rhodamine 123 permeability in paracrine Transwell models throughout the assay period shows a general rapid increase in permeability followed by a plateau phase whereby permeability values stop increasing .....</b>	<b>355</b>
<b>Figure 6.16: Time course analysis of Rhodamine 123 permeability in 3D Alvetex tissue equivalent models throughout the assay period shows a general rapid increase in permeability followed by a plateau phase whereby permeability values stop increasing .....</b>	<b>356</b>
<b>Figure 6.17: Efflux ratio permeability calculation of 2D Transwell paracrine models for Rhodamine 123 - .....</b>	<b>359</b>
<b>Figure 6.18: Efflux ratio permeability calculation of 3D Alvetex Caco-2/ Fibroblast models for Rhodamine 123 .....</b>	<b>360</b>
<b>Figure 6.19: B-A transport of Rhodamine 123 in KGF treated Caco-2 layers shows decreased transport in treated layers versus controls with addition of Verapamil Hydrochloride having a dose dependant increasing effect on membrane permeability .....</b>	<b>363</b>
<b>Figure 6.20: Schematic representation of the expected directional travel mechanisms for Atenolol in Transwell and 3D Alvetex® models.....</b>	<b>365</b>
<b>Figure 6.21: Apparent Caco-2 permeability of Atenolol in Transwell Snapwell model systems.....</b>	<b>367</b>

<b>Figure 6.22: Apparent Caco-2 Transwell permeability of Atenolol in Transwell Co-culture systems .....</b>	<b>368</b>
<b>Figure 6.23: Apparent Caco-2 Transwell permeability of Atenolol in 3D Alvetex Scaffold models systems.....</b>	<b>371</b>
<b>Figure 6.24: Apparent Caco-2 Transwell permeability of Atenolol in Alvetex Scaffold co-culture systems .....</b>	<b>372</b>
<b>Figure 6.25: Efflux co-efficient calculations shows no significant directional bias in 2D model atenolol transport.....</b>	<b>374</b>
<b>Figure 6.26: Efflux co-efficient calculations shows significant differences in the transport bias of HDFn models to other 3D systems and Transwell co-cultures..</b>	<b>374</b>
<b>Figure 6.27: Schematic representation of the expected permeability routes of Propranolol across Transwell and Alvetex models .....</b>	<b>376</b>
<b>Figure 6.28: 2D comparison of Propranolol transport across Control and treated Transwell models shows HDFn and HIC treatments increase propranolol permeability.....</b>	<b>378</b>
<b>Figure 6.29: 3D comparison of Propranolol transport across Control and 3D Alvetex models with both CCD-18co and HIC models displaying attenuated propranolol permeability compared to controls.....</b>	<b>379</b>
<b>Figure 6.30: Efflux co-efficient of Propranolol across 2D and 3D intestinal constructs suggests no bias in directional drug transport .....</b>	<b>381</b>
<b>Figure 6.31: Schematic overview of the expected permeability routes of Etoposide through Caco-2 Transwell and 3D Alvetex intestinal models.....</b>	<b>382</b>

<b>Figure 6.32: Etoposide 2D paracrine media Transwell comparison shown large significant increases compared to control values in all culture conditions.....</b>	<b>384</b>
<b>Figure 6.33: 3D HIC and HDFn Alvetex models show significant Etoposide permeability increases over their 2D paracrine counterparts and 2D Caco-2 Control layers. 3D CCD-18co models similar to CCD-18co conditioned media models ....</b>	<b>385</b>
<b>Figure 6.34: Efflux co-efficient values show significant bias toward B-A transport in all conditions, both 2D and 3D .....</b>	<b>388</b>
<b>Figure 6.35: Schematic diagram of the expected permeability routes of Methotrexate in both Transwell and 3D Alvetex intestinal models .....</b>	<b>389</b>
<b>Figure 6.36: Methotrexate membrane permeability analysis of 2D paracrine Caco-2 co-cultures shows a trending increase in membrane permeability in CCD-18co, HIC and HDFn co-cultures .....</b>	<b>392</b>
<b>Figure 6.37: Methotrexate membrane integrity analysis of 3D Alvetex/ Caco-2 co-cultures shows significant increases in membrane permeability in HIC cultures</b>	<b>393</b>
<b>Figure 6.38: Efflux co-efficient values of Methotrexate comparing controls with paracrine media and 3D Alvetex models .....</b>	<b>395</b>
<b>Figure 6.39: Schematic diagram of expected lucifer yellow transportation routes through both Transwell and Alvetex scaffold intestinal models.....</b>	<b>396</b>
<b>Figure 6.40: Lucifer yellow membrane integrity analysis of 2D paracrine Caco-2 co-cultures .....</b>	<b>398</b>
<b>Figure 6.41: Bi-directional transport of Lucifer Yellow shows significant increase in membrane permeability in 3D Alvetex based intestinal models compared to 2D Transwell alternatives.....</b>	<b>399</b>

<b>Figure 6.42: Efflux co-efficient of lucifer yellow analysis suggests Control and 2D CCD-18co layers have a B-A directional bias .....</b>	<b>401</b>
<b>Figure 6.43: Summary of the complete analysis of 2D Caco-2 Transwell models with the model compounds tested in this study .....</b>	<b>412</b>
<b>Figure 6.44: Summary of the complete analysis of 3D bioengineered models with the model compounds tested in this study .....</b>	<b>413</b>
<b>Figure 6.45: Reported human and animal tissue values compared to Caco-2 Transwell controls .....</b>	<b>414</b>
<b>Figure S1: Negative control images for 2D fibroblast cell lines –.....</b>	<b>464</b>
<b>Figure S2: Negative control images for 2D Epithelial – .....</b>	<b>465</b>
<b>Figure S3: Negative control images for wholemount and transverse Caco-2 Transwell models –.....</b>	<b>466</b>
<b>Figure S4: Negative control images for Sectioned Transwell models – .....</b>	<b>467</b>
<b>Figure S5: Negative control images for Sectioned 3D models –.....</b>	<b>468</b>
<b>Figure S6: Negative control images for human tissues –.....</b>	<b>469</b>
<b>Figure S7: Preliminary data for the intrinsic permeability of different Alvetex formats to Crystal Violet dye – .....</b>	<b>470</b>
<b>Figure S8: MDR1 primer optimisation and efficiency check.....</b>	<b>471</b>
<b>Figure S9: MRP2 primer optimisation and efficiency check .....</b>	<b>472</b>
<b>Figure S10: OATP-B primer optimisation and efficiency check .....</b>	<b>473</b>
<b>Figure S11: Occludin primer optimisation and efficiency check .....</b>	<b>474</b>
<b>Figure S12: Villin primer optimisation and efficiency check.....</b>	<b>475</b>

<b>Figure S13: BCRP primer optimisation and efficiency check .....</b>	<b>476</b>
<b>Figure S14: GAPDH primer optimisation and efficiency check.....</b>	<b>477</b>
<b>Figure S16: Green channel for Figure 3.4 .....</b>	<b>478</b>
<b>Figure S15: Green channel for Figure 3.3 .....</b>	<b>478</b>
<b>Figure S18: Green channel for Figure 3.6 .....</b>	<b>479</b>
<b>Figure S17: Green channel for Figure 3.5 .....</b>	<b>479</b>
<b>Figure S19: Green channel for Figure 3.7 .....</b>	<b>480</b>
<b>Figure S20: Green channel for Figure 3.12 .....</b>	<b>481</b>
<b>Figure S21: Green channel for Figure 3.26 .....</b>	<b>482</b>
<b>Figure S23: Green channel for Figure 3.14 .....</b>	<b>483</b>
<b>Figure S22: Green channel for Figure 3.13 .....</b>	<b>483</b>
<b>Figure S24: Green channel for Figure 3.20-23 .....</b>	<b>484</b>
<b>Figure S26: Green channel for Figure 5.22/23 .....</b>	<b>485</b>
<b>Figure S25: Green channel for Figure 4.11 .....</b>	<b>485</b>
<b>Figure S27: Green channel for Figure 5.25-27 .....</b>	<b>486</b>
<b>Figure S28: Green channel for Figure 5.28 .....</b>	<b>486</b>
<b>Figure S30: Green channel for Figure 5.30 .....</b>	<b>487</b>
<b>Figure S29: Green channel for Figure 5.29 .....</b>	<b>487</b>

## Abbreviations

GI	Gastro-intestinal
Conventional culture	Gold standard Caco-2 Transwell epithelial models
ADME	Absorption, Distribution, Metabolism and excretion
3D	Three Dimensional
2D	Two Dimensional
iPSC	Induced Pluripotent Stem cell
Caco-2	Colon Adenocarcinoma cell line
NCE	New chemical entities
ZO-1/2	Zonula Occludens – 1/2
CAM	Calcium dependant adhesion molecule
LGR5	Leucine-rich repeat-containing G-protein coupled receptor 5
MRP1,2,3	Multidrug resistance-associated protein 1,2,3
BCRP	Breast cancer resistance protein
MDR1	Multidrug resistance protein
MHC	Major Histocompatibility Complex
ECM	Extracellular Matrix
$\alpha$ SMA	Alpha Smooth muscle actin
CD4	Cluster of differentiation 4
MUC	Mucin protein
EC cells	Enterochromaffin cells
CYP3A4	Cytochrome P450 3A4
PTS domain	Phosphotransferase systems domain
HT29-MTX	Colon Carcinoma Goblet “like” cell line
CCD-18co	Colon carcinoma normal fibroblast cell line
NHF	Normal Human Fibroblast
Ki67	Antigen encoded by MK167 gene
CEA	Carcinoembryonic antigen
KGF	Keratinocyte growth factor
HDF	Human Dermal Fibroblasts
TEER	Transepithelial electrical resistance

LY	Lucifer yellow
P-gp	P-glycoprotein
Papp	Apparent permeability
Poly HIPE	Polymers high internal phase emulsions
HIC	Human intestinal cells
MTT	MTT 3-(4,5-dimethylthiazol-2-yl)-2,5-diphenyltetrazolium bromide
qPCR	Quantitative PCR
OATP-B	Organic anion-transporting polypeptide B
mRNA	Messenger RNA
DAPI	4',6-diamidino-2-phenylindole DNA stain
ELISA	Enzyme Linked Immunosorbent Assay
ECACC	European collection of authenticated cell cultures
IBD	Irritable Bowel Disease
hMSC	Human mesenchymal stem cells
IGF-1	Insulin growth factor 1
VEGFR-1	Vascular endothelial growth factor receptor-1
MCP-1	Monocyte Chemoattractant Protein-1
IL-6	Interleukin 6
HUVEC	Human vascular endothelial cells
MMP 9	Matrix metalloproteinase 9
TGF- $\beta$	Transforming growth factor beta
EGF	Epidermal growth factor
PAS	Periodic acid Schiff
TEM	Transmission electron microscopy
SEM	Scanning electron microscopy
DMEM	Dulbecco's modified eagles medium
PFA	Paraformaldehyde
NHE8	Sodium/Hydrogen Exchanger 8
TNF- $\alpha$	Tumour necrosis factor alpha
IEC	Intestinal epithelial cells
MSC	Mesenchymal Stem cells
FDA	Federal drug administration
H&E	Haematoxylin and Eosin

ALI	Air liquid interface
PBS	Phosphate buffered saline
PBST	0.5% Tween in Phosphate buffered saline
THF	Tetrahydrofuran
DCM	Dichloromethane
DBE	Dibenzyl ether
PMN	Peripheral mononuclear cells
PET	Polyethylene terephthalate
HBSS	Hanks Buffered saline solution
DMSO	Dimethyl sulfoxide
HPLC	High Performance Liquid Chromatography
AgCl	Silver Chloride
KCl	Potassium Chloride
mm	Millimetre
µm	Micrometre
nm	Nanometre
mg	Milligram
µg	Microgram
ng	Nanogram
pg	Picogram



## 1. General Introduction

### 1.1 Challenges of modern drug discovery

The gastro-intestinal (GI) tract is a major specialised organ. Its purpose during normal function is the breakdown of ingested substances into digestible molecules and the homeostatic removal of waste products produced within the body. Secondary functions, include protection against poisons, perceived or otherwise through expulsion mechanisms and as a major immunologically active area, again protecting the body against ingested pathogens (1) this time biological in nature.

Ingested substances refer largely to food taken in for sustenance but in the modern world may often also refer to orally administered therapeutic drug compounds. Often the intestines natural defence mechanisms will detect and treat these ingested compounds as poisons, blocking them from absorption and as such significantly reducing compound uptake and bioavailability. Ultimately, this acts to limit therapeutic bioavailability and activity. Therefore, it goes without saying that a foundation of knowledge of the intestine, its structure, function, how the two relate and the likely interactions between compounds of interest and *in vivo* biology is of vast importance when understanding the bodies capability to absorb novel, pharmacokinetically untested compounds.

Pharmaceutical development is as ancient as human history itself, however, with the scientific enlightenment, new methodologies were devised to understand the mechanistic action of medicines in the body. Early modern pharmaceutical pioneers such as Louis Pasteur *et al* would utilise animals, often in great numbers, to test their hypothesis. However, whilst animal usage can be effective, demonstrated by two of Pasteur's more famous discoveries, vaccines for Anthrax (tested on Sheep and cattle) and Rabies (tested on rabbits, dogs and humans)(2) the ethical and moral use of animals as test subjects limits their use in modern science. Indeed, Pasteur himself had a reputation of unethical practices, even in the mid 1800's. Not only is animal use ethically challenging, more recent studies have begun to question their *in vivo* validity when comparing to human

tissues. With issues ranging from differences in underlying animal disease mechanisms compared to humans, non-similar drug toxicities and pharmacokinetics (3,4)

During the 20<sup>th</sup> century cell isolation and culture became a more time and cost-effective method to do biological research. Starting with the first continuously growing immortalised cell line, HeLa (5), cells of almost any tissue are now relatively readily available for use in *in vitro* tissue models. Some more modern approaches to cell culture focus on the culture and directed differentiation of stem cell lines to create more *in vivo* physiologically relevant cells for use in tissue models. As such, cellular models of human and animal tissues have slowly become one of the most prominent research tools in pharmaceutical biology, particularly in very early stage compound development where they can be used to efficiently screen large numbers of compounds in a single study. (6) New, models based on simple, familiar techniques such as the standard Caco-2 model have an improved likelihood of being adopted whilst occupying a significant niche in the early stages of drug discovery, lowering costs through improved predictability of NCEs' *in vivo*.

The current gold standard for the pharmacokinetic ADME (absorption, distribution, metabolism, and excretion) testing of novel compounds in the intestine is the Caco-2 Transwell assay. This well-defined model consists of Caco-2 intestinal epithelial cells cultured on Transwell semi-permeable membranes.(7) Caco-2 cells were first isolated in the mid to late 1970s by Fogh *et al* (8) and have been utilised for a wide variety of purposes over the intervening decades, evolving from their original purpose as a cell to study cancer phenotypes (9) and understanding intestinal bacteriology (10,11) to their current gold standard use in drug permeability and toxicity. They are able to form confluent, differentiated monolayers with apically expressed, well-defined brush border formation and production of intestinal specific compound transporters. Additionally to this, Caco-2 cells bind to one another through the formation of tight junctional complexes to create a highly polarised cellular epithelium with quantifiable membranal resistance, a phenotype which will be discussed in detail later in this chapter. The value of the Caco-2 cell line in intestinal research is hard to overstate with even a simple literature search demonstrating a large number of published applications.

The Caco-2 intestinal model has been critical in the development and pharmacokinetic testing of numerous NCEs (new chemical entity) and their translation into clinical drug compounds. Other techniques such as PAMPA (parallel artificial membrane permeability assay), an artificial membrane able to be utilised in high throughput applications are able to model the passive para/ transcellular transport but do not incorporate the active movement of NCE compounds across the membrane by influx/ efflux protein pumps. PAMPA experiments are often ran co-currently with the Caco-2 Transwell model, together creating a strong predictive basis for NCEs *in vitro*, particularly those absorbed passively through the cell membrane. (12)

A major issue with the Caco-2 system as a gold standard for intestinal research is its poor inter-lab reproducibility. It has been shown that, even at the earliest stages of Caco-2 isolation and development, Caco-2 populations are highly heterogenous. Heterogenicity in itself isn't necessarily a disadvantage, indeed the intestine itself is a highly heterogenous organ system with multiple cell types and functionalities in the epithelium alone. (13) However, differing culture techniques between labs in the intervening decades since initial isolation has caused large variations in Caco-2 cell phenotypes. Ultimately, unless comparable studies utilise the same master cell bank of Caco-2 cells, cellular phenotypes are unlikely to be directly comparable. Trans-epithelial electrical resistance (TEER) measurements are an obvious example of this with reported Caco-2 values ranging from 2-300 to 2-3000 Ohms.cm<sup>2</sup> depending on the lab whilst in each case reported as normal Caco-2. (7,14–18) Even so, as before, variable phenotype is not necessarily a disadvantage so long as known cellular phenotypes are taken into consideration at the beginning of a study. The difficulty however is that differences in Caco-2 sub-clone phenotypes from multiple master cell banks are not often quantified, with no easy way to distinguish one sub-clone from another. Other inherent disadvantages of the Caco-2 system include no intrinsic CYP3A4 expression (a highly important cell surface enzyme molecule known to metabolise a number of drug classifications)(19), high TEER and low P-gp (efflux protein with a wide substrate base important in drug absorption and availability) (19). There is growing concern that the Caco-2 model of the intestinal epithelium is insufficiently reproducible for accurate modelling the cell-drug interaction of the human intestine.(20)

NCE clinical translation success rates generally lie in the low to mid-single figure percentages. (21) Figure 1.1 demonstrates how these extremely high attrition rates can lead to high development costs for new compounds to market, putting the average cost of development at almost 2.6 billion dollars per drug. With a capitalised cost in the mid 2010s of over 1 billion dollars for the pre-human phases alone, over double the cost of the previous decade, an order of magnitude higher than costs in the 70s and 80s and accounting for nearly half the total cost to market. (22) Indeed recent figures show that more money is spent in the pre-clinical phases today than was spent getting a drug to market in the mid-2000s. (22) Increasing drug to market prices are always going to be a multifactorial process with inflation, new highly accurate but more expensive tests and improved testing and safety standards all contributing to developmental costs. When one considers some of the main reasons for compound attrition during the development process such as; clinical safety, efficacy and bioavailability (23) it clearly highlights how new systems for the large-scale testing of novel compounds which are more able to mimic the human intestine are required to reduce compound attrition in late stage clinical trials.

Oral administration of drugs is the most common pathway by which pharmaceuticals are ingested.(24) This will likely continue to remain true due to oral administration being

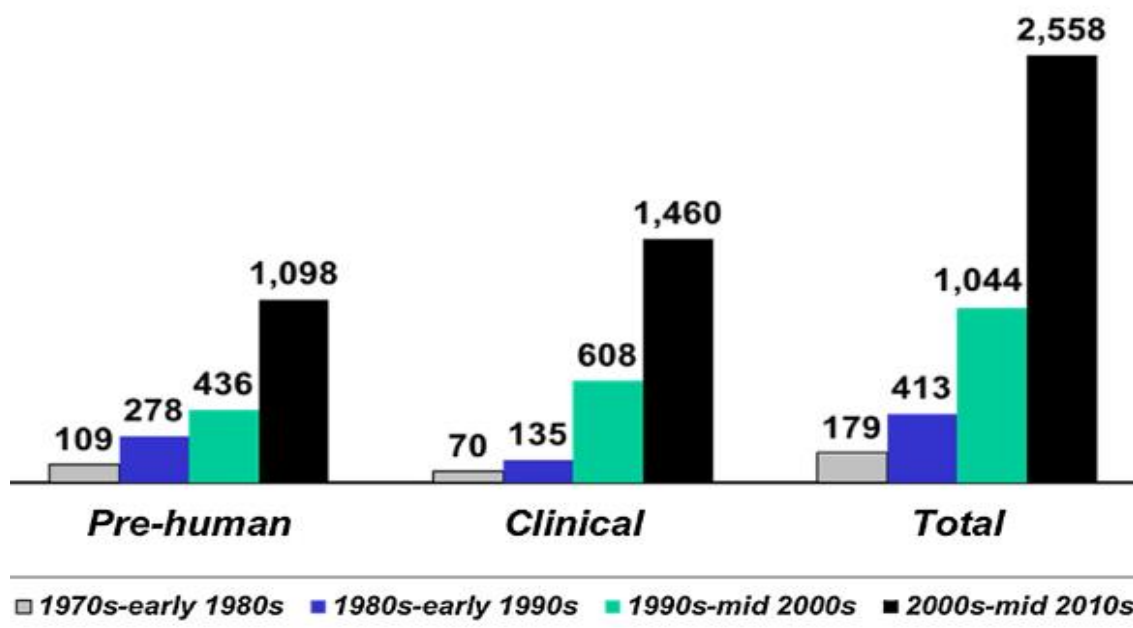


**Figure 1.1: Understanding the costs for the development and testing of novel drug compounds** – The cost of bringing new drugs to market has shown a steady increase over the last 40 years with pre-clinical phase testing now costing over a billion dollars on average per new drug to market. Source DiMassi *et al* 2016 (21)

both the easiest for patients to correctly administer as well as being the least invasive method available when considered against intra-venous (IV) methods which bypass the intestine at the cost of being highly invasive. (25) As such improving the tools for pharmacological research will allow for more *in vivo* mimetic responses in tissue models which is key to future NCE development which rely on oral administration. The limitations of current intestinal models ultimately cause large levels of wasted time and effort on the validation of either toxic or non *in vivo* effective compounds (either by absorption or metabolism) that, with a more *in vivo* representative early stage model of the intestine, could have been removed as possibilities earlier in the process.

Most current studies are focussed on the utilisation of the Caco-2 cell line in novel ways to adapt these well characterised cells to be more structurally and functionally relevant to *in vivo* tissue. This includes being utilised as an addition to a 3D model, growth upon tissue mimetic basement membrane proteins (26,27) or as a direct or paracrine co-culture with other cell types.(28) The use of iPSC, intestinal derived stem cells (29) or other

existing cell lines in intestinal model construction is another way in which new research is creating more *in vivo* representative models. It is hypothesised that these new technologies (3D scaffold based models, hydrogels and organoids) will have a great impact on the methods utilised for pharmaceutical development in the future.

## 1.2 The general anatomy of the gastro-intestinal tract

The gastro-intestinal (GI) tract is an organ system of great diversity and complexity with each point tailored to a specific purpose and function. The upper tract consists of the mouth, responsible for the initial breakdown of ingested substances through mastication and secretion of salivary enzymes. The stomach contains a highly acidic environment with a complex array of digestive enzymes tailored for the breakdown of foods to small, absorbable component parts. (30) However, it is important to note that a significant part of digestion does take place within the intestine in addition to the stomach. (31) Gross digestive system structure is detailed in Figure 1.2.

Intestinal biology begins at the pylorus, ending at the ileocecal valve. (32) Intestinal morphology is split into 2 major sections, the small intestine and the large, each of which can then be further broken down into distinct regions. The small intestine is the first of the two and is a major point in the body for compound digestion and the primary place of nutrient absorption, with 90% of useful compounds absorbed here. In total the intestine is approximately 4 meters long with the small intestine grossly described as consisting of 3 parts;

### 1. Duodenum

The duodenum is the smallest section of the small intestine at approximately 25cm long and is located immediately after the pyloric sphincter of the stomach. The function of this region of the small intestine is in the neutralisation of stomach acid and continued breakdown of proteins and fats into absorbable states through secretions from the liver, pancreas and the intestinal wall itself (bile, digestive enzymes and neutralisation agents respectively). Brunner's glands are primarily localised in the proximal Duodenum. (33) Their role lies primarily in the secretion

of bicarbonate containing mucous which has the dual role of neutralisation and lubrication through the intestine. Proteases and antimicrobial compounds are also seen within the Brunner's gland secretome and are thought to protect the mucous layer against digestion by pancreatic enzymes. Another important distinction of the duodenum is its lack of mesentery support when compared to other regions of the small intestine. (31)

## 2. Jejunum

The jejunum is the middle and longest section of the small intestinal system at approximately 1.5 meters long and is primarily responsible for the absorption of digestive products; sugars, fatty and amino acids. The greatest levels of absorptive adaptation can be found here with large contiguous villus structures and circular (plicae) folds to further increase absorptive surface area. Anatomically, there is no distinctive differences between the jejunum and the ileum.

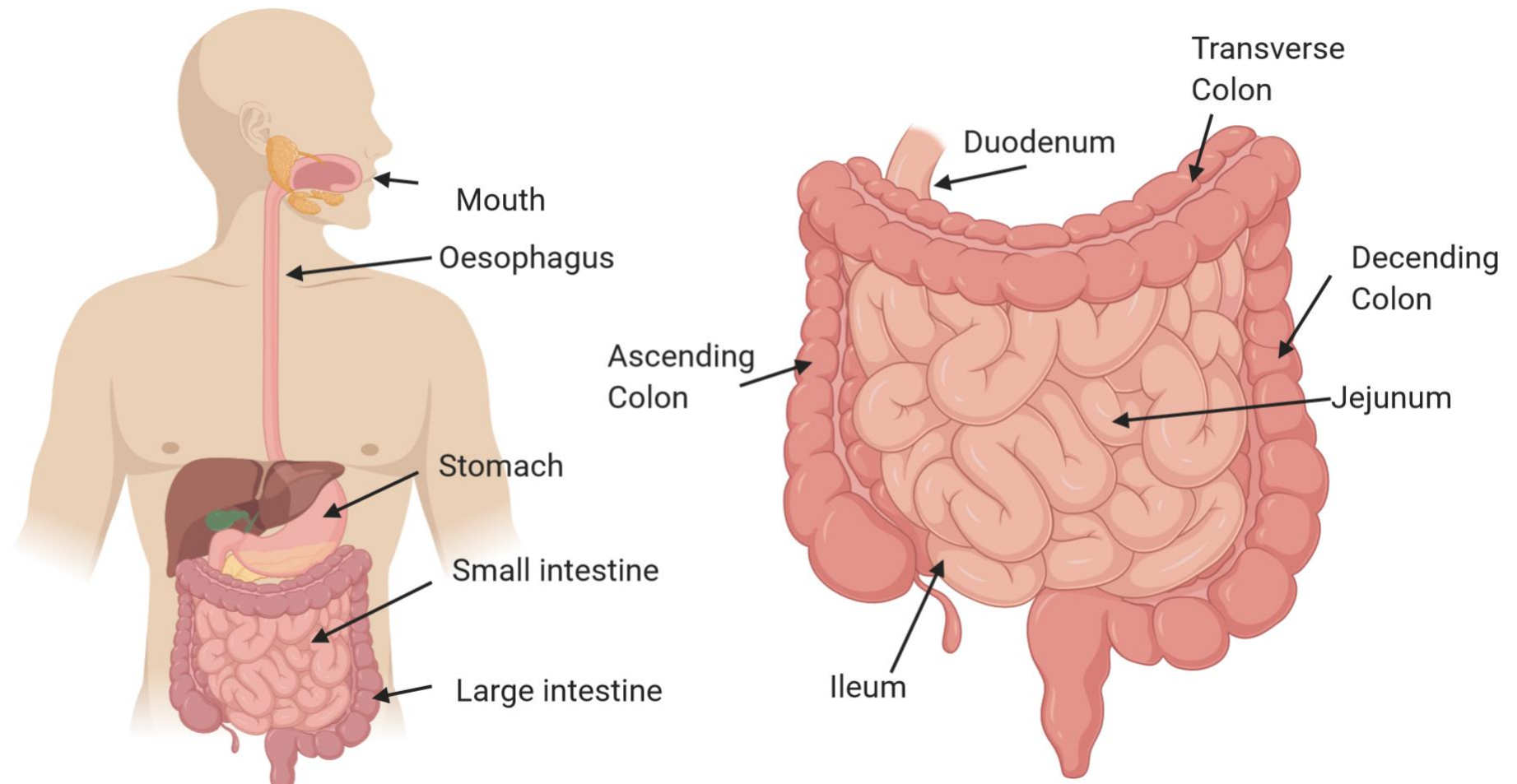


**Figure 1.2: The gross anatomy of the digestive system with specific focus on the structure of the intestine** – The digestive tract is split into 4 distinct sections; mouth, stomach, small intestine and large intestine. The intestinal structures are further split into distinct regions, each with specific yet largely overlapping function.



### 3. Ileum

The ileum is the final section of the small intestine and is generally considered to be the point whereby bile salts and vitamin B<sub>12</sub> is absorbed alongside any left over, unabsorbed compounds from the jejunum. Additionally, the ileum is characterised by a highly developed gut associated lymphoid tissue (GALT).(34) Aggregations of lymphoid tissues known as Payer's patches are located here primarily and span the lamina propria through to the submucosa. (35) Paneth cells in the ileum secrete antimicrobial peptides due to the increased bacterial load caused by proximity to the proximal large intestine. The ileal lumen diameter decreases compared to the jejunum and the circular folds decrease towards the terminal end of the ileum. The ileocecal valve is responsible for the controlled movement of matter from the small intestine to the large and is located at the terminal end of the ileum.

Also known as the colon, the large intestine has three major functions in the absorption of water and electrolytes, producing and absorbing vitamins and movement of waste products towards the anus. Indeed, the colon is thought to reabsorb approximately 400-1000ml of water per day from waste matter. Although this number varies drastically, it is important to remember that 80-90% of water is absorbed in the small intestine. The large intestine in an average adult is approximately 1.5 meters long and has a significantly wider lumen diameter than the small intestine. A higher proportion of goblet cells can be found within the large intestine when compared to the small, due to the less absorptive functionality and the importance of lubrication as the faecal matter becomes more desiccated. Columnar cells of the intestine are the primary functional unit responsible for water and salt absorption in the large intestine as described above. They are the most numerous epithelial cell of the colon and are found sandwiched between the much larger goblet cells. (32)

The large intestine can also be further split into 3 main sections however unlike the small intestine the function of the large intestine varies less significantly with distinctions primarily due to gross anatomy and organ location within the body The sections are:

1. Ascending colon

This is the first section of the large intestine and, as the name suggests, ascends away from the rectum on the right side of the abdomen.

2. Transverse colon

This is the longest region of the colon.

3. Descending Colon

This is the final main stage of the colon and as the name suggests descends towards the sigmoid colon and the rectum

It is in the large intestine where resident bacterial populations have a significant role in the breakdown of indigestible intestinal content into digestible forms to be absorbed by the colonic epithelium such as vitamin B and K. (36) Additionally, bacteria are able to

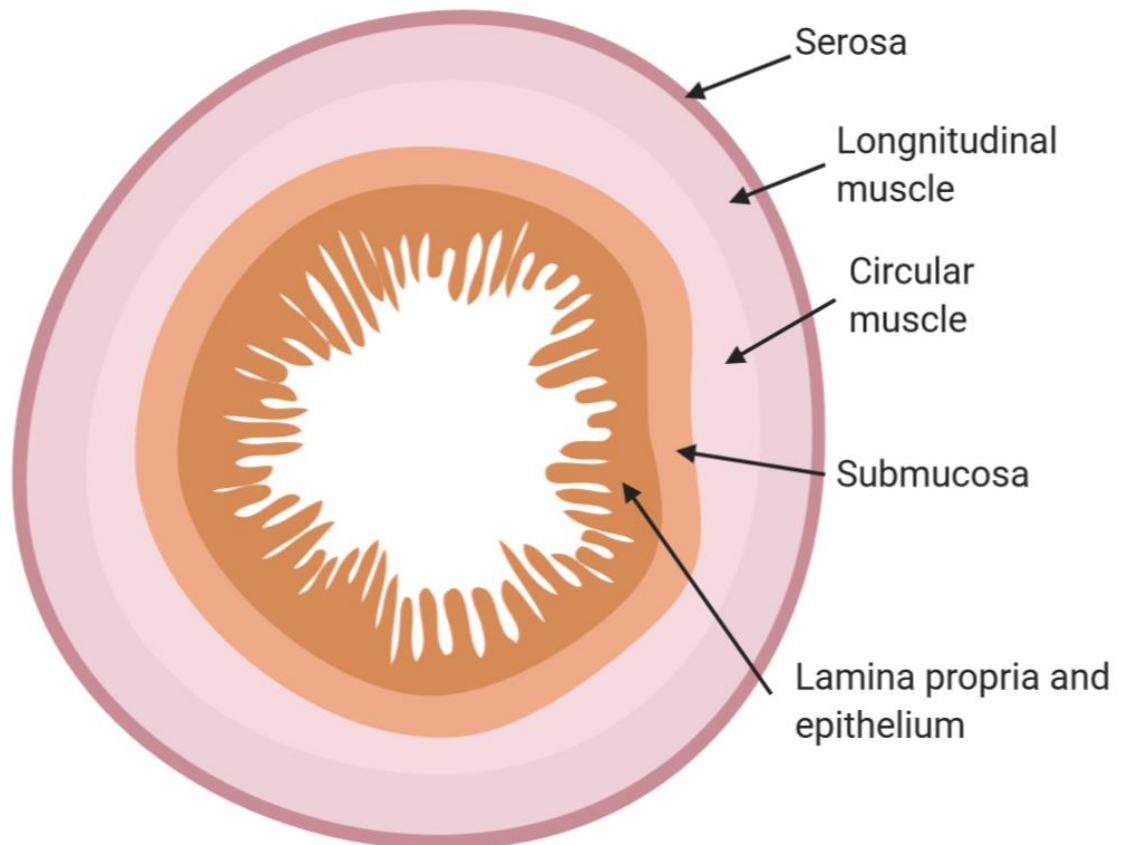


**Figure 1.3: The structural layers of the intestine** – A simple schematic of the constituent layers of the intestine. The outer serosal layers provide a protective membrane around the entire organ. Muscularis layers support the peristaltic movement of digestive chyme. Submucosal layers are home to glands, muscularis and lamina propria layers support the functional epithelium.

ferment non-absorbable carbohydrates such as cellulose and lipids. It is the digestion of these lipids in particular into short fatty chains which are readily absorbed into the colonic epithelium, catalysing the uptake of water and sodium ions at the same time. It is important to note that the colon itself is poorly organised for efficient nutrient absorption. Both villi and circular folds, critical for increasing the surface area of the absorptive epithelium in the small intestine are lost in the colon, significantly reducing absorptive efficiency. Smooth muscle banding around the outside of the colonic tissue is increased compared to the small intestine to reflect the function of the colon in the efficient removal of non-digestible waste matter.

Whilst the detailed histology of intestinal epithelial tissues is highly variable dependant on the area of the intestine under study, the basic structure of the intestinal wall varies little through the length of the intestine. Figure 1.3 shows a simple schematic of the constituent layers of the intestine.

The serosa is a protective layer covering the entire surface of the intestine consisting of connective tissues and a monolayer of squamous epithelium. Immediately below these serosa are the 2 muscle layers, longitudinal and circular, which together make up the *muscularis externa*. The purpose of these muscle layers is two-fold. 1. To mix up the intestinal contents to ensure optimal digestion, 2. Through peristaltic movement, force the intestinal contents through the intestinal lumen. Smooth muscle around the intestine forms sphincters at regular intervals, controlling the rate of intestinal content movement. The submucosa is a loose collection of fibroblasts, collagen and acellular connective tissues containing the majority of the intestinal lymphatics, blood vessels and nerves. Dependant on the part of the intestine under study, the submucosa may also be home to submucosal glands such as the Brunner's glands mentioned earlier. The lamina propria and the epithelium are then supported by a thin layer of muscle tissues both longitudinal and circular. The lamina propria is home to resident fibroblast and myofibroblast populations whose function it is to support the development and maintenance of the surface epithelium whose histology varies greatly dependant on the region of the intestine. (31,32,37)

### **1.3 Epithelial anatomy, the relation of structure and function.**

The epithelium is most generally described as a cellular layer which extensively covers the outermost surfaces of the body, both internally and externally.(38) Often the internal interface epithelial layers are covered with small cytoplasmic extensions known as either microvilli or cilia. The former being an adaption for improved cellular absorption through provision of larger surface area for substrate transport and the latter being an adaption for the transport of mucous. Alternatively, the epithelium on the “outer” interfaces of the body, namely the skin, are adapted to express a highly keratinised outer layers with several specialised functions such as defence against external pathogens and retention of moisture.(39) The epithelium of the body are as diverse as the organs they support, deriving from all three germ layers with their function dependant on their location and structure. For example skin epithelium derives from the ectoderm, gastrointestinal epithelium from the endoderm and mesoderm creates blood vessel endothelium. (40–43)

Epithelia are structured differently throughout the body with their structure directly related to their function. Primarily the structures can be split into two broad categories, 1. Simple and 2. Squamous. A simple epithelium is described as a single layer of cells supported by a basement membrane (44) with primary functions as a selective interface for the absorption (Diffusion/ Active) and secretion at external body interfaces. Further subcategories of simple epithelium are based on the epithelial cell morphology. (38) Squamous cells are flattened cells whose lateral dimensions far exceed the cell height. These cells can be found in the blood vessel system as well as type I pneumocytes of the lung alveoli. (45) These cells are mostly involved in passive processes due to their cellular shape being unsuitable for complex differentiation and development. (Figure 1.4 A) Cuboidal cells are described as cells whose height and width are approximately equal and includes cells found in the kidney epithelium (46) and ciliary body of the eye. (47) (Figure 1.4 B) Columnar cells are tall cells whose height exceeds their lateral dimensions. These cells are found in the intestine where they undergo complex differentiation into absorptive enterocytes or secretive goblet cells amongst others. (48) (Figure 1.4 C) Finally, pseudostratified epithelial layers are columnar cells whereby the arrangement appears to

be organised into multicellular layers. However, all the cells into a pseudostratified epithelium are in contact with the basement membrane and hence only one cell thick. (Figure 1.4 D)

Stratified epithelium (Figure 1.5) is composed of multiple layers of cells, with each layer consisting of cells at different stages of differentiation. Basal layer cells are often cuboidal and home to the self-replicating stem cell niche and the proliferating cells for the maintenance of the epithelial layer. E.g. the stratified epithelium of the skin. Cells of the basal layer migrate toward the apical surface of the epithelium over time, as cells move away from sources of nutrients, they become more squamous, functionally differentiated

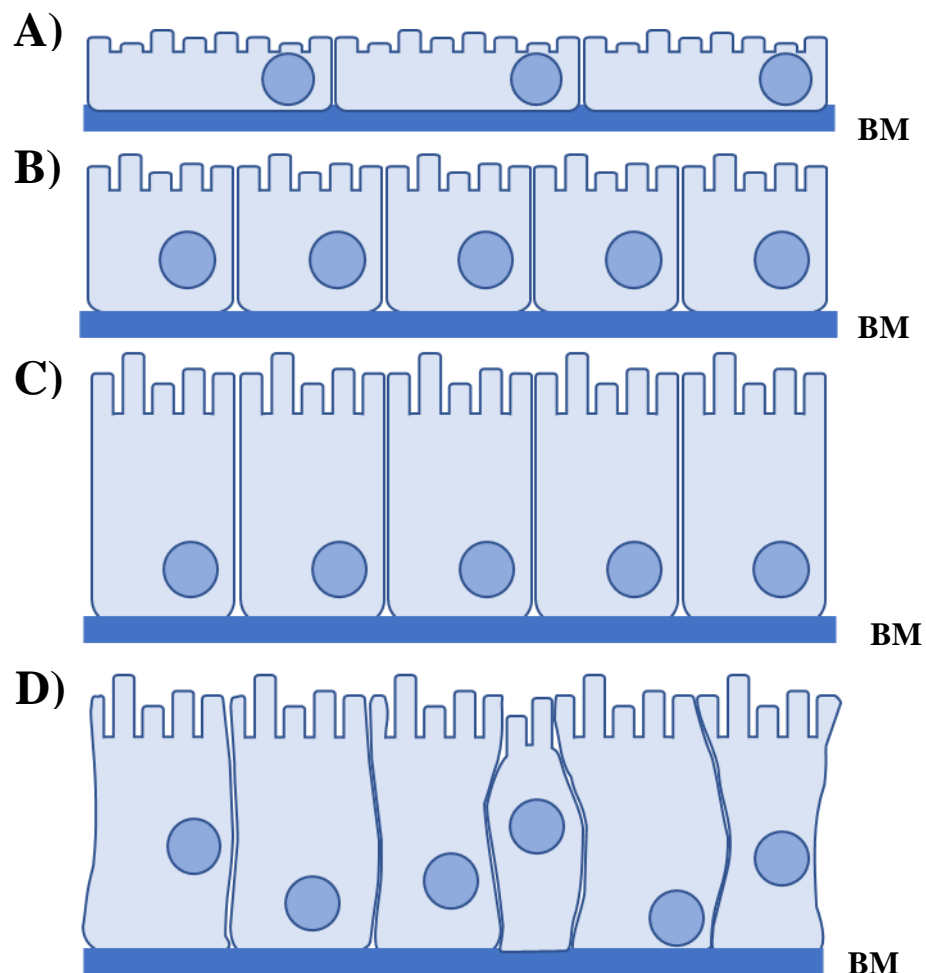


**Figure 1.4: Structural characteristics of simple epithelial layers in the human body** – Schematic showing the structures of different types of simple epithelium A) Squamous, B) Cuboidal, C) Columnar, D) Pseudostratified. Basement membrane (BM) is extremely important in the development and maintenance of the epithelial layer. A key feature lacking in the Caco-2 Transwell gold standard of the intestinal epithelium.

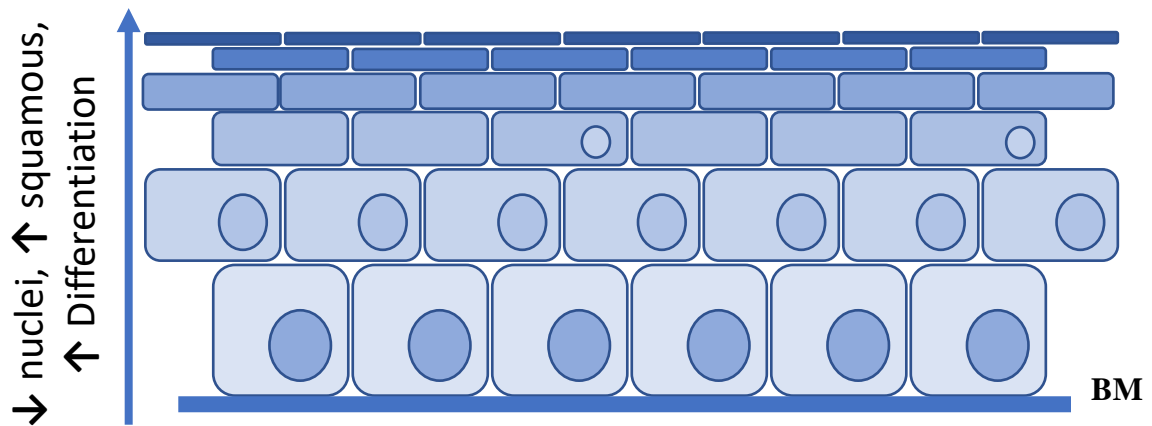


**Figure 1.5: Complex squamous epithelial show gradients of differentiation across the thickness of the epithelial layer** – Simple schematic of a classic stratified epithelium such as the skin. Notice the loss of nuclei as cells differentiate and the change in cell shape from a proliferative base layer to a non-proliferative differentiated surface barrier.

and lose proliferative capability. (49) Stratified epithelium can be described as keratinised (Skin) or non- keratinised (Buckle, Vagina) depending on their location and function.(50)

The purpose of this thesis is the description of the intestinal epithelium, its adaption to its function and how it can mimic the human intestine *in vivo*. As such stratified epithelium will not be discussed in any more detail.

The function of the epithelium of the body are diverse. Broadly speaking these functions can be categorised 3 ways; 1. Protection, 2. Absorption, 3. Secretion. Protective epithelium includes those such as the skin which is developed to include a denucleated highly keratinised external layer. (51–53) This acts as a physical barrier to external pathogens and desiccation of the underlying tissue through secretion of an outer oil layer. Other protective characteristics of epithelium include the creation and maintenance of a sterile mucous layer. These mucous layers are created and maintained through use of specialised epithelial cells known as goblet cells. This is most evident in tissues such as the colon or airway mucosa. Colon tissues in particular have complex bi-layer mucous structures including both secreted and membrane bound mucins. (54) These mucous layers, in much the same way as the skins keratinised outer layer, provide a physical barrier to the passage of outside pathogens such as bacteria. The mucous layer of the colon achieves this whilst maintaining some level of absorptive capability. Another primary function of the mucus layer of the colon is the provision of a niche for population with symbiotic bacteria. These bacteria are responsible for breaking down indigestible

components into useful compounds such as vitamin K which cannot be created by the body. (55–57) An important distinction for epithelial layers is their ability to form highly polarised cell layers, necessary for their proper function. The focus of this work is on the absorptive/ transportation capabilities of the intestinal simple epithelium and as such stratified epithelia will not be discussed further.

## **1.4 Understanding the functional absorptive component of the intestine, the enterocyte.**

The intestinal mucosa is split into two main compartments, the epithelium and the lamina propria. The most abundant cell type of the epithelium is the absorptive enterocyte followed by mucous secreting goblet cells in addition to enteroendocrine and Paneth cells (small intestine) which are prevalent at a lesser rate. All cells in the epithelium arise from an intestinal LGR5+ve stem cell population located within the crypt of Lieberkühn. (58) Except for Paneth cells which reside in the small intestinal crypt and migrate downwards, all cells of the epithelium migrate from the crypts of Lieberkühn up to the villus tip. (59) The intestinal epithelium is one of the most highly turned over epithelia of the body with cell lifespan limited to a matter of 3-5 days for most mammals. (55) For example, in humans it is estimated that  $10^{11}$  intestinal epithelial cells are lost daily. (60) As such the intestine exists in a carefully maintained homeostatic balance between cell renewal and apoptosis, with disruption to this homeostasis being the basis for many intestinal diseases.

The enterocytes are the main absorptive cell in the intestinal epithelium. Their main role is in the selective absorption of nutrients and compounds through the epithelium, and ultimately into the blood stream. Phenotypically, enterocytes are organised into a single monolayer of columnar cells with an apically expressed brush border of microvilli and well-defined apical lateral tight junctional complexes. Nutrients in the intestinal lumen travel through the epithelium by two main routes, paracellularly and transcellularly. Transcellular transport can occur through a variety of mechanisms and is defined as the passive or active uptake of compounds by cellular mechanisms into the cell, creating concentration gradients which the cell must overcome to allow for continuous supply of nutrients.

Paracellular absorption is characterised by the passive diffusion of compounds between the cells through the tight junctional complexes. Selective Paracellular absorption is primarily achieved through selection by compound size and charge. Additionally, enterocytes are bound by a thick membrane associated mucous layer and microvilli associated glycocalyx. The mucous layer is formed from variable length mucins made from carbohydrate side chains attached to a protein core whilst the glycocalyx is comprised of glycoproteins which are structurally similar to mucin proteins. (61) In both instances the main function of the glycocalyx and the mucous layer is as a diffusion barrier and filter of macromolecules in addition to pathogens such as viruses and bacteria. The glycocalyx also has an important function as a reservoir of glycoprotein enzymes responsible for the digestion of macromolecule prior to enterocytic absorption.

In addition, to the enterocytes role in absorption they also have further protective roles in compound expulsion. Transporter protein complexes found on the basal and apical membranes of the enterocytes such as P-gp, MRP1,2,3 and BCRP are ABC transporter proteins implicated in drug and toxin clearance within the intestine. (62) These transporters are of particular interest as they are involved in drug resistance and poor pharmaco-availability within the blood stream. Creating intestinal models more able to recapitulate the drug resistance aspects of the intestinal epithelia will have major uses in the development and testing of new drug compounds. Enterocytes have also been shown to have active roles in the intestinal immune response as antigen presenting cells through MHC class II expression, stimulating CD4<sup>+</sup> T cell responses under inflammatory conditions.



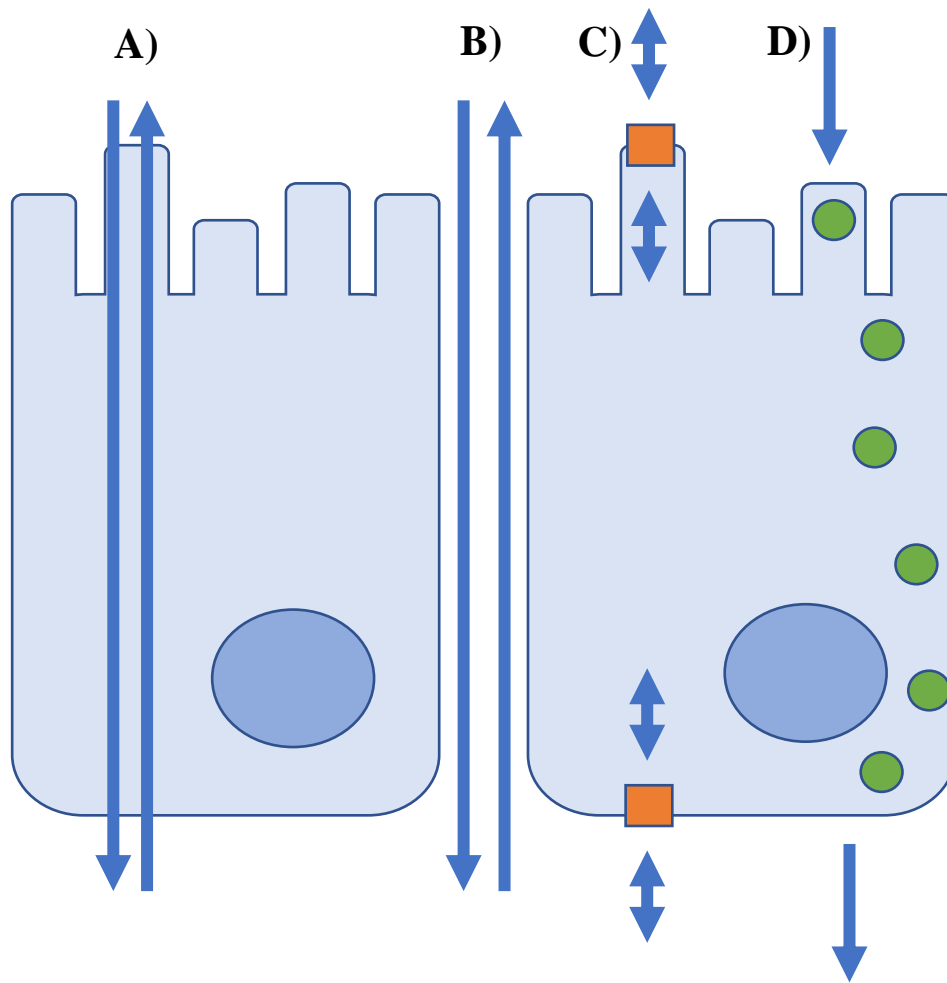


**Figure 1.6: General methods of permeability through epithelial barriers** – A) Passive transcellular. Compounds can readily pass through the lipid cell membrane to enter the cell. B) Passive Paracellular. Compounds do not readily cross the cell membrane but can pass through the intercellular junctional complexes. C) Carrier mediated, compounds cannot passively cross the epithelial barrier and must be transported through active carrier mediated mechanisms. D) Transcytosis, Compounds are captured inside membrane bound vesicles and move through the cytoplasm.

## **1.5 Methods of epithelial permeability and epithelial junctional composition, development of a selective passive paracellular barrier.**

Epithelial cells are bound together with several junctional types, namely; Occluding junctions which provide a tight bound barrier (63), Anchoring junctions (Macular Adherens/ Zonula Adherens/ Adhering junctions) which give the epithelial layer mechanical stability and communicating junctions (Gap junctions) which allow the passage of signalling molecules between cells. (64) Intestinal epithelial cells, primarily those of the small intestine, are relatively weakly bound to one another due to the absorptive adaptations of the intestinal mucosae. TEER values of intestinal tissue for example are well known to be in the low 100s ohms.cm<sup>2</sup> at the most, compared to skin which is regularly in the 1000s of ohms.cm<sup>2</sup>. (65)

### **1.5.1 Methods of permeability through epithelial barriers**

Figure 1.6 demonstrates the 4 main routes of transepithelial permeability, two passive (Trans– and Paracellular) and two active (Carrier mediated and Transcytosis). Compound chemistry largely determines the method of permeability and can fall into one or multiple categories. For example, Lipophilic compounds generally move Transcellularly as they are readily able to pass through the lipid bilayer membrane of the cell. Propranolol is an example of a lipophilic compound thought to travel in this manner exclusively. (66) Other such as etoposide move in more complex manners with a combination of passive and active transport mechanisms such as through OCT 2, MDR1, BCRP and MRP2. (67–69) Compounds such as vitamin B12 are known to move through the cell via transcytosis whereby they attached to membrane receptors and are packaged into membrane bound vesicles to cross the cell membrane.(70)

### **1.5.2 Occluding junctions**

Tight junctions (Zonula occludens/ Occluding junctions) are one of the main junctional complexes important to the intestinal epithelium. (71) These junctions, as the name would suggest, work to tightly bind cells together at their apical interface preventing passive paracellular movement of molecules between cells and entering the blood stream. This is highly important to the intestinal epithelia in particular as it functions as a gatekeeper to the body, selectively absorbing/ rejecting molecules it comes into contact with. Tight junctions are important for the setup and maintenance of concentration gradients and establishment of membrane polarity, a key factor for the correct functioning of many transporter systems found within the intestine. Furthermore preventing back diffusion of compounds into the intestinal lumen ensures absorbed compounds are efficiently translated into the blood stream and the wider body. (72) Some of the key proteins involved in the tight junction complex are Occludins, Claudins and ZO-1/ ZO-2. Occludins and Claudins are structured similarly and as such have similar functions. (73) Both protein systems have 4 transmembrane complexes with two extracellular loops and in internal protein domain which binds to the anchoring protein ZO-1. These proteins have the function of bridging the intercellular gap, creating tightly bound cross-cell complexes and maintaining the integrity of the tight junction, essentially locking the cells together in a band circumnavigating the cell, creating an impermeable barrier to luminal contents. (74) Figure 1.7 outlines the general structure of tight junctional complexes.

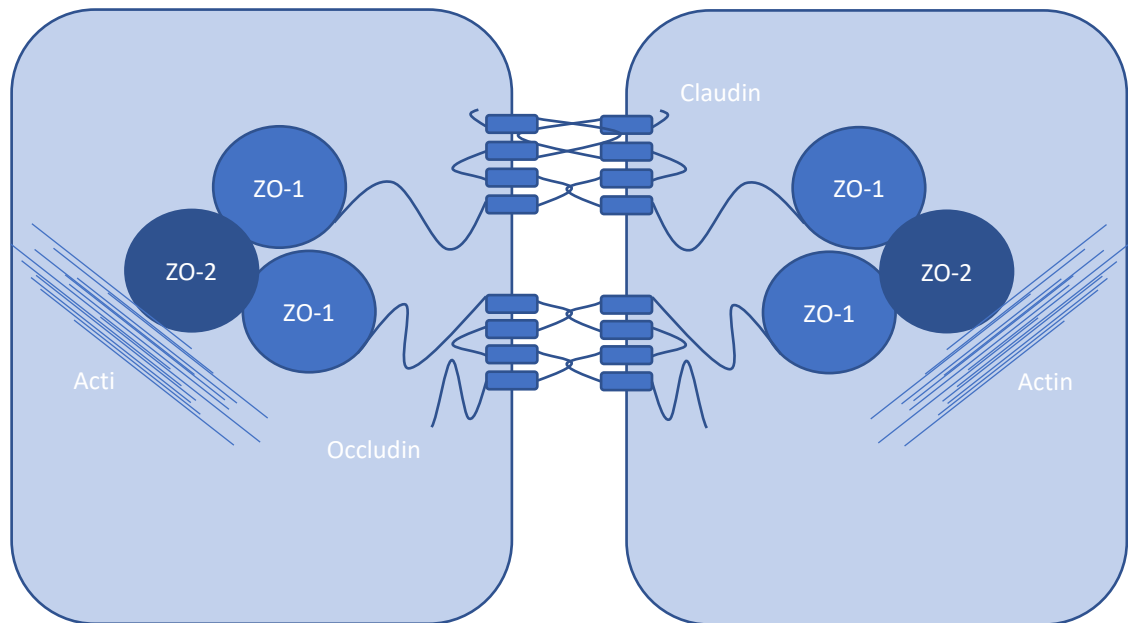


**Figure 1.7: General organisation of a tight junction complex** – Diagram showing the arrangement of some of the key proteins involved in the function of a developed tight junction. Adapted from *Schneeberger et al, 2004*

### 1.5.3 Anchoring junctions

Whilst the tight junctions work to create an impermeable barrier, they do not provide membrane stability between cells to any great extent. The purpose of anchoring junctions is in forming strong protein complexes between the lipid bilayers of neighbouring cells, anchoring to the cells cytoskeleton and providing stability. Anchoring junctions are observed throughout the bodies tissues but are generally more prevalent in areas which are exposed to high levels of mechanical stress such as the epidermis layers of the body and the blood vessels. (75)

In general, there are two main categories for anchoring junctions; 1. Adherens junctions and desmosomes which bind cells to one another (76), 2. Focal adhesions and hemidesmosomes which bind cells to the ECM (77,78)

A *zonula adherens* is described as a continuous belt of Adheren junctions immediately beneath the tight junctions of the cells.(79) Adheren junctions work to connect the actin cytoskeleton of adjacent cells to one another. The Cadherins, members of the Calcium-dependant cell adhesion molecules (CAMs) are the inter-membrane spanning proteins which attach to inner membrane protein complexes made from Alpha/ Beta Catenin and Vinculin. (63,80) The primary cadherin of epithelial tissue is E-Cadherin and as such is found throughout the intestine, (81,82) which along with N-cadherin is also thought to be highly important during development, driving correct cellular localisation and differentiation. As such, Cadherins, specifically the switch in expression from E to N cadherin, is thought to signify a change towards a less differentiated, more proliferated phenotype and as such is a key marker for the malignancy of cancer cells. (81)

Desmosomes are similar in function to the Adheren junctions, consisting of a cytoplasmic protein plaque made of the anchor proteins desmoplakin and plakoglobin. The inter-membrane adhesion proteins of these junctions, desmoglein and desmocollin, are also members of the Cadherin family of proteins. Unlike adherens junctions, desmosomes attach primarily to keratin filaments within the cytoplasm instead of actin, and as such are of significant importance in keratin rich cells such as those seen in the skin. (83,84)

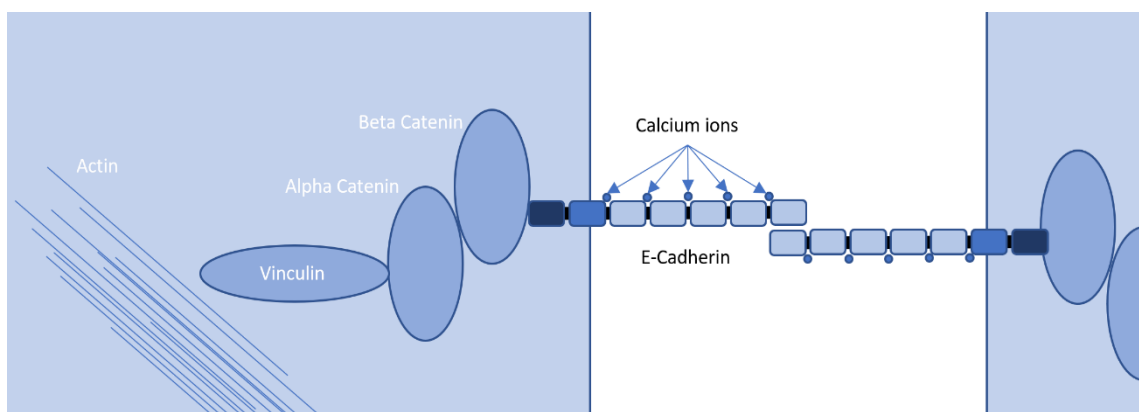


**Figure 1.8: Basic structural anatomy of the adherens junction complex**– Diagram showing the basic protein arrangement of a simple adherens junction. In this instance E-cadherin expression would likely indicate cells of an epithelial origin. Adapted from *Neissen et al 2007*

Figure 1.8 outlines the general structure of adherens junctions.

### 1.5.4 Gap Junctions

The function of gap junctions within the intestinal epithelium and indeed throughout the body is to allow direct communication between adjacent cells. They achieve this through the direct linkage of cell cytoplasm's to one another through the formation of channels by the protein family connexins, 21 genes of which are known to exist in humans. (85) Connexin proteins form hexameric complexes called connexons which form together to create the mature gap junction channel. Interestingly, connexons can be formed from a heterogenous composition of the 14 different human connexin types, the function of the junction changing with the composition of its connexons. (86) In addition to chemical signalling, gap junctions are critical for the electrical excitability of cell layers. (87) As such, cells which are regularly innervated generally contain higher proportion of gap junctions than those that are not. Figure 1.9 shows the basic anatomy of the gap junction complex and demonstrated the orientation of the protein relative to the cellular membrane. (88)

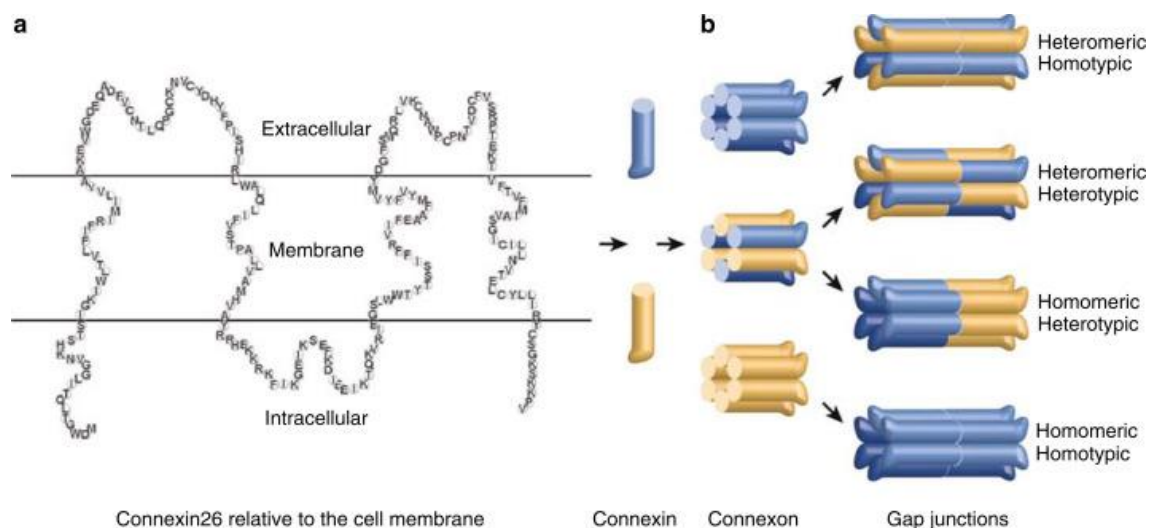


**Figure 1.9: Basic anatomy of gap junction physiology** – Basic gap junction structure showing the capability of gap junctions to be made from a number of different connexin proteins in mixtures of hetero and homogenous combinations. Image taken from Meşe *et al* 2007 (82)

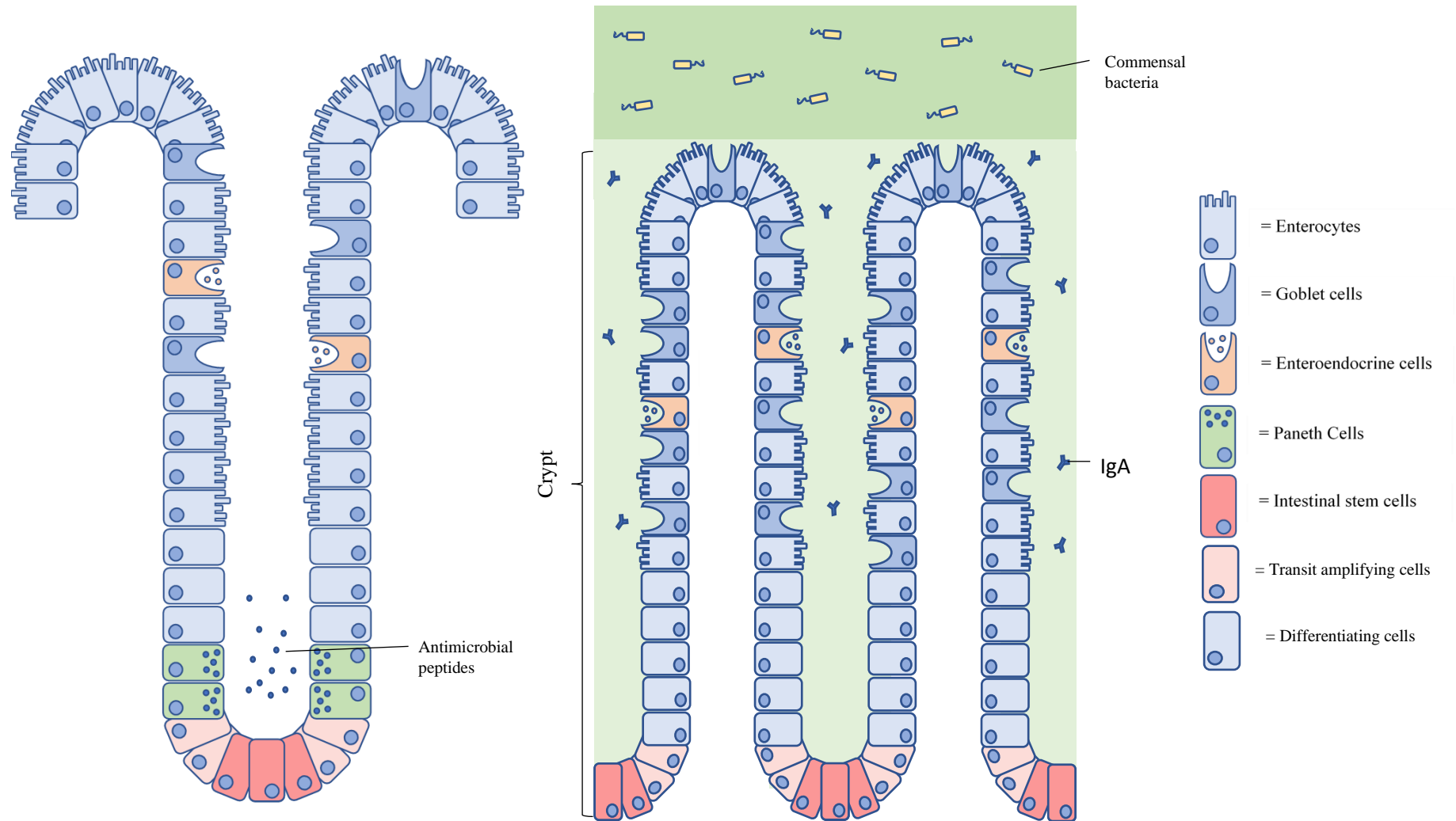


**Figure 1.10: Basic anatomy of human small and large intestine** - Left, Small intestinal anatomy highlighting the importance of the paneth cells in the stem cell crypt nestled between the intestinal stem cells and transit amplifying cells. Large intestine (Colon), Right, Is generally characterised by deep crypt structures and a high proportion of goblet cells forming both a membrane bound and secreted mucous layer.

## 1.6 Quantitative techniques for monolayer integrity and tight junction formation measurement.

Transwell model systems are valuable models of many epithelia throughout the body. Unfortunately, they often take multiple weeks to culture to maturation and as such a method of measuring the development of the model throughout the culture time is required as barrier integrity is crucial to the models function. Transepithelial electrical resistance (TEER) is one widely accepted method whereby the development of the epithelium can be non-directly and non-invasively quantitatively measured throughout the differentiation period. Additionally, TEER measurements are often used as basic acceptance criteria before a model is utilised to give functional data. For example, the widely accepted TEER criteria for a Caco-2 monolayer is 500 ohms/cm<sup>2</sup>. The resistance measurement deemed as acceptable will vary, often greatly, dependant on the cell types used (14) within the model and the type of epithelium created. E.g. simple cuboidal epithelium will have a different TEER from a keratinised stratified epithelium. Furthermore, temperature, media composition and cell passage can all have large effects on the TEER values. (17) Temperature for example is normally controlled through incubating the cells for a short time in pre-warmed media, with the measurement taken at approximately the same time within each well to limit temperature change.

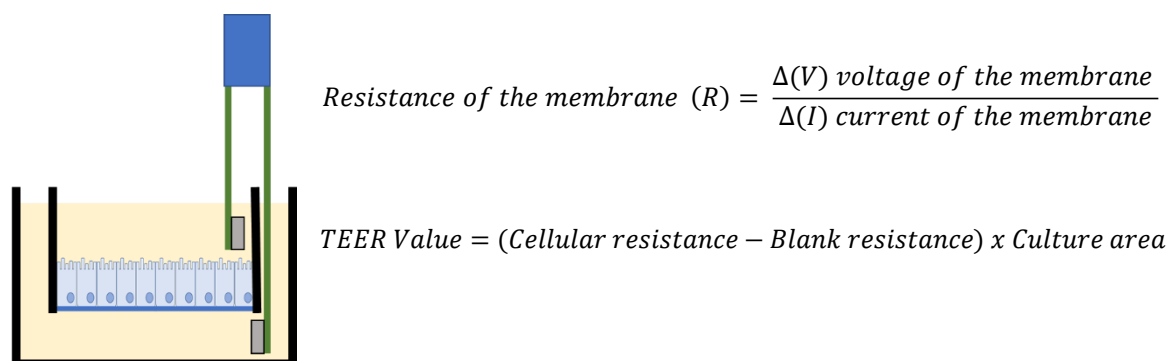


**Figure 1.11: Transepithelial resistance chopstick equipment and calculations** – Raw TEER values are a sum of the internal resistance of the equipment, Electrodes and the polycarbonete membrane. In order to accurately measure the TEER of the membrane along a blank measurement is taken of an acellular membrane which is then subtracted from the raw values.



Alternatively, Blume *et al* worked on mathematically modelling the changes in TEER with the changes in temperature of the media. (15) Hypothetically, utilising their equations you could “correct” the TEER values gained back to 37°C so long as the temperature of the solution is known when the measurement is taken. As such, these conditions need to be carefully controlled in each instance in order to gain a reliable quantification of TEER levels. In addition to the use of TEER as a monitoring tool, quantitative TEER measurements can be used to assess membrane damage, either as a result of scratch healing or compound toxicity assays.

TEER equipment works through the application of an alternating current across the cellular membrane. The change in voltage is measured and utilising Ohms law a resistance can be calculated. Chopstick electrodes are most commonly used when culturing Transwell systems. These electrodes have a long and a short leg which allows for the complete submersion of both silver-chloride electrode pellets into the media without risk of damaging the epithelium being measured. Whilst commonly used throughout the industry for routine analysis of model development, significant variation in TEER response can be induced through small changes in the application of the probes to the culture media. Newer, more accurate systems for TEER analysis have been developed to negate this issue through the application of the model to a sterile chamber, removing the human added error. The cell membranes are blanked in fresh medium and the measurement is taken before being area and blank well corrected. The TEER equipment simply measures the conductive properties of the membrane. As such TEER is an indirect tool with some flaws and cannot be used as a predictor of membrane activity or functionality. For example, a membrane could have a low resistance value but still be highly impermeable to a compound and vice-versa. Even paracellular compounds whose transport across the membranes is governed by the abundance of tight junctional complexes is not always accurately modelled by quantification of TEER values alone.

## **1.7 Paracellular permeability, measuring membrane integrity**

In addition to the use of TEER as a measurement of membrane barrier function the integrity of a cellular membrane can also be assessed through the addition of paracellular

transported compounds to the system. These can include compounds such as inulin, mannitol or lucifer yellow. (89,90) These compounds are used in much the same way as a normal transport assay would be set up, namely the compound of known concentration is added into either the apical or basal compartment and then samples after a set amount of time, from which an apparent permeability can be calculated for the model. The downside to using this method to quantify barrier integrity is that it is significantly more time consuming and invasive when compared to the TEER system of measurement. As such, unless the model resistance is being continuously monitored by equipment such as Ussing chambers these compounds are often run alongside the compounds of interest and measured at the end of the assay to ensure that the models have remained intact throughout the assay time period.

## **1.8 Other cells of the intestinal epithelium and mucosa**

### **1.8.1 Goblet cells**

The main function of the goblet cell in the intestine is in the secretion of mucins into the intestinal lumen to create a mucous barrier over the surface of the intestinal epithelium. This mucous layer has several functions and is split into one or two main layers depending on the position within the intestine (Small intestine does not have a secreted mucous layer). Figure 1.10 shows the overall histology of the colonic structure with deep crypts and a higher proportion of goblet cells when compared to other regions of the alimentary tract, namely the small intestine.

The primary function of the mucous layer is as a barrier to pathogens and physical damage of the intestine in addition to be a selective barrier to macromolecules. The mucins that make up the mucous layer have distinct functions. (91) MUC 2 makes up the main secretory glycoprotein and is the backbone of the secreted mucous layer. It is here that the majority of commensal bacterial populations are within the intestinal lumen. (92) Additionally, bioactive molecules such as MUC 1, 3 and 17 are membrane bound mucins and form the membrane bound mucous layer which is present on most cells of the intestinal epithelium. Bacteria of the small intestine are usually only associated with the enterocytes at the villus tips whereas the presence of the secreted mucous layer in the

colon renders the inner membrane mostly sterile with no regular bacterial contact with colonic epithelial cells. (93)

The distribution of goblet cells through the intestine changes with the lowest frequency being in the duodenum with increasing frequency throughout the jejunum and ileum with the largest goblet cell populations being in the distal colon. It has been shown that the amount of mucous produced in the intestine is correlated with the bacterial load, with bacterial colonisation increasing in a proximal-distal direction.

### **1.8.2 Enteroendocrine cells**

The enteroendocrine cells of the intestine are primarily located within the mucosa and only comprise of a small minority of intestinal epithelial cells (<1%) with the highest abundance in the proximal small intestine and the lowest in the distal colon. There are over 30 different hormones secreted asymmetrically throughout the intestine with highly variable functions such as stimulation of peristaltic movement, appetite and enterocyte proliferation. There are many diverse populations of enteroendocrine cells in the gut with the most abundant being the EC (Enterochromaffin) cells which have primary functions in the secretion of serotonin into the intestinal lumen. (94)

### **1.8.3 Paneth cells**

Paneth cells are a secretory cell type like enteroendocrine cells which are located exclusively within the small intestine and appendix. The range of peptides secreted by Paneth cells is large and variable with some of the main secreted peptides being alpha defensins and lysozyme, antimicrobial peptides that when secreted within the crypt act as both as a response to pathogenic invasion and as a method for the homeostasis of commensal gut bacteria. Additionally, Paneth cells have been majorly implicated in the regulation of the stem cell niche itself. In such a high turnover organ such as the intestine careful regulation of the stem cell niche is imperative for the continued homeostasis and function of the intestinal epithelium. A recent study by Pentimikko *et al* showed how Paneth cells potentially attribute to changes in the intestinal epithelium with age through

the production of the Notum protein, an extracellular Wnt inhibitor, as such decreasing stemness maintaining Wnt signalling. (95)

As mentioned previously, Paneth cells differ from the other epithelial cell types of the intestine in that instead of migrating to the villus tip they instead migrate downwards into the crypt. Furthermore, Paneth cells also have a significantly longer lifespan of around 60 days in contrast to 2-6 days of other intestinal epithelial cells. (96)

### **1.8.4 Fibroblasts and myofibroblasts**

The intestinal epithelium is supported by a stromal population of myofibroblasts immediately beneath the epithelial basement membrane. Myofibroblasts in this work and others are characterised phenotypically as being positive for Vimentin (mesenchymal fibroblast marker) and Alpha-smooth muscle actin (Smooth muscle maker) whilst being negative for Desmin (a muscle lineage marker). (97) The location of these cells in close proximity to the epithelial layer suggests a role in the maintaining and controlling the epithelial layer through paracrine and direct-action effects. Epithelial-mesenchymal cross talk has been shown in the past to be of critical importance in the development and maintenance of epithelia throughout the body with signalling breakdowns often resulting in the development of tissue pathologies such as cancers. (98–100) In regards to the effects of paracrine factors on continuous cell lines, Montesano *et al* showed how advanced cellular phenotypes could be observed in MDCK cells when co-cultured with 3T3 fibroblasts. Cells suspended in a collagen gel were able to form a branching tubular morphology similar to that seen *in vivo* (101) which was not seen in cells which were not co-cultured with fibroblasts. Epithelial cells are also able to modulate the function of fibroblast populations. Lichenberger *et al* in their study of epithelial-mesenchymal cross talk in skin derived cells, showed that  $\beta$ -catenin produced by epithelial cells was able to modulate and remodel the underlying dermis. (102) Growing evidence is also been seen in the effects of 3D cultured stromal tissues on the development of epithelia, specifically in the modulation of membrane resistance through tight junction abundance. Matsusaki *et al* (103) showed how co-culture of Caco-2 intestinal epithelial cells with normal human dermal fibroblasts significantly affected the epithelial resistance of the resultant model,

decreasing it in comparison to conventionally cultured control models with further significant decreases in relative mRNA for tight junction proteins (Occludin, Claudin 1,2, ZO-1). Biologically, Caco-2 cells are known to produce heightened non-physiologically relevant epithelial resistance values when cultured by conventional mechanisms. This study highlights the effects of increased model complexity in regards to *in vivo* relevancy and how said conditions drive relevant changes in functional phenotype.

## 1.9 The Villus-crypt axis and the stem cell niche

To facilitate the rapid turnover of intestinal tissues a constant supply of new proliferating and differentiating epithelial cells are required to replace cellular attrition at the villus tip. A resident stem cell population of adult intestinal stem cells is found at the base of the crypt structures found within the intestine. Holistically, the stem cell populations and differentiating epithelium is known as the villus crypt axis and can be considered the single individual functional unit of the intestine. Figure 1.10 shows a simple schematic representation of the villus-crypt axis within the small intestine with the basally located stem cells maintained within their pluripotent states by paneth cell populations located adjacently. Transit amplifying cells are intermediaries between stem cell populations and differentiated enterocytes, undergoing 4 to 5 divisions as they move up the crypt axis. (104) Careful maintenance of stem and transit amplifying cells allows the functional unit of the crypt niche to be functional immortal through a human lifespan. Age related disfunction in intestinal stem cells is a large contributor to age related intestinal disease such as impaired intestinal barrier function (105) , impaired nutrient absorption (106) and an increase in the risk of GI cancers. (107,108) Cells at the base of the crypt can be considered to be less differentiated than the apical surface with increasing differentiation towards the villus tip. Cellular lineage differentiation is controlled by a complex environment of interacting cytokines and secreted factors, Notch, Wnt and BMP playing significant roles. (41,109,110)

## **1.10 *In Vitro* models of the intestinal epithelium**

The Ussing chamber developed by Hans Ussing in the mid-20<sup>th</sup> century is a critical piece of equipment for the measurement of transport kinetics *in vitro*. The first methods utilised to test intestinal function in the human body primarily utilised animal systems to assess pharmacological properties of NCE *in vitro*. (111) Essentially, animal tissues would be excised and prepared before addition into the chamber system in which electrophysical and transport kinetic properties of tissue epithelia could be measured through addition of model compounds designed to stimulate specific responses. The use of these model substrates alongside inhibitory and stimulatory substances could build up a picture of intestinal function over time. MDR1 for example can be inhibited by a number of highly specific compounds, both competitively and non-competitively. Comparison of control and inhibited transport rates of NCE in *in vitro* animal intestinal models can build a picture of NCE MDR1 specificity. Following this logic you can build a picture of the NCE pharmacokinetic properties in a number of transport specific mechanisms.

There is a huge variety of methods for the culture and creation of intestinal models throughout the literature, with many having specific advantages and disadvantages compared to one another such as improved *in vivo* relevancy or expression of a protein absent in the standard model such as CYP3A4 in Caco-2 cells. (18) Most new emerging models of the intestine have moved away from the simplistic monocultures of the past and focus more on the incorporation of multiple cell lines/ types together in a single culture or in a 3D matrix through use of scaffolds and hydrogels. Additionally, new organ on chip approaches to tissue development promise the complexity of 3D co-cultures with the simplicity of high throughput design.

### **1.10.1 Caco-2 Transwell models of the intestinal epithelium**

The Caco-2 cell line as previously described was first isolated by Fogh et al (112) during the 1970s with its early uses as a generic colorectal carcinoma cell line. The cell line as the name would suggest was originally isolated from a colon carcinoma but has a functional protein expression profile able to more closely mimic the small intestines

absorptive properties. Caco-2, since the pioneering papers in 1980s by Pino et al (113) and Hidalgo et al (114) among others, has been the main workhorse for intestinal research and model construction throughout the pharmaceutical and biological communities. Caco-2 cells are characterised by their capability to maturely differentiate over a culture period of 15-21 days into mature enterocytic cells with defined brush border expression, good cellular polarisation as shown by apical lateral tight junction formation and functional transport capabilities through the cells into the underlying “lumen”. Indeed, in 2D cell culture these cells can form heterogenous layers of cells with characteristic monolayer doming upon reaching maturity and are particularly good at modelling the passive absorption of compounds like that of the jejunum.

The Caco-2 cell line is also known to express proteins such as P-gp, MRP1/2 and BCRP which, as efflux ABC transporters, act to pump compounds from the cell back into the intestinal lumen. (115) Naturally, this efflux is an intrinsic way of removing waste compounds from the cell or as a defence mechanism against exogenous ingested toxins.

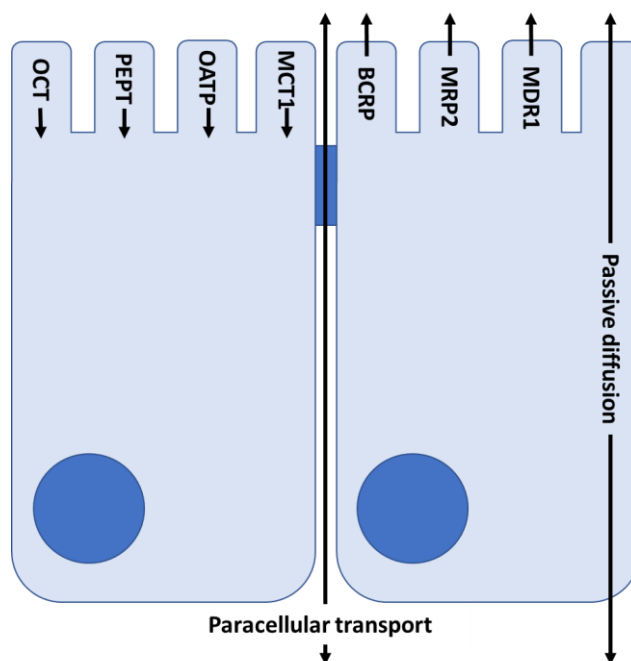


**Figure 1.12: Expression of key proteins by Caco-2 cells in Transwell** – A small selection of the important transporter proteins and cell surface enzymes present in the caco-2 system. Figure modified from Sun *et al* (144)

The result is that the Caco-2 cell line shows a natural resistance to the absorption of compounds which are the substrates of these efflux proteins in a way similar to the *in vivo* intestine (jejunum). Often however, the expression levels of these critical efflux proteins do not mimic that of the intestine, with some under expressed such as P-gp (especially if not allowed to fully differentiate) (116) and others overexpressed in comparison to *in vivo* tissues. As such the Caco-2 Transwell assay is limited in its capabilities to completely model the intestine especially for efflux substrate compounds.(115) Additionally, whilst these cells are positive for the expression of many critical markers of the intestine it is generally known that the Caco-2 cell line is lacking in the correct expression of many important proteins such as CYP3A4, a surface bound enzyme known to be expressed in the intestine at the apical surface of enterocytes, but absent in the Caco-2 cells line. Interestingly, it has been shown that CYP3A4 can be induced through the addition of  $1\alpha,25$ -dihydroxyvitamin D<sub>3</sub>.(115) Whilst CYP3A4 is not directly involved in the absorption of compounds in the intestinal lumen it is a major contributor to pharmacological metabolism in the intestinal lumen. The consequence of a lack of CYP3A4 expression in Caco-2 models can artificially increase relative permeability due to a lack of substrate metabolism.

The Caco-2 model has been key to the development of new drug compounds over the past three decades and has a number of significant advantages over other systems such as:

1. Rapid assessment of drug permeability.
2. Useful for testing how drugs are transported (Pathway analysis).
3. Shows biologically relevant efflux transporter, apical enzymes and brush border proteins of a differentiated small intestine epithelium.
4. Useful for toxicity in addition to permeability studies.
5. Large scale screening application due to easy high throughput culture.
6. Is a well characterised reference model with which to compare NCEs to model drugs in a highly controlled manner.

However, Caco-2 models are well known to be both under representative in some aspects (P-gp expression) whilst over representative in others (heightened TEER values) and as such are not a perfect model for the intestinal epithelium. Indeed, whilst enterocytes are



the most abundant cell type in the small intestine, they are by no means the only cell represented *in vivo*. Transwell Caco-2 models can be modified in a number of physiologically relevant ways such as addition of goblet cells which will be discussed in detail later in this chapter.

### **1.10.2 Stem cells applied to the Transwell system**

Other new methods based on the high throughput Transwell system are able to recreate the entire range of epithelial heterogeneity are being developed through the application of stem cells to the culture system. (117) Wang *et al* (118) showed how ground state intestinal stem cells in their model displayed positive immunofluorescence staining for enterocytic markers such as E-cadherin and Villin whilst also demonstrating a significant mucous component of the model through positive staining of MUC 5ac and MUC 2 mucin proteins. Additionally, cells were shown to multilayer and form villus like structure, drastically increasing the available surface area of the model for functional experimentation such as drug permeability not unlike that seen in *in vivo* tissues. Unfortunately, the functional aspects of this model were not tested in this study but one could see the potential benefits of this model over Caco-2 monolayers. It was hypothesised that with increasing complexity, variation will increase at a similar rate. Therefore, there will always be a place for highly simplistic models such as the Caco-2 systems when high degrees of reproducibility are preferred over *in vivo* replicability.

Intestinal epithelial cells are known to be particularly challenging to culture *in vivo* from primary tissue sources unless highly complex/ expensive media compositions are used. Hence, this is one of the primary reasons why the Caco-2 cell line is still commonly utilised 30 years after its initial isolation. Primary cells are always preferred over cells of carcinoma origin if possible due to phenotypical changes caused during the transformation process. Stem cell culture and application to current *in vivo* model systems is thought to be one method by which the limitations of intestinal epithelial cell culture can be bypassed whilst concurrently creating greater *in vivo* relevancy. Another interesting application of stem cells in model systems generally comes in the creation of either disease state or patient specific models. Cystic fibrosis, cancer, ulcerative colitis and crohns disease are all genetic based examples of where stem cells have been utilised

to create disease state models of the intestine. (119–121) More *in vivo*-like models of the intestine allow a more refined understanding of the basic biological principles underlying the formation of these disease phenotypes. Bio-banks of patient derived stem cells are an exciting direction for future development potentially allowing for, among a great many other applications, a more refined study of drug interactions in people of differing genetic backgrounds or ethnicity, allowing for more tailored personalised medicines. (122) However, as yet intestinal models based on stem cell cultures are limited in their characterisation and adoption in industry compared to older Caco-2 based systems. Essentially, the same issues apply to stem cell based models as does to complex 3D cultures in that they are expensive and technically challenging to culture. The justification for using Caco-2 cells in this project is as such in addition to allowing for easy adoption into an industrial setting. Creating a more *in vivo* relevant model, whilst still relying on the Caco-2 cell line is designed to bridge the gap towards even more *in vivo* mimetic model systems such as stem cell based cultures in the future.

### **1.10.3 Utilising HT29-MTX as a goblet cell component of the epithelial layer**

The HT29 cell line was originally derived from a colorectal adenocarcinoma of a 44 year old Caucasian female (123) and, much like the Caco-2 cell line, was isolated in the 60/70s by Fogh *et al* (8). Most of the cells within the small intestinal epithelium are of enterocytic origin. However, the intestine is also resident to a significant population of mucous producing goblet cells which have important physiological applications on the function of the intestine. Mucous secreted by these goblet cells has a variety of functions such as, aiding the passage of material through the intestine, the creation of a protective barrier effect to exogenous compounds and promoting the sterility effect of mucous on the small intestinal epithelium. (124,125)

The mucous environment within the human body is quite variable dependant on the epithelium in question with over 20 mucin genes identified and tissue specific mucin expression. (92,126–128) Structurally, mucins are built of a protein core consisting mainly of Proline, Threonine and Serine. These so-called PTS domains are then highly

glycosylated to form the mature mucin glycoprotein. Mucins can vary quite drastically in size, structure and function with the smallest being on the scale of hundreds of amino acids and the largest multiple thousands.(124,129) For example MUC2, one of the most abundant mucins in the intestine is thought to be approximately 2200/2300 amino acids long.(125,129) Generally, mucins are split into two categories; the secretive gel forming and the transmembrane mucins.

Differential expression of mucins and mucous layer formation is seen within the intestine; For example, the small intestine has only a single, transmembrane mucous layer whereas in contrast the Colon has a mucous bi-layer containing both transmembrane and secretory components.(125) The inner mucous layer of both the small intestine and the colon generally acts as a sterile environment so as to limit the direct exposure of the surface enterocyte cells to the intestinal bacteria. (126,127,130) It does this by organising into a dense layer, acting as a rudimentary filter. Commensal bacterial population survive in the gut in the secreted outer layers of the colon whose mucous layers are significantly less dense, providing a home for bacterial colonisation. These mucous layers are then slowly digested by the bacteria as an energy source.

Most of the cell lines of the intestine reflect the relative abundance of enterocytes and as such very few goblet cell lineages exist for researchers to utilise. The HT29 line is one of the few which has been shown to, at least partially, mimic the function of a goblet cell; with enhanced mucous secretion over other, terminally differentiated enterocytic cell lines. The HT29 line of cells has can be further split into sub-populations which have been stimulated for a specific phenotype. For example, the HT29-MTX sub clone is created by treatment of HT29 cells with the drug Methotrexate. This treatment and the resultant cell line have been shown to have improved mucous secreting phenotypes over the parental HT29 populations. Attempts at incorporating the HT29-MTX line into cellular models of the intestine have been trailed with variable success, with the majority of Caco-2/ HT29-MTX co-cultures being utilised for model: bacterial interactions rather than pharmacological assessment. (131–134)

## **1.11 Understanding the growing use of CCD-18co cells in intestinal model cell culture.**

The CCD-18co cell line is a normal colon cell line utilised through intestinal cell research as a myofibroblast lineage. It has been noted through the literature that the CCD-18co cells are able to secrete paracrine factors which are able to affect the co-cultured epithelium.(135,136)

For example Visco *et al* (137) highlighted in their 2009 paper the effects of secreted KGF on the development of a co-cultured Caco-2 cells layer. They showed that KGF, both in a pure added form and as a result of CCD-18co or NHF (normal human fibroblasts) co-culture, resulted in the increased expression of Ki67 and carcinoembryonic antigen (CEA). These markers correlate with increased Caco-2 cell proliferation and differentiation respectively. In addition to showing the effects of secreted factors on epithelial cell proteome expression they were also able to show differences between intestinal and skin fibroblast KGF expression. This additional information works to highlight the importance of choosing tissue specific fibroblasts which match the phenotypical characteristics of the model being created. In this instance the CCD-18co cell line was shown to express approximately 3 times the expression of KGF when compared to NHF.(137)

Pereira *et al* (138) created a simple 3D co-culture model of the intestine utilising the CCD-18co and Caco-2 cells for the purpose of creating a new method to test the *in vitro* permeability of the intestine to new compounds, similar to that done in this study. They found that direct co-culture of the cells together on a permeable membrane, created a model with significantly lower TEER values than the conventionally cultured Caco-2 intestinal equivalent. Additionally, the authors tested the functionality of the model, specifically transcellular integrity, by loading the models with insulin and calculating the Papp over time. They showed that the membrane which had been co-cultured with intestinal fibroblasts were more permeable to insulin than the standard Caco-2 membrane layers. The authors in this case attribute the increase in permeability to a decrease in tight junction abundance and “tightness”, although they did not directly test this hypothesis in

their study and they do acknowledge that the changes in insulin permeability could be due to other processes such as an increase in transporter expression of which insulin is a substrate.

There is significant evidence that the co-culture of Caco-2 epithelial cells with fibroblasts has significant effects on the expression of several key transporters such as MDR1, MRP2, BCRP etc. Matsusaki et al (103) showed this in their paper creating a 3D model of Caco-2 cells with neonatal HDF (HDFn). Relative mRNA expression of these key transporters was shown to change significantly over controls when co-cultured with HDFn cells. This has the potential to have large repercussions on the activity of the overall model and as such the importance of the stromal component of any intestinal model shouldn't be underestimated. Changes in transporter expression and relative changes in model functionality in co-culture and 3D systems will be discussed further in chapter 7.

## **1.12 The growing use of advanced 2D and 3D models of the intestine over the current 2D standards.**

The 2D culture of cell lines for use as pharmacologically reliable markers of drug bioavailability and metabolism has been a common practice within the pharmaceutical industry for decades. These model cell lines have significant advantages in that they are; readily available, cheap to use and expand, highly reproducible and quick to culture. The advantages allow for the mass production and use of cheap *in vitro* models, allowing for the high throughput screening of novel drug compounds in early clinical testing. This is especially valuable in the first phases of compound discovery whereby hundreds of compounds with high structural homogeneity may be tested for their pharmacological effects, toxicity and bioavailability. Additionally, most model cell lines when cultured in this method produce highly reproducible cellular models allowing for easy cross-comparison of data between labs, as such increasing the reliability of data from these methods. The disadvantages to utilising simply cultured cells in isolation are many. One of the most significant shortcomings is that they lack the *in vivo* cues, both direct and paracrine, that they would normally be exposed to in the body allowing for a level of genetic drift overtime.

New intestinal models developed to replace the 2D monoculture assays have focussed more on the incorporation of *in vivo* like conditions such as three-dimensionality and through the culture of multiple complementary cell types together. One of the main focusses is in the addition of enterocytes with goblet like cells which can include the parental line HT29 but more often work with induced sub-clones such as HT29-MTX. An example of this can be seen in the work by Beduneau *et al* (139), in which they aim to create a tuneable co-culture model with the enterocytic cell line Caco-2 and the goblet-like properties of the transformed cell line HT29-MTX. They created a simplistic co-culture model which demonstrates a change in the functional characteristics of their model compared to simple control monocultures. They demonstrated changes in P-gp mediated transporter action through measurement of the permeability of the compound Rhodamine 123 to control Caco-2 and their own tuneable Caco-2/ HT29-MTX model. When HT29-MTX cells are added early in the culture period the apparent permeability of the membrane to Rhodamine 123 decreases. A decrease in permeability, e.g. A decrease in the movement of compound from the basal to apical compartments, would suggest a decrease in the active transport incurred by the P-gp present in the model, a non-physiological change compared to human intestinal P-gp levels. The aim of their project is to create a model which can begin to mimic not only the absorption characteristics of the enterocytes but also model the effects of mucous secretion on drug bioavailability. Indeed, the mucous layer of the intestine has been shown to be incredibly important in gut homeostasis and has significant effects on drug availability *in vivo* primarily through the creation of an unstirred water layer on the surface of the intestinal epithelium.(140) In this instance the bio-availability of the drug will rely primarily on the drugs hydrophobicity and its capability to diffuse through this unstirred layer to reach the cells beneath. Additionally, compounds have been shown to be able to bind to mucin molecules such as tetracycline hydrochloride (140), further limiting their availability as mucous is continuously produced and shed from the GI tract. (140,141)

Ferraretto *et al* have also created a simple co-culture model utilising the Caco-2 and HT29 cell lines.(142) Contrastingly, they showed that incorporating the HT29 cell line and mucous layer actually increased the levels of Lucifer yellow apparent permeability (Papp) in their models. As such this highlight the complexity that is added to the model through co-culture, with the mucous layer blocking some compounds but aiding the absorption of

others. Another explanation for the apparent increase in lucifer yellow availability could also be deduced by looking at TEER values. Lucifer yellow is a marker of membrane integrity, moving exclusively through the paracellular absorption pathway. The TEER values of the 70/30 Caco-2/ HT29 layers that the authors created in this paper were markedly reduced compared to Caco-2 controls. As such one might expect an increase in LY movement through the membrane regardless of the presence of a mucous layer. Co-culture Caco-2/ HT29-MTX models in general still suffer from a number of significant drawbacks such as even lower P-gp expression due to the addition of HT29-MTX cells and a lower, but yet not physiological TEER values. (139,142) Goblet cells are specialised secretory cells with little active function in the transport of compounds across the epithelial membrane. Therefore, logically one might expect that adding a higher proportion of non-transport capable goblet cells to the epithelial barrier would correlate with the decrease in the transport capabilities of the epithelial membrane as shown here. This paper can show how simple changes to the culture of cellular models can result in significant changes in the function of the resultant models. However, this paper doesn't look at how the co-culture of the epithelial lineages is affecting the gene and protein expression of the cells themselves, a key consideration when adding cells to a co-culture which don't have intrinsic "functional" epithelial characteristics such as fibroblasts or immune cells.

Recent work has highlighted the effects of the fibroblasts of the underlying supportive mucosae and the ECM microenvironment on the development and maintenance of an epithelial layer of high functionality. Schweinlin *et al* demonstrated this approach in their intestinal model made from decellularised porcine intestinal tissues. They showed that the addition of fibroblasts to the models had significant effects on both the TEER of the organoid model and its permeability to dextran-4000, a commonly utilised measurement of membrane integrity similar to Lucifer yellow.(143) Additionally to the addition of fibroblasts to the model culture they also demonstrated the effects of fluid flow mechanics on the development of the epithelial layer. They described how perfused cultures with physiological sheer stresses were able to influence model functionality, changing its permeability to model drug compounds such as Rhodamine 123, Propranolol and Fluorescein. The underlying mesenchymal layer of the intestinal crypt has also been shown to be critical in the maintenance of the intestinal stem cell niche, allowing for long

term homeostasis of the stem cell population and the rapid turnover of stem cells into new epithelium seen in the intestine. (144,145) Additionally, the paracrine effects of myofibroblasts have been shown to induce differentiation and proliferation of epithelia. For example, Visco *et al* showed that the myofibroblast cell line CCD-18co was able to have effects on Caco-2 monolayers through the paracrine actions of keratinocyte growth factor (KGF), increasing the expression of the proliferation marker Ki-67 and the differentiation marker carcinoembryonic antigen (CEA). (137)

Compound absorption studies are commonly done utilising the Transwell system, whereby a population of cells are cultured on one side of the permeable transport insert to create a polarised epithelial tissue model. Whilst widely accepted as the standard for compound screening, the Transwell system suffers from the same negatives as mentioned above in addition to lacking morphological similarity to the tissue being modelled. One of the main research directions being explored is the replacement of the Transwell systems with more physiological systems which incorporate multiple cell types, in 3D matrices and with tissue specific ECM deposition. There are multiple ways in which this is being achieved with one of the main being the utilisation of tissue specific stem cells to create organoid models. These organoid models often contain the most complexity of the advanced *in vitro* tissue models with multiple differentiated cell types and complex tissue specific 3D architecture. The work on intestinal organoids was first driven by the lab of Hans Clevers *et al.* (146) Their work demonstrates the value of utilising intestinal organoids as models for human physiology in a number of ways; through their work in the identification of the function of paneth cells in the intestinal crypt, (96) understanding the roles of cancer mutation in intestinal cancers (147) or in disease states such as cystic fibrosis (148) to name a few. One major drawback to the use of organoid cultures for routine drug testing is the inability to control the macro structure of the model. Organoids naturally develop in suspension and as such are naturally shaped as a mass of cells with the functional epithelial layers orientated to the inside of the macro-structure. In order for application to a drug validation platform a single, layered epithelium with consistent directional polarity is necessary for Papp studies, something organoid cultures, as yet cannot recapitulate.



Other promising methods for the creation of 3D models with physiological function rely on the use of scaffolds, both biological and synthetic, for the 3D culture of cells. Biological scaffold generally encompass extracellular matrix constituents such as collagen matrigel gels in their simplest form all the way up to decellularised tissues for the most complex models. (143,149–151) Decellularised tissues in particular have clinical applications in organ transplant/ regeneration research with the idea being that decellularised scaffold could be recellularised with patient derived stem cells, forming a new, functional tissue that could be transplanted with reduced fears of rejection. (152,153) Synthetic scaffold encompass any material of non-biological origin. For example, work discussed in this study primarily focusses on the use of Alvetex<sup>®</sup>, a polystyrene polyHIPE scaffold treated to allow the routine culture of human and animal cells. Other examples could include electrospun scaffolds which can be constructed from a wide range of available materials with properties fine tuned to the use of the model. The advantages and disadvantages of each system will be discussed later in detail in chapter 5.

### **1.13 Regulatory alignment and the challenges of applying new, more complex models to the drug development process.**

Studies involving humans suffer from a number of key challenges. Experiments using *in vitro* tissue segments and Ussing chamber devices are extremely expensive, technically challenging and low throughput. Whereas, *in vivo* human clinical trials are all of the aforementioned plus ethical considerations regarding screening of potentially toxic compounds in human subjects. As such, the FDA and other bodies have accepted model systems such as Caco-2 as surrogates for human intestines, albeit primarily for assessment of passive paracellular transport. (154)

The Biopharmaceutics classification system (BCS) was originally developed as a tool to assess the correlation between jejunum permeability rates and drug absorption to facilitate the approval of Class I drugs known to be highly permeable and dissolvable within the intestine, important for an orally administered compound. BCS is used to classify compounds and is widely accepted in both academia and industry. Classifications fall into 4 categories; Class 1, are highly soluble and permeable, Class 2 have low solubility but

high intestinal permeability, Class 3 are highly soluble but have a low permeability and Class 4 are both poorly soluble and have low permeability.

The code of federal regulations forms the basis of regulatory approval of new, innovative cellular products. These regulations cover a huge range of considerations such as biological evaluation, safety, manufacturing processes (GMP) etc. (155)

What is clear is that current research pharmacokinetic practices do not function at close to tissue relevant levels in many instances. The development of new and more advanced research tools for the study of drug dynamics in the intestine is key to optimising the drug discovery and validation process. Regulatory approval for bodies such as the FDA required multidisciplinary expertise and must include those with experience in fields such as medicine, pharmacology/toxicology, cellular therapies, and cell biology, as such compounding the complexity for regulatory approval.(156) *In silico* modelling is one new area within which new regulatory models are being approved for use.(157) It is hoped that these models can accurately predict the permeability characteristics of certain compounds through simple model layers such as Caco-2 without the requirement for “wet work” in the lab. These models would have a clear advantage over current practices however validating their efficacy is complex, primarily due to the inherent heterogeneity of Caco-2 populations dependant on origin and culture conditions. Any *in silico* model would need to pool data sets of Caco-2 of varying origins to assess for any variability. Other methods such as 3D models are more able to mimic the structural complexity of *in vivo* tissues and, as such, can help to bridge the gap between current standards and animal models. However, increasing model complexity through the addition of additional cell lines compounds on the already inherent variability in Caco-2 cells. Regulatory approval would require extensive characterisation and validation to assess for any changes in cellular phenotype. The challenge for new systems lay in the demonstration of significant improvement over current standards sufficient to justify the complex process which is FDA approval.

## 1.12 Project Hypothesis

The main hypothesis of this project was that, through use of either paracrine influences or 3D culture, the Caco-2 Transwell system could be improved to better recapitulate both the gross anatomy of the human intestine and its functional characteristics. Furthermore, it was hypothesised that simple Caco-2 3D models could be adapted for use in a 96 well system to better allow for adoption and use throughout industry as a direct replacement for the current Caco-2 Transwell gold standard. Additionally, the base architecture of the 3D model could be further developed to include additional cell lines such as goblet cells to expand the functionality of the resultant model.

## 1.13 Project Aims

This project aims to create both advanced Transwell model variants of the Caco-2 standard through the co-culture of Caco-2 membranes with conditioned media from fibroblasts of varying origins and to create a 3D model of the intestine, again using Caco-2 cells in order to demonstrate how increased complexity allows for tissue models with more *in vivo* like properties.

Additionally, work undergone in this project will include the analysis of such models including structural assessments through a range of techniques such as histological and immunological stains in addition to TEM and SEM. Assessment of model function will be achieved through the use of an Ussing type chamber measuring the apparent permeability of model drug compounds within each model system. Values gained in this work will be cross referenced against both internal and literature derived values for standard Caco-2 models in addition to assessment against human tissue values, again gained from the literature where possible. It was hypothesised that the advanced co-culture Transwell models and the full mucosal 3D models of the intestine will improve the structure and function of models, as such improving the *in vivo* reliability of these models compared to data with human tissues.

## **1.14 Project Objectives**

1. Develop and optimise a novel 3D mucosal intestine equivalent utilising Alvetex Scaffold and multiple cell types including; Caco-2, CCD-18co, HDFn and HIC fibroblast lineages.
2. Develop and optimise the culture of advanced paracrine Transwell models utilising conditioned media gained from 2D cultured CCD-18co, HDFn and HIC cell lines.
3. Structurally characterise all models through the use of techniques such as histological staining of paraffin embedded samples in addition to immunostaining from key protein elements of cellular function and SEM/ TEM analysis of cellular ultrastructure.
4. Utilising model drug compounds functionally characterise the models created during this study to assess their comparability to Caco-2 controls and human tissues. Another aim was to design and create novel tools for the culture and functional analysis of intestinal equivalents.
5. Introduce HT29-MTX cells into the paracrine Transwell models to assess the effect of the mucous layer on the function of the epithelial models.
6. Postulate and test a potential mechanism for any differences in structural and functional phenotypes observed in the characterisation of the models.

## **2. Materials and methods**

### **2.1 Materials**

#### **2.1.1 Chemicals and miscellaneous lab reagents**

Kits for periodic acid Schiff (PAS) (RRSK15-100) and Massions Trichrome with Methyl blue (RRSK20-100) were both obtained from Atom scientific (UK). Rhodamine 123, Verapamil Hydrochloride, Etoposide, Methotrexate, Atenolol, Propranolol, Lucifer yellow, L-alanine-4-nitroanilide hydrochloride, 4-Nitroanaline, Hanks Buffered salt solutions (HBSS) and DPX (#06522-100ml) were obtained from Sigma Aldrich, UK. 3-(4,5-Dimethylthiazol-2-yl)-2,5-Diphenyltetrazolium Bromide (#158990050) used for MTT studies of metabolic activity was obtained from Fisher Scientific along with embedding wax (#12624077), Methanol (#11976961), Acetone (#11453483), Isopropanol (#10588630) and microscope slides (#10149870). Vectorshield plus DAPI was obtained from Vector labs (#H1500)

#### **2.1.2 Cells and cell culture media components**

Caco-2 (#86010202) and HT29-MTX (#12040401) cells were obtained from the European Collection of Authenticated Cell Cultures (ECACC) (Porton Down, UK) and were used between passages 44-50 and 55-60 respectively. CCD-18co (CRL-1459) fibroblasts were obtained from ATCC (UK) and used between PDL 10 and 15. HDFn cells (#C0045C) were obtained from Thermo Fisher Scientific (UK) and were used up to passage 4. HIC cells were isolated in lab as described later. HIC cells were used up to passage 5.

High glucose containing DMEM with Pyruvate (#21969-035) cell culture media and supplements (L-glutamine (#25030-081), penicillin and streptomycin (#15140-122 10,000 U/ml), FBS and 0.25% Trypsin (#25200-056)) were obtained from Thermo Fisher Scientific. DMSO (#D8418) and Trypan Blue (#T8154-100ml) were obtained from

Sigma. KGF (#100-19) recombinant protein was obtained from PeproTech. KGF ELISA kit (#DKG00) was purchased from R&D systems. Cryovials for the long term storage of cell populations were purchased from Greiner (#121263)

### 2.1.3 Plastic ware

Cell culture grade polyester Snapwell inserts 12 mm diameter with 0.4µm pore size were purchased from Sigma Aldrich (CLS3407-24EA). 12 and 24-well Alvetex<sup>®</sup> Scaffolds (12 (AVP005-12), 24 (AVP012-48)) and 96 (Prototype) well sized Alvetex Scaffold inserts were purchased from Reprocell, UK. Alvetex<sup>®</sup> Scaffolds were purchased at 200µm thickness.

Supplier	Item	Catalogue #
Greiner Bio-one	6 well plates	657160
	12 well plates	665180
	24 well plates	662160
	T25 cell culture flask	658175
	T75 cell culture flask	660175
	T175 cell culture flask	690175
	50ml Falcon centrifuge tube	227261
	15ml Falcon centrifuge tube	188271
	50ml syringe	SYR5-L5
	Cell storage cryovials	121263
Sarstedt	50ml cell culture stripettes	86.1689.001
	25ml cell culture stripettes	86.1685.001
	10ml cell culture stripettes	86.1254.001
	5ml cell culture stripettes	86.1253.001
	P1000 pipette tips	70.762
	P200 pipette tips	70.760.002
	P10 pipette tips	70.153

Fisher Scientific	0.2µm Syringe filter	15181499
	96 well plate	10334791
	1ml Syringe	15889142

**Table 2.1: Summary of plastic materials consumed during the course of this project including cell culture grade and general lab reagents.**

## 2.1.4 Antibodies

Antibodies were purchased from a number of sources dependant on price, availability and efficacy for a given use. Dilutions shown here were determined based on manufacturer recommendations. Antibodies used in this study are detailed below:

Supplier	Target protein	Catalogue #	Use & Dilution
Abcam	Collagen I	ab34710	Immunofluorescence (1/100 Dilution)
Abcam	Fibronectin	ab23750	Immunofluorescence (1/500 Dilution)
Abcam	Villin	ab130751	Immunofluorescence (1/200 Dilution)
Abcam	E-cadherin	ab1416	Immunofluorescence (1/200 Dilution)
Abcam	Collagen IV	ab6586	Immunofluorescence (1/100 Dilution)
Abcam	αSMA	ab7817	Immunofluorescence (1/100 Dilution)
Abcam	Elastin	ab9519	Immunofluorescence (1/100 Dilution)
Abcam	Tubulin	ab176560	Immunofluorescence (1/100 Dilution)
Abcam	Cyto-Keratin	ab118817	Immunofluorescence (1/200 Dilution)

Protein Tech	Collagen III	22734-1-AP	Immunofluorescence (1/100 Dilution)
Santa Cruz Biotechnologies	Vimentin	sc-6260	Immunofluorescence (1/ 50 Dilution)
Santa Cruz Biotechnologies	Occludin	sc-133256	Immunofluorescence (1/ 50 Dilution)
Santa Cruz Biotechnologies	MDR1	sc-55510	Immunofluorescence (1/ 50 Dilution)
Santa Cruz Biotechnologies	Desmin	sc-23879	Immunofluorescence (1/ 50 Dilution)
Santa Cruz Biotechnologies	MRP2	sc-71603	Immunofluorescence (1/ 50 Dilution)
Thermo Fisher Scientific	Donkey anti rabbit (488)	A21206	Secondary antibody (1/ 500 Dilution)
Thermo Fisher Scientific	Donkey anti mouse (488)	A21202	Secondary antibody (1/ 500 Dilution)

**Table 2.2: List of antibodies used in this project including secondary Alexa Fluor conjugated secondaries.**

### 2.1.5 qPCR primers and PCR reagents

qPCR primers used in this study were taken directly from literature resources prior to optimisation and use within this study. Below is a list of the relevant primers utilised here:

Gene of interest	Code	Reference
GAPDH (S) GAPDH (AS)	ATGGGGAAGTGAAGGTCGGAG TCGCCCTTGATTTTGGAGG	(158)
MDR1 (S) MDR1 (A/S)	GCCAAAGCCAAAATATCAGC TTCCAATGTGTTCGGCAT	(159)
BCRP (S)	TGCAACATGTACTGGCGAAGA	(159)



BCRP (AS)	TCTTCCACAAGCCCCAGG	
MRP2 (S)	TGAGCAAGTTTGAAACGCACAT	(159)
MRP2 (A/S)	AGCTCTTCTCCTGCCGTCTCT	
OATP-B (S)	TGATTGGCTATGGGGCTATC	(159)
OATP-B (AS)	CATATCCTCAGGGCTGGTGT	
Occludin (S)	CTCCCATCCGAGTTTCAGGT	(160)
Occludin (AS)	GGAGTGTAGGTGTGGTGTGT	
Villin (S)	AGGATGATGTGTTCTACTAGATGTCTG	(159)
Villin (AS)	GTTGCTGCGGCCTTCTTC	

**Table 2.3: qPCR primers including reference of origin.**

Supplier	Item	Catalogue #
Bio-Rad	Hard-shell PCR plates	HSP9601
	Quick start SYBR	1725271
Thermo Fisher	PCR plate seals	AB0558
Qiagen	RNeasy Plus mini kit	74134
Promega	GoScript reverse transcriptase	A2791
Sigma	RNase ZAP	R2020

**Table 2.4: qPCR reagents for the isolation of RNA, reverse transcription into cDNA and expansion SYBR based detection methods.**

## 2.2 General methods

### 2.2.1 General cell culture

Cells were routinely cultured in T75 or T175 cell culture flasks maintained in a humid environment at 37°C, 5% CO<sub>2</sub> in air. In 2D culture, cells were fed with their respective media, prewarmed to 37°C in a temperature-controlled water bath, at a rate of every other day unless otherwise stated. Cells were deemed ready for passage at 80% confluency. Cell lines were visually checked for contaminants daily and checked by phase microscopy immediately prior to media change.

### **2.2.2 Passaging**

Cells were removed from the incubator and washed twice in sterilised PBS prior to incubation with 0.25% Trypsin/EDTA (2500mg/L) containing phenol red (2ml T75, 4ml T175). Cells were incubated in a humidified environment at 37°C, 5% CO<sub>2</sub> for 3 minutes or until cells had detached from the tissue culture surface. For strongly adherent cell lines such as Caco-2 this could take up to a maximum of 10 minutes. If after 10 minutes cells were still attached to culture plastic flasks were gently tapped to liberate cells into solution. Cells were liberated and collected by gentle washing on the cell surface with 10% FBS containing culture media. This also acts as the trypsin neutralisation step. The media volume was then topped up to 15ml in a Falcon tube. To remove trypsin containing media, cells were centrifuged for 3 minutes at 500g unless otherwise stated. Media was then removed being careful not to disturb the cell pellet which was then subsequently carefully resuspended in an appropriate volume of fresh prewarmed culture media (usually 1ml). Cells were re-seeded into new sterile cell culture flasks at the appropriate density as per the manufacturer's instructions or were counted for use in experimental procedures.

### **2.2.3 Trypan Blue cell counting**

To allow for the accurate seeding density within Transwell and 3D models or when manufacturers guidelines specified cell seeding numbers per flask, total cell number must be quantified prior to use. Cells were passaged as above and resuspended in an appropriate volume of fresh cell culture medium (usually 1ml but more if large quantities of cells were being counted so as to ensure accurate sampling of cell numbers). A 9:1 dilution of trypan blue: cell suspension was created in a separate Eppendorf tube. This cell suspension is carefully pipette mixed (gently to avoid unnecessary cell damage) before being added to a haemocytometer. Live/dead cell counts can be made microscopically by counting the ratio of dyed (Blue) cells to dye excluded (White) cells, with dye exclusion indicating cellular viability. A total of 3 quadrants on a standard haemocytometer were

counted to create an average of one quadrant with a known volume of 0.1µl. Raw cell numbers were converted into total cell population by the following equation.

$$\frac{\text{Raw quadrants values}}{3} = \text{Quadrant average}$$

$$\text{Quadrant average} \times \text{Dilution factor} = \text{Dilution corrected}$$

$$\frac{\text{Dilution corrected}}{\text{Quadrant volume (ml)}} = \text{Total cellular population}$$

## 2.2.4 Cryopreservation

Cells were passaged as previously described. Cells were resuspended in an appropriate volume of 10% FBS containing complete culture medium and counted with a haemocytometer. The volume for the correct number of cells to be frozen per vial (usually 1-2 million) was calculated and added to a 1ml cryovial. DMSO and 10% complete cell culture medium was added to each tube to create a final volume of 1ml and a final DMSO concentration of 5%. Cell vials were then added to a Mr Frosty™ (Thermo-Fisher) for a minimum of 24 hours at -80°C. Cells were then placed at -150°C or in liquid nitrogen vapour phase for long term storage until required for use.

## 2.2.5 Cell revival

Cells vials were quickly warmed in a 37°C water bath until only small ice crystals remained floating in suspension. Cells were gently resuspended and added to an appropriate volume of 10% FBS cell culture medium. Cells were allowed to attach for 24 hours in an appropriately sized flask ( <1,000,000 = T25, 1,000,000-2,000,000 = T75) before DMSO containing medium was removed and replaced with fresh pre-warmed

culture media. Any unattached cells after 24 hours were carefully removed and pelleted before resuspension and addition back into the culture flask. Unattached cells after this point were discarded with media changes.

## 2.3 Embedding techniques for study samples

### 2.3.1 Paraffin embedding

Samples to be processed for paraffin embedding were first washed in PBS before being fixed in 4% Formalin for a minimum of 30 minutes at room temperature but more generally overnight at 4°C. Actual fixation length was determined by the sample type with tissue samples preferably being fixed for longer at cooler temperatures to ensure complete tissue fixation. Samples were removed from fixative and washed twice in PBS before being dehydrated through a series of ethanol concentrations 30-100% (v/v) for a minimum of 10 minutes per concentration with an extended incubation time of 30 minutes for 100% ethanol solutions. Samples were then incubated for 30 minutes in HistoClear II (National diagnostics) at room temperature. Paraffin wax is added to HistoClear II samples to make a final ratio of 50:50 HistoClear: Paraffin for 30 minutes at 65°C. Finally, samples

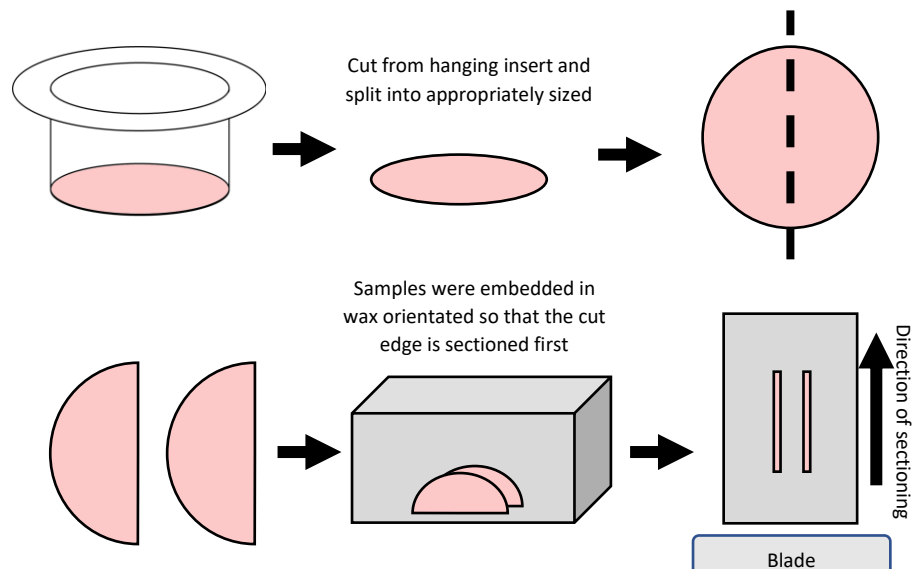


**Figure 2.1: Schematic representation of the embedding and sectioning process for both Transwell and Alvetex® based intestinal models** – Samples are cut in half and embedded with the cut end to the bottom of the block (first to be trimmed). Blocks are sectioned at 5µm.

were washed twice in 100% Paraffin at 65°C for a minimum of 20 minutes per wash (longer for larger tissues before embedding in cassette moulds and allowing to cool.

### **2.3.2 OCT embedding**

Samples to be processed for OCT embedding were first gently washed in PBS to remove all culture media. Samples were then fixed for 10 minutes in an ice cold mixture of 50:50 methanol: acetone. OCT freezing moulds were made from aluminium foil and clearly labelled with the sample name before samples were added. OCT freezing solution was added to the foil moulds. Samples were cut to size and completely submerged in OCT for a period of 15 minutes before freezing. Liquid nitrogen was added to a polystyrene freezing box below a metal plate. Liquid nitrogen was not allowed to touch the surface of the metal plate as freezing will occur at vapour phase. Samples were added to the pre-chilled plate and left to fully freeze for a period of 30 minutes. Samples were stored at -80°C for long term storage.

## **2.4 Immunohistochemistry**

### **2.4.1 Paraffin embedded samples**

Paraffin embedded 4% PFA fixed sections (7µm) were dewaxed for 15 minutes in Histoclear I and brought to water through a series of alcohol solutions (90, 70% ethanol). Samples were antigen retrieved by incubation for 30 minutes at 95°C in citrate buffer.

Should permeabilisation be required samples were incubated for 5 minutes in a 0.5% Triton/ PBS solution. Samples were washed in PBS before being blocked to limit non-specific protein binding in a 10% Normal Goat Serum (NGS)/ PBS solution for 30 minutes at room temperature. Primary antibodies were incubated in a 1%NGS, 0.1% PBST solution at an antibody specific concentration for a minimum of 1 hour at room temperature or overnight at 4°C. Following primary antibody incubation samples were washed 3 x 5 minutes in 0.1% PBST to remove any unbound and non-specific primary antibody. Fluorescently tagged secondary antibodies were diluted at an antibody specific

concentration in PBS and incubated with the samples for a minimum of 30 minutes at room temperature. Samples were protected from light at this stage onwards in order to protect the samples from photobleaching. Samples are then washed 2x in 0.1% PBST. Nuclei were stained using either DAPI or Hoechst which were added at an active concentration to the final wash step post-secondary antibody incubation. Excess nuclei stain was removed by one final wash in PBS followed by mounting with soft set Vectorshield fluorescent mounting media. Slides were sealed before imaging through the minimal application of clear nail varnish to the edges of the coverslip.

### **2.4.2 OCT embedded samples**

Samples were allowed to warm to -20°C prior to sectioning. Sections were allowed to air dry for 10-20 minutes before being washed gently in PBS to remove excess freezing media. Samples were then fixed in ice cold 50:50 methanol: acetone before being brought back to water. OCT embedded methanol: acetone sections do not require antigen retrieval or permeabilisation steps. All other steps in this protocol are the same as Section 2.4.1 Step 4 onwards.

### **2.4.3 Wholemout cell coverslips, wells and Transwell inserts.**

Cells were fixed in ice cold methanol: acetone for 10 minutes at -20°C. Methanol: acetone fixed cells do not require antigen retrieval or permeabilisation steps. All other steps in this protocol are the same as Section 2.4.1 Step 4 onwards.

For all immunochemistry negative controls were used routinely (Samples processed without primary antibody incubation). Where possible positive controls of either human tissues or specific cell lines were used.

## **2.5 Histological staining techniques of paraffin embedded samples.**

### **2.5.1 Haematoxylin and eosin**

Paraffin embedded samples were sectioned at 7µm and heat dried to glass slides. Slides were de-paraffinised in Histoclear for 15 minutes. De-paraffinisation was followed by rehydration through ethanol to water (100, 95, 70%) for 1 minute per ethanol concentration. Samples were then placed in haematoxylin for 5 minutes in order to stain the cellular nuclei. Excess stain was washed off in water followed by a 30 second wash in alkaline ethanol to blue the stained nuclei. Samples were dehydrated in ethanol (70, 95%) once more and incubated in eosin solution for 30 seconds. Finally, samples were rapidly washed in 95 and 100% (v/v) ethanol and cleared in Histoclear for 10 minutes. Slides were then mounted with a coverslip and left to dry before viewing under a microscope.

### **2.5.2 Periodic acid Schiff stain**

Paraffin embedded samples were sectioned at 7µm and heat dried to glass slides. Slides were de-paraffinised in Histoclear for 15 minutes followed by rehydration through ethanol (100, 95, 70%) to water for 1 minute per ethanol concentration. Deparaffinised sections were oxidised in periodic acid solution for 5 minutes. Samples were then gently washed in distilled water and stained with Schiff reagent for 20 minutes at ambient temperature. Slides were then washed in running tap water until appearing pink macroscopically followed by staining of the cellular nuclei with Mayer's Haematoxylin for 1 minute. Finally, samples were differentiated in 0.5% (v/v) acid alcohol and blued in running tap water. Samples were then dehydrated through an ethanol series, mounted and allowed to dry before viewing and imaging.

### **2.5.3 Masson trichrome stain with methyl blue**

Paraffin embedded samples were sectioned at 7µm and heat dried to glass slides. Slides were de-paraffinised in HistoClear for 15 minutes followed by rehydration through ethanol (100, 95, 70%) to water for 1 minute per ethanol concentration. Weigert haematoxylin was prepared by mixing part A and B solutions in a 50:50 ratio immediately prior to use. Samples were incubated with Weigert haematoxylin for 20 minutes at room temperature. This was followed by quickly washing with water and differentiating in 1% acid alcohol. Nuclei were blued by rinsing in water. Next slides were stained with Ponceau Fuchsin solution for a period of 5 minutes then rinsed in water. Slides are then differentiated in phosphotungstic acid for 15 minutes and stained with methyl blue for 1 minute without rinsing. Finally, samples were rinsed in distilled water, dehydrated through alcohols, cleared and mounted. Slides were allowed to dry before viewing and imaging.

### **2.6 Scanning electron microscopy (SEM)**

Biological samples were fixed for SEM for 1 hour in Karnovsky fixative. Samples are washed 3x with 0.1M Cacodylate Buffer at pH 7.6. Karnovsky fixed samples were further fixed for a period of one hour in a 1:1 ratio of 2% (v/v) Osmium Tetroxide and 0.2M Cacodylate buffer at pH 7.4. Samples were then dehydrated through ethanol gradients (30-100% v/v ethanol) for 3 x 5 minutes per ethanol solution. The dehydration process was completed through use of critical point drying equipment. Critically dried samples were orientated on chips and sputter coated with platinum. Critically dried and coated samples were stored under vacuum. Images were taken on an S5200 Field emission scanning electron microscope.



## **2.7 Transmission electron microscope (TEM)**

Samples were fixed in Karnovsky fixative followed by osmium tetroxide treatment and dehydration in the same way as detailed for samples which were processed for SEM. Post dehydration samples were infiltrated with a 1:1 mixture of Ethanol (100% v/v) and propylene oxide for 15 minutes. This was followed by a further infiltration step of propylene oxide alone for 15 minutes. The resin used for embedding biological samples was the epoxy resin Agar 100 (Agar scientific, UK). Resin was pre-prepared at 37°C following kit instructions prior to use. Samples were infiltrated with 1x wash of 1:1 propylene oxide and Epon resin for 15 minutes followed by 3x 1 hour infiltrations with Epon resin at room temperature on a rotating incubator. Samples were added to setting moulds and left to set at 37°C for at least 24 hours prior to sectioning. Ultra-thin sections were created using either a glass or diamond knife before being stained with uranyl acetate and lead citrate. Sections were then viewed under the H7600 Transmission electron microscope

## **2.8 Drug permeability transport assays.**

Transport studies were conducted utilising a standard Ussing chamber set up (WPI, UK) with the chamber insert determined by the model/ tissue being tested. The general protocol for the experiments follows routinely utilised procedures. Transport buffer consisted on HBSS pH 7.4 with 2mM supplementary glucose. Stock solutions of all drug compounds were dissolved in a substance specific vehicle (DMSO/ Ethanol) before being added to the HBSS.

Models to be tested were carefully removed from culture, washed twice in PBS and added into the Ussing chamber system. TEER measurements were taken both immediately before addition to the chamber and at the end of the experiment. 15ml of 37°C prewarmed HBSS was carefully added to both the apical and basal sides of the chamber system simultaneously, media was kept at 37°C throughout the experimental period through use of a circulating heated water jacket. Transport media was mixed and oxygenated utilising a bubble lift of 95% Oxygen and 5% CO<sub>2</sub>. Drug compounds were spiked into the Ussing

chamber at T=0. Timepoints were taken every 30 minutes by removal and replacement of transport media directly from the test chamber, either the apical or basal side. Lucifer yellow was run alongside test compounds as an additional measure of barrier integrity throughout the experimental procedure where possible. Compound concentration within the transport medium was assessed through use of either the compounds fluorescent properties or through detection with HPLC equipment.

Papp was calculated utilising the following equation;

$$P_{app} = \frac{V_R * dC_R}{dt * A * C_{D0}}$$

Whereby  $V_R$  is the volume of the receiver compartment  $dC_R/dt$  is the change in the analyte concentration of the receiver compartment over time,  $A$  is the area of the transport interface and  $C_{D0}$  is the concentration of the donor compartment at time zero.

## **2.9 qPCR analysis of cell models and tissues**

### **2.9.1 mRNA purification and extraction from whole cell and tissue lysates.**

Firstly, mRNA was extracted from biological samples through use of the RNeasy RNA extraction kit (Qiagen, USA).

Cells were lysed through addition of buffer RLT and mechanical disruption of the cell layer with either a cell scraping device or a pipette tip. Cell homogenate was then further homogenised through passing through a blunt 20-gauge needle tip at least 5 times. An equal amount of alcohol was added to the cell lysate. The alcohol/ lysate mix was then added to an RNeasy spin column and spun for 15 seconds at 10,000 RPM. Pass through was discarded and DNase digestion was performed on column. Cell lysate was then washed once with RW1 buffer before being spun for 15 seconds at 10,000 RPM. Samples were then washed twice with RPE buffer before being spun for 15 seconds and 2 minutes

respectively at 10,000 RPM. Pass through was discarded each time. Finally, the spin column was added to a fresh collection tube and 30µl of RNase free water was added. This was then spun for 1 minute at 10,000 RPM to collect the purified RNA.

Purified RNA was either stored at -80°C or was quantified using a Nanodrop and reverse transcribed immediately.

### **2.9.2 mRNA quantification of purified cell model lysates.**

mRNA isolated from cell models through RNA easy extraction kits was quantified through the use of a Nanodrop spectrophotometer device.

Briefly, 2µl of RNA free H<sub>2</sub>O was added to the Nanodrop and to allow for a blank to be read. 2µl of purified mRNA is then added to the reading pedestal and the top level carefully lowered. The droplet is visually checked to be in contact with both the top and bottom reading points before mRNA quantification. mRNA levels are read and concentration is automatically quantified by the software provided by the manufacturer. In addition to mRNA concentrations, 260/280 and 260/230nm reading ratios are calculated. Samples were deemed sufficiently contaminant free when 260/280 and 260/230 ratios were  $\geq 1.8$  and  $\leq 2.2$ .

Samples were quantified only immediately prior to reverse transcription and were re-evaluated after a freeze-thaw cycle.

### **2.9.3 mRNA reverse transcription into single strand complementary DNA**

Reverse transcription of known amounts of mRNA was done using the GoScript™ Reverse Transcriptase Kit from Promega. 500-2000ng of mRNA was added to a single reverse transcription reaction. Kit specific amounts of random primer mixes and reverse transcriptase were added to the mRNA sample. The mixture was gently mixed and then

ran on a thermocycler utilising manufacturer stated temperature and time settings using the following protocol:

Reaction buffer is made from constituent kit components by adding 4µl of GoScript™ Reaction Buffer, Oligo(dT) to 2µl of GoScript™ Enzyme Mix. Up to 5µg of RNA was added to a reaction vessel containing premixed reaction buffer and volume is made up to a total of 20µl using Nuclease-Free water. Pipette mix the reaction buffer/ RNA solution. Add reaction tubes containing Buffer/ RNA mix into a thermocycler set to the following settings:

Step	Temperature (°c)	Time (Min)	No# of cycles
Anneal Primer	25	5	1
Extension	42	60	1
Inactivation	70	15	1
Hold	4	∞	1

#### **2.9.4 cDNA quantification and comparative analysis to controls.**

cDNA was quantified utilising an SYBR based detection method. For initial optimisation of primers (list below) multiple concentrations of cDNA were tested with the most appropriate carried forward into testing. Primer efficiency was determined through analysis of melt curve dynamics and by plotting concentration curves onto a graph and calculating the  $R^2$  value. Primer specificity was tested by running qPCR end products through a polyacrylamide gel and comparing product length against the Primer BLAST database.

## 2.10 Bradford assay assessment of protein abundance

Samples were lysed directly with MPER lysis buffer (Sigma, UK), scraped and added to a 1.5 ml Eppendorf tube before being mechanically homogenised every 5 minutes for 30 minutes using a vortex mixer. Samples were then sonicated for 30 minutes and centrifuged for 20 minutes to pellet cell debris. Cell lysates not used immediately were stored at -80°C until further processing. Total protein concentration of the cell lysates was quantified by Bradford assay. Briefly, 5µl of cell lysate was added to a standard clear bottom 96 well plate. 195µl of Bradford reagent (Bio-Rad) was added to the wells containing the lysed samples. Colour was allowed to develop for at least 10 minutes at room temperature on an orbital shaker set to 100rpm. Colour change was assessed on a plate reader at 595nm wavelength. Protein levels were quantified against a standard curve of known BSA concentrations.

## 2.11 Quantification of aminopeptidase activity

Aminopeptidase activity was quantified through the catalysation of the cleavage of the substrate L-alanine-4-nitroanilide hydrochloride into the breakdown product 4-nitroaniline. Briefly, 0.5ml of prewarmed 1.5mM of L-alanine-4-nitroanilide hydrochloride solution was added to the apical compartment of both Transwell and 3D models. These models were then incubated for a period of 1 hour under standard cell culture conditions on an orbital shaker set at 100rpm. After 1 hour 100µl of the cleavage product was transferred to a well of a clear 96-well plate. All samples were analysed in duplicate replicate to assess for intraassay variation and pipetting errors. A standard curve was created from a stock solution on 4-nitroaniline to allow for cleavage product quantification. Wells were quantified at 405nm using a plate reader and blank values were used for sample correction. End data was expressed as activity per cm<sup>2</sup>/ minute using the following equation:

$$\text{Raw absorbance} - \text{Blank} = \text{Blank reduced value}$$

Blank reduced value is then used to find the concentration of 4-nitroaniline utilising the equation of the standard curve line.

$$\frac{\text{Calculated 4 – nitroaniline concentration}}{\text{Area of the model}} = \text{Activity/Cm}^2$$

## **2.12 Standard Caco-2 Transwell experimental set up and conditioned media creation and application.**

For the creation of Caco-2 Snapwell® (Corning) cultures, 80% confluent flasks of 2D grown Caco-2 cells were passaged utilising the standard passaging technique mentioned earlier. Caco-2 cells are counted utilising a haemocytometer and Trypan Blue staining before being diluted in a 15ml falcon tube (Corning) to a concentration of 250,000 cells per 500µl of complete growth medium. 500µl of the cell mixture is added to the apical compartment of the Snapwell insert, resulting in a seeding density of 250,000 cells per insert or 223,000 cells/cm<sup>2</sup>. Caco-2 cells were allowed to settle and attach overnight (at least 12 hours) before experimental conditions were changed.

Conditioned media was created by incubating complete Caco-2 medium with fibroblast cells for a period of 24 hours. 25ml of media was added to a confluent T175 flask of fibroblasts at a medium density of 0.143 ml/cm<sup>2</sup>. After 24 hours of fibroblast media conditioning, media was removed from the cells and sterile filtered through a 0.4µm pore syringe filter. Before addition to Transwell models, conditioned media was diluted at a 1:1 ratio with fresh complete DMEM to ensure the media was sufficiently nutritious for continued Caco-2 growth and development. Conditioned media was added to Snapwell Transwell experiments on day 2 at the first media change post Caco-2 seeding. Conditioned media was stored at 2°C for a maximum of 7 days before use.

Caco-2 Transwell models were media changed by careful aspiration of both apical and basal compartments before addition of 500µl and 3 ml of fresh media apically and basally respectively. Caco-2 Transwell models were cultured for a minimum period of 21 days with media changed on alternative days. Caco-2 Transwell models were used in experiments between 21 and 25 days.

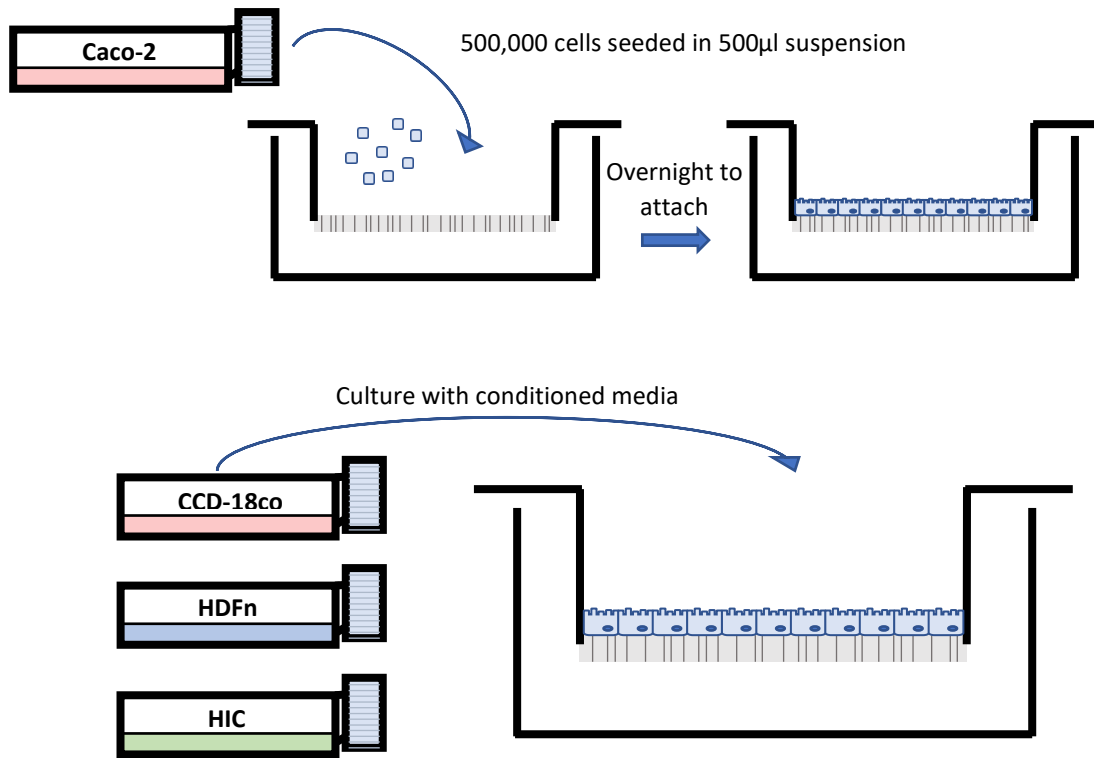


**Figure 2.2: Schematic representation of the process for setting up and culturing Transwell based intestinal models in control and conditioned media systems**

## 2.13 Human tissue processing and staining

Human tissues were obtained both pre-fixed and fresh from Bioptra (Glasgow, UK). All tissue samples were cut into pieces no larger than 5mm<sup>3</sup>. Pre-fixed tissue samples were processed for paraffin wax embedding following the standard protocol mentioned in section 2.3.1 of alcohol dehydration followed by HistoClear and paraffin incubation and embedding. Fresh tissue samples were cut to appropriate sized pieces and processed in a

number of ways. Paraffin, OCT and resin embedding were done following the previously mentioned protocols (Sections 2.3.1, 2.3.2 & 2.7). All human tissues were used and processed under HTA licence following HTA guidelines.

## **2.14 Outgrowth of myofibroblast primary cell cultures from human tissue sections**

Myofibroblast outgrowth was achieved from the culture of human tissue slices in the following method. Firstly, Human intestinal tissue was received from Biopta and washed twice in sterile PBS containing 3% P/S. The muscular layers of the tissues were carefully dissected from the tissue leaving only the epithelium and underlying mucosa. A 6 well plate was scored in a grid pattern with a sterile scalpel. The dissected tissue was placed onto the scored grid mucosa side down and incubated overnight in FBS containing concentrations of 4% Penicillin and Streptomycin (P/S) and gentamycin and amphotericin (G/A). After incubation overnight tissue sections were confirmed to be attached to the plate through gentle rocking. Tissue sections were incubated in FBS for up to 48 hours to allow for attachment. When confirmed to be attached tissue sections were carefully submerged in Hams F12 media (Fisher) containing 10% FBS, 4%P/S and 2%G/A. Submerged tissues were carefully media changed daily and microscopically checked for contaminants (early contamination was generally by bacteria whereby later contamination was usually fungal). Cell outgrowth was usually first seen 7-10 days after initiation of cell culture.

Cells were passaged by carefully removing tissue sections from the plate and then following standard trypsinisation and seeding procedure as described previously. Tissues were added back into culture in fresh plates and cultured as described above. Passaged cells were cultured in standard DMEM conditions (10%FBS with supplemented L-glutamine and P/S). Once tissues were no longer viable for cell culture they were disposed of through standard human tissue disposal practices as described by the HTA.



## 2.15 Generation of a 3D intestinal model

The generation of the intestinal model has been optimised for both the 24-well and 96-well formats of Alvetex Scaffold®. This methods section will detail the process for both of the Alvetex® system although it is important to note that the functional model analysis was undertaken in the 96 well system.

Firstly, Alvetex® Scaffold® is prepared for the seeding of cells through the submergence into 70% ethanol for a period of at least 15 minutes. Scaffold are then wash twice in PBS to remove the ethanol prior to the addition of the cells. Fibroblast cells are seeded into the Scaffold at the air liquid interface at a density of 250,000 cm<sup>2</sup> (192,000 for 24 well, ~50,000 cells for 96 well model). Fibroblasts are seeded in a volume of prewarmed media which is appropriate for the Scaffold size in use ( 24-well = 200µl, 96-well = 25µl). Once seeded these cells are left at the air liquid interface (base compartment filled with media) for 12 hours (overnight) to allow for complete surface attachment before being submerged and cultured submerged for a period of 7 days within the scaffold in an 12-well standard culture plate (24-well model) or an Alvetex® Deep well plate (ADW) (96 well model). Media is changed every 48 hours for optimal cell feeding (4.5ml in the 24 well format and 1.5 ml in the 96 deep well format). After 7 days of initial fibroblast culture further seeding of fibroblasts into the models is done twice more at 2 day intervals (day 7 and 9) at the same seeding density per cm<sup>2</sup> as previously described. At 14 days of total cell

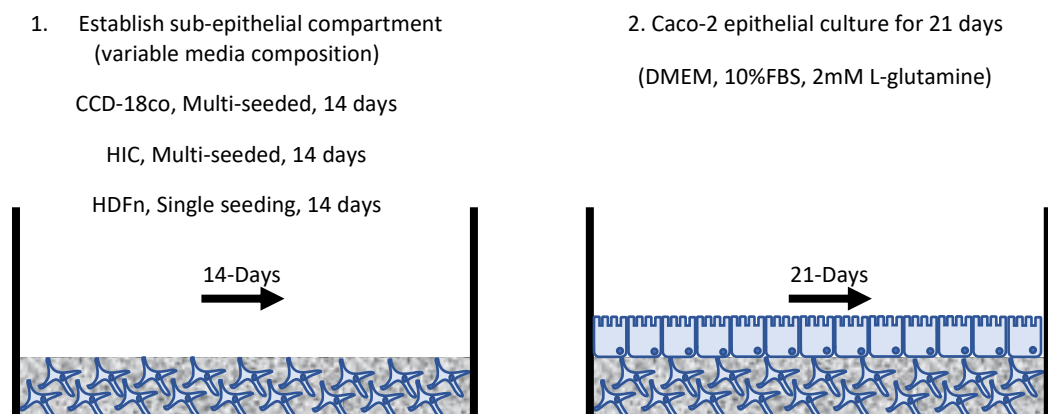


**Figure 2.3: Schematic representation of the process for setting up and culturing Alvetex® based intestinal models.**

culture the fibroblast models are seeded with the cellular epithelium of Caco-2 colon adenocarcinoma cells (ECACC) at a density of 220,000 cells per cm<sup>2</sup>. After epithelium seeding models are cultured submerged in standard Caco-2 DMEM based media (described previously) for a further period of 21-25 days before use in downstream analysis.

## **2.16 Epithelial electrophysical resistance measurements of Transwell models of the intestine.**

Samples are first washed in pre-warmed sterile PBS before fresh pre-warmed media is added to the models. Models are placed into a 37°C incubator and allowed to normalise for a period of at least 30 minutes. During this time TEER electrode probes (WPI) were first sterilised in 70% ethanol for a period of 5 minutes before being placed in sterile PBS to allow for electrode normalisation for 30 minutes before readings are taken by placing the electrodes into the model media (longer probe to the outside of the model) and reading the values from the attached EVOM TEER equipment. Models were removed from the incubator immediately prior to taking a measurement and were taken as quickly as possible in order to limit any variations due to temperature fluctuations. Raw TEER measurements are processed to remove blank values which are taken at the same time as the non-blank wells through the culture of an insert without cells alongside experimental cultures, and then normalised to culture area to give the final value. It is important to remember that raw TEER measurements are inversely proportional to the culture area so normalisation is achieved through multiplication of culture areas rather than division.

## **2.17 Statistical analysis of study data**

All data analysis achieved in this study was done utilising Prism5 software (GraphPad). A standard unpaired students T-test was used where statistical significance was required between 2 data sets. Study sets containing greater than 2 data sets were analysed by one-way ANOVA with Tukeys post-test analysis. \*\*\*=p <0.0005, \*\*=p<0.005, \*=p<0.05.

### **3. Development Transwell co-culture models**

#### **3.1 Introduction**

##### **3.1.1 Caco-2 Transwell, the gold standard for intestinal pharmacokinetics.**

The intestine is a highly complex 3D architecture consisting of multiple populations of distinct, functionally niche cells with the capability to cross talk with one another, existing together in a complex 3D architecture to maintain intestinal homeostasis and function. It is well understood that current Caco-2 Transwell models do not recapitulate the complexity of the intestinal mucosae; indeed they were never designed too with current models only supporting a single cell type within a basic 2D architecture. For the most part however, Caco-2 monocultures remain the primary model used within industry due to a number of reasons, the most important of which are:

1. Simplicity allows for mass production,
2. Simplicity allows for highly reproducible data with low inter/intra-assay variability.
3. Less likely for human error in model construction

That isn't to say that attempts haven't been made in the past to improve this model. HT29 and HT29-MTX cell lines were one of the first to be used and have been cultured within Caco-2 Transwell models in order to attempt to create a mucous barrier which is present in *in vivo* intestine.(161) Addition of these cells has had some success and is discussed further in the following chapter.

##### **3.1.2 Understanding the role of sub-epithelial fibroblasts on the homeostasis of the intestinal epithelium.**

The role of the sub-epithelial cell populations in the intestine and similarly the addition of myofibroblast cell cultures into the Caco-2 models was, until recently, a poorly

understood method in which to improve Caco-2 models' phenotypes. Conventional, thinking placed fibroblasts as having limited function in the development and maintenance of the epithelium, serving a simple role in ECM secretion and tissue structure. Advances in the understanding of stromal-epithelial dynamics indicates the sub-epithelial cell layers have significant effects on epithelial growth, barrier integrity, repair and cellular differentiation. (162–165)

Sub-epithelial mucosal fibroblasts in the intestine have also been implicated in a number of disease phenotypes. Crohn's disease for example is an inflammatory condition of the bowel which ultimately leads to tissue fibrosis with excessive ECM deposition and fibroblast activation protein (FAP) expression.(166) inflammatory bowel disease (IBD) and ulcerative colitis are similarly related conditions involving excessive tissue fibrosis. (167)

### **3.1.3 Methods for the advancement of model *in vivo* relevancy.**

In recent decades there has been an increase in the general focus towards tissue engineering more complex, tissue mimetic models and the culture of multiple cell lines together in both 2D and 3D environments. This has resulted in significant advances in the creation of biological tissue models representative of many tissue types within the body, such as; Skin, Bone, eye, brain, muscle etc. Skin models, for example, are one of the most thoroughly developed and routinely created models of tissue encompassing the full range of technologies available. (168–170) Indeed, establishment of continuous keratinocyte cultures *in vitro* and the creation of simple keratinocyte layers for clinical use within human patients go as far back as 1975 with the work by Rheinwald and Green (169,171). These first Keratinocyte constructs were simple monolayers and were reasonably effective for their simplicity. To use skin as another example, epidermis of structurally relevant composition can be created utilising modern techniques by simply growing a monoculture of keratinocytes on a semi-permeable 2D membrane such as Transwell or Millicell. (168) The uses of these models often go beyond simple *in vitro* models utilised within the lab and can be applied to *in vivo* applications as tissue implants or devices.

*In Vitro* intestinal models have undergone significant changes and advancement over the past decade in order to more accurately recapitulate the full intestinal mucosae rather than the simple mono-cell type epithelium of current gold standard industrial models. Primarily, work has focussed on the creation of improved intestinal mucosae models encapsulating not only the epithelial layer, but also the sub-epithelial fibroblasts populations. These have the most relevance in the pharmaceutical industry as test pads for the pharmacokinetic and pharmacodynamic properties of novel and pre-clinical drug compounds. Whilst the purpose of this study is to improve upon the conventional Caco-2 system, current simple cellular models of the intestine are already able to drastically reduce the reliance of animal models which in the past have been shown to be quite often non-physiologically aligned with human ADME phenotypes. (172) Even simple changes to current mono-culture models such as the inclusion of goblet cells to create the mucous layer (142) or co-culture with myofibroblasts to provide the tissue specific paracrine microenvironment (173) could have significant effects on the reliability of simple models.

### **3.1.4 Understanding the importance of 3D architecture on model development.**

In a stepwise increase in model complexity, the provision of a 3D scaffold for the culture of cells could provide a more physiological platform of 3D mechano-transduction, resulting in improved cellular phenotypes. Even extremely small changes in substrate composition such as matrix stiffness can lead to large effects in cellular phenotype such as driving EMT in tumour cells (174) and regulating ECM deposition. (175) Dependent upon the model created the applications of complex 2D or 3D models are not necessarily limited to drug ADME and can range from potential tissue transplants to simple models for understanding the cancer dynamics.

A very recent study by Castano *et al* (176) demonstrated how 3D scaffolds can be designed to more accurately mimic the tissue being modelled. Utilising a UV setting polymer hydrogel they were able to reliably create villi structures in their 3D scaffold. Scaffolds could then be functionalised and cultured with Caco-2 cells. These cells were shown to create confluent layers across the full length of the scaffolds 3D architecture.

Actin viewed by immunofluorescence staining demonstrated a well formed monolayer structure with clear apical polarisation of cells. ZO-1 staining was also utilised to display the presence of tight junctions between adjacent cells. Interestingly TEER measurement of models showed a highly significant reduction in the epithelial resistance of 3D models which correlated well with an increase in FITC-dextran 4kDa, a commonly utilised marker for trans-cellular passive permeability. This system demonstrates a physiological change based on substrate morphology alone. It was hypothesised that this model could be further improved by either establishing fibroblast populations within the polymer scaffold or through paracrine conditioned media of physiologically important cell lines as achieved in this chapter.

It is hoped that the creation of more tissue mimetic models will have the effects of lowering the time and cost taken to identify and test potential compounds, savings which can be passed onto consumers and allow for greater funding to be allocated to compound discovery. This chapter will focus first on the simple modification of conventionally cultured Caco-2 models through their culture with the released paracrine factors of human fibroblast cells of varying origin.

## **3.2 Hypothesis, aims and objectives**

### **3.2.1 Hypothesis**

The hypothesis for this chapter was that the co-culture of Caco-2 cells with the paracrine influences of fibroblast conditioned media would have significant effects on the development and function of the Caco-2 epithelial layer. Furthermore, it is hypothesised that fibroblasts from differing origins, (CCD-18co - Intestinal Carcinoma, HIC – Normal Intestine, HDFn – Normal skin) would have different mechanistic effects on the Caco-2 layer and work through a variety of morphogenic pathways. Finally, it is hypothesised that KGF is one of the main signalling molecules present in the fibroblast conditioned media based on similar experiments in the literature. (137,177)

### **3.2.2 Aims**

The aims of this chapter were to develop simple co-culture alternatives to the 2D Caco-2 Transwell cell model, currently the gold standard in the industrial pharmacokinetic testing of drugs and novel drug compounds.

Initially, the aim was that Caco-2 models were to be modified through culture of Caco-2 cells in conditioned media from a variety of sources. Namely, these were: HDFn (Human Dermal fibroblasts from neonatal foreskin biopsies), CCD-18co (Non-transformed colonic adenocarcinoma cell line) and HIC (Human intestinal cells isolated from normal Human small intestine biopsies). All of the above cell lines have been shown to possess myofibroblast like properties either in the literature or from in-house testing and as such were deemed suitable for conditioned media testing.

The project aimed to characterise 2D Caco-2 models through a number of techniques such as immunofluorescence staining and qPCR analysis of key proteins of interest.

The final aim of this chapter is to provide a mechanism of action for some/ all of the paracrine medias utilised in the creation of advanced Transwell models.

### 3.2.3 Objectives

The objectives of this chapter are summarised below;

- Characterise the structural and protein expression phenotype of HDFn, CCD-18co and HIC cells.
- Investigate the effects of conditioned media on the structure of Caco-2 cells grown on Transwell inserts.
- Investigate the effects of conditioned media on epithelial resistance and cell metabolic rate.
- Understand the development of tight junctional complexes overtime both in control and paracrine fibroblast conditions.
- Characterise key protein expression in Transwell CCD-18co conditioned media through immunofluorescence.
- Understand the relative abundance of mRNA of key proteins in different media conditions
- Provide evidence of a mechanism of action for the changes seen in Caco-2 epithelial layers when co-cultured in conditioned media.



### **3.3 Methods**

#### **3.3.1 Immunohistochemical characterisation of intermediate filament expression in CCD-18co, HDFn and HIC cells.**

HIC cells were isolated from Human Small intestinal biopsies as previously described (Section 2.14). CCD-18co, HDFn and HIC cells were seeded onto the base of 12-well plates at a density of 25,000 cells per well. Cells were cultured in standard DMEM composition for a period of 5 days before being fixed and stained as described previously (Section 2.4.3). Cells were stained for Vimentin,  $\alpha$ SMA, Desmin, Actin, Elastin and alpha tubulin. Stained cells were imaged on a Zeiss 880 confocal microscope and images processed utilising Zen Blue software.

#### **3.3.2 Characterisation of Caco-2 and HT29-MTX in pre and post confluency states through immunohistochemistry.**

Caco-2 and HT29-MTX were seeded on the base of 24-well cell culture plates at a density of 12,500 cells per well and cultured in a standard DMEM composition for a period of 5 days for pre-confluency samples and 10 days for post-confluency samples. Samples were fixed as described previously (Section 2.4.3) and processed using the standard immunostaining protocol (Section 2.4.1). cells were stained for Pan-cytokeratin, Occludin, MDR1, MRP2, Actin, vimentin and E-cadherin. After staining samples were all imaged on a Zeiss 880 confocal microscope and images processed utilising Zen Blue software.

#### **3.3.3 Co-culture model formation**

Caco-2 Transwell models were formed as described in Section 2.12. Briefly, 80% confluent flasks of Caco-2 cells were passaged and counted with a haemocytometer. Cellular viability was assessed with Trypan blue. 250,000 Caco-2 cells were diluted in 500 $\mu$ l of pre-warmed DMEM before addition to each Snapwell insert. Caco-2 cells were allowed to attached overnight before addition of conditioned media.

Conditioned media was created as previously described (Section 2.12) with media changed ever two days for a minimum of 21 days total culture time. TEER measurements were taken every 7 days as described previously (Section 2.16).

After 21 days models were processed for histological characterisation by both 4% PFA fixation for paraffin embedding (Section 2.3.1) and methanol: Acetone fixed for OCT embedding (Section 2.3.2).

### **3.3.4 Trans-Epithelial Electrical Resistance (TEER) measurement of epithelial layers**

Cell cultures were removed from the incubators and media changed as per normal procedure using 37°C prewarmed 10% FBS containing complete medium. Cell cultures were returned to the incubator and allowed to equilibrate for at least 30 minutes prior to TEER measurement. Measurements of Transwell models were done using the EVOM2 Voltohmeter with STX2 Chopstick probes. Chopsticks were completely submerged in media and allow 5-10 seconds to equilibrate before a measurement was taken. Raw TEER measurements were normalised to cell culture area utilising the following equation.

$$R_{\text{TISSUE}} (\Omega) = R_{\text{RAW}} - R_{\text{BLANK}}$$

$$R_{\text{TISSUE}} (\Omega) \propto 1/M_{\text{AREA}} (\text{cm}^2)$$

$$\text{TEER}_{\text{MODEL}} = R_{\text{TISSUE}} (\Omega) \times M_{\text{AREA}}$$

[1] TEER measurement techniques for *in vitro* barrier model systems

### **3.3.5 MTT assay for the assessment of metabolic function**

Cell layers to be assessed by MTT assay were first washed in sterile PBS twice to remove all phenol containing medium and moved to a clean cell culture plate . Thiazolyl Blue Tetrazolium Bromide salt was dissolved at a concentration of 1mg/ml into sterile PBS

and allowed to reach 37°C in a thermostatically controlled water bath for at least 30 minutes before use. 1ml of Thiazolyl Blue Tetrazolium Bromide solution was added to cell layers and incubated in the dark at 37°C in standard cell culture conditions for 1 hour.

After 1-hour cell layers were washed twice in PBS to remove excess Thiazolyl Blue Tetrazolium Bromide solution. Cells were lysed and the developed dye was liberated in an appropriate amount of acidified isopropanol. Liberation volume was the same for all experiments where a direct comparison between conditions was made. Solution intensity was then quantified on a plate reader at 450nm.

### **3.3.6 Assessment of conditioned media and KGF on the metabolic activity of Caco-2 epithelial cells.**

For conditioned media and KGF spiked media assays, Caco-2 cells were seeded into 12-well plates at a density of  $2.86 \times 10^3$  cells per  $\text{cm}^2$  (~10,000 cells/ well) and allowed to attach in complete Caco-2 DMEM culture media for a period of 2 days before the addition of conditioned/ spiked media. MTT assays were performed as described in section 3.2.5 on wells every 48 hours to assess for changes in cellular metabolism up to a maximum of 14 days. MTT values were normalised to the protein concentration of a sister well, set up at the same time as the analysis well and assessed through use of a Bradford assay (protocol as previously described in Section 2.10).

### **3.3.7 Assessment of tight junction formation in conditioned media treated cellular layers through immunostaining of the tight junction protein Occludin.**

Control and conditioned media wells were set up at a density of 10,000 cells per well as previously described in 12-well plates (Section 3.2.6). Samples were fixed by Methanol: Acetone fixation (Section 2.3.2) every 2 days for a total of 10 days (5 samples). Occludin was stained utilising normal immunostaining techniques (Section 2.4.3) with Occludin

diluted at manufacturer recommended levels. Samples were imaged utilising a Zeiss 880 confocal microscope and images were processed utilising Zen Blue software.

### **3.2.8 Immunostaining of wholemount Transwell models**

Transwell models were set up as described in section 2.12 and cultured for a minimum of 21 days. Transwell models were fixed and immunostained following the previously described protocol (Section 2.4.3)

### **3.3.9 qPCR analysis of Transwell model lysates**

Transwell models were set up and cultured as previously described (Section 2.12) for a total of 7, 14 and 21 days to understand the development of Caco-2 Transwell layers over time in culture. Section 2.9 describes the basic protocol for the isolation of mRNA from cell and tissue samples. Specifically, Transwell Snapwell models were removed from culture and washed twice gently in room temperature PBS. Snapwell models were removed from the outer support and placed into clean 6 well plates. 500µl of ice cold RLT buffer was added to the apical side of the cells model. A pipette tip was used to scrape the surface of the Transwell to remove all of the cellular material. Scraped material was then placed into 500µl Eppendorf vials and placed on ice for further processing. The remaining protocol is identical as to what is described in Section 2.9.

### **3.3.10 Aminopeptidase quantification of Transwell models compared to 3D cultures.**

Conditioned media, KGF spiked Snapwell Transwell models and 3D Alvetex models were created as specified in sections 2.12 and 2.15 respectively. Aminopeptidase activity quantification assay was performed as described in section 2.11.

### **3.3.11 Keratinocyte growth factor (KGF) conditioned media experiments in Snapwell format inserts.**

Snapwell Caco-2 models are set up as previously describes (Section 2.12) and allowed to grow under normal conditions for a period of 48 hours in order to allow for normal cellular attachment to the Snapwell surface. KGF (PeproTech) is reconstituted in sterile PBS and nominally stored at -20°C before use. KGF is spiked into freshly prepared, prewarmed complete DMEM medium at an experimental dependant concentration. Snapwell cultures are then grown normally up to a total culture time of 21-25 days with KGF spiked medium changed every 48 hours.

Processing of Transwell Snapwell layers for histological structural analysis was done as described in sections 2.3.1 and 2.3.2 for paraffin and OCT embedding procedures respectively. Wholmount Immunostaining of KGF spiked samples was processed as previously described (Section 2.4.3)

### **3.3.12 MTT assessment of KGF treated Caco-2 layers.**

Caco-2 layers were set up as described in Section 3.2.6. KGF treatment was started 48 hours after initial seeding with variable concentration of KGF added to different cellular conditions. MTT assay assessment of metabolic activity of treated cell layers was achieved as previously described (Section 3.2.5).

### **3.3.13 Assessment of tight junction formation in KGF treated cell layers through immunostaining of the tight junction protein Occludin.**

Control and KGF treated wells were set up at a density of 10,000 cells per well as previously described in 12-well plates (Section 3.2.6 and 3.2.7). Samples were fixed by Methanol: Acetone fixation (Section 2.3.2) every 2 days for a total of 10 days (5 samples).

Occludin was stained utilising normal immunostaining techniques (Section 2.4.3) with Occludin diluted at manufacturer recommended levels. Samples were imaged utilising a Zeiss 880 confocal microscope and images were processed utilising Zen Blue software.

### **3.3.14 ELISA quantification of KGF abundance in conditioned media samples.**

CCD-18co, HDFn and HIC fibroblasts were seeded at a density of 50,000 cells per either 6-well plate or 96-well (deep dish) format Alvetex Scaffold® insert. Cells were allowed to grow for a period of one week before the addition of Caco-2 conditioned media (As described previously) to “treated” wells or fresh DMEM to control wells. Media was changed every 2 days throughout the culture time. After a further 7 days of culture (14 days culture total) 1.5 ml of fresh DMEM was added to all samples and cultured under normal conditions for 24 hours. After 24 hours 1 ml of media was removed from each condition and placed in a sterile deep dish plate following the preestablished assay plate map. Conditioned media samples were placed at 2-8°C for no longer than one hour before being used in the ELISA assay.

2D cell layers and 3D models were placed in RLT DNA/RNA lysis buffer (Qiagen). 3D models were fully lysed, with lysate stored at -80°C before analysis.

ELISA kit for KGF quantification was purchased from R&D systems. The assay was run following the manufacturers guidelines.

Briefly;

Standards curve was created and 100µl Assay diluent added to each well of the plate. 100µl of standard, sample or control was added to each well (200µl well volume total). Plate was incubated at room temperature for 3 hours. Plate was taped dry and washed 4 times in assay wash buffer. 200µl of KGF conjugate was added to each well and incubated for a total of 1.75 hours. Repeat step 3. 200µl of substrate solution was added and incubated in the dark for 30 minutes. 50ul of stop solution was added and the plate

was gently mixed (100rpm rotating plate) for 5 minutes in the dark. Plate was read at 450nm with 570nm correction.

### **3.3.15 DNA concentration quantification for KGF ELISA normalisation**

DNA lysates stored at -80°C (Section 3.2.12) were thawed and vortexed 5 x 30 seconds to ensure complete cell lysis and DNA dissolution.

DNA quantification was performed utilising a DNA quantitation kit (Sigma).

Briefly:

Contents were thawed and DNA standard was incubated at 50°C for 30 minutes. 100µg DNA stock was created in MG H<sub>2</sub>O. 2µg/ml bisBenzimide H 33258 solution was created in MG H<sub>2</sub>O and 190µl of solution added to each assay well of a flat bottom 96 well plate. 10µl of standard, sample and blank was pipetted in to relative wells in duplicate. Plate was read at 360nm excitation and 460nm emission at room temperature.

### **3.3.16 Transport assays utilising the Ussing chamber system for Transwell and Alvetex Lucifer Yellow permeability assays**

Transport studies were conducted utilising a standard Ussing chamber set up (WPI, UK) with the chamber insert determined by the model/ tissue being tested. The general protocol for the experiments follows routinely utilised procedures. Transport buffer consisted on Hanks buffered saline solutions, (HBSS) (Sigma , UK) pH 7.4 with 2mM supplementary glucose. Stock solutions of all drug compounds were dissolved in a substance specific vehicle, usually DMSO, Ethanol or dH<sub>2</sub>O, before being added to the HBSS.

2D Transwell conditioned media models to be tested were carefully removed from culture, washed twice in PBS and added into the Ussing chamber system. A CHM5 chamber from WPI was used for all Snapwell culture experiments.

3D models were all cultured in the 96 well format for Ussing chamber analysis (detailed further in chapter 7). Models were carefully snipped from the strip holder after washing before being added to the custom made Ussing chamber systems. A small amount of plastic supports were left attached to the model to allow for a snug fit within the chamber when the opposite ends are sandwiched together. TEER measurements were taken both immediately before addition to the chamber and at the end of the experiment.

15ml of 37°C prewarmed HBSS was carefully added to both the apical and basal sides of the chamber system simultaneously utilising 50ml syringes fitted with 2mm capillary tubing. Transport media was kept at 37°C throughout the experimental period through use of a circulating heated water jacket. Transport media was mixed and oxygenated utilising a bubble lift of 95% Oxygen and 5% CO<sub>2</sub> (BOC, UK). Models were allowed to acclimatise to the assay system for a minimum of 30 minutes before t=0.

Drug compounds were spiked into the Ussing chamber at T=0. Timepoints were taken every 30 or 60 minutes by removal and replacement of transport media directly from the test chamber, either the apical or basal side. Lucifer yellow was run alongside test compounds when pertinent as an additional measure of barrier integrity throughout the experimental procedure. Compound concentration within the transport medium was assessed through use of either the compounds fluorescent properties and a spectrophotometer or through detection with HPLC equipment.

The apparent permeability ( $P_{app}$ ) of the models was calculated utilising the following equation;

$$P_{app} = \frac{V_R * dC_R}{dt * A * C_{D0}}$$

Whereby  $V_R$  is the volume of the receiver compartment  $dC_R/dt$  is the change in the analyte concentration of the receiver compartment over time,  $A$  is the area of the transport interface and  $C_{D0}$  is the concentration of the donor compartment at time zero.  $P_{app}$  values show in this thesis are converted into reasonable number for comparison by amplifying



the Papp value by  $1 \times 10^6$ . This amplification step is not technically necessary but is standard procedure for the reporting of Papp values throughout the literature.

### 3.3.17 qPCR analysis of conditioned media and KGF spiked Caco-2 2D layers.

Caco-2 cells were passaged and counted utilising the normal protocol as described previously (Section 2.2.1). Cells were then seeded into T25 flasks at a density of 50,000 cells per flask. n=1 of each condition was set up with replicates cultured at weekly intervals from a separate bank of parental Caco-2 cells. Cell layers were cultured for a period of 21 days to allow for full differentiation prior to lysing and analysis. Cells were lysed and processed utilising the standard Qiagen miniRNA kit, as described previously (Sections 2.9). Analysis was achieved with a SYBR based detection system, as described previously (Section 2.9.4) along with complementary primers to sequences of interest.

Primer sequences used are detailed below

Gene/ Protein of interest	Sequence	M W	Secondary Structure	Primer Dimer	Melting temperatur e	GC content (%)
MDR1/ABCB 1 (S)	GCCAAAGCCAAAAT ATCAGC	608 8.00	N	N	63.3	45.00
MDR1/ABCB 1 (A/S)	TTCCAATGTGTTCGG CAT	548 0.54	V.W	N	62.7	44.44
MRP1/ABCC 1 (S)	GGGCTGCGGAAAGT CGT	529 1.44	N	N	66.6	64.71
MRP1/ABCC 1 (A/S)	AGCCCTTGATAGCCA CGTG	578 8.75	N	N	65.2	57.89
MRP2/ABCC 2 (S)	TGAGCAAGTTTGAAA CGCACAT	676 7.42	V.W	N	66.6	40.91
MRP2/ABCC 2 (A/S)	AGCTCTTCTCCTGCC GTCTCT	627 5.00	N	N	65.8	57.14
BCRP/ABCG 2 (S)	TGCAACATGTACTGG CGAAGA	647 9.23	N	N	66.6	47.62
BCRP/ABCG 2 (AS)	TCTTCCACAAGCCCC AGG	540 4.50	V.W	N	66.4	61.11
Villin (S)	AGGATGATGTGTTCC TACTAGATGTCTG	864 9.6	M	N	65.3	42.86
Villin (AS)	GTTGCTGCGGCCTTC TTC	544 8.5	N	N	66.1	61.11
Occludin (S)	CTCCCATCCGAGTTT CAGGT	604 4	W	N	65.3	55
Occludin (AS)	GGAGTGTAGGTGTGG TGTGT	631 5	N	N	60	55

GAPDH (S)	ATGGGGAAGTGAAG GTCGGAG	664 0	N	N	61.52	57.14
GAPDH (AS)	TCGCCCTTGATTTTG GAGG	582 6	W	N	57.74	52.63

## **3.4 Results**

### **3.4.1 Morphological characterisation of stromal and epithelial cell lines.**

All cell lines utilised within this study were first cultured in conventional 2D cell culture techniques on cell treated culture plates and flasks. Figure 3.1 & 3.2 shows the morphological characteristics of the cell lines utilised within this study, The commercially available stromal cell lines namely the CCD-18co and HDFn (Figure 3.1 A-B, E-F) lines exhibit a stellate morphology without defined cellular junctions, classical of fibroblast and myofibroblast phenotypes. Cellular size at low passage is similar between the two cell lines with similar growth patterns in conventional 2D culture. The HIC (Human intestinal cells) cells (Figure 3.1 C-D) utilised here were isolated from human small intestine tissue explants (Biopta, Glasgow, UK as detailed in section 2.14). These cells have the same structural similarities to the commercially available cells with a noticeable stellate morphology and lack of cellular junctions.

Contrastingly, the epithelial cell lines utilised here, Caco-2 and HT29-MTX (Figure 3.2 A-D) exhibit a flattened continuous monolayer of cells with clear cellular junctions and a “cobblestone” morphology of growth. When cultured at low confluency these cells grow in colonies, staying in contact with each other rather than growing independently as seen in fibroblast cell populations. The HT29-MTX cells grow similarly to Caco-2 cells in culture with close cellular positioning, forming confluent monolayers of cobblestone patterned cells. Structurally, when grown in 2D HT29-MTX cells are smaller than Caco-2 cells and form more densely packed formations.

### **3.4.2 Immunostaining characterisation of myofibroblasts for characteristic cytoskeletal markers.**

CCD-18co, HDFn and HIC cells were all shown to be positive for the type II intermediate filament protein Vimentin (Figure 3.3 A, G & M). This cytoskeletal protein is found throughout all mesenchymal cells and as such is used as a positive control and as a

determiner of cellular structure. All fibroblasts cell types show similar stellate formations and strong staining throughout the cellular cytoplasm. Alpha smooth muscle actin ( $\alpha$ SMA) is used as a designator of myofibroblast morphology (Figure 3.3 B, H & N). As with Vimentin, CCD-18co, HDFn and HIC cells all were shown to positively express this protein. The intestinal cell lines CCD-18co and HIC both appear to express  $\alpha$ -SMA at a significantly higher rate than HDFn cells which stained with a much lesser intensity. Desmin is a muscle specific type II intermediate protein, of which none of the cell lines tested were positive for this muscle lineage marker (Figure 3.3 C, I & O). Additionally, all cells were shown to be weakly positive for actin, a key component of the cellular cytoskeleton (Figure 3.3 D, J & P). No significant elastin staining was seen in any of the cell lines tested (Figure 3.3 E, K & Q). All cell lines were positively stained for microtubule protein Tubulin (Figure 3.3 F, L & R). HDFn cells were stained homogenously with strong expression seen throughout all of the cells. CCD-18co and HIC cells were all positively stained for tubulin however staining was seen to be less homogenous. All staining was done in the presence of a negative control (not shown)

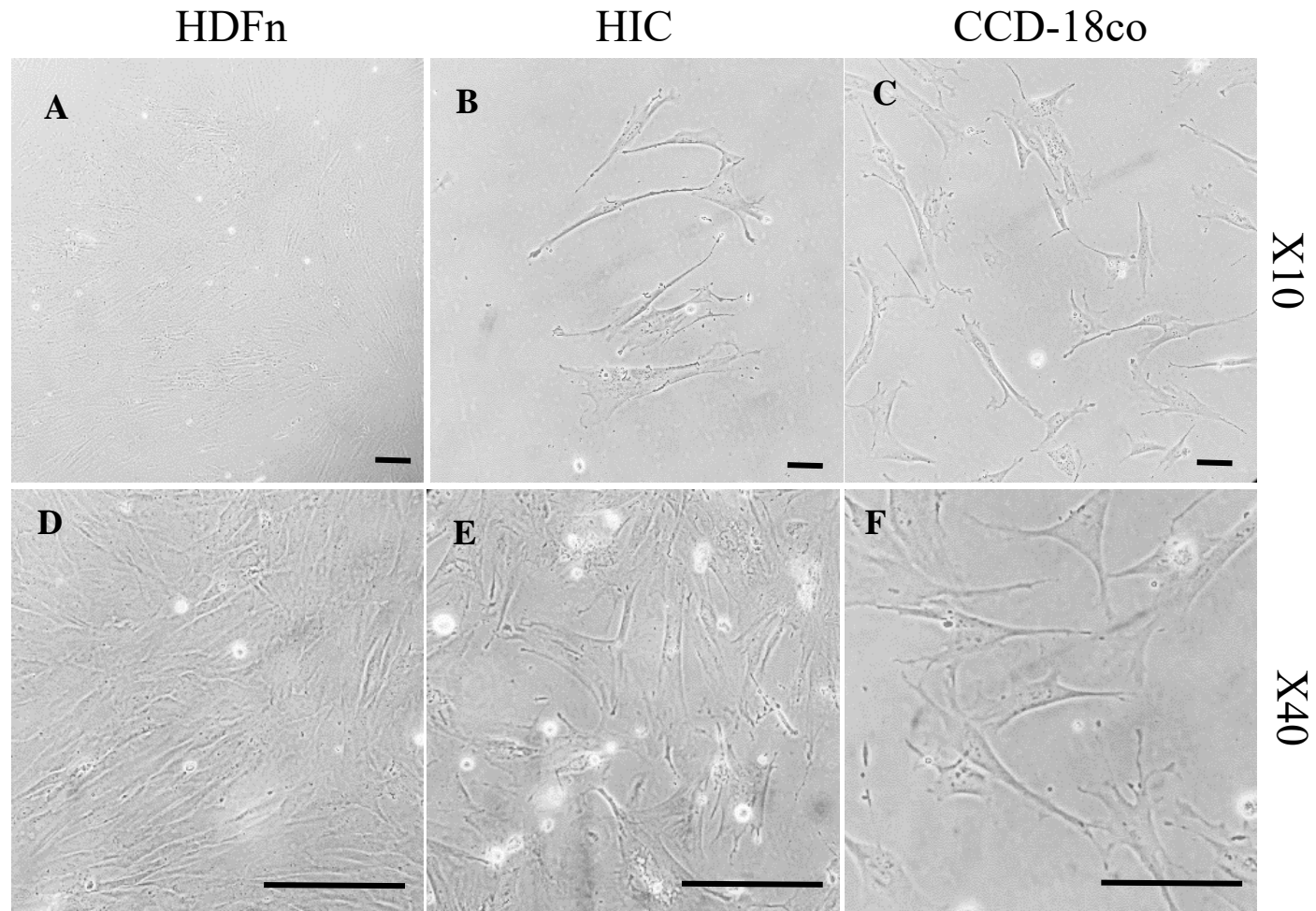


**Figure 3.1: Fibroblasts from differing origins are indistinguishable morphologically by phase contrast microscopy** – Representative phase contrast images of stromal cells utilised within this thesis. Stromal lines, CCD-18co, colonic fibroblast, Primary human small intestinal cells (HIC), HDFn, Human dermal fibroblasts. All cells exhibit a classical fibroblast morphology under phase contrast microscopy with a large stellate phenotype. Images are representative of repeated observations. Scale 25μm.

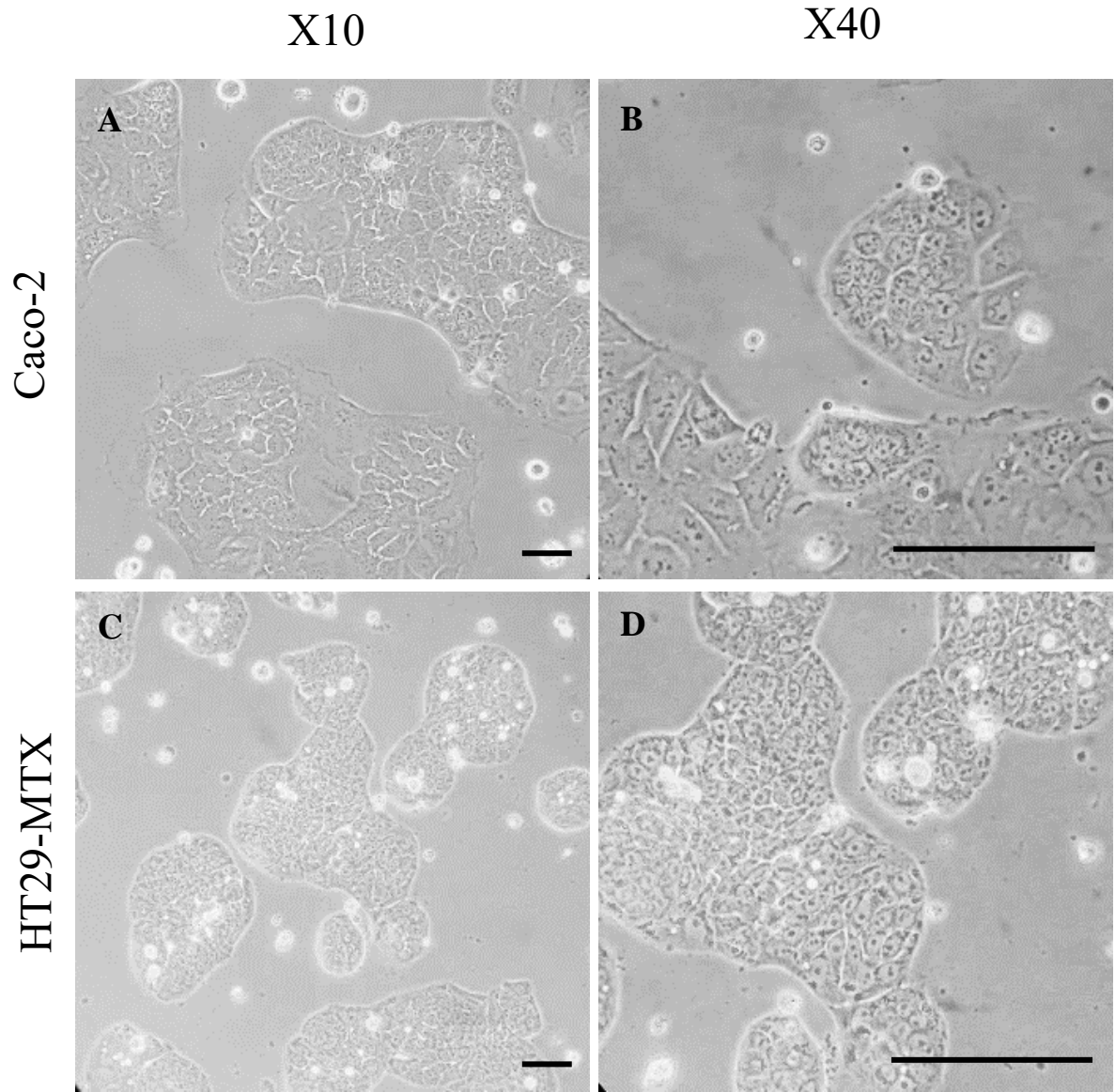


**Figure 3.2: Epithelial cells grow in densely packed “cobble stone” colony formations –** Representative phase contrast imaged of epithelial cells utilised within this thesis. Epithelial lines, Caco-2, colonic epithelial, HT29-MTX, a colonic HT29 cell lineage treated with methotrexate. Panel D is a magnified image of panel C. Panels A and B are unrelated. Images are representative of repeated observations. Scale 100µm and 25µm respectively.

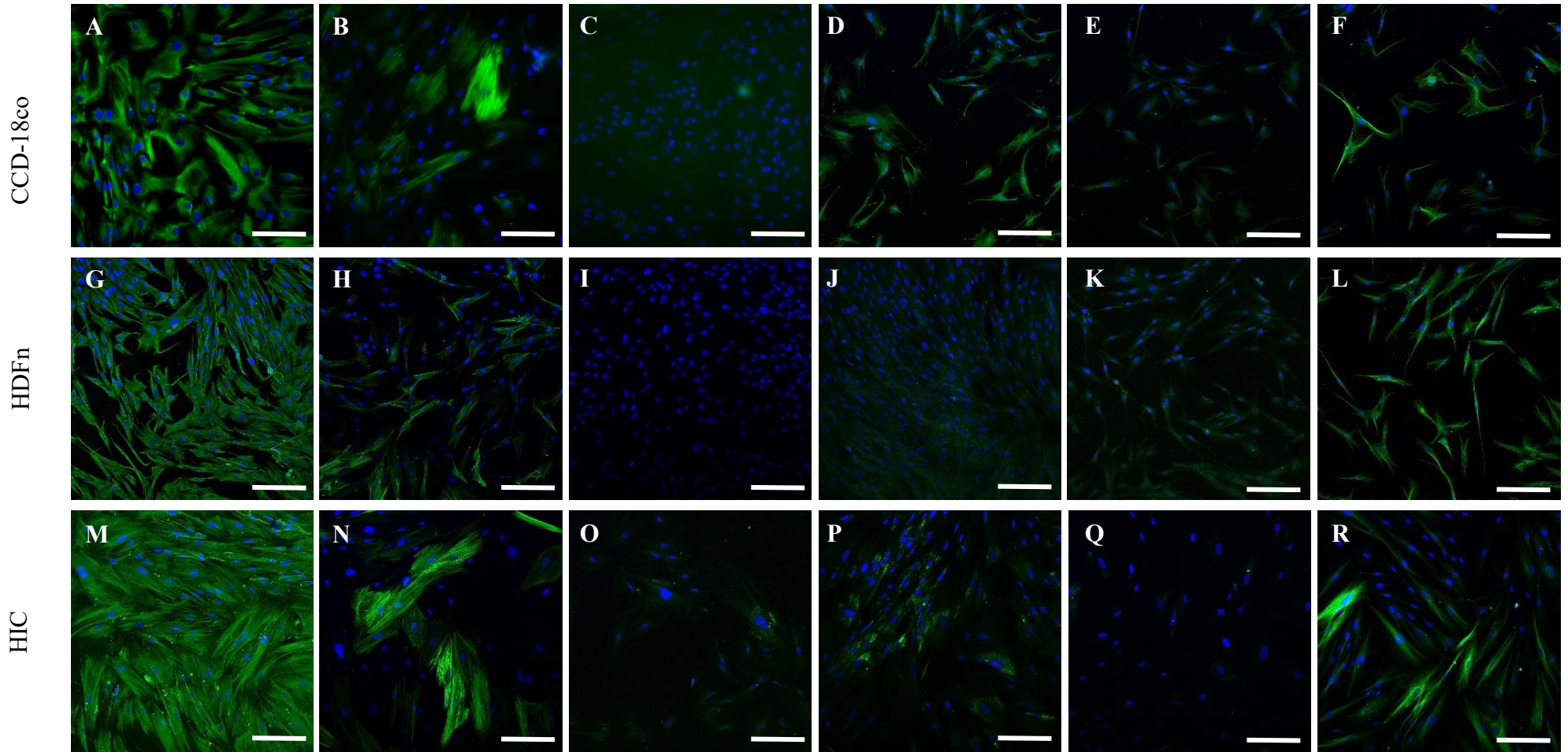


**Figure 3.3: Lineage specific intermediate filament expression analysis in 2D shows similar expression patterns between the three cell lineages.** – A-F) CCD-18co colonic carcinoma cells, G-L) HDFn dermal skin fibroblasts, M-R) HIC primary small intestinal cell. Blue staining represents cellular nuclei (DAPI), Green colour represents positive staining. All cells are positive for the general fibroblast lineage markers such as Vimentin, Alpha-SMA and Pan-Tubulin. Desmin is a stain specific to muscle lineages, as such no staining expression is expected. All staining was done alongside a negative control (See appendix). Images are representative of N=3 staining Scale: 200 $\mu$ m

### **3.4.3 Analysis of the changing characteristics of Caco-2 cells in pre and post confluency states.**

The Caco-2 cell lines was characterised by immunofluorescence for key proteins of interest in both pre-confluency and post confluency 2D cultured samples.

Pan-cytokeratin (Figure 3.4 A&E) is an intermediate filament protein found specifically within cells of epithelial origin. Pan-cytokeratin was used as both a marker of cellular structure and as a positive control. Caco-2 cells were shown to be strongly positive of pan-cytokeratin in both pre and post-confluency states with no obvious difference in staining intensity noticed between samples. Occludin (Figure 3.4 B & F) was used as a marker of tight junction expression within the cell populations. Caco-2 cells were shown to be weakly positive for Occludin when in pre-confluency and strongly positive when post confluence. MRP2 and MDR1 (Figure 3.4 C&G, D & H respectively) are both ATP-binding cassette proteins belonging to sub-families C and B respectively. These proteins are expressed at a low rate when cells are pre-confluent with increasing expression as the cells differentiate when they reach confluency. Low levels of Actin (Figure 3.5 A, D) expression was seen in both pre and post-confluency Caco-2 samples. Vimentin (Figure 3.5 B, E) was used as the negative control to show that cells were not of mesenchymal origin. Both pre and post-confluency states were negative for Vimentin. Finally, E-cadherin (Figure 3.5 C, F) was used as a marker of Adherens junctions. E-cadherin was shown to be expressed similarly to Occludin whereby low levels of non-homogenous E-cadherin staining was observed in the pre-confluency state whereby when post-confluent the cells express E-cadherin significantly more strongly throughout the sample.



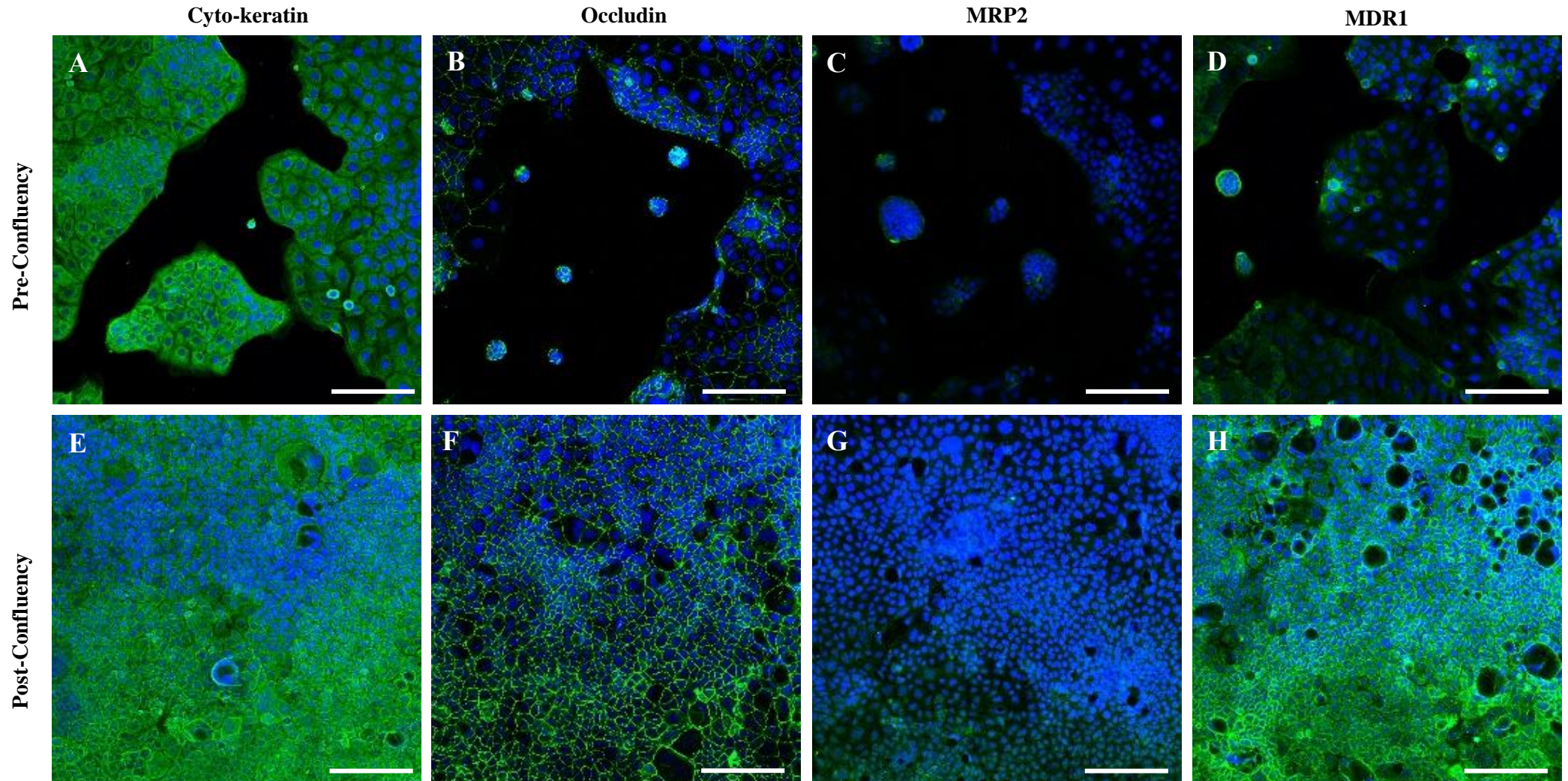


**Figure 3.4: Post-confluent Caco-2 cells express heightened levels of junctional marker, Occludin and surface efflux protein, MDR1** – Characterisation of Pre-confluency Caco-2 stained images, A) Cyto-Keratin, B) Occludin, C) MRP2, D) MDR1. Post-confluency Caco-2 stained images E) Cytokeratin, F) Occludin, G) MRP2, H) MDR1. Post confluency cells express all markers at significant levels. MDR1 specifically is an efflux transporter protein important in the efflux of drug compounds from the cell back into the intestinal lumen. MDR1 is known to be over expressed in Caco-2 cells All staining was done alongside a negative control (See appendix). Images are representative of N=3 staining Scale: 200µm



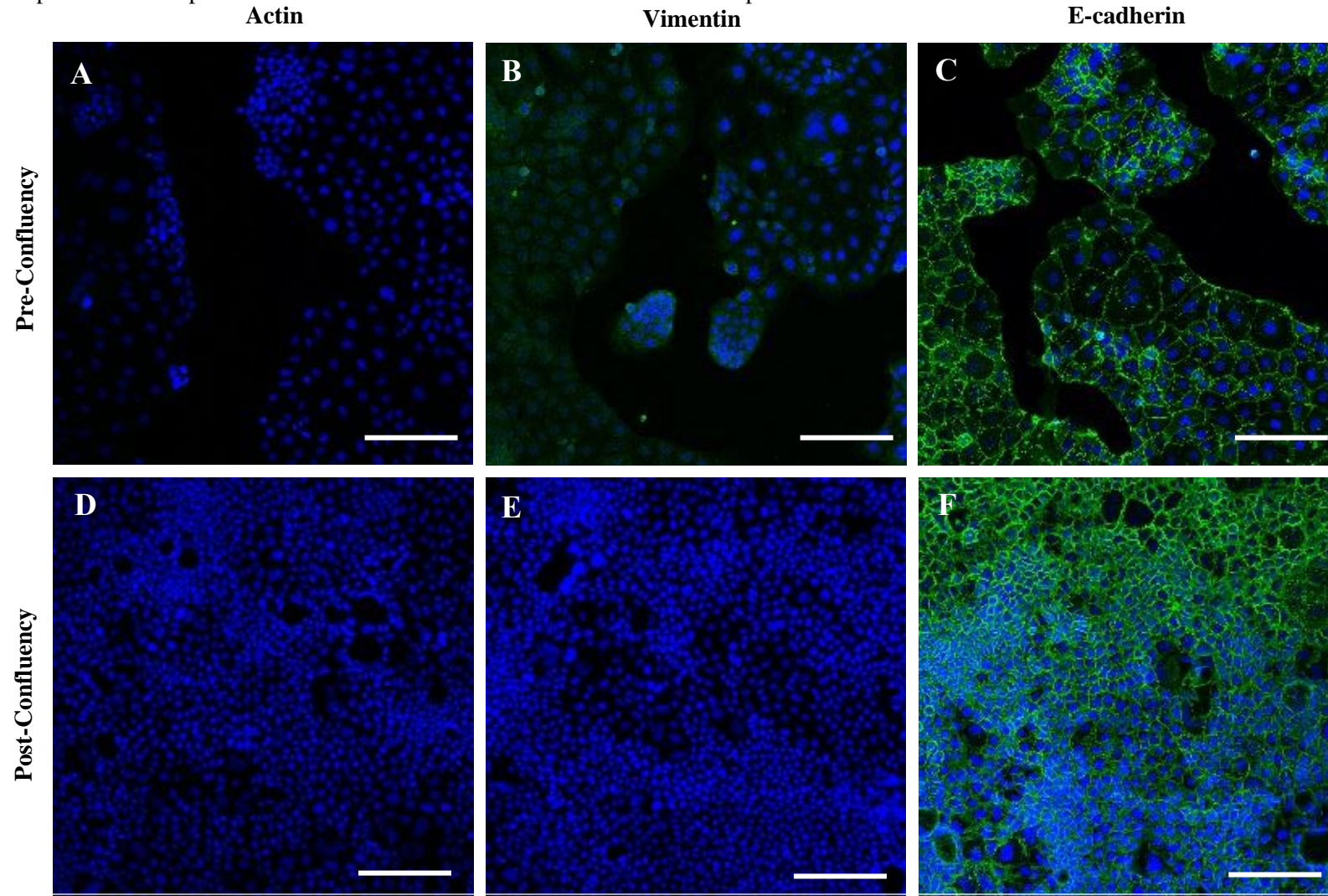


**Figure 3.5: Caco-2 cells are negative for Vimentin and E-cadherin staining remains proportional in pre and post-confluency states –** Characterisation of Pre-confluency Caco-2 stained images, A) Actin, B) Vimentin, C) E-cadherin. Post-confluency Caco-2 stained images D) Actin, E) Vimentin, F) E-cadherin. Lack of Vimentin expression shows these cells are not of mesenchymal origin All staining was done alongside a negative control (See appendix). Images are representative of N=3 staining Scale: 200µm

### **3.4.4 Understanding the effects of confluency on the differentiation of HT29-MTX cells in 2D culture.**

HT29-MTX cells were cultured on standard tissue plastic and immunostained as described previously (Section 2.4.3). HT29-MTX cells were stained for key proteins of interest in both pre and post confluency states.

Cyto-keratin (Figure 3.6 A, E) was expressed throughout both pre and post-confluency states as a marker of epithelial intermediate filaments. Occludin (Figure 3.6 B, F) shows a very low expression rate in the pre-confluency state with very little non-homogenous positive staining seen in the sample. The post-confluency state shows a significantly higher rate of staining throughout the samples however expression of Occludin was non-homogenous between the cells. HT29-MTX was negative for MRP2 (Figure 3.6 C, G) with no positive staining seen in either the pre or post-confluency samples. MDR1 (Figure 3.6 D, H) staining was seen at a high rate in both pre and post-confluency states with no noticeable difference in expression in confluent samples. This is out of character for HT29-MTX cells as they are generally thought to lack most enterocyte properties. Additionally, the staining seen in these samples compared to Caco-2 (Figure 3.4) is far less defined. It was hypothesised that positive staining seen here is most probably a consequence of membrane bound mucins sequestering the primary antibody. Actin (Figure 3.7 A, C) was not expressed at high rates in either of the samples. Vimentin (Figure 3.7 B, D) was not expressed in the pre-confluency state but some weak staining was seen when the cells were post-confluence. E-cadherin staining (Figure 3.7 C, F) was seen in both pre and post confluency states. Strong staining indicates continuous expression of adherens junctions between the cells, a hall mark of differentiated epithelial cells.



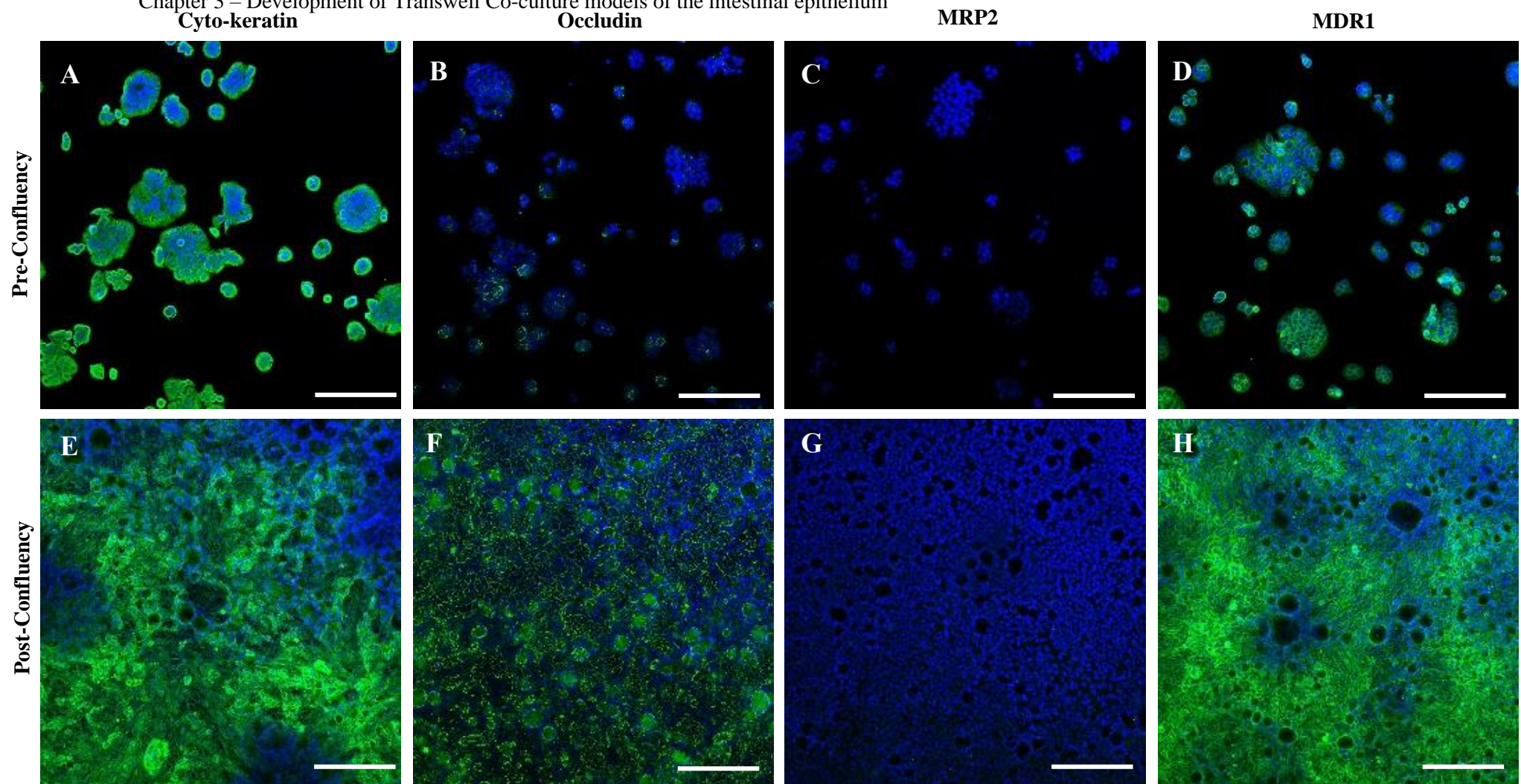


**Figure 3.6: Immunofluorescent characterisation of 2D epithelial cells Pre and Post-confluency shows increasing differentiation expression with time in culture –** Characterisation of Pre-confluency HT29-MTX stained images, A) Cyto-Keratin, B) Occludin, C) MRP2, D) MDR1. Post-confluency HT29-MTX stained images E) Cytokeratin, F) Occludin, G) MRP2, H) MDR1. Interestingly, HT29-MTX cells appear to also highly express MDR1. This is unusual due to HT29-MTX supposed function as a goblet cell lineage. However, due to HT29-MTX's epithelial origins some left over epithelial characteristics could be possible All staining was done alongside a negative control (See appendix). Images are representative of N=3 staining Scale: 200µm

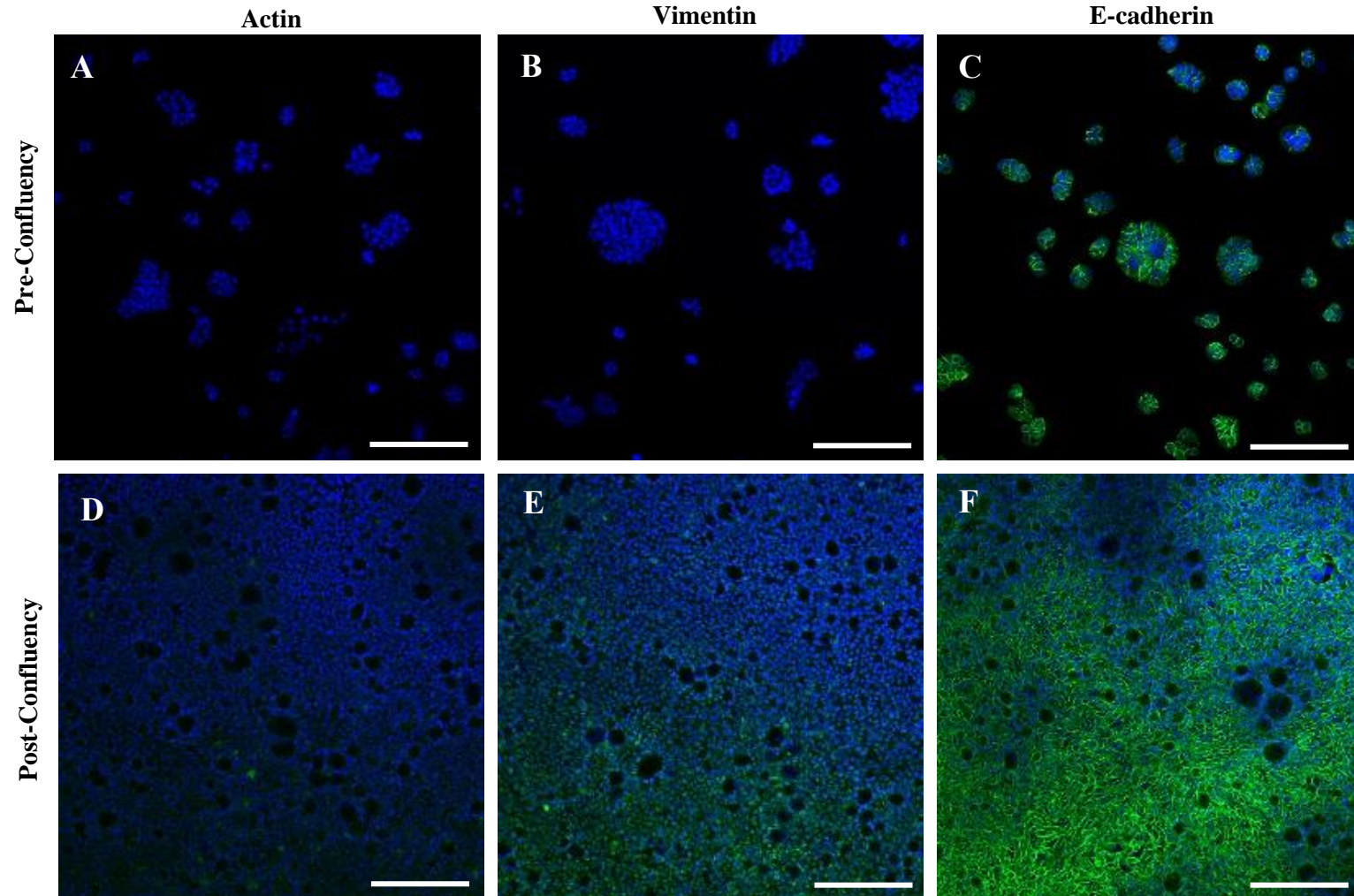


**Figure 3.7: Immunofluorescent characterisation of 2D epithelial cells Pre and Post-confluency** – Characterisation of Pre-confluency HT29-MTX stained images, A) Actin, B) Vimentin, C) E-cadherin. Post-confluency HT29-MTX stained images D) Actin, E) Vimentin, F) E-cadherin. All staining was done alongside a negative control (See appendix). Images are representative of N=3 staining Scale: 200µm



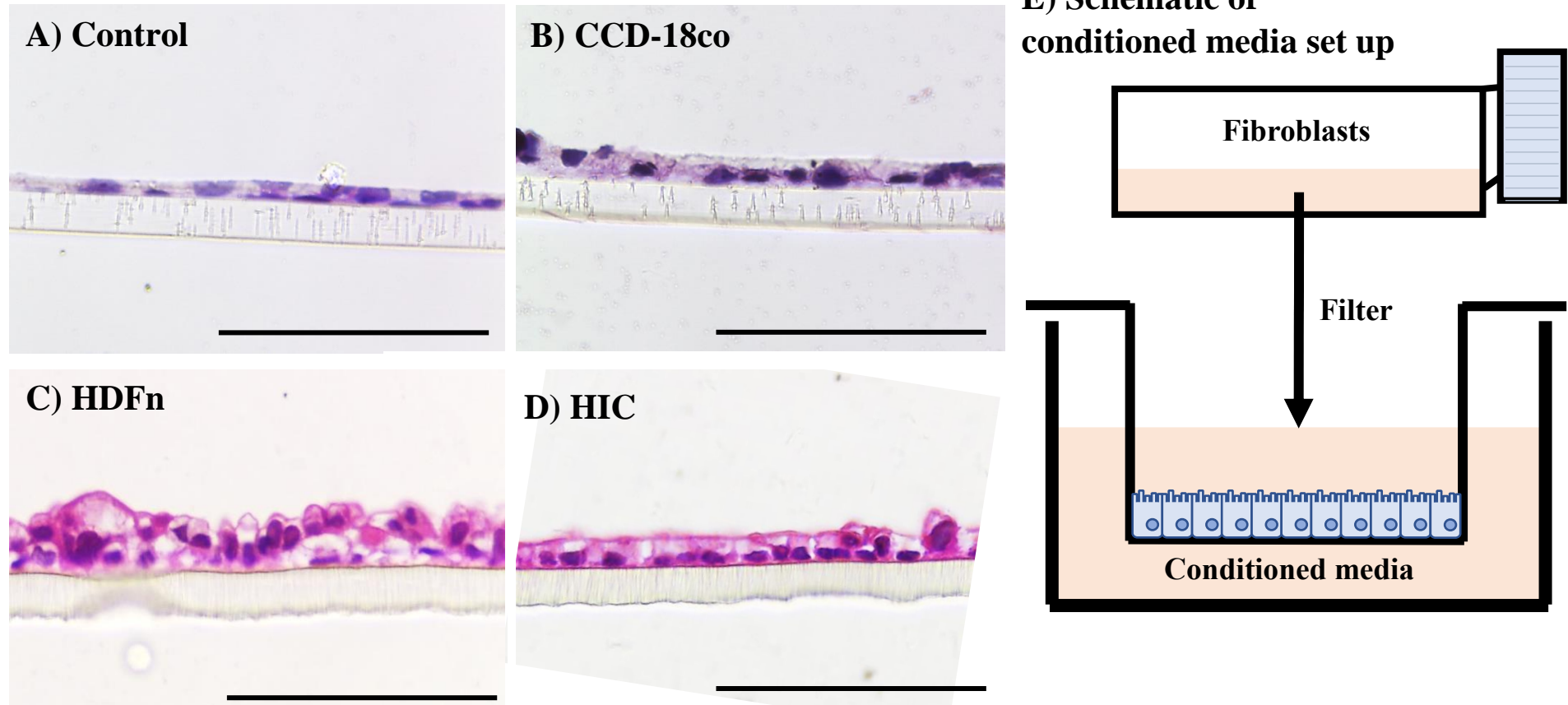


**Figure 3.8: H&E stained comparison of Caco-2 conditioned media co-culture models shows consistent monolayer formation in each of the model conditions. Cells are clearly able to differentiate and polarise in conditioned media at differential rates than in Control conditions** – Snapwell Transwell samples were fixed in 4% PFA and embedded into wax before being sectioned at 7 $\mu$ m and stained with Haematoxylin and Eosin to differentiate between nuclei and cytoplasm. A) Caco-2 control, B) Caco-2/ CCD-18co, C) Caco-2/ HDFn, D) Caco-2/ HIC. Addition of conditioned media to the Caco-2 epithelial equivalents appears to induce significant changes in cellular morphology when compared to control layers. HIC conditioned media specifically shows a highly regular structure with basally located nuclei, suggesting enhanced cellular differentiation. E) Shows a schematic of the process for the creation and culture of conditioned media Transwell models. Media is conditioned in 2D flasks on top of fibroblast cells for a period of 24 hours before being filtered and mixed in a 50:50 ratio with fresh culture medium before application to Transwell models. Images are representative of a minimum of 3 repeats. Scale = 100 $\mu$ m

### **3.4.5 Paracrine conditioned media has differential effects on epithelium development dependant on the origin of the fibroblasts.**

Caco-2 cells were cultured on Snapwell Transwell for a period of 21 days in the presence of conditioned media from the CCD-18co, HDFn and HIC fibroblast cell lines. Histologically it could be observed that samples were homogenous along their entire length. Caco-2 control (Figure 3.8 A) samples showed a polarised yet flattened morphology similar to that seen in cells grown in similar 2D culture systems.

CCD-18co conditioned media (Figure 3.8 B) resulted in a slightly improved structural morphology over Caco-2 controls with increased cell height and basally located nuclei. Cells under high magnification could be seen to develop microvilli structures indicating cellular differentiation within the models. HDFn conditioned media (Figure 3.8 C) showed a drastically different morphology than that seen in the control samples. Cells were significantly taller with some cellular multilayering across the samples. HIC conditioned media (Figure 3.8 D) models were similar in histology to those gained in CCD-18co conditioned media experiments with a heightened cellular morphology and basally located nuclei with continuous brush border development apparent when viewed under light microscopy.

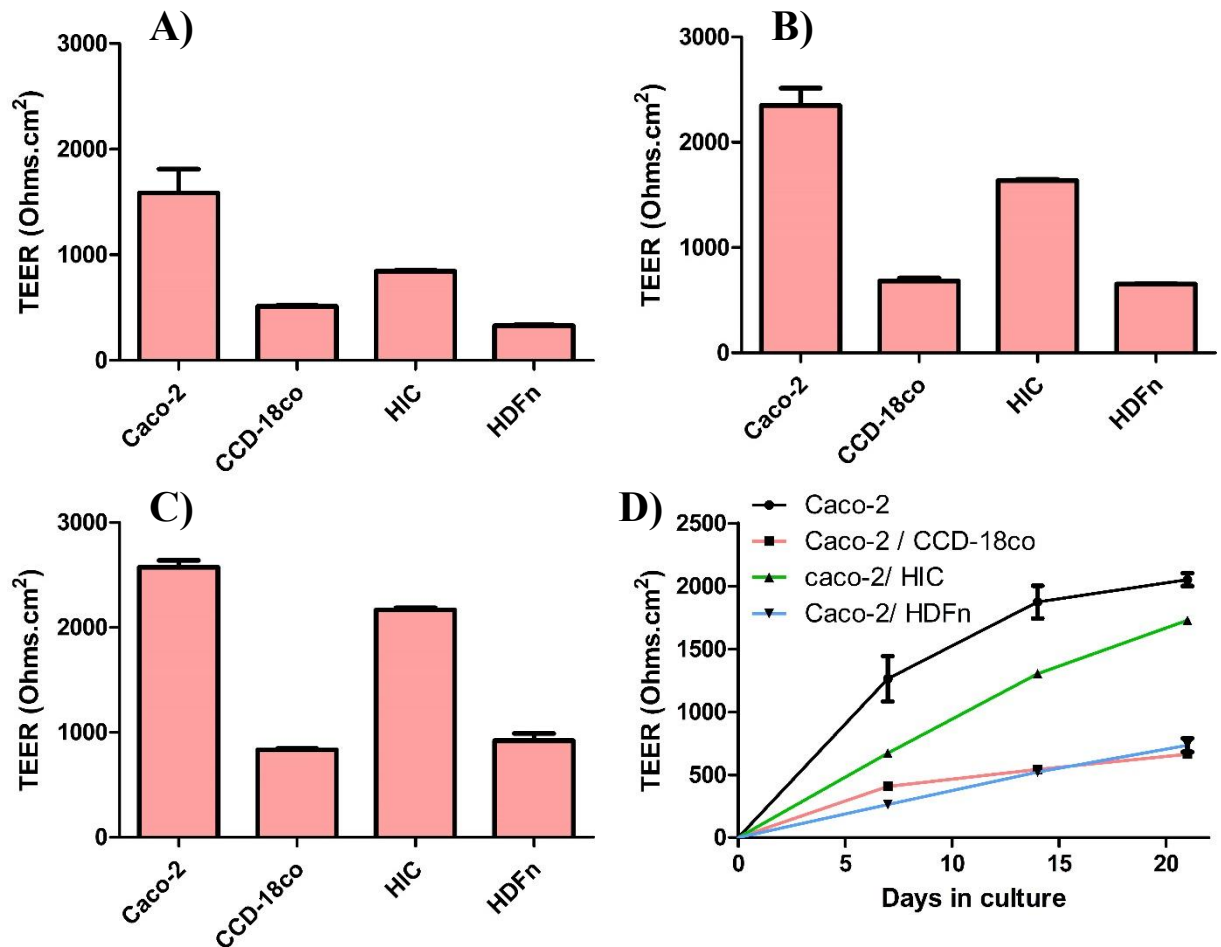


**Figure 3.9:** 7, 14 & 21 day TEER measurements of Caco-2 cells on Transwell Snapwell in control and conditioned media experiments shows that addition of conditioned media to the Caco-2 cellular layers results in a variable decrease in TEER values compared to control layers – Caco-2 cells were grown on Snapwell Transwell inserts and were co-cultured in conditioned media from CCD-18co, HIC or HDFn cells. A) 7 Day, B) 14 Day, C) 21 Day comparative TEER measurement between culture conditions. D) 21 day line graph showing the development of the Caco-2 layers over the course of the experiment. All cellular layers showed increased TEER values over time with the highest TEER values per model being at the 21 day time point. n=3-8 N=3. Scale bars represent +SEM.

7 Days		14 Days		21 Days	
Caco-2 vs CCD-18co	***	Caco-2 vs CCD-18co	***	Caco-2 vs CCD-18co	***
Caco-2 vs HIC	ns	Caco-2 vs HIC	*	Caco-2 vs HIC	**
Caco-2 vs HDFn	***	Caco-2 vs HDFn	***	Caco-2 vs HDFn	***
CCD-18co vs HIC	ns	CCD-18co vs HIC	**	CCD-18co vs HIC	***
CCD-18co vs HDFn	ns	CCD-18co vs HDFn	ns	CCD-18co vs HDFn	ns
HIC vs HDFn	ns	HIC vs HDFn	**	HIC vs HDFn	***

**Table 3.1 Statistical analysis of Transwell model TEER measurements:** One way ANOVA with Tukeys post-test analysis was used to calculate signficacy between v n=3, N=3



### **3.4.6 Trans-epithelial resistance is shown to decrease in the presence of conditioned media from all origins with a variable degree of response.**

The effects of paracrine media culture on the membrane integrity of Caco-2 monolayers was assessed utilising the commonly used TEER measurement system. All tested cultures demonstrate an increase in epithelial resistance values over the course of the 21 day culture period. Control models show the sharpest increases between Day 0 and 7 up to a resistance of approximately 1000-1500 ohms (Figure 3.9 D). This initial sharp rise in resistance measurements is followed by an increasingly slower rise in TEER values up to day 21 when resistance values are shown to have plateaued, with maximum TEER values seen of up to 2000 Ohms.

In contrast to this in all instances the co-culture of Caco-2 cells with the paracrine media of CCD-18co, HDFn and HIC fibroblasts results in the decrease in the TEER values of the epithelial monolayer compared to control epithelial resistance values. HIC co-culture epithelial models show the smallest, yet still significant, attenuation of TEER values compared to control models. In contrast to control samples which showed an initial rapid increase in TEER values, HIC conditioned media treated Caco-2 cells show a shallow, almost linear increase in TEER values between the 0 and 14 day timepoints. Around day 14 a small attenuation in the gradient of the TEER curve indicated the beginnings of a plateau up to day 21. Statistical analysis of the Caco-2/ HIC cultures shows that the lines are non-significantly different (Figure 3.9 A,B) until the 14 days timepoint (Figure 3.9 C) whereby a significant decrease in the maximum TEER value of the epithelial membrane is seen with a maximum value at 21 days of around 1700 ohms.

CCD-18co and HDFn co-culture epithelial layers are almost indistinguishable from one another over the course of the 21 day co-culture (Figure 3.9 D). Statistically, CCD-18co and HDFn co-cultures are significantly lower than the control samples from the day 7 timepoint onwards until the terminal 21 day values of around 500 Ohms. Similarly to HIC co-culture layers, HDFn cells show an almost constant linear increase in TEER values up to 21 days. CCD-18co co-cultures show an initial sharp increase in TEER between the 0

and 7 day timepoints. This increase is shown to plateau after day 7 with a shallower linear increase up to day 21.

### **3.4.7 MTT metabolic measurements of Caco-2 2D paracrine co-culture models shows CCD-18co conditioned media increases the metabolic activity of Caco-2 cells at later timepoints by delaying lag phase onset.**

Due to the significant changes seen in the epithelial TEER values when co-cultured with fibroblast conditioned media the logical next question was to assess whether these changes in barrier resistance were due to physiological changes in membrane phenotype rather than due to induced necrosis or apoptosis.

Figure 3.10 A-D shows the comparative MTT values of 2D Caco-2 cells grown in control and conditioned media environments. HIC and HDFn (Figure 3.10 B,C) MTT curves follow the same approximate trend with an initial lag phase followed by an exponential phase of growth, ending with a plateau of MTT values by day 10. Contrastingly, control samples reach a maximal MTT value at day 8 which decreases at day 10. In HDFn and HIC instances there is no significant differences seen in MTT value at the day 10 timepoint when compared to the control samples (Table 3.2). CCD-18co conditioned media (Figure 3.10 A) samples show a similar increase in MTT values as the control up until day 6 whereby the rate of increase is lower than that of the control until day 8. Whereas, by day 10 the control, HDFn and HIC samples have reached plateau the CCD-18co samples show a linear rate of growth past the day 10 timepoint.

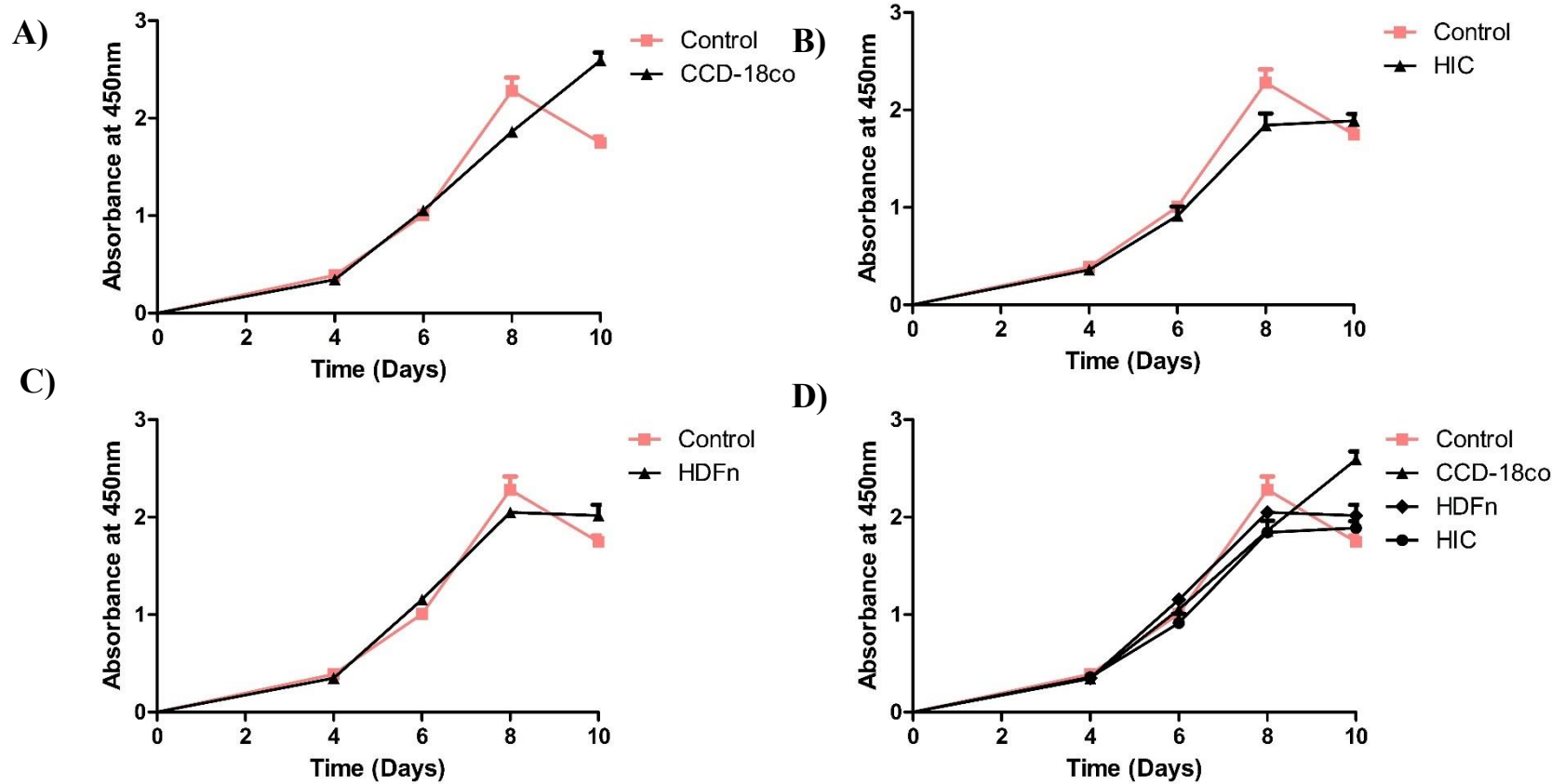


**Figure 3.10:** The effects of fibroblast conditioned media on the MTT values of 2D cultured Caco-2 cells shows that CCD-18co paracrine influences have the most effect on Caco-2 cells with a continuation of growth up to 10 days in culture – Cell viability was assessed by MTT assay of 2D cells at set time points. All cell lines were shown to have effects on the metabolic activity of the Caco-2 cells, shifting the classical growth curve to the right, delaying the onset of the lag and death phases. CCD-18co conditioned media appears to delay the onset of the lag phase significantly more in comparison to other conditions. Data is from at least 3 different experiments,  $n=3$ .  $N=3$  Scale bars represent  $\pm$ SEM.

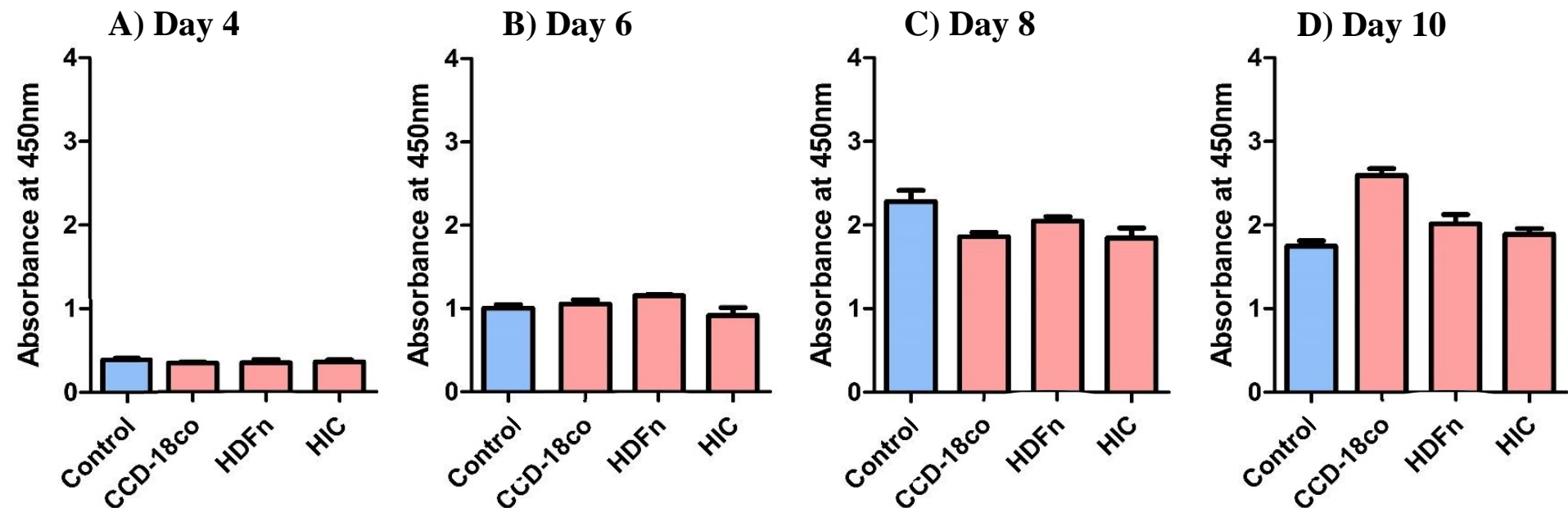


**Figure 3.11: Time-point comparison of all conditioned media conditions** – Control and conditioned media Caco-2 cells were assessed for metabolic activity by MTT assay. A) Day 4, B ) Day 6, C) Day 8, D) Day 10. Values represent means + SEM. All experiments n=3 N=3.

Day	Con vs CCD-18co	Con vs HDFn	Con vs HIC
4	ns	ns	ns
6	ns	*	ns
8	*	ns	ns
10	**	ns	ns

**Table 3.2: Significances of conditioned media MTT data** – All comparative significances were tested by one way ANOVA with Tukeys post-test analysis of variance \*\*\*=p <0.0005, \*\*=p<0.005, \*=p<0.05

### **3.4.8 Understanding the differential development of tight junction formation in Caco-2 cells treated with fibroblast conditioned media.**

The formation of tight junctions in Caco-2 monolayers was assessed through the staining of Occludin, a tight junctional component protein found in the membrane and inter-membranal space between epithelial cells.

Figure 3.12 shows that regardless of cellular confluency Occludin was expressed as early as day 2, weakly in cells with no other cellular contacts and more strongly in cells localised into small groups or colonies in all conditions tested. Initially, the staining appears to be patchy with non-continuous staining along the apical surface of the cellular membranes when cells are adjacent to the membranes of other cells. Furthermore, earlier timepoint samples appear to have significantly more intracellular/ cytoplasmic staining of the occludin than in later samples where the occludin appears to be more localised to the membranes. The cells in the immunostained samples appear to be larger in apparent size when at lower confluency and pack together more tightly as the cells mature and begin to differentiate. Immunologically there are no significant differences seen in the Occludin staining either in localisation or strength between the different paracrine models up to day 6. After day 6 the intensity of the stained samples seemingly increases in the conditioned media examples compared to the control although this observation was not quantified. Additionally, control cells show a homogenous cell size phenotype up to day 8 in culture with a classic cobblestone pattern seen throughout the samples. Conditioned media stained samples appear to be more heterogenous in morphology earlier in the culture period at around day 6 with some cells significantly bigger in size than other.



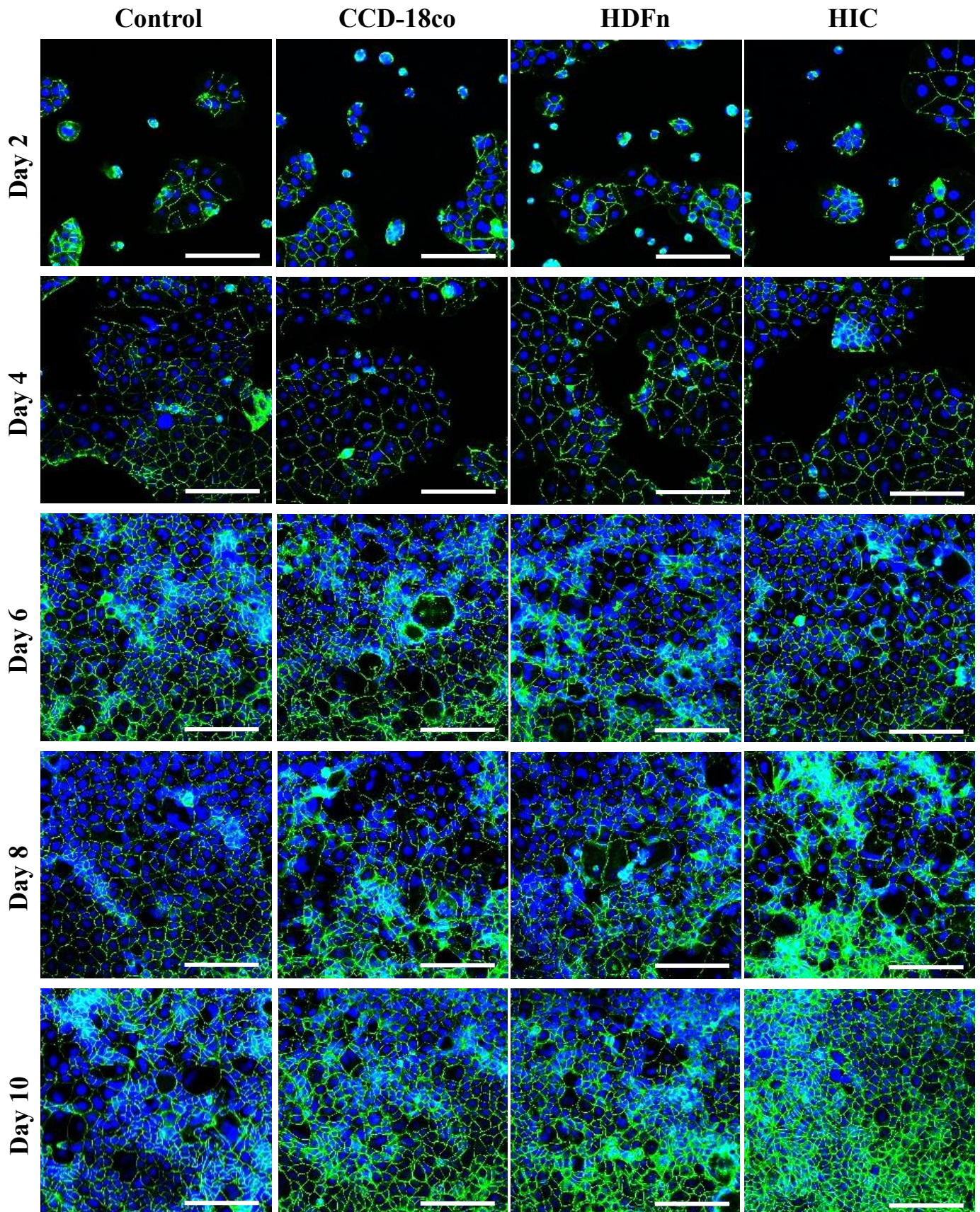


**Figure 3.12: Tight junction expression between conditioned media conditions shows increased cellular packing in conditioned media samples** – Control and conditioned media treated Caco-2 cells were cultured on 2D plastic for a varying number of days before fixation and staining for the tight junction protein Occludin. Staining intensity appears to increase in conditioned media models at day 10, especially in HIC models which appear to be more consistently, strongly stained with more cells packed into the same area. Images are representative of N=3. Scale = 200µm



### **3.4.9 Immunostaining of cells grown in Snapwell Transwell and CCD-18co effects on functional differentiation of Caco-2 cells with regards to P-gp expression and brush border formation.**

Figure 3.13 A & E, shows the staining of E-cadherin of Caco-2 cells grown on the permeable membrane Snapwell Transwell. Positive E-cadherin staining is localised to the membranes of the cells with homogeneity throughout the samples (Figure 3.13 A). The transverse sectioned sections (Figure 3.13 E) of E-cadherin shows primary baso and lateral staining localisation. Contrastingly, Figure 3.14 (A & E) shows the comparative E-cadherin staining of Caco-2 Snapwell Transwell cultures grown in the paracrine CCD-18co conditioned media. Staining for E-cadherins shows significant changes in both staining intensity and in cellular structure with a far more heterogenous cell morphology throughout the samples. Transverse sections of these samples (Figure 3.14 E) shows significantly less cellular organisation with positive staining seen apically in addition to laterally and basally.

Similarly, Occludin staining of control (Figure 3.13 B & F) and CCD-18co conditioned media (3.14 B & F) samples shows much the same pattern with less structural homogeneity seen in the conditioned media samples.

P-gp/ MDR1 staining of Control samples (3.13 C & G) shows a heterogenic pattern of expression with areas of high intensity and low intensity staining observed. Transverse sections of high density areas of staining (Figure 3.13 G) shows localisation of primary staining to the apical boundary of the cells. P-gp/MDR1 staining of CCD-18co conditioned media treated samples (Figure 3.14 C & G) shows significantly less positive staining of P-gp throughout the sample. Transverse sections of high intensity stained areas (Figure 3.14 G) shows a similar pattern to that seen in other stained targets with significantly different structural organisation of the positive staining. However, the CCD-18co conditioned samples still maintain the strong apical expression expected of this protein.

Control samples stained for actin expression (Figure 3.13 D & H) show clear positive staining throughout the surface of the sample (Figure 3.13 D) with clear microvilli staining seen under high magnification. Figure 3.13 H shows the transverse section of the control sample showing staining primarily located to the actin rich brush border layer and to the junctional complexes in the lateral membranes of the cells. Similarly, CCD-18co conditioned media treated samples show consistent staining across the entire surface layer of the models (Figure 3.14 D). Transverse sections (3.14, H) of the models show strong positive staining at the actin rich brush border layer but significantly less staining across the lateral membrane when compared to the control samples.



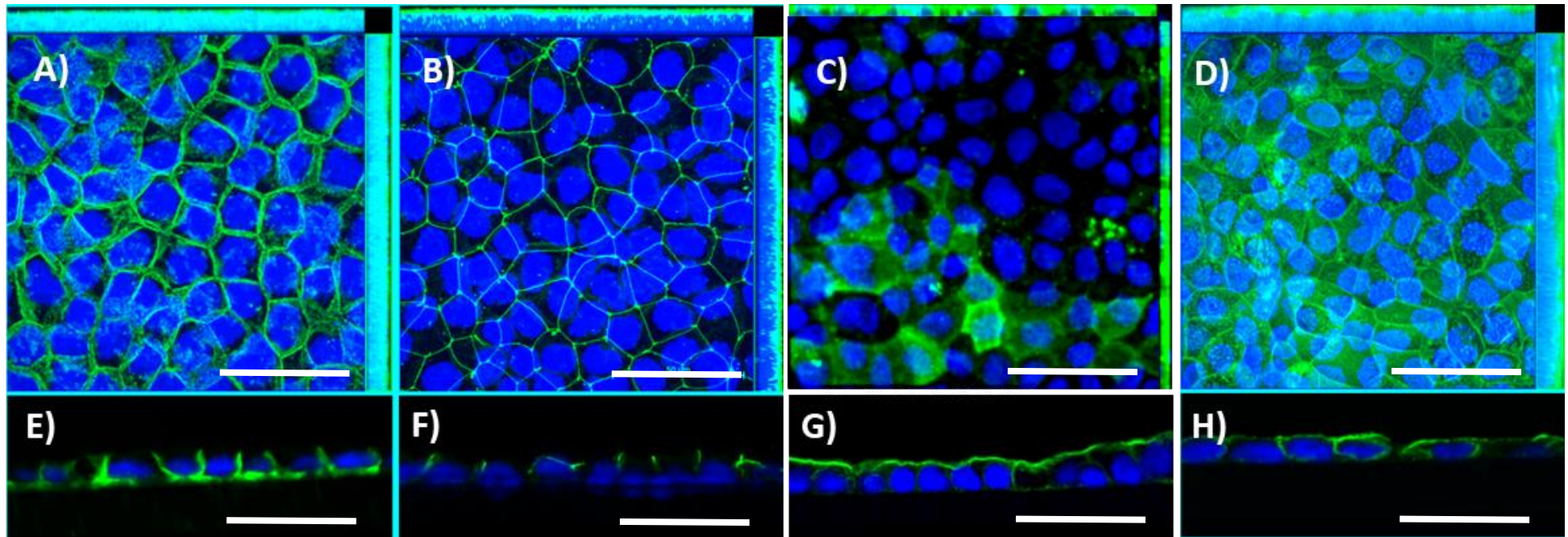


**Figure 3.13: Caco-2 control models appear to be well differentiated through expression of key proteins for model differentiation and function –** Representative stained images of Methanol: Acetone fixed Caco-2 cells for A&E) E-cadherin, B&F) Occludin, C&G) P-gp, D&H) Actin. Scale = 50μm for wholemount and sectioned images. Images are representative of N=3.

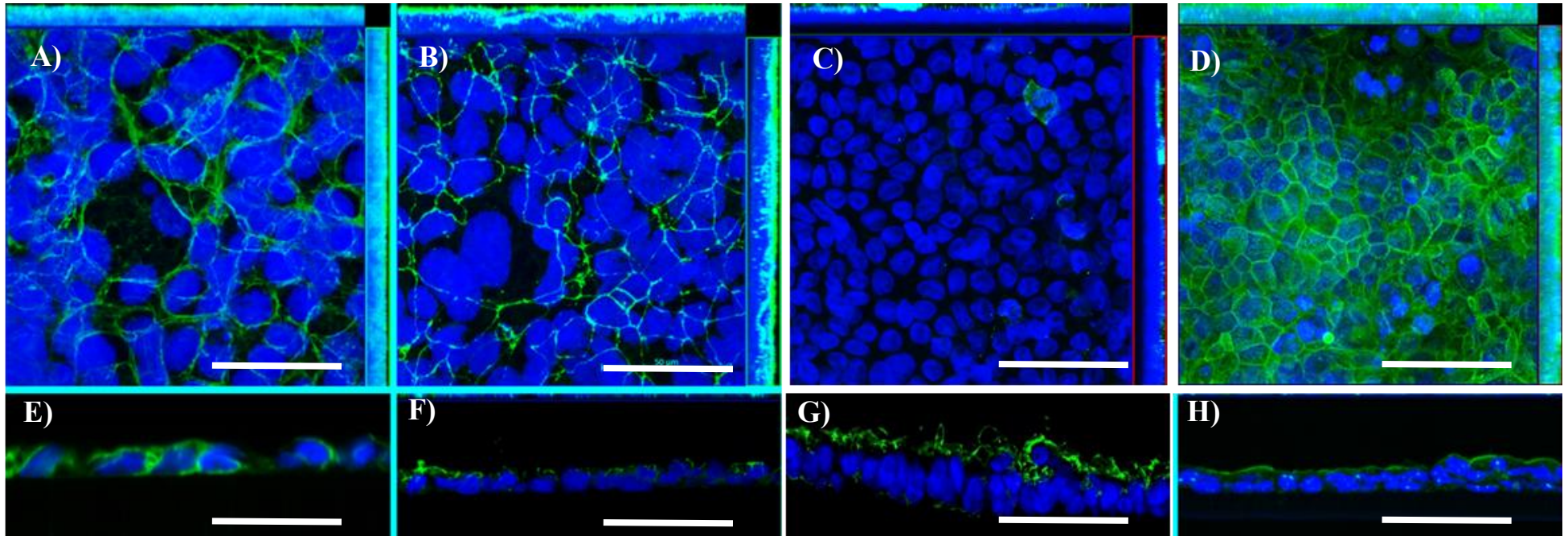


**Figure 3.14: Caco-2 cells grown in CCD-18co conditioned paracrine media shows differences in the cellular organisation as analysed through expression of key proteins for model function** – Representative stained images of Methanol:Acetone fixed Caco-2 cells co-cultured with CCD-18co conditioned media for A&E ) E-cadherin, B&F) Occludin, C&G) P-gp, D&H) Actin. Both A and B show junctional proteins outlining the periphery of cells. Compared to control layers significant differences can be seen in cellular organisation with less homogenous structures seen in conditioned media treated epithelial constructs. Scale = 50 $\mu$ m for wholemount and sectioned images. Images are representative of N=3.

### **3.4.10 qPCR analysis of the development of Caco-2 layers in relation to key targets of function and the effects of CCD-18co paracrine media on Caco-2 layer development.**

Figure 3.15 shows the qPCR results of Caco-2 monolayers cultured on Snapwell Transwell taken at 7, 14 and 21 day time intervals with and without the addition of CCD-18co conditioned media. Figure 3.15 A shows the results for the expression of Villin mRNA. Villin mRNA expression is shown to slowly increase in control samples between 7 and 14 days in culture before a rapid increase in mRNA levels up to 21 days. Addition of CCD-18co conditioned media to the Transwell layers results in a gradual increase in levels over the full 21 day period, with terminal levels in CCD-18co conditioned media samples approximately 50% that of the control. Significance values for comparative Villin expression reflect these observations with significances in control samples only between the 21 day timepoints. No significant change is seen between 7 and 21 day samples treated with CCD-18co conditioned media although an upwards trend can be observed. Interestingly, 21 day timepoints of CCD-18co treated Caco-2 layers are not significantly different from 7 day non treated controls when comparing relative expression of Villin, OATP-B or BCRP. Although, in each case the 21 day timepoint of CCD-18co treated layers tends to be higher than 7 day controls.

Occludin, OATP-B and MRP2 levels (Figure 3.15 B, C & Figure 3.16 A respectively) shows a similar expression profile to that of Villin. CCD-18co conditioned media results in a decrease in mRNA expression of these genes at the 21 day period timepoint when compared to the control 21 day samples. With levels dropping to between 50 and 60% that of the control. Whilst a downwards trend in relative expression rates of samples cultured in CCD-18co conditioned media can be observed in each of the three samples mentioned above only OATP-B and MRP2 21 day +/- CCD-18co comparisons results in a significant decrease in relative expression. No significant differences can be seen when comparing Control and CCD-18co treated epithelial layers at 7 and 14 day timepoints.

Figure 3.16 B shows the expression levels of BCRP. Control layers show a steady increase in mRNA levels until the 14 day timepoint whereby the levels plateau and remain

at the same approximate level until 21 days. Conversely, CCD-18co conditioned media Caco-2 layers show an initial rapid rise in mRNA levels up until 7 days at which point levels rise steadily until the 21 day experimental endpoint. The mRNA levels of the conditioned media models 7 day time point is approximately equal to that of the 21 day matured non-treated Caco-2 layers with BCRP mRNA expression of the 21 day timepoint being approximately twice that of the control. Interestingly however, no significant differences can be seen between any combination of samples in this experiment. Although, as before, general increasing trends over time can be observed.

Finally, MDR1 (Figure 3.16 C) shows a similar pattern to that of BCRP but to a lesser extent with conditioned media Caco-2 models being approximately 1.5x the levels of control layers. In the case of MDR1 however increases mediated by CCD-18co paracrine media culture can be shown to be significantly different from control Caco-2 epithelial model layers.

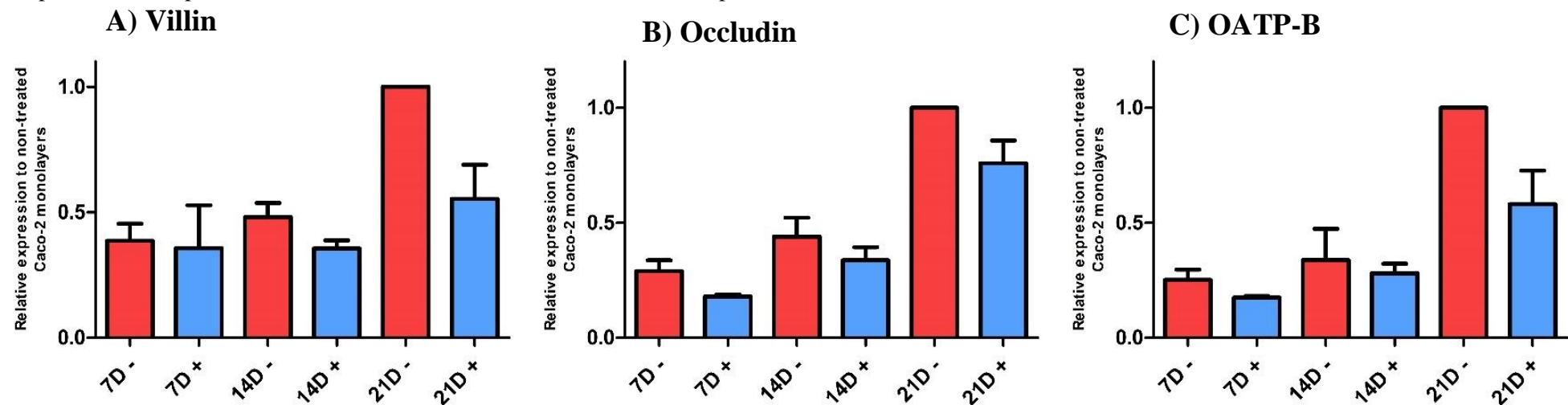


**Figure 3.15: Transwell time course models PCR for Villin, Occludin and OATP-B** - Graph shows the relative expression of 3 different markers of cellular differentiation at different timepoints of monolayer maturation and in the presence of CCD-18co compared to the 21D Caco-2 standard. A) Villin, B) Occludin, C) OATP-B. Relative expression rates of Villin and OATP-B are significantly lower in CCD-18co treated epithelial layers at 21 days than in controls. Occludin levels do not significantly change over the 21 day culture period suggesting something else is responsible for the significant changes in TEER observed in conditioned media cultures n=3 N=3 in all cases **except 7D + where n=2 N=2**. Significance calculations are omitted for N=2 data points. Scale bars represent +SEM.

	7D +	14D -	14D +	21D -	21D +
7D -		ns	ns	***	ns
7D +					
14D -			ns	***	***
14D +				***	ns
21D -					*

	7D +	14D -	14D +	21D -	21D +
7D -		ns	ns	***	*
7D +					
14D -			ns	**	ns
14D +				***	*
21D -					ns

	7D +	14D -	14D +	21D -	21D +
7D -		ns	ns	***	ns
7D +					
14D -			ns	**	ns
14D +				***	ns
21D -					*

**Table 3.3: Significances for comparative Villin expression in time course samples** – Comparative sample analysis was achieved utilising One way ANOVA with Tukeys post-test analysis \*\*\* = P<0.0001, \*\* = P<0.001, \* = P< 0.01

**Table 3.4: Significances for comparative Occludin expression in time course samples** – Comparative sample analysis was achieved utilising One way ANOVA with Tukeys post-test analysis \*\*\* = P<0.0001, \*\* = P<0.001, \* = P< 0.01

**Table 3.5: Significances for comparative OATP-B expression in time course samples** – Comparative sample analysis was achieved utilising One way ANOVA with Tukeys post-test analysis \*\*\* = P<0.0001, \*\* = P<0.001, \* = P< 0.01



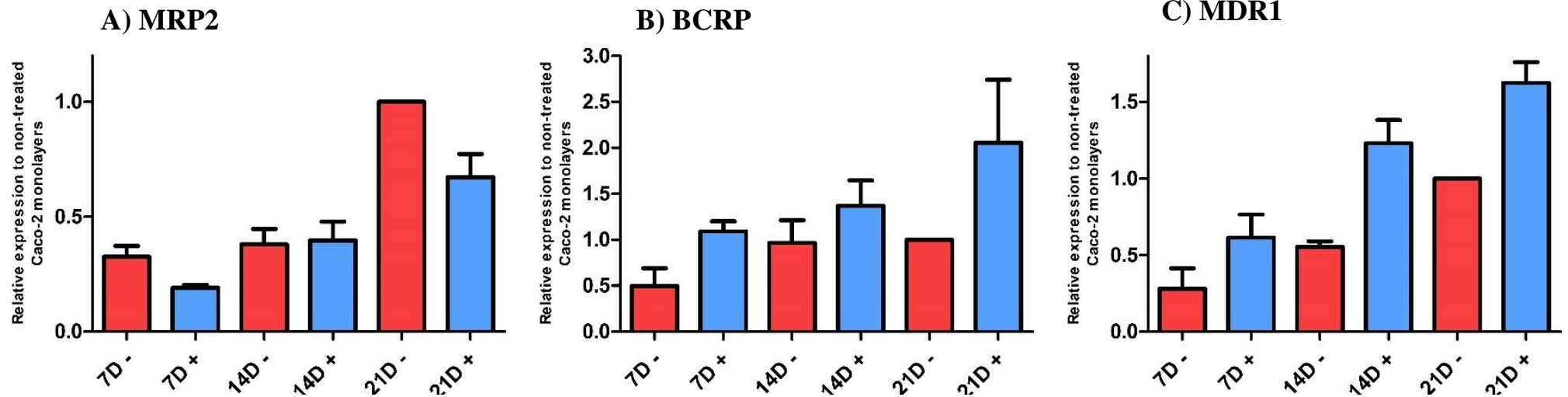


**Figure 3.16: Transwell time course models qPCR of MRP2, BCRP and MDR1-** Graph shows the relative expression of 3 different markers of cellular differentiation at different timepoints of monolayer maturation and in the presence of CCD-18co compared to the 21D Caco-2 standard. A) MRP2, B) BCRP, C) MDR1. MDR1 is the only marker to show significant differences over the control with a significant increase in relative mRNA abundance.  $n=3$ ,  $N=3$  in all cases except 7D + where  $n=2$ ,  $N=2$ . Significance calculations are omitted for  $N=2$  data points. Scale bars represent  $\pm$ SEM.

	7D +	14D -	14D +	21D -	21D +
7D -		ns	ns	***	*
7D +					
14D -			ns	***	ns
14D +				**	ns
21D -					*

**Table 3.6: Significances for comparative MRP2 expression in time course samples** – Comparative sample analysis was achieved utilising One way ANOVA with Tukeys post-test analysis. \*\*\* =  $P<0.0001$ , \*\* =  $P<0.001$ , \* =  $P<0.01$

	7D +	14D -	14D +	21D -	21D +
7D -		ns	ns	ns	ns
7D +					
14D -			ns	ns	ns
14D +				ns	ns
21D -					ns

**Table 3.7: Significances for comparative BCRP expression in time course samples** – Comparative sample analysis was achieved utilising One way ANOVA with Tukeys post-test analysis \*\*\* =  $P<0.0001$ , \*\* =  $P<0.001$ , \* =  $P<0.01$

	7D +	14D -	14D +	21D -	21D +
7D -		ns	**	**	**
7D +					
14D -			*	***	**
14D +				ns	ns
21D -					*

**Table 3.8: Significances for comparative MDR1 expression in time course samples** – Comparative sample analysis was achieved utilising One way ANOVA with Tukeys post-test analysis \*\*\* =  $P<0.0001$ , \*\* =  $P<0.001$ , \* =  $P<0.01$

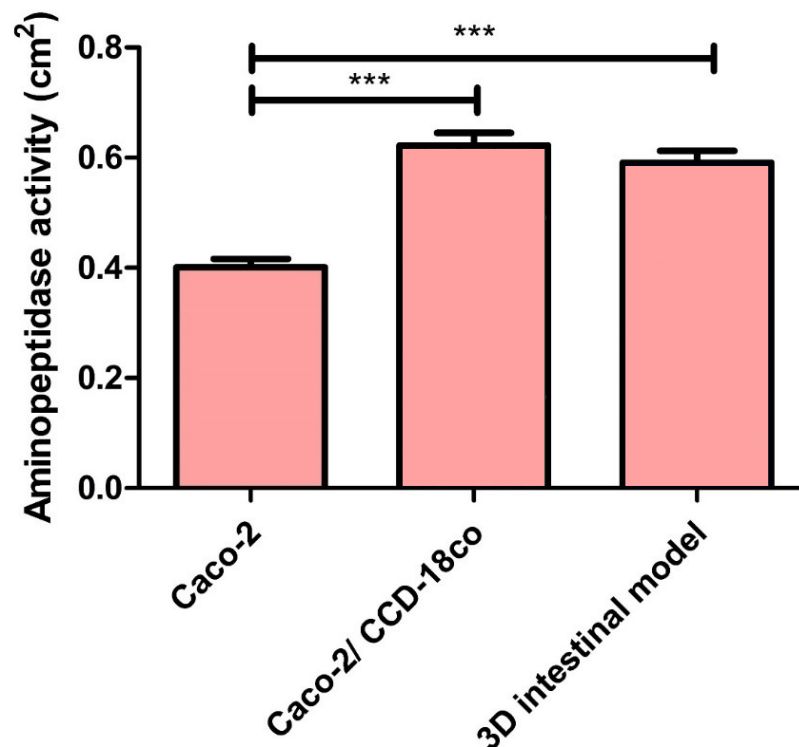


**Figure 3.17: Amino-peptidase activity levels increase in both paracrine and 3D CCD-18co cultures** – Amino-peptidase enzyme activity assessed at 21 days of Caco-2 culture in control, Paracrine treated and 3D CCD-18co models. When corrected to culture area both CCD-18co paracrine and 3D models resulted in a modest yet significant increase in amino-peptidase activity, suggesting improvements in cellular differentiation.  $n=6$   $N=3$ . Significance compared to control was assessed by students unpaired T-test. \*\*\*= $p < 0.0005$ , \*\*= $p < 0.005$ , \*= $p < 0.05$  Scale bars represent +SEM.

### 3.4.11 Co-culture of Caco-2 cells increases the amino-peptidase activity within intestinal models.

Amino-peptidases are expressed in the intestine as a surface enzyme of enterocytes for the catabolism of the breakdown of amino acids through breakage of the N-terminus of proteins. Caco-2 monolayers were tested in comparison to both 2D and 3D CCD-18co models. 3D CCD-18co models in this instance refers to the Alvetex<sup>®</sup> based 3D model discussed further in chapter 5. In both cases amino-peptidase activity was seen to increase by approximately 50% compared to control levels. There was no significant differences between the effect of 2D and 3D culture systems on the stimulation of Caco-2 layers.

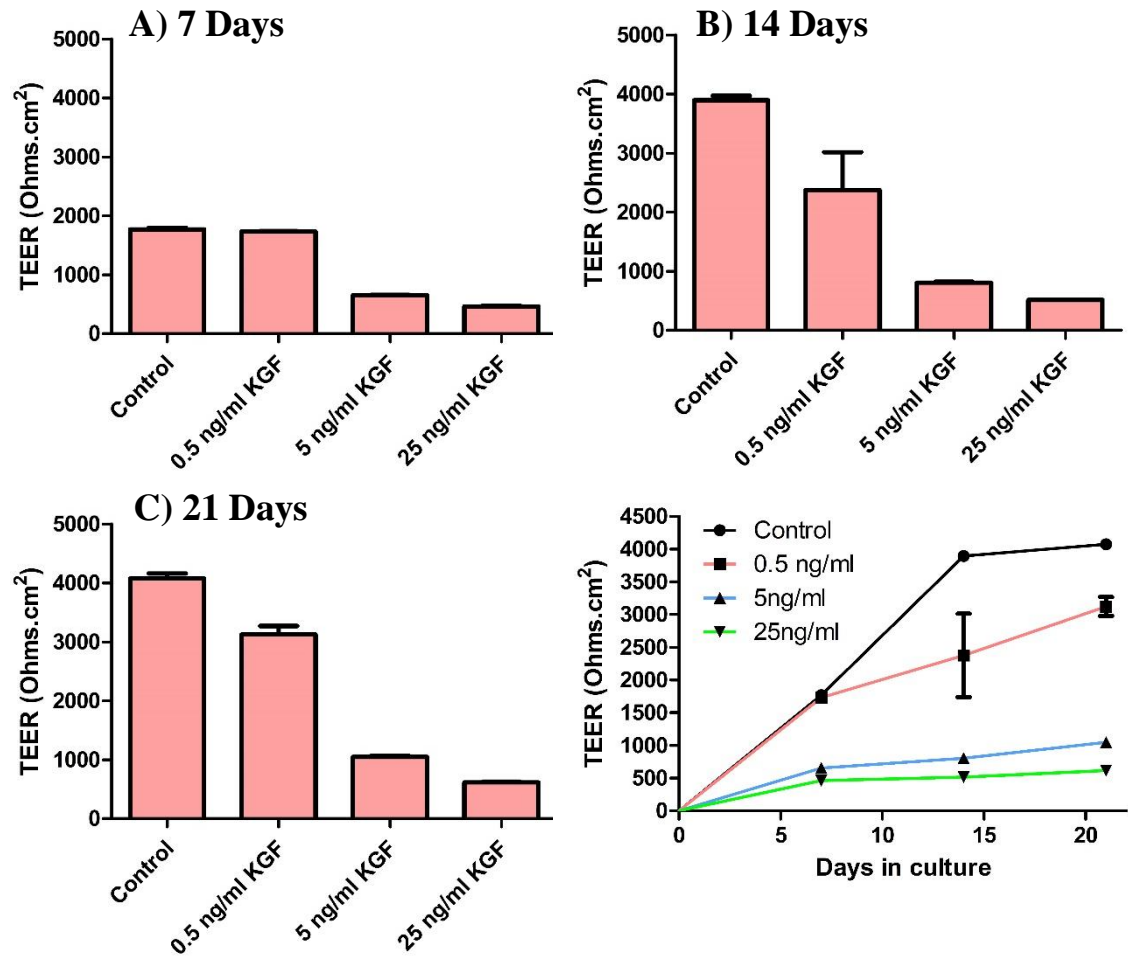


**Figure 3.18: 7, 14 & 21 day TEER measurements of Caco-2 cells on Transwell Snapwell in control and KGF spiked media conditions shows that addition of KGF to the Caco-2 models results in highly significant decreases in epithelial construct TEER values – KGF was spiked into Caco-2 culture media at a concentration of 0.5, 5 and 25ng/ml. TEER assessment was made to quantify changes in barrier integrity mediated by KGF. A) 7 Day Caco-2 culture, B) 14 days, C) 21 days, D) Comparative TEER measurements of spiked media cultures. n=3, N= a minimum of 3 independent experiments.. Scale bars represent +SEM.**

7 Days		14 Days		21 Days	
Control vs 0.5 ng/ml KGF	ns	Control vs 0.5 ng/ml KGF	*	Control vs 0.5 ng/ml KGF	***
Control vs 5 ng/ml KGF	***	Control vs 5 ng/ml KGF	***	Control vs 5 ng/ml KGF	***
Control vs 25 ng/ml KGF	***	Control vs 25 ng/ml KGF	***	Control vs 25 ng/ml KGF	***
0.5 ng/ml KGF vs 5 ng/ml KGF	***	0.5 ng/ml KGF vs 5 ng/ml KGF	*	0.5 ng/ml KGF vs 5 ng/ml KGF	***
0.5 ng/ml KGF vs 25 ng/ml KGF	***	0.5 ng/ml KGF vs 25 ng/ml KGF	*	0.5 ng/ml KGF vs 25 ng/ml KGF	***
5 ng/ml KGF vs 25 ng/ml KGF	***	5 ng/ml KGF vs 25 ng/ml KGF	ns	5 ng/ml KGF vs 25 ng/ml KGF	*

**Table 3.9 Statistical analysis of Transwell model TEER measurements:** One way ANOVA with Tukeys post-test analysis was used to calculate significacy between values \*\*\*=p<0.0005, \*\*=p<0.005, \*=p<0.05. n=3



### **3.4.12 KGF changes the structural physiology of Caco-2 monolayers and decreases membrane TEER levels in a dose-dependent manner.**

The addition of KGF to the media of Caco-2 Transwell models and its effects on the TEER measurement of the membrane over time were assessed using the same methods as measured previously.

Figure 3.18 D shows the relative TEER curves of all variable concentration conditions together. The Caco-2 non-spiked media controls show a rapid increase in TEER values between 0 and 14 days. This is followed by a plateau of any further increase in membrane resistance until 21 days in culture, with maximum TEER values of around 3200 ohms. When 0.5 ng/ml of KGF is added to the culture media the initial increase in TEER values between 0 and 7 days is indistinguishable over the control values. 0.5 ng/ml values differ from control samples in that the beginning of the plateau phase of culture begins at day 7 onwards, with TEER values increasing at a significantly reduced rate until day 21 whereby 0.5 ng/ml cultures have a significantly reduced maximal TEER values over the controls (Figure 3.18 C). 5 ng/ml KGF spiked into the Caco-2 culture media is shown to have highly significant effects on the TEER values of the resultant models throughout the entire 21 days of culture (Figure 3.18, A-C). Initial expansion TEER measurement phase between 0 and 7 days is at a significantly decreased level over both control and 0.5 ng/ml models. Post day 7 this reduced rate of increase reduces further into a plateau phase which lasts until 21 days in culture (Figure 3.18 D). Similarly, 25 ng/ml has an overall culture TEER curve of the same general shape as 5 ng/ml KGF. 25 ng/ml culture results in a significantly decreased model TEER value throughout the course of the culture when compared against the Control models, with an end TEER values of approximately 500 ohms, significantly closer to the TEER values of Human intestinal tissue.

Histologically, Transwell models are shown in Figure 3.19 to change depending on the levels of KGF supplemented to the culture media. Figure 3.19 A, shows Caco-2 control models. Figure 3.19 B-D shows the addition of 0.5, 5 and 25 ng/ml of KGF respectively. 0.5 ng/ml (Figure 3.19 B) shows the least amount of change as expected with cells being

mostly flattened albeit more strongly stained than the control samples. Models which contain higher levels of KGF can be observed to show a heightened cellular phenotype with more cuboidal like cells which are densely packed together to create a continuous layer. Additionally, cells appear to stain more strongly than controls with eosin and appear more polarised.

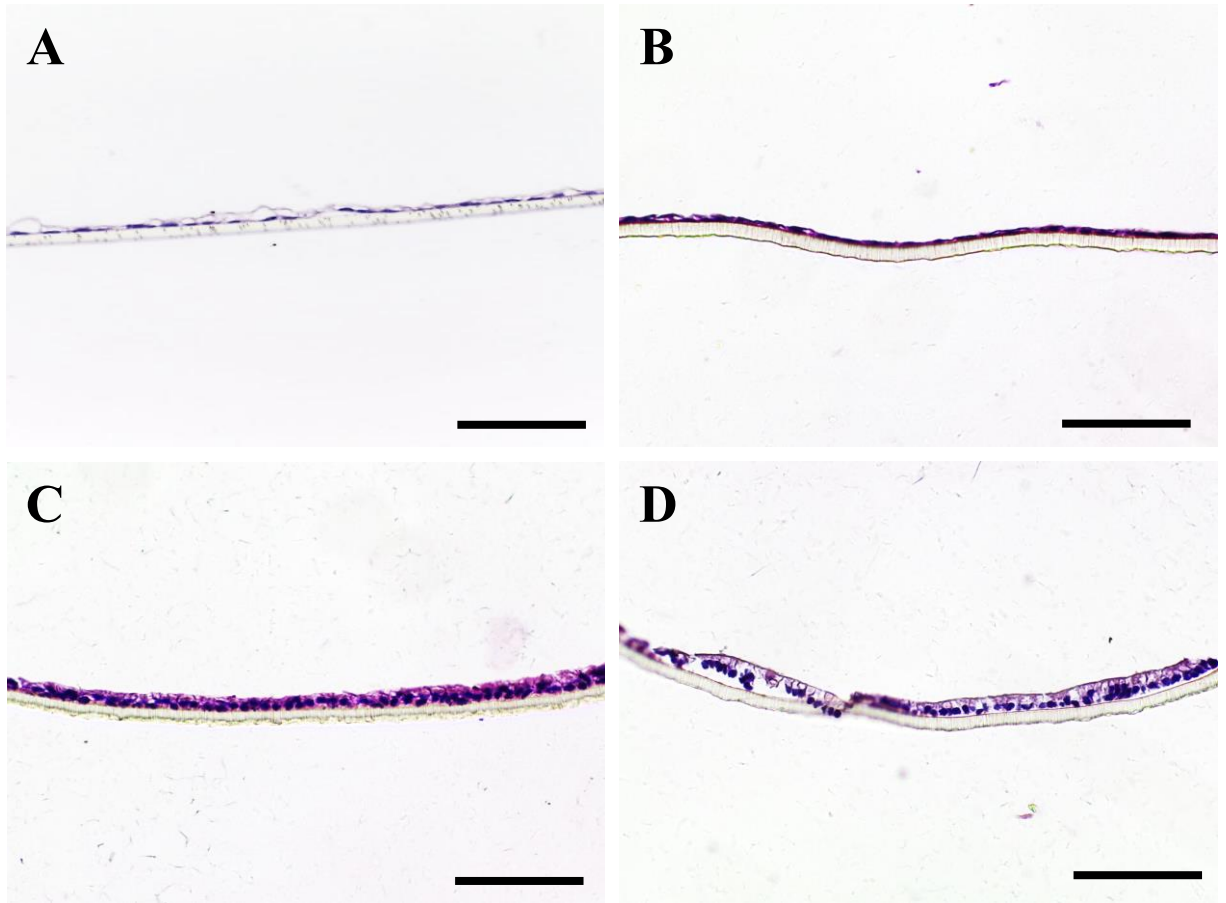


**Figure 3.19: H+E of KGF spiked media Caco-2 Transwell models shows similar histology to the addition of paracrine media with increased cellular height and cytoplasmic staining – H&E histology of 7 $\mu$ m sectioned, PFA fixed, Caco-2/KGF models cultured on Transwell Snapwell ®. A) Control, B) 0.5ng/ml, C) 5ng/ml, D) 25ng/ml. Images are representative of a minimum of 3 independent repeats. Scale= 200 $\mu$ m**

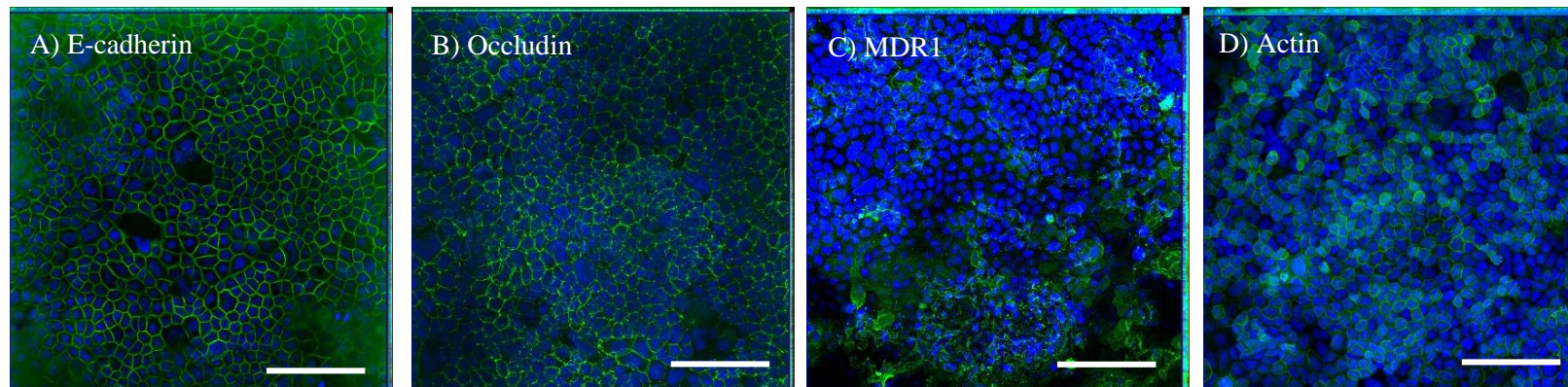


**Figure 3.20: Immunofluorescence staining of Control Caco-2 Snapwell models** – Representative images of wholemount immunostained Caco-2 Transwell Snapwell® intestinal models cultured for a period of 21 days in culture. A) E-cadherin, B) Occludin, C) MDR1, D) Actin. Images are representative of a minimum of 3 independent repeats. Scale = 200 $\mu$ m

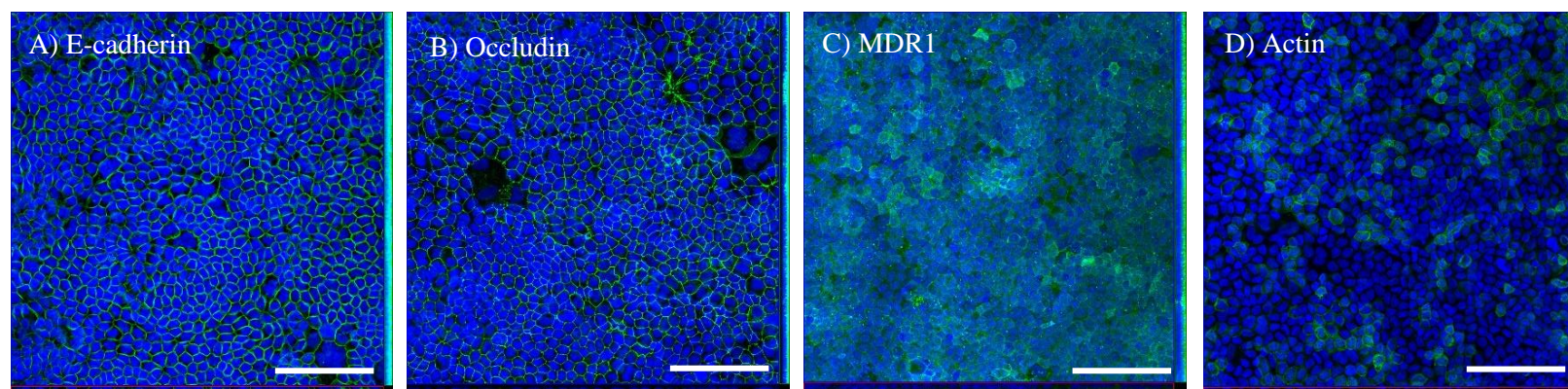


**Figure 3.21: Immunofluorescence staining of 0.5ng/ml KGF spikes Caco-2 Snapwell models** – Representative images of wholemount immunostained Caco-2 Transwell Snapwell® intestinal models cultured with 0.5ng/ml of human recombinant KGF for a period of 21 days in culture. A) E-cadherin, B) Occludin, C) MDR1, D) Actin. Images are representative of a minimum of 3 independent repeats Scale = 200 $\mu$ m



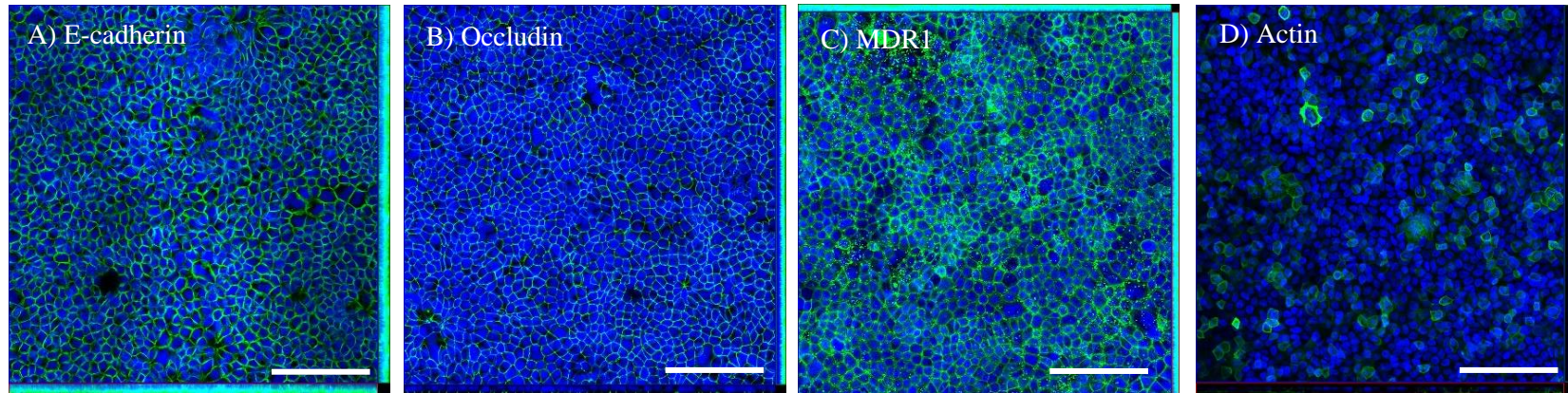


**Figure 3.22: Immunofluorescence staining of 5ng/ml KGF spikes Caco-2 Snapwell models** – Representative images of wholemount immunostained Caco-2 Transwell Snapwell® intestinal models cultured with 5ng/ml of human recombinant KGF for a period of 21 days in culture. A) E-cadherin, B) Occludin, C) MDR1, D) Actin. Images are representative of a minimum of 3 independent repeats Scale = 200µm

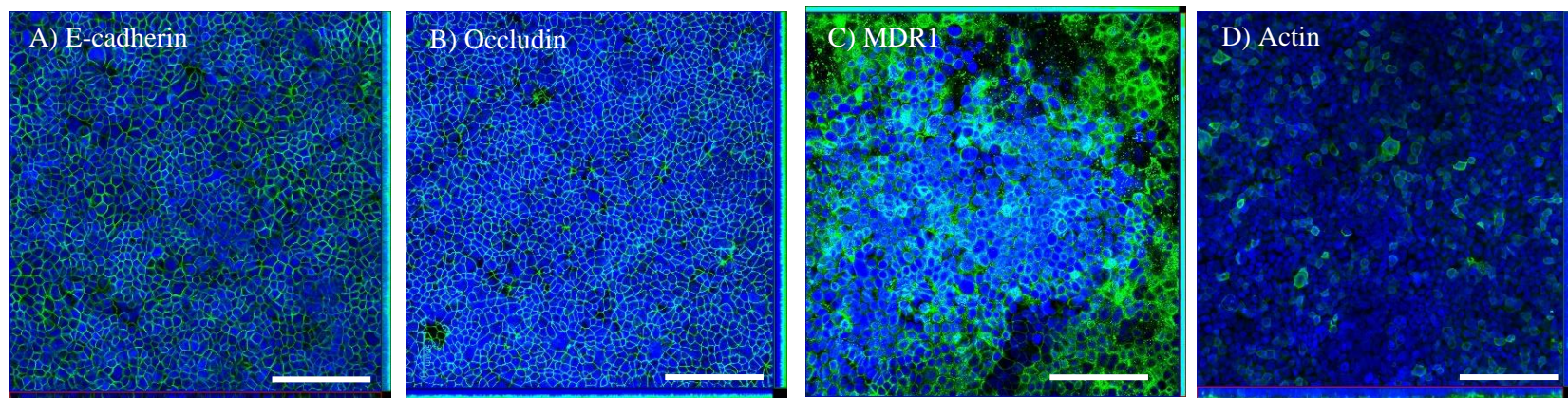


**Figure 3.23: Immunofluorescence staining of 25ng/ml KGF spikes Caco-2 Snapwell models** – Representative images of wholemount immunostained Caco-2 Transwell Snapwell® intestinal models cultured with 25ng/ml of human recombinant KGF for a period of 21 days in culture. A) E-cadherin, B) Occludin, C) MDR1, D) Actin. Images are representative of a minimum of 3 independent repeats Scale = 200µm

### **3.4.13 Immunostaining characterisation of KGF treated Caco-2 layers shows increased Villin expression with higher KGF concentrations.**

Figure 3.20 shows the wholemount expression profile of key protein markers, E-cadherin, Occludin, MDR1, Pan-Actin and Villin. E-cadherin of control layers shows consistent homogenous staining across the entire model layer. Orthogonal view of E-cadherin shows staining, apical to base, along the full length of the cell indicating consistent lateral membrane staining. Comparatively, in KGF treated layers E-cadherin shows a similar pattern of staining throughout all of the models. Occludin (Figure 3.20 B) staining of the same control models shows a similar wholemount pattern as E-cadherin with cell-cell junctional tracing. In contrast, the orthogonal view of Occludin shows localisation to the apical surface of the cells indicating apical lateral tight junction staining. Figure 3.20 C, shows MDR1 (p-gp) staining across control layers. Sample shows inconsistent staining across the surface of the model. Staining, where positive, is located apically to the DAPI stained nuclei, indicating apical microvilli expression as is expected for MDR1. Pan-actin is utilised here (Figure 3.20 D) as a marker for both the surface brush border and actin dense junctional complexes. Control layers are inconsistently stained for actin with some junctional and surface staining seen. However, whilst inconsistent, control layers are shown to have significantly higher staining abundance and intensity when compared to 0.5, 5 and 25 ng/ml KGF conditioned layers (Figure 3.21, 22 & 23, D). Indeed, the 25ng/ml KGF (Figure 3.23 D) conditioned media sample shows extremely inconsistent pan-actin staining with only sporadic junctional staining seen and very little/no surface brush border staining.

### **3.4.14 KGF in Caco-2 culture media increases the metabolic activity of Caco-2 cells in a dose-dependent manner.**

In addition to analysis of the TEER of KGF spiked culture epithelial models, Figure 3.24 shows the effects of the same spiked media concentration on the metabolic activity as measured by the MTT assay. In control wells (Figure 3.24 A-D) it can be observed that the cells undergo an initial lag phase of growth followed by an exponential growth phase and a plateau/ death phase after day 8 whereby the cells have become full confluent.

The addition of 0.5 ng/ml of KGF to the media (Figure 24 A) results in no significantly different changes in the metabolism measured at any point during the culture of the cells. In contrast, both 5 and 25 ng/ml KGF supplementations (Figure 3.24 B, C) to the growth media results in significant increases in Caco-2 metabolic rates by day 20 of culture. Indeed, with regards to the 25ng/ml media concentration the increase in metabolic rate shown by the Caco-2 cells was significantly higher than the controls from day 6 onwards. Generally speaking, the curve shape is the same in ns tested up until day 8 whereby changes can be seen in the shape of the 5 and 25 ng/ml curved. Whereas the Control and 0.5 ng/ml conditions both show a clear decrease in metabolic activity between days 8 and 10, 5 and 25 ng/ml conditions show a more plateau like shape with 25 ng/ml continuing to rise but at a less steep gradient.

When compared together (Figure 3.24 D) the data shows a stepwise increase in Caco-2 metabolism and a less pronounced plateau/ death phase with increasing concentration of KGF spiked into the media.

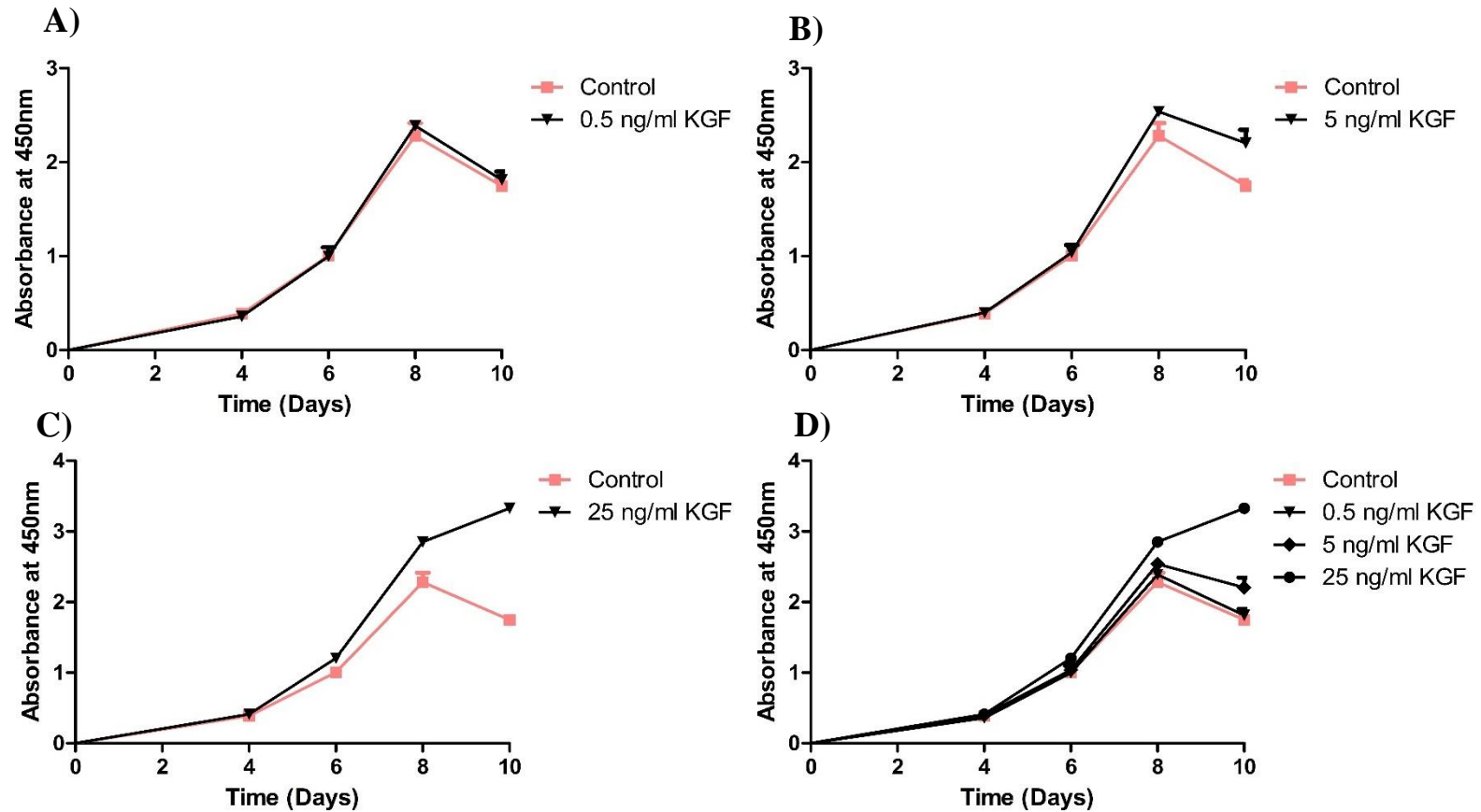


**Figure 3.24: MTT assessment of cellular viability over 10 days culture period (2D) with and without KGF spiked media.** – Cell viability was assessed by MTT assay of 2D cells at set time points. Significant changes in model metabolic activity can be seen in a dose dependant manner with increasing KGF levels resulting in an increase in metabolic activity. Very similar to the effects of CCD-18co conditioned media. All experiments n=3 N=3. Statistical significance is summarised in Table 3.10. Error bars represent  $\pm$ SEM.

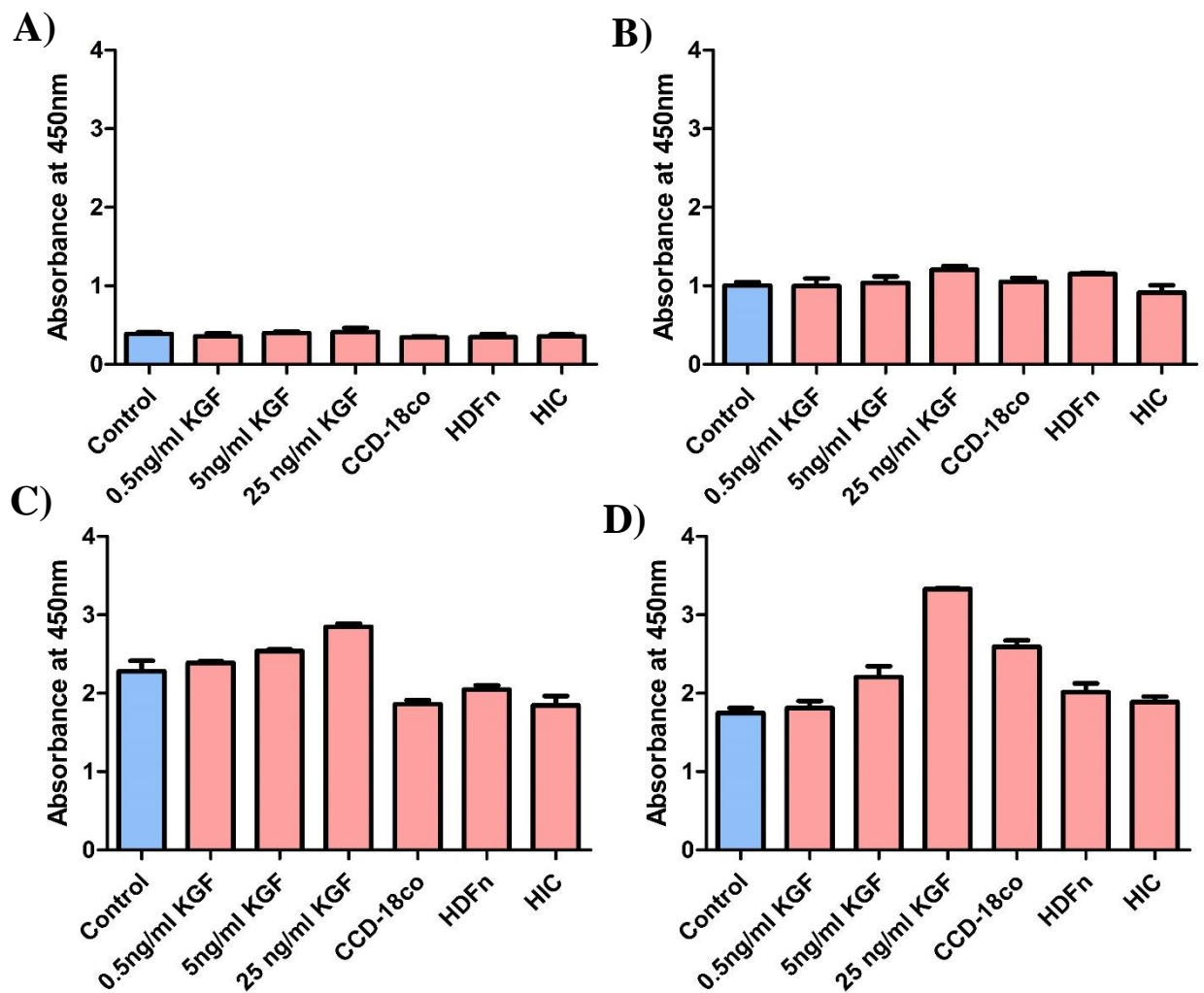


**Figure 3.25: Time-point comparison of all conditions** – A) Day 4, B ) Day 6, C) Day 8, D) Day 10. Values represent means + SEM. All experiments n=3 N=3.



### Chapter 3 – Development of Transwell Co-culture models of the intestinal epithelium

4 Days		6 Days		8 Days		10 Days	
Control vs 0.5ng/ml KGF	ns	Control vs 0.5ng/ml KGF	ns	Control vs 0.5ng/ml KGF	ns	Control vs 0.5ng/ml KGF	ns
Control vs 5ng/ml KGF	ns	Control vs 5ng/ml KGF	ns	Control vs 5ng/ml KGF	ns	Control vs 5ng/ml KGF	*
Control vs 25 ng/ml KGF	ns	Control vs 25 ng/ml KGF	ns	Control vs 25 ng/ml KGF	**	Control vs 25 ng/ml KGF	***
Control vs CCD-18co	ns	Control vs CCD-18co	ns	Control vs CCD-18co	*	Control vs CCD-18co	***
Control vs HDFn	ns	Control vs HDFn	ns	Control vs HDFn	ns	Control vs HDFn	ns
Control vs HIC	ns	Control vs HIC	ns	Control vs HIC	*	Control vs HIC	ns
0.5ng/ml KGF vs 5ng/ml KGF	ns	0.5ng/ml KGF vs 5ng/ml KGF	ns	0.5ng/ml KGF vs 5ng/ml KGF	ns	0.5ng/ml KGF vs 5ng/ml KGF	ns
				0.5ng/ml KGF vs 25 ng/ml KGF	*	0.5ng/ml KGF vs 25 ng/ml KGF	***
0.5ng/ml KGF vs 25 ng/ml KGF	ns	0.5ng/ml KGF vs 25 ng/ml KGF	ns	0.5ng/ml KGF vs CCD-18co	**	0.5ng/ml KGF vs CCD-18co	***
0.5ng/ml KGF vs CCD-18co	ns	0.5ng/ml KGF vs CCD-18co	ns	0.5ng/ml KGF vs HDFn	ns	0.5ng/ml KGF vs HDFn	ns
0.5ng/ml KGF vs HDFn	ns	0.5ng/ml KGF vs HDFn	ns	0.5ng/ml KGF vs HIC	**	0.5ng/ml KGF vs HIC	ns
0.5ng/ml KGF vs HIC	ns	0.5ng/ml KGF vs HIC	ns	5ng/ml KGF vs 25 ng/ml KGF	ns	5ng/ml KGF vs 25 ng/ml KGF	***
5ng/ml KGF vs 25 ng/ml KGF	ns	5ng/ml KGF vs 25 ng/ml KGF	ns	5ng/ml KGF vs CCD-18co	***	5ng/ml KGF vs CCD-18co	ns
5ng/ml KGF vs CCD-18co	ns	5ng/ml KGF vs CCD-18co	ns	5ng/ml KGF vs HDFn	**	5ng/ml KGF vs HDFn	ns
5ng/ml KGF vs HDFn	ns	5ng/ml KGF vs HDFn	ns	5ng/ml KGF vs HIC	***	5ng/ml KGF vs HIC	ns
5ng/ml KGF vs HIC	ns	5ng/ml KGF vs HIC	ns	25 ng/ml KGF vs CCD-18co	***	25 ng/ml KGF vs CCD-18co	***
25 ng/ml KGF vs CCD-18co	ns	25 ng/ml KGF vs CCD-18co	ns	25 ng/ml KGF vs HDFn	***	25 ng/ml KGF vs HDFn	***
25 ng/ml KGF vs HDFn	ns	25 ng/ml KGF vs HDFn	ns	25 ng/ml KGF vs HIC	***	25 ng/ml KGF vs HIC	***
25 ng/ml KGF vs HIC	ns	25 ng/ml KGF vs HIC	ns	CCD-18co vs HDFn	ns	CCD-18co vs HDFn	**
CCD-18co vs HDFn	ns	CCD-18co vs HDFn	ns	CCD-18co vs HIC	ns	CCD-18co vs HIC	**
CCD-18co vs HIC	ns	CCD-18co vs HIC	ns	HDFn vs HIC	ns	HDFn vs HIC	ns
HDFn vs HIC	ns	HDFn vs HIC	ns				

**Table 3.10: Time-point comparison of Conditioned media and KGF spiked conditions** – Summary of comparative significances between data sets. Standard one way ANOVA with Tukeys post-test analysis was performed between data sets. \*\*\* = P<0.0005, \*\* = P<0.005, \* = P< 0.05, n=3, N=3

### **3.4.15 Understanding the development of tight junction expression in Caco-2 cells grown in control and KGF spiked media conditions.**

As described previously in section 3.4.8, tight junctional abundance was assessed through the staining of epithelial layers with Occludin, an intermembrane component of the tight junctional complex.

Figure 3.20 shows the expression of Occludin in each of the samples with timepoint taken 2 days apart for 10 days. As before it can be seen that Occludin expression is abundant even in very low confluency cells and even as cytoplasmic staining of single cells without cell-cell contacts. This expression gets gradually stronger and more abundant over time in each of the spiked media conditions. By day 10 there is a clear difference in cellular confluency between the spiked media samples and the control, with an increasing level of cellular packing with increasing KGF concentration. This results in smaller more tightly packed cellular layers in models exposed to higher concentrations of KGF (5 and 25 ng/ml) than the control. Additionally, cell layers appear to be more homogenous at higher KGF concentrations with little heterogenicity in cell size seen in the layers, probably as a consequence of more tightly packed epithelial layers.

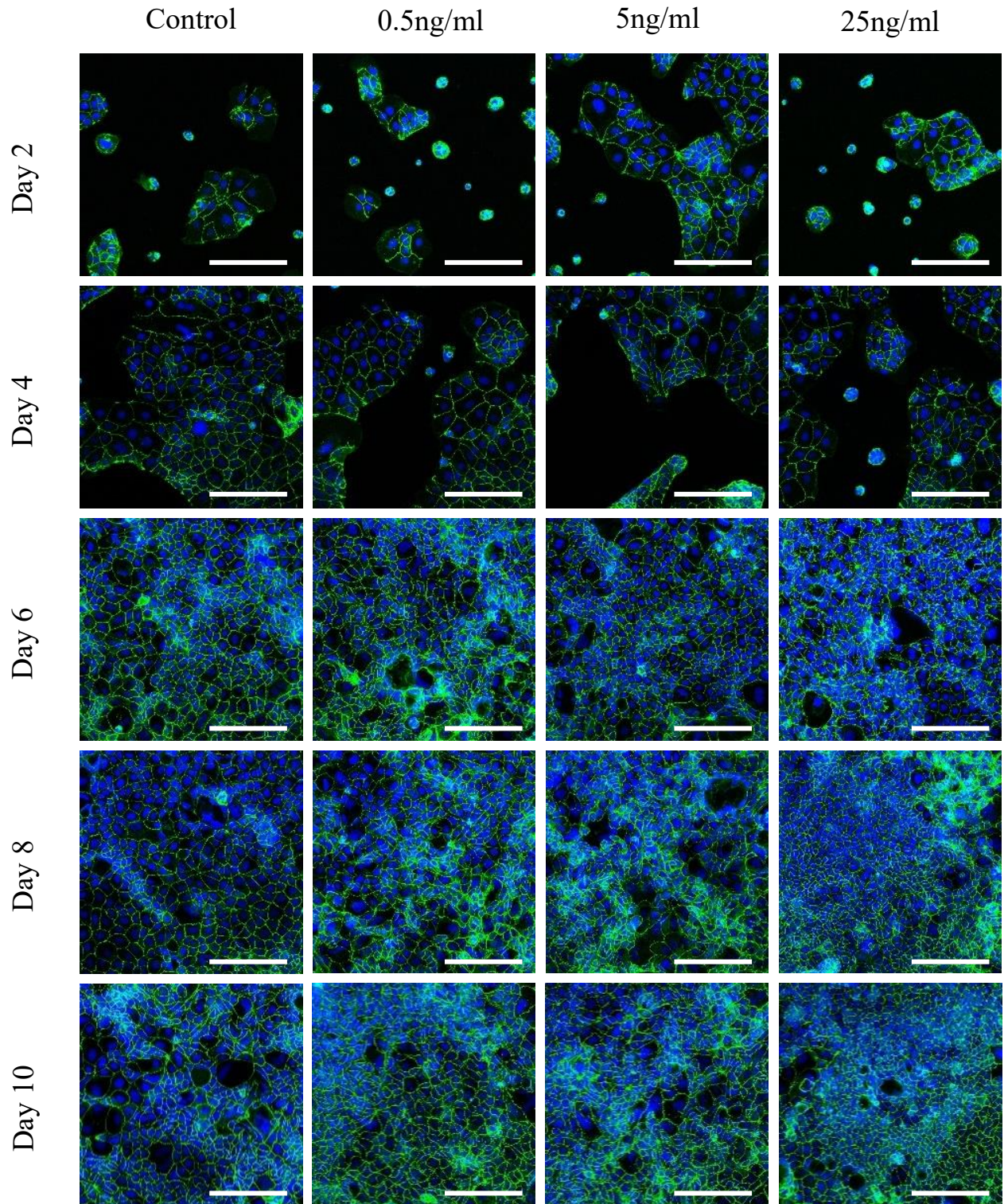


**Figure 3.26: Tight junction expression of Caco-2 cells treated with different KGF concentrations over 10 days** – Control and KGF media treated Caco-2 cells were cultured on 2D plastic for a varying number of days before fixation and staining for the tight junction protein, Occludin. Images are representative of 3 independent repeats Scale = 200µm

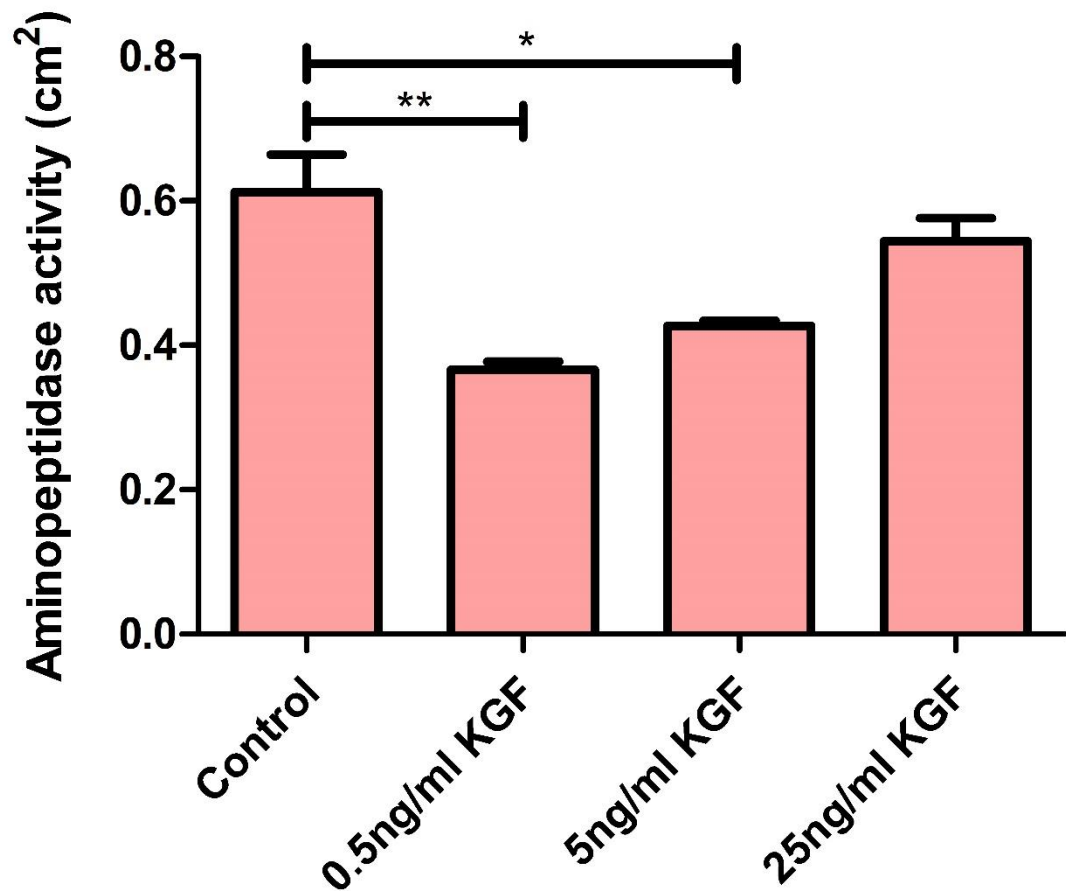


**Figure 3.27: Aminopeptidase activity of KGF treated Caco-2 layers** – Caco-2 treated layers were tested for their Aminopeptidase activity through their ability to convert L-alanine-4-nitroanilide hydrochloride into 4-Nitroaniline. Significances calculated through Student T-test. n=3 N=3. Scale bars represent +SEM.

### 3.4.16 Differential aminopeptidase activity of KGF conditioned layers.

Figure 3.27 shows the relative aminopeptidase activity of Caco-2 membranes treated with 0.5, 5 and 25 ng/ml of KGF. What can be seen is that a small amount of KGF added to the Caco-2 layers, namely 0.5 and 5 ng/ml, results in a significant drop in aminopeptidase activity after 21 days of total culture time. Interestingly, this decrease in enzyme activity is recovered with the addition of further KGF, with 25ng/ml showing no significant decrease over the control samples.

### **3.4.17 Quantification of the levels of KGF present in paracrine conditioned media samples.**

Figure 3.28 shows the relative amounts of KGF secreted into the conditioned media by CCD-18co , HIC and HDFn fibroblasts both cultured in standard DMEM and in Caco-2 paracrine media. KGF levels within the media were normalised to total DNA levels within the samples.

Figure 3.28 A shows the conditioned media gained from 2D cultured fibroblast cells compared with 2D fibroblasts cultured for a period of 7 days in Caco-2 DMEM conditioned media. CCD-18co conditioned media is shown to contain significantly higher levels of KGF than both HDFn and HIC conditioned medias, with an approximate 14-fold increase in KGF abundance per ng of DNA. HDFn and HIC fibroblasts are not shown to have significantly different KGF abundance in cultured in standard DMEM. The application of Caco-2 conditioned media to the CCD-18co cells appears to induce a significant reduction in KGF abundance per ng of DNA over the untreated samples. Conversely, HDFn and HIC Caco-2 conditioned media treated layers do not appear to significantly change from their respective non-treated controls. However, 2D HDFn KGF levels are shown to be significantly different from 2D HIC Caco-2 conditioned media KGF levels. Significances for Figure 3.28 A are summarised in Table 3.11.

The KGF levels of cells cultured in 3D (Figure 3.28 B) shows a similar trend to the comparison in 2D with CCD-18co cells secreting the highest levels of KGF per ng of DNA albeit the difference in KGF secretion between CCD-18co and other fibroblasts is less than in 2D conditions. Similarly to 2D conditions, the addition of Caco-2 conditioned media to the CCD-18co cell layers results in a significant decrease in the KGF abundance overall with this change not reflected in the HDFn of the HIC samples. Significances for Figure 3.28 A are summarised in Table 3.11.

Figure 3.28 C shows the comparative KGF levels between 2D and 3D cultures cells normalised to ng of DNA. As in other comparisons 2D CCD-18co results in the highest levels of KGF per ng of DNA than any other condition. Growth of cells within a 3D

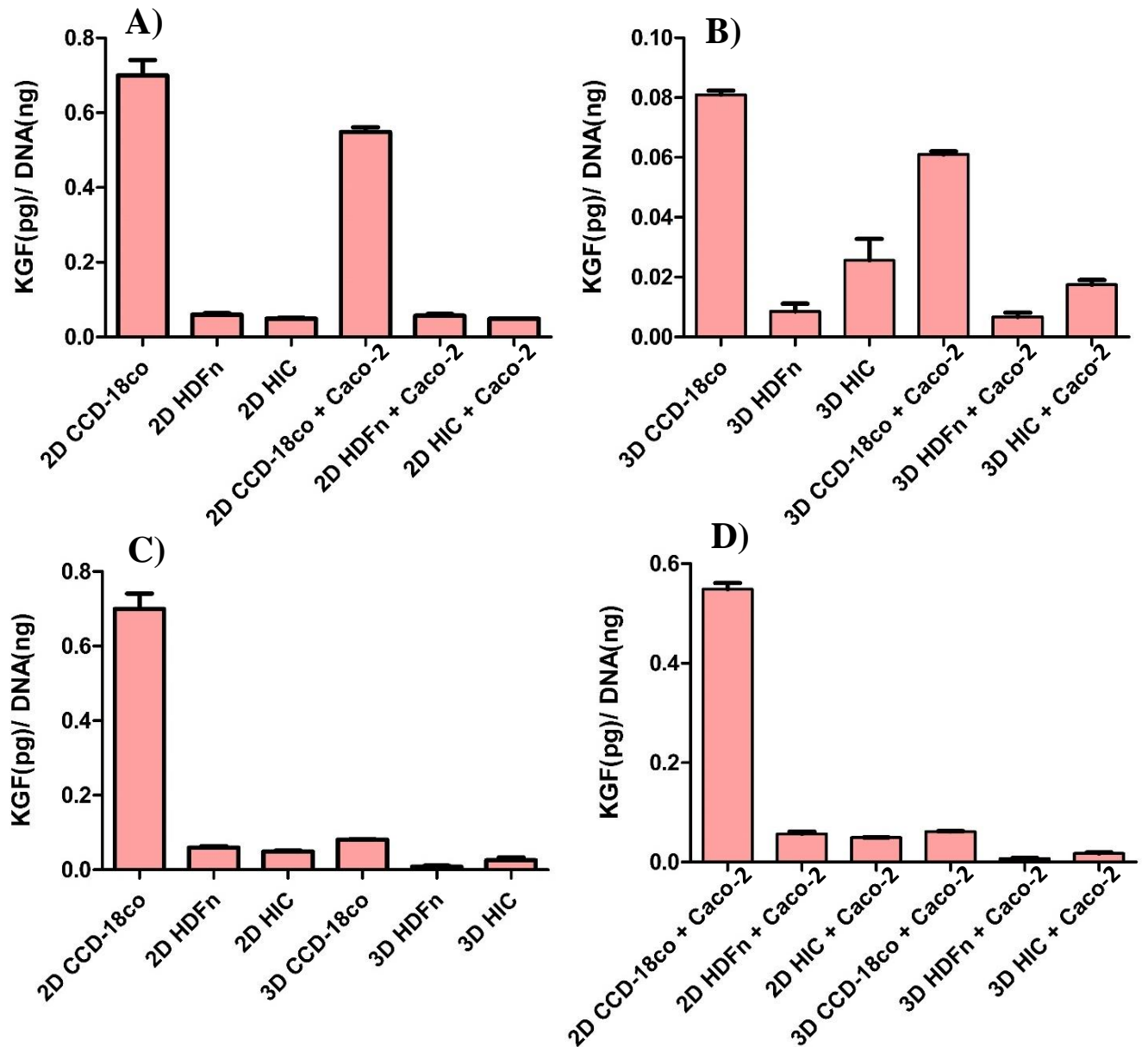
scaffold results in a significant decrease in the levels of KGF over the 2D condition. Indeed, KGF levels of CCD-18co conditioned media grown in 3D reduce down to levels similar to that seen in HDFn and HIC samples. Significant reductions in KGF abundance are also observed in HDFn and HIC cultures although the amount of change is less than that seen in CCD-18co conditioned media experiments. Significances for Figure 3.28 C are summarised in Table 3.11.

Figure 3.28 D shows the comparative KGF abundance between 2D and 3D cells grown in Caco-2 conditioned media. The trends are similar to that seen in Figure 2.20 C with a significant reduction of KGF in 3D cultures compared to 2D grown cells. Significances for Figure 3.28 C are summarised in Table 3.11.

Figure 3.29 shows the total KGF levels of the conditioned media without the normalisation to cellular DNA concentration. Essentially, this graph shows the abundance of KGF in the paracrine conditioned media which would be effecting the Caco-2 epithelium when added to the growing epithelial constructs. Similar to that seen in Figure 3.28, 2D CCD-18co conditioned media has highest levels of KGF at approximately 700-800 pg/ml. These levels are a whole order of magnitude higher than other 2D paracrine media conditions which generally express KGF in the mid to high tens of picogram.

Treatment of fibroblast cultures with Caco-2 conditioned media prior to sampling of fibroblasts conditioned media resulted in a modest decrease in the levels of KGF within the CCD-18co samples with no significant differences in the others. Additionally, as seen in the DNA concentration corrected layers, culture of fibroblasts in 3D resulted in the significant decrease in secreted KGF. In the case of CCD-18co cells, this decrease brought the KGF expression rates in line with levels seen in Hic and HDFn fibroblast conditions. Figure 3.30 shows the relative abundance of DNA isolated from each of the fibroblast conditions. The graph shows that very little variation in DNA abundance can be seen between conditions. This suggests that the controlled seeding amounts at the beginning of the experiment were maintained throughout the culture period in both 2D and 3D. Additionally, treatment of fibroblast layers with Caco-2 conditioned media did not have any meaningful effects on fibroblast growth with Caco-2 conditioned DNA content non-significantly different from the 2D counterparts.





**Figure 3.28: DNA normalised KGF ELISA** – Conditioned media from 2D and 3D fibroblast cultures were assessed for levels of secreted KGF. KGF levels were quantified and normalised with total DNA concentration of 2D and 3D cell lysates. A) 2D vs 2D + Caco-2 conditioned media, B) 3D vs 3D + Caco-2 conditioned media, C) 2D vs 3D, D) 2D + Caco-2 conditioned media vs 3D + Caco-2 conditioned media. n=3 N=3 Error bars represent + SEM

2D CCD-18co vs 2D HDFn	***	2D HIC vs 2D CCD-18co + Caco-2	***
2D CCD-18co vs 2D HIC	***	2D CCD-18co + Caco-2 vs 2D HDFn + Caco-2	***
2D CCD-18co vs 2D CCD- 18co + Caco-2	***	2D CCD-18co + Caco-2 vs 2D HIC + Caco-2	***
2D CCD-18co vs 2D HDFn + Caco-2	***	2D CCD-18co + Caco-2 vs 3D CCD-18co	***
2D CCD-18co vs 2D HIC + Caco-2	***	2D CCD-18co + Caco-2 vs 3D HDFn	***
2D CCD-18co vs 3D CCD- 18co	***	2D CCD-18co + Caco-2 vs 3D HIC	***
2D CCD-18co vs 3D HDFn	***	2D CCD-18co + Caco-2 vs 3D CCD-18co + Caco-2	***
2D CCD-18co vs 3D HIC	***	2D CCD-18co + Caco-2 vs 3D HDFn + Caco-2	***
2D CCD-18co vs 3D CCD- 18co + Caco-2	***	2D CCD-18co + Caco-2 vs 3D HIC + Caco-2	***
2D CCD-18co vs 3D HDFn + Caco-2	***	3D CCD-18co vs 3D HDFn	*
2D CCD-18co vs 3D HIC + Caco-2	***	3D CCD-18co vs 3D HDFn + Caco-2	*
2D HDFn vs 2D CCD-18co + Caco-2	***		

**Table 3.11: KGF levels in conditioned media normalised to DNA concentration of 2D cellular layers** – Summary of comparative significances between data sets. Standard one way ANOVA with Tukeys post-test analysis was performed between data sets. \*\*\* =  $P < 0.0005$ , \*\* =  $P < 0.005$ , \* =  $P < 0.05$ ,  $n=3$ ,  $N=3$



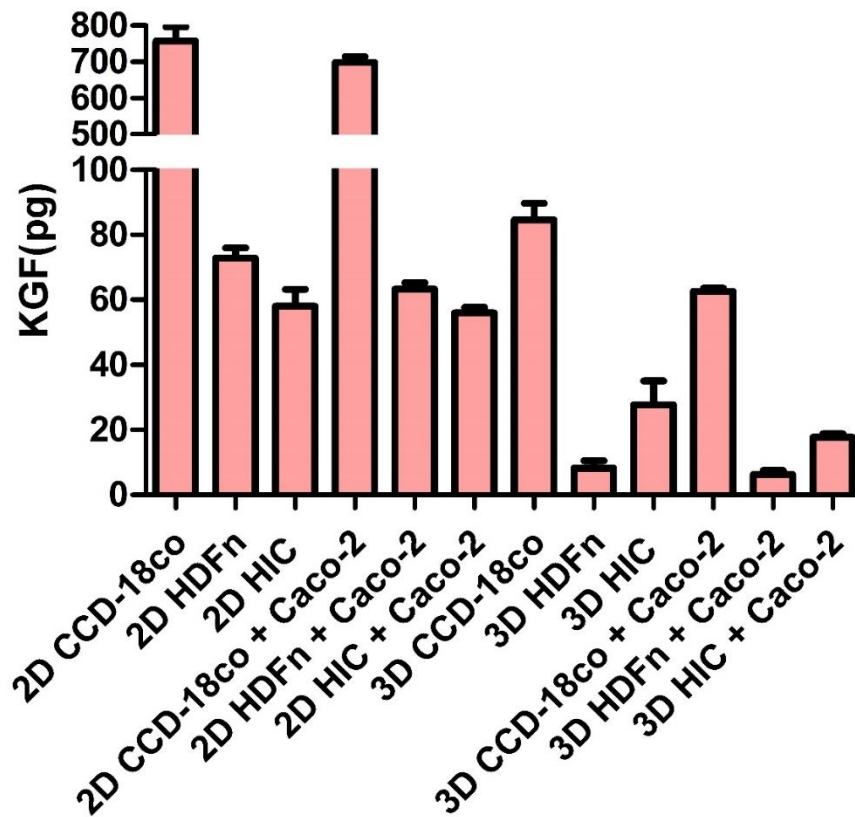


**Figure 3.29: Total KGF concentration of conditioned media** – Total KGF concentration of the different conditions without the DNA concentration corrected. 2D CCD-18co cells can be seen secrete the most KGF of all conditions tested by approximately an order of magnitude. Culture of CCD-18co in 3D attenuates the high KGF secretion rates to levels much more similar to those seen in other conditions. n=3, N=3. Scale bars represent +SEM.

2D CCD-18co vs 2D HDFn	***	2D HIC vs 2D CCD-18co + Caco-2	***
2D CCD-18co vs 2D HIC	***	2D CCD-18co + Caco-2 vs 2D HDFn + Caco-2	***
2D CCD-18co vs 2D HDFn + Caco-2	***	2D CCD-18co + Caco-2 vs 2D HIC + Caco-2	***
2D CCD-18co vs 2D HIC + Caco-2	***	2D CCD-18co + Caco-2 vs 3D CCD-18co	***
2D CCD-18co vs 3D CCD-18co	***	2D CCD-18co + Caco-2 vs 3D HDFn	***
2D CCD-18co vs 3D HDFn	***	2D CCD-18co + Caco-2 vs 3D HIC	***
2D CCD-18co vs 3D HIC	***	2D CCD-18co + Caco-2 vs 3D CCD-18co + Caco-2	***
2D CCD-18co vs 3D CCD-18co + Caco-2	***	2D CCD-18co + Caco-2 vs 3D HDFn + Caco-2	***
2D CCD-18co vs 3D HDFn + Caco-2	***	2D CCD-18co + Caco-2 vs 3D HIC + Caco-2	***
2D CCD-18co vs 3D HIC + Caco-2	***	3D CCD-18co vs 3D HDFn	*
2D HDFn vs 2D CCD-18co + Caco-2	***	3D CCD-18co vs 3D HDFn + Caco-2	**
2D HDFn vs 3D HDFn	*	3D CCD-18co vs 3D HIC + Caco-2	*
2D HDFn vs 3D HDFn + Caco-2	*		

**Table 3.12: Absolute KGF levels in conditioned media statistical analysis** – Summary of comparative significances between data sets. Standard one way ANOVA with Tukeys post-test analysis was performed between data sets. \*\*\* = P<0.0005, \*\* = P<0.005, \* = P< 0.05, n=3, N=3

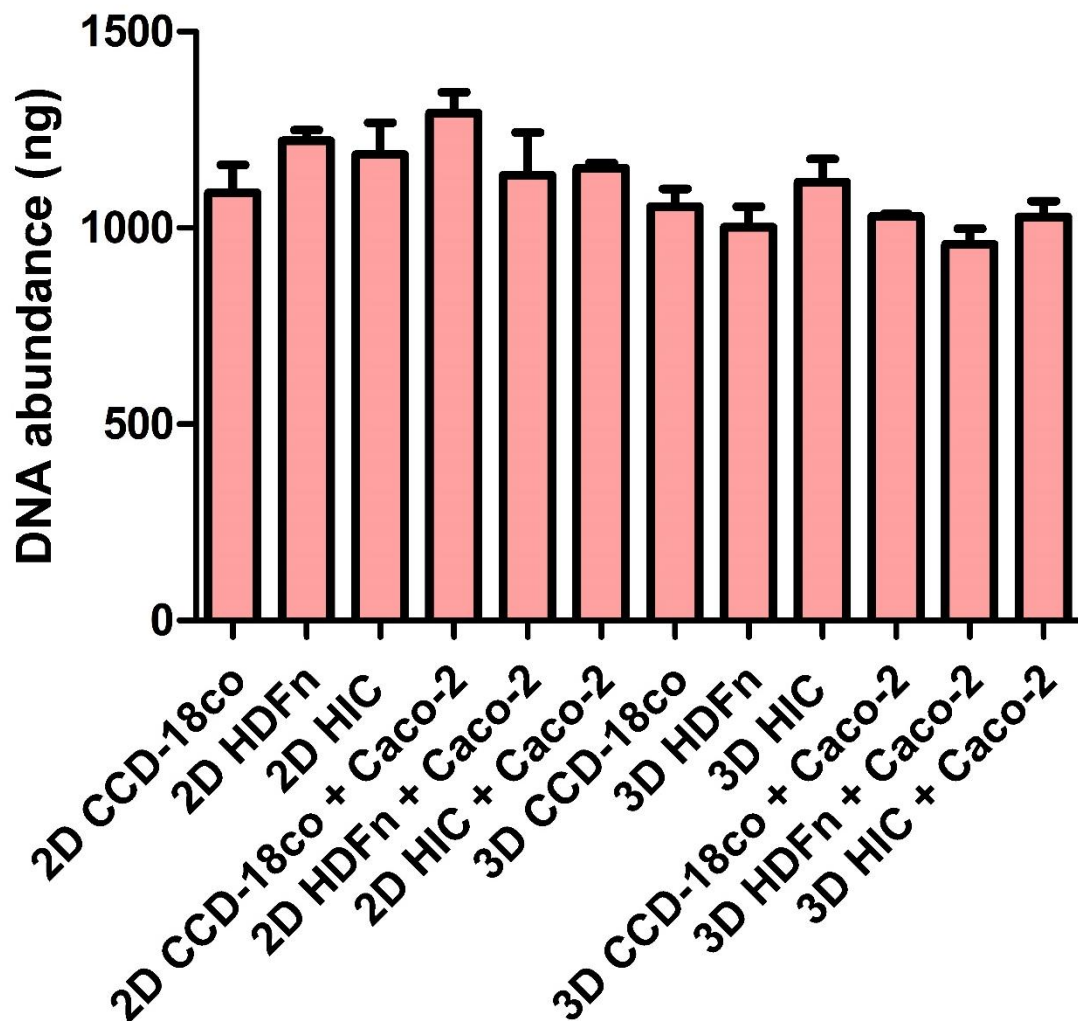


**Figure 3.30: Total DNA abundance of fibroblasts utilised for the generation of conditioned media shows no significant differences between like-samples–** Total DNA abundance in fibroblasts utilised to create the conditioned media utilised in the KGF concentration analysis experiment. Very little variation is seen between conditions suggesting that cell numbers in each conditions are approximately equal. Small variation in the DNA levels explains why similar trends are seen in corrected and total KGF graphs. n=3, N=3. Scale bars represent +SEM.

2D CCD-18co + Caco-2 vs 3D HDFn	*
2D CCD-18co + Caco-2 vs 3D HDFn + Caco-2	*

**Table 3.13: DNA concentration of 2D fibroblast cellular layers statistical analysis –** Summary of comparative significances between data sets. Standard one way ANOVA with Tukeys post-test analysis was performed between data sets. \*\*\* =  $P < 0.0005$ , \*\* =  $P < 0.005$ , \* =  $P < 0.05$ , n=3, N=3

### 3.4.18 The effects of conditioned and KGF spiked media on the passive paracellular transport of Lucifer yellow.

Figure 3.31 shows the passive paracellular transport of the fluorescent compound Lucifer Yellow. Caco-2 control layers show a Papp value of around  $1 \times 10^{-6} \text{ cm/s}$ , a normal value for Caco-2 layers when compared to the literature. A small non-significant increasing trend is seen when Caco-2 cells are cultured in the paracrine media of CCD-18co fibroblasts. This increasing trend continues when comparing Caco-2 controls to 3D CCD-18co Alvetex® models. A trend which is also shown to be non-significant when analysed by unpaired student T-test.

2D HIC and HDFn layers show a decrease in the levels of permeability to Lucifer yellow compared to control to a similar level of that seen in KGF spiked conditions. 3D HIC and HDFn models however have an increased permeability, similar to the levels of 3D CCD-18co. This increase could be attributed to the change in culture system rather than a physiological change in the cells. Addition, of KGF to the Caco-2 media results in a decrease in overall membrane permeability, albeit as before, in a non-significant manner when compared to control layers.

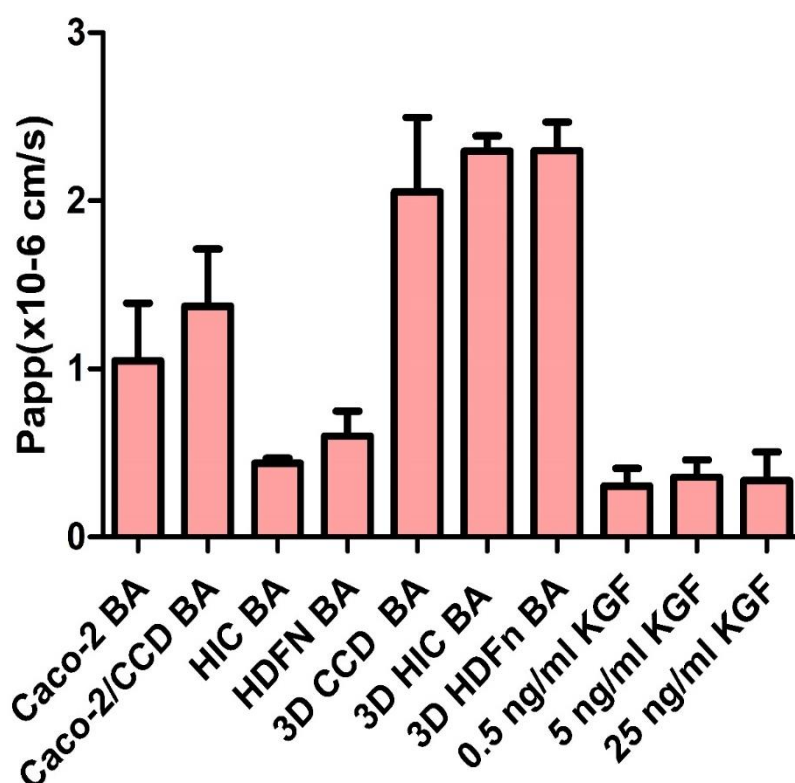


**Figure 3.31: Lucifer yellow paracrine transport across treated epithelial layers -** Lucifer Yellow is utilised as a marker of membrane integrity by acting as a passive, paracellular transported compound. Membranes with low integrity would show higher Papp values. n=3 , N=3. Significance was assessed by one way ANOVA with Tukeys post-test analysis. No significant difference was observed between samples. Scale bars represent +SEM.

### **3.4.19 qPCR analysis of conditioned and KGF spiked media samples for the relative abundance of mRNA for key tight junctional components.**

Figure 3.32 shows the relative junctional mRNA expression rates of conditioned and KGF spiked media samples. Figure 3.32 A, shows relative Occludin mRNA abundance. Generally, there is either no significant changes in mRNA levels (CCD-18co and HDFn conditioned media) or there is a small decrease in relative abundance (HIC conditioned media along with all KGF spiked media samples).

A similar pattern of expression rates is seen in Figure 3.32 B, for the expression of mRNA encoding the protein Claudin 2 with HIC and KGF samples showing a small decrease in relative expression and CCD-18co and HDFn samples showing little relative change.

Conversely, Figure 3.32 C shows the relative expression of ZO-1. Interestingly, CCD-18co and HDFn conditioned media see large increased in relative expression compared to control Caco-2 layers. HIC conditioned and KGF spiked media samples also show significant increases in relative mRNA expression albeit to a lesser extent than CCD-18co and HDFn samples. Interestingly, whilst compared to the control all ZO-1 samples are increased, the overall pattern between samples is similar to that seen in Occludin and Claudin-2 analysis.

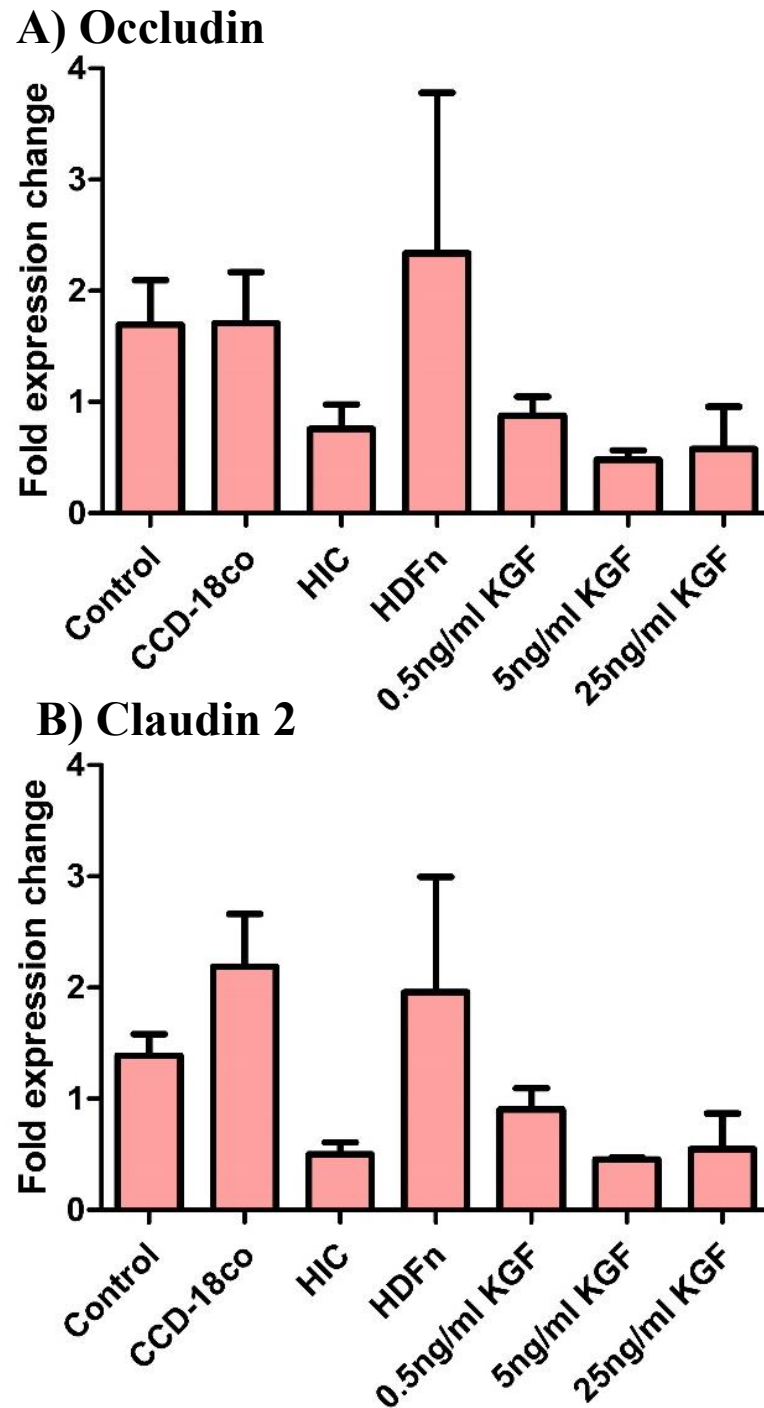


**Figure 3.32: qPCR analysis of relative tight junctional component expression in 2D conditioned media studies – A) Occludin, B) Claudin 2, C) ZO-1.** Changes in expression patterns can be seen between different conditioned media samples. Generally, CCD-18co and HDFn models show increases in junctional proteins compared to HIC conditions which generally decrease compared to other conditions. KGF samples show decreases in Occludin and Claudin-2 whilst ZO-1 levels generally increase. n=3 (HIC n=2) N=3 (HIC N=2). Significance test were performed utilising one way ANOVA with Tukeys post-test analysis. No significance between data points was observed. Scale bars represent mean +SEM.

### **3.5.20 qPCR analysis of conditioned and KGF spiked media samples for the relative abundance of mRNA for efflux transporter protein important in the function of Caco-2 cells.**

Figure 3.33 shows the relative mRNA abundance of key efflux proteins involved in the functionality of Caco-2 cells when utilised as models of drug permeability. Figure 3.33 A shows the relative expression rate of MDR1, commonly known as P-glycoprotein (P-gp) between different conditions. P-gp is thought to be under/ normally expressed in control Caco-2 layers. Addition of CCD-18o and HIC conditioned media to Caco-2 monolayers results in a significant decrease in the relative levels of MDR1 mRNA. Conversely, addition of HDFn and KGF spiked media samples resulted in a significant increase in MDR1 levels compared to control sample expression rates.

In contrast, Figure 3.33 B shows the relative expression rates of MRP1 between all samples. CCD-18co conditioned media is shown to increase mRNA levels significantly with all other conditions having no significant effects on the overall relative expression. KGF spiked media samples do not appear to be significantly changed compared to the control layers however, a trend in expression rates between KGF spiked samples can be observed here which is also seen in other mRNA targets whereby 5ng/ml KGF causes a relative decrease in mRNA expression levels compared to 0.5ng/ml which is then corrected through an increase in relative expression when samples are cultured in 25ng/ml KGF. This could suggest some kind of KGF regulation whereby 5ng/ml KGF addition into the media is being suppressed by some unknown mechanism which, when cultured with 25ng/ml KGF is overwhelmed, resulting in further changes, usually increases, in relative mRNA abundance.

Figure 3.33 C shows the relative expression rates of mRNA encoding for MRP2. As can be seen by looking at Figure 3.33 B & C, very different expression changes are seen between the both MRP1 and 2, both of which are highly related and have many overlapping functions. HIC conditioned media along with all of the KGF spiked media conditions saw a decrease in the relative mRNA levels compared to the control. Whereas

CCD-18co and HDFn were both non-significantly different from Control levels with a trend towards a slight increase.

Finally, relative Villin expression rates are shown in Figure 3.33 D. All conditions except 5ng/ml KGF spiked media were non-significantly different from Control layers. CCD-18co did show a trend to increased relative levels however the variability was too high for significance. 5ng/ml KGF spiked levels showed a decrease in relative Villin mRNA expression compared to controls. Interestingly, this decreases in reverted in 25ng/ml KGF levels in a similar manner as previously described.

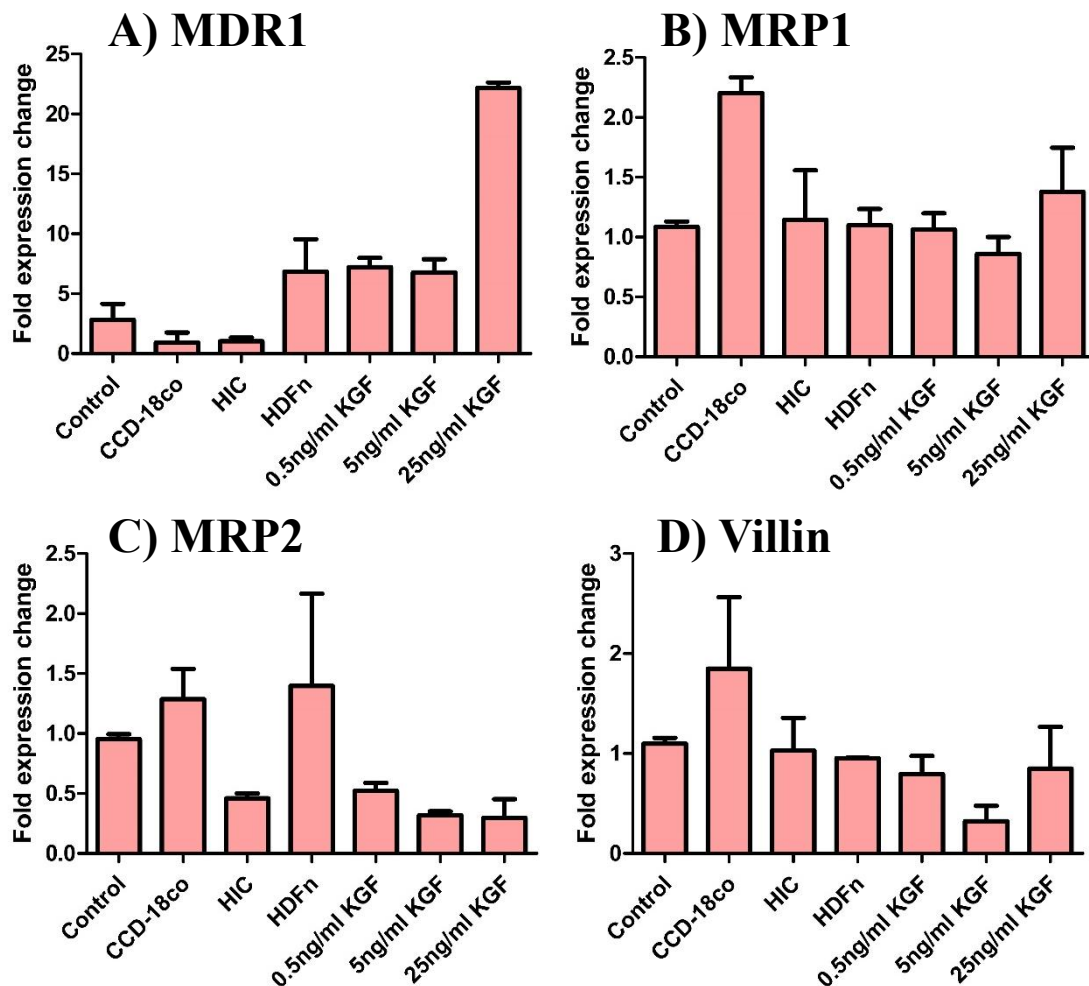


**Figure 3.33: qPCR analysis of relative functional efflux protein component and Villin expression in 2D conditioned media studies – A) MDR1, B) MRP1, C) MRP2 D) Villin.** Variable differences can be seen between different conditioned media samples. KGF spiked samples show increases MDR1 and MRP1 (A & B) expression over controls. Especially at 25 ng/ml levels. Conversely MRP1 and Villin levels are seen to decrease compared to controls. Significance values were not calculated for this data set due to low replicate number of n=2-3 N=2-3. Scale bars represent mean +SEM.

## **3.5 Discussion**

### **3.5.1 Chapter overview**

The aims of this chapter were to evaluate the suitability of a number of prospective cell lines for co-culture with Caco-2 cells in a Transwell Snapwell epithelial model and to postulate a potential mechanism by which said cell lines were having physiological action. The commercially available cells lines utilised were CCD-18co (Colon Carcinoma) & HDFn (neonatal Human dermal fibroblasts), along with primary human intestinal cells (HIC) isolated from tissue in the lab. Fibroblast cell lines were characterised for their structural and protein morphology before being applied to Caco-2 models through the use of conditioned media containing paracrine released factors released by the fibroblasts. The effects of said conditioned media on Caco-2 Snapwell® cell layer development was assessed by a number of techniques, namely, TEER, MTT assay and drug transport (discussed later).

The barrier integrity of Caco-2 membranes is critically important to their function as pharmacokinetically useful models within the lab. As such barrier integrity of Caco-2 layers was assessed through the immunostaining of Occludin (Tight junction marker) alongside TEER measurements of control and conditioned models and MTT assessment of model metabolism. The metabolic activity of Caco-2 cells within Snapwell model is also a good indicator of the transport capabilities of the developed epithelium. Cell layer metabolic activity was assessed both in 2D over time and at 21 days in culture in Snapwell® models by use of MTT assay.

Changes in the functional components of the Caco-2 epithelial layers such as surface aminopeptidase and efflux protein expression was assessed by N-nitroaniline assay and qPCR for transporter mRNA abundance respectively. Finally, a potential mechanism for the change in Caco-2 layers seen to be induced by paracrine conditioned medium, was investigated through quantification of KGF and comparison of KGF spiked media layers to conditioned media values.



### **3.5.2 Fibroblast characterisation through phase contrast and immunohistological microscopy.**

ATCC (American Type Culture Collections) describes CCD-18co cells as normal neonatal colon fibroblast cells. Phase contrast analysis of these cells shows a classical fibroblast like morphology with long protruding, spindle-like extensions and small cellular bodies. (178) There is some evidence to suggest that fibroblasts differentiate along the villi-crypt axis in much the same way that epithelial cells do, going from a discoid shape in the crypt to a spindle shape at the villus tip. As such the fibroblast morphology seen in 2D culture here is more reminiscent of the “differentiated” fibroblasts of the villus tip rather than those of the crypt. (179) Fibroblast cell layers are motile, spacing equidistantly from one another before replicating to confluency, at which point cells become contact inhibited and further replication stops after a period of cellular packing.

When immunostained for cell lineage specific markers positive staining of the major mesenchymal intermediate filament protein Vimentin alongside alpha smooth muscle actin ( $\alpha$ SMA) were shown. No positive staining is seen for Desmin (a smooth muscle lineage marker), which along with positive Vimentin staining suggests cells are not of a smooth muscle origin.  $\alpha$ SMA staining is often used as a marker for myofibroblast identification (180) but is also seen to be expressed in many other cell types within the intestinal mucosae, some of which are dependent on the location within the intestine. E.g. Smooth muscle of the small intestine or in lymphatic pericytes found within the colon. (180)

Past literature shows that myofibroblast populations exist throughout the intestine, primarily located beneath epithelial layers and are responsible for the development, maintenance of the epithelial layer (179,180), principally through the secretion of paracrine factors. (179) Indeed, they are thought to not only support the development of the mature epithelium at the villus tip but also be important regulators of the stem cell niche in the crypt base. (173) Lei *et al*, worked to support this theory by assessing the effects of myofibroblast paracrine factors on their ability to promote the creation of

differentiated intestinal epithelium enteroids and for their successful engraftment *in vivo* into C57BL/6 mice. They found that *in vitro* enteroid development was enhanced by co-culture with myofibroblast and that *in vivo* implantation was not possible with monoculture organoids, suggesting an important role in sub-epithelial myofibroblasts in crypt and epithelial maintenance and development. Additionally, there is further evidence that intestinal myofibroblast populations act as mediators of inflammation within the intestine, playing a key role in inflammatory bowel diseases such as Crohn's disease. (181,182)

Pericytes are often thought to be supportive cells of endothelial layers rather than epithelial, important in the development and maintenance of blood vessels in much the same way myofibroblasts are thought to maintain epithelial layers. (183,184) Pericytes structural morphology is similar to that of myofibroblasts making them impossible to identify apart with simple light microscopy. Pericytes are also shown to be  $\alpha$ SMA positive and as such distinguishing immunofluorescence between myofibroblasts and pericytes is difficult, due to their overlapping function in addition to their expression profile. Indeed, many have argued that  $\alpha$ SMA cells located immediately below epithelial layers are more likely to be pericytes than myofibroblasts. (185) However, in this instance smooth muscle or pericyte lineages in the cells is unlikely due to the absence of positive Desmin staining, a key marker for both *in vivo* with smooth muscle cells staining strongly positive and pericytes staining weakly for Desmin expression. (180,186–188)

Tubulin is a highly conserved microtubule protein found within eukaryotic cells. In this instance Tubulin staining was utilised as a marker of cellular structure rather than as a tool for the distinguishing of cell type. Actin was used in a similar way. Actin should be strongly conserved and stained in all fibroblast cells and as such weak staining seen here may not be physiologically mimetic, potentially suggesting a failure in the staining process.

The expression profile of immunostained fibroblasts utilised in this study suggests a myofibroblast type cell in all instances, phenotypically somewhere between a true fibroblast and a smooth muscle cell. HDFn and HIC cells show a similar expression profile to that of CCD-18co suggesting myofibroblast lineage. It should be noted that far

weaker  $\alpha$ SMA staining was seen of HDFn cells when compared to myofibroblasts derived from the intestine. This could potentially reflect the decreased proportion of myofibroblasts that are naturally found within the human skin (generally produced as a consequence of damage as a wound healing response) compared to the intestine mucosa. (189) However, the similarity in the overall HDFn expression profile lends validation as potential cells to be utilised within intestinal models; with benefits including improved availability, replicative potential and cost over similar primary intestinal fibroblast cells.

### **3.5.3 Paracrine influences on structural morphology and Trans-Epithelial Electrical Resistance (TEER).**

The change of structural morphology seen in co-culture intestinal models implies that paracrine factor(s) present within the conditioned media are having effects on the development/ differentiation of the Caco-2 membrane over time. Interestingly, the phenotype change between models is different dependant on the myofibroblasts utilised to create the conditioned media, suggesting multiple mechanisms of action. What is more likely is that a complex cocktail of paracrine factors are being released into the conditioned media, resulting in the variable effects seen. In all cases except Caco-2/ HDFn culture a monolayer of cells was observed with varying polarity along the membrane length. Caco-2/ HDFn layers resulted in a taller multilayer epithelium.

Changes in structure have been shown to have intimate effects on the function of cells. Indeed, the intestine itself has been shown to change the structure of epithelial enterocyte cells in response to a number of external stimuli such as the composition of dietary lipids in the intestine. (190) TEER is the foremost way in which the membrane integrity of Caco-2 Transwell layers is monitored throughout the models culture period. Furthermore, TEER is used as a quality control mechanism whereby models with a TEER above or, more usually, below, pre-set values are excluded from analysis. The utilisation of this method, whilst prevalent throughout industry, can be flawed, with low intra-lab but high inter-lab variation between models. Indeed, Caco-2 Transwell models have reported 14-21 day culture TEER values of anything from 150 to 3000 ohms per  $\text{cm}^2$ , (16,161,191,192) with differences seen without any changes in protocol between labs.

Caco-2 cells are well known to express a heterogeneous population of cell morphologies when cultured in standard 2D conditions. (193) Beaulieu and Quaroni *et al* were one of the first to quantify this heterogeneity by demonstrating the mosaic expression of sucrase-isomaltase within Caco-2 populations. (194) Caco-2 heterogeneity is seen in this study in the images of Caco-2 cells conducted within this work, with simple phase microscopy and cell shape as outlined by Occludin staining. A multitude of variable cell sized throughout pre and post confluent Caco-2 monolayer can be observed. Additionally, expression of surface transporter proteins such as MDR1 (p-gp) and MRP2 are expressed inconsistently across the membrane, highlighting single or small groups of cells in a mosaic fashion as described in other works. (193,195) This can be most clearly seen when cells have been cultured on Transwell membrane and allowed to differentiate for 21 days. MDR1 staining in particular is shown to be clearly positive in very specific cell sub-populations throughout the model, especially in those treated with CCD-18co conditioned media.

One possible explanation for the variation seen in Caco-2 studies between different labs is the accidental formation and utilisation of Caco-2 subclone populations and is a huge issue in the reproduction of results between labs. Indeed, there are many well-known sub-population of Caco-2 cells which have different structural and functional morphologies.(196) A simple experiment conducted by Woodcock et al (197) highlights the heterogeneity of Caco-2 populations. They showed that by taking a parental Caco-2 cell line, diluting a trypsinised solution to 100 cells per flask, isolating colonies and utilising the cell lines produced, that significant differences could be seen in cloned populations TEER values in addition to changes in their transport capabilities of taurocholic acid.

Close following of protocols is critical to maintaining reproducible TEER values over time and include close regulation of factors such as measurement media temperature(198), pH(199), passage number of cells used (200) and measurement point in culture period. In this study Caco-2 controls are seen to display an area corrected TEER value of around 2000 ohms per cm<sup>2</sup>, which, whilst on the higher end of reported values for Caco-2 cells, does have precedence within the literature. (201,202) Caco-2 cells are provided by ECACC at passage 44 with the majority of Transwell work occurring

between passage 48 and 55. Briske-Anderson *et al* showed in their study of TEER in Caco-2 cell models that TEER values tend to increase with increasing passage number up to approximately P70 whereby TEER values rapidly decrease. In fact the reported values of around 2000 ohms per cm<sup>2</sup> correlate almost exactly with the TEER values of Caco-2 cells at passage 50 in this study.(200) When compared to human tissue TEER values, Caco-2 cells, due to their colonic origin, are expected to provide values more in line with those seen in the distal regions of the intestine. Indeed, TEER values of 300 ohms per cm<sup>2</sup> would be in line with that seen in *in vivo* colon (203), but not small intestine which has general TEER values of below 100 ohms per cm<sup>2</sup>. (204)

CCD-18co, HDFn and HIC conditioned medium was shown to have a significant decreasing effects on the TEER values of the epithelial membrane models. CCD-18co and HDFn have the largest effects on TEER values, causing a significant reduction after day 7 and an end TEER measurement of approximately 500 Ohms per cm<sup>2</sup> when measured at 21 days in culture, a value which is significantly more physiologically relevant (300 ohms per cm<sup>2</sup> in colonic tissue) when compared to control Caco-2 layers.

Whilst it is possible that changes in TEER in conditioned mediums could be effected by factors such as medium temperature, pH and presence of metabolic factors (17), a number of redundancies were used in the experimental design to mitigate these factors. Temperature, pH and the presence of metabolites was controlled in two mechanisms. First, conditioned medias were mixed 1:1 with fresh medium prior to being added to Caco-2, diluting any negative implications brought about by depletion of key media components by “conditioning” fibroblast cells. Additionally, mixing with fresh media allowed for a further buffering of pH levels back to normal. Second, Temperature was controlled through a normalisation period of 30 minutes at 37°C prior to taking measurements, ensuring all wells were back to 37°C during the measurement procedure.

Changes in TEER measurements of Caco-2 monolayers in the presence of paracrine fibroblasts have also been observed in past studies. Pereira *et al* also showed significant decreases in TEER measurement when Caco-2 cells were cultured with CCD-18co cells in their *in vitro* model of the intestine. (162) They hypothesised that this decrease in TEER was due to the interspersing of CCD-18o cells within the Caco-2 layer, creating areas of

low resistance and as such lowering the total resistance measurement of the complete model. These experiments however, do not include direct co-culture of CCD-18co with Caco-2 cells within the model. Instead, models relied here on the use of conditioned media to induce changes in epithelial development. This media is rendered acellular through syringe filtering before application to the Caco-2 models, suggesting that the changes seen in this model are due to a secreted paracrine factor having effects on the growth and development of Caco-2 cells layers. As will be shown and discussed later, when direct co-culture in 3D models is achieved there is no evidence to suggest that CCD-18co physically disrupts the epithelial layer within the model. Indeed, staining of epithelial specific markers such as E-cadherin or Occludin shows a consistent monolayer of Caco-2 cells on the surface of the model without interruption from stromal located fibroblast populations.

#### **3.5.4 Tight junctional formation in Caco-2 control and paracrine treated layers and its effect on epithelial layer TEER and permeability.**

TEER, as previously described is the main way in which Caco-2 layers are observed throughout the cell culture process. The cell membrane is a poor conductor of electrical activity (205) and a basic principle of electrical current is that it will always follow the path of least resistance. Therefore, epithelial resistance measurements mostly measure, and are dependent on, tight junctional formation and composition between cells, with higher TEER values generally correlating with increased tight junction formation and consistency over the entire epithelial layer. The function of tight junctions are to provide a barrier against the passive absorption of large macromolecular molecules which cannot cross the membrane passively.(206,207) These molecules are normally either enzymatically processed in the intestinal lumen before absorption or are actively transported across enterocyte membranes by the multitude of transporter protein complexes found embedded within the apical microvilli epithelial surface layer.

Occludin is a protein found within the tight junctional complex and as such is utilised in this study as a marker of tight junction abundance and localisation within a cell. Caco-2

cells within this study are shown to express Occludin between cellular boundaries after as little as 2 days in culture. This staining remains strong throughout the culture period and increases in abundance as cells become more confluent. After confluency has been reached further increases in Occludin staining are difficult to quantify through immunofluorescence alone. Cells appear to become smaller and more uniform overtime, especially within HIC treated samples which can be seen visually (Not quantified) to be significantly smaller than control and CCD-18co/ HDFn treated samples. Smaller more tightly packed cells would infer an increased abundance of tight junctional complexes throughout the model. This observation when referred back to the TEER values gained in the previous section correlate well, with HIC treated monolayers having a significantly higher TEER value compared to other treated samples whilst still being significantly lower when compared to the control samples.

With a decrease in model TEER measurement, one would expect the overall paracellular permeability of the epithelial model to increase. Lucifer yellow was utilised here as a marker of paracellular transport. Interestingly, changes in TEER measurement did not correlate directly with increases in permeability of lucifer yellow. Significant decreases in TEER values did not result in a significantly more “leaky” epithelial models, suggesting changes in TEER values are potentially through a different mechanism than modulation of tight junction complex integrity or abundance. Although, a non-significant increasing trend in permeability is seen with conditioned media samples compared to controls.

Addition of KGF to the epithelial layers resulted in a highly significant decrease in TEER, whilst also decreasing membrane permeability. This is in contrast to paracrine media layers which, whilst non-significantly different from control layers, did show a moderate increase in permeability values. The opposite effect when culturing Caco-2 cells with KGF suggests that KGF is not the driving factor in conditioned media experiments, with apparent differences in mechanistic action. However, these differences could also be due to any number of complex small molecule co-interactions present in the conditioned media which are not present in the pure KGF spiked samples.

Kim *et al* (208) conducted a similar experiment whereby they co-cultured Caco-2 Transwell monolayers with direct and Paracrine CCD-18co conditioned media in addition

to adding supplemental KGF to culture media. Their results reflect what is seen in this present study whereby CCD-18co conditioned and KGF supplemented media both had the effect of reducing TEER values of mature models. Interestingly, the authors also show that addition of KGF to culture media results in an increase in Claudin 2 (Tight junctional component protein) without any increases in other significant tight junctional proteins such as Claudin 1, Occludin or ZO-1. On the surface, increased expression of a tight junctional component, resulting in a decreased epithelial resistance, seems to lack sense. However, more recent studies of the function of Claudin-2 have implicated it in the creation of “leaky” tight junctions through channel formation within the tight junctional complexes, making them more permeable to paracellular water flux. (209–211) This leakier tight junctional complex could then explain the decreases seen in TEER values of myofib conditioned and KGF treated layers. This “leaky” tight junctional complex is thought to be permeable to  $\text{Li}^+$ ,  $\text{Na}^+$  and  $\text{K}^+$  ions in addition to being permeable to water molecules less than  $2.8\text{\AA}$  in diameter.(209) Lucifer yellow has been shown to have a diameter of approximately  $9.9\text{\AA}$  in diameter, (212) and as such would be too large to fit through the “leaky” claudin-2 expressing tight junctions. This puts the data found in this study into context whereby TEER has been shown to decrease without any significant changes in Lucifer Yellow permeability. Increases in claudin-2 expression can also be seen in diseases such as IBD, where by the proliferative progenitor cells at the base of the intestinal crypt show heightened levels of Claudin-2 expression correlating with an increase in the rate of proliferation. (211,213)

The addition of KGF to Caco-2 monolayers has significant effects on the metabolic activity of the cells. Indeed, close analysis of the curve created by measuring the change in metabolic activity over time shows that KGF prolongs the exponential phase of growth, resulting in a significantly higher MTT value after 10 days in culture. Whilst not tested in this study my hypothesis would be that the more metabolically active cell layers show similarly heightened levels of Claudin-2 expression mediated by KGF paracrine factors. Indeed, when looking at growth curves of models grown in conditioned media it was clear that addition of CCD-18co conditioned media has a similar effect on metabolic activity over time to that seen in the KGF spiked media assays. Interestingly, HIC and HDFn conditioned media does not create the same effect, with no significant differences seen between the growth curves of those conditions compared to the controls. CCD-18co MTT



curves in particular do not reach plateau like values seen in control samples. This could suggest the initiation of a proliferative (inflammatory) repair response as discussed earlier.

KGF levels secreted into the conditioned media by ELISA was quantified to assess changes in secretion amounts between culture conditions. The results show that compared to other conditions, CCD-18co cells secrete far more KGF than their HIC and HDFn counterparts both in 2D and 3D models (3D model development will be discussed in chapter 5). This ties in nicely with the data discussed previously, whereby CCD-18co conditioned media experiments have a significantly lowered TEER value, an increased MTT growth curve reminiscent of KGF spiked media experiments and a non-significantly different passive permeability to lucifer yellow.

Interestingly, when comparing 2D to 3D cultured CCD-18co fibroblasts there is a significant decrease in KGF secretion, when normalised to DNA content, down to approximately the same levels of KGF secreted by normal (Non-carcinoma origin) human cells. 3D culture within Alvetex<sup>®</sup> therefore appears to be modulating the physiology of a cancer derived cell line back into a normal phenotype. Saavedra *et al* (214) utilised Alvetex Scaffold<sup>®</sup> for the culture of human mesenchymal stem cells (hMSC) in 3D to assess the secretome changes of these cells between 2D and 3D conditions. They found that significant changes were induced through 3D culture, some small molecules such as IGF-1 were shown to increase whilst others such as VEGFR-1, MCP-1 and IL-6 decreased in 3D culture. In each case they showed that 3D paracrine media has beneficial effects on the differentiation of both HUVEC and Osteoclasts into functional tissues, highlighting the physiologically relevant changes induced through 3D culture. Other studies such as the Melissaridou *et al* showed that the 3D culture of cells created a more mimetic model of cancer growth by enhancing the inherent phenotype of the cells used within the model. (215) It could be hypothesised that normal KGF levels within the intestine are similar to those secreted by HDFn and HIC cells seen within this study. Under this assumption culture of CCD-18co cells in 3D reduces the KGF amount secreted to more physiological levels. Indeed, previous studies have shown that cancer cells are well known to over express KGF within the intestine.(213,216) For example, Watanabe *et al* showed in their study that 10 out of 12 cases showed significantly increased KGF

expression within cancerous tissues compared to normal tissues of the same origin. KGF is a known regulator of cell proliferation as discussed previously, and as such is thought to have proliferation promoting effects on epithelial cells within cancer tissues, potentially contributing to the rapid proliferating cancer phenotype and hence the significant effects in Caco-2 cells. Riedl *et al* (217) recently showed how Colorectal adenocarcinoma cell lines, normally utilised for intestinal modelling such as Caco-2 and HT29, when grown in 3D spheroids, significantly reduced their proliferative “cancer-like” phenotype as well as rewiring in signalling and a reduction in the AKT–mTOR–S6K pathway, known to be important in regulation of the cell cycle.(217,218) To suggest that CCD-18co cells “lose” their cancer phenotype based on evidence in this study is premature. However, evidence does seem to point to a more physiologically “normal” cell compared to their 2D cultured counterparts.

Analysis of KGF ELISA results also shows that when CCD-18co cells are cultured in the paracrine media of Caco-2 cells there is a significant reduction in KGF secreted into the paracrine media. This decrease is seen in both 2D and 3D cultured cells and is decreased proportionally by approximately the same relative amount in each. Evidence of Caco-2 cross-talk with underlying myofibroblasts is seen throughout the literature. Drygiannakis *et al* studied the effects of Caco-2 conditioned media on myofibroblasts (Human Crohns and CCD-18co) paracrine secretion. They found that Caco-2 cells secreted significant levels of TGF- $\beta$ 1 without any additional stimuli. (219) This secretion was seen to induce modulation of myofibroblast secretome, with changes in MMP-9 and collagen secretion. Further to this, Brenmoehl *et al* showed that TGF- $\beta$  has differentiation inducing effects on sub-epithelial myofibroblasts,(220) with increased levels of smooth muscle actin formation in treated cells.. This activation event mediated through TGF- $\beta$  secretion is normally important in tissue repair and remodulation. This study was one of the first to show that Caco-2 conditioned media has the effect of decreasing KGF secretion in carcinoma derived sub-epithelial myofibroblasts, specifically CCD-18co cells. Whilst not shown here it was hypothesised that stimulation of CCD-18co cells by TGF- $\beta$ 1 causes CCD-18co cells to differentiate further, expressing greater levels of  $\alpha$ SMA and decreasing KGF secretion into paracrine media.

HIC cells only induced a marginal decrease in TEER values and have no significant effects on membrane metabolic activity suggesting any physiological differences between control and HIC layers are not induced through the paracrine effects of KGF. This is further suggested through analysis of KGF concentration within conditioned media samples. Only marginal levels of KGF were detected within HIC conditioned media (~KGF concentration of 30-40 pg/ml).

Interestingly, HDFn paracrine co-culture reduces the TEER values of Caco-2 models to a similar degree as CCD-18co conditioned media, without the similar changes in metabolic activity. KGF ELISA results show only marginal secretion of KGF into HDFn conditioned media at levels far lower than those tested in KGF treated samples (~KGF concentration of 50 pg/ml). This suggests that the reduction in TEER mediated by HDFn conditioned media is not induced through KGF secretion but by some other paracrine small molecule. KGF is thought to be secreted in the dermis of the skin but evidence shows that heightened levels are only observed in the case where cells are activated in a disease state. (221) Canady et al showed through ELISA based detection that normal HDFn cells secrete KGF at a rate of approximately 10 pg/ml. Levels very similar to those seen in this study. What then could be effecting the Caco-2 layer in such a way to significantly reduce TEER?

FGF-10, epidermal growth factor (EGF) and interleukin 6 (IL-6) have all been shown to be released by HDFn cells, having effects on the development and maintenance of the overlying keratinocyte layers. (222) FGF-10(223) and EGF(224) both are known as epithelial mitogens, as such are unlikely to be involved in the phenotypic change seen in Caco-2 cells in this study. Interestingly, IL-6 has been shown to modulate Claudin-2 expression, increasing tight junction permeability similarly to the mechanism induced by KGF. (225) Miyake et al showed that IL-6 also has effects on the transport capabilities of the Caco-2 membrane, increasing P-gp and MRP mediated transport. (226). The transport capabilities of the models will be discussed in further depth in Chapter 7.

### **3.5.5 Understanding the effects of conditioned media and KGF spiked media on the relative expression of key junctional and transporter proteins as assessed through qPCR analysis of 2D Caco-2 layers.**

Quantitative mRNA analysis of Caco-2 layers shows significant changes occur when cells are cultured in the paracrine effects of CCD-18co, HIC and HDFn cells. The first analysis that was attempted was in understanding the effects of different culture conditions on the composition of the tight junction complex. Three mRNA sequences were tested, Occludin, Claudin 2 and ZO-1. As discussed previously here Claudin-2 was of particular interest due to the hypothesis described earlier whereby KGF enhances the production of Claudin-2, increasing the permeability of the resultant tight junction to ions and small water soluble compounds. What was discovered however was the converse with KGF treated layers having significantly less Claudin-2 mRNA in comparison to control levels.

Whilst this at first may seem to disprove the hypothesis formulated here it is important to remember that mRNA analysis of lysed samples provides only a single snapshot of the cells expression levels. Essentially, mRNA levels do not always reflect the abundance of a particular protein within a cells. For example, data shown earlier in this work shows that tight junctions formation between Caco-2 cells begins immediately upon cell contact, with even sub-confluent populations of cells showing strong expression of Occludin, a key tight junctional component between adjacent cells. By 21 days in culture one would expect tight junctions to be completely constructed through the cells. As such any new mRNA translation would be to maintain expression levels rather than creating new junctions. Indeed, Claudin-2 has been shown to be a relatively long lived tight junctional component with Van Itallie *et al* (227) demonstrating how the cytoplasmic tail of Claudin-2 is important in the proteins longevity, with a half-life in excess of three times that of Claudin 4. These could have significant effects on the levels of mRNA expression within the cells with lower levels not necessarily representing true protein abundance.

Expression levels of important efflux proteins such as MDR1, MRP1 and MRP2 also showed significant variation between models with conditions often showing the largest changes in relative mRNA whereas HIC conditioned media either resulted in no significant differences or a reduction relative to the control. MDR1 levels were seen to drastically and significantly increase in the presence of KGF supporting the conclusion that KGF is important in the maturation and differentiation in the intestinal epithelium. MDR1/ P-gp levels are generally thought to be under expressed in the Caco-2 layer. An increase in the amount of P-gp present within the Caco-2 layer has implications in the functionality of the resultant models, allowing for more sensitive assays for the detection of potential substrate of P-gp in the human intestine. Potentially, heightened P-gp levels could identify compounds which fall under the functional detection range of current models.

Analysis of both mRNA expression levels and protein abundance through western blot would give a more representative idea of the mechanisms within the cells resulting in the observed changes in phenotype. Often these mechanisms are far too complex to get a definitive answer without utilising multiple methods of analysis and testing the models through multiple mechanisms. The mRNA analysis done here is simply a first step in this process and could not be justified utilised as standalone data.

### **3.6 Conclusion**

A complete understanding the complexity of the formation, maintenance and differentiation of Caco-2 cells in addition to intestinal epithelia in general is far beyond the scope of this work. What was shown here is that the paracrine secretome of intestinal fibroblasts, both of normal and carcinoma origins along with general skin fibroblasts can have significant effects on epithelial structure, TEER values of a membrane, cellular metabolism and on the expression of functional mRNAs important in the production of key tight junctional and functional efflux transporter proteins. It was postulated that KGF was one of the paracrine influences having a significant effect on the above phenotypes. It was found that KGF does indeed have many of the same effects as conditioned media samples and that CCD-18co cells were able to secrete KGF at physiological concentrations into the conditioned media. Differences were seen on further downstream

analysis between conditioned media samples and pure KGF spiked media conditions, suggesting that whilst KGF does have an important role to play, at least in CCD-18co conditioned media samples, it is not the only paracrine factor which is having effects on the epithelial phenotype. HDFn and HIC mechanistic action is more difficult to identify with only small amounts of secreted KGF detected in conditioned media samples. Indeed, without a large scale broad study of the paracrine media, finding potential candidates is largely a matter of careful reading of past literature and, to a greater scale, luck.

Further work in this area should include said broad, large scale analysis of the fibroblast secretome, perhaps through modern sequencing techniques, in order to precisely identify potential candidates for further analysis and quantification. Additionally, further work could be done on the quantification of total protein levels through western blot analysis alongside qPCR analysis to understand the proteome of the modified Caco-2 layer.

## **4. Epithelial - Goblet cell co-culture and its effect on model function.**

### **4.1 Introduction**

Many attempts over the past decade have been made to improve the standardised Caco-2 models in such a way to increase the relevance of Caco-2 studies whilst maintaining the high throughput nature of the assay and its low cost. As described in the previous chapter, one simple way of achieving this is through the paracrine action of tissue specific fibroblasts on the development of the epithelial membrane. Another strategy is through the addition of other cell lines with distinct functions to the Caco-2 cellular models at the appropriate physiological ratios. The addition of goblet cells is one of the main areas in which this concept has been applied.

#### **4.1.1 Understanding the structure of the mucus layer and its importance on the functional aspects of the human intestine.**

The goblet cells and the associated mucous layer is highly variable dependant on the region of the intestine studied. Structurally the mucus layer changes in distinctive ways from the proximal small intestine to the distal colon, with the changes in structure correlating with distinct changes in function. (129) The small intestine mucus is primarily formed of MUC2 and forms a single layer over the surface of the villus tips. This mucus layer is not impermeable to bacteria as the small intestine requires ease of movement of soluble nutrient to facilitate uptake into the body. (91) Instead, this single layer of mucus is populated with secreted antimicrobial proteins and peptides in order to limit enterocyte/bacterial contact. In contrast the colon consists of an outer mucus layer which is home to many commensal bacterial populations with an inner layer which is essentially acellular. (54)

Very generally, the mucus layer is important in a number of key functions of the intestine, namely as a matrix for the colonisation of bacteria away from the surface epithelial layer, maintaining a sterile layer immediately above the epithelial layer and in the controlled

absorption/ as a barrier to macromolecules.(91) Indeed, the mucous layer has been demonstrated repeatedly to be highly important in assessing the absorption kinetics of drug compounds into the blood stream. (228–231)

The mucous produced within the intestine is composed of proteins known as mucins which can be further categorised in to 2 main types; 1. Transmembrane and 2. Secretory mucins. Transmembrane mucins are created by enterocytes and, as the name suggests, are anchored to the enterocyte apical membrane. The exact function of the transmembrane mucins within the body is poorly understood. Enterocytic transmembrane proteins such as MUC3 (232), 13, 12 and 17 are most likely to form a physical absorption barrier to large macromolecules, not readily absorbed by the intestinal epithelium and are almost certainly the components which make up the Glycocalyx in the intestine. (56,233) Additionally, it is thought that the cytoplasmic domains of these transmembrane proteins interact with signalling pathways within the enterocyte cytoplasm which are involved in the apical membrane organisation, inflammation, differentiation, apoptosis and ion channel presentation. (234,235) This suggests that these transmembrane mucins may be utilised as a primitive sense organ, allowing for some dynamic, active, remodelling dependant on cellular environment. Interestingly, regarding the immune component of mucins there is further evidence to support the hypothesis that resident probiotic microbes within the intestine may also be important in the intestines innate immunity through their ability to induce mucin secretion in the presence of competing pathogenic organisms. (236) The transmembrane mucins have been shown to contain with extracellular domains able to bind bacteria, initiating a shedding of affected mucin complexes and the stimulation of an inflammatory response. (234,237)

#### **4.1.2 Limitations of the Caco-2 system to model the effects of mucus on the drug pharmacokinetics and methods to more accurately mimic the intestinal epithelium.**

Caco-2 cells have been shown to produce a very small, if any, amount of mucous. (238) Therefore, in its gold standard format, the Caco-2 cell assay poorly recapitulates the mucous layer of the intestine, lacking structure and the complex cocktail of mucin



proteins produced by true goblet cell lineages and hence the complex signalling environment created by a mucous membrane. (239)

The HT29-MTX cell line is a methotrexate treated sub-population of the parental HT29 population.(240) This line is known to exhibit goblet cells “like” characteristics with ample mucous production seen in standard cell culture conditions.(241,242) The benefit of this cell line lies in its easy availability and reproduction, making it a valuable tool for application into standardised epithelial models. Since the protocol for its formation was published in the early 90s, HT29-MTX cells have been explored as potential co-culture candidates with Caco-2 cells quite extensively with the aim of creating an epithelial construct with absorptive and mucus barrier functions. Careful optimisation and calibration of culture conditions is required in co-culture systems in order to maintain the correct cellular ratios throughout the culture period and in the final models. Many differing methods have been developed to tackle this with the simplest such as in the study by Hilgendorf *et al* (161) where they create the co-culture models through ratio seeding of Caco-2 and HT29-MTX cells at day 0 of the model culture period. Also in the study by Lozoya-Agullo *et al* (131) where they did the same at a 90:10 Caco-2 to HT29-MTX ratio. Even these simple culture methods however resulted in a stepwise decrease in TEER in models with higher HT29-MTX content with an increasing permeability to passive absorption test compounds as the percentage of Caco-2 cells per model decreased. Unfortunately, neither of the authors quantified the absolute levels of HT29-MTX cells in the end culture so it is impossible to know if the original seeding ratios were maintained throughout the culture period.

More complex culture methodologies such as that by Béduneau *et al* (243) focus on the addition of HT29-MTX cells at different stages of development of the Caco-2 epithelial constructs. This method is able to create models with decreasing TEER with increasing levels of HT29-MTX and changes in the functional permeability of the resultant model in the same way as day 0 ratio culture achieves. Whilst the authors here did attempt to quantify the extent of HT29-MTX cells in the end cultures, primarily through p-gp expression rates, no definitive test has been created which can give definite cellular ratios in co-culture intestinal equivalents. The addition of further complexity to this co-culture model is highly limited in the literature, with a few examples attempting to add an

immune component to the epithelial models, (131) in understanding the complex cross talk between bacterial populations and intestinal epithelial layers (244,245) or in fibroblast effects on goblet cell morphology. However, regardless of the culture methodology widespread adoption of a Caco-2/ HT29-MTX model of the intestinal epithelium is still unfortunately limited. New methods for the formation of co-culture models which can reliably form constructs with defined cellular ratios are required before extensive use can be expected.

As shown in the previous chapter addition of fibroblast conditioned media can have distinct effects on the physiology and function of intestinal epithelial cells, namely Caco-2. Examples of co-culture models of Caco-2/ HT29-MTX cells with influences from fibroblast conditioned media are lacking in the literature. The novel aspect of this chapter is in the attempted creation of a reliable intestinal model incorporating goblet cell morphology through ratio based seeding techniques and co-culture with conditioned media from CCD-18co fibroblast cells.

## **4.2 Hypothesis, Aims and Objectives**

### **4.2.1 Hypothesis**

It is hypothesised that the co-culture of Caco-2 cells with HT29-MTX “goblet-like” epithelial cells will result in an epithelial construct with improved functional capabilities over current Caco-2 gold standards. Further to this it is hypothesised that paracrine factors from CCD-18co fibroblast cells will improve overall model morphology and functional characteristics.

### **4.2.2 Aims**

The aims of this chapter were to create an epithelial co-culture model of the intestinal epithelium, incorporating both Caco-2 enterocytes and HT29-MTX “goblet” cells and assessing the effects of paracrine media on the formation of the enterocyte/ goblet cell co-cultures. Resultant models were to be assessed in terms of both structure and function. E.g. mucous production

### **4.2.3 Objectives**

The objectives of this chapter are summarised below;

- Assess changes in TEER values caused by goblet cell co-culture and CCD-18co paracrine media.
- Structurally assess resultant models through H+E staining and mucous production rates by PAS staining.
- Immuno-characterisation of key junctional and transporter proteins.
- TEM ultra-structure analysis.
- qPCR quantification of relative expression of key genes of interest involved in junction formation and transporter protein expression.
- Functional assessment of co-culture models through Rhodamine 123 transport.

## 4.3 Materials and Methods

### 4.3.1 Generation of epithelial co-culture models consisting of Caco-2 and HT29-MTX cells.

Caco-2 and HT29-MTX cells were passaged and counted as previously described (Section 2.2). 250,000 cells were seeded per Snapwell Transwell insert in 500µl of pre-warmed DMEM. The number of models was calculated before hand and a master mix of seeding solution was prepared to reduce the variability between models of a single batch. 500µl of seeding solution containing Caco-2 and HT29-MTX cells at the correct seeding density and ratio was added to the apical compartment of the Snapwell Transwell and 3ml of DMEM is added to the outside compartment. Models were incubated for 21-25 days before analysis with media changes occurring every two days. TEER measurements were

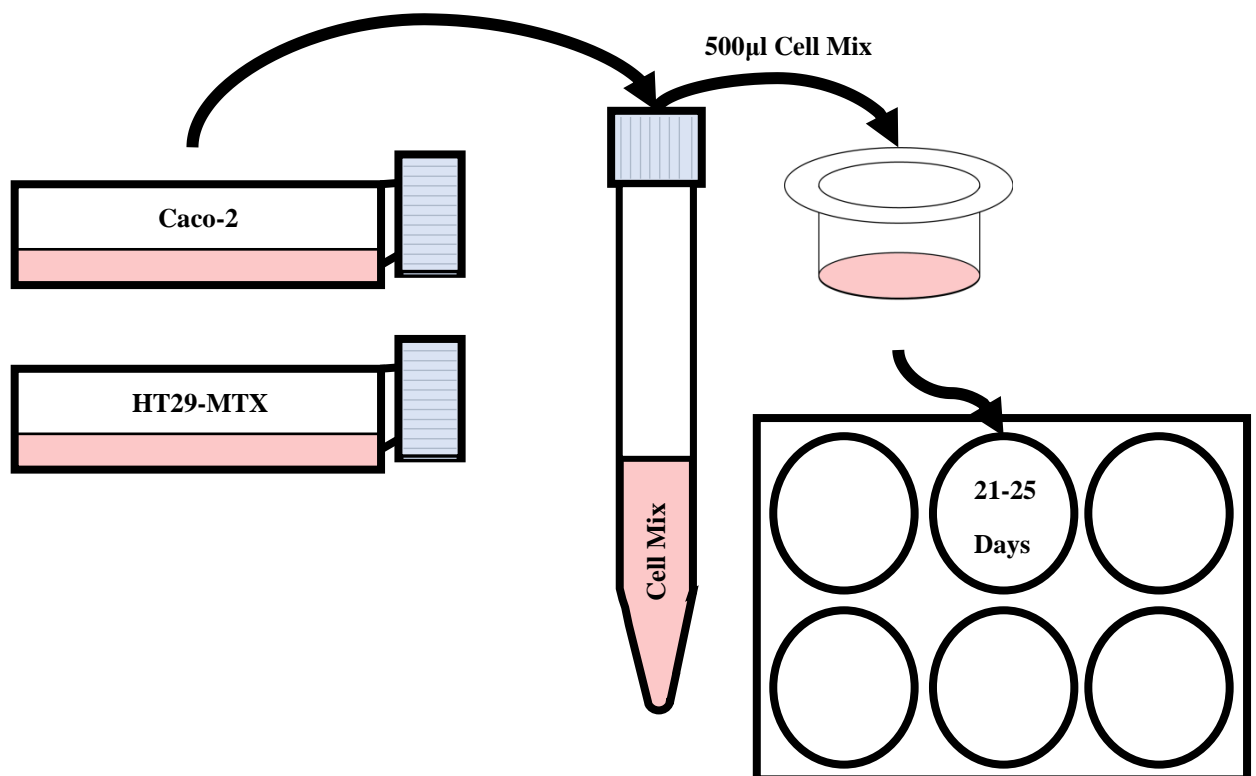


**Figure 4.1: Schematic diagram of the process for the set up and culture of Caco-2/ HT29-MTX co-culture mucus models of the intestinal epithelium** – Caco-2 and HT29-MTX cells are trypsinised as normal and placed at the correct proportions into a cell mix. Cells are diluted to 250 000 total cells/ 500µl and cultured in Snapwell inserts

taken throughout the culture assay when required or immediately before analysis. TEER measurements were taken as previously described (Section 2.16)

For CCD-18co paracrine co-culture, models are initially set up as described above. CCD-18co paracrine conditioned media is created as previously described (Section 2.12) before being added to the models after an initial 2 days of culture in normal DMEM to allow for establishment of cells onto the Transwell surface. CCD-18co media is replaced every two days for a growth period of 21-25 days.

### **4.3.2 H&E, PAS staining of sectioned and wholemount Caco-2/HT29-MTX co-culture models.**

Epithelial co-culture models were fixed in PFA, embedded and sectioned as previously described (Section 2.3.1). For sectioned slides H&E and PAS staining was also as previously described (Section 2.5.1 and 2.5.2 respectively). Whole mount staining was achieved utilising the previously described (Section 2.4.3). Briefly, all processing and staining steps were done with the Transwell still attached to the Snapwell insert. Samples were fixed in 4%PFA before being dehydrated through ethanol, incubated in HistoClear and rehydrated. This step was done to reasonably limit any variations in staining colour/intensity when comparing against paraffin embedded sectioned samples which must go through the previous steps. H&E or PAS staining was then done following a normal protocol as described previously. Stained Transwell models were removed from Snapwell inserts immediately prior to mounting on a standard Super frost microscope slide. After mounting of the sample, gentle pressure was applied to the slide whilst drying in order to ensure Transwell layers remained flat against the glass.

### **4.3.3 Toluidine blue staining of epithelial co-culture models.**

Samples were processed into resin as previously described in the main methods sections (Section 2.7). Semi-thin (1µm) sections were placed onto a glass slide suspended in water before being heat dried using a medium heat hot plate. Once dry samples were stained by addition of one drop of Toluidine Blue (pH 2-2.5) for a period of 2 minutes. Stained

sections were washed well with distilled water until the slide and water ran off clear. Slides were dehydrated, cleared and mounted utilising normal protocols.

#### **4.3.4 TEM analysis of Caco-2/ HT29-MTX co-culture constructs.**

Samples were processed into resin as previously described (Section 2.7) before sectioned ultra-thin and transferred to copper grids. Copper grids were then double contrast stained with Uranyl Acetate and Lead citrate before being imaged on (H7600 TEM)

#### **4.3.5 qPCR analysis of Snapwell Transwell epithelial co-culture constructs.**

Samples were processed as described previously (Section 2.9). RNA was isolated and quality checked utilising a nanodrop spectrometer. RNA was immediately converted into cDNA and stored at -20°C. A SYBR detection system was used.

#### **4.3.6 Rhodamine 123 transport analysis of epithelial co-culture constructs.**

Snapwell epithelial construct were removed from culture after 21-25 days and first washed gently in PBS to remove remaining media. Inserts were carefully added into the Ussing system into CH8 chambers specifically designed for use with Snapwell inserts. 15ml of prewarmed HBSS containing 1g glucose per litre, which will be referred to as Transport media from here onwards, was added to each side of the Ussing chamber reservoirs. 95% O<sub>2</sub> 5% CO<sub>2</sub> was gently bubbled through the HBSS. The entire equipment set up was maintained at 37°C through use of a circulating water bath and a fluid jacket. Models were left in the chamber for a minimum of 30 minutes to allow for full acclimatisation. Rhodamine 123 was then added to the donor compartment to create a final concentration of 5µM. Samples were taken from the receiver reservoir at 60 minute intervals. Any volume removed was replaced with fresh transport media.

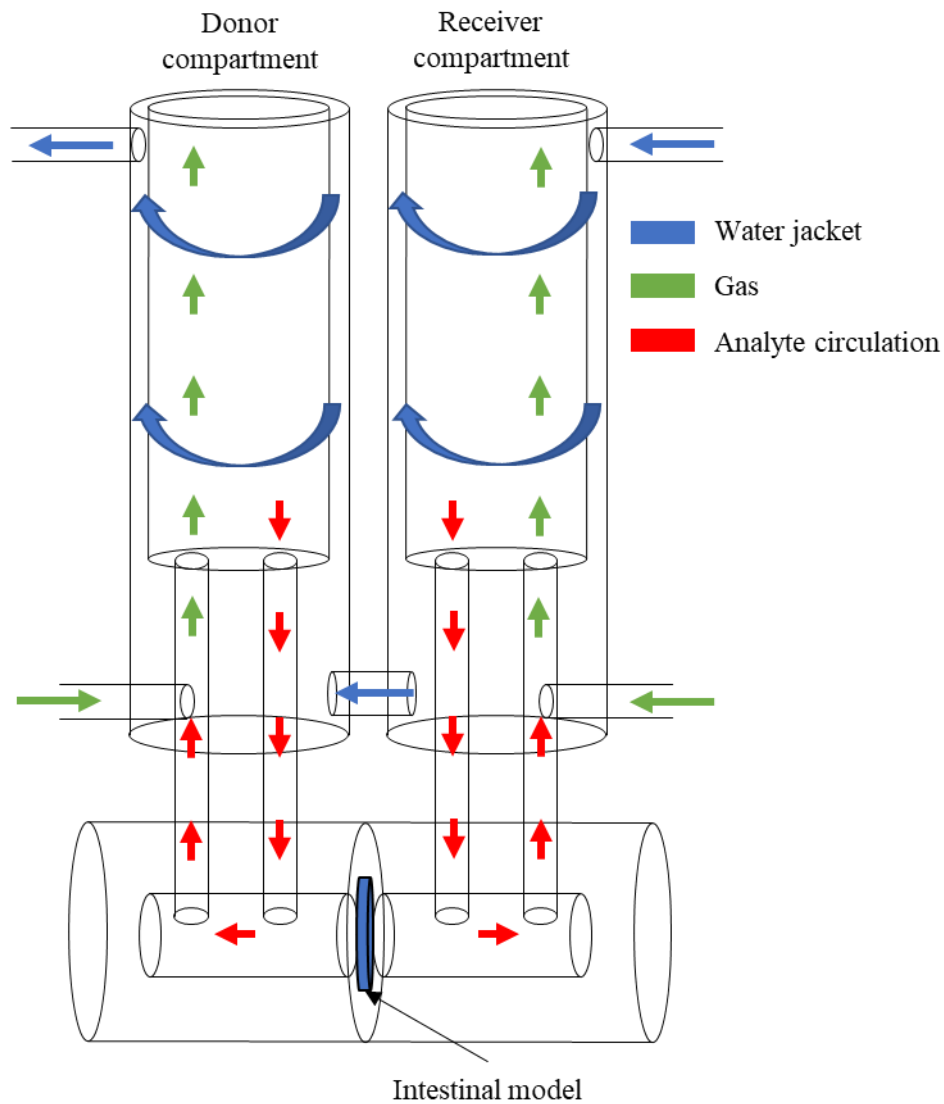


**Figure 4.2: Schematic diagram of the process for the set-up of Caco-2 co-culture models within an Ussing chamber system** – The systems consists of two reservoirs encircled by a circulating water bath maintaining an constant 37°C. Analyte of interest is added to either of the reservoirs dependant on the experiment (B-A or A-B). Carbogen gas is bubbled through the reservoirs to both oxygenate and circulate the system. Models are placed in a chamber system attaching to the reservoirs providing a singular interface between reservoirs. Samples are taken after set time points with any volume removed being replaces so as not to induce pressure changes between chambers.

## **4.4 Results**

### **4.4.1 Trans-epithelial resistance measurements of Caco-2:HT29-MTX co-cultures and the effects of CCD-18co conditioned media on resultant co-culture layers.**

Caco-2 cells were co-cultured in a number of key ratios, determined through analysis of histological section of Human intestine, with HT29-MTX cells on Snapwell Transwell. Figure 4.2 shows the data gained from analysis of TEER of resultant Transwell models over the course of 21 days culture. As seen previously untreated Caco-2 layers show a relatively linear phase of growth with a short lag phase before a rapid increase in TEER values between days 6 and 16 followed by a final plateau until 21 days in culture. Final TEER values of untreated Caco-2 layers as similar to that as seen previously at approximately 2000-2500 ohms (Figure 4.2 A)

The addition of HT29-MTX cells to the Caco-2 layers results in a significant decrease in TEER values throughout the course of the culture period with maximal 21 day TEER values of 1200 and 1000 ohms in 90 and 80% Caco-2: HT29-MTX co-cultures respectively. The curve generated through analysis of co-culture TEER over the 21 day culture period results in a trend line with a linear increase in TEER values over time with less pronounced lag, log and plateau phases. Culture of HT29-MTX cells alone results in a maximal TEER value of <100 ohms, significantly less than Caco-2 cells (Figure 4.2D)

The addition of CCD-18co conditioned media to the co-culture Transwell layers has differential effects depending on the ratio of HT29-MTX cells which are present in the culture. Caco-2 cells control models show a similar phenotype as to that shown earlier in the previous chapter (Figure 3.9) with a significant decrease in measured TEER values under conditioned media conditions. Conversely, the addition of CCD-18co conditioned media to Caco-2: HT29-MTX co-culture layers results in a significant increase in the resultant models measured TEER values over control values of the same cellular ratios. Figure 4.2 B shows a consistent, stable increase in TEER value of between 500 and 1000 ohms over the 90% control after day 6 in culture. Figure 4.2 C shows a trend in the 80%



co-culture with an increase in TEER values over the control samples consistently throughout the course of the 21 day co-culture. By day 21 the difference in TEER values between the control and CCD-18co treated samples is approximately double that of the control. HT29-MTX cells grown in the paracrine presence of CCD-18co fibroblasts shows a significantly increased TEER value over the HT29-MTX control. 21 day HT29-MTX co-cultures ended with a TEER value of approximately 2000 ohms in comparison to the less than 1000 ohms of the control samples. Interestingly, the TEER values of the treated HT29-MTX co-culture was very similar to that of the Caco-2/ CCD-18co paracrine culture suggesting a change from a goblet cell phenotype to one more similar to that of a standard enterocyte.

Figure 4.3 shows the different culture conditions compared to one another, both in control and CCD-18co paracrine conditions. Figure 4.3 A, shows the stepwise decrease in TEER values induced through co-culture of Caco-2 cells with HT29-MTX without the effects of paracrine media. As can be seen, increasing levels of HT29-MTX presence directly correlates with a decrease in overall TEER value of the models. Figure 4.3 B shows the effects of the same ratios together with CCD-18co paracrine media. As seen be seen the result of this effective triple co-culture is the convergence of TEER values to a similar level in each condition regardless of the HT29-MTX ratio in the models.

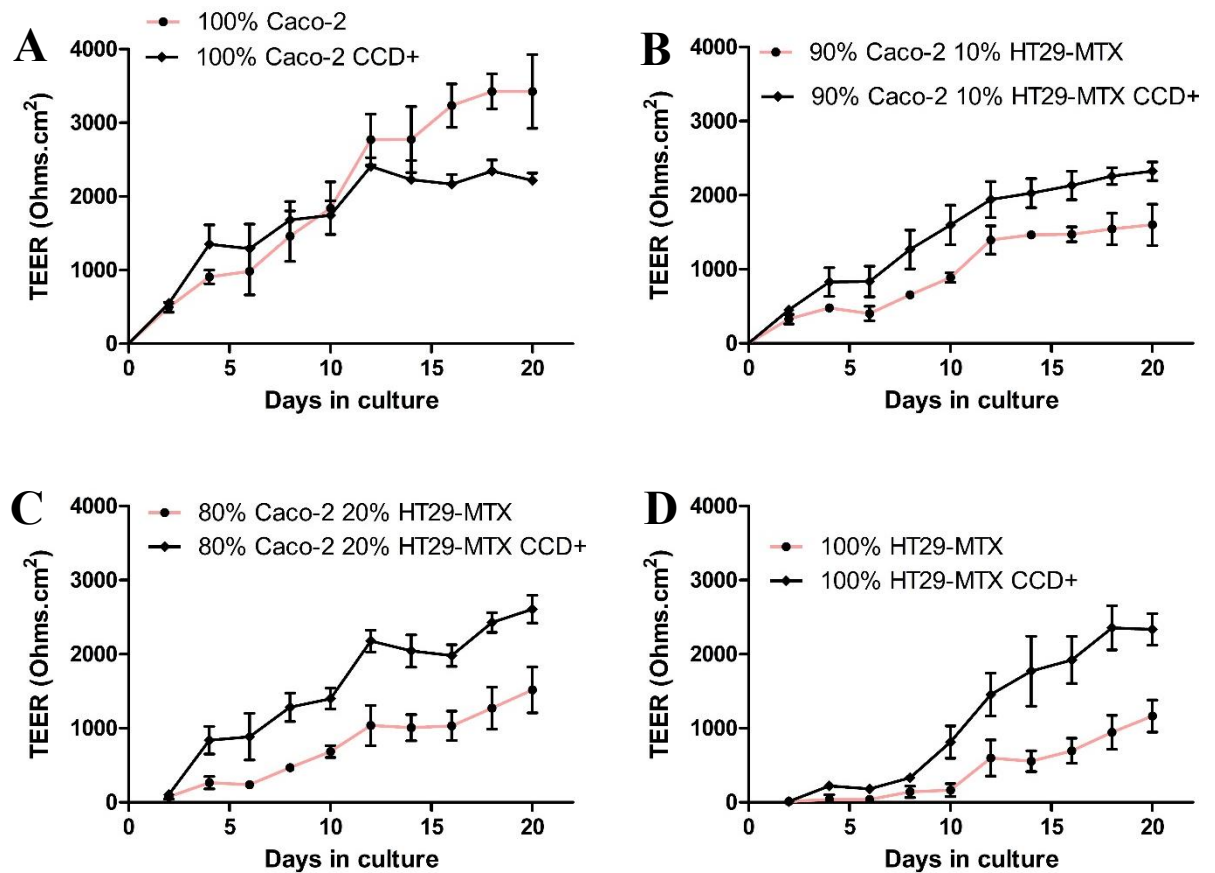


**Figure 4.3: Caco-2/ HT29-MTX co-culture decreases the TEER values of resultant epithelial constructs** – A) 100% Caco-2, B) 90%/10% Caco-2/ HT29-MTX, C) 80%/20% Caco-2/HT29-MTX, D) 0%/100% Caco-2/ HT29-MTX. All cellular ratios were performed in the presence (+) and absence (-) of CCD-18co conditioned media. Addition of CCD-18co paracrine media to HT29-MTX cells results in an increase in the TEER levels of the resultant model. The converse is true in Caco-2 monocultures which decrease in TEER. n=3-6 from a minimum of 3 independent experiments. Significant differences calculated by one way ANOVA with Tukeys post-test analysis \*\*\* =  $P < 0.0001$ , \*\* =  $P < 0.001$ , \* =  $P < 0.01$ . (Tables 4.1) Error bars represent  $\pm$ SEM of average values.

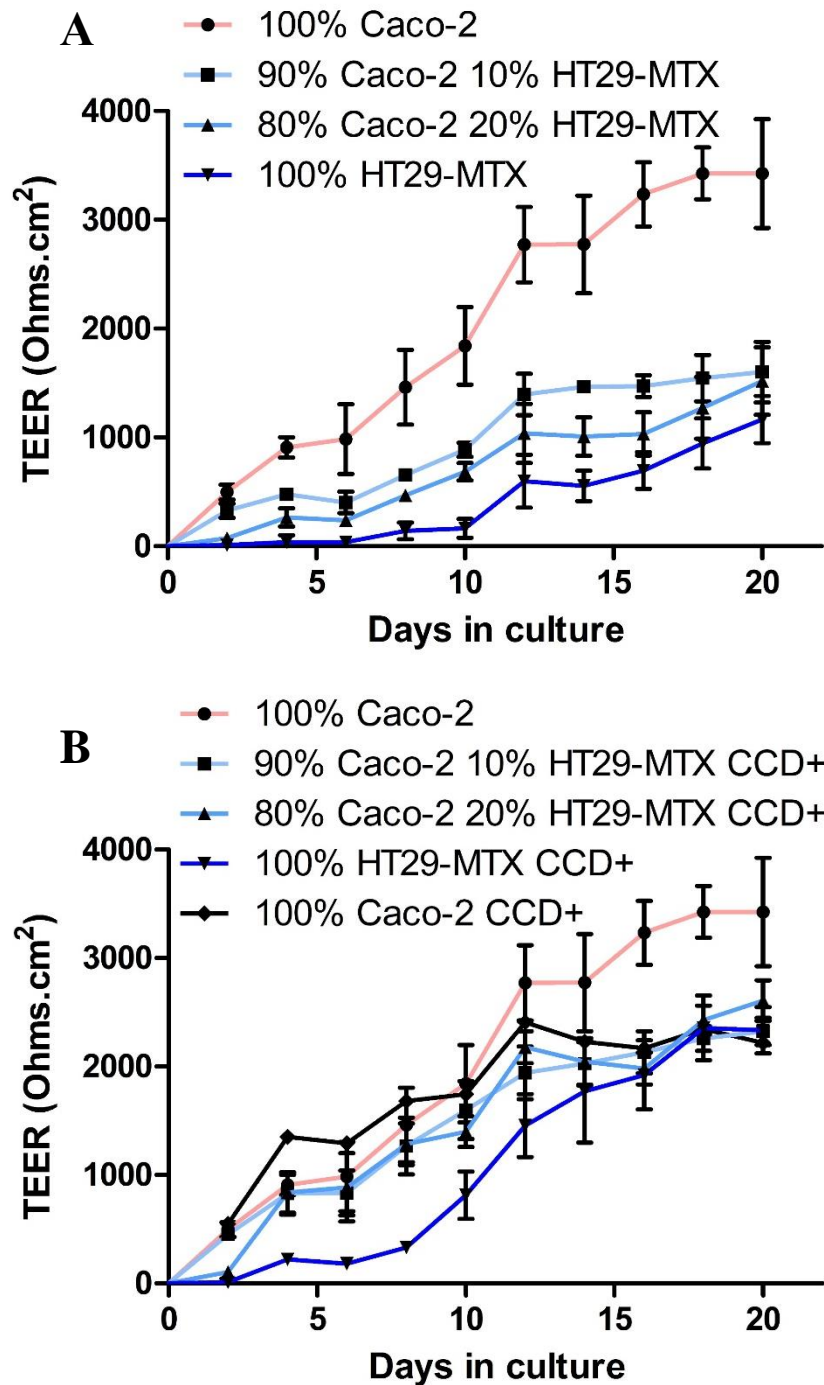


**Figure 4.4: CCD-18co paracrine co-culture with Caco-2/ HT29-MTX epithelial constructs increases TEER values compared to non-treated controls** – A) Co-cultures without the presence of CCD-18co conditioned media. Co-culture layers show increasing TEER values over time with maximal TEER values decreasing correlating to increased HT29-MTX proportion. B) Co-culture Transwell models in the presence of CCD-18co conditioned media show increased TEER compared to control layers. Treated models show approximately double the TEER values of control conditions. n=4-8 N=from a minimum of 4 independent experiments. Error bars represent  $\pm$ SEM of average values.

#### Chapter 4 – Goblet cell co-culture model of the intestinal epithelium

Caco-2 Day 8 vs Caco-2 Day 14	*	90%/10% Day 8 vs Caco-2 CCD+ Day 14	***	80%/20% Day 14 vs 80%/20% CCD+ Day 14	*
Caco-2 Day 8 vs Caco-2 Day 20	***	90%/10% Day 8 vs Caco-2 CCD+ Day 20	***	80%/20% Day 14 vs 80%/20% CCD+ Day 20	***
Caco-2 Day 8 vs 80%/20% Day 8	**	90%/10% Day 8 vs 90%/10% CCD+ Day 14	**	80%/20% Day 14 vs HT29-MTX CCD+ Day 20	***
Caco-2 Day 8 vs HT29-MTX Day 8	**	90%/10% Day 8 vs 90%/10% CCD+ Day 20	***	HT29-MTX Day 8 vs Caco-2 CCD+ Day 8	***
Caco-2 Day 14 vs 90%/10% Day 8	***	90%/10% Day 8 vs 80%/20% CCD+ Day 14	**	HT29-MTX Day 8 vs Caco-2 CCD+ Day 14	***
Caco-2 Day 14 vs 90%/10% Day 14	***	90%/10% Day 8 vs 80%/20% CCD+ Day 20	***	HT29-MTX Day 8 vs Caco-2 CCD+ Day 20	***
Caco-2 Day 14 vs 80%/20% Day 8	***	90%/10% Day 8 vs HT29-MTX CCD+ Day 14	*	HT29-MTX Day 8 vs 90%/10% CCD+ Day 14	***
Caco-2 Day 14 vs 80%/20% Day 14	***	90%/10% Day 8 vs HT29-MTX CCD+ Day 20	***	HT29-MTX Day 8 vs 90%/10% CCD+ Day 20	***
Caco-2 Day 14 vs HT29-MTX Day 8	***	90%/10% Day 14 vs Caco-2 CCD+ Day 14	***	HT29-MTX Day 8 vs 80%/20% CCD+ Day 14	***
Caco-2 Day 14 vs HT29-MTX Day 14	***	90%/10% Day 14 vs Caco-2 CCD+ Day 20	**	HT29-MTX Day 8 vs 80%/20% CCD+ Day 20	***
Caco-2 Day 14 vs HT29-MTX Day 20	**	90%/10% Day 14 vs 90%/10% CCD+ Day 14	*	HT29-MTX Day 8 vs HT29-MTX CCD+ Day 14	**
Caco-2 Day 14 vs 90%/10% CCD+ Day 8	**	90%/10% Day 14 vs 90%/10% CCD+ Day 20	**	HT29-MTX Day 8 vs HT29-MTX CCD+ Day 20	***
Caco-2 Day 14 vs 80%/20% CCD+ Day 8	*	90%/10% Day 14 vs 80%/20% CCD+ Day 20	***	HT29-MTX Day 14 vs Caco-2 CCD+ Day 14	***
Caco-2 Day 14 vs HT29-MTX CCD+ Day 8	***	90%/10% Day 14 vs HT29-MTX CCD+ Day 20	**	HT29-MTX Day 14 vs Caco-2 CCD+ Day 20	**
Caco-2 Day 20 vs 90%/10% Day 8	***	90%/10% Day 20 vs 80%/20% Day 8	*	HT29-MTX Day 14 vs 90%/10% CCD+ Day 14	*
Caco-2 Day 20 vs 90%/10% Day 14	***	90%/10% Day 20 vs HT29-MTX Day 8	*	HT29-MTX Day 14 vs 90%/10% CCD+ Day 20	***
Caco-2 Day 20 vs 90%/10% Day 20	**	80%/20% Day 8 vs Caco-2 CCD+ Day 8	***	HT29-MTX Day 14 vs 80%/20% CCD+ Day 14	*
Caco-2 Day 20 vs 80%/20% Day 8	***	80%/20% Day 8 vs Caco-2 CCD+ Day 14	***	HT29-MTX Day 14 vs 80%/20% CCD+ Day 20	***
Caco-2 Day 20 vs 80%/20% Day 14	***	80%/20% Day 8 vs Caco-2 CCD+ Day 20	***	HT29-MTX Day 14 vs HT29-MTX CCD+ Day 20	***
Caco-2 Day 20 vs 80%/20% Day 20	**	80%/20% Day 8 vs 90%/10% CCD+ Day 14	***	Caco-2 CCD+ Day 8 vs HT29-MTX CCD+ Day 8	**
Caco-2 Day 20 vs HT29-MTX Day 8	***	80%/20% Day 8 vs 90%/10% CCD+ Day 20	***	Caco-2 CCD+ Day 14 vs HT29-MTX CCD+ Day 8	***
Caco-2 Day 20 vs HT29-MTX Day 14	***	80%/20% Day 8 vs 80%/20% CCD+ Day 14	***	Caco-2 CCD+ Day 20 vs HT29-MTX CCD+ Day 8	***
Caco-2 Day 20 vs HT29-MTX Day 20	***	80%/20% Day 8 vs 80%/20% CCD+ Day 20	***	90%/10% CCD+ Day 14 vs HT29-MTX CCD+ Day 8	**
Caco-2 Day 20 vs Caco-2 CCD+ Day 8	***	80%/20% Day 8 vs HT29-MTX CCD+ Day 14	**	90%/10% CCD+ Day 20 vs HT29-MTX CCD+ Day 8	***
Caco-2 Day 20 vs 90%/10% CCD+ Day 8	***	80%/20% Day 8 vs HT29-MTX CCD+ Day 20	***	80%/20% CCD+ Day 14 vs HT29-MTX CCD+ Day 8	**
Caco-2 Day 20 vs 80%/20% CCD+ Day 8	***	80%/20% Day 14 vs Caco-2 CCD+ Day 14	***	80%/20% CCD+ Day 20 vs HT29-MTX CCD+ Day 8	***
Caco-2 Day 20 vs HT29-MTX CCD+ Day 8	***	80%/20% Day 14 vs Caco-2 CCD+ Day 20	***	HT29-MTX CCD+ Day 8 vs HT29-MTX CCD+ Day 14	*
Caco-2 Day 20 vs HT29-MTX CCD+ Day 14	**	80%/20% Day 14 vs 90%/10% CCD+ Day 14	**	HT29-MTX CCD+ Day 8 vs HT29-MTX CCD+ Day 20	***
90%/10% Day 8 vs Caco-2 CCD+ Day 8	**	80%/20% Day 14 vs 90%/10% CCD+ Day 20	***		

**Table 4.1: Significance calculation between TEER values measured in epithelial co-culture Transwell models of the intestinal epithelium** - Significance was calculated by one way ANOVA with Tukeys post-test analysis with 95% confidence rating. \*\*\* =  $P < 0.0005$ , \*\* =  $P < 0.005$ , \* =  $P < 0.05$ . Only days 8, 14 and 20 were used in significance calculations. n=4-8 N=4-8

#### **4.4.2 Histological investigation of Caco-2:HT29-MTX 2D co-culture on Snapwell Transwell membranes.**

Figure 4.4 shows the H&E stained models of Caco-2 (Figure 4.4 A, D & G), 90:10 Caco-2: HT29-MTX (Figure 4.4 B, E & H) and HT29-MTX (Figure 4.4 C, F & I).

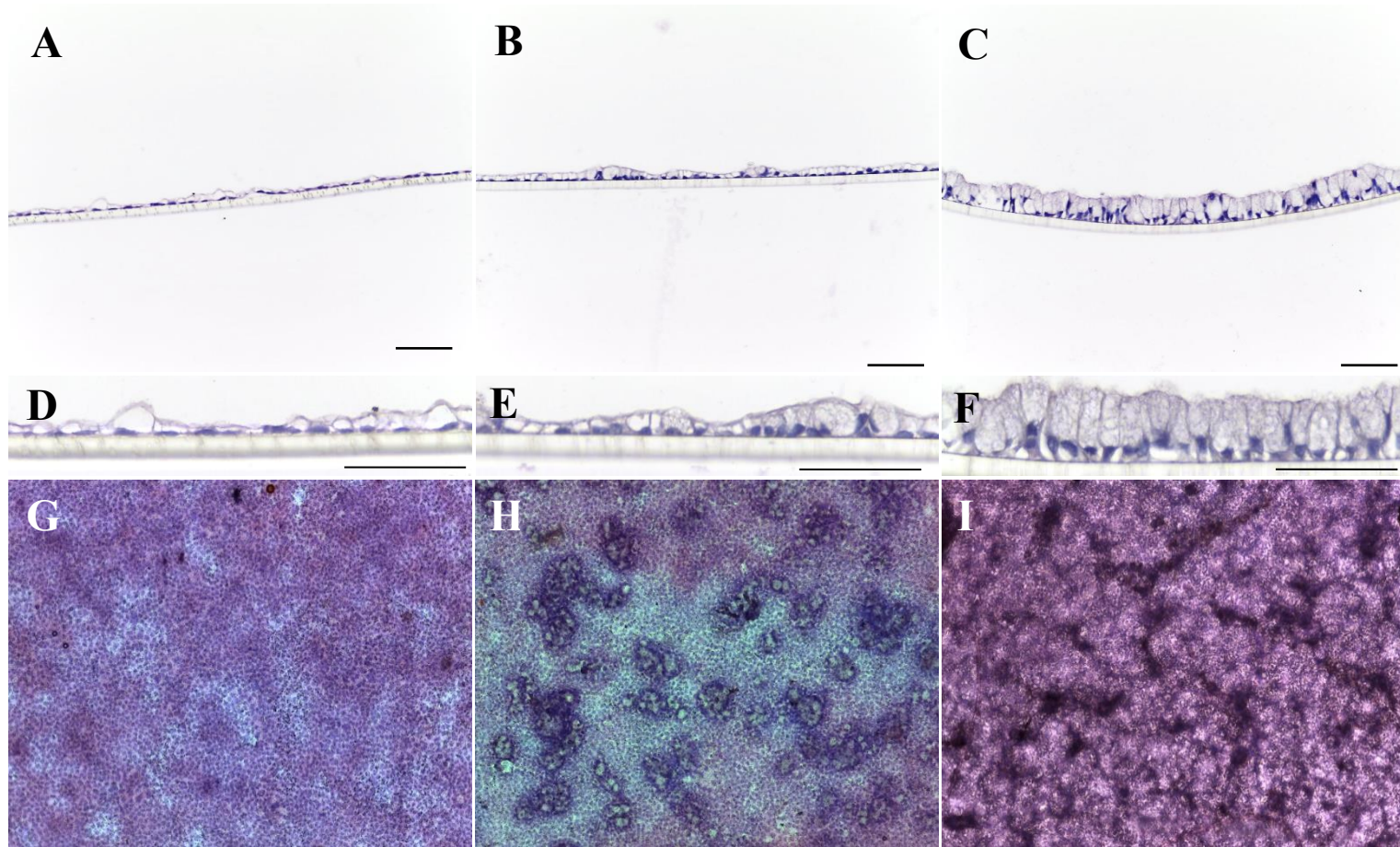
Histologically, Caco-2 control membranes exhibit a flattened squamous monolayer morphology which is consistent through the length of the samples (Figure 4.4 A, D). Figure 4.4 G shows the top down stained model membrane. Staining is consistent over the entire samples with little heterogeneity, as would be expected from a single cell type phenotype. Conversely, figure 4.4 B & E shows the 90:10 co-culture membranes. It can be clearly shown that two cell types are present in this sample with the Caco-2 cells having weaker cytoplasmic staining when compared to HT29-MTX cells in addition to being far flatter than their goblet cell comparisons. Interestingly, the Caco-2 cells, even when non-adjacent to goblet cells, appear taller in co-culture samples than the controls.

Figure 4.4 H shows the top down staining of 90:10 co-culture model membranes. Goblet cells can be seen to be growing in island colonies within the Caco-2 cell monolayer. HT29-MTX cells appear to take up a larger proportion of the final cell model area than the 90:10 original culture ratio would suggest. Therefore, it can be inferred that HT29-MTX cells grown within 2D co-culture Transwell models grow at a faster rate than the Caco-2 cells, overtaking then in the areas in which they are seeded.

HT29-MTX monocultures grown on Snapwell Transwell exhibit a heightened cell morphology when compared to Caco-2 controls (Figure 4.4 C & F). This heightened layer is shown to have basally located nuclei with large, strongly staining vacuole like structures located apically to the nuclei. Figure 4.4 I, shows the top down staining of HT29-MTX monolayers. These stain strongly with eosin to produce a deeper purple stain than compared to Caco-2 monolayers. Areas of darker staining indicate places of mucous build up, released by the HT29-MTX goblet cell like membrane.

Figure 4.5 shows the Periodic acid Schiff (PAS) staining of the same Caco-2 control, 90:10 Caco-2: HT29-MTX co-culture and HT29-MTX control layers previously. Figure 4.5 A & D shows that control Caco-2 layers have weak staining for acidified mucosubstances, the PAS positive staining target. Figure 4.5 G confirms that Caco-2 cells are naturally weakly positive for acidified mucosubstances, potentially indicating a limited ability for Caco-2 cells to express membrane bound and secreted mucins.

The 90:10 Caco-2: HT29-MTX co-cultures show areas of weak PAS staining and areas of strong positive staining, with the strong staining isolated to the taller with more densely stained cytoplasm, as seen by H+E staining in Figure 4.5 B, E & H and hypothesised to be the goblet cells in culture. The Caco-2 cells in this model don't appear to express acidified muco-substances at a higher rate than in the control samples. Figure 4.5 H, shows the wholemount staining of Caco-2: HT29-MTX co-culture. It is clear from the image that the staining of the co-culture model is significantly stronger than the staining seen in the Caco-2 monoculture control models. Additionally, the staining is seen in a heterogenous manner with areas of light and dark staining within the epithelial layers. Finally, Figure 4.5 C & F show strong PAS stained cells with a heightened cell morphology. When looking at the whole mount staining of this sample (Figure 4.5 I) it is clear to see a significantly darker stained homogenous layer of cells within the model.



**Figure 4.5: Caco-2:HT29-MTX epithelial co-cultures shows significant differences in cellular morphology between models** – H+E stained sections of 21 day matured Caco-2: HT29-MTX co-cultures on Transwell polyester membranes. A) 100% Caco-2, B) 90% Caco-2 with 10% HT29-MTX, C) 100% HT29-MTX. Samples were fixed in 4% Formalin overnight before dehydration and embedding in wax. HT29-MTX goblet cells show increased cell height and polarisation with clear basally located nuclei. Caco-2 cells exhibit a flattened squamous cell morphology with little polarisation evident. 90:10 Caco-2 HT29-MTX co-culture appears to improve the structural morphology of caco-2 cells with a moderately more polarised cuboidal cell phenotype. Sections were cut at a thickness of 5 $\mu$ m. Images are representative of a minimum of 3 independent observations. Scale 25 $\mu$ m.



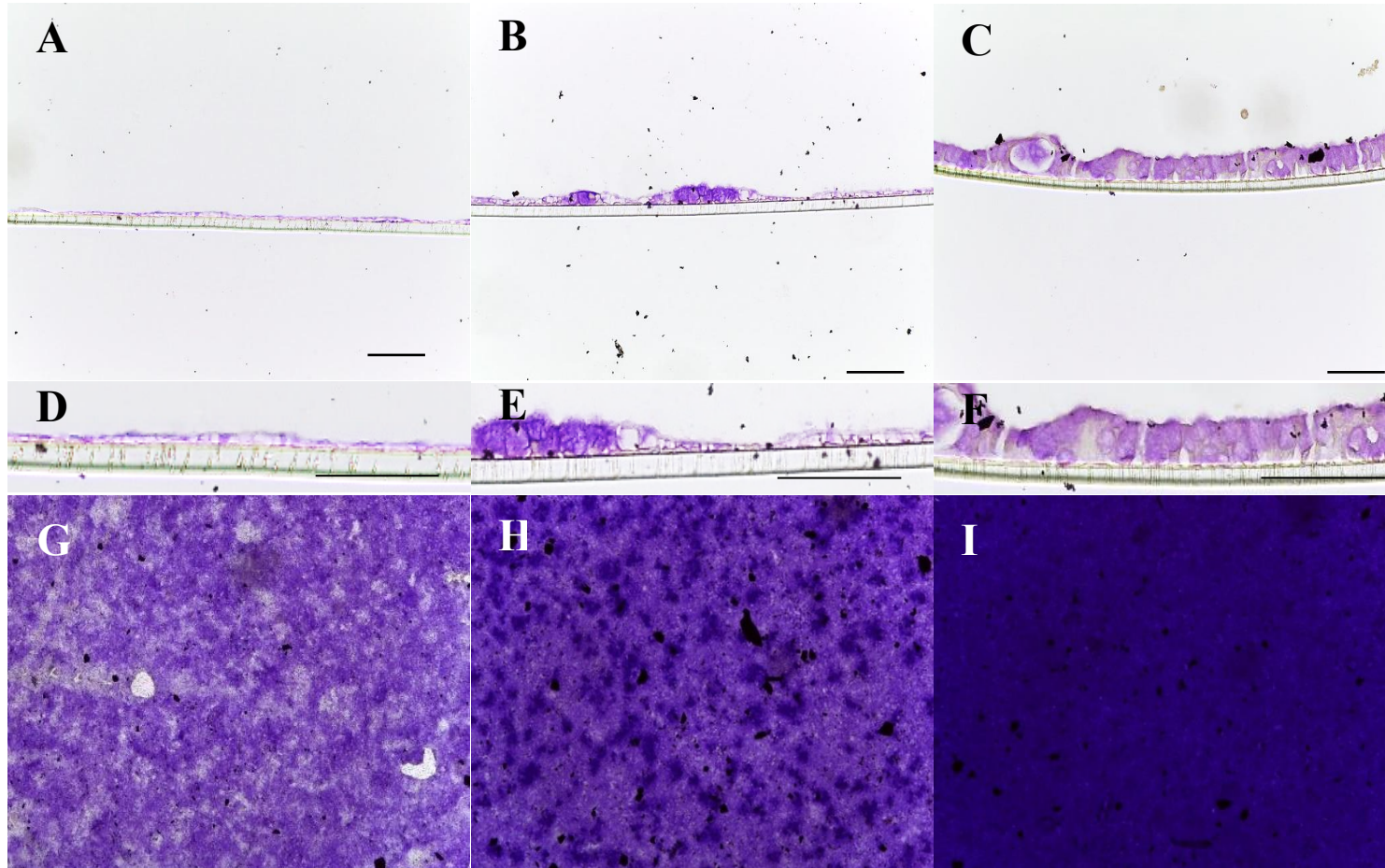


**Figure 4.6: Mucous staining in Caco-2:HT29-MTX epithelial co-cultures** – Periodic acid Schiff (PAS) stained sections of 21 day matured Caco-2: HT29-MTX co-cultures on Transwell polyester membranes. A) 100% Caco-2, B) 90% Caco-2 with 10% HT29-MTX, C) 100% HT29-MTX. D-F) Sectioned samples of the corresponding model co-cultures. G-I) Top down viewed wholemount stained samples of corresponding co-culture models. Samples were fixed in 4% Formalin overnight before dehydration and embedding in wax. Pas staining intensity can be seen to increase with increasing proportion of HT29-MTX cells into the co-culture models. PAS stained goblet cells can be easily identifiable in sectioned samples of the models by intense PAS staining compared to less intensely stained Caco-2 cells. Control layers of Caco-2 monocultures show weak PAS staining indicating low levels of mucin production. Sections were cut at a thickness of 5 $\mu$ m. Images are representative of a minimum of 3 independent observations. Scale 25 $\mu$ m



### **4.4.3 Understanding the effects of CCD-18co paracrine culture on the development of Caco-2/HT29-MTX co-culture Snapwell® membranes.**

Figure 4.6 shows the H&E stained layers of Caco-2 and HT29-MTX when cultured in the presence of CCD-18co conditioned media. Figure 4.6 A, B & C, shows a low powered magnification of the Caco-2 (Figure 4.6 A), 90/10 Caco-2/ HT29-MTX co-culture (Figure 4.6 B) and HT29-MTX (Figure 4.6 C). In each instance the cells express a flattened or cuboidal cell morphology with no obvious goblet cell like morphologies in any of the conditions. Caco-2 cells when treated with CCD-18co paracrine media do not appear significantly different in structure from control samples. However, HT29-MTX cells become significantly shorter than their control counterparts, with no obvious goblet cell phenotype as seen in Figure 4.4 C & F.

When looking at a wholmount perspective, Caco-2 monolayers treated with CCD-18co paracrine media do not look significantly different from their control counterparts with a normal cobble-stone distribution of approximately equal size cells. A similar phenotype can be seen in 90/10 Caco-2/ HT29-MTX samples (Figure 4.6 H) with a reasonably homogenous epithelial layer observed. On close inspection some differences can be seen throughout the layer betraying the presence of the HT29-MTX cells. However, when compared to no CCD-18co treated control layers (Figure 4.4 H) the differences are significant with HT29-MTX cells in control layers easily distinguishable compared to treated models. Finally, H&E staining of treated HT29-MTX monocultures (Figure 4.6 I) shows a significantly less homogenous structure compared to control models (Figure 4.4 I). Cells appear to form a uniform monolayer across the surface of the Transwell Snapwell® insert with areas of doming, similar to what is seen in Caco-2 monolayers cultured on non-permeable membranes. In this instance it is more likely to be areas on higher mucous production.

Figure 4.7 shows the effects of CCD-18co paracrine treatment on the mucous production of the resultant epithelial models assessed by PAS staining. Structurally there is no differences seen in these Periodic acid Schiff stained samples over those stained for H&E.

Firstly, looking at the transverse sections it was shown that the levels of positive PAS staining is not noticeably different between any of the epithelial co-culture conditions. Wholemout staining of the epithelial constructs does show differences in PAS staining across the surface of the monolayers. Similarly to untreated conditions, increasing staining presence is seen with increasing proportion of HT29-MTX cells added into the culture. However, what should be noted is that compared to control layers (Figure 4.5) , treated cultures express significantly less mucous production.

Figure 4.7 H, shows PAS specifically staining populations of HT29-MTX cells which are growing in isolated colonies as seen in control layers. HT29-MTX monocultures shows a highly heterogeneric surface expression of mucin elements, with higher levels of staining seen primarily in the areas identified earlier as likely to be areas of mucous production.

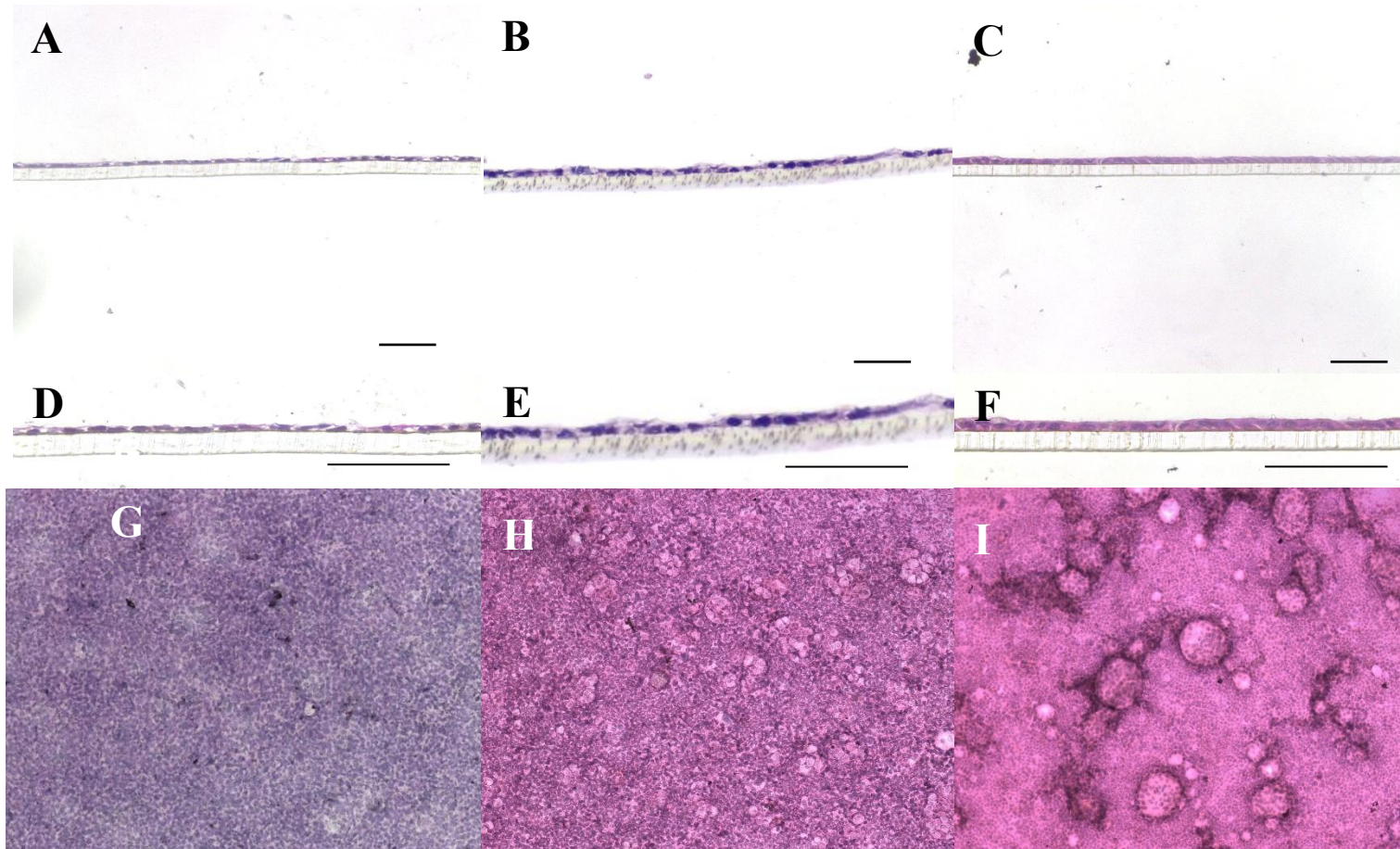


**Figure 4.7: CCD-18co effects on Caco-2:HT29-MTX epithelial co-cultures** – H&E stained sections of 21 day matured Caco-2: HT29-MTX co on Transwell polyester membranes. A) 100% Caco-2, B) 90% Caco-2 with 10% HT29-MTX, C) 100% HT29-MTX. D-F) Sectioned samples of the corresponding model co-cultures. G-I) Top down viewed wholemount stained samples of corresponding co-culture models. Samples were cultured in the paracrine media produced by CCD-18co fibroblasts. Samples were fixed in 4% Formalin overnight before dehydration and embedding in wax. Distinct differences can be seen between Control H+E stained models (Figure 4.3) and CCD-18co treated models with changes in goblet cell morphology in treated samples. HT29-MTX exhibit a more flattened phenotype with a loss of the tall polarised morphology. Sections were cut at a thickness of 5 $\mu$ m. Images are representative of a minimum of 3 independent observations. Scale 25 $\mu$ m

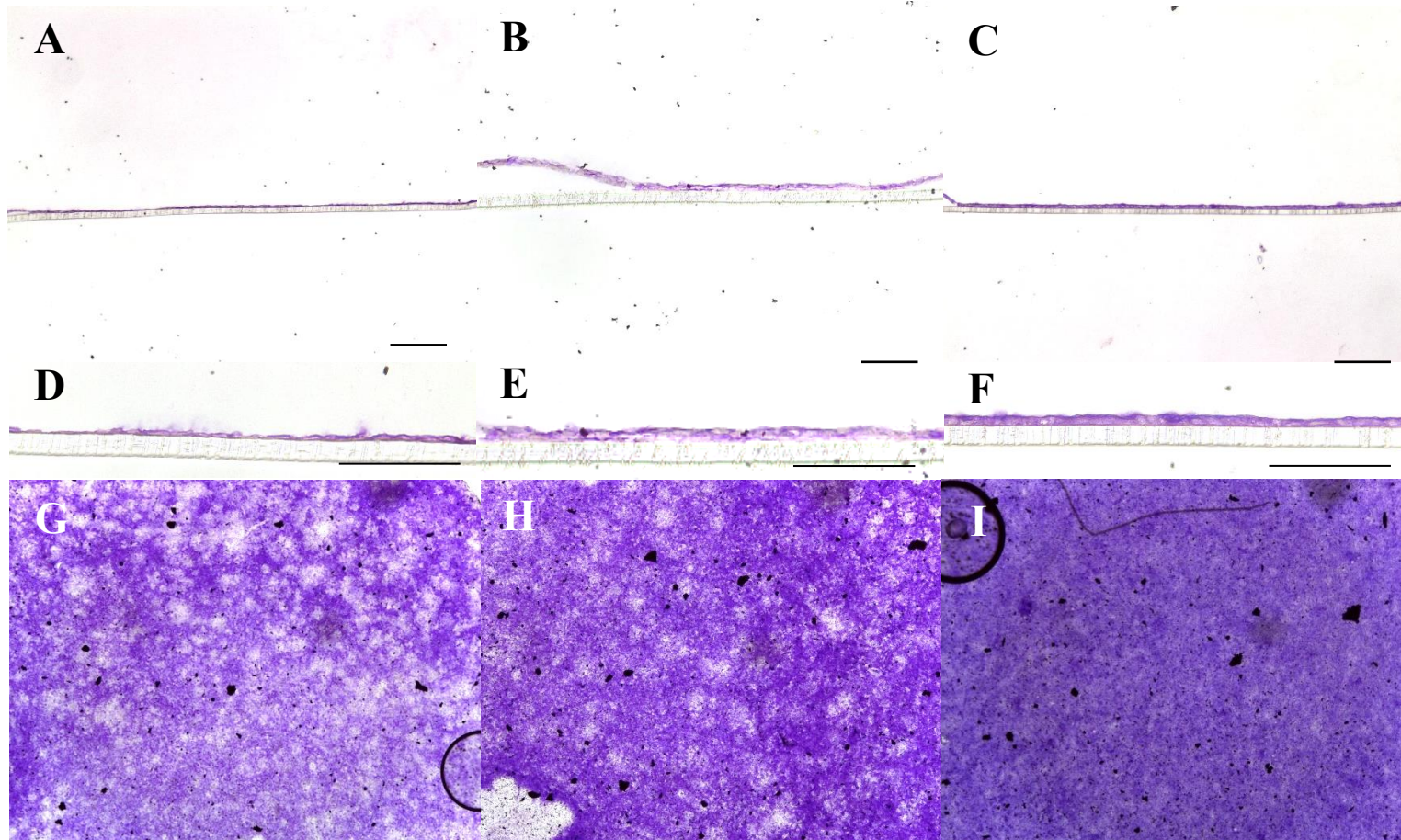


**Figure 4.8: Caco-2:HT29-MTX epithelial co-cultures with CCD-18co paracrine media** – Periodic acid Schiff (PAS) stained sections of 21 day matured Caco-2: HT29-MTX co-cultures on Transwell polyester membranes cultured in the presence of CCD-18co paracrine media. A) 100% Caco-2, B) 90% Caco-2 with 10% HT29-MTX, C) 100% HT29-MTX. D-F) Sectioned samples of the corresponding model co-cultures. G-I) Top down viewed wholemount stained samples of corresponding co-culture models. Samples were fixed in 4% Formalin overnight before dehydration and embedding in wax. A clear loss in PAS staining can be observed over control models (Figure 4.4). Less PAS staining suggests that models are secreting less mucous than in control conditions. Sections were cut at a thickness of 5µm. Images are representative of a minimum of 3 independent observations. Scale 25µm

#### **4.4.4 Analysis of Co-culture model cellular phenotype under CCD-18co conditioned media by Toludine blue staining of resin embedded sections.**

CCD-18co conditioned media was applied to Caco-2: HT29-MTX co-culture membranes and the structural histology was analysed through Toludine Blue staining of resin embedded samples.

Figure 4.8 shows more clearly the effects of CCD-18co on co-culture membranes than paraffin embedded samples. Figure 4.8 A, shows Caco-2 controls without modification embedded in Resin. It can be seen that resin embedding procedures are more able to preserve the structural histology of the epithelial membrane with clear improvement in cellular height and staining resolution over the PFA fixed paraffin embedded samples. Figure 4.8 B & C, shows similar phenotypes as seen in the paraffin embedded samples (Figure 4.4 B & C) with clear distinction between the Caco-2 and HT29-MTX cell types present in the model (Figure 4.8 B). The increased resolution staining achieved by resin embedding and Toludine blue staining highlights the seemingly pseudostratified nuclei of the HT29-MTX control membrane. (Figure 4.8 C)

Contrastingly, Figure 4.8 D-F shows the phenotype of the Caco-2 epithelial cells in the presence of CCD-18co paracrine media. As before Caco-2/ CCD-18co models are not noticeably structurally different from Caco-2 controls. However, it can be clearly seen in Figure 4.8 E & F that the HT29-MTX cells re-organise themselves into a very different structure over the 21 day culture period when in the presence of CCD-18co conditioned media. Figure 4.8 F, highlights this most clearly by showing HT29-MTX cells in isolation. It can be seen that the cells have lost their clear goblet cell like phenotype and have reverted into a cell more reminiscent of a standard epithelial cell such as the Caco-2. The cells are much shorter than the control HT29-MTX and have lost the distinctive goblet cell vacuole seen apically in control cells.



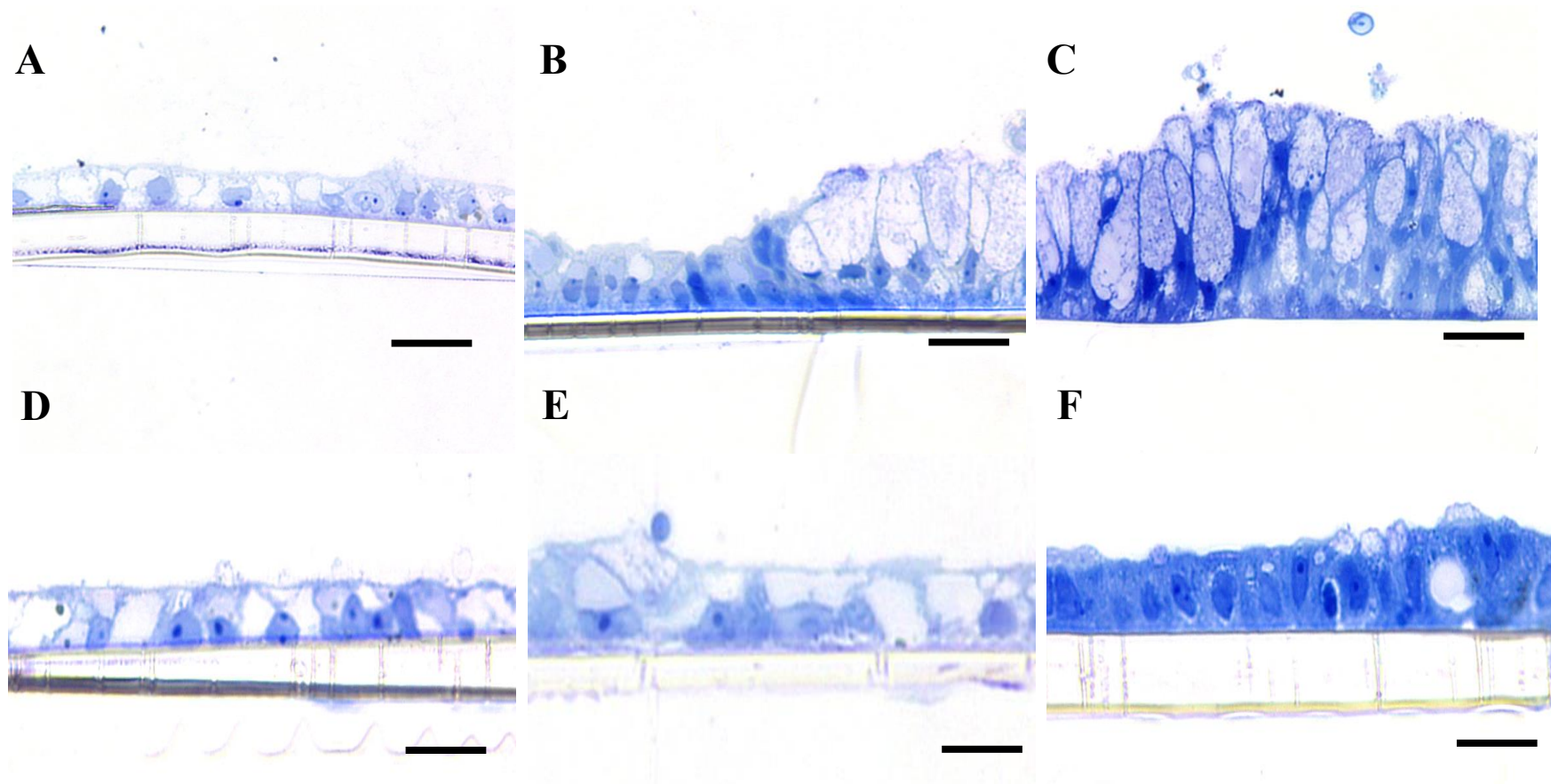


**Figure 4.9: Toluidine blue stained sections of Caco-2/ HT29-MTX co-cultures with and without CCD-18co conditioned media on Transwell membranes** – A) Caco-2 control, B) 90:10 Caco-2: HT29-MTX co-culture, C) HT29-MTX control, D) Caco-2/ CCD-18co, E) Caco-2:HT29-MTX/ CCD-18co, F) HT29-MTX/ CCD-18co. Toluidine Blue stained sections allow for the high magnification analysis of cellular morphology, not possible with paraffin embedded sections. A-C) Shows the Control conditions highlighting the flattened Caco-2 phenotype (A) and the tall morphology of HT29-MTX cells (C). CCD-18co treated Caco-2 layers highlights the drastic change in morphology, particularly HT29-MTX cells which appear similar in structural phenotype to Caco-2 cells when treated. Images are representative of a minimum of 3 independent observations. Scale = 20µm

#### **4.4.5 Analysis of Caco-2:HT29-MTX co-cultures structural phenotype through high resolution transmission electron microscopy (TEM).**

Transmission electron microscopy (TEM) was used to assess the ultrastructure of the Caco-2, Caco-2/HT29-MTX epithelial co-culture membranes. Figure 4.9 A & B, shows both the apical and basal ultra-structure of the Caco-2 control layers. Caco-2 have large continuous microvilli along the apical cell surface. Additionally, microvilli associated glycocalyx can be seen along the surface of the Caco-2 cells. Cell membranes between adjacent cells follow a convoluted line with many invaginations between the cells, beginning at the surface (Figure 4.9 A) and continuing to the base (Figure 4.9 B). This results in a large total membrane contact length between adjacent cells. Tight junctional complexes can be seen along the apical section of the adjacent cell membranes as electron dense areas of staining. Cytoplasm staining of the Caco-2 cells shows abundant organelles throughout. However the cytoplasm itself has weak electron dense staining.

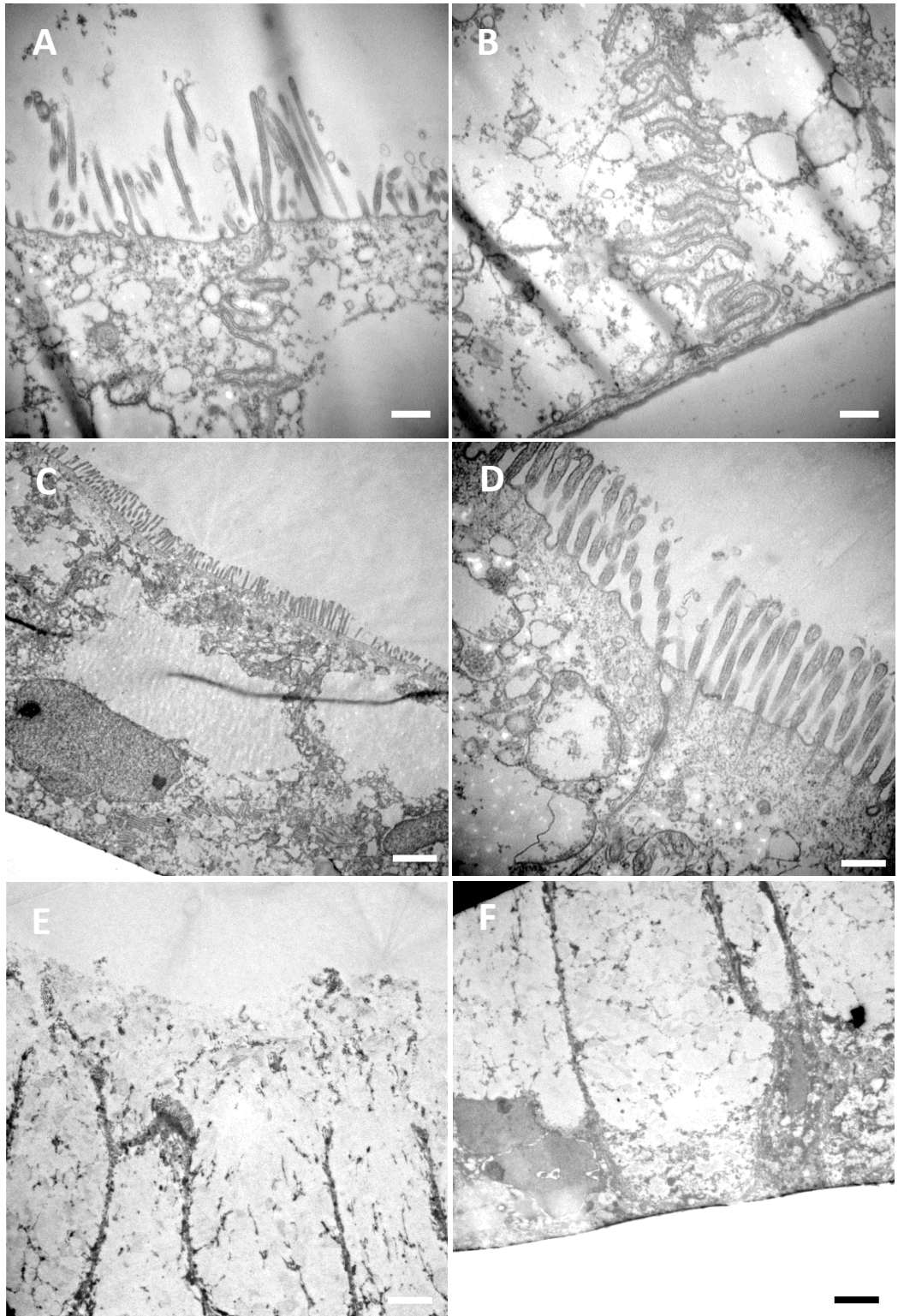
Figure 4.9 C & D, shows the TEM imaging of the 90:10 Caco-2:HT29-MTX co-culture membranes. As in the Caco-2 control layers there is a continuous microvilli surface layer across the length of the model which seem to be shorter but more densely packed and consistent. Interestingly, The cell-cell membranes are significantly less invaginated than in the Caco-2 control layers with less electron dense staining indicating junctional points. ON the whole distinguishing between Caco-2 and HT29-MTX cells in these cultures is difficult due to a high degree of similarity in structural phenotype between cells.

Finally, Figure 4.9 E and F shows the detailed structural morphology of the HT29-MTX cells grown on the Transwell membranes. These cells show none of the epithelial cell phenotypes such as continuous microvilli formation along the apical cell surface and tight junctional abundance along cell-cell membranal contacts. Instead these cells are shown to have a much decreased microvilli confluency, arranged into small clusters along part of the apical membrane. Additionally, membrane contacts between cells are long and straight without any invaginations as seen in Caco-2 layers. Nuclei are basally located with the majority of the remaining space in the cell taken up by large vacuole like

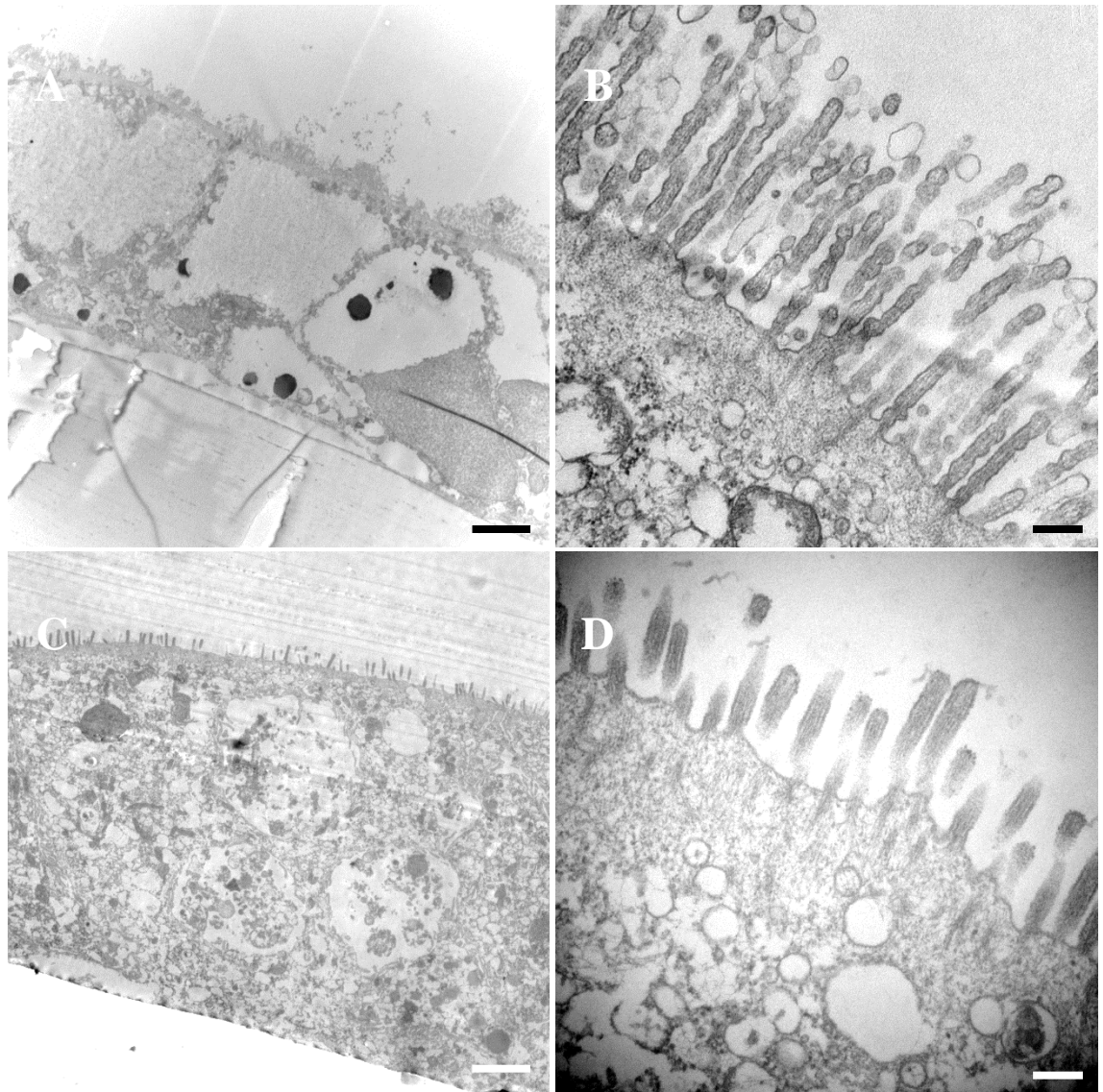
structures filled with mucin and with a thick mucus layer can be clearly seen attached to the apical surface membrane.

Figure 4.10 shows the effects of the addition of CCD-198co paracrine media to the Caco-2/ HT29-MTX cellular model. Figure 4.10 A & B shows the Caco-2 epithelium alone. No noticeable differences can be observed in Caco-2 structure when co-cultured in CCD-18co media. Contrastingly, Figure 4.10 C & D shows the effects on HT29-MTX cellular structural morphology when cultured in CCD-18co media. Large vacuole structured observed in non-treated samples are noticeably lost with denser cytoplasmic staining and a more differentiated epithelial surface. Consistent microvilli expression is observed along the apical membrane of treated HT29-MTX cells. In essence, HT29-MTX cells appear, in the presence of CCD-18co media, to revert back to a more enterocytic phenotype with a loss of goblet cell function.





**Figure 4.10: TEM images of Caco-2/ HT29-MTX co-cultures – A-B)** Caco-2 cell control cultured on a Transwell membrane for a period of 21Days, Cells show good differentiation with apically expressed microvilli seen throughout the section. Cells are tightly bound together with extensive cellular junctions throughout the length of the cell. Scale 500nm. **C-D)** 90/10 Caco-2/ HT29-MTX co-culture, extensive well developed brush border is seen along the length of the cell. Brush border in co-culture modes appears to more consistent throughout the length of the cell and shorter than caco-2 monocultures. Scale 2um and 500nm. **E-F)** HT29-MTX cells cultured on Transwell membranes for a period of 21 days showing classic goblet cell morphology. Images are representative of a minimum of 3 independent observations. Scale 4μm.



**Figure 4.11: TEM images of Caco-2 and HT29-MTX cultures in the presence of CCD-18co conditioned media – A-B)** Caco-2 grown on Transwell membranes for a period of 21 days in the presence of CCD-18co conditioned media **C-D)** HT29-MTX cells grown on Transwell membranes for a period of 21 days in the presence of CCD-18co cells conditioned media. Changes in morphology are seen when compared to normal goblet cell cultures. Cells express an epithelial like morphology with extensive brush boarder and cell junctions. Images are representative of a minimum of 3 independent observations. Scale 2μm, 250nm

#### **4.4.6 E-cadherin staining of Caco-2/ HT29-MTX layers highlights the changes in structural morphology when HT29-MTX cells are exposed to CCD-18co paracrine media.**

Figure 4.11 shows the E-cadherin staining of Caco-2/ HT29-MTX co-cultured Transwell membranes in the absence (Figure 4.11 A-D) and presence of CCD-18co paracrine conditioned media (Figure 4.11 E-H). Progressively increasing HT29-MTX cell proportions can be easily seen between samples with the presence of tall goblet like cells, easily distinguishable from epithelial Caco-2 cells. This goblet cell phenotype is significantly attenuated in CCD-18co paracrine media treated conditions with 100% HT29-MTX layers exhibiting a morphology very similar to that of the Caco-2 cell line.

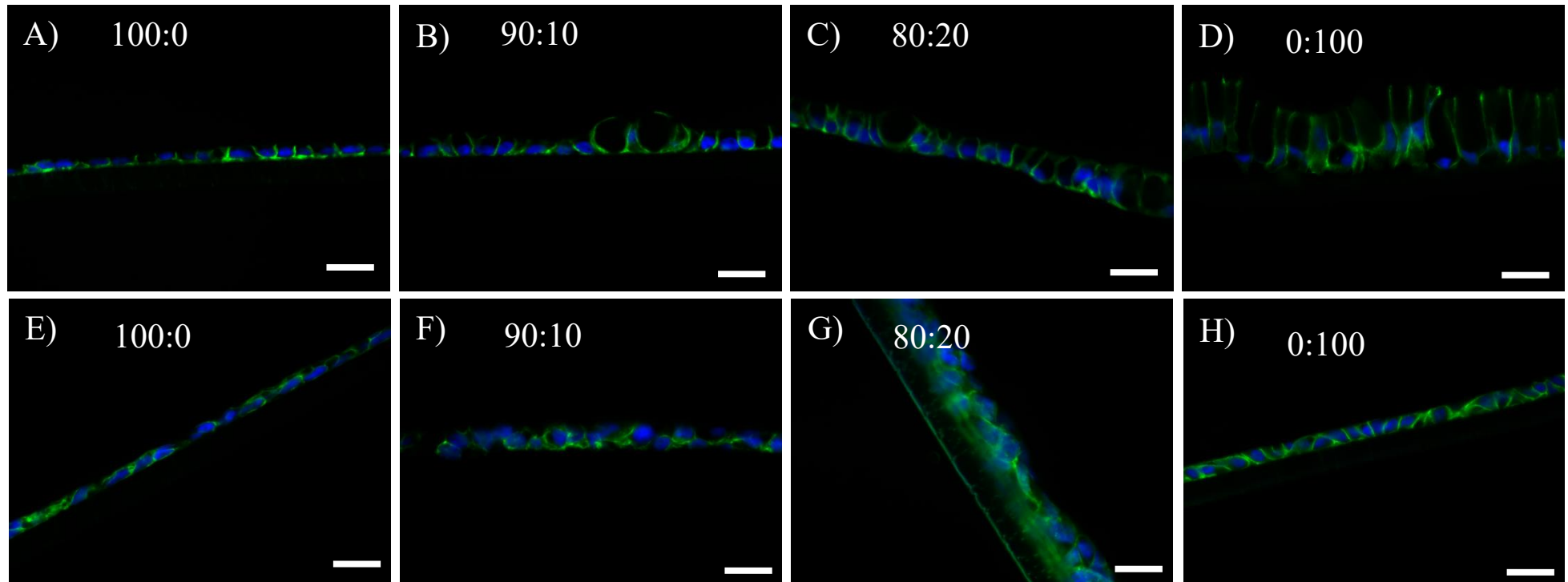


**Figure 4.12: E-cadherin stained Caco-2/ HT29-MTX co-cultures in the presence and absence of CCD-18co conditioned media** – Significant attenuation of HT29-MTX structural phenotype can be seen when exposed to CCD-18co conditioned media with resultant cellular phenotype similar to enterocyte morphology. A) 100% Caco-2, B) 90% Caco-2, 10% HT29-MTX, C) 80% Caco-2, 20% HT29-MTX, D) 100% HT29-MTX, E) 100% Caco-2 + CCD-18co, F) 90% Caco-2, 10% HT29-MTX + CCD-18co, G) 80% Caco-2, 20% HT29-MTX + CCD-18co, H) 100% HT29-MTX + CCD-18co. Images are representative of a minimum of 3 independent observations. Scale 20µm

#### **4.4.7 qPCR analysis of the development of Caco-2:HT29-MTX co-culture layers in relation to key targets of function.**

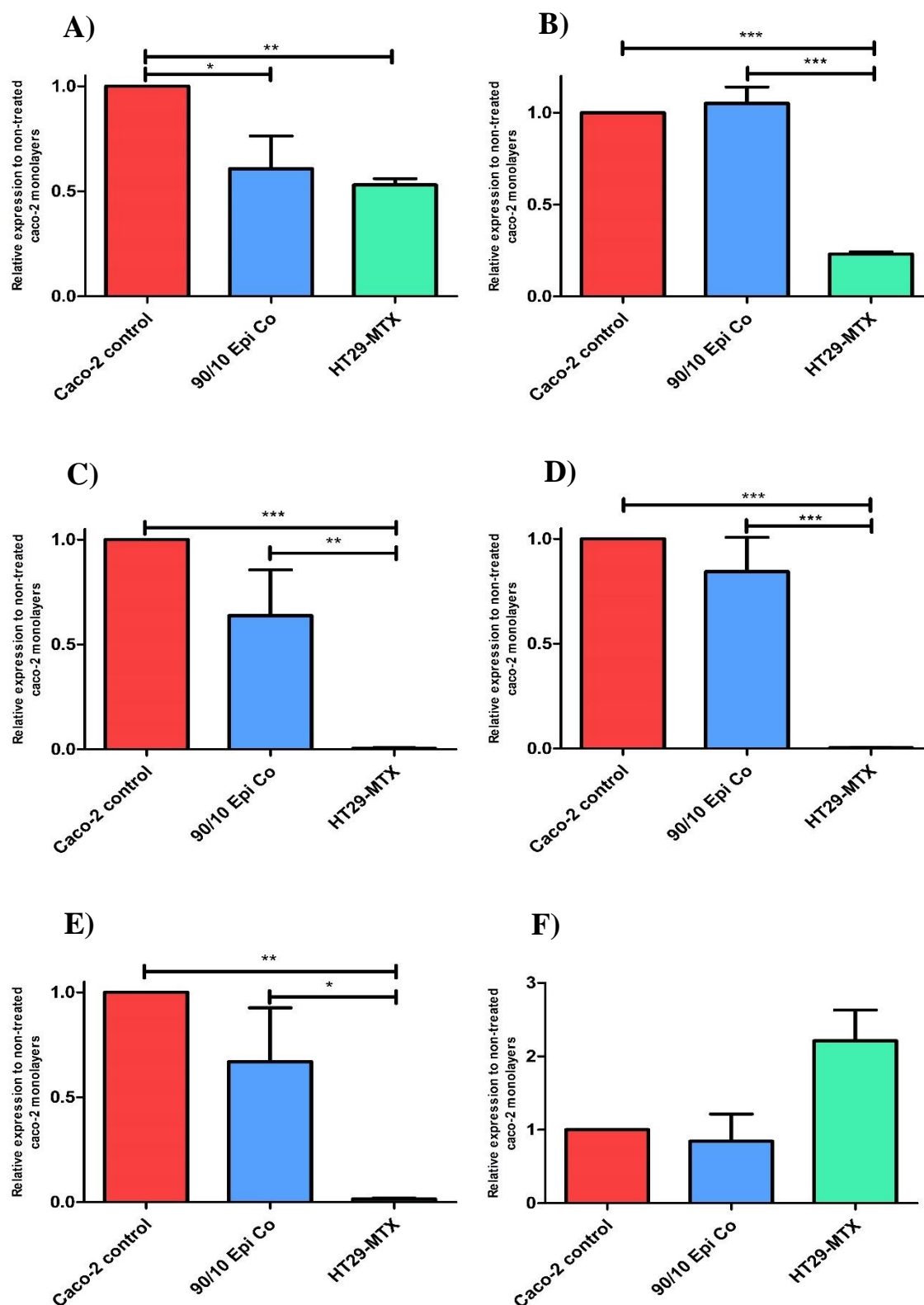
mRNA expression levels of key genes of interest namely; Villin, Occludin, MRP2, MDR1, OATP-B and BCRP, were quantified through the use of SYBR based qPCR expansion and detection methods.

Figure 4.12 A, shows the mRNA expression levels of the protein Villin. Villin is an apically expressed microvilli protein which is often used as a method of quantifying microvilli expression and as such enterocyte epithelial differentiation. Figure 4.12 A, shows a stepwise decrease in Villin mRNA expression dependant on the ratio of HT29-MTX cells within the epithelial culture. When normalised to Caco-2 control expression levels it was demonstrated that addition of 10% HT29-MTX cells at the beginning of the culture period induces a significant decrease in Villin expression by approximately 40% that of the control. HT29-MTX cells grown in isolation do express Villin mRNA, albeit at a significantly reduced level compared to Caco-2 at approximately 50% expression of the control.

Occludin as discussed previously is an important component of the tight junctional complex. Figure 4.12 B, shows the relative expression levels of Occludin when normalised to Caco-2 controls. Both Caco-2 control and 90:10 Caco-2: HT29-MTX co-culture layers show no significant difference in Occludin levels between the models. Contrastingly, HT29-MTX layers show a significant decrease in Occludin mRNA expression when compared to all other conditions to a levels approximately 25% of Caco-2 layers.

MRP2, MDR1, OATP-B and BCRP are all apically expressed transporter protein shown to be involved primarily in the efflux of toxins from the intestine, including therapeutic drugs. The function and abundance of these proteins in the human intestine and their effects on the bioavailability of drug compounds within the intestine is a key area of consideration when designing an improved biological model for use as a tool in biological research. MRP2, MDR1, OATP-B (Figure 4.12 C, D and E) all follow the same

basic stepwise decrease in expression rates with increasing HT29-MTX involvement compared to Caco-2 and HT29-MTX controls. Indeed, MRP2, MDR1, OATP-B are shown to be negligibly expressed within the samples with expression rates only a few percent of the control levels. In each case, the 90:10 Caco-2: HT29-MTX co-culture shows strong expression levels compared to HT29-MTX but are less than Caco-2 monocultures. Contrastingly, BCRP expression shows a significant increase in mRNA expression in HT29-MTX cells when compared to Caco-2 controls. However, 90:10 ratio co-cultures were shown to be not significantly different from the Caco-2 controls in this instance.



**Figure 4.13: qPCR analysis of Caco-2/ HT29-MTX co-culture Transwell models shows differential expression between Caco-2 and HT29-MTX cells lines** – qPCR data shown here demonstrates the differential expression of key protein mRNA between Caco-2 and HT29-MTX cells. A) Villin, B) Occludin, C) MRP2, D) MDR1, E) OATP-B, F) BCRP. In most instances A-E, HT29-MTX cells show a reduction in the relative expression of mRNA of the key proteins tested here. This is as expected as most of the targets are enterocyte efflux or tight junction proteins. Interestingly however, BCRP levels are seen to increase in HT29-MTX cells in comparison to Caco-2 cells. This could affect the sensitivity of co-culture models to BCRP substrate compounds. Significance was calculated by one way ANOVA with Tukeys post-test analysis with 95% confidence rating. \*\*\* =  $P < 0.0005$ , \*\* =  $P < 0.005$ , \* =  $P < 0.05$ . n=2-3 N=2-3. Significance values calculated between value n=2, N=2 have been omitted from the graphs (Panel F). Error bars represent + SEM of average values.

#### **4.4.8 Functional characterisation of Caco-2/ HT29-MTX co-culture Rhodamine 123 transport in Snapwell culture.**

Figure 4.12 shows the basal to apical (B-A) transport of Rhodamine 123 across Caco-2/ HT29-MTX co-culture layers both in control states and in CCD-18co paracrine treated conditions. All data points within Figure 4.13 were taken after 120 minutes within the Ussing chamber system with absolute donor compartment concentration calculated by comparison of values against a standard curve. Control layers show an approximate Papp of  $0.4 \times 10^{-6}$  which is well in line with values gained in similar experiments throughout the literature. Addition of the paracrine effects of CCD-18co cells resulted in an increase in B-A transport by about double, although the standard error here is large with significant variation seen between samples making differences non-significant from control layers. No significant differences in B-A transport can be seen in 90/10 ration cultured Caco-2/ HT29-MTX epithelial models from controls. However, similarly to control samples an increase in Rhodamine Papp can be seen in CCD-18co treated 90/10 epithelial layers although the magnitude of the change is less than that of control layers.

Finally, HT29-MTX cultured modes show some Rhodamine 123 transport at a significantly reduced levels than all other conditions. Treatment with CCD-18co conditioned media has very little to no effects on the transport of Rhodamine 123 in HT29-MTX layers with Papp values non significantly different from Control HT29-MTX models.



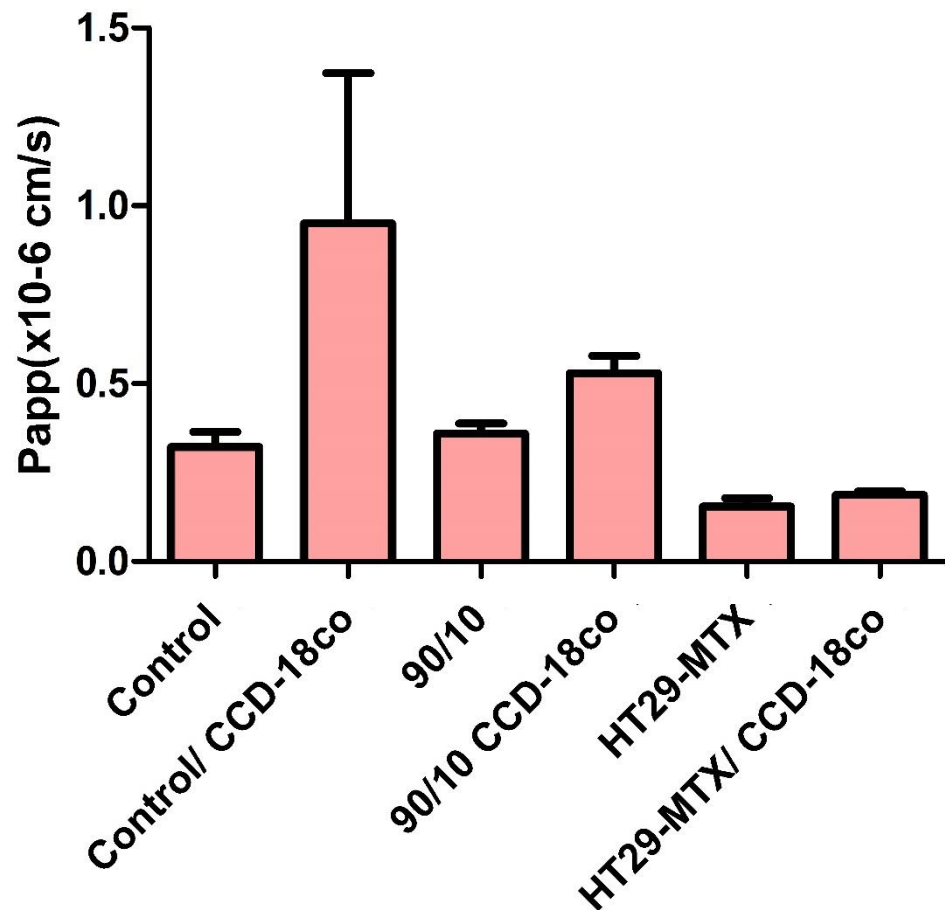


**Figure 4.14: B-A Rhodamine 123 transport dynamics of Caco-2/ HT29-MTX co-cultures in control and CCD-18co paracrine treated Snapwell layers** – Epithelial cell models were tested for transport of Rhodamine 123 within an Ussing chamber systems as previously described. All measurements were taken after 120 minutes assay length. Paracrine CCD-18co models were created as previously described. HT29-MTX models have a significantly reduced Rhodamine transport capability over Caco-2 Transwell systems. 90/10 co-culture models show no significant changes suggesting goblet cells can be added to a model in small amounts without compromising the capability of said model in a functional manner, in this case in its capability to transport Rhodamine 123, primarily through P-gp mediated means. n=3-6 N=3 Significance was calculated by one way ANOVA with Tukeys post-test analysis. No significance was observed between samples. Error bars represent + SEM of average values.

## 4.5 Discussion

The aims of this chapter were to attempt to create an epithelial co-culture model incorporating both the mucous element of the intestinal epithelium and the paracrine cross talk of supportive stromal cells, in this case CCD-18co myofibroblasts. The barrier function of the resultant constructs was assessed through TEER measurements as previously described and structure was evaluated through the use of histological techniques and electron microscopy. Finally, epithelial constructs were assessed functionally through their capability to transport the p-gp substrate, Rhodamine 123.

### 4.5.1 Epithelial co-culture and the effects of differing seeding ratio on the Trans-Epithelial Electrical Resistance (TEER) of the tissue construct.

Caco-2 cellular models are well known to exhibit significantly higher TEER values than *in vivo* intestinal tissues due to a heightened expression of tight junctional proteins within Caco-2 cells. Additionally, Caco-2 models overexpress the surface efflux protein p-gp. As such, these models are often poor indicators of for the transport of hydrophilic compounds (which primarily move paracellularly) which can appear to be highly impermeable to the Caco-2 constructs. (243) The usefulness of HT29-MTX cells in culture is primarily in their ability to produce a mucous layer along their apical surface when grown in 2D culture and in their significantly lower TEER values when compared to Caco-2 cells through interspersed of goblet cells between enterocytes. As such these cells have been widely utilised as a stand in for goblet cells in many cellular models of the intestinal epithelium. (131,243,246–248) In this study the co-culture Caco-2 cells with HT29-MTX at a range of physiological ratios, specific to differing sections of the intestine was attempted. For example, there is a significantly higher proportion of goblet cells in the colon (25-55%) (249) than the small intestine, with a gradual increase as the small intestine descends. (92)

Figure 4.2 and 4.3 of this chapter show the effects of epithelial cell co-culture on the development of the model TEER values over the course of 21 days in culture. HT29-

MTX cells are generally known to express lower TEER values than Caco-2 cells with reported values ranging from less than 50 to ~200 ohms per cm<sup>2</sup>. (243,244) Whilst the TEER values gained here for HT29-MTX monocultures are significantly higher than some of the values which are published, they are still significantly lower than the TEER values of the Caco-2 cells utilised in the co-culture models. The methodology for the measurement of TEER values of HT29-MTX layers differs significantly lab to lab and, much like how Caco-2 reported TEER values can vary between individuals and labs the same applies to other cell lines. Additionally, the possibility of the membrane associated and secreted mucous on the TEER values of the epithelial layers was not tested for here and is not fully understood. Theoretically, the density of the mucous layers could contribute to the overall TEER values of the models. (230)

When looked at histologically, HT29-MTX cells can be seen to be organised into tall, often multicellular layers. As such this could in part explain why TEER values for these cells were so high due to the long convoluted membrane length and multicellular nature of the model. HT29-MTX cells are seen to become more organised when co-cultured with Caco-2 cells, with clear monolayer formation and basally located nuclei. As such one would expect that these cells within the co-culture model exhibit a decreased TEER compared to their control HT29-MTX counterparts. Therefore, the decrease in TEER which is seen when co-culturing Caco-2 cells with HT29-MTX follows a logical course assuming that Caco-2 and HT29-MTX cells don't interact with one another in a way to change their individual epithelial resistances.

Indeed, this stepwise decrease in TEER value was also observed by Béduneau *et al* in their tuneable co-culture model in which they culture both of these cells lines together. (243) In this study the authors created Caco-2: HT29-MTX models on Transwell membranes utilising a culture method different from that used in this study. Different density models were created through the simple seeding of mix ratio dependant populations with all cells seeded on day 0. Béduneau *et al* also cultured different ratios of cells but also changed the time at which the HT29-MTX cells were added to the model with additions ranging from -1-7 days post Caco-2 seeding. Whilst this is an interesting methodology for controlling the end model population ratio of cells this study doesn't appear to have controlled for the fact that cells will be of different maturities in the end

model. For example, HT29-MTX cells seeded 7 days post Caco-2 seeding will have a full week less time to grow and importantly, differentiate than their day 0 counterparts. This again highlights the difficulties in directly comparing model results between studies as the culture methods and materials often differ significantly.

Similarly to the work here, Béduneau *et al* evaluated their models through Rhodamine transport and lucifer yellow permeability. They found that increasing the number of HT29-MTX cells within the co-culture system resulted in decreases in overall construct TEER measurements in addition to stepwise decreases in the Papp of lucifer yellow, indicating that models with high proportions of HT29-MTX cells were more passively leaky than Caco-2 controls. Additionally, they observed that rhodamine transport decreased with increasing HT29-MTX percentage most likely due to less active enterocytes in the end culture and the effects of the mucous barrier created by the HT29-MTX cells.

#### **4.5.2 Functional transport characteristics of epithelial co-culture layers.**

Figure 4.13 of this study shows the B-A Rhodamine 123 transport conducted in this study. Significant differences between Caco-2 and 90/10 co-culture conditions was not observed. However, HT29-MTX monocultures did transport Rhodamine 123 at a significantly lower rate than Caco-2 controls. Having said that however, the HT29-MTX B-A Papp values for Rhodamine 123 were still a significant proportion of the control Caco-2 levels. This along with the abnormally heightened TEER values in control HT29-MTX layers compared to values normally published in the literature lends evidence to the idea that these cells used in this study may be a different subtype. Alternatively, culture conditions have been shown to significantly affect the structure and differentiation of matured cell lines. For example, Navabi *et al* (250) cultured HT29-MTX in RPMI 1640 media compared to the DMEM utilised in this study. As such, the histology of the control HT29-MTX layers in their study appear significantly different in structural morphology than seen here with their cells forming cuboidal monolayers more reminiscent of enterocytes than the goblet cell morphology seen in this study. Interestingly, even through

the morphology of their cells appear more enterocyte like the TEER values of the resultant HT29-MTX models were still low at around 150 ohms, significantly less than seen here. Unfortunately, there is little standardisation between labs in the methods to culture these cells thereby increasing the likelihood of differences arising between studies.

The model by Beduneau *et al* showed the functional transport of Rhodamine 123 across HT29-MTX/ Caco-2 layers of varying ratio. (243) Essentially, the outcomes of their study are reflected here with a decreased functional transport of Rhodamine 123 in HT29-MTX cell systems, an expected outcome due to HT29-MTX's known function as a goblet cell rather than an enterocyte. Given the usual under representation of Caco-2 cells models regarding MDR1 activity, addition of HT29-MTX cells which further reduce the models functional MDR1 based capabilities would be counterproductive. Culture of HT29-MTX cells with Caco-2 sub-populations known to possess a more homogenous expression profile such as Caco-2/TC7 (251) are another possibility to attempt to counteract efflux protein under expression. Pontier *et al* showed the transport capabilities of a number of compounds between Caco-2/TC7 and HT29-MTX. Interestingly, they showed how HT29-MTX cells are able to increase permeability to a number of compounds compared to Caco-2 monocultures. Taken together they suggest that differences between the two cell lines are relatively minimal when a wide range of compounds are taken into account. However, in their TEER analysis the HT29\_MTX cells in their cultures has a significantly higher resistance value than their control Caco-2 monocultures. This is in complete contrast to the phenotype observed here and again highlights the importance of culture conditions on cellular phenotype.

### **4.5.3 Understanding the effects of CCD-18co conditioned media on the development of the epithelial construct layers.**

To my knowledge, whilst the co-culture of Caco-2 and HT29-MTX cells together is a routinely, if not widely adopted, model of the intestine as previously discussed. Addition of the paracrine factors present in CCD-18co conditioned media is a novel addition to this system. As has been discussed and shown in the previous chapter, one of the main known components of CCD-18co paracrine media, with biological morphogenic properties, is

KGF. A search of the literature suggests that the action of KGF on HT29-MTX cells specifically is poorly understood and understudied, although it is logical to assume that KGF will have many of the same functions on HT29-MTX cells as with any other intestinal epithelial cell lines, namely; cellular/ lineage differentiation and regulating cellular proliferation. (213)

In this study, HT29-MTX cells when cultured with CCD-18co conditioned media are shown to change significantly in both their structure as seen by H&E, Toluidine Blue staining and TEM, and in function as seen with changes in PAS staining, a stain which specifically targets acidified mucosubstances normally produced by goblet cells. Indeed, close analysis of HT29-MTX cells after co-culture with CCD-18co conditioned media shows that the cells have morphed into an enterocyte like cell line with regular cuboidal structure, basally located nuclei and a single monolayer formation without evidence of multilayering. When further investigated with TEM HT29-MTX cells are seen to transform from a large vacuous cell with significant apical mucous and only sporadic microvilli formation into a densely cytoplasmic enterocyte with continuous well-formed apical brush border and cell junctions. This change can also be seen reflected in the TEER assessment at the beginning of the chapter whereby the culture of HT29-MTX containing models with CCD-18co conditioned media increases TEER values in each case. This is in direct contrast to co-culture with Caco-2 cells which results in a TEER decrease with paracrine co-culture.

HT29-MTX cells as discussed earlier are in reality simply HT29 cells which have been treated with Methotrexate in order to isolate a goblet cell like subclone from the parental line. (240) It was hypothesised that the co-culture of HT29-MTX cells with CCD-18co paracrine media results in a reversion of this goblet cell like phenotype back into a cell more similar to the parental HT29 morphology. This could be potentially through a KGF mediated pathway (KGF is important in cancer phenotype homeostasis in the intestine) (213) although this was not looked into in any depth in this study. This kind of cellular reprogramming can be seen throughout the literature. In the context of HT29-MTX cells specifically, Xu *et al* considered the effects of small molecules on HT29-MTX cells in their paper studying the role of NHE8, its regulation by TNF- $\alpha$  and its effect on the production of mucous in HT29-MTX cells. (252) Briefly they found that NHE8 was

downregulated by TNF- $\alpha$  resulting in a decrease in the mucous production of the HT29-MTX cells. TNF- $\alpha$  is a proinflammatory cytokine primarily produced by cells of the immune system, namely activated macrophages (253) but can also be produced by endothelial cells and importantly, fibroblasts. Whilst not tested for it is possible that CCD-18co cells are able to produce TNF- $\alpha$ , especially if in a proinflammatory state as seen by high levels of  $\alpha$ -SMA, potentially reducing HT29-MTX mucous production through this method. With structure comes function, therefore a reduction in functional ability would imply similar variations in cellular structure. However, whilst Xu *et al* did provide indicative evidence suggestive that downregulation of NHE8 reduced mucous production they did not analyse the structure of the resultant cells so it is not possible to know if the same morphological changes were seen in their study as here.

Visco *et al* (179) showed in their study that KGF was able to have effects on the growth rate of HT29 cells *in vitro* with significant increases seen in Ki67 expressing cells, suggesting an improved rate of proliferation. Interestingly, in this study the authors also note that CCD-18co conditioned media has stronger proliferation inducing effects than KGF treatment alone, suggesting that other small molecules are being released by CCD-18co cells that are having compounding morphogenic effects on Caco-2 and HT29 epithelial cultures. Whilst this study doesn't go into any depth about the change in function of treated cells it does show that HT29 cultures are sensitive to KGF treatment. As such one could expect that HT29-MTX cells, derived from HT29 parental lines, would also be sensitive to KGF and in similar ways, which in this instance was an increase in cell proliferation.

## 4.6 Conclusion

Work done in this chapter highlights the importance of simulating multiple aspects of the intestinal epithelium when creating a co-culture model of the intestine. Goblet cells can have significant effects on the capability of the resultant epithelial constructs with changes in transport capabilities induced through a reduction in transport capable enterocytes and the formation of a mucous layer which can have inhibitory effects on compound movement and availability to the enterocyte epithelium. Additionally, CCD-18co cells have been further shown to have bioactive effects on the development of epithelial layers. Indeed, reversion of HT29-MTX cells into a less goblet cell state, whilst

not ideal for the resultant model, could be argued to be more biologically relevant, with increasing model complexity enhancing cell phenotypes. As HT29-MTX cells are not true goblet cells, in this instance the enhanced phenotype that would be expected is that of the enterocyte. Results found within Chapter 3 along with the work discussed here has been invaluable in understanding the effects of simple cell co-cultures in Transwell based systems.

Future work within the scope of this chapter could include further elucidation of the exact mechanism for the changes in structural phenotype seen when Caco-2 cells are cultured with CCD-18co conditioned media. For example, understanding if this mechanisms is controlled through KGF secretion could help to identify the function of KGF in the development and maintenance of epithelial layers. The initial purpose to optimising Caco-2/ HT29-MTX/ CCD-18co cells in Transwell was to apply the knowledge gained into a 3D model of this intestine. Due to the negative interactions of HT29-MTX cells with CCD-18co paracrine factors it was decided that no further development would take place in this study. Further work should focus on overcoming these challenges to create a true 3D intestinal model which incorporates the mucous aspect of the intestinal epithelium.



## 5. Optimisation & characterisation of an *in vitro* model of the intestinal mucosa and development of associated technology.

### 5.1 Introduction

#### 5.1.1 The biological relevance of 3D culture.

Conventional Transwell culture as seen in the previous chapters of this work is clearly the gold standard technique for the modelling of the human intestinal epithelium in both industry and academia. Since the inception of the Caco-2 cell line in the early 90's and its application to drug discovery purposes there has been little change seen from the original model principle developed by Artusson *et al* (254) and others of Caco-2 cell layers cultured on permeable hanging inserts.

As has been discussed previously, others have attempted to modify/ enhance the Caco-2 model system through the application of other cell types/ cell lines such as the addition of goblet cells into the culture in order to recapitulate the mucous layer (228,255) or in the co-culture of Caco-2 cells in paracrine media such as at by Ghadban *et al* in their work with immune cells and their effects on the differentiation and function of the Caco-2 and

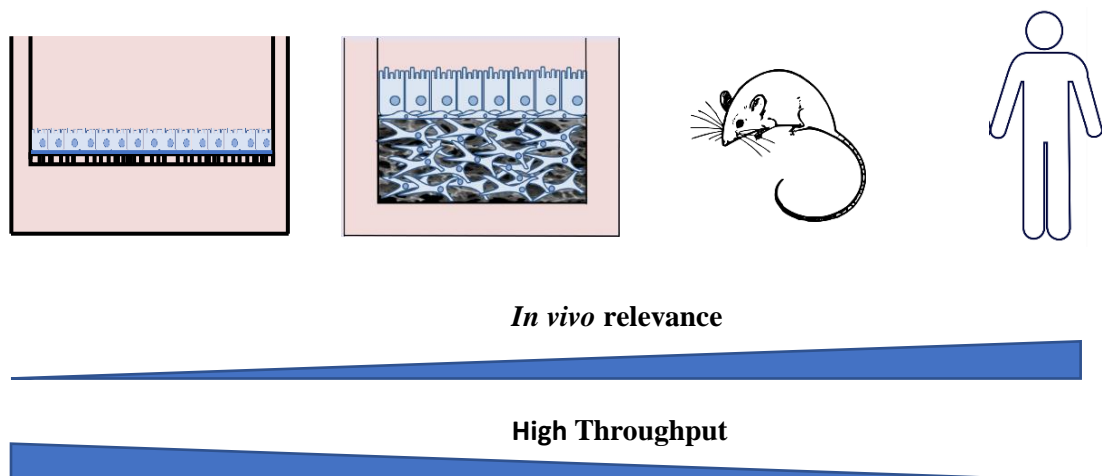


**Figure 5.1: The progressive complexity of biological research** – With increasing relevance comes increasing cost, 3D models are designed to be a midpoint between simple 2D models of the intestine and more ethically challenging options such as animal and humans testing.

IEC epithelium.(256) Generally, these modifications still rely on the original hanging insert technique without much additional innovation.

The immediate reasons for this are three-fold;

1. The Caco-2 model is reasonably predictive of the pharmacokinetic properties of the intestine of a number of drug classifications without additional modification, especially when utilised alongside other simple models such as PAMPA.
2. The Caco-2 model is inexpensive and well characterised compared to novel 3D systems.
3. The Caco-2 model is simple to culture and as such is relatively easy to apply to high throughput applications.

Whilst the advantages of the Caco-2 cell line seem numerous, the models do suffer from a number of major drawbacks, primarily in their bio predictability of certain drug classifications such as in their poor indicatives of lipophilic compounds due to retention within the Caco-2 cell layer and non-specific binding to the Transwell surface. (257) As such the Caco-2 models are often utilised alongside more ethically challenging systems such as *in vivo* animal models which are simultaneously far less high throughput and significantly more expensive than their 2D cell-based model counterparts. More sophisticated models of the intestinal epithelium which are able to bridge the gap between simple cell based and animal systems have the potential to streamline the drug discovery process; increasing the identification rates of pharmacokinetically viable compounds, decreasing the reliance on animal models and ultimately saving both time and money throughout the process.

### **5.1.2 Different applications of the Caco-2 cell line to 3D systems of the intestinal epithelium.**

In an effort to close the gap between cell based and animal models new and emerging models of the intestinal epithelium are published on a regular basis focussing primarily on the application of the Caco-2 cell line to 3D culture systems. As discussed in the

general introduction to this thesis, one of the main powers of 3D culture is its flexibility, allowing it to take many forms and be tailored to the required specifications of the user.

For example, Yu *et al* (258) created a model which incorporated the 3D architecture of the intestinal villus through the use of a hydrogel construct formed into villi structures, cultured in a hanging insert, onto which they cultured Caco-2 epithelial cells. They demonstrated that simply changing the architecture onto which the cells were cultured had significant effects on the differentiated phenotype of the resultant model. For example, they showed significantly reduced TEER values in 3D constructs over 2D controls and hydrogels without the 3D structure. This TEER decrease when compared to rat intestinal tissues which showed a significantly more *in vivo* TEER phenotype in the 3D constructs. Additionally, calculated permeability co-efficients were more physiologically relevant in 3D models when compared to human tissues than 2D model controls.

The most important part of this model was its simplicity. No additional cell lines or supplementary signalling were required to produce an model with improved “*in vivo*” characteristics over 2D controls. As such, this highlights the power of the 3D environment, suggesting that the structure of the cells implies their function, a critical phenotype missing in 2D cultures. This concept of structure influencing the function of cells is often referred to as mechano-transduction and is a relatively well studied area of biology. For example Wang *et al* (259) in their recent paper looked at the effects of the organisation of the ECM on the phenotype of MSC cells cultured within a tuneable ECM scaffold. They found that by altering the properties of their material such as fibre diameter, stiffness and alignment they could alter the 3D structure of the scaffold. The microscopic structures within the scaffolding materials (Voids and channels) had significant effects on the shape and actin cytoskeleton morphology of 3D cultured cells. This lead to changes in cellular differentiation and as such the function of the tissues created by the 3D cultured cells. Again, this is another example whereby cell fate is influenced by the 3D structure in/ on which the cells are cultured without any additional influencers. One postulated mechano-transduction mechanism in Caco-2 cells works through integrin adhesions (an adhesion to the ECM) and the YAP pathway. (260) In many ways the simple scaffold created by Wang *et al* is similar to Alvetex® (utilised in

this study) in that scaffold pore size can be altered to suit experimental needs. These levels of 3D tunability are simply impossible in 2D cultures in which cells are expected to differentiate in an alien environment and without the signalling queues found *in vivo*.

Organoid cultures are another area of current intense research interest since their inception and by Hans Clever. (117) These models utilised primary intestinal stem cells or isolated intestinal crypts to grow highly advanced, well differentiated cellular epithelium with a whole range of different cell types with variable function. Unfortunately, their application to drug discovery functions are limited due to the inability to create a single polarised monolayer from these cells. However, these models are still highly valuable for a range of uses such as understanding tissue development (261) and disease modelling (262). Newer techniques are being developed to apply these advanced culture systems to pharmacokinetic applications. Onozato *et al* described a process whereby they tested a number of compounds on organoid cultures such as Rhodamine 123 and FD-4. (263) Their model however, still suffered from the aforementioned disadvantages of their technique such as; only A-B transport could be tested and quantification of total drug absorption/ efflux was not possible.

Scaffolding technologies, as utilised in this study are another potentially powerful tool for the creation of 3D culture models. Scaffolds can come in a range of formats from decellularised matrices which straddle the boundaries between tissues, hydrogels and scaffolds, to polystyrene structures (as used in this study) which are significantly more reproducible, standardised formats, good for use in routine sample analysis etc whilst sacrificing the intrinsic signalling properties of scaffolds made from biological substances such as ECM components. In many instances however models are created to utilise multiple technologies together. The coating of the often bio-inert surfaces of polymer based scaffolds with hydrogels such as collagen I is a fairly ubiquitous technique to improve the attachment and differentiation of cells in culture through the provision of a basement membrane. Indeed, collagen coating techniques are used regularly even in 2D culture, in many ways blurring the definitions of 2D and 3D culture systems. (264–268)

3D models for all of their advantages do have a number of significant drawbacks which have ultimately stopped their widespread use throughout industry. Often it is the very

advantages of 3D culture which works against their extensive use. For example, as discussed previously, 3D culture technologies can be highly variable, have very niche applications, and allow for tailor made models incorporating a single or multiple methods. Whilst this is an advantage in academia, allowing for the creation of distinct models with unique capabilities it effectively dilutes the ongoing characterisation of each model most often to the lab from which it originated.

Unlike the Caco-2 Transwell model which has been widely characterised the world over, there is no gold standard 3D model of the intestine. As such, many labs have their own model variation which differs from others in its own unique ways, be that in terms of: cell line used, hydrogel composition, scaffold material, surface treatments, media composition/ small molecule additives, model culture time, etc. This lack of cross comparability between unique models and their generally limited characterisation means that individual models cannot be trusted to be more pharmaco-predictive than Caco-2 Transwell models already being utilised. (162,246–249,251,258,269) Furthermore, lack of characterisation leads to non-approval by regulators such as the FDA, a key step that must be taken for a concern to be utilised as an appropriate test model for novel compounds. Ultimately, in order for the cutting of the red tape limiting 3D model progression one model has to “win out” over the others as a new gold standard. Without this the amount of variation which can be incorporated between 3D models make it unlikely any will be sufficiently characterised and approved for large scale use in industry in a reasonable timescale.

Other considerations which have to be made when utilising 3D models are their expense and labour costs. 2D models are “cheap”, with Caco-2 cells, DMEM and Transwell being relatively low cost. Contrastingly, 3D models often utilise technologies which either have not been commercialised or if they have to a relatively low volume and scale compared to 2D systems. Essentially, 3D models will be more expensive than 2D alternatives, at least until high volume production of a single gold standard 3D model is achieved. In terms of labour, 2D Transwell models are relatively easy to culture with 2-3 media changes per week, requiring minutes of work per model. Often 3D models incorporate more cells, of varying lineages, with more complex media requirements, increasing the time required per model and the potential for mistakes in the more complex system.

Additionally, 3D constructs are often created in stages, together taking longer to culture than their 2D counterparts, increasing overall labour and material needs. The burden is for 3D models to prove that the added cost is worth the increased functionality and bio-predictability. A 3D model which is 10% improved at predicting clinical outcomes in humans but costs twice as much and takes three times the work is unlikely to be utilised over simpler models. Especially when the alternatives are more scalable to high-throughput work.

The data novel herein will cover the creation and optimisation and structural characterisation of three 3D models of the intestinal mucosa one for each of CCD-18co, HDFn and HIC lineages as discussed previously. Additionally, work in this chapter will cover attempts at creating a high throughput version of the 3D models through the design and construction of advanced 3D culture plates and Ussing chamber devices.

## **5.2 Hypothesis, Aims and Objectives**

### **5.2.1 Hypothesis**

It is hypothesised that a novel intestinal mucosal model can be created utilising Alvetex Scaffold® and a range of intestinal fibroblasts (CCD-18co, HDFn and HIC) and epithelial cells (Caco-2). Additionally, it was expected that through advanced culture methods a well populated sub-epithelial layer could form to create a dense ECM cellularised matrix for the support and population of Caco-2 cells apically, forming a single monolayer of enterocyte epithelium. Furthermore, it was hypothesised that cells of different lineages will show a degree of cross talk and interaction through the formation of a basement membrane and the differential effects on the structure and function of the Caco-2 epithelium.

### **5.2.2 Aims**

The aims of this chapter are two-fold

1. To create an advanced 3D model of the intestinal mucosae utilising multiple cell types from both stromal and epithelial compartments. It was proposed to understand how fibroblasts from multiple origin points as used in Chapter 3, namely CCD-18co, HDFn and HIC cell lines, are able to form a well populated basement scaffold on which could be cultured Caco-2 epithelial cells for a period of 21 days. Protein expression profile and structure of 3D models was compared to the expression seen in human tissue sections to show close similarity.
2. To create tools in which the functional characteristics of the 3D models could be quantified. E.g. creation of bespoke Ussing chambers to study drug /ion transport and electrophysical characterisation of newly created intestinal models.

### 5.2.3 Objectives

The objectives of this chapter are summarised below:

- Development of fibroblasts stromal compartment of the model to allow for the culture of Caco-2 in a monolayer without invasion into the underlying stromal layers.
- Immunohistochemical characterisation of 3D constructs and comparison to human intestinal tissues to highlight similarities and enhance the differences seen in Transwell models
- Utilise TEM to show cellular ultra-structure and cross talk between epithelial and stromal cell lines.
- Create novel bespoke Ussing chambers for the functional transport analysis of 3D models.
- Develop a method for the higher throughput production and functional analysis of Alvetex<sup>®</sup> based 3D models.



## **5.3 Materials and methods**

### **5.3.1 Seeding Caco-2 cells onto Alvetex® of varying format.**

Alvetex® 12-well discs were processed for cell culture through submersion into 70% ethanol for 5 minutes followed by two washes in sterile PBS to remove any remaining ethanol. This was done to render the Scaffold hydrophilic for cell culture. Cells were seeded at a density of 250,000 cells per insert and cultured in DMEM for a period of 7 days. At culture end models were fixed in 4% paraformaldehyde and processed into wax utilising the standard paraffin embedding protocol described previously (Section 2.3.1)

### **5.3.2 Basement membrane addition to Alvetex Scaffold®.**

Alvetex® 12-well discs were processed to be hydrophilic for culture as described previously (Section 5.3.1). Collagen I, Matrigel® and Puramatrix® solutions were made up following manufacturers specification to a concentration of 2 mg/ml. Basement membrane solutions were added to scaffolds at a density of 200µl per scaffold and allowed to gel completely in a humidified environment at 37°C for 30 minutes before the addition of cells. Caco-2 cells were seeded onto Alvetex®/ Gel constructs at a density of 250 000 cells/ insert and left to culture for either 14 or 28 days. At the end of cell culture models were fixed in 4% paraformaldehyde and processed into wax as previously described (Section 2.3.1)

### **5.3.3 Differential CCD-18co seeding density on model development.**

The epithelium of the intestine is formed of a monolayer of enterocytes and other cell lineages supported by a basement membrane and an underlying stroma of myofibroblasts and fibroblasts. 24-well scaffold with area of 0.77cm<sup>2</sup> were seeded with 77,000 (100,000/cm<sup>2</sup>), 192,000 (250,000/cm<sup>2</sup>), 385,000 (500,000/cm<sup>2</sup>) and 777,000 (1,000,000/cm<sup>2</sup>) fibroblast cells per model. Cells were grown in standard media as

described previously (Section 2.2) for a period of 2 weeks. After 2 weeks of culture Caco-2 cells were added to the apical side of two thirds of the models and allowed to attach at air liquid interface overnight before subsequent submergence in Caco-2 complete medium (complete DMEM) for a further period of 2 weeks. The remaining models were analysed by MTT assay at the 14 day timepoint without Caco-2 addition as previously described (section 3.2.5). At experiment end, replicates of individual models were either fixed and processed into paraffin as previously described (Section 2.3.1) or were analysed by MTT as previously described (Section 3.2.5)

Paraffin embedded samples were sectioned at 7µm and stained with H&E. Images were taken along the length of each sample with a ICC50 HD microscope (Leica) and stitched together and analysed using image J. Multiple sections per condition were measured ensuring each section was a minimum of 50µm from the previous section. Image analysis consisted of measuring the epithelial area relative to the area of the entire model. This was achieved by overlaying images with a 500µm<sup>2</sup> grid with grid squares chosen for analysis by random number generator.

### **5.3.4 The effect of culture time on model development.**

CCD-18co cells were seeded into culture treated Alvetex<sup>®</sup> Scaffold discs at a density of 250,000 cells/ cm<sup>2</sup> (192,000 cells per insert). Scaffold were cultured for 14, 21 or 28 days before analysis. One third of the models were stopped at their respective timepoints and tested for metabolic activity by MTT assay. Other models were seeded with Caco-2 cells at a density of 223,000 cells per cm<sup>2</sup> (172,000 cells per insert, the same as the seeding density of Transwell). Caco-2 cells were allowed to attach overnight at the air liquid interface (ALI) before being subsequently cultured for a period of 14 Days. After 14 days of Caco-2 culture models were either processed into paraffin as previously described (Section 2.3.1) or were analysed by MTT as previously described. (Section 3.2.5)

Paraffin embedded samples were sectioned at 7µm analysed in Image J for the % Caco-2 penetration into the scaffold as previously described.

### **5.3.5 MTT assay analysis of CCD-18co cells grown in Alvetex®**

#### **Scaffold.**

MTT assay analysis of CCD-18co metabolic activity was achieved as previously described (Section 3.2.5)

Briefly, whole Alvetex® Scaffolds containing CCD-18co cells were washed in sterile PBS twice. 3-(4,5-Dimethylthiazol-2-yl)-2,5-Diphenyltetrazolium Bromide was dissolved into phenol free DMEM at 2mg/ml. Solution was heated to 37°C and agitated sufficiently to ensure complete dissolution. MTT solution was sterile filtered through a 0.2µm filter before use. 4.5 ml of MTT solution per well was added to the 24 well format Alvetex Scaffold® and left at 37°C for 1 hour. After 1 hour models were removed from MTT solution and washed twice in sterile PBS. Models were then unclipped carefully from the well supports to limit any disturbance of the cell layers and placed at the bottom of a fresh 12 well plate. 1ml of acidified isopropanol was added to the models to liberate the dye. Models were placed at 150 RPM for 15 minutes to ensure complete dye removal from the 3D scaffold material. 200µl of dye solution was placed into a 96 well microtiter plate and read at 590nm

### **5.3.6 SEM processing of differential seeded CCD-18co**

#### **Alvetex® layers.**

CCD-18co cells were liberated from 80% confluent T175 culture flasks and counted as previously described (Section 2.2.3). Cells were seeded onto cell culture treated Alvetex Scaffold® layers at differential densities of 77,000, 192,000, 385,000 and 777,000 cells per model equating to 100,000, 250,000, 500,000 and 1,000,000 cells per cm<sup>2</sup> or by utilising the multiple seeding technique which involves seeding 192,000 cells on days 0, 7, 9 and 11 for a total of 768 000 cells per model. Models were cultured in standard DMEM formulation for 14 days with media changes every other day. After 14 days models were fixed and processed for SEM as previously described (Section 2.6)

### **5.3.7 3D model processing for TEM analysis**

The general protocol for the processing and staining of samples for TEM analysis is described previously (Section 2.7)

### **5.3.8 Toluene Blue stained samples**

3D models stained for Toluene Blue were set up utilising the standard 3D model set up protocol as previously described (Section 2.15). Samples were cultured for the full culture period before being processed into resin (Section 2.7). Resin embedded samples were sectioned semi-thin (approx. 1µm) utilising a glass knife. Resin embedded sections heat fixed onto a glass slide before being submerged in Toluene Blue solution for a period of 5 minutes. Stained samples were rinsed in cold running water to remove excess stain. Stained samples were mounted with DPX before being imaged on a light microscope (ICC50 HD, Leica)

### **5.3.9 Clearing of Alvetex Scaffold for high resolution lighsheet imaging of 3D intestinal models.**

3D models were fixed in 4% PFA as previously described before being washed twice in PBS for 30 minutes each time. Samples were dehydrated in methanol following a 50%, 80% and 100% gradient (Methanol: PBS) for one hour at each concentration. Samples are bleached in 5% H<sub>2</sub>O<sub>2</sub> in 20% DMSO/ Methanol overnight at 4°C in the fridge. Samples are washed twice in 20% DMSO/ Methanol for one hour each time. This is followed by rehydration through methanol (80%, 50%) for one hour each before being washed in PBS twice and PBS/0.2% Triton for at least one hour before further processing. Samples were Immunostained utilising the normal protocol for immunostaining as previously described (Section 2.4.1) Samples are incubated overnight in 50:50 tetrahydrofuran (THF): H<sub>2</sub>O. Samples are incubated in 80% THF and 100% THF for 1 hour per concentration. Samples are then processed into dichloromethane (DCM) for 30 minutes followed by storage in dibenzyl ether (DBE) at room temperature at which point Alvetex Scaffold® becomes completely transparent within DBE. Protocol taken from a method devised by Renier *et al* (270)

For imaging on a lightsheet microscope (Zeiss lightsheet Z.1) Alvetex<sup>®</sup> must remain within DBE to remain transparent. Alvetex<sup>®</sup> sections were attached to a metal rod with agar before being placed within a capillary tube containing DBE. The tube was sealed so that DBE could not leach into the microscope imaging chamber.

### **5.3.10 Immunostaining of 3D models and human intestinal tissue.**

Both tissues and models were fixed and embedded in paraffin wax as previously described (section 2.3.1) prior to sectioning at 7µm intervals and heat fixing to glass slides. Prior to staining slides were dewaxed in Histoclear and brought to water through a series of ethanol gradients. The general protocol for the process of immunostaining 4% PFA fixed tissues and models is described previously (Section 2.4.1). All slides were analysed on a Zeiss 880 confocal microscope

### **5.3.11 Developing a 24 and 96 well Ussing chamber design for the efficient functional analysis of Alvetex intestinal models.**

Both 24 and 96-well Ussing chamber designs were created by myself in the 3D CAD software Autodesk. Schematics for finalised designs were sent to mechanical engineering services, a part of the Department of Physics at Durham university for manufacture. Chambers were made out of optically transparent Acrylic. It is important that chamber systems at no point are in contact with ethanol of any concentration as plastic will fracture on/ shortly after contact.

Deep well plates for the culture of 96-well inserts were designed by myself and 3D modelled in collaboration with e3design ltd (Newcastle, UK). Concept and application were developed and optimised in house.

## 5.4 Results

### 5.4.1 Caco-2 growth characteristics in different Alvetex® configurations.

In order to understand the best way to construct the 3D model of the intestine the first thing that must be understood is the growth characteristics of the cell lines within Alvetex®. Alvetex® comes in 3 different formats; Scaffold, Strata and Polaris, with the difference between each of the formats linked to the void size of the material. Scaffold has the largest void size at an average of 42µm, Strata has a void size of an average of 15µm and Polaris has the smallest pore size (not quantified)

Caco-2 cells were seeded onto each of the Alvetex® formats at a seeding density of 250,000 cells per cm<sup>2</sup> for a period of 7 days before being processed into paraffin wax as previously described. Figure 5.1 shows the H&E staining of Caco-2 cells on A) Alvetex Scaffold®, B) Alvetex Strata® and C) Alvetex Polaris®. Figure 5.1 A shows that in the scaffold format Caco-2 cells are able to form a well-defined multilayer of cells at the surface of the scaffold structure. Additionally, Caco-2 cells can be clearly seen to line the surface of the scaffold voids creating a pore like structure within. Cells are shown to be able to penetrate through some of the Alvetex scaffold® but generally remain within the upper third of the 200µm thickness. When cells are grown on Alvetex Strata® (Figure 5.1 B) Caco-2 cells are shown to create a monolayer not dissimilar from that seen in Caco-2 Transwell models. Cells are confined to the surface of the material without any invasion into the underlying stroma. Similarly, when cells are grown on Polaris (Figure 5.1 C) no invasion through the Alvetex® material is seen. However, Polaris culture seems to induce a multilayering phenotype within the Caco-2 cells not seen in Strata or scaffold.

Alvetex Scaffold was chosen as the preferred substrate for model development because of its high porosity. Initial experiments (Data not shown) suggested that both Strata and Polaris Alvetex® formats would be poorly suited to pharmacokinetic analysis due to compound sequestration. Additionally, Scaffold® allowed for the culture of fibroblasts cells throughout the length of the substrate with ample room for ECM deposition.

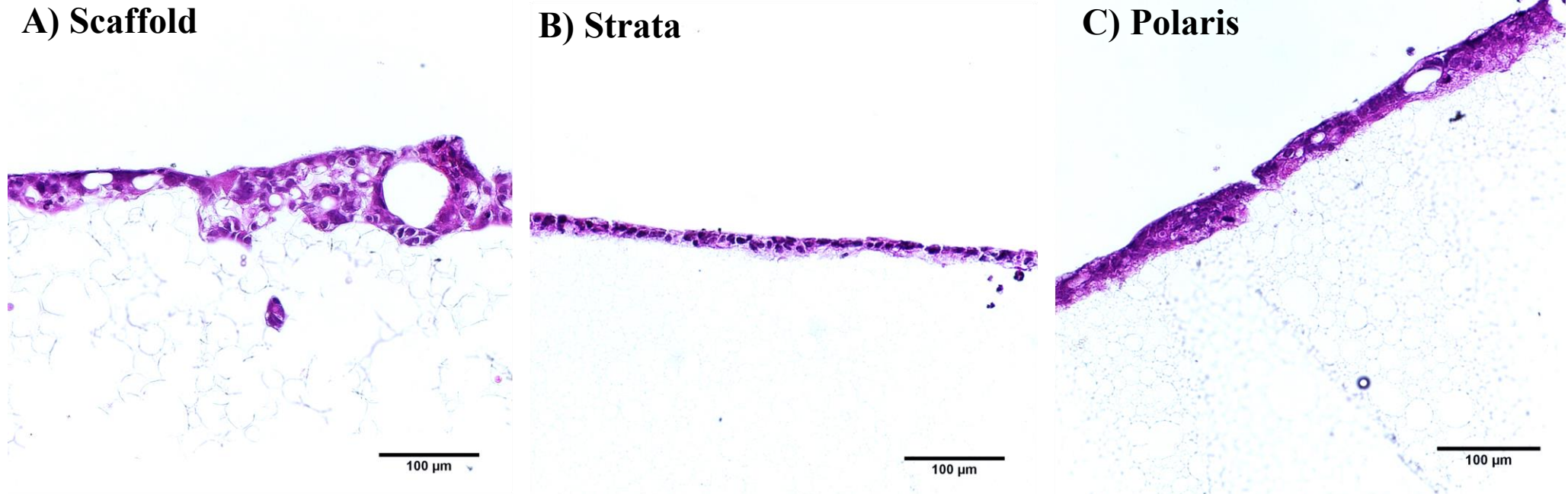


**Figure 5.1: Understanding the growth characteristics of Caco-2 cells in different formats of Alvetex® polystyrene supports** – A) Alvetex Scaffold® has the largest pore size of the different formats with an average void of (33-55µm). Caco-2 cells can be seen growing along the first third of the scaffold thickness, lining the pores to create small epithelial lines spheroids. B) Alvetex Strata® has an average pore size of (<20µm). Caco-2 cells form a monolayer across the surface of the model with no invasion into the underlying support. C) Alvetex Polaris® has the smallest pore size with an average diameter of (3-4µm). Similar to that seen in Strata, Polaris allows for the formation of a monolayer along the surface of the support, with some areas of multilayering. Images are representative of a minimum of 3 independent observations.

### **5.4.2 Addition of a basement membrane protein to the surface of Alvetex Scaffold®.**

Figure 5.1 shows that it is impossible to culture Caco-2 within a 3D Alvetex Scaffold® and create a consistent monolayer without the addition of some other factor to limit Caco-2 cell invasion. One method attempted to limit Caco-2 movement was application of basement membrane proteins to the surface of the Scaffold, onto which cells could be seeded. Figure 5.2 shows Caco-2 cells on Collagen I, Puramatrix and Matrigel layers.

Figure 5.2 A shows Caco-2 cells forming a continuous layer with good cellular morphology on Collagen I layers. No invasion into the underlying stromal section indicates a continuous gel layer. Puramatrix (Figure 5.2 B) and Matrigel (Figure 5.2 C) layers result in significant stromal Caco-2 invasion by 14 days of culture. Cells are seen lining the internal pores of the Alvetex Scaffold®. Puramatrix® Caco-2s' remain in the upper third of the Scaffold whereas Matrigel induces cellular invasion almost to the full thickness of the scaffold at a greater rate than the uncoated surfaces (Figure 5.1 A).

The phenotype described above is the same at 21 days of culture, with Collagen layers limiting Caco-2 cells to a single monolayer at the surface and Puramatrix and Matrigel layers allowing full cellular infiltration across the depth of the scaffold over 28 days of culture. As such, from a structural standpoint alone, Collagen I was shown to be the best suited Basement membrane protein for long term culture of Caco-2 cells in 3D.

Figure 5.3 shows the optimisation of Collagen I layers on the surface of Alvetex Scaffold®. Figure 5.3 A, shows the Analine Blue staining of Collagen I of 2mg/ml, 200  $\mu$ l per cm<sup>2</sup> scaffold area, B is 1 mg/ml and C is 0.5 mg/ml. It can be clearly shown that only 2mg/ml was able to form a continuous layer of collagen across the surface of the model as such this concentration was utilised through the proceeding experiments. It was decided at this time that focus on the development of a populated stromal fibroblast layer was more in line with the overall goals of the project. As such addition of a collagen membrane was dropped in favour of optimisation of a sub-epithelial fibroblast



compartment, sufficiently populated to limit Caco-2 invasion without the requirement of the addition of further basement membrane proteins.

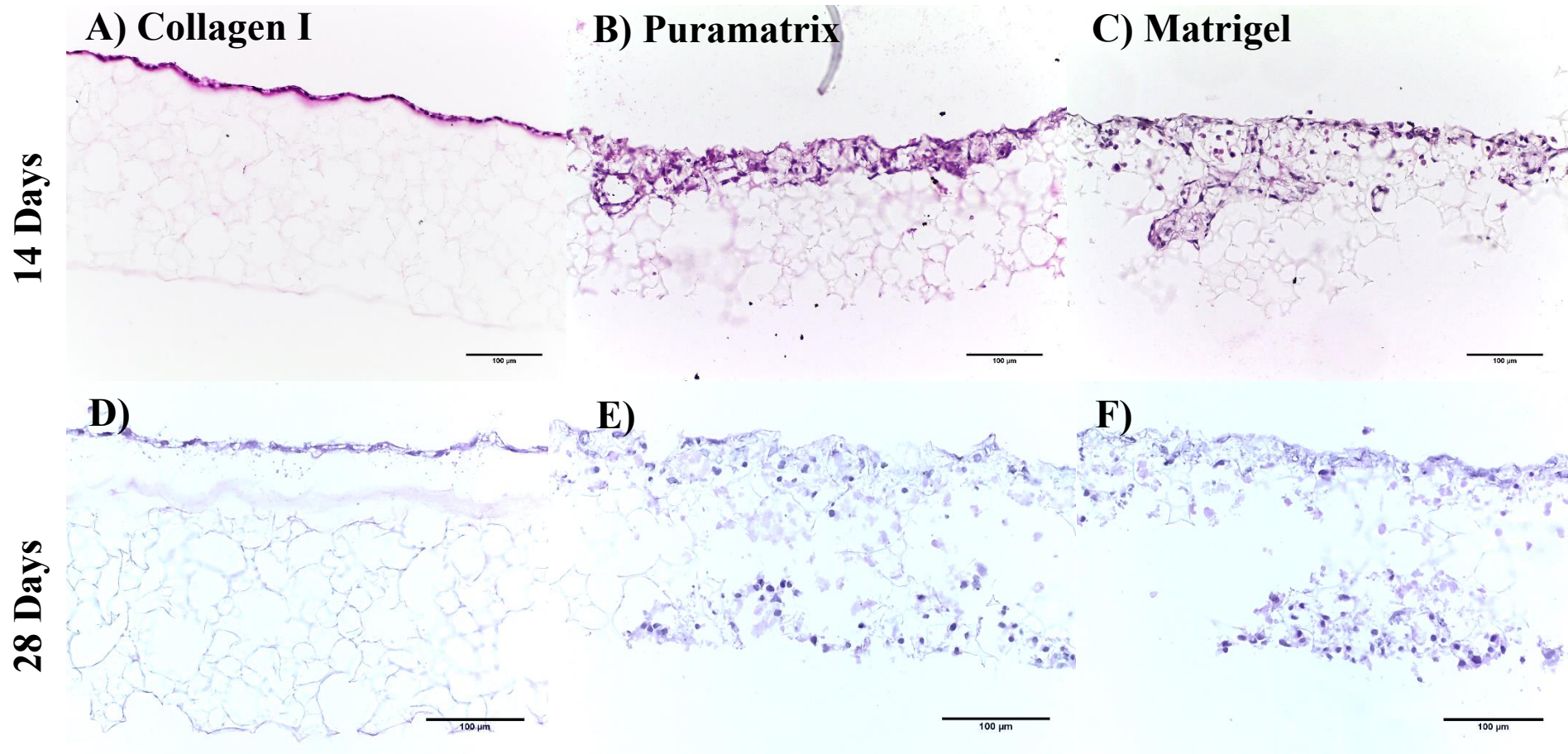


**Figure 5.2: Application of basement membrane proteins to Alvetex Scaffold® to limit the invasion phenotype into the underlying stromal compartment.** – A) Caco-2/Collagen I, 14 days, B) Caco-2/ Puramatrix, 14 days, C) Caco-2/ Matrigel, 14 days, D) Caco-2/Collagen I, 28 days, E) Caco-2/ Puramatrix, 28 days, F) Caco-2/ Matrigel, 28 days. Collagen I was the only protein gel mix that experienced reasonable success in the limiting of Caco-2 invasion with clear monolayer formation on the apical side of the collagen gel at days 14 and 28. Matrigel and Puramatrix had little effects on the limiting cellular invasion. Indeed, in both instances it could be easily argued that these protein mixes had the opposite effect, promoting cellular growth and motility into the Scaffold. Scale =100μm Images are representative of a minimum of 3 independent observations.

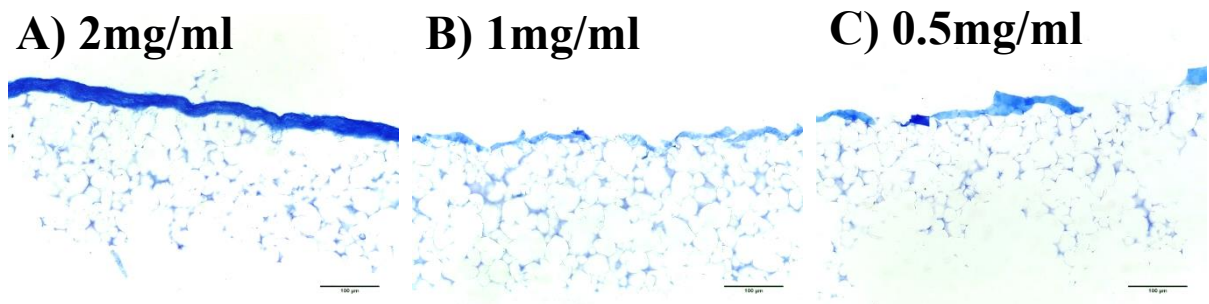


**Figure 5.3: Optimising the volume and concentration of Collagen I gels to add to the surface of the Scaffold to limit cellular invasion.** – Aniline blue staining of collagen I gel on the surface of Alvetex Scaffold®. A) 2mg/ml, B) 1mg/ml, C) 0.5mg/ml. Staining clearly shows that only 2mg/ml was capable of creating a consistent layer across the surface of the Alvetex Scaffold®. All other conditions created weak layers at the surface and lined the pores of the Alvetex Scaffold®. Images are representative of a minimum of 3 independent observations. Scale =100µm.

### 5.4.3 CCD-18co conditioned media effects on Caco-2 development on Collagen I Basement membranes in Alvetex Scaffold®.

Figure 5.4 A-F, shows the morphology of Caco-2 cells grown on Alvetex® Collagen I membranes in the presence of CCD-18co conditioned media. Figure 5.4 A shows H+E staining of 7 day paracrine cultures. Analysis of staining shows strong nuclei staining and weak cytoplasmic staining, characteristic of Caco-2 cells. Cells appear to grow in a homogenous monolayer across the entire samples with no obvious places whereby cells have penetrated into the underlying stromal compartment. This same morphology is also seen in both the 14 and 21 day cultures (Figure 5.4 B&C respectively).

Higher magnification analysis of the slides (Figure 5.4 D, E & F) shows how the Caco-2 cells are tall and undifferentiated at day 7, possibly arranged into thick multilayers of cells. Over time this phenotype decreases until by day 21 there is a continuous monolayer of cells across the membrane with well-defined polarity with Nuclei clearly arranged close to the basement membrane and cuboidal shaped epithelial cells. Darker eosin staining at the surface of the 21 day differentiated Caco-2 cell models (Figure 5.4 F) potentially indicates the presence of microvilli and associated glycocalyx.

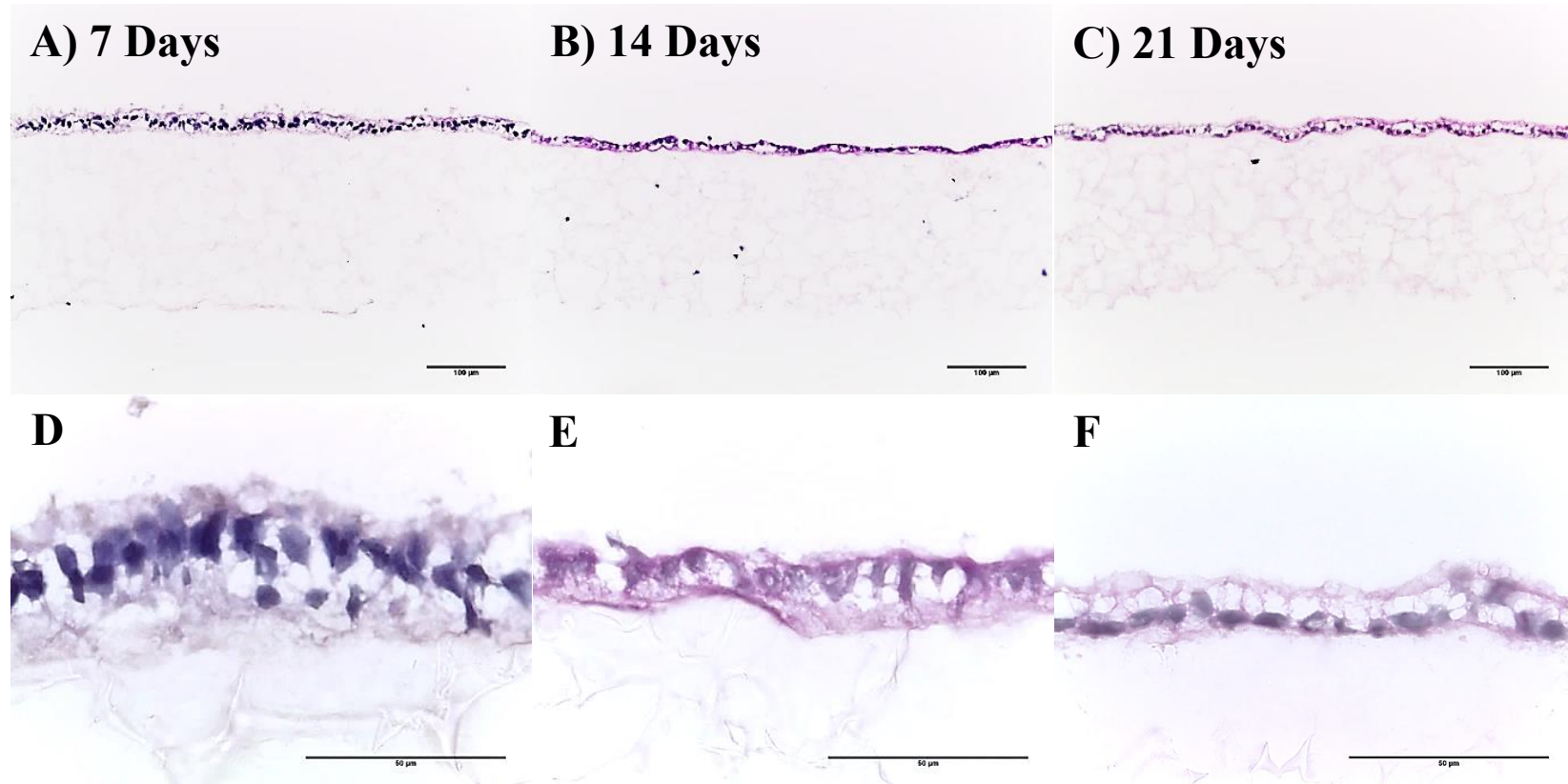


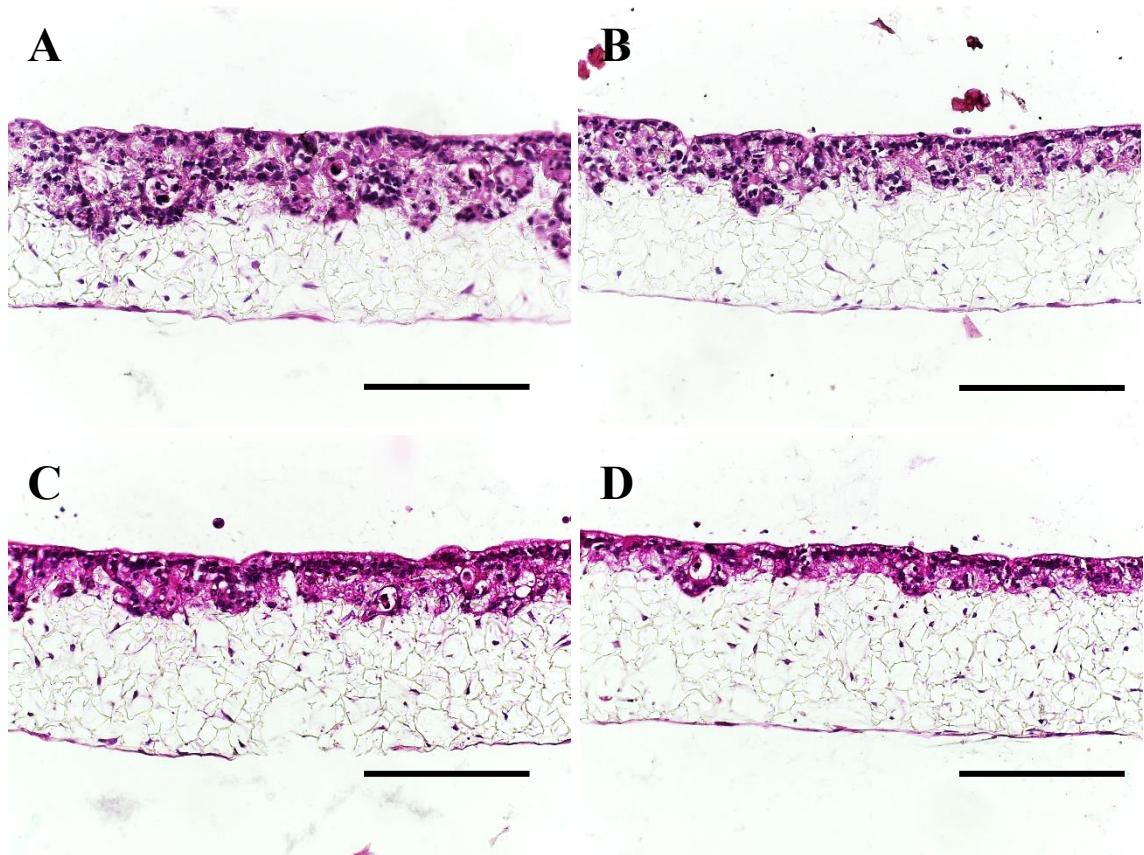
**Figure 5.4: CCD-18co paracrine treatment of Caco-2 cells cultured on 2mg/ml Collagen I gel layers shows an enhanced Caco-2 phenotype over control layers** – CCD-18co paracrine media was cultured with Caco-2 collagen models for a period of A) 7 days, B) 14 days, C) 21 days. Caco-2 cells can be seen to increase in membrane organisation over time, starting with a disorganised multilayer of cells, progressing over time to form a single monolayer of polarised epithelium at day 21. Images are representative of a minimum of 3 independent observations. Scale 100µm and 50µm respectively.

### **5.4.5 Optimisation of CCD-18co cells seeding density within Alvetex Scaffold® to create a surface layer to support the culture of Caco-2 epithelial cells.**

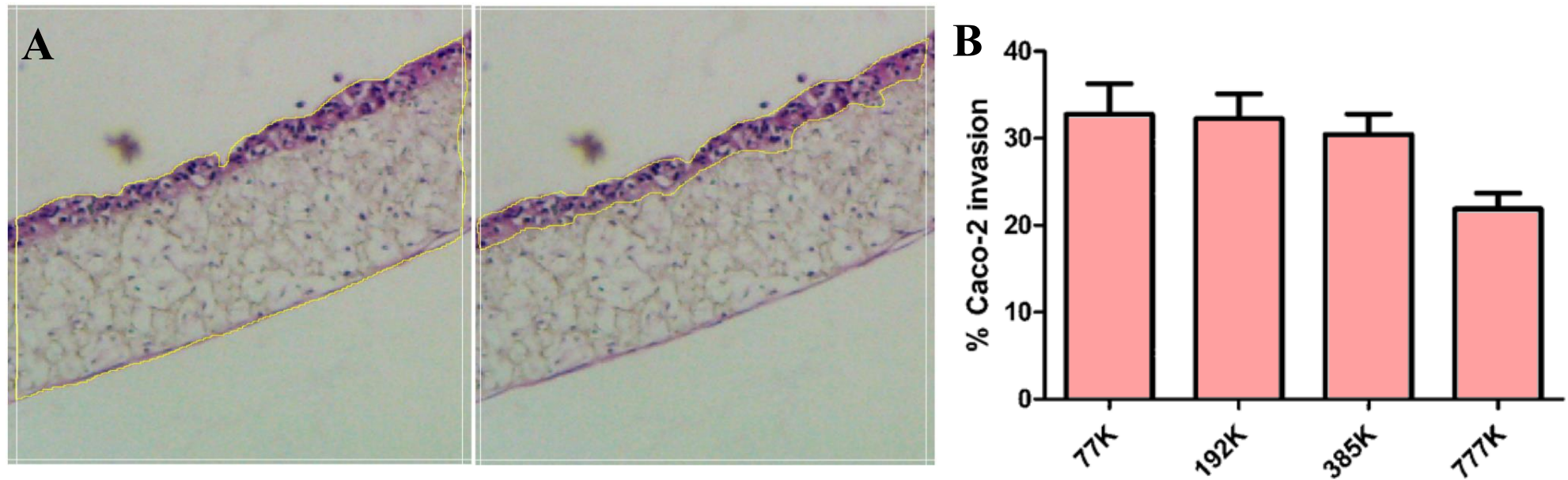
The use of Collagen I as a substitute basement membrane was ruled out at this point. All further experiments with the development of a 3D model system are done so without the addition of exogenous collagens. Figure 5.5 A-D shows the effect of CCD-18co seeding density on the ability of Caco-2 cells to create an epithelium. Figure 5.5 A shows Caco-2 cells cultured on an Alvetex Scaffold® populated with 77,000 cells per insert (100,000 cells/ cm<sup>2</sup>) after being cultured for 14 days. Caco-2 cells invade up to halfway through the scaffold with cells growing characteristically as described previously within the Alvetex®. Figure 5.5 B, C and D shows the same phenotype as described for Figure 5.5 A however the initial fibroblast seeding densities in each case are 192k (250,000 cells/ cm<sup>2</sup>), 385k (500,000 cells/ cm<sup>2</sup>) and 777k (1,000,000 cells/ cm<sup>2</sup>). Interestingly, the initial seeding density of CCD-18co cells does not appear to have a significant effect on the rates of Caco-2 invasion until the 777k seeding density. The 777k condition (Figure 5.5 D) does appear to have a small effect on Caco-2 invasion rates but is still insufficient to stop some cellular infiltration into the underlying stroma.

Figure 5.6 shows the quantified effect of CCD-18co seeding density on Caco-2 invasion rates. Figure 5.6 A, shows the methodology whereby “Invasion rate” is quantified as a percentage of the area of Caco-2 staining compared to the total area of scaffold present. Values are normalised to a 500µm<sup>2</sup> grid. Figure 5.6 B, shows the quantified difference in Caco-2 invasion rates between the different seeding concentrations. There is no significant difference between the rate of Caco-2 invasion between any of the conditions although a downwards trend is seen with increasing CCD-18co density, with the maximum decrease seen in the 777k samples of around 10-15% compared to 77k. Significance was calculated by one way ANOVA with Tukeys post test analysis however no significance between values was observed.





**Figure 5.5: Optimisation of fibroblast seeding density to limit the invasive characteristics of Caco-2 cells** – Multiple seeding densities (Cells/ cm<sup>2</sup>) were tested for their capabilities to create a well populated, ECM rich foundation for the culture of Caco-2 cells. Ideally, CCD-18co populated Alvetex should be able to support the culture of a Caco-2 monolayer without the need for additional basement membrane protein additions. CCD-18co cells were cultured for a period of 14 days prior to the addition of Caco-2 cells which were also cultured for 14 days prior to invasion analysis. A) 77K, B) 192K, C ) 385k, D) 777K. As can be seen here, no singular seeding density was sufficient for complete repulsion of Caco-2 cells from the internal Alvetex Scaffold. Representative images of 14 day Caco-2 calls on different seeding densities. Images are representative of a minimum of 3 independent observations.



**Figure 5.6: Creating a quantifiable technique for the analysis of model sections for the percentage invasion of Caco-2 cells within the Alvetex scaffold®**– A method was required which was able to quantify the levels of invasion of the overlying Caco-2 cells into the underlying stromal compartment. A percentage invasion was calculated by first measuring the area of the stained caco-2 cells and then the area of the whole model. Percentage invasion is calculated through comparison of the two measured areas. A) Methodology for the measurement of Caco-2 infiltration into underlying scaffold. A full length image of the sections was taken and stitched together in image J. For quantification an overlying grid of  $500\mu\text{m}^2$  was used to take random samples along the model. Minimum of 4 images were quantified per section. B) Graph showing results as a percentage of area quantified.  $n = 12$  from a minimum of 3 independent experiments. Significance was calculated by one-way ANOVA, No significance was observed between samples. Error bars represent +SEM of average values.

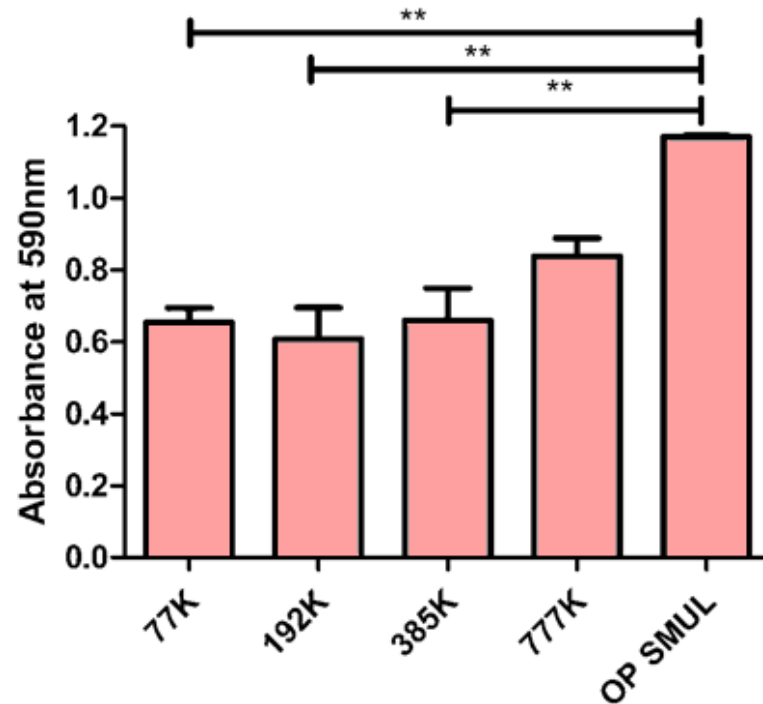
### **5.4.6 Metabolic activity assessment of CCD-18co seeding optimisation experiments.**

Figure 5.7 A, shows the MTT assay results of the 14 day cultures of CCD-18co in Alvetex Scaffold® with differential starting seeding densities. No significant differences can be seen in the metabolic activity between any of the seeding densities at the 2 week timepoint, although there is a small non-significant trend toward increasing MTT value with increasing cell seeding density. However whilst there is a small trend the difference is disproportionate to the increase in cell number at the beginning of the experiment. For example, 777k seeding density with 10 times the original starting density of CCD-18co cells compared to 77k only shows a marginal increase in MTT absorbance of approximately 10-20% over the 77k seeding condition. In contrast, the multiple seeding technique as described previously (Section 2.15) seeds a total of 576k cells into the scaffold over the duration of the 14 day culture time. This is 201k cells less than the 777k condition but produces a significantly higher absorbance value than any other condition suggesting a compounding effect.

When Caco-2 cells are added to the fibroblast stromal models and cultured for a further 14 days (Figure 5.7 B) there is no significant differences seen in the terminal MTT values, suggesting that Caco-2 cells have invaded into the underlying stroma and scaffold and have proliferated to similar extents in each of the conditions, providing evidence that these seeding densities are unable to stop Caco-2 invasion into the underlying stroma.



**A**



**B**

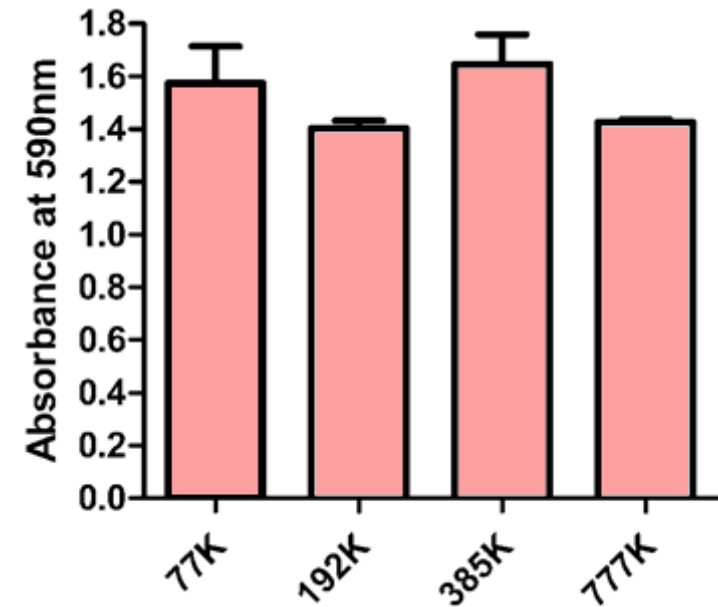


**Figure 5.7: Metabolic activity of the models shows that seeding higher densities of CCD-18co cells at the beginning of model culture has little effect on the number of surviving fibroblasts at the time of analysis – A) MTT data of differing seeding densities of fibroblasts grown in Alvetex Scaffold for 14 days. Compared to current multiphasic seeding method. Data shows that there is a non-significant difference between low number seeding densities (77,000/ model) and high number seeding densities (777,000/ model) multiphasic seeding (OP SMUL) whereby 777,000 cells are added over time rather than all on day 0 shows significant increases over other conditions suggesting a higher proportion of surviving fibroblasts. B) MTT values of 14 day fibroblast models plus 14 days of caco-2 culture. Heightened MTT values indicate significant Caco-2 cellular infiltration into the underlying scaffold. No significant difference between models suggests all of the models allow for Caco-2 infiltration at similar rates. n=3, N=3 Significance was calculated by one way ANOVA with Tukeys post-test analysis. Error bars represent +SEM of average values.**

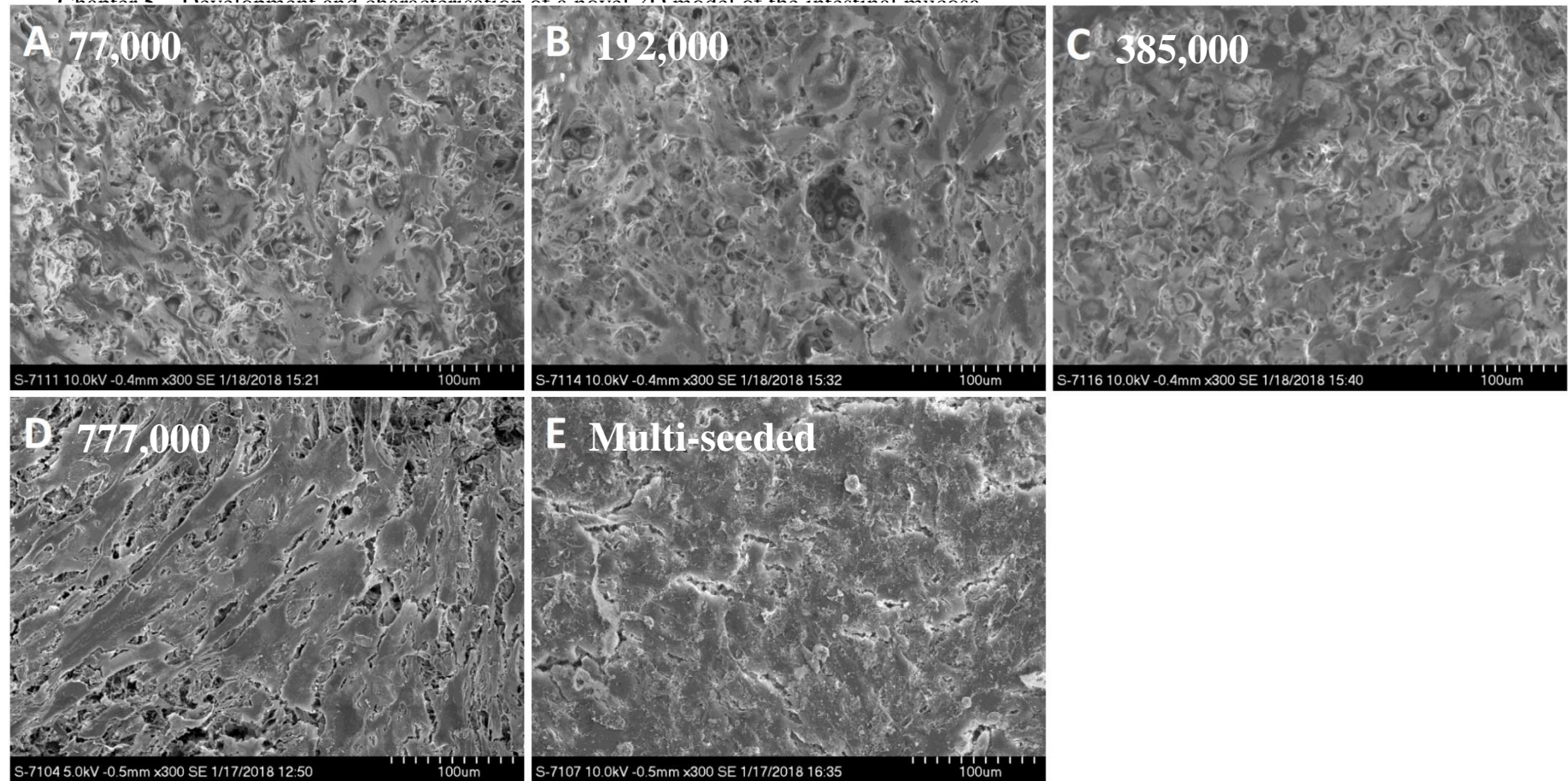


**Figure 5.8: SEM topographical analysis of optimisation CCD-18co layers shows significant gaps in the surface support for the culture of Caco-2 cells –** Different seeding densities of fibroblasts were added to Alvetex Scaffold. A) 77k, B) 192k, C) 385k, D) 777k, E) Multiple seeding technique. Areas for the invasion of Caco-2 cells into the underlying stromal support can be clearly seen in all conditions except when CCD-18co cells are seeding into models utilising the multiple seeding technique. Images are representable of the average phenotype of the entire surface layer and multiple observations.

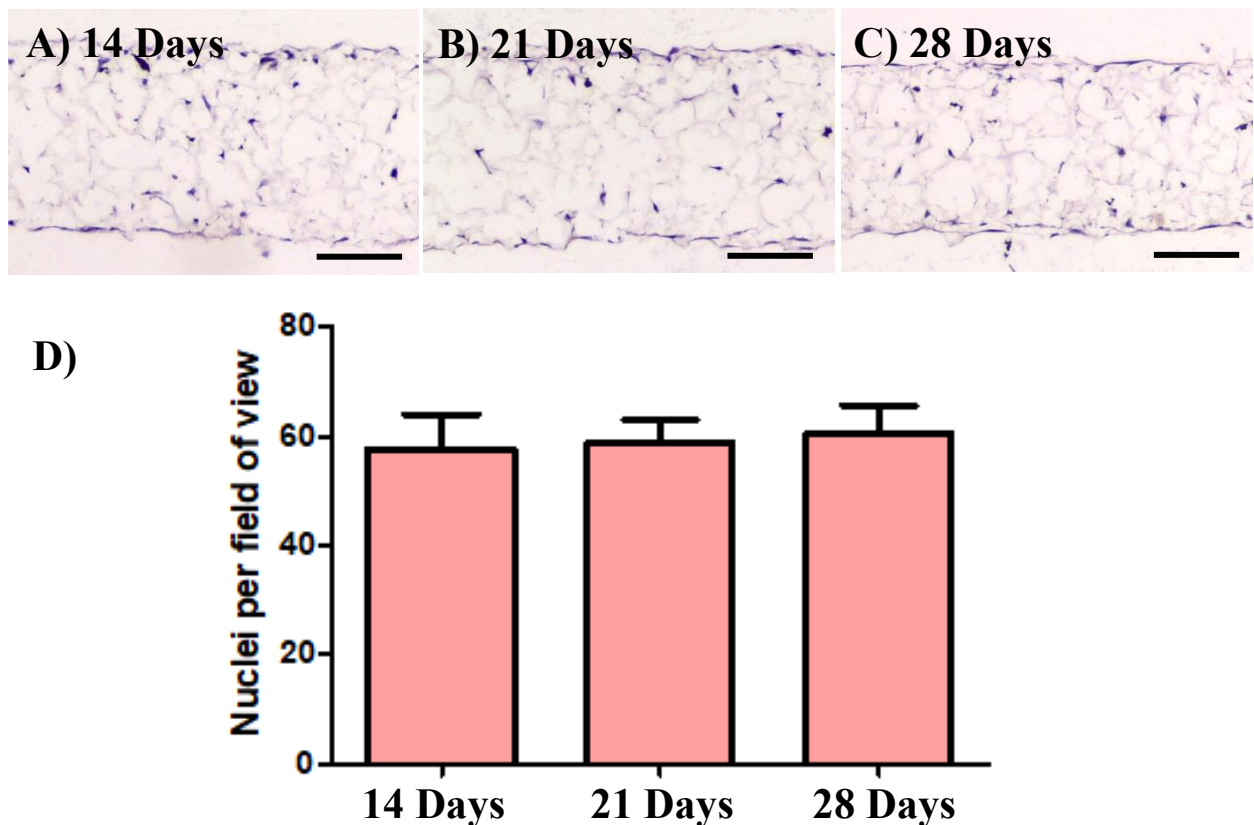
#### **5.4.7 SEM analysis of the surface topography of CCD-18co seeding density layers.**

Surface topography of CCD-18co cells grown in Alvetex scaffold® is clearly shown through SEM imaging. Figure 5.8 A, shows 77k seeding density at the 14 day timepoint. Whilst cells can be clearly seen on the surface of the Scaffold®, there are clear gaps in the surface fibroblast layers, inevitably resulting in Caco-2 invasion into the Alvetex Scaffold® below. Figure 5.8 B, C & D correspond to higher seeding densities, show similar gaps, albeit appearing to decrease in regularity, in the surface layer. Figure 5.8 E however shows the effects of multiple seeding on CCD-18co surface layers. A continuous layer of cells is demonstrated across the entire surface of the model with no gaps available for the invasion of Caco-2 cells into the scaffold. Indeed, the cracks seen on the SEM images are due to processing of the samples for SEM analysis rather than for a biological reason.

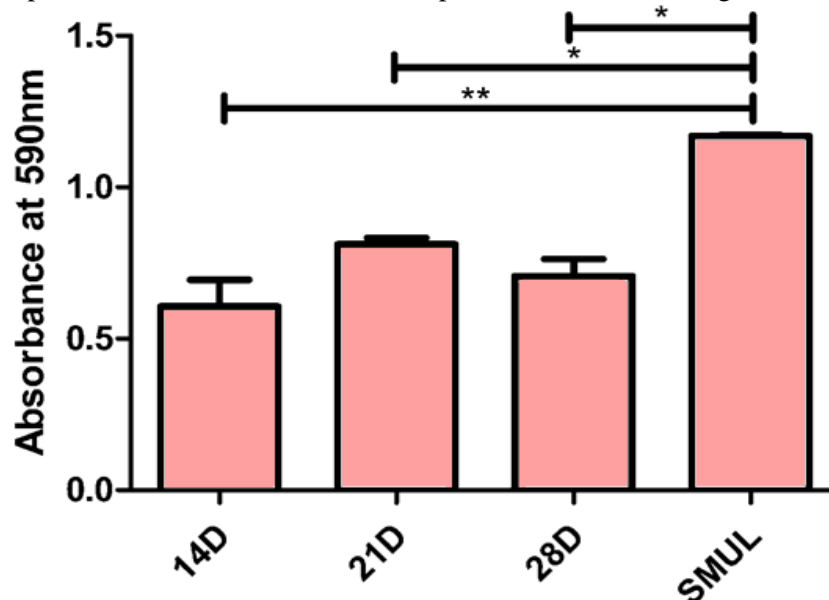
#### **5.4.8 The effects of extended culture time on the population of Alvetex Scaffold® with CCD-18co cells.**

Figure 5.9 shows the histological sections of samples cultured for a period of either 14, 21 or 28 days. Observation of the slides highlights the lack of CCD-18co growth over time when cultured in 3D. Cells appear to colonise the substrate before proliferatively quiescing, maintaining cell numbers without proliferation (Figure 5.9 D).

Figure 5.10 shows the effects of fibroblast culture time on the MTT values of the stromal cell models. What is clear is increasing culture time seemingly has no effect on model metabolic activity, suggesting that CCD-18co cells do not proliferate in 3D. Analysis of Caco-2 invasion (Figure 5.11) as described previously, reflects MTT values with no significant differences. In contrast multiphasic culture significantly increases the MTT absorption values and decreases Caco-2 invasion into the underlying stroma when compared to other timepoint conditions.



**Figure 5.9: The effects of time on the growth of CCD-18co population in 3D Alvetex models shows little active proliferation when cultured in 3D – A) 14 days CCD-18co culture, B) 21 days, C) 28 days. D) Quantified data showing nuclei per field of view between samples.  $n=3$   $N=3$ . Histological analysis of paraffin embedded sectioned samples shows no significant differences between 14, 21 or 28 days of culture on the population of CCD-18co cells populating the Alvetex Scaffold. Images are representative of a minimum of 3 independent observations. Error bars represent + SEM of average values.**



**Figure 5.10: Understanding the effects of time on the growth of CCD-18co population in 3D Alvetex models – MTT data of 192k cells/cm<sup>2</sup> at differing timepoints. 14D, 21D, 28D. Data shows that time has little effect on the overall population size of CCD-18co cells cultured in Alvetex Scaffold. No significant differences can be observed between 14, 21 and 28 day timepoints with the highest levels being at around 21 days in culture, after which levels once again begin to drop. Multiphasic culture design is added here for comparison only, cell numbers and time are not controlled in multiphasic cultures in the same way as other conditions here.  $n=3$   $N=3$ . Significance calculation performed by one way ANOVA with Tukeys post-test analysis.  $n=3$ ,  $N=3$ . Error bars represent + SEM of average values.**

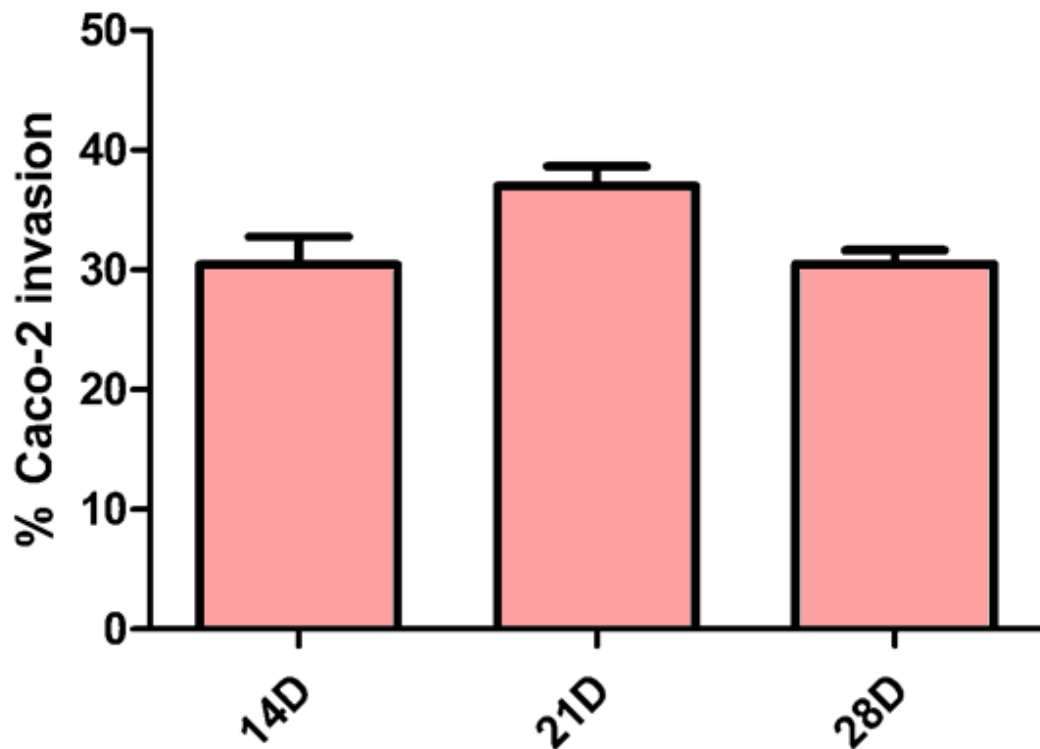


**Figure 5.11: Caco-2 invasion characteristics show that CCD-18co culture time has no significant effects on reducing the levels of Caco-2 invasion in Alvetex models** – 192 000 cells were added to Alvetex Scaffold on day 0 and allowed to grow in 3D for either 14, 21 or 28 days. Results show no significant effect of culture time on the capabilities of the resultant model to limit Caco-2 cellular ingrowth with an average invasion amount of approximately 30% of the model area. Error bars represent + SEM of average values. n=3, N=3

#### 5.4.9 SEM analysis of stromal fibroblast cell layers.

Figure 5.12 shows the protocol for the culture of CCD-18co cells growing within the Alvetex Scaffold® support. Figure 5.12 A shows the full thickness of the Alvetex scaffold® with CCD-18co growing within. It can be clearly shown that CCD-18co cells grow throughout the full 200µm scaffold thickness. ECM growing within the Alvetex® voids (Figure 5.12 B) is seen as strands of proteins spanning along the void spaces. ECM does not fully fill the space within the voids but instead spans between the cells and the voids. Figure 5.12 C & D shows the CCD-18co fibroblast phenotype along the surface of the Scaffold with a classical spindle shape layering the surface. The purpose of optimising the culture of the CCD-18co cells within the Alvetex Scaffold® was to limit the number of places whereby Caco-2 cells could invade into the underlying stroma. Figure 5.12 C shows that whilst the multiphasic culture strategy is more capable at creating said layer than all other conditions, there are still instances of areas on the surface of the scaffold whereby Caco-2 penetration could feasibly occur.



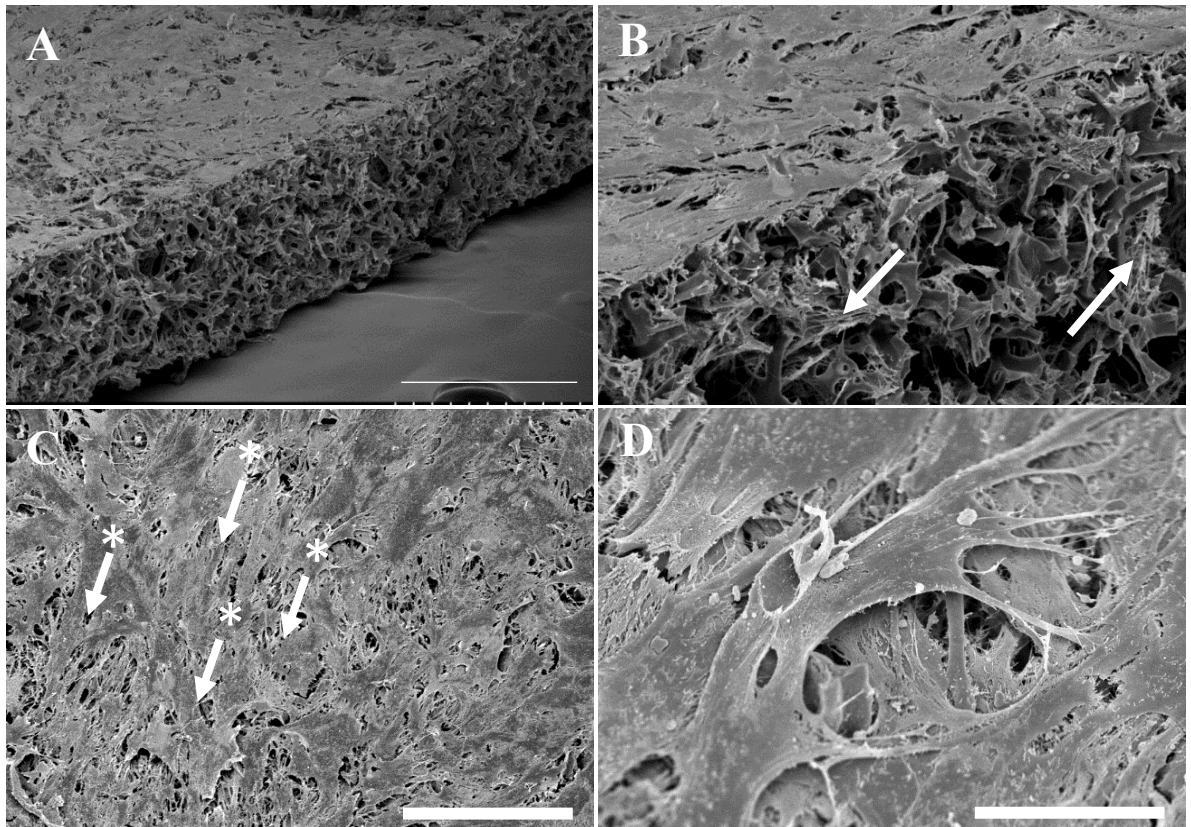


**Figure 5.12: SEM Images of CCD-18co cells cultured in Alvetex Scaffold for a period of 21 days shows significant ECM depositions within the Scaffold matrix-** A-B) Fibroblasts provide a continuous surface layer in addition to penetration of the Alvetex inter-pore spaces and deposition of ECM proteins. Scale 200 and 50  $\mu\text{m}$  C) High magnification image of the surface layer of the intestinal model. Image shows multiple layers of stretched fibroblasts providing supportive layer. Arrows (\*) indicate points in the surface layer where Caco-2 penetration could occur. D) High magnification image of surface CCD-18co cells showing stellate morphology. Images are representative of a minimum of 3 independent observations. Scale 100 and 20 $\mu\text{m}$  respectively.

#### 5.4.10 Structural analysis of optimised multiphasic seeded Caco-2/ CCD-18co Alvetex Scaffold<sup>®</sup> intestinal models.

Histological cross sections of 3D Alvetex<sup>®</sup> models highlights the structural morphology of cells within the Scaffold support (Figure 5.13 A & B). All models were cultured for a period of 35 days (14 days stromal culture followed by 21 days Caco-2 differentiation). High quality images show the heightened Caco-2 cells morphology located apically in the models. Caco-2 cells appear to create a single monolayer of cells for the majority of the models length however there are areas where multilayering seems to occur. However,

differentiation between Caco-2 and CCD-18co cells is difficult at the epithelial-mesenchymal boundary so these areas of “multilayering” could simply be CCD-18co and Caco-2 cells closely interacting. The cells growing within the Alvetex Scaffold® matrix can be clearly identified as CCD-18co cells from their basic cell morphology and growth patterns. Cells can be seen to be evenly dispersed throughout the model with thin layers at the base of the model in addition to the surface whereby they create a supportive foundation for the culture of the Caco-2 epithelium. This supportive layer is clearly able to limit the invasion of Caco-2 cells into the Scaffold with no evidence of invasion seen in this sample.

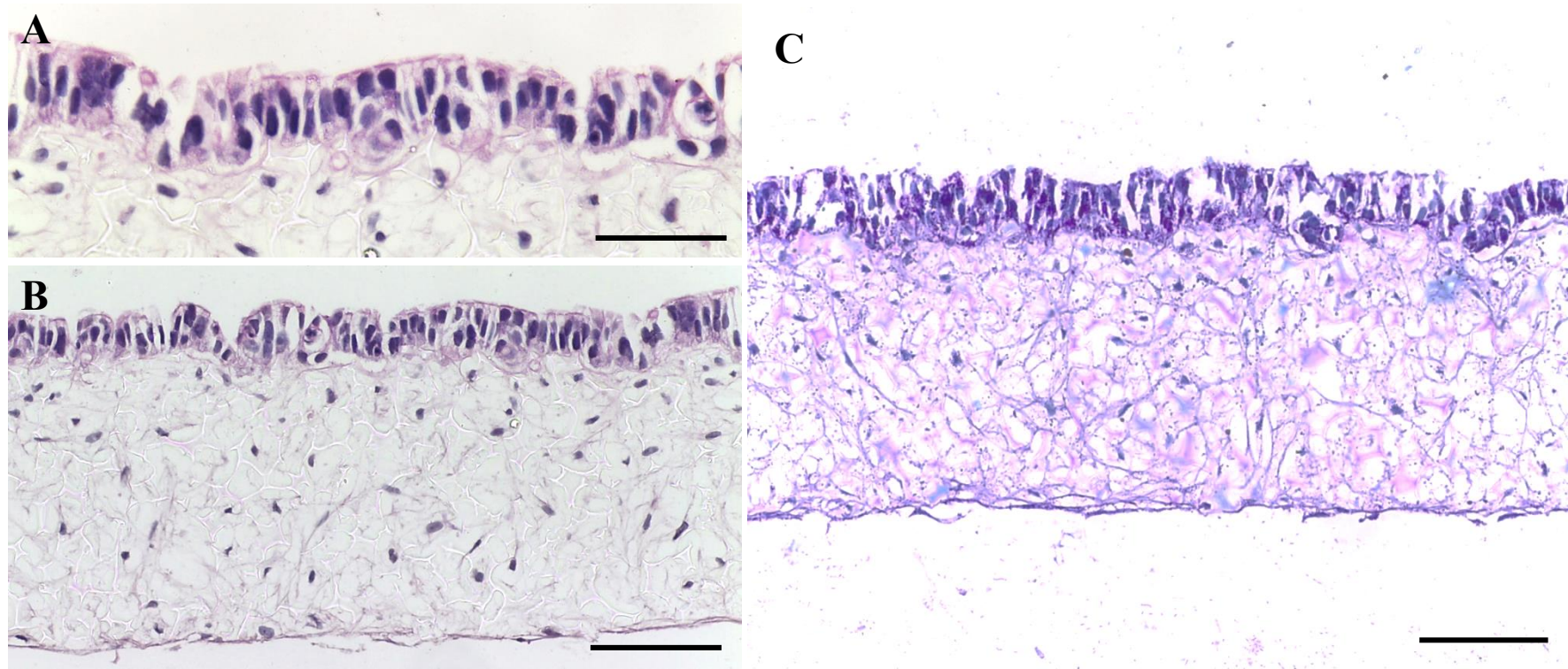
Periodic Acid Schiff staining (Figure 5.13 C) of the 3D model cross section for detection of acidified mucosubstances, indicating mucous production, shows strong positive staining in both the CCD-18co and Caco-2 cell layers. throughout the model but primarily located within the Caco-2 layer. Caco-2 cells are not known to secrete significant levels of mucous.

Figure 5.14 shows Toluidine blue stained semi-thin resin embedded sections of 3D CCD-18co Alvetex Scaffold. Resin embedding allows for a higher resolution image. Unlike in Figure 5.13, Caco-2 cells can be clearly seen to arrange themselves into a monolayer epithelium at the surface of the model with a supporting fibroblast mucosa. Brush border formation can be observed apically to the epithelial cells in addition to membrane associated glycocalyx proteins.

SEM ultra-structural analysis of the surface of 3D Caco-2/ CCD-18co models shows the classical cobblestone morphology of epithelial cells growing on the supporting fibroblast surface layer (Figure 5.15 A). A closer analysis of the surface shows a homogenous layer of microvilli formation across the surface of the sample which can be identified as short column like protrusions from the apical cell membrane (Figure 5.15 B). A mesh-like mix of glycocalyx glycoproteins and acidified mucosubstances can be seen associated with the microvilli on the surface of the model, making individual microvilli difficult to isolate due to the overlapping glycocalyx weave.

TEM structural analysis of 3D Caco-2/ CCD-18co models reaffirms what is seen in the SEM analysis of the model. Figure 5.16 A & B highlights the apically based microvilli structures seen across the entire surface of the model. Additionally, Figure 5.14 A shows apical-lateral electron dense staining at cell-cell junctions indicating the presence of tight junction complexes between cells. A clear boundary between Caco-2 and CCD-18co cells can be seen at the base of the epithelial layer within the model (Figure 5.16 C). Electron dense staining at the epithelia-mesenchymal boundary suggests the formation of a basement membrane between the two cell populations. Additionally, active vesical formation at the base of Caco-2 cells suggests cross talk between cellular compartment (Figure 5.16 D).





**Figure 5.13: 14 day multi-phasic culture design using young intestinal CCD-18co fibroblasts results in the formation of an intestinal model with little observable Caco-2 infiltration** – A) 40x B) 20X H+E staining of model. Note heightened epithelial cell morphology and well populated sub-epithelial compartment. Caco-2 cells grow and self-organise into a monolayer epithelium without the added necessity for basement membrane protein additions to the model. Naturally secreted ECM creates a support structure for the culture of Caco-2 cells apically. C) PAS staining of intestinal models reveals moderate secretion of acidified mucosubstances in line with that seen in normal Caco-2 culture. Total model culture time = 35 days. All images were taken after 35 days in culture (21 days post-Caco-2 addition) Images are representative of a minimum of 3 independent observations. Scale: 50µm and 100µm respectively

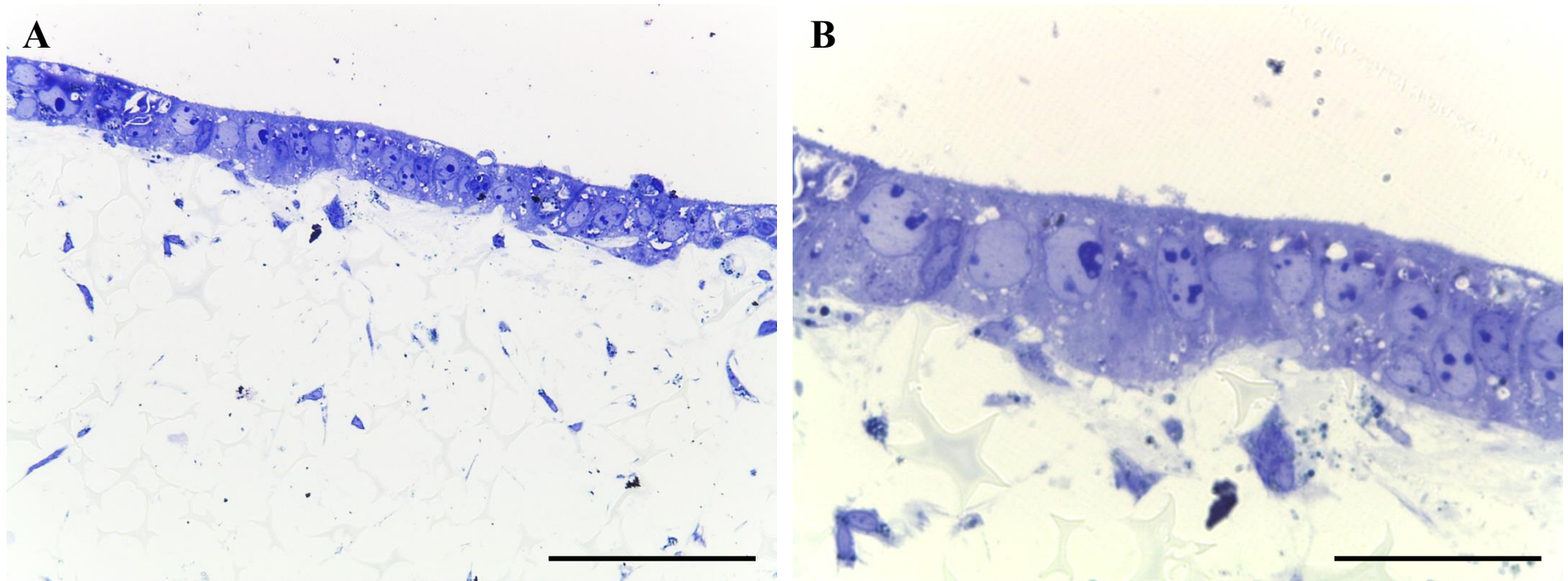


**Figure 5.14: Toluidine blue stained samples provides enhanced resolution over H&E stained images allowing for closer analysis of the structural morphology of Caco-2 layers on the surface of CCD-18co models** – Representative images of CCD-18co/ Caco-2 Toluidine blue stained semi thin resin embedded sections. A) 40 x magnification image of multiphasic culture CCD-18co/ Caco-2 intestinal model, B) 100x magnification. Total model culture time = 35 days. All images were taken after 35 days in culture (21 days post-Caco-2 addition) Images are representative of a minimum of 3 independent observations. Scale bar 100µm and 50µm respectively.

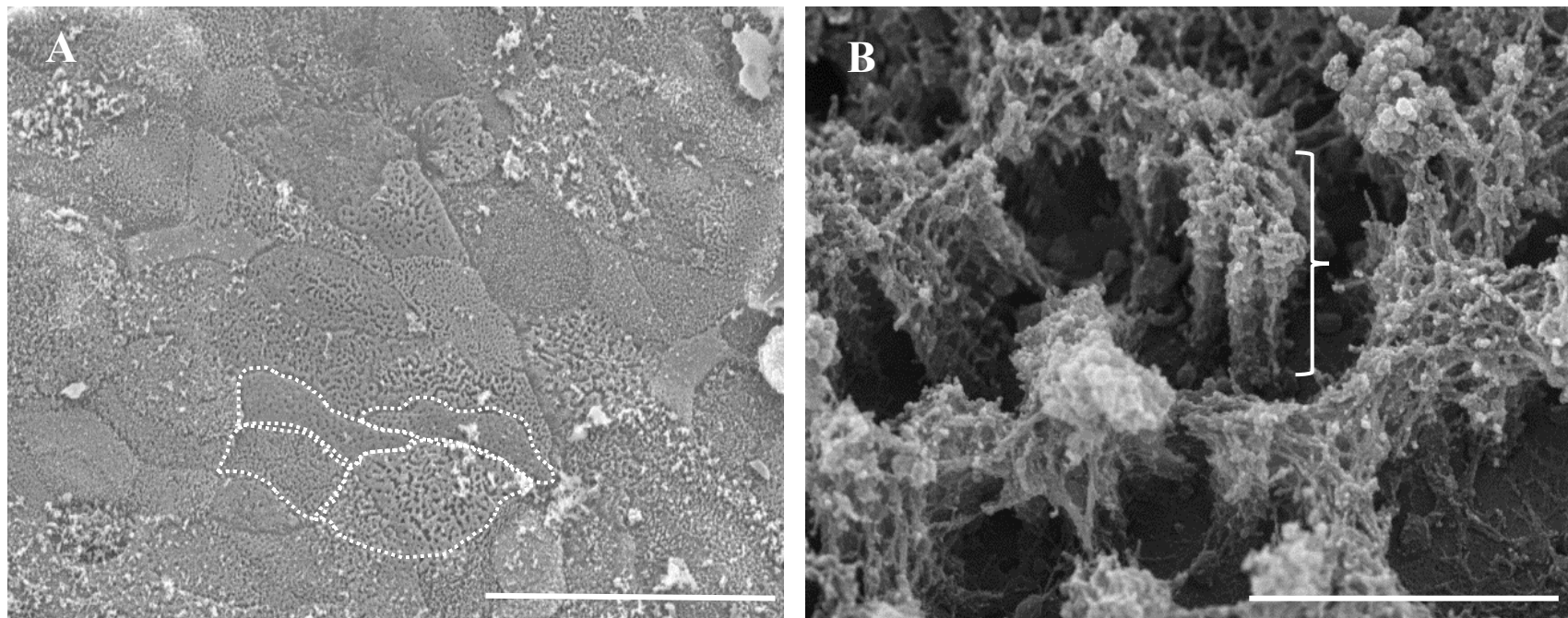


**Figure 5.15: High magnification analysis of Caco-2/ CCD-18co 3D models reveals differentiated enterocytes with clear microvilli formation and associated glycocalyx** – Samples, increasing magnification from left to right. Surface structures seen through SEM microscopy are highly reminiscent of microvilli structures seen in the literature. These structures indicate a well-established and differentiated caco-2 layer within the model. Total model culture time = 35 days. All images were taken after 35 days in culture (21 days post-Caco-2 addition). Images are representative of a minimum of 3 independent observations. Scale bars: 30 and 1  $\mu\text{m}$  respectively.



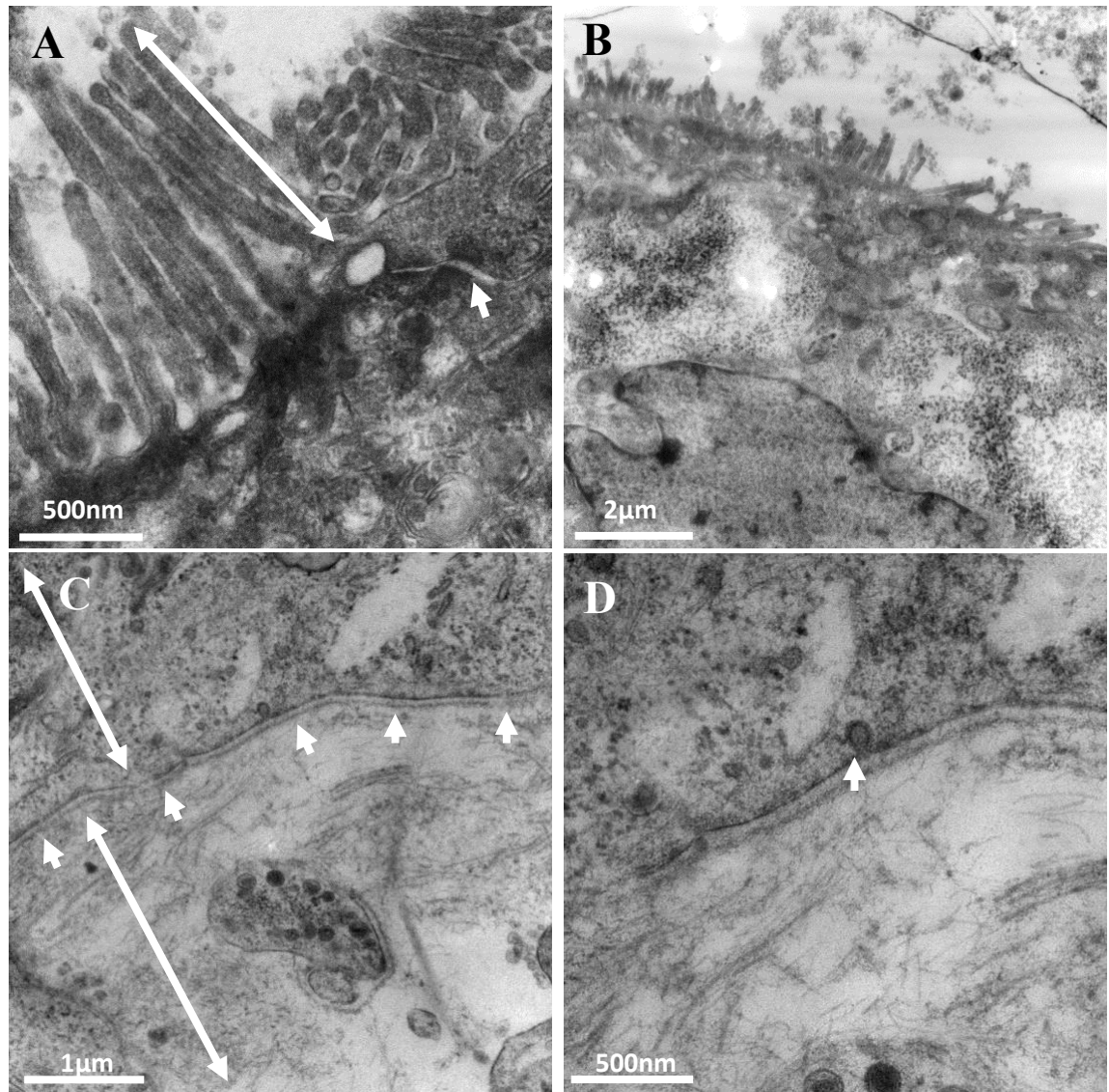


**Figure 5.16: TEM ultra-thin cross sections of CCD-18co 3D co-culture model showing microvilli, intercellular junctions and basement membrane formation** – A) Microvilli formation on the apical surface of Caco-2 cells, B) Low magnification image of the surface of one Caco-2 cell showing microvilli formation along the total apical length of the cells, C) Caco-2/ CCD-18co contact points showing electron dense basement membrane, D) Vesicle formation between CCD-18co and Caco-2 cells. Total model culture time = 35 days. All images were taken after 35 days in culture (21 days post-Caco-2 addition). Images are representative of a minimum of 3 independent observations.

### 5.4.11 Optimisation and structural analysis of Caco-2/ HDFn

#### Alvetex Scaffold® intestinal models.

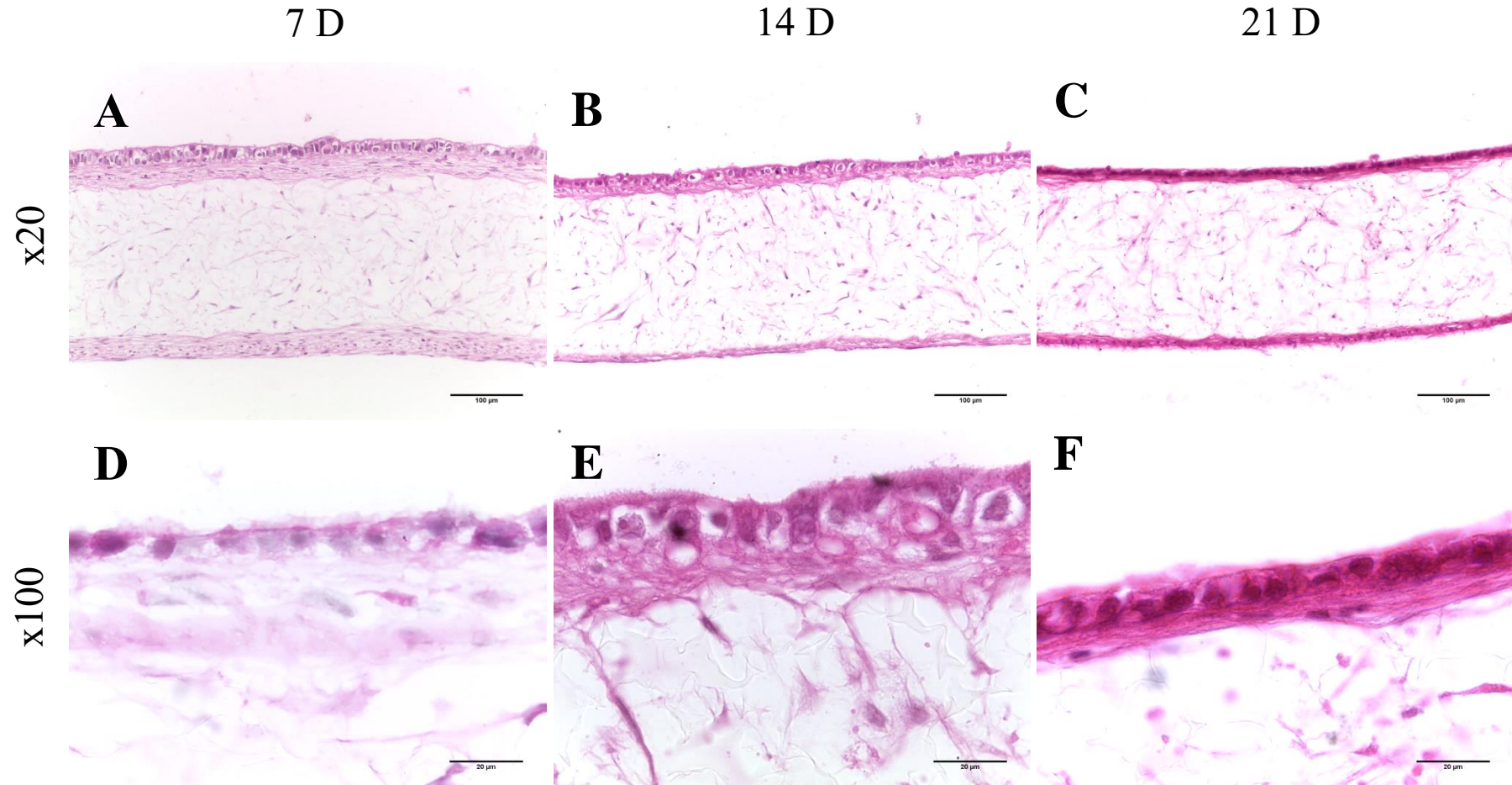
Figure 5.17 shows the differential morphologies of cells seen in 3D at different timepoints of Caco-2 culture on the surface of the HDFn models. The purpose of this experiment was to observe the 3D model during the culture period. The culture of HDFn models in the absence of Caco-2 cells shows good model stability overtime without any significant effects in model morphology even over long periods (data not shown). The addition of Caco-2 cells for a period of 7 and 14 days (Figure 5.17 A,B & D,E) shows good Caco-2 morphologies with tall columnar cells, basally located nuclei and, under close examination, apical microvilli formation. However, Fibroblast layers are seen to dramatically decrease in size between 7, 14 and 21 days.

Caco-2 cells were not expected to have any negative effects on the culture or morphology of the HDFn membrane however by 21 days in culture significant decreases in cellular number and changes in cell morphology can be easily observed with fibroblast cells taking on a flattened, compacted morphology, potentially indicating cell death. Caco-2 cells at day 21 (Figure 5.17 C & F) are cuboidal in cell, cytoplasmically dense and form a tight monolayer at the surface of the model. Whilst this morphology is significantly different than 7 and 14 day cultures, compared to 2D Caco-2 cells shown previously, there is still a significant improvement toward *in vivo* like characteristics of polarised columnar cells.

Figure 5.18 shows methyl blue staining of the 3D HDFn cultured models described previously in Figure 5.17. Methyl Blue is a well-known stain for Collagen showing a high specificity here with little background staining often seen in Alvetex® based models. 7 and 14 day cultures (Figure 5.18 A-B, D-E & G-H) show clear collagen deposition within the scaffold matrix, with long fibrous strands stretching across voids and pores. This allows for the full 3D culture of the cells within the scaffold through the deposition of tissue specific hydrogels and proteins within the 3D matrix itself. By day 21 Collagen deposition within the scaffold is seen to be significantly diminished over 7 and 14 day samples, with only weak, diffuse staining seen.

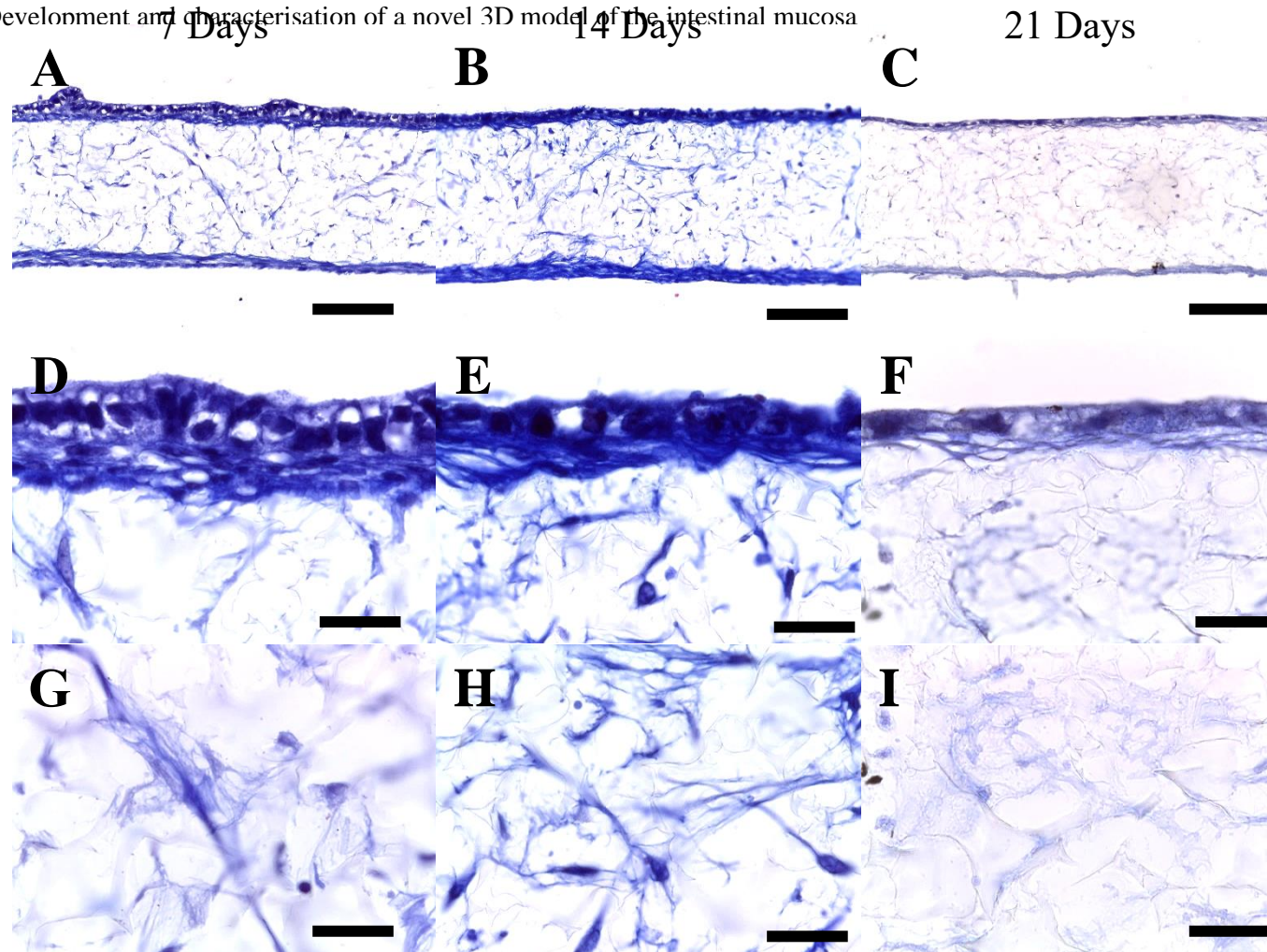
Due to the decreases in cell numbers and collagen deposition as seen in Figures 5.17 and 5.18 respectively, the multiphasic approach to fibroblast culture was attempted with the same methodology as was proven to be successful with CCD-18co cells previously.

Figure 5.19 shows the H&E staining of multi-seeded mature HDFn intestinal models. Figure 5.19 A shows the Caco-2 epithelial layer at high magnification, highlighting the cuboidal shape of the cell layer and the lack of both invasion into the underlying scaffold and the ability of the cells to create a single layer thick monolayer epithelium as would be seen in the human intestine. Figure 5.19 B shows the H&E stained model at a lower magnification, highlighting the well populated Alvetex<sup>®</sup> Scaffold substrate and the dense fibroblast layers at both the apical and basal sides of the HDFn intestinal model. PAS (Figure 5.19 C) staining shows a similar morphology to that seen previously in the CCD-18co intestinal model (Figure 5.13 C) whereby Caco-2 cells stain weakly positive, suggesting some low level mucous production in these cells. HDFn cells appear to also weakly stain with PAS reagent suggesting some level of background staining within the image.



**Figure 5.17: H+E staining of 7, 14 and 21 day cultures of Caco-2 on 28 day matured dermal equivalents show a changing fibroblast morphology over time** - 500 000 Caco-2 cells were seeded per 12 well format Alvetex Scaffold insert pre-cultured with dermal cells after day 28 of HDFn growth within Alvetex Scaffold. Caco-2 cells were cultured for variable time for either 7 days (A,D), 14 days (B,E) or 21 days (C,F). HDFn layers can be seen to reduce in thickness over time at both the apical and basal sides of the Alvetex Scaffold. Additionally, Caco-2 Morphology is clearly seen to change from a relatively tall, columnar shape to the more regular cuboidal culture after 21 days. Samples were fixed in 4% PFA overnight at 4°C prior to dehydration and embedding in paraffin. Images are representative of a minimum of 3 independent observations. Scale 100µm (A-C) and 20µm (D-E)





**Figure 5.18: Methyl Blue stained Collagen staining of the 7, 14 and 21 day cultured Caco-2 models shows how Collagen deposition decreases after 21 days in culture** – Collagen levels indicated through blue staining of structures within the Alvetex Scaffold® show clearly that fibrous collagen deposition has occurred during the culture of the HDFn cells within the Scaffold prior to the seeding of Caco-2 cells apically. Interestingly, deposited Collagen within the Scaffold seems to decrease over time with the length of Caco-2 culture diminishing both Collagen deposition and HDFn populations. Images are representative of a minimum of 3 independent observations. Scale 100µm (A-C) & 20µm (D-I) respectively.



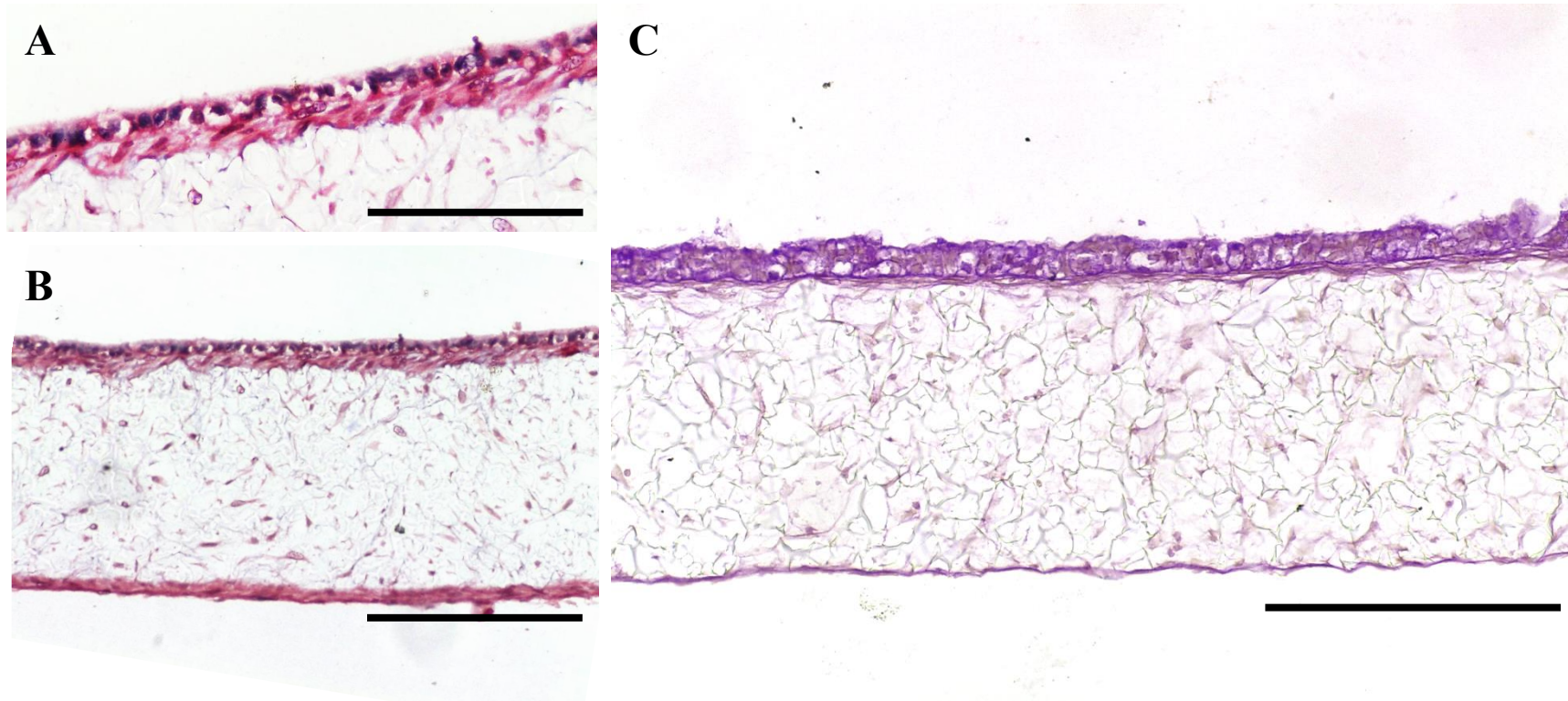


**Figure 5.19: 14 day multi-phasic culture design using low passage HDFn fibroblasts results in the formation of an intestinal model with little observable Caco-2 infiltration** – A) 40x B) 20X H+E staining of model. Note cuboidal epithelial cell morphology and well populated sub-epithelial compartment. HDFn cells can be seen growing within the interior of the Alvetex Scaffold® in the self-organised 3D environment created by long term 3D cell culture. Similar to that seen in the CCD-18co 3D model, Caco-2 cells grow and self-organise into a monolayer without the addition of basement membrane proteins to the model. Naturally secreted ECM creates a support structure for the culture of Caco-2 cells apically. C) PAS staining of intestinal models reveals moderate secretion of acidified mucosubstances in line with that seen in normal Caco-2 culture and a similar intensity to that seen in the CCD-18co 3D model. Images are representative of a minimum of 3 independent observations. Scale 100µm (A), and 200µm (B-C).

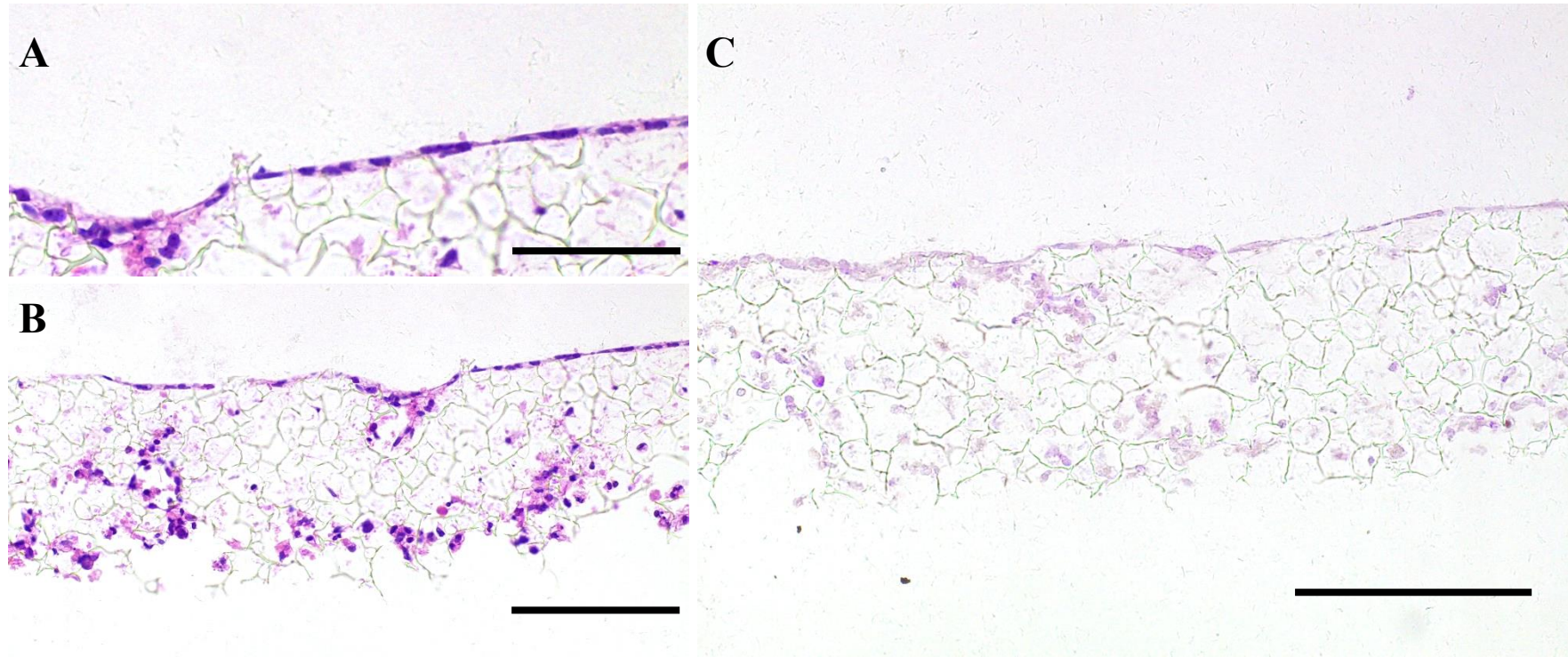


**Figure 5.20: 14-day multi-phasic culture design using low passage HIC fibroblasts results in the formation of an intestinal model with poor Caco-2 structure when compared to CCD-18co and HDFn optimised models** – A) 40x, B) 20x H&E staining of the model shows poor Caco-2 differentiation across the surface of the model. Relatively low levels of Caco-2 cellular infiltration are observed however infiltration is more prevalent than CCD-18co and HDFn models. C) PAS staining of HIC 3D model sections shows no positive staining throughout the model, unlike in other conditions. Images are representative of a minimum of 3 independent observations. Scale 100µm (A), and 200µm (B-C)

### **5.4.12 Histological analysis of the structure of Caco-2/ HIC**

#### **Alvetex Scaffold® intestinal models.**

Figure 5.20 shows the histological analysis of Caco-2/ HIC models created utilising a multi-seeding approach with Alvetex® Scaffold. Figure 5.20 A & B, shows H&E stained sections at high and low magnification respectively. A consistent Caco-2 epithelium is observed across the length of the model however, cellular morphology is highly squamous similar to that seen in control Caco-2 Transwell cultures. PAS staining (Figure 5.20 C) shows no positive staining throughout the section. This is in contrast with both CCD-18co and HDFn cultured models in which a small degree of mucous producing capability, especially in Caco-2 epithelial layers, could be observed. Caco-2 cells are primarily of enterocyte origin and function therefore, it is possible that this is a physiologically consistent change in cellular phenotype.

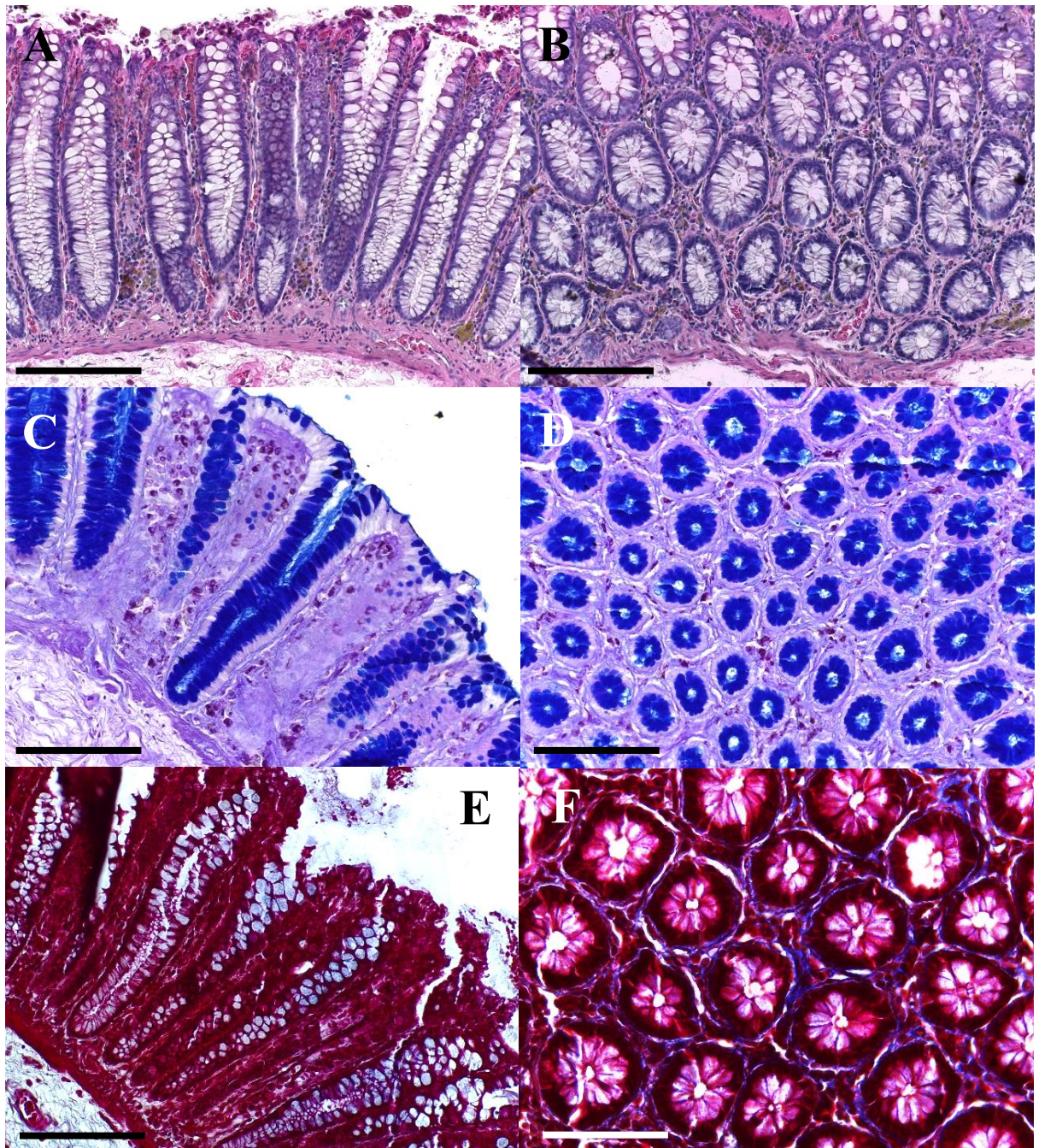
### **5.4.13 Human colonic and small intestinal characterisation for comparison to 3D co-culture models.**

Figure 5.21 shows the histological characterisation of normal human colonic tissue obtained from Biopra (Glasgow, UK). Figure 5.21 A & B, shows samples of normal human colonic tissues which have been H&E stained to view the cellular morphology. Tissue is shown in both transverse and longitudinal sections showing abundant goblet cells within the epithelium and deep crypt formations. Goblet cell abundance is confirmed through PAS staining of tissue sections with strong positive staining seen along the length of the epithelium and into the crypt structures. Figure 5.21 E & F Masson's Trichrome staining highlights the extracellular matrix compositions seen along the base of the epithelial layers, secreted by sub-epithelial myofibroblasts, supporting epithelial differentiation.

Immunofluorescence characterisation of human colon tissue sections (Figure 5.22, 5.23) shows the characteristic staining patterns of some key proteins of interest, namely of ECM deposition, junctional formation and functional efflux protein expression. Collagen I, III and IV are intercellular and secreted collagen proteins found extensively throughout the

body. Figure 5.22 A-C, shows the deposition patterns of these collagens in human colonic tissues. Collagen I (Figure 5.16 A) is clearly seen to be highly abundant in both the crypt walls and the basal muscular layers with no positive staining seen in epithelial tissues. Collagen III (Figure 5.22 B) shows limited staining throughout the colon tissue section with only small amounts of positive staining seen, primarily located in the crypt core and the underlying smooth muscle layers. Collagen IV (Figure 5.22 C) shows extensive staining throughout the crypt core and the sub mucosal layers. Collagen IV is normally known as a basement membrane protein, primarily located on the basal lamina. Interestingly, whilst some of the staining does seem specific to the areas immediately beneath the epithelial layer, staining seen here suggests a more diffuse expression profile with extensive staining also seen in the sub-mucosal layers. Negative controls (Data not shown) do not show any positive staining in the absence of the primary antibody, suggesting the staining seen here for Collagen IV particularly is true staining. It is possible however, that some levels of cross specificity between Collagen types is present with this antibody, resulting in the non-physiological diffuse pattern of staining.  $\alpha$ SMA staining designates myofibroblast locations within the sub-epithelial mucosa.  $\alpha$ SMA staining here, compared to vimentin (Figure 5.23 A, D staining (general mesenchymal marker) shows a high proportion of myofibroblasts within the colonic tissues compared to total mesenchymal population. Elastin staining (Figure 5.23 B, D) is primarily located within the muscle layers immediately beneath the crypt structures. MDR1 (P-gp) colonic staining (Figure 5.23 C,E) demonstrates positive localisation to the crypt tips alone, generally thought to be the tissue within the colon most fully differentiated for enterocytic functions. No positive staining is seen within the crypt structured suggesting good staining specificity. Interestingly, MDR1 cellular localisation is not specific to the apical membrane as would be hypothesised, with staining also seen along lateral membrane boundaries.





**Figure 5.21: Histological analysis of normal human colonic tissue sections –** A-B) H+E staining of longitudinal and transverse sections of the colonic crypt. C-D) PAS staining of longitudinal and transverse sections of the intestinal crypt. E-F) Masson's Trichrome staining showing the collagen deposition between the intestinal crypts. A-E Images were taken at 20x, F) was taken at x40 magnification to show subtle blue staining. Images are representative of a minimum of 3 independent observations. Scale bar: A-E) 200 $\mu$ m, F) 400 $\mu$ m



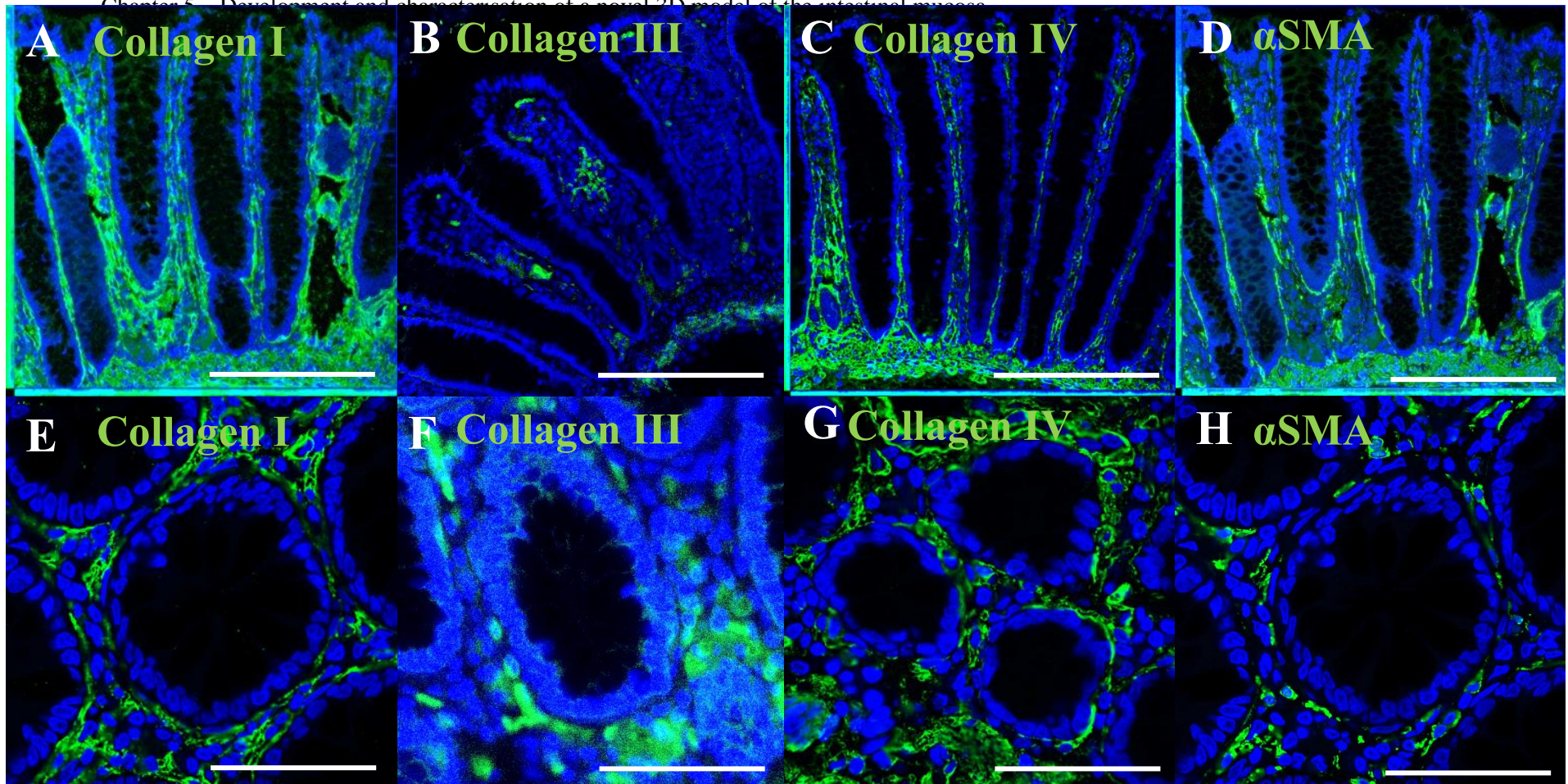


**Figure 5.22: Immunofluorescence analysis of normal Human Colonic tissue sections shows significant Collagen I, III and IV staining located at the sub-epithelial compartment of the tissues – A-D) longitudinal sections of Human Colonic tissue. Collagen deposition can be seen throughout the core of the crypt structures.  $\alpha$ SMA staining indicated the presence of myofibroblasts located in the sub-epithelial compartment of the tissues. E-H) Shows the transverse sections of the crypt structures. Again, Collagen can be seen to be deposited immediately beneath the epithelial layers in the tissues. Internal non-stained circular areas mark the internal crypt space, normally absent of cells. Images are representative of a minimum of 3 independent observations. Scale: A-D) 200 $\mu$ m E-H) 100 $\mu$ m**



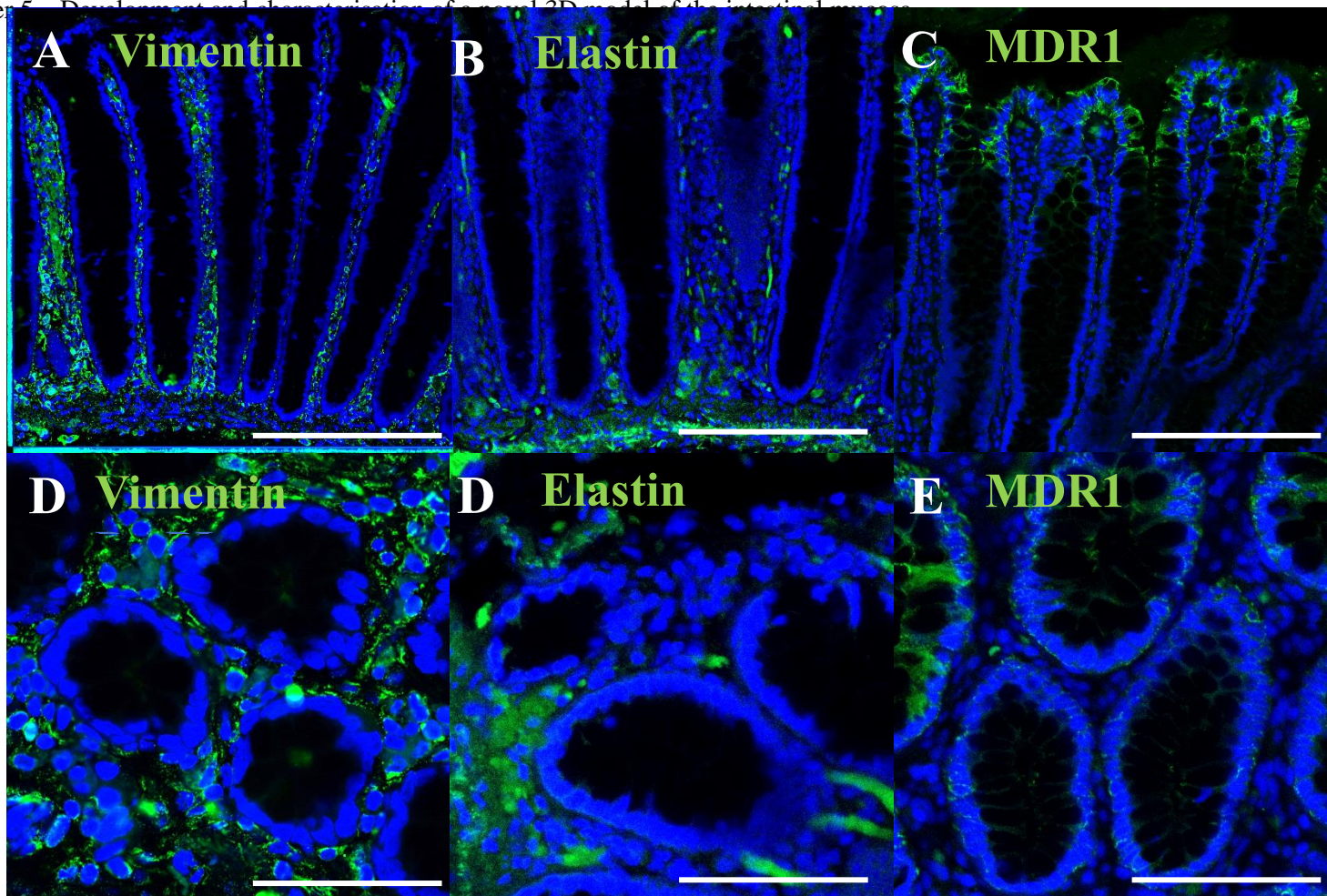


**Figure 5.23: Immunofluorescence analysis of normal human colonic tissue sections highlights the two distinct cellular populations between epithelial and stromal lineages** – A,D) Shows the longitudinal and cross sectional staining of the protein Vimentin, a type III intermediate filament protein found in mesenchymal cells. Staining intensity shows primary location in the sub-epithelial stromal compartment, highlighting the location of supportive fibroblast cells beneath the epithelial structures. B,E) Stains for Elastin, a component of the ECM of many tissues, important for tissue elasticity. C,E) MDR1 staining is shown to be located primarily at the crypt surface with less intense staining seen further into the crypt structure. Longitudinal staining shows only small expression in some crypt structures. Images are representative of a minimum of 3 independent observations. Scale: A-C) 200 $\mu$ m, D-F) 100 $\mu$ m

#### **5.4.14 Human small intestine characterisation for comparison to 3D co-culture intestinal models.**

Small intestinal tissue was also acquired from Biopta (Glasgow, UK). Figure 5.24 A, B shows the histological staining of the small intestinal tissue with H&E. Classical tall villus structures can be seen with a well-defined epithelium, supportive mucosa and basal smooth muscle layers. Transverse sections of the tissue show round structures indicating the cross sectioned villus. Large numbers of supportive fibroblasts can be easily identified with seemingly much denser staining than that seen in the colon tissue (Figure 5.21 A,B). Figure 5.24 C, D show PAS staining of the intestinal tissue. Goblet cells, as identified by positive PAS staining are shown to be interspersed throughout the villus crypt axis between non-stained enterocyte lineages. Small intestinal tissue sections when compared to their colonic counterparts (Figure 5.21 C, D) show significantly less positive goblet cell staining indicative of the change in function between the tissues, with small intestine primarily tooled towards high absorptive properties. Trichrome staining (Figure 5.24 E, F) shows significant collagen deposition throughout the entirety of the tissue but primarily located at the base of the villi structures.

Similar to that seen in colonic tissues, Collagen I, III and IV staining (Figure 5.25 A-C) is observed throughout the tissue structures, primarily in the sub-epithelial compartment immediately beneath the epithelial layers.  $\alpha$ SMA staining (Figure 5.25 D) is equally dispersed throughout the tissue. However, compared to Vimentin (Figure 5.26 A)  $\alpha$ SMA is only a small proportion of total mesenchymal staining. This is in contrast to staining of the colon and suggests that the small intestine harbours a smaller number of myofibroblast cells as a percentage of the total fibroblast population. Elastin staining (Figure 5.26 B) shows a specific, punctate staining throughout the small intestine mucosae most likely representing smooth muscle cells. MDR1 (Figure 5.26 C) shows a similar expression profile in small intestine as was observed in colonic tissues, namely a localisation to the apical cells of the villi structures and apical/ apical-lateral staining in the cells themselves. Small intestinal tissue sections were also stained for Occludin and E-Cadherin (Figure 5.27 A, B) which were localised to the epithelial layer alone, with either apical or lateral staining for Occludin and E-cadherin respectively, as expected.



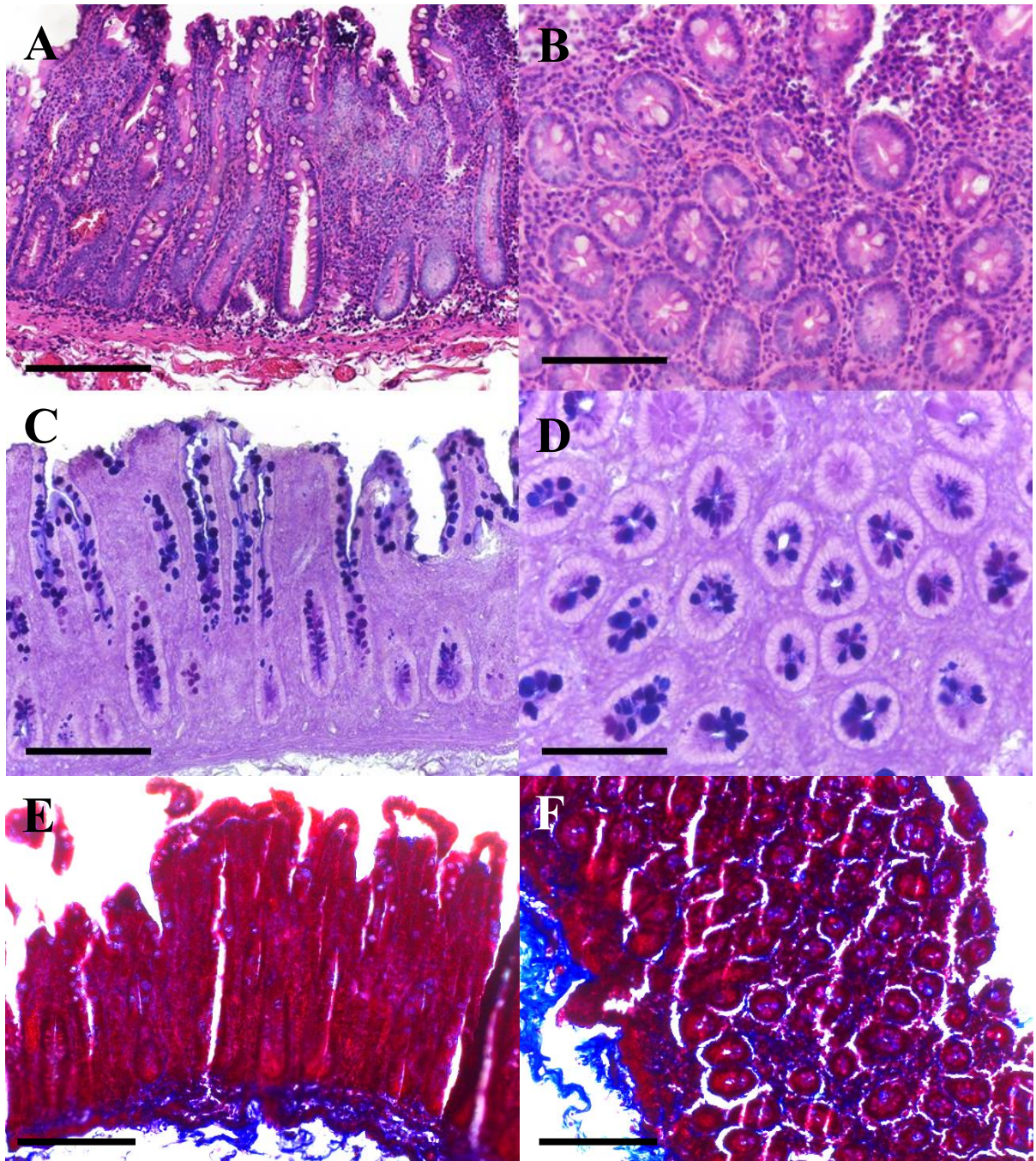


**Figure 5.24: Histological analysis of normal Human Small intestinal tissue sections – A,B)** Histological analysis of tissue structure by H&E staining of intestinal villi and muscularis layers. **C,D)** PAS staining of goblet cell populations within the small intestinal villus. Significant numbers of goblet cells can be seen throughout the length of the intestinal Villus. Goblet cell population rates are significantly lower than that seen in the large intestinal sections (Figure 5.15 C,D). **E,F)** Masson's Trichrome staining of intestinal sections showing collagen depositions along the villus axis, Intense staining can be seen around the serosal layer of the tissue and in between villus structures. Images are representative of a minimum of 3 independent observations. Scale 200 $\mu$ m

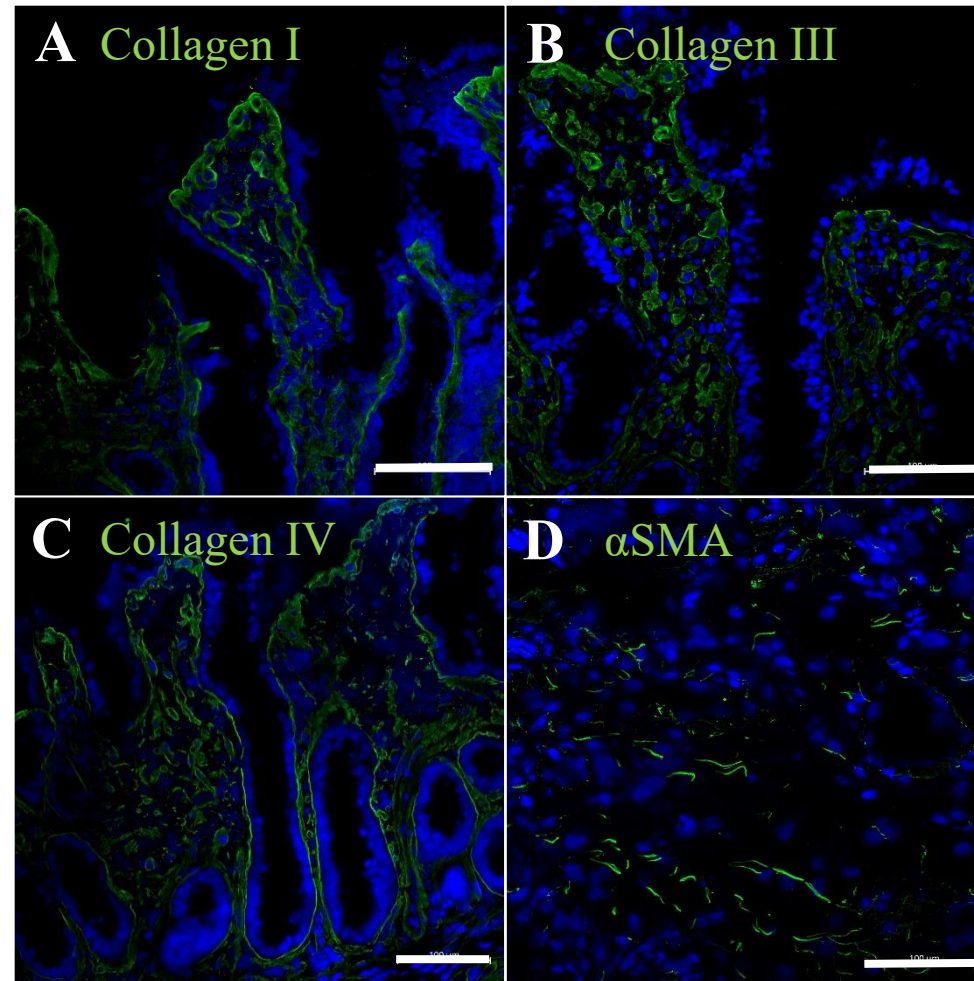


**Figure 5.25: Immunofluorescence study of normal Human Small intestinal tissue sections for the analysis of ECM deposition in the stromal intestinal tissues** – As was seen with immunofluorescence staining of Colonic tissues, ECM deposition can be located primarily beneath the Epithelial layers with a strong band of staining showing the supportive basement membrane of the epithelial layer. Low levels of  $\alpha$ SMA (D) staining can be seen throughout the tissue sections, especially in the stromal and smooth muscle layers of the tissues. Images are representative of a minimum of 3 independent observations. Scale 100 $\mu$ m



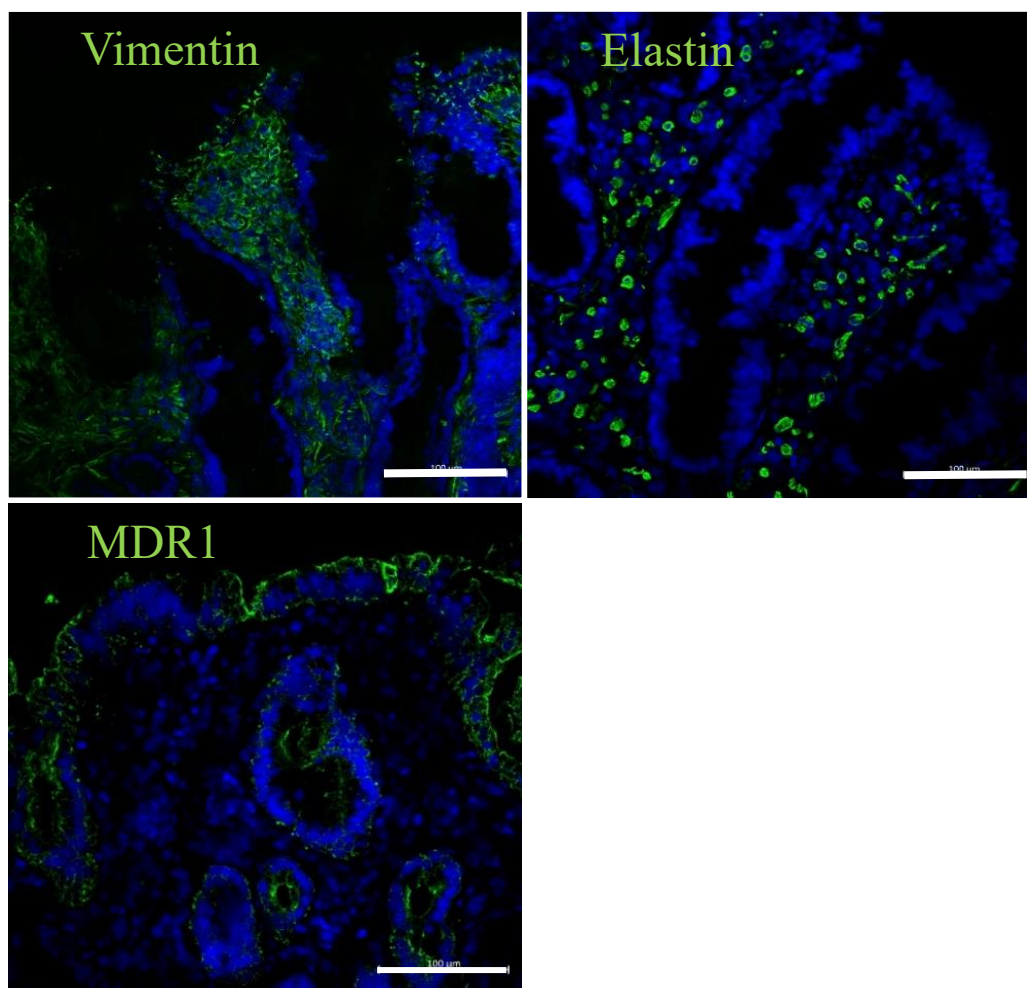


**Figure 5.26: immunofluorescence analysis of normal Human Small intestinal tissue sections shows distinct population of cells within the epithelial and stromal compartments – A) Vimentin, Mesenchymal intermediate filament protein B) Elastin, a secreted ECM component found within many body tissues, important for tissue elasticity C) MDR1, Apically expressed efflux protein found in enterocytes within the intestine Images are representative of a minimum of 3 independent observations. Scale 100µm**

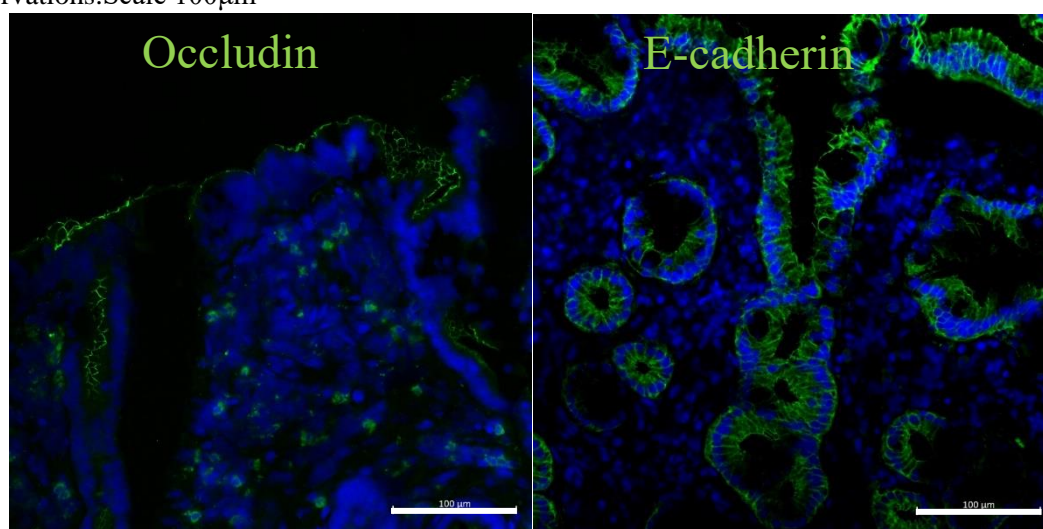


**Figure 5.27: Immunofluorescence analysis of normal Human Small intestinal tissue sections – A) Occludin, tight junctional component protein, B) E-cadherin, Adherens junction component protein. Images are representative of a minimum of 3 independent observations. Scale 100µm**

### **5.4.15 3D CCD-18co intestinal model immunostaining characterisation.**

Figure 5.28 shows the immunostaining characterisation of the 3D CCD-18co Alvetex<sup>®</sup> model of the intestinal mucosae. A-C shows the extracellular Collagen deposition by the CCD-18co fibroblasts within the Alvetex Scaffold<sup>®</sup>. Namely, Collagen I, III and IV are shown here and are seen to be homogenously dispersed throughout the Alvetex<sup>®</sup>, covering the pore surfaces and in some cases are seen spanning the void distance.

Figure 5.28 D and E, shows Vimentin and  $\alpha$ SMA staining respectively. Vimentin is used in this instance as a marker for cells of mesenchymal origin and should therefore stain fibroblasts specifically, including both normal and myofibroblast cells.  $\alpha$ SMA is a marker specifically for cells of a myofibroblast origin. By comparing the relative expression of Vimentin to  $\alpha$ SMA one could understand the frequencies of different cell populations within the intestinal and 3D model stromal compartments. Figure 5.28 D & E, shows staining of both markers within the 3D model.  $\alpha$ SMA is shown to be significantly less expressed than Vimentin and as such suggesting a mixed population of normal and myofibroblasts within the 3D model stroma, as was seen in the human colonic and small intestine tissue sections (Figure 5.21 E & F and Figure 5.25/26).

Cellular junctions within the 3D model were assessed through the staining of E-cadherin and Occludin (Figure 5.28 F & G). Clear junctional formation could be observed in the epithelium of the 3D model with consistent E-cadherin formation along the length of the entire epithelium. Additionally, E-cadherin staining shown how cells are arranged into a tall epithelial monolayer rather than multilayering. Tight junction expression as assessed through Occludin staining is also seen throughout the epithelium with staining primarily located at the apical lateral point of the Caco-2 cells membrane with specific tight junction localisation also inferring cell polarisation. Finally, MDR1 staining (Figure 5.28 H) is shown to be specific to the epithelial layer. However, MDR1 does not show the expected apical localisation within the cells with significant expression seen along the length of the apical and basal membrane along with some disperse cytoplasmic staining similar when compared to the expression seen in tissue.

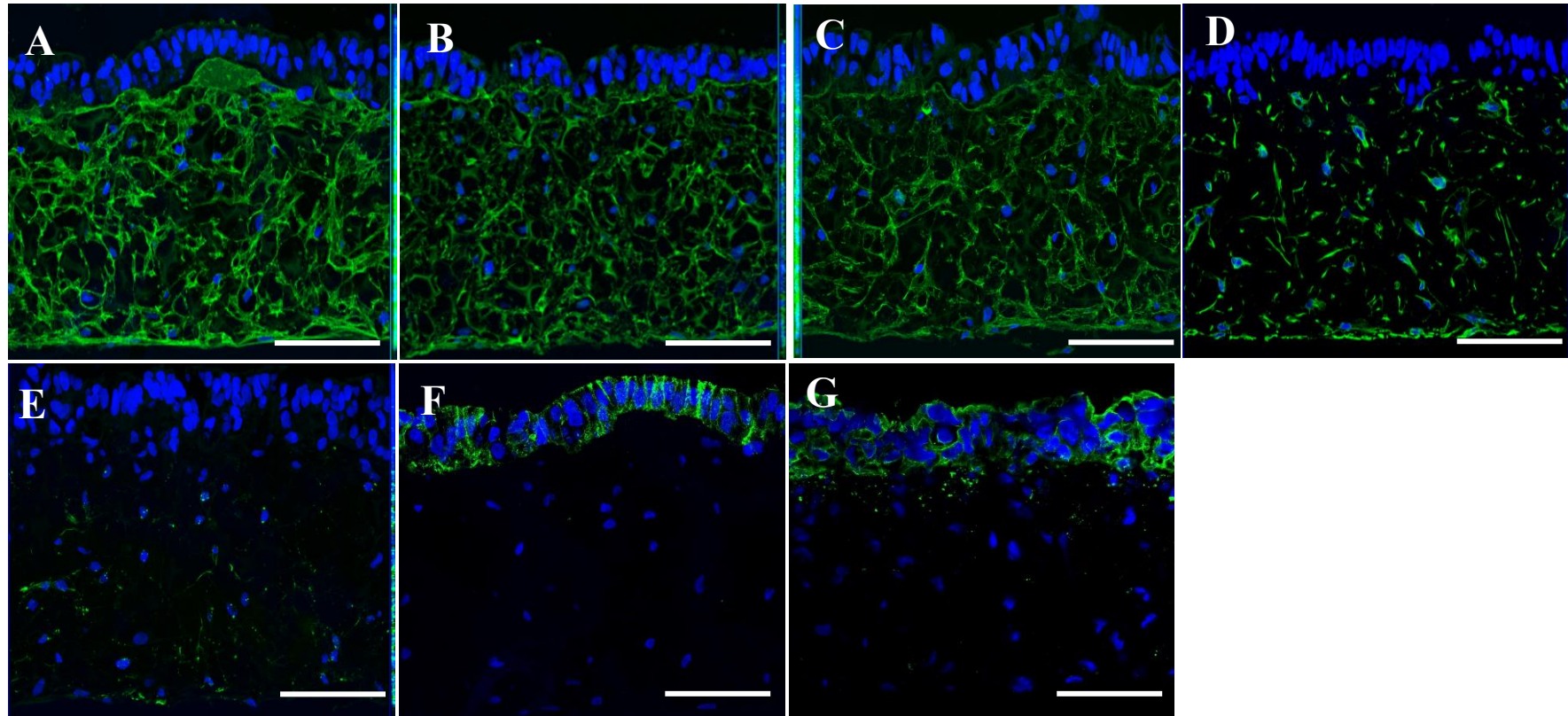


**Figure 5.28: Immunofluorescence analysis of CCD-18co/ Caco-2 Alvetex 3D models shows significant ECM deposition within the substrate in addition to well defined epithelial layers - A) Collagen I, B) Collagen III, C) Collagen IV, D) Vimentin, E) Alpha- SMA, F) E-cadherin, G) MDR1. Images are representative of a minimum of 3 independent observations. Scale 100µm.**

#### **5.4.16 3D HDFn intestinal model immunostaining characterisation.**

Figure 5.29 shows the immunofluorescence staining for optimised HDFn 3D Alvetex Scaffold® models of the intestine. Figure 5.29 A-C shows the extra and intra-cellular staining of Collagen proteins important in normal tissue function and homeostasis, namely, Collagen I, III and IV. Collagen I shows a limited amount of expression within the Scaffold, primarily located to the basal and apical surfaces of the Scaffold. This is most likely intracellular Collagen I as the positive staining location strongly correlates where the largest population of HDFn cells reside within the model. Collagen III (Figure 5.29 B) is, for the most part, absent from this model. Collagen IV (Figure 5.29 C) is by far the strongest stained of the Collagen so far, with extensive deposition throughout the model.

Figure 5.29 D and E show vimentin and  $\alpha$ SMA staining respectively. Vimentin is utilised as a stain for mesenchymal cells, and as such, specifically stains HDFn cells at a higher intensity than Caco-2. Vimentin staining shows significant fibroblast populations throughout the model, however, there does appear to be a bias toward the apical surface of the models, most probably due to the sequential seeding techniques. Figure 5.29 E shows  $\alpha$ SMA, very little positive staining is seen within the HDFn model. Some positive staining can be observed indicating a small subpopulation of  $\alpha$ SMA positive fibroblasts/myofibroblasts. Figure 5.29 F shows E-Cadherin staining along the entire length of the Caco-2 epithelium. Caco-2 cells are able to differentiate forming well defined junctions between cells within the epithelium. Occludin staining (Figure 5.29 G) shows a similar pattern with primarily apically located expression along the epithelial layer. Finally, MDR1 staining (Figure 5.29 H) is shown to be strongly located to the basal layer of the epithelium, generally not where MDR1 expression is to be expected.



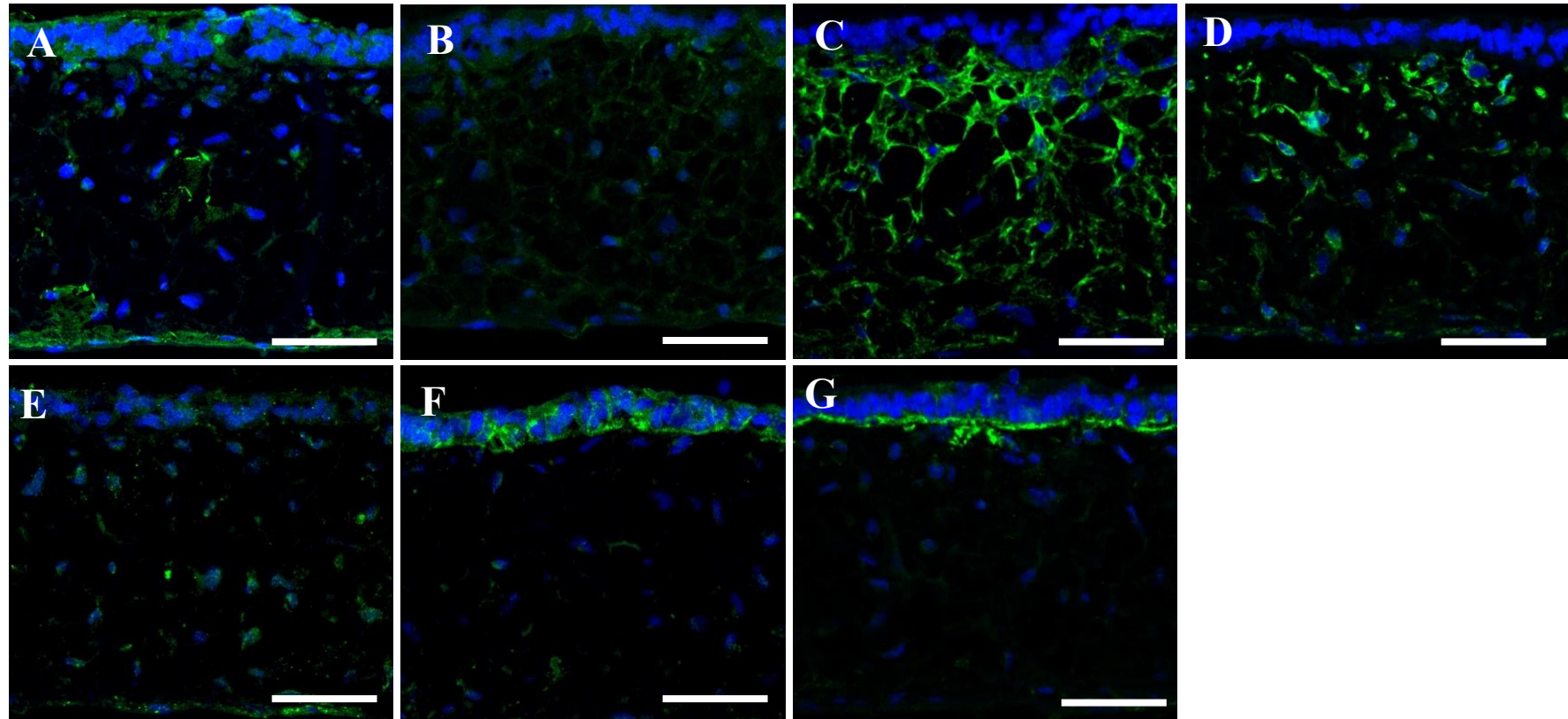


**Figure 5.29: HDFn/ Caco-2 Alvetex models show well defined epithelial layers without the significant Collagen deposition within the substrate as seen in CCD-18co models - A) Collagen I, B) Collagen III, C) Collagen IV, D) Vimentin, E) Alpha- SMA, F) E-cadherin, G) MDR1. Images are representative of a minimum of 3 independent observations.**

#### **5.4.17 3D HIC intestinal model immunostaining characterisation.**

Figure 5.30 shows the immunostaining characterisation of 3D cultured models created with the HIC cells (Human intestinal cells, isolated in Durham). Histological analysis seen previously (Figure 5.20) shows how the 3D structure in this model is limited in its *in vivo* mimicry of the intestine. Therefore, it would be unreasonable to expect the immunofluorescence staining to show anything less than the disorganised structure already analysed histologically. Similar to HDFn staining, Collagen I and III (Figure 5.30 A & B) show limited deposition within the Alvetex Scaffold similar to HDFn primary cells. Collagen IV (Figure 5.30 C) shows significant staining throughout the scaffold with an even deposition moving from the apical to basal sides of the substrate. Vimentin and  $\alpha$ SMA staining is similar to that seen in other models with higher levels of Vimentin than  $\alpha$ SMA when compared, suggesting a mixed myofibroblast population. E-cadherin and Occludin staining highlights the failure of the HIC cells to create a foundation for the culture of Caco-2 cells localised to the apical surface of the model. Whilst some epithelial organisation can be observed, there is a large amount of Caco-2 infiltration into the 3D scaffold as suggested by positive junctional staining throughout the substrate. MDR1 similarly shows a lack of organisation with positive staining seen throughout the scaffold. Structure implies function. Therefore, without the correct tissue organisation one would expect a decrease in the functional attributes of a model and its capabilities to mimic the *in vivo* intestine.

HIC 3D models were a late addition to the project. Additionally, only limited numbers of HIC cells were available for use. As such only minimal optimisation of culture techniques was achieved with HIC 3D models. The model disorganisation in comparison to the other models utilised in this study highlights the importance of optimisation in the culture process. 3D HIC models were carried through to functional pharmacokinetic assessment to maintain consistency and provide a comparison with HIC paracrine media cultured achieved in Transwell.



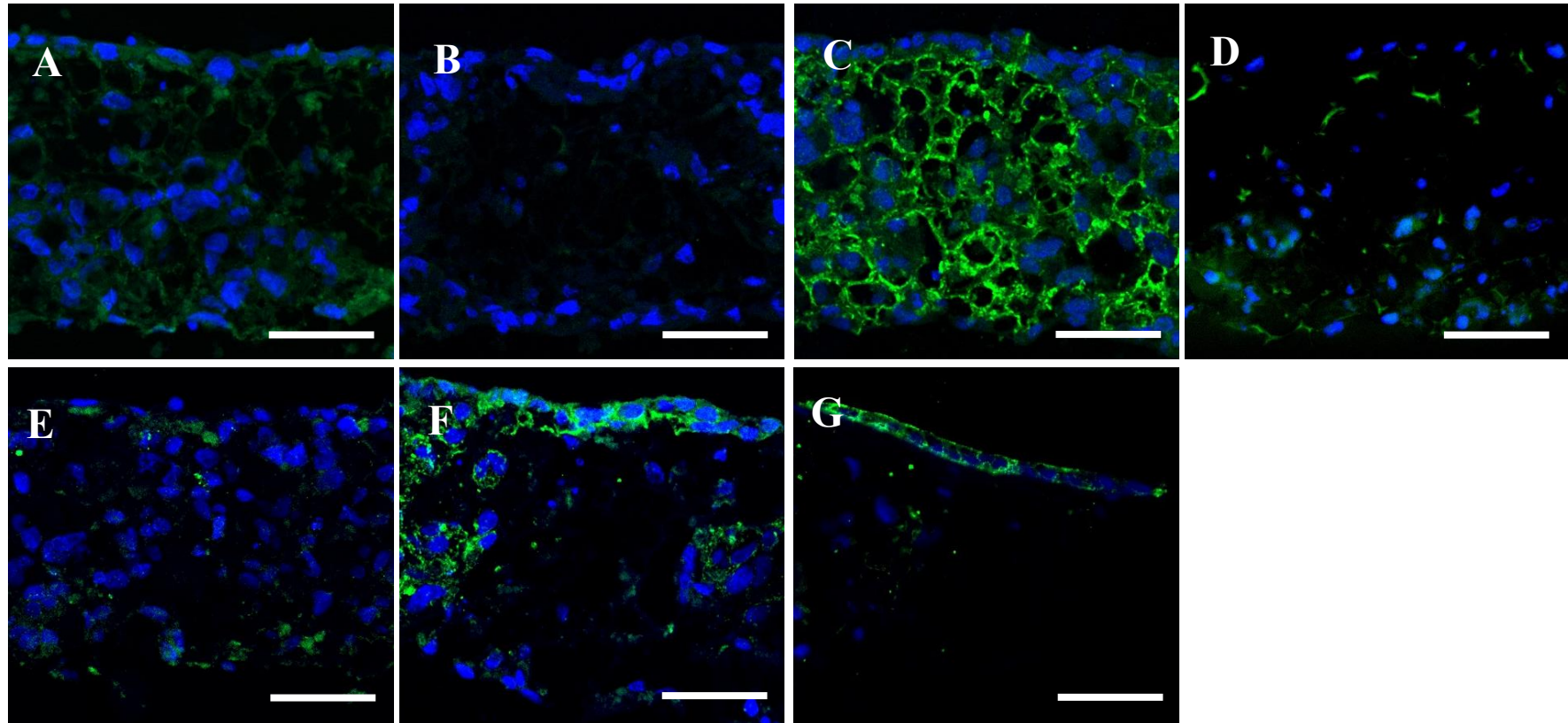


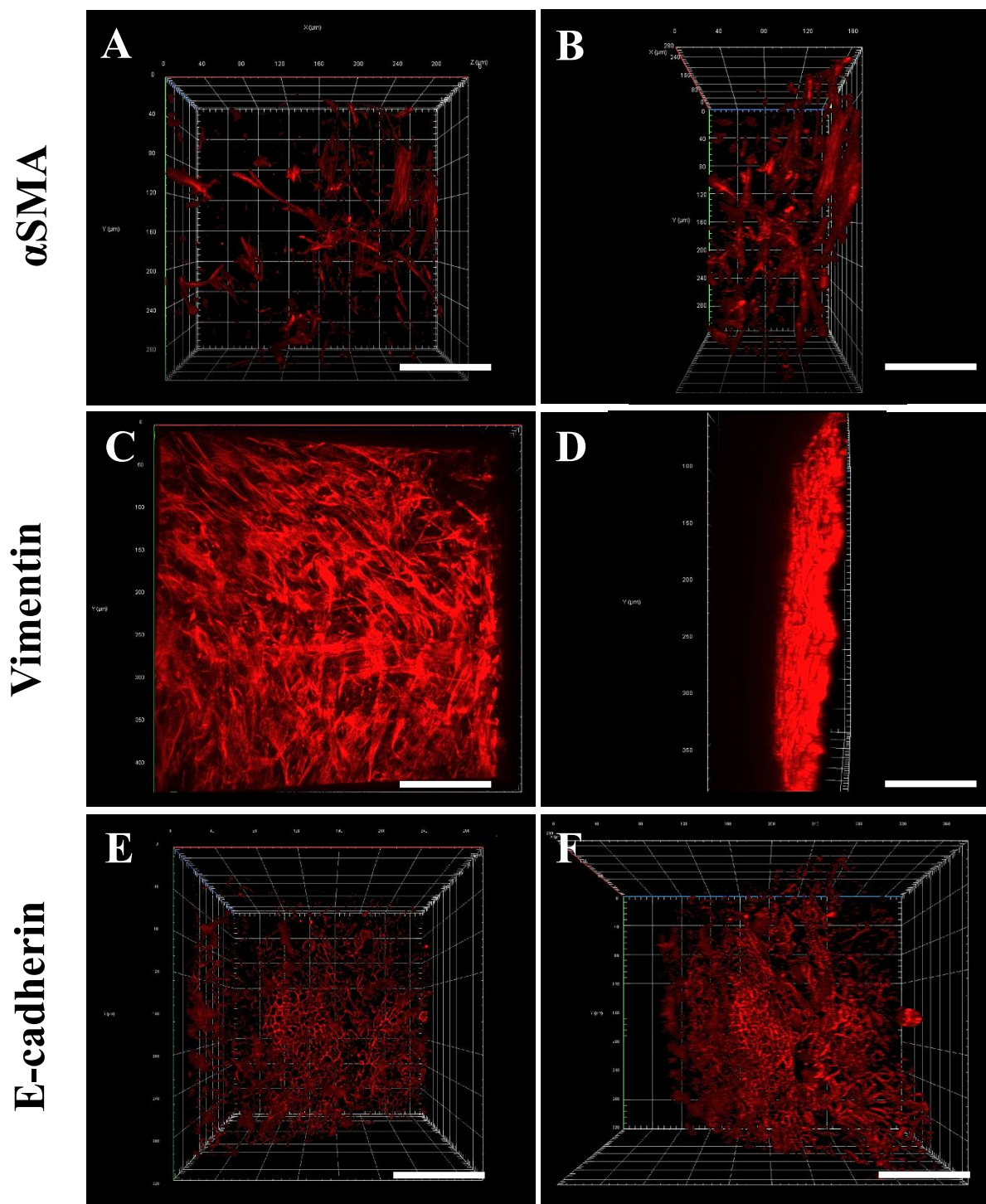
**Figure 5.30: HIC/ Caco-2 3D models are shown to secrete significant levels of Collagen IV with only minor amounts of other ECM components, epithelial layering is significantly diminished compared to other model systems - A) Collagen I, B) Collagen III, C) Collagen IV, D) Vimentin, E) Alpha- SMA, F) E-cadherin, G) Occludin, H) MDR1. Images are representative of a minimum of 3 independent observations. Scale 100μm.**

### **5.4.18 Lightsheet analysis of 3D model immunostaining morphology.**

Light sheet analysis was attempted to form a 3D immunostaining image of the intestinal model in order to understand the dispersion of ECM within the Alvetex Scaffold<sup>®</sup>. Due to the limitations of the Alvetex Scaffold's<sup>®</sup> optical properties a novel clearing method based on the paper by Renier *et al* (270) was required to penetrate any significant distance into the Alvetex<sup>®</sup> model.

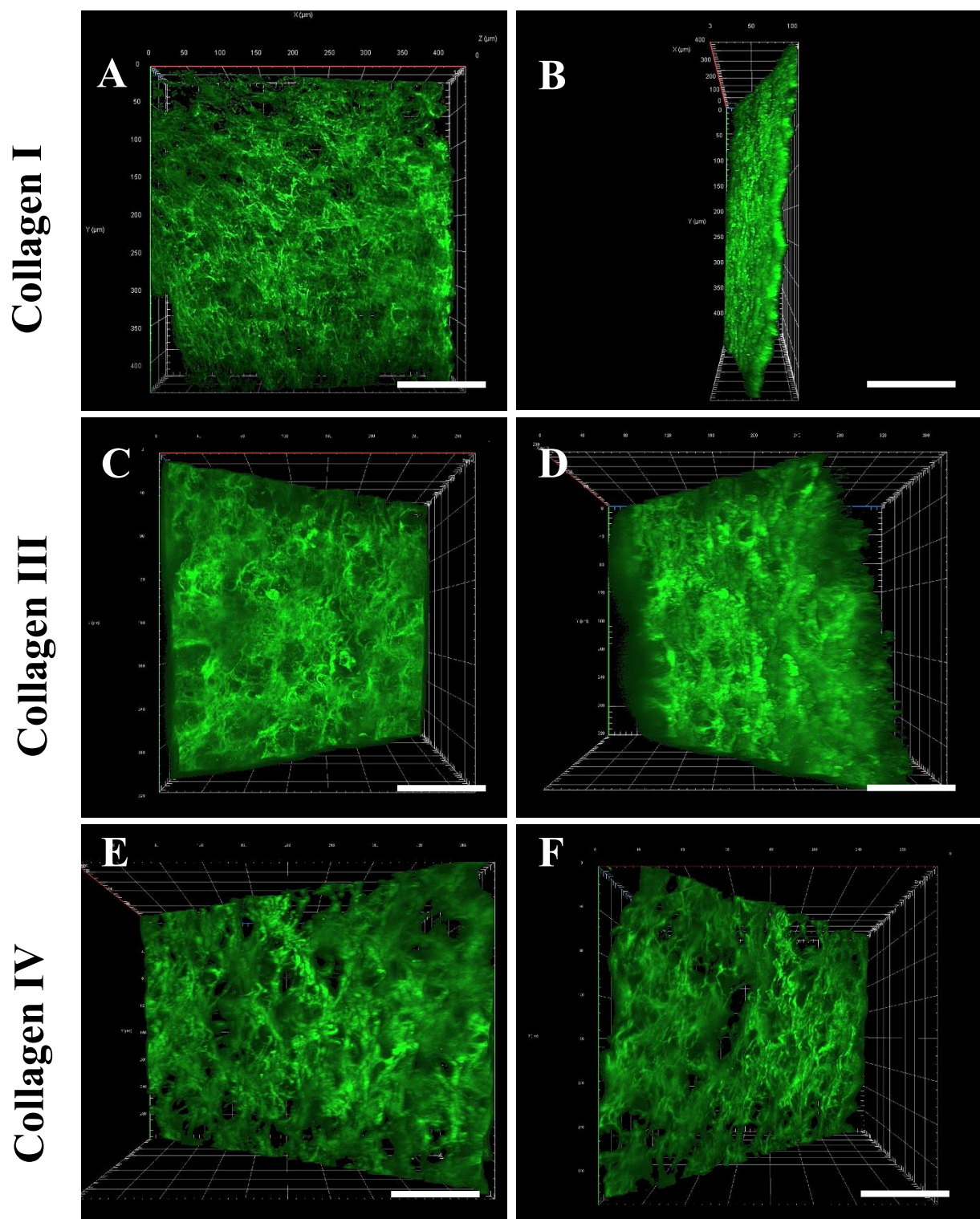
Figure 5.31 shows the expression of  $\alpha$ SMA and Vimentin (Both markers of myofibroblasts and mesenchymal cells respectively) in addition to E-cadherin, utilised here to highlight the formation of the epithelial layers. The differential expression rates of  $\alpha$ SMA and Vimentin clearly show that  $\alpha$ SMA positive cells are a small yet significant sub-population of the added fibroblasts. Vimentin staining shows the levels of CCD-18co population within the Alvetex Scaffold<sup>®</sup>. It clearly shows that the cells form a continuous layer across the surface of the scaffold, sufficient for the subsequent seeding and culture of Caco-2 cells across their surface with minimal epithelial invasion into the underlying stromal section of the model. The continuous monolayer formation of Caco-2 cells in the model is further highlighted by the E-cadherin expression showing a clear monolayer across the surface of the construct.

Figure 5.32 highlights the levels of collagen deposition within the scaffold. The tested collagens, Collagen I, III and IV all show significant deposition within the scaffold with collagen III being potentially the most abundant and Collagen IV the least. In either case it is clearly shown the CCD-18co cells are able to secrete significant levels of ECM into the Alvetex Scaffold<sup>®</sup> throughout the culture period. It was decided that light sheet analysis for this application did not provide significant additional value over sectioned samples due to the poor penetration of the imaging into the sample. As such full scale immunological assessment did not proceed past this point with this technique.



**Figure 5.31: 3D cellular organization of CCD-18co fibroblasts and Caco-2 cells – A, B)  $\alpha$ SMA staining of myofibroblast sub populations, B) 90° rotation of A. C, D) Vimentin staining of mesenchymal cells, D is a 90° rotation of C. E, F) E-cadherin staining of Caco-2 cells, F is a 90° rotation of E. Images are representative of a minimum of 3 independent observations. Scale 100 $\mu$ m**





**Figure 5.32: 3D cellular organization of CCD-18co fibroblasts and Caco-2 cells – A, B)** Collagen I, B) 90° rotation of A. C, D) Collagen III staining of mesenchymal cells, D is a 90° rotation of C. E, F) Collagen IV staining of Caco-2 cells, F is a 90° rotation of E. Images are representative of a minimum of 3 independent observations. Scale 100μm

#### **5.4.19 Development of an Ussing chamber for the incorporation of the 24-well format Alvetex Scaffold®.**

Alvetex Scaffold®, unlike Transwell in the Snapwell format, does not come in formats friendly to easy addition into Ussing chamber designs currently available on the market. All model development and optimisation steps were performed in the 24-well Alvetex Scaffold® format due to its small culture area, reducing cellular load and ease of use in standard format 12-well plates. It was necessary to ensure that the model would have minimal disruption when taken from cell culture to utilisation within the Ussing chamber. As such, unclipping the Alvetex® model (disrupting the epithelium) from the 24-well format inserts would impart mechanical stresses ultimately damaging the intestinal construct, prior to addition into the Ussing chamber for analysis.

Figure 5.33 shows the chamber design allowing for the incorporation of the entire 24-well insert into the Ussing chamber. The design ensures equal amounts of fluid on either side of the membrane when in the system. This limits any static fluid pressures which could ultimately influence the transport kinetics of the model. The full insert is added into the middle of the 3 sections and, when closed together creates a watertight seal across the membrane stopping any passive movement of fluid across the chamber, not associated with passive movement through the membrane.

Ultimately, the transport experiments conducted in the following chapter utilised the 96-well format instead of the 24-well format due to improved high throughput applications. The 96 well format became available after the design and construction of the 24-well Ussing chamber. Models were moved to the 96-well format due to its enhanced capabilities to allow for higher throughput model culture, more simplistic/ reproducible chamber design and requirement of a reduced number of population limited cells for creation of a full intestinal model.

Figure 5.34 shows pictures of the final product.

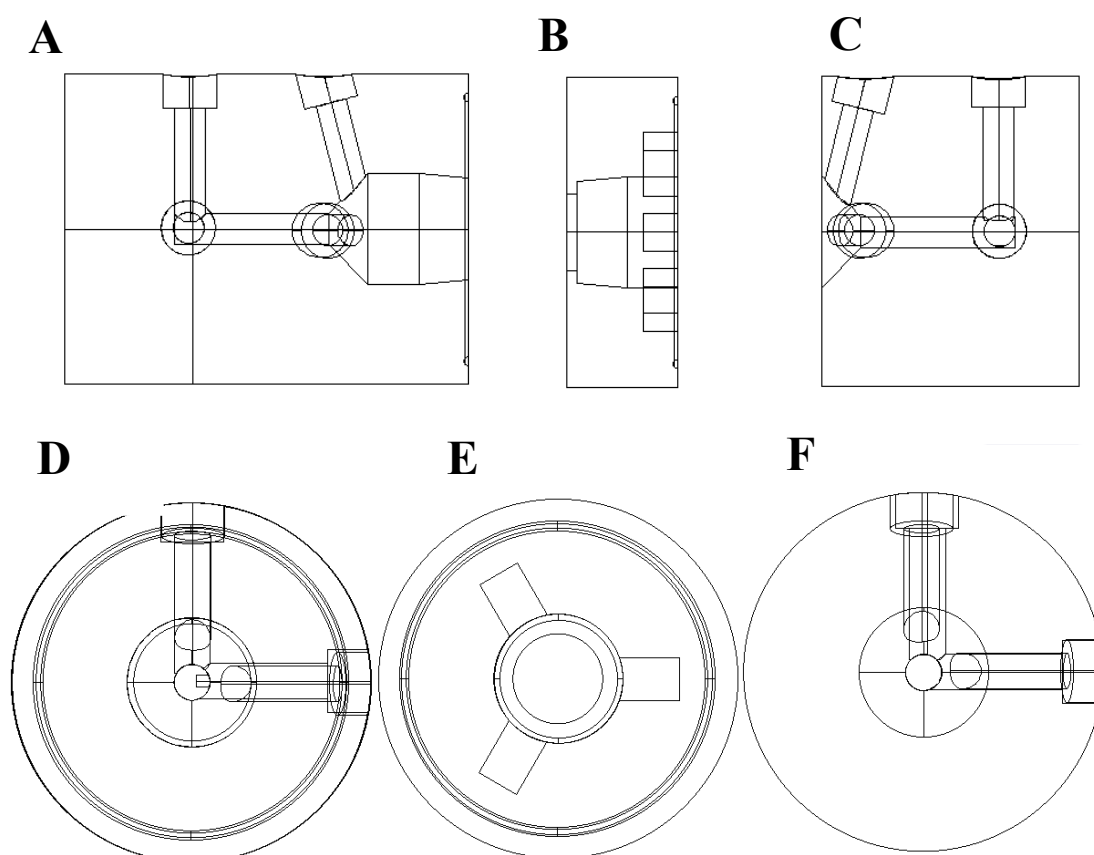


**Figure 5.33: Wireframe schematic diagram of the 24-well Alvetex Scaffold Ussing chamber design** – The design comes in 3 distinct sections to allow for the full incorporation of the 24-well insert into the Ussing chamber system. This is done in an effort to minimise the mechanical disruption to the model prior to analysis which unclipping the Alvetex from the culture insert would induce. The entire culture insert fits within part B of the chamber design with parts A and B mirroring the internal measurements of the 24 well format to ensure equal amounts of media on either side of the membrane. Parts D-F are cross sections of the corresponding A-C parts.

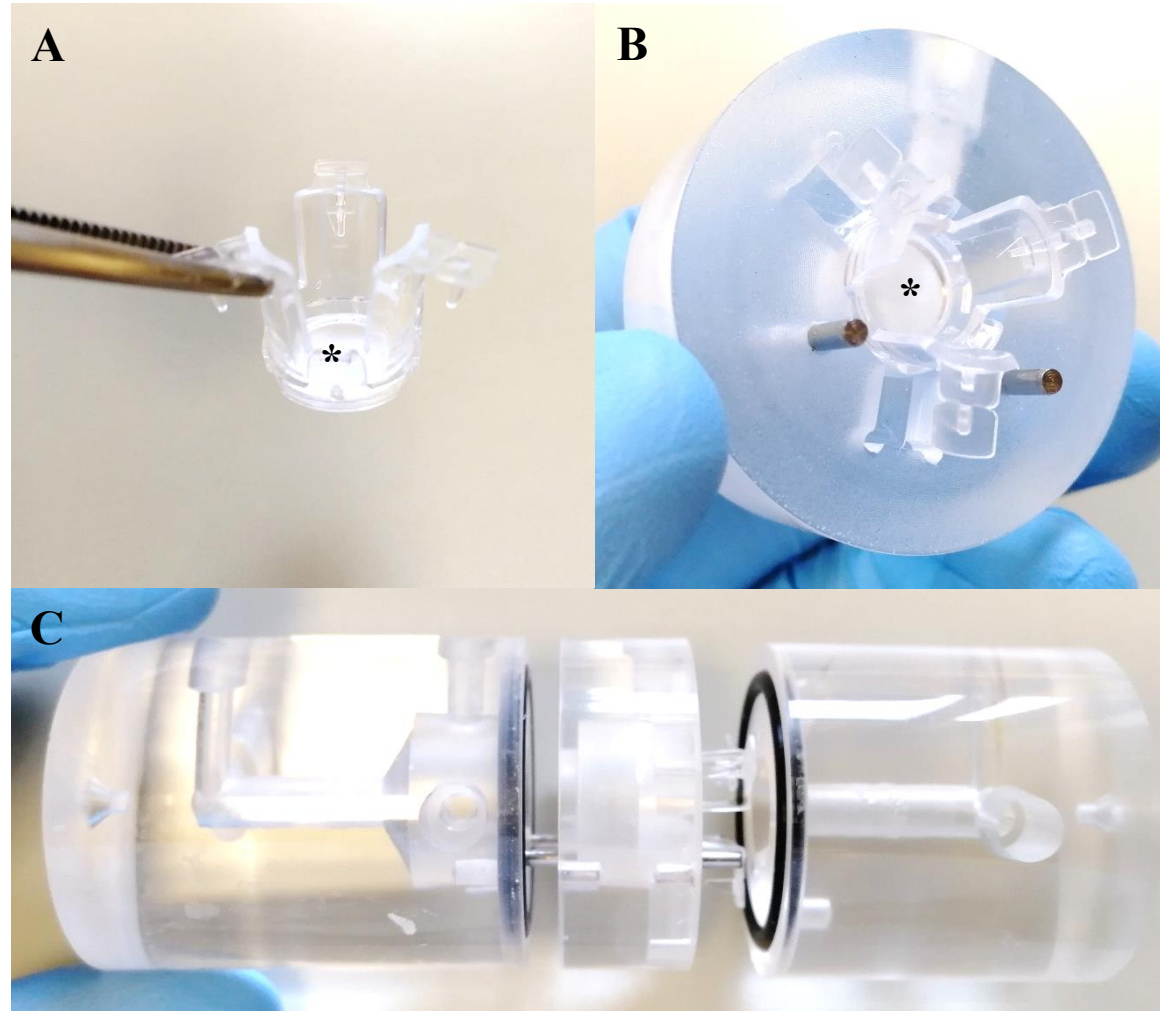


**Figure 5.34: Photographic images of the 24-Well format manufactured Ussing chamber** – A) 24 well insert with Alvetex layer (\*), wing span of the insert is sufficient for suspension culture within a 12 well plate. B) 24 well insert placed within the acceptor compartment of the Ussing chamber device. When inserted fully the surface of the 24 well insert is flush with the Ussing chamber plastic. Alvetex layer (\*) C) The whole Ussing chamber device with the 24 well insert ready to be sandwiched together and used for analysis.

#### **5.4.20 Creating a high throughput solution for the culture of 96-well format 3D Alvetex® models.**

24-well Alvetex Scaffold®, whilst small in its own right and on a similar scale as 12 and 24-well Transwell inserts is not high throughput to the extent required in the pharmaceutical industry for the large-scale analysis of potential drug compounds. As such the prototype 96-well Alvetex® format was created. The 96 well models were created in strips of 8 wells per model with size and distancing sufficient for the culture in a standard 96-well plate. However, it was observed that due to the extremely small media volumes added to a standard 96-well plate that the models were being insufficiently fed and media evaporation was clearly an issue for models at the edges of the plate (Data not shown). As such a new culture system was designed to limit the above described disadvantages. Figure 5.35 shows the schematic of the resultant design created for the culture of 96-well format models. A deep reservoir was incorporated into the design around the edges of the plate in order to limit any effects of evaporation seen in the culture wells. At the air liquid interface 1ml of media can be fit into the wells beneath the models with the final submerged volume of 1.5 ml. This provides ample media for the growing cellular models within the Alvetex Scaffold®, with media changes every other day. Utilisation of the 96-well plate resulted in the creation of models with indistinguishable histology than other formats.

The main advantage of this culture system over 24, 12 and 6-well Alvetex® formats is in the higher throughput capabilities of the system. A total of 24-models can be created in a single plate with a media availability per cm<sup>2</sup>, significantly higher than any other format by over an order of magnitude. 1.5 ml of media per model is sufficient for only a twice weekly feeding schedule. Minimising the work/ time needed to culture the model, reducing failure rates (e.g. through infection or manual mishandling of models) and saving money by reducing expensive media volumes required. Images of final products are shown in Figure 5.36



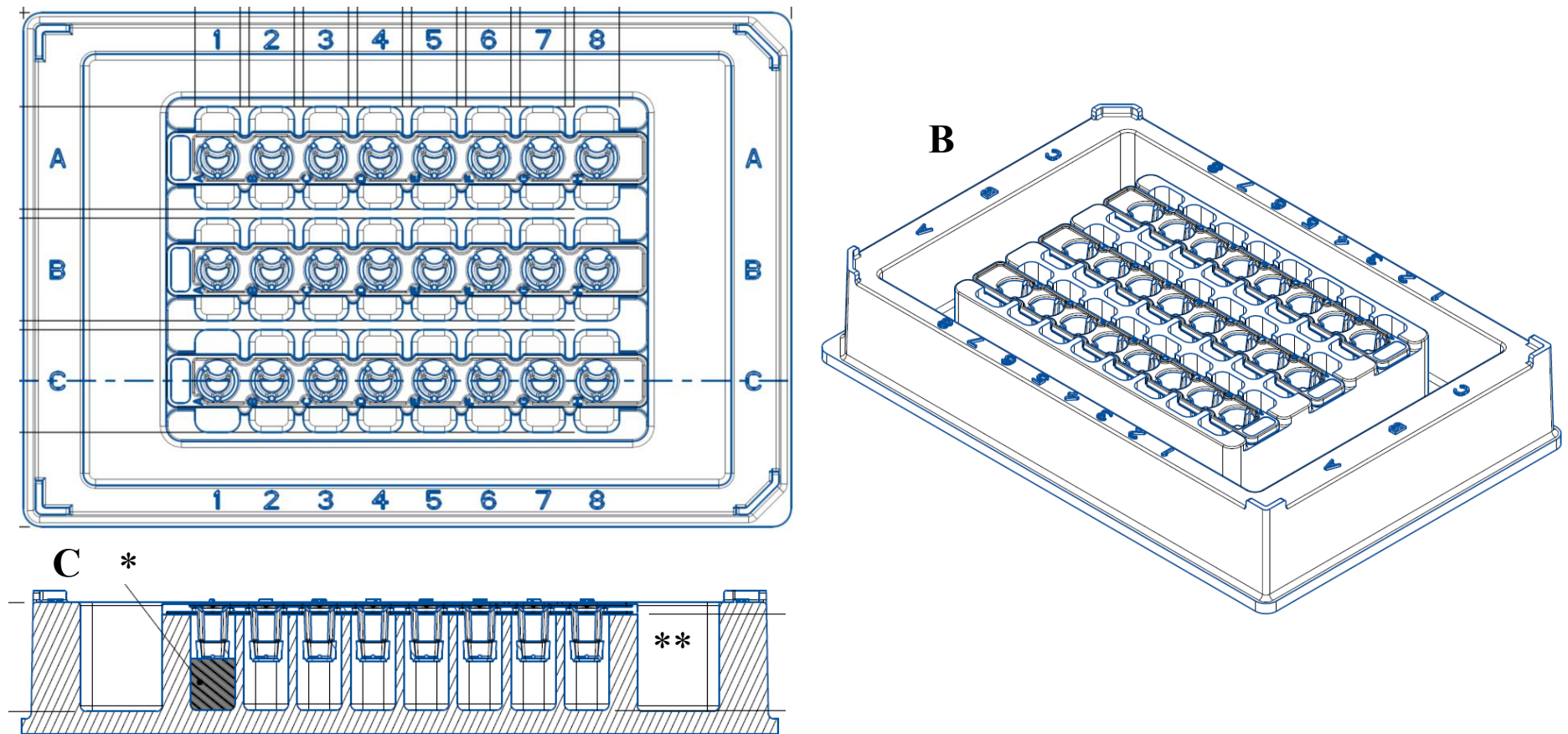


**Figure 5.35: Creating a Deep well culture dish for the maintenance of the ideal conditions to allow for 3D intestinal model growth in 96 well formats** – A,B) Shows a top down and rotated view of the 96 well deep culture dish with 96 well inserts resting within the plate, C) shows a cross section of the plate through the centre of one of the 3 culture strips. \* = the 1 ml void beneath the hanging culture insert to allow for the air-liquid interface culture of the models with sufficient media to promote cellular viability and growth. Total chamber fill amount is 2ml, 1.5 ml is the standard volume required to submerge the models completely. \*\* = the external reservoir for the addition of either sterile H<sub>2</sub>O or sterile PBS. This reservoir ensures sufficient humidity is maintained in the plate, limiting media loss through evaporation, important for models at the air-liquid interface.

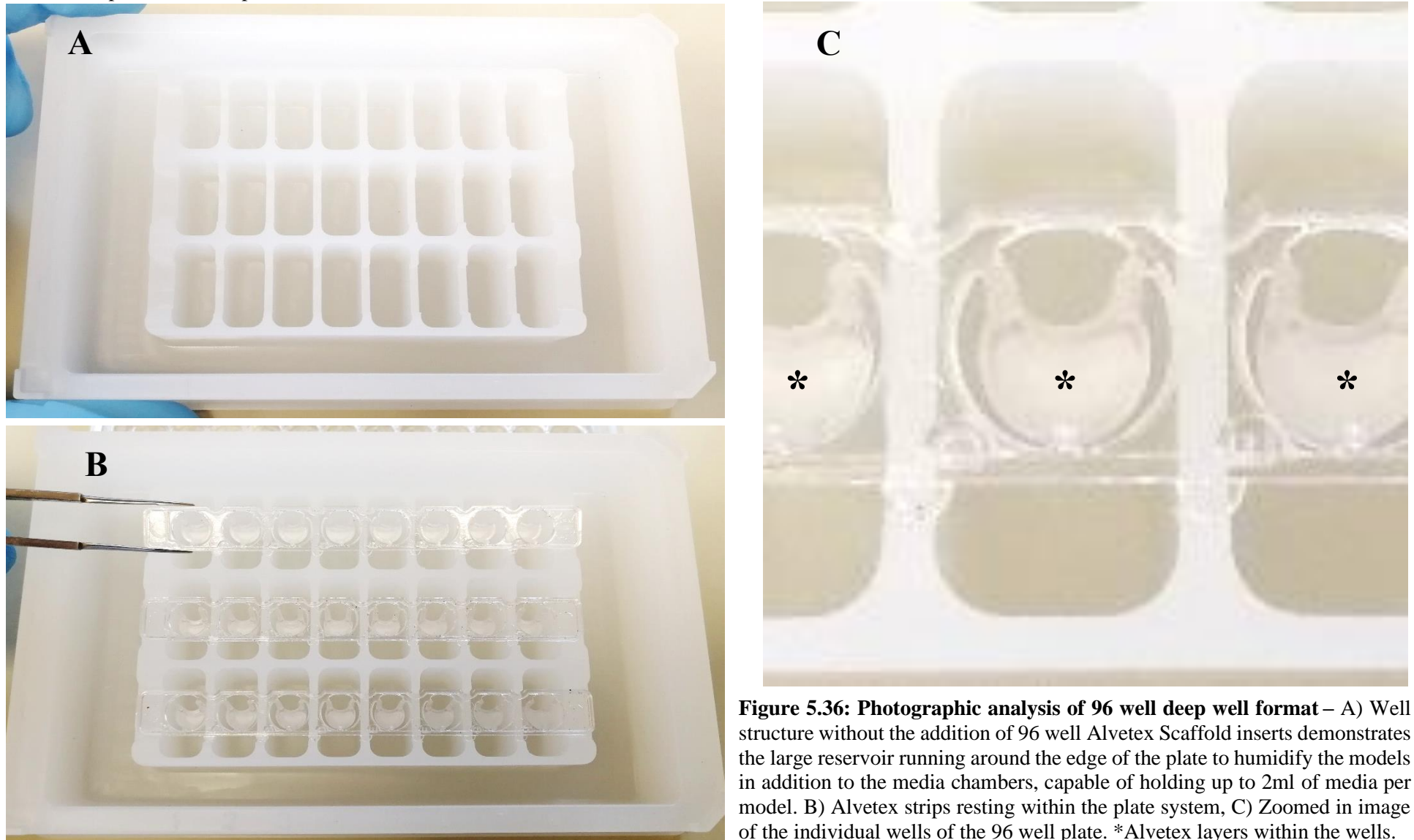


**Figure 5.36: Photographic analysis of 96 well deep well format –** A) Well structure without the addition of 96 well Alvetex Scaffold inserts demonstrates the large reservoir running around the edge of the plate to humidify the models in addition to the media chambers, capable of holding up to 2ml of media per model. B) Alvetex strips resting within the plate system, C) Zoomed in image of the individual wells of the 96 well plate. \*Alvetex layers within the wells.

### **5.4.17 Development of an Ussing chamber suitable for the analysis of 3D cultured 96 well format models.**

Assessment of a models functional capabilities can involve any number of assays and experiments in order to understand the physiological relevance of a model. This study primarily utilised an Ussing chamber design for all of the transport kinetic work, displayed in the following chapter.

In order to utilise the 96-well Alvetex<sup>®</sup> format within an Ussing chamber, a custom designed and manufactured chamber system was created to incorporate the bespoke nature of the 96-well format. Figure 5.37 shows the wire frame 3D model of the resultant design. Figure 5.37 A shows the aperture within which the Alvetex<sup>®</sup> and insert rests throughout the transport assay. Much in the same way as the 24-well chamber was designed the 96-well chamber is designed to incorporate the entire model insert, reducing the need for manual handling of the models and as such limiting the possibilities for accidental damage to the 3D models prior to use in the system. Unfortunately, due to the 96-well models design with 8 wells heat bonded per strip some manual handling is required for the 96-well format when applying to the chamber by clipping away the models from the culture strip. This is easily and cleanly done with a pair of wire snips prior to addition to the chamber. Figure 5.39 shows the steps for the processing of 96 well format Alvetex Scaffold<sup>®</sup> models into the custom designed Ussing chamber. Once models are in the chamber the basic premise of the system is the same as any other Ussing chamber device. There are ports for the connection of reservoir in and out tubing in addition to ports for the attachment of Ag/Cl electrode for the measurement of the electrophysiology of epithelial layers.

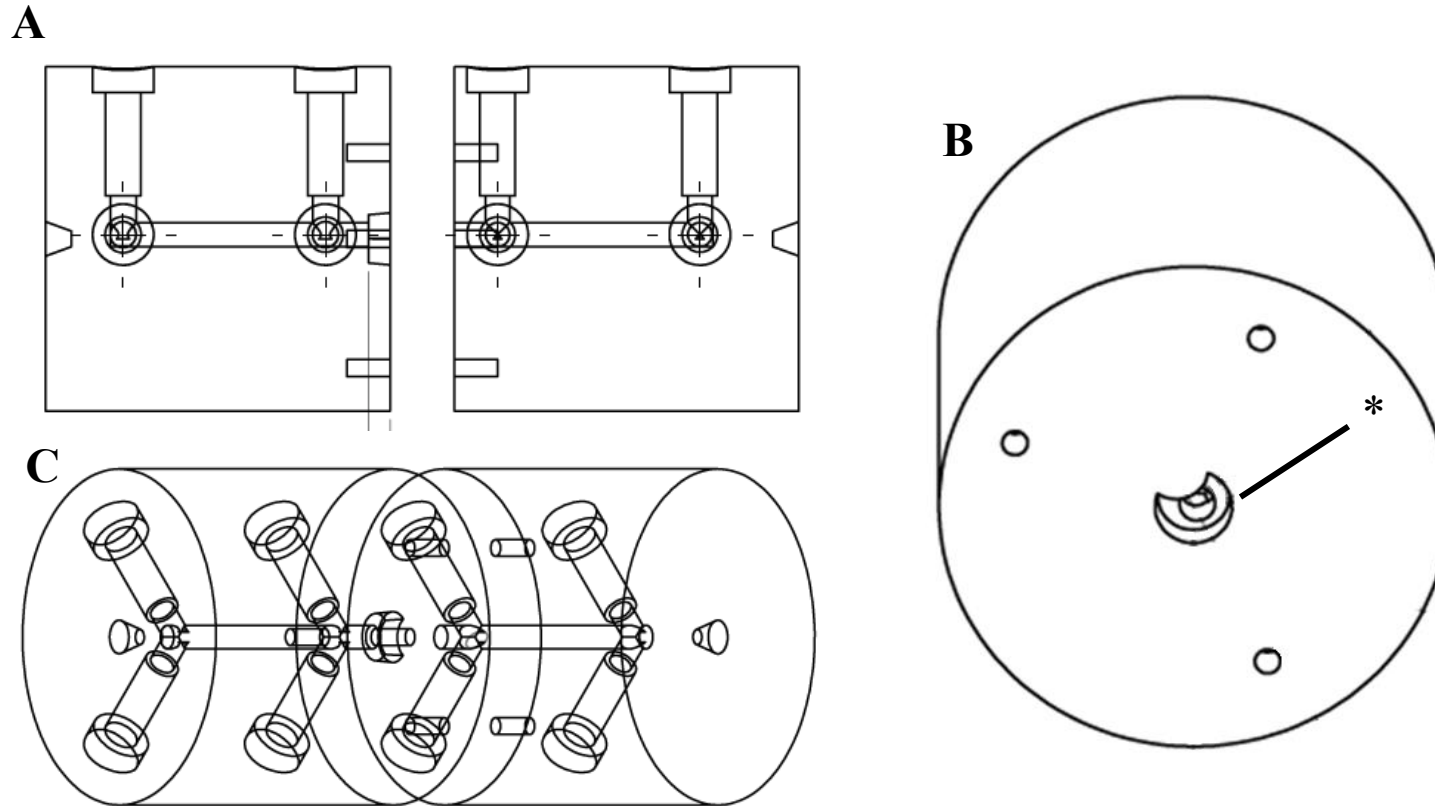


**Figure 5.37: Wireframe schematic of the 96 well Ussing chamber system, designed for the incorporation and functional testing of 96 well format Alvetex intestinal models** – A) A profile view down the centre line of the chamber giving a view of the orientation of the internal ports and fluid lines. B) Shows the acceptor compartment for the addition of Alvetex Scaffold models, \* = Acceptor port. C) Shows the wireframe of the complete design when sandwiched together. The model is sandwiched between both sides of the chamber system. A small amount of the apical surface of the hanging insert protrudes from the Acceptor port. This design ensures that the model is secure and water tight when the chamber system is sandwiched together.

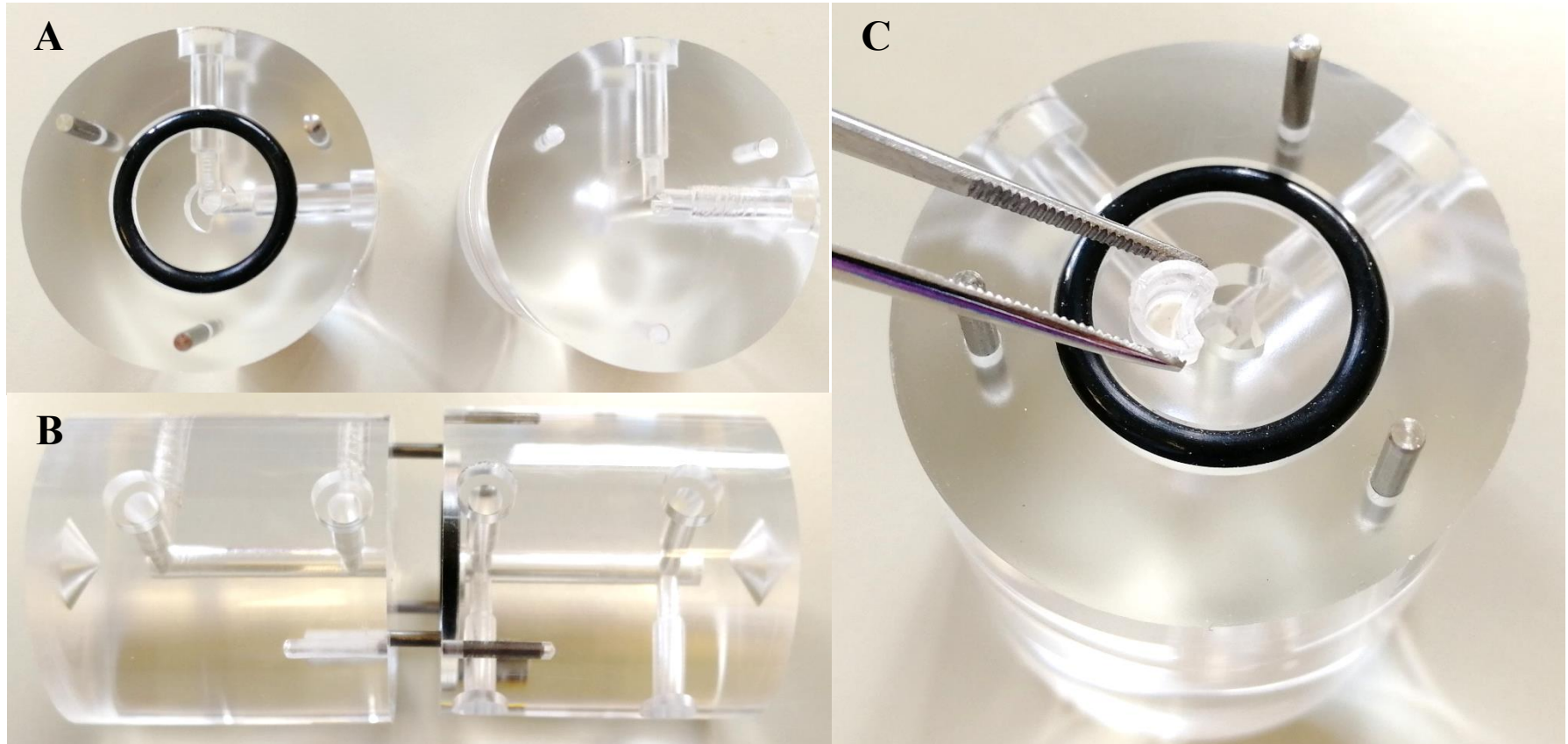


**Figure 5.38: Photographic images of the 96 well format Ussing chamber with added 96 well Alvetex insert** –A) Face view of the internal aperture of the 96 well chamber. Left) 96 well receiver chamber, Right) Sealing chamber. B) Both left and right pieces of the Ussing chamber immediately before sealing. The middle is completely flush with the O-ring sealing the chamber when closed. C) 96 well receiver compartment with a pre-prepared 96 well Alvetex Scaffold model ready for insertion into the chamber.



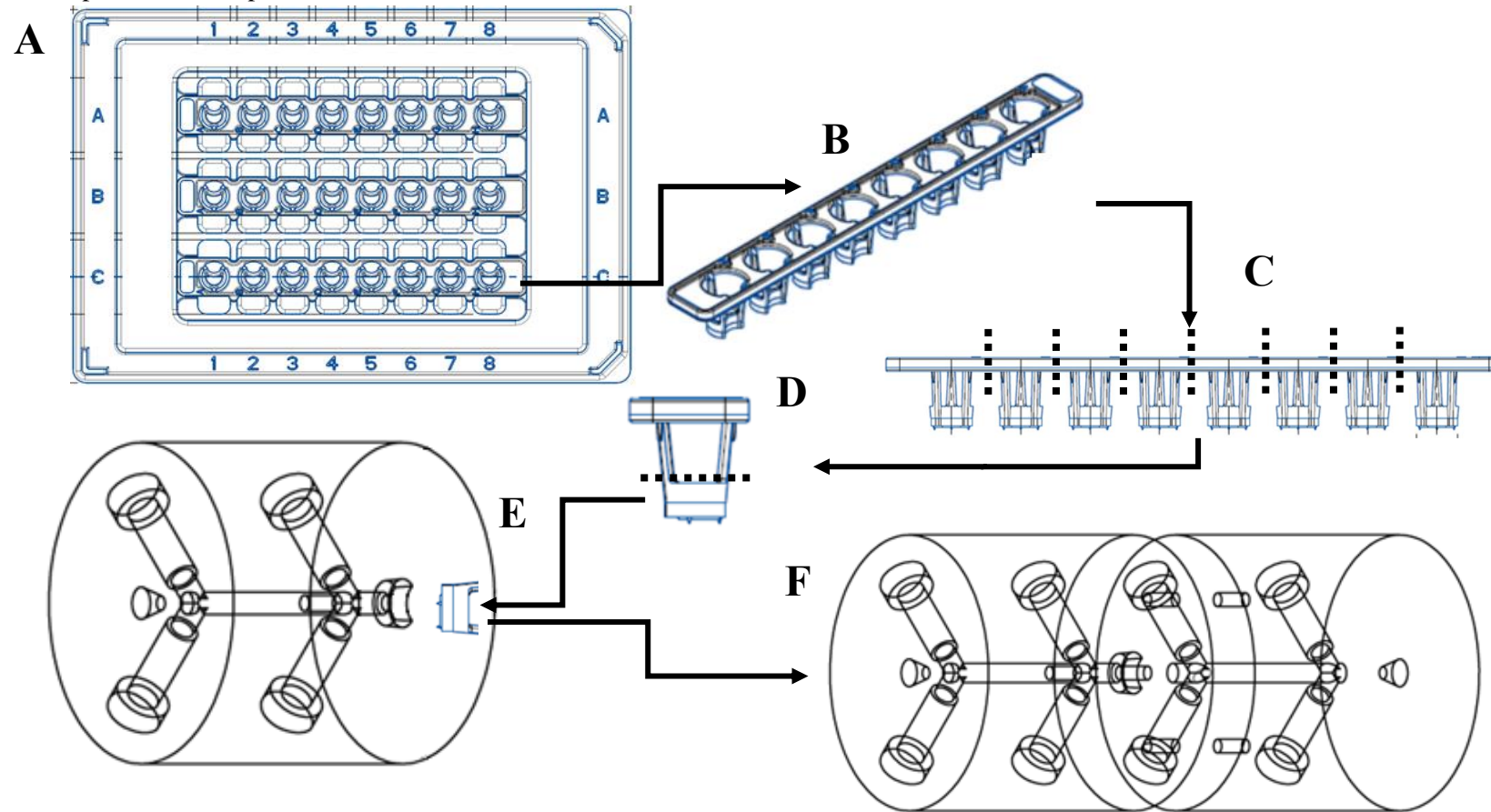


**Figure 5.39: Schematic diagram of the process require for addition of 96 well format inserts into the custom designed 96 well Ussing chamber** – A) 96 well models are cultured in the custom designed 96 well format culture plate for a total period of 5 weeks, B) After 5 weeks in culture the models are ready for analysis. Firstly, the model strip is removed from the culture plate. C) The model strip is cut along the supporting material to allow for manipulation of individual models (Depending on the total number of models being analysed only part of the strip may be cut with the rest remaining in culture until required. D) Models for use in the Ussing chamber system are first washed twice gently in sterile PBS before snipping away the remaining support material, leaving just the base insert with the heat welded Alvetex Scaffold, E) The base insert is added to the receiving Ussing chamber, ensuring a snug fit. F) The remaining chamber is attached with the model sandwiched between the two sides. The chamber system is not complete and can be attached to an Ussing chamber for model analysis.

## 5.5 Discussion

Work within this chapter has focussed on the optimisation and development of several 3D models of the intestinal epithelium utilising one of three fibroblast cell lines co-cultured with Caco-2 cells. Alvetex Scaffold® is the principle material that has been utilised in the construction of these models due to its high porosity, important for the expected function of these models as a tool for drug permeability analysis. Models have been structurally characterised here with functional analysis contained within Chapter 6. Novel equipment designed for the culture and analysis of prototype 96-well Alvetex® formats have been created for use in this work.

### 5.5.1 The properties of Alvetex® and its potential uses as a substrate for 3D culture systems.

Alvetex Scaffold® is a polystyrene polyHIPE (High internal phase emulsions) with an average void size of 42µm allowing for the culture of cells in 3D within the scaffold material.(271) The large pore size and the 200µm(272) thickness of the Scaffold allows for the culture of cells in conditions that more accurately recapitulate the *in vivo* characteristics of human tissues. A high porosity allows free cellular movement, alongside easy exchange of nutrients and cellular waste. Additionally, large pore sizes allow for culture of multiple cell lines together, initiating direct contact and permitting a level of cellular cross talk which is simply not possible in two dimensions. Indeed, throughout the literature there are many instances of models involving the utilisation of multiple cell lines within Alvetex®. For example, Forrest *et al* (273) achieved a stable co-culture through the direct co-culture of H441 Human lung epithelial cells and peripheral mononuclear cells (PMN). H441 were first cultured in the Alvetex Scaffold® at air liquid interface for a period of 14 days before the addition of PMN to the base of the model. The purpose of the experiment was to assess the rate at which these mononuclear cells could move through the 3D epithelial tissues. Whilst this model is suitable for answering the biological question of this study one would not consider this as tissue “mimetic” in the sense that simply culturing cells in 3D does not always infer *in vivo* like characteristics on the resultant model.

Outside of this work Alvetex<sup>®</sup> has been utilised for the creation of tissue mimetic models for a number of targets including; Skin (53,274), Lung (275) and Bone (276), with varying degrees of complexity and *in vivo* relevance. Generally, there are two decision branches regarding the creation of 3D models. The first involves the design and creation of a scaffold material containing all the necessary ECM components, signalling molecules and 3D structures before the addition of cells which colonise the substrate and are actively directed.(149,277,278) The second methodology, one which is utilised in this study and indeed in most Alvetex<sup>®</sup> based models, is of cell driven construction.(53,275) In short, cells are allowed to populate a Scaffold, secrete their own ECM and paracrine environment with models being allowed enough time in culture to form tissue mimetic structures spontaneously and without excessive outside direction. That is not to say there is no direction in the culture of these models entirely. The layering of cells in or model construction in this study and the use of small molecules are good examples of this.

Optimisation of the fibroblasts cultured within the Alvetex Scaffold<sup>®</sup> in this study showed a number of interesting observations regarding the variable phenotype of cells when cultures in 3D. It was observed that cellular proliferation of CCD-18co was limited in 3D resulting in a weakly colonised scaffold, unable to support a Caco-2 epithelium without significant cellular invasion. This was confirmed both by MTT assessment of fibroblast model metabolic activity and by histological analysis of cellular population of the scaffold. Previous experiments with the application of ECM proteins onto the surface of the Alvetex Scaffold<sup>®</sup> had shown that Collagen I was able to create a thin layer able to support the growth of a monolayer of Caco-2. However, it was decided that ideally, a model which was able to self-organise without the need for non-human exogenous protein application whilst also having phenotypic effects on the Caco-2 cells was an improved methodology. Additionally, use of Collagen gels increased the cost and variability of the model. Addition of fibroblasts over time was a new technique which allowed for the proper colonisation of the Scaffold, with far higher cellular retention rates and significantly lower Caco-2 invasion rates.

The ability of cells to self-direct their differentiation is also shown in the model of the Human skin by Costello and Rogers *et al*, (53,274) with clear multilayer epithelial structures highlighting how *in vivo* relevant organisation can be spontaneously formed



within a 3D cultured tissue. Again however, cells do have to be minimally instructed through the addition of TGF- $\beta$  and KGF to the culture system in order to create complex differentiation. It would be interesting to see how the addition of TGF- $\beta$  and KGF expressing cells to these models could affect the final model. Potentially, creating a true self organising model of *in vivo* complexity.

The simplicity of the Alvetex Scaffold<sup>®</sup> allows for a wide range of uses, not limited to the construction of tissue mimetic models. For example work with this substrate has included carcinoma modelling (279–282), migration studies of cells within a 3D environment (283), host pathogen interaction (284). Indeed, the simplicity of the system allows for a wide range of functions, both in terms of the study of core biological processes and in the construction of 3D systems for specific downstream applications such as drug discovery and cancer research. The power of 3D technologies such as this is that they can be tailored/ modified in many different ways to suit specific needs. Whilst no one 3D technology is perfect in all ways, the ability to modify culture substrates either through direct material chemistry (285) or protein or epitope coating (286,287) of culture substrates, broadens the use to a wide range of applications. The simple construction and use of Alvetex Scaffold<sup>®</sup> also lend itself well to high throughput applications, a necessary property for use in industrial applications such as as a tool for drug discovery and development.

Other 3D culture systems were considered for use in this study such as nanofiber membranes and hydrogel systems. Indeed, both of these methods have been utilised throughout the literature to create intestinal models of reasonable complexity and reproducibility (162,258,288–291). One of the primary benefits of electrospun scaffolds is their ease of modification. Utilisation of different plastics for example can change the hardness/ stiffness of the substrate whereas subtle changes in the manufacturing protocol can affect properties such as fibre thickness and density. polyHIPE scaffolds, as previously stated, can also boast a variety of modifications although generally these are less simple to achieve than electrospun scaffolds. (292–294) The potential application of modified scaffolds can be seen in the intestinal model created by Faralli *et al* (295) whereby they cultured Caco-2 cells on electrospun scaffolds incorporating a bioactive compound, in this case Curcumin. Cells were able to grow on the electrospun Scaffold

and were shown to be bioactive influenced by the encapsulated compound, with changes in permeability to model compounds such as Lucifer yellow and Fluorescein. One could imagine the capability to encapsulate highly tailored levels of compounds into a scaffold material in order to direct differentiation and improve functional phenotypes.

Another recent paper by Patient *et al* (269) assessed the differences in Caco-2 functional morphology between the Transwell gold standards and a PET nanofiber construct with Caco-2 cells grown on the surface. Interestingly, even though no stromal cells were present in the study, simply changing the surface architecture of the membrane on which Caco-2 cells were cultured had significant effects on the Papp values of the model drugs tested in the study with improvements in the *in vivo* characteristics of the resultant Caco-2 membrane. This highlights how small changes in 3D structure can have significant effects on the phenotype of the resultant model.

Generally, however, electrospun scaffolds do not allow for full 3D culture with the capability of the cells to fully immerse themselves into the substrate. These scaffolds are more akin to a basement membrane than a true mucosal scaffold. When studying the histology of the model produced by Patient *et al* one can see how the electrospun scaffold looks very much like Transwell, consisting of a simple layer on which the Caco-2 cells are cultured. Indeed, function follows structure in regard to the functional capabilities of cells *in vivo*. When looking at Caco-2 cells cultured on nanofiber scaffolds compared to those cultured on Transwell inserts, little difference can be seen. This is in contrast with the 3D models created here in this study which show significant changes in cellular structure compared to Transwell layers, with improvements in cellular height and polarisation of the membrane.

### **5.5.2 Optimisation of a 3D model of the intestinal epithelia utilising Alvetex Scaffold®.**

Initial investigations into the phenotype of Caco-2 cells in 3D culture demonstrated that, without additional modification to the model protocol, Caco-2 epithelial cells would invade into the top third of the Scaffold material before self-limiting their invasive

characteristics, proliferating and differentiating. There could be many possible reasons as to why Caco-2 cells lose their motile characteristics; two of the most probable being are due to the limitations of nutrient diffusion into the scaffold or reprogramming of the cellular phenotype due to the three dimensionalities of the substrate. Nutrient diffusion is difficult to quantify and will differ significantly dependant on the substrate in use. Conditions such as the material utilised to create the scaffold, the size of the molecule diffusing, its charge and its mass can all have effects on its availability.

A recent study by McMurtrey (296) took a mathematical approach to understanding the Oxygen requirements of different cells within the body and the supply rates of different tissues. He concluded that the average human cell required  $2.5 \times 10^{-18}$  mol/cell x s with the average supply rate in human tissues and hydrogels being approximately  $1 \times 10^{-10}$  to  $1 \times 10^{-9}$  mol<sup>2</sup>/s. Alvetex Scaffold® is highly porous with an average porosity of over 90%. This is far higher than would nominally be found in most tissues and hydrogels. As such it could be expected that Oxygen availability is less likely to be reducing cellular motility within the Scaffold structure.

Alternatively, although there is no direct data available here to support this observation, it has been noted that many cell lines from variable origins appear to proliferate and migrate much more slowly in Alvetex scaffold® than in 2D. The attenuation of proliferation rates can be observed in this study when looking at the seeding density and time course optimisation steps for the creation of the 3D model. In particular the time course experiments (Figure 5.11) shows no significant increases in cell metabolic rates at 14, 21 or even 28 days in culture. As such a novel multi-layering approach, seeding fibroblast multiple times over the course of 14 days was developed, allowing for more dense populations of cells within the Scaffold with an apical bias allowing for the culture of Caco-2 cells onto the stromal construct without invasion into the underlying Alvetex®. One hypothesis which could explain this phenotype is that many cell types simply differentiate upon addition to a 3D matrix, losing much of their proliferative potential in the process. Indeed, there was a high proportion of  $\alpha$ SMA positive cells (Normally utilised as a marker of myofibroblast terminal differentiation) within the 3D constructs.

Alvetex Strata<sup>®</sup> and Polaris<sup>®</sup> (Not commercially available) have increasingly smaller pore sizes allowing less invasion into the scaffold material. As such Caco-2 cells in these formats sit on the surface of the substrate without much cellular infiltration. Strata<sup>®</sup> and Polaris<sup>®</sup> substrates were not carried forward into full scale model optimisation as easy access to the internal substrate structure is needed for the culture of fibroblasts. Alvetex Scaffold<sup>®</sup> was chosen as the best candidate to allow for maximal direct cell contact and cellular crosstalk.

### **5.5.3 What does 3D tissue engineering demonstrate about the biology of tissues, understanding the limitation of 3D models.**

Most of this chapter so far has discussed how the main benefit of 3D culture is in the higher *in vivo* relevancy of the 3D substrates, allowing for cellular growth in an environment more similar to the natural state than 2D. Whilst it would be difficult to argue the converse, with, on the surface levels at least, 3D substrates appearing to be improved growth mediums than 2D culture, work so far has focussed less on the actual phenotypical changes induced by 3D culture on cells. This is true for both this work and the literature in general, with a whole multitude of 3D cellular models but little dedicated research on 3D induced phenotype changes.

Indeed, there could be an argument made to question if a 3D environment is necessary in the first place. For example, an epithelium is by definition, a polarised layer of cells. Many cellular models, not just of the intestine, already recapitulate the epithelium of tissues to a high level of complexity. A good example is of the skin where commercially available epidermal models already exist which show the multi-layered, highly differentiated cell morphology seen in *in vivo* tissues. EpiDerm<sup>™</sup> from MatTek is a great example of this with a full structure recapitulating the skin epidermis. (297) Roger *et al* (53) created both a 2D epithelial model utilising Millicell, a semi-permeable membrane similar to Transwell in structure allowing for the 2D culture of cells with some passive movement of compounds through the membrane, and a 3D cultured Alvetex model consisting of HDFn cells and keratinocytes. Histological H&E images comparing the epithelial structure of the 2D system to the 3D system in this model showed relatively

little difference in the epithelial structure of the tissue. Keratin 10 and 14 are regularly utilised markers able to show the differentiation gradient within the skin epidermis, both of which could be observed in both the 2D and 3D systems. (53)

The epithelial keratinocyte cells in the 3D Alvetex model are cultured upon a dense layer of HDFn fibroblasts and are not in physical contact with the 3D substrate. The same observations could be made with the models created in this study and it begs the question, are the changes in function due to direct 3D influences on the epithelial development or simply due to direct and paracrine influences from co-cultured fibroblasts? Influences which may or may not be modified by culture of fibroblast in a 3D environment. It is my belief that these models are more a study in the effects of fibroblasts on the physiology of cultured epithelia and the effects of 3D culture on the phenotype of cultured fibroblasts specifically rather than a study into the effects of 3D culture on tissues in general.

Due to the gold standard models now incorporating any paracrine fibroblast influences comparison of Gold standard Caco-2 models to 3D intestinal models is not a fair contrast. Fundamentally, the epithelial cells in both models are cultured in very similar ways, application onto a 2D surface. It is the addition of the paracrine effects of fibroblasts and the effects of 3D culture on those populations which is of more importance to the overall physiology of the model. Unfortunately, understanding the importance of fibroblasts within a tissue is often overlooked, even more so when it comes to determining the effects of 3D culture on their function.

### **5.5.3 Overcoming the technical limitation of 3D models by designing a method of high throughput culture and analysis.**

One general disadvantage to 3D cell culture that is often described as potentially the main factor preventing the large-scale adoption within industry, is the capability to perform high throughput culture and analysis. Often when it comes to testing new compounds large scale studies could require hundreds or thousands of models for a complete analysis. Current 3D culture systems for the high throughput analysis of model pharmacokinetics fall into two categories; 1. Organ on chip/ simplistic systems which allow for high

throughput analysis but don't recapitulate *in vivo* tissue organisation or 2. 3D cultures which recreate tissue architecture but are not best suitable for high throughput culture. Newer studies however are attempting to adapt these organ on chip systems to be more applicable to the drug screening process. For example, Workman *et al* (298) worked with iPSCs to create intestinal organoids which they applied to a chip system with direct comparison to a Caco-2 equivalent. Through western blot analysis they showed increased phosphorylation of STAT1 in response to increasing IFN- $\gamma$ , a marker of inflammatory response. This response was attenuated in Caco-2 systems compared to that of intestinal organoids. Furthermore, western blot analysis of biomarkers for both paneth and goblet cells showed marked upregulation in iPSC derived intestinal models. However, their work also displays some of the continued challenges associated with organ on chip systems. Transverse sections of the models highlight the multi-layered nature of the organoid model in this study with a clearly diminished structural organisation compared to a Caco-2 monolayer. Additionally, there was no evidence of brush border formation in the models, key for *in vivo* correlative molecular transport of chemical entities. Furthermore, large numbers of intestinal organoid cells were required for complete colonisation of the chip structure (~6 000 000 cells). This factor is of key importance for application to a pharmaceutical setting whereby large numbers of models are required for screening purposes. Adding to this is the complex nature of iPSC differentiation, further limiting this models capability of large scale manufacture.

Others such as Kasendra *et al* have created similar organ chip systems. This study focussed instead in using patient derived primary cells instead of iPSC whilst still favouring the organoid method for cellular expansion. Similarly they show villus “like” structures and in this instance, clear brush border formation. Transcriptomic analysis of their models compared to Caco-2 and Human tissue highlights clear improvements over Caco-2 in regards to gene expression, their models closely representing Human duodenum although some differences still remain, primarily in genes responsible for drug transport. Interestingly, sucrase-isomaltase activity of both their models and Caco-2 controls shows similar activity levels between models suggesting all cells are capable of differentiation into absorptive enterocytes. As with the previous example the primary challenges for this model lay in scalability to large studies. It is clear that these models provide an improved system with regards to *in vivo* correlation to intestinal tissues than

Caco-2 models (assessed by transcriptomic analysis). However, both studies lack key transporter data for the permeability to key model compounds to highlight the scale of any potential improvement. Gene analysis alone can often be misleading in regards to protein expression. Therefore further development of these models should focus on quantitative measurements of proteins such as P-gp, MRP, OCT etc.

The Alvetex Scaffold used in this study was chosen due to its relatively homogenous structure between samples and its similarity in chemical composition to 2D cell culture plastics. This has allowed for the creation a culture system for models in 96 well inserts and the capacity to analysed them through custom designed Ussing chambers.

In terms of membrane functionality, Caco-2 monolayers and 3D models are often ultimately compared to human tissue to show whether each model is more or less representative in its values for the absorption/ transport of compounds through the epithelial layer. It could be argued however that direct comparison like this is inherently flawed. The intestinal epithelium is far more complex than a 2D epithelium or even a 3D epithelium supported by sub-epithelial fibroblasts. It is the complex 3D architecture of the intestine, specifically the small intestine, that enables it to be the highly absorptive site that it is. 3D models are often more physiologically mimetic of human tissues however without the 3D architecture, 2D and 3D models are unlikely to be directly comparable to tissues in terms of functional transport even if normalised to model area due to the vast increase in surface area created by the villus crypt axis. Future work on this model should include development of a villus structure within the 3D model, possibly either through creating hydrogel templates for the surface of Alvetex or by micropatterning the Scaffold surface directly to create some level of 3D architecture.

## 5.6 Conclusions

This chapter has focussed on the optimisation, creation and construction of tools for the analysis of 3D models of the intestine based on the Alvetex Scaffold 3D culture platform. 3 models have been created in this study for the functional analysis discussed in the following chapter. These models differ in the origins of the fibroblasts utilised in order to understand the influence of the stromal compartment on the development of the epithelial

membrane. Models including cells of different origins were created to observe differences in the functionality of the resultant models which could hint to the influences these fibroblasts have during the development of the epithelium. Equipment designed and manufactured during this study will allow for the full scale analysis of 3D models going forwards in terms of both permeability/ compound transport and electrophysiology experiments.



## **6. 3D Alvetex<sup>®</sup> and paracrine Transwell model transport dynamics of CCD-18co, HDFn and HIC/ Caco-2 co-culture models.**

### **6.1 Introduction**

#### **6.1.1 Chapter goals**

Three dimensional cell culture models of many organ systems are beginning to become more popular as research tools within both academia and industrial laboratories. Generally speaking, simple 2D models are still used throughout biology due to their low cost and simplicity which allows for a high degree of automation in many cases in addition to high throughput manufacture of models for application such as compound screening purposes. Indeed, since its inception in the late 70s Caco-2 cells cultured on semi-permeable membranes are still a popular *in vitro* model utilised for the testing of intestinal cells for a wide range of applications.

This chapter and introduction will focus on advanced 2D and 3D cultured models currently recorded throughout the literature and where possible comment on the functional characteristics of these models, comparing conventionally cultured systems to actual transport seen in human tissues. The results section of this chapter will cover the functional analysis of the models created in this study, both 2D paracrine and 3D tissue models for their permeability to model drug compounds, which will be detailed in this introduction.

#### **6.1.2 Understanding the disadvantages of 2D culture and methods for improved model in vivo physiology.**

It is reasonably well known that conventional 2D cultured models do not fully recapitulate the complexity of the systems they are mimicking. Indeed, in some instances this can be seen as an advantage as it allows researchers to specifically test cells of single lineages or

populations instead of whole tissues, whose complexity can often hide the interactions being studied. However, for the majority of applications, especially those associates with testing NCE's for use in humans, there is a clear need for more complex models of human tissues than are currently available.

Bioengineered 3D models can be based on a number of technologies, with each having both advantages and disadvantages over the others. The 3D model created within the scope of this thesis for example is based on an inert scaffold technology within which cells are cultured, setting up their own molecular cross talk and micro-environments. Myofibroblast and fibroblast addition to Caco-2 models of the intestinal epithelium is an area of research which is only just seeing significant insights into the physiologically relevant effects that these cells can have on model layers. (299–301) CCD-18co fibroblast cells are the primary cell line which has been used in this study and indeed are used in the literature as tools for understanding myofibroblast influences on epithelial development in both 2D and 3D systems.

Pereira *et al* created a model of high complexity similar to what was created in this thesis by co-culturing CCD-18co, Caco-2 and HT29-MTX cells in a single 3D model. (162) CCD-18co cells were cultured within a matrigel matrix atop a Transwell membrane with Caco-2 and HT29-MTX cells directly seeded onto CCD-18co/ Matrigel layers. The results are a well-defined model with good differentiative potential as evidenced by significant microvilli formation on the apical surface of the epithelium. Additionally, TEER values of the resultant 3D models showed a physiologically relevant, significant decrease compared to control Caco-2 layers. To my knowledge, prior to work done in this study, this remains the only significant study into the effects of CCD-18co cells on Caco-2 epithelial membranes in a 3D setting. Unfortunately, as is common with the development of 3D models, the systems created by Pereira *et al* is poorly characterised, focussing on the transport characteristics of insulin only. Another disadvantage with the model created here is its reliance on exogenous matrix proteins in the models construction. Not only is Matrigel non-human in origin, it's also created from carcinoma cells and is not fully defined, with manufacturer specified inter-batch variances in protein composition. (302) Indeed, isolation of proteins from cells of tumour origin is inadvisable as ECM constituents of ECM have been shown to alter during a cancer phenotype.

(149,303) In fairness however, models created utilising the CCD-18co cell line in this study could also be suggested to contain cancer derived ECM proteins, hence why models utilising normal human fibroblasts were cultured and optimised concurrently. Regardless, the physiological changes in Pereira's model function can, at least in part, be attributed to fibroblast addition within the model, and as such lend further weight to the involvement of myofibroblast influence on epithelial development.

The 3D models created in this study and that of the aforementioned example by Pereira *et al* focussed on the addition of cells to a scaffold and allowing to spontaneous self-organisation with varying degrees of instruction. Newer methods however are being developed which are able to take some of the “guess” work out of the equation through direct bioprinting of tissue structures *in vitro*. Madden *et al* in their recent study were able to create complex 3D models consisting of both a subepithelial fibroblast compartment containing adult human intestinal myofibroblasts printed into a Matrigel hydrogel, and an epithelial layer consisting of epithelia cells isolated from ileal tissues. (28) Comparison to Caco-2 monolayers and human tissues showed a more physiologically relevant membrane structure with defined cellular junctions and clear mucous expression, something lacking from standard Caco-2 models. Analysis of gene expression showed clear differences in 3D bioprinter models compared to Caco-2 controls with a significantly more *in vivo* expression profile when compared to human tissues analysed in the same experiment.

The simplest “bio-printed” systems come in the form of organs-on-chip, whereby cells are directly printed/ cultured on a chip scaffold in the precise organisation designed by the investigator. These have a number of important advantages, primarily in that they allow for the most direct yet controlled culture of cells together to assess changes in cellular phenotype. Ultimately this makes results gained from these platforms generally highly reproducible and highly attuned to the requirements of the project. Delon *et al* utilised this chip based methodology to investigate the effects of fluid sheer stress on Caco-2 culture in a miniaturised system. (304) They designed their culture system to provide a gradient of sheer stresses over the length of the chip. Utilising this method they quantified the change in expression levels between the different sheer conditions. Large differences in actin, villin, ZO-1 and occludin expression were seen in cultured layers in

addition to changes in mucous production and, most interestingly, upregulation of CYP3A4, a protein commonly known to not be expressed by standard Caco-2 cells. Fluid stress analysis lends itself to miniaturisation as conditions can be more finely tuned than in larger scale systems.

3D printing is another area drawing significant attention (not only in biology) for the application of the construction of 3D models. Hsieh *et al* (305) demonstrated that complex 3D designs mimicking tissues in the body can be constructed utilising this approach. Seeding of these tissues with stem cells, similar to that seen in decellularised tissue scaffolds, has the potential to be a new frontier in the construction of tissue replacements in a clinical setting. There is still limitation in these systems regarding the direction of complex differentiation and the formation of tissue relevant structures before true clinical applications can be considered.(306)

The above examples utilised a scaffold based approach similar to this study whereby fibroblast cells were added to a matrix, in this case polystyrene, were cultured for a set amount of time before the addition of epithelial cells. That is not to say however that this is the only method for the creation of 3D models. Indeed, a wide variety of methods can be utilised such as organoid culture demonstrated by Sato *et al* (307) and Hans Clevers. The nature of the intestinal epithelium is one of rapid turnover and cell apoptosis, constantly making way for new cells differentiating up the villus-crypt axis. Long term stable culture of primary intestinal epithelial cells has for a long time been a goal of intestinal biologists hoping to form more *in vivo* correlating intestinal models. Stable intestinal stem cell propagation is one method whereby scientists hope to be able to recapitulate the entire epithelial morphology of the *in vivo* tissue.

Current organoid techniques for the culture of said stem cells however are ill suited for the testing of drug compounds across the surface due to a number of factors such as lack of easy access to the inter-luminal space of the organoids and relatively low transport rates per organoid unit making Papp quantification difficult to achieve. Groups in the past have attempted to create intestinal monolayers from these organoids with poor results due to increased stem cell apoptosis when cultured on monolayer cultures. Recent advances have had some success in forming monolayers of advanced complexity compared to

Caco-2 controls. Wang *et al* in their recent paper were able to culture adult colonic stem cells in a neutralised collagen hydrogel whose surface had been stamped with a mould in order to create crypt structures as part of the collagen architecture. Through application of a chemical gradient across the crypt micro architecture they were able to not only culture adult stem cell in a monolayer with physiologically relevant shape, but also recreated the stem cell niche with only those cells at the base of the crypt structure showing positive markers for stem cell pluripotency. (308) This study demonstrates the potential for the formulation of new models incorporating both *in vivo* relevant cells and 3D architecture. Wang *et al* showed a proof of concept, further studies onto the differentiation of cells within the scaffold matrix and their functional phenotype could well lead to a new advanced model of the intestine with *in vivo* like properties.

### **6.1.3 Model drugs, their mechanisms of action and relevance to this study.**

The following section overviews the model compounds used in this study to evaluate the functional characteristics of the *in vitro* models, and specifically to test Transwell paracrine and 3D Alvetex models against conventional Caco-2 Transwell monolayers. This section will detail the compounds physiologically relevant properties alongside a basic overview of the transport mechanisms within the model systems.

#### **6.1.3.1 Rhodamine 123**

Rhodamine 123 has been utilised for many years as a model substrate for MDR1/ P-gp mediated transport in the intestine and in intestinal models.(309–312) Rhodamine 123 is lipophilic and as such was assumed to pass into the cell through a transcellular mechanism, bypassing the lipid bilayer.(309) Troutman *et al* sought to confirm this assumption in their study. (309) Interestingly, they made a number of observations which contradicted the perceived knowledge in a number of ways. Firstly, they noticed that Rhodamine 123 is preferentially transported B-A and that A-B Rhodamine 123 Papp was low, approximately as low as compounds known to travel

paracellularly through tight junctions. Transportation rates were unaffected by increasing donor Rhodamine 123 concentration. Secondly, disruption of tight junction complexes by calcium/ magnesium starvation caused an increase in Rhodamine 123 transport in the A-B direction, as such insinuating that this increase in compound movement was through paracellular mechanisms. Finally, fluorescence imaging of Rhodamine 123 Caco-2 layers showed Rhodamine localisation to only the paracellular spaces in control and MDR1 inhibited A-B conditions. Entry of Rhodamine 123 into the cell in the B-A direction must then occur through a carrier mediated mechanism as membrane composition is not appreciably different on the basally than apically. Indeed, inhibition of MDR1/ P-gp resulted in an intracellular accumulation of Rhodamine 123 in the epithelial cell, further suggesting that carrier mediated uptake is not effected by standard MDR1/ P-gp inhibitors. Figure 6.1 shows a brief overview of Rhodamine 123 potential methods of transport.

The same functional phenotype has been observed by Hirsch-Ernst *et al* in rat hepatocytes, demonstrating phenotypical conservation both between species and tissues.(310) They postulated that OCT 1 may be the unknown transporter able to actively transport Rhodamine 123 across the basal membrane of cells. However, OCT 1 inhibition with Verapamil did not significantly effect Rhodamine 123 accumulation. However, as seen in this study, Verapamil is a potent inhibitor of MDR1 activity, as such overlapping protein inhibitions could potentially confuse phenotypic observations. OATP1 and 2 also appear to be potential candidates for basolateral uptake however their efficacy in this regard is as yet unknown.

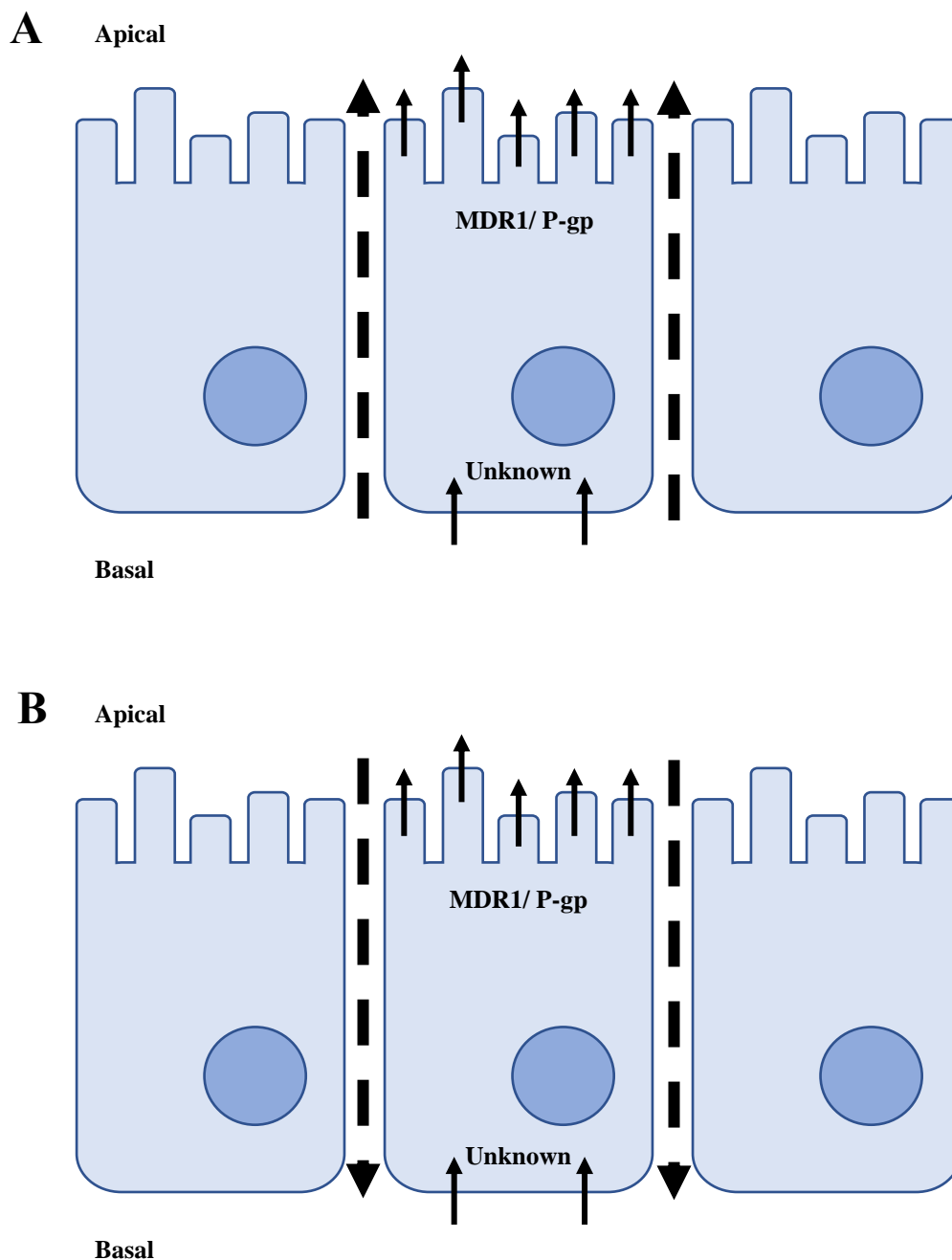


**Figure 6.1: Theoretical Rhodamine 123 permeability routes** – A) B-A directional travel is thought to move in both carrier mediated and paracellular mechanisms. B) A-B permeability is thought to be paracellularly only, with no movement of Rhodamine 123 passively across the lipid bilayer. Hashed arrows indicate passive movement, solid arrows indicate carrier mediated.

### 6.1.3.2 Atenolol

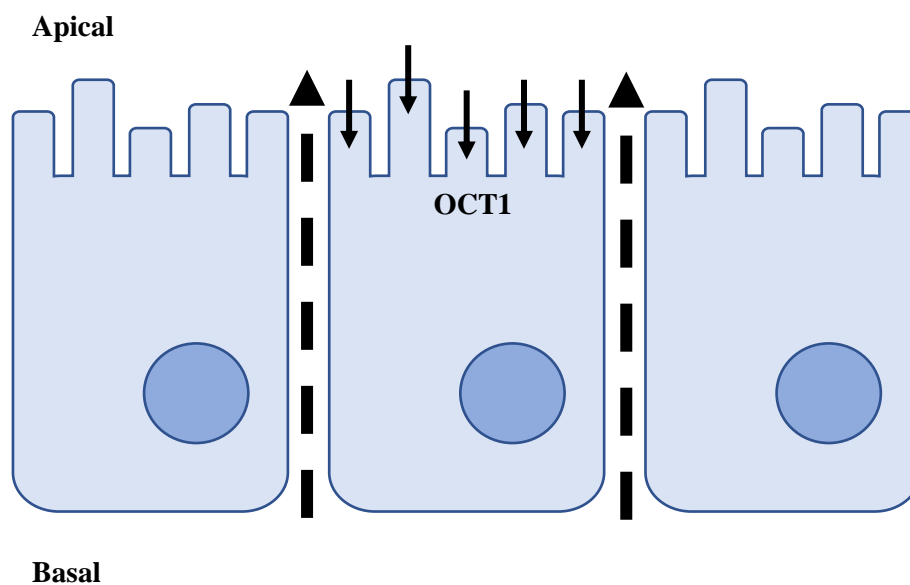
Atenolol is a hydrophilic molecule normally utilised as a beta-blocker. Atenolol in this study was used as a low permeability paracellular transported compound, as is commonly done to assess the hydrophilic transcellular absorption routes of intestinal and blood brain barrier models. (66,313–315) Essentially, due to Atenolol's highly hydrophilic nature, and hence inherent lipophobicity, it cannot easily cross the cell lipid bilayer. However, recent data does show that Atenolol may be subjected to active transport through some membrane associated transporter proteins such as OCT 1(313,315)

There is some disagreement regarding the cellular organisation of OCT 1 in human enterocytes with evidence for both basal and apical expression. (316) Han *et al* used the Caco-2 models and human and mouse enterocytes to show a bias towards apical OCT1 expression. Unlike MDR1/P-gp, OCT 1 is an uptake protein and as such, expression at the apical membrane would result in an increase in Atenolol transport into the enterocytes. However, unless a similar transporter mechanism also exists on the basolateral sides of the enterocytes, Atenolol will be limited to intercellular accumulation. As such only passive paracellular transport will be detected and reported in permeability values. Perhaps a method of fluorescently tagging Atenolol could illuminate its transport pathways as was done with Rhodamine in the previous example. If observations by Han *et al* are accurate with basally located OCT 1 expression then logically it was expected that B-A permeability will be lower than A-B due to the active uptake and accumulation of Atenolol within the cells. However, transportation experiments are conducted at or above drug saturation, as such masking the small concentration change induced by intracellular accumulation. Figure 6.2 shows a brief overview of potential transport mechanisms for Atenolol.

.



### A) B-A Transport



### B) A-B Transport

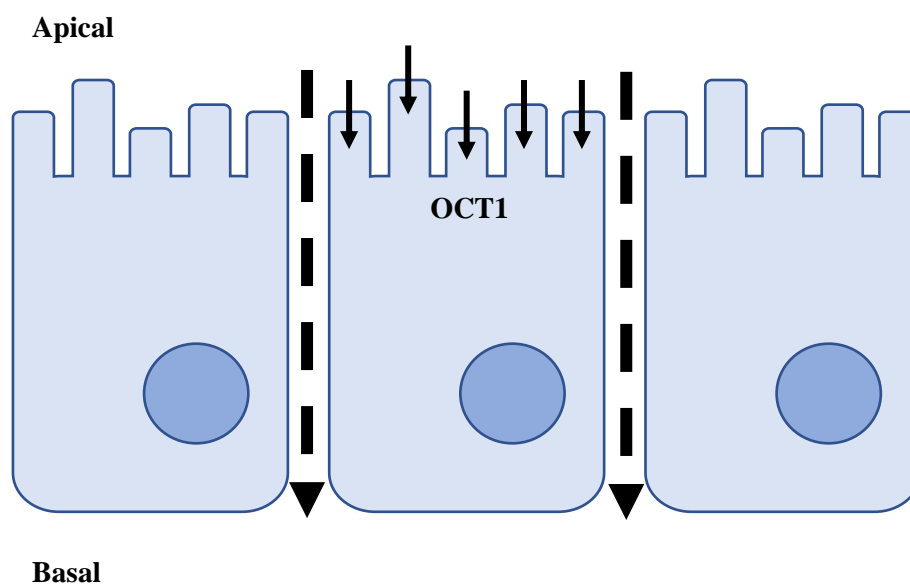


**Figure 6.2: Theoretical Atenolol permeability routes** – A) B-A directional travel is thought to move in both carrier mediated and paracellular mechanisms. B) A-B permeability is thought to favour paracellular travel. Hashed arrows indicate passive movement, solid arrows indicate carrier mediated.

### 6.1.3.3 Propranolol

Similarly to Atenolol, Propranolol is a beta blocker. Unlike Atenolol however, Propranolol is highly lipophilic and as such is thought to readily move through the epithelial lipid bilayer.(317–319) As such passive absorption rates for Propranolol are significantly higher than less lipophilic compounds. Zheng *et al* (320) conducted a study into the effects of P-gp expression on the rate of Propranolol transport in MDCK and Caco-2 cells. They found that in standard conditions efflux ratios (a measurement of directional bias) for Propranolol were less than one, indicating no bias. Interestingly, they observed that when the apical transport medium was adjusted to a slightly lower pH of 6.5 (approximate pH of the jejunum where propranolol is primarily absorbed) , afflux ratios increased to 3.63, suggesting a strong bias towards B-A transport. They attribute this change in permeability to the pH partition hypothesis, whereby weakly basic Propranolol will exist in a non-ionised form at higher pHs'. As such for Propranolol a lower pH provides a smaller driving force for membrane permeability. This assumes that only the neutral (ionised) form may easily pass through the membrane. (321) Weak bases are best absorbed in neutral pH conditions whereas acidic compounds are more readily absorbed in acidic conditions as outlined by Shore *et al*. Therefore, more acidic conditions results in less Propranolol transport. (322,323)

Whilst temperature and pH (320,324) of the transport media are known to effect Propranolol permeability there is little evidence for carrier mediated transport activity. Indeed, passive transportation through the cellular membrane occurs at such a high rate that even were Propranolol a substrate for one or more transporters, it would be difficult to observe this active transport and is unlikely to be clinically relevant. Propranolol is an excellent model compound for transcellular diffusion. However this limits the use of Propranolol because of its unsuitability for use in inhibition / tight junction integrity studies etc. Figure 6.3 summarises Propranolol transport.

## A) B-A Transport

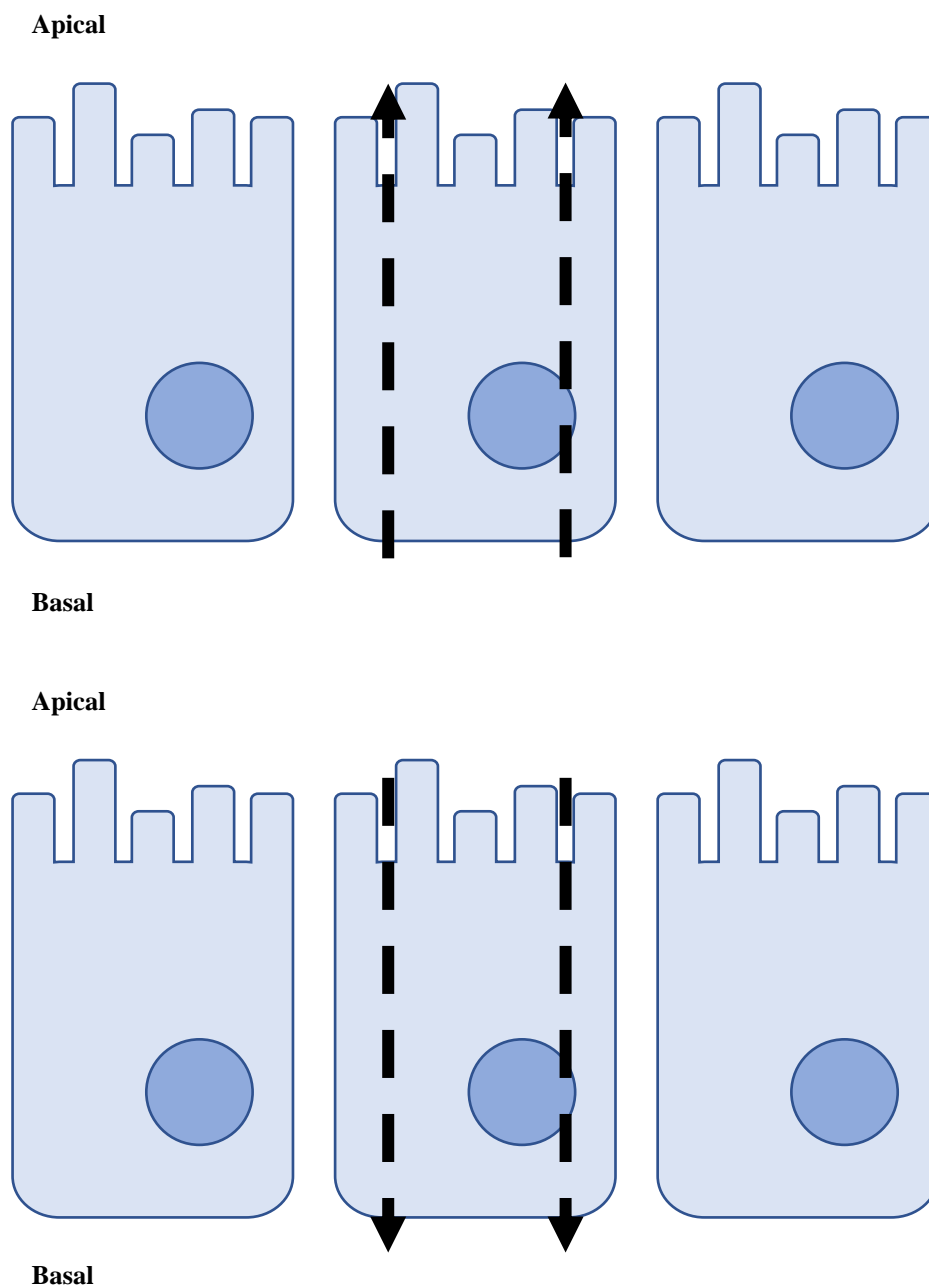
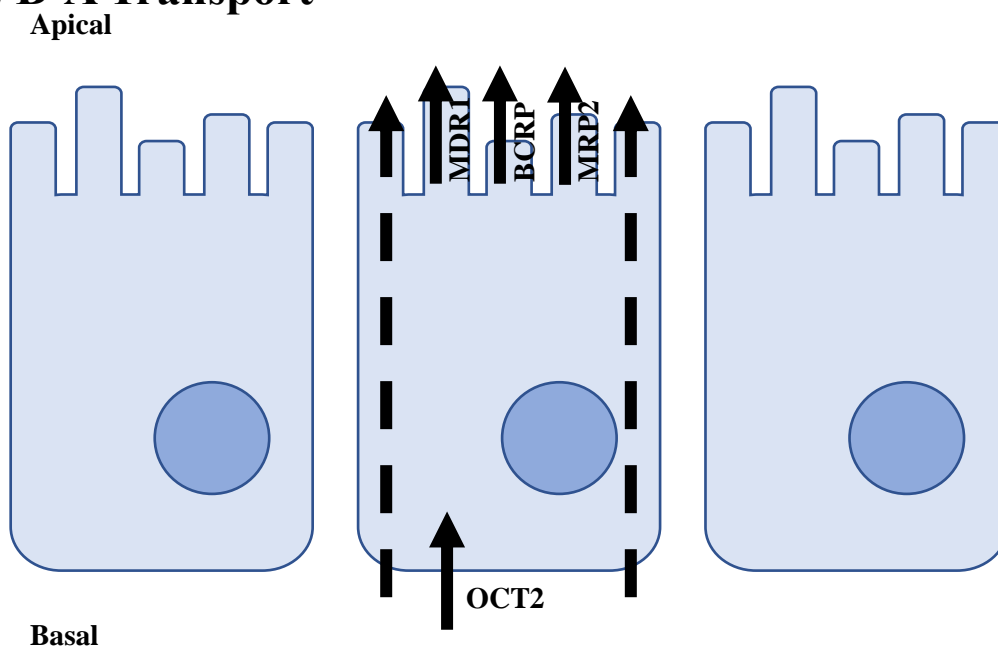


**Figure 6.3: Theoretical Propranolol permeability routes – A,B)** Both B-A and A-B directional transport is thought to be passive transcellular. Hashed arrows indicate passive movement, solid arrows indicate carrier mediated.

#### 6.1.3.4 Etoposide

Etoposide is a chemotherapeutic well known for low oral bioavailability in humans. (67) It was used as a model drug in this instance to measure the activity rate of MRP1/2. Whilst it is generally considered that MRP2 is the main transport mechanism, that is not to say that MRP family transporters are the only methods by which Etoposide is transported *in vivo/ in vitro*. (68,325) Indeed Etoposide is a substrate for many ABC transporters with significant overlap observed in the literature; including MDR1/ P-gp (326), BCRP (327) and OCT 2 (328). Kunta *et al* in their study utilising rabbit intestinal sections came to the conclusion that A-B (Absorptive) transport was not mediated to any significant extent by transporter mechanisms, whereby conversely B-A transport can be inhibited by verapamil and saquinavir. (69) Passively, Etoposide is thought to move through the lipid bilayer, transcellularly. (329) Etoposide transport mechanisms are summarised in Figure 6.4.

### A) B-A Transport



### B) A-B Transport

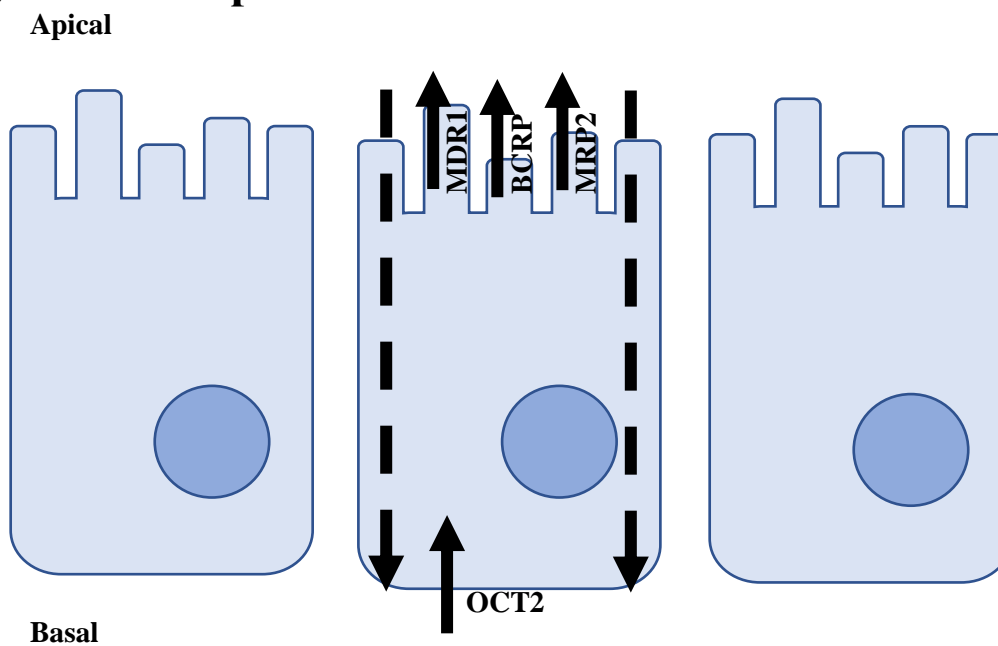


**Figure 6.4: Theoretical Etoposide permeability routes** – A) B-A, B) A-B, Transport in either direction is thought to be either through paracellular mechanisms or active transport by MDR1, BCRP or MRP2.

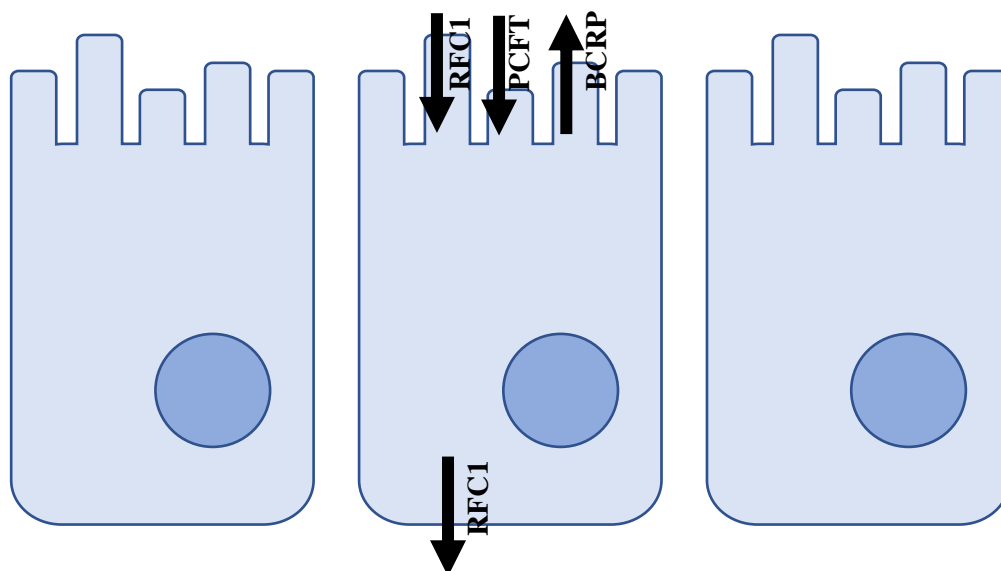
### 6.1.3.5 Methotrexate

Methotrexate is a Biopharmaceutical classification system (BCS) class III compound. Originally designed as a chemotherapeutic for use in the treatment of lymphoblastic leukaemia it has since been applied as an immunosuppressant for rheumatoid arthritis and Crohn's disease.(330) The primary clinical pharmacological mechanism is through inhibition of dihydrofolate reductase, decreasing thymine production required for mitotic cell division. Absorption is through a number of proton dependant active transport mechanisms, the two known ones being RFC and PCFT, both of which are well known to have a high affinity for Methotrexate due to its structural similarities to folate. (331) RFC is expressed in virtually all cells within the body and is the primary method by which cells are able to uptake folates. Primarily, folates and hence Methotrexate are absorbed by PCFT in the duodenum and jejunum within the acidified microenvironment at the cellular surface. (332) Methotrexate is a hydrophilic compounds and so, as such is poorly permeable through lipid bilayer membranes with long gut times required for efficient drug uptake. Novel methods for increasing gut longevity have included microencapsulation and liposome usage. Unlike other drug systems whereby some level of passive transport is seen either trans or paracellularly, Methotrexate is primarily transported by influx/efflux proteins only.

BCRP is as an active methotrexate efflux protein, (333) and is important when studying the bioavailability of methotrexate when administered orally. BCRP efflux assessment E.g Methotrexate, is the primary goal for the use of this drug in this study into the fitness of new models of the intestine to test for negative drug interactions of NCE *in vitro*. Maeda *et al* showed that methotrexate can increase membrane permeability to FD-4, a marker known for paracellular absorption.(334) As such suggesting methotrexate may behave in such a way to disrupt tight junction integrity in the intestine, (335) a common phenotype of chemotherapeutic compounds in the intestine. Methotrexate transport is summarised in Figure 6.5.

### A) B-A Transport

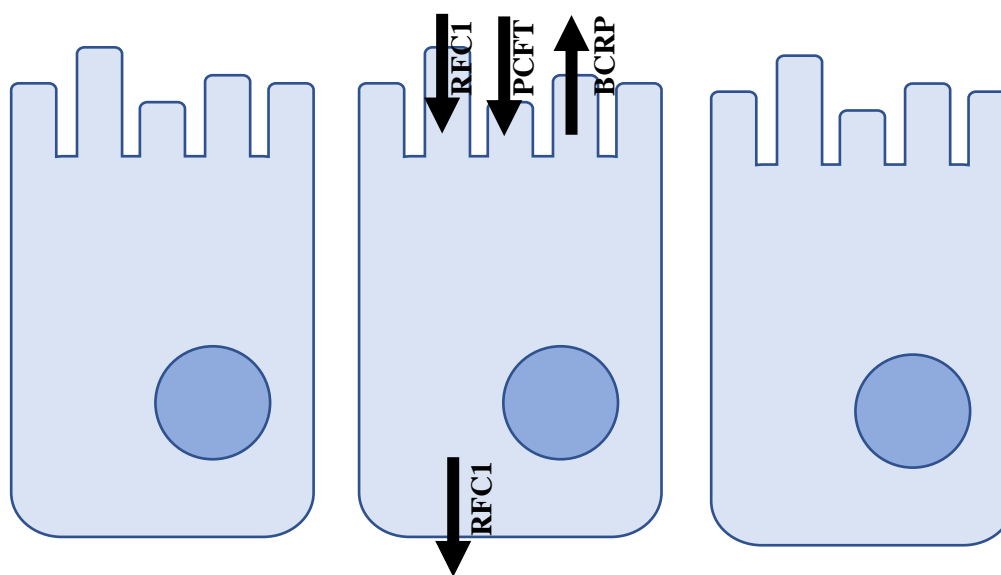
Apical



Basal

### B) A-B Transport

Apical



Basal

**Figure 6.5: Theoretical Methotrexate permeability routes** – A)B-A, B) A-B, Methotrexate is not thought to have any appreciable trans or paracellular passive movement across the epithelial layers. As such active protein action is the same in either direction with RFC and PCFT responsible for methotrexate uptake and BCRP the main efflux protein.

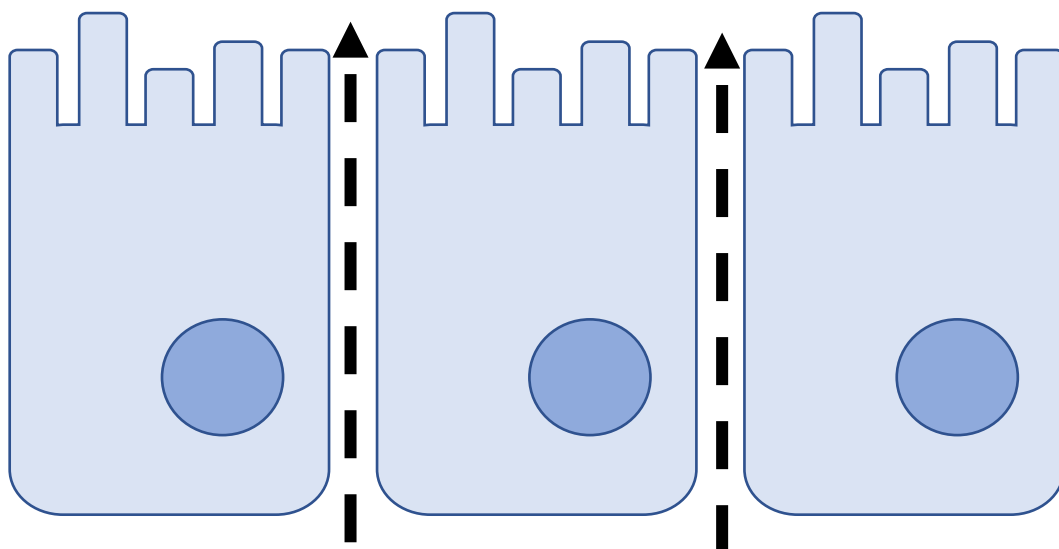
#### **6.1.3.6 Lucifer Yellow**

Lucifer Yellow is the final compound discussed in this thesis and is commonly utilised as a passive paracellular marker in the intestine and intestinal models. Lucifer yellow is a hydrophilic compound and as such as discussed earlier will not passively pass through the lipid bilayer membrane of the enterocyte. (295,336,337) Active transport of lucifer yellow is not known within the intestine although some evidence exists that suggests some cells in the body such as those in the retina are able to specifically uptake Lucifer Yellow into the cytoplasm through an unknown uptake mechanism. (90) Passive paracellular permeability of Lucifer yellow is often utilised alongside TEER as the primary methods for analysis of membrane integrity. Co-incubation of lucifer yellow with other drug compounds throughout the permeability testing is not uncommon to show a maintenance of membrane integrity through the assay. However care must be taken as molecules such as methotrexate are known to have effects on membrane passive paracellular permeability through tight junction disruption. Lucifer yellow transport is detailed in Figure 6.6



## A) B-A Transport

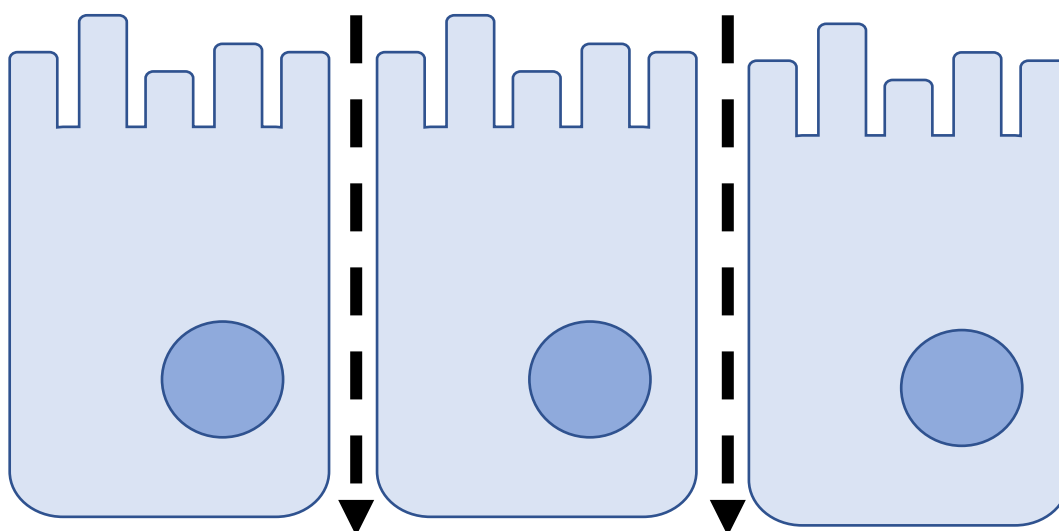
Apical



Basal

## B) A-B Transport

Apical



Basal

**Figure 6.6: Theoretical Lucifer yellow permeability routes – A)B-A, B) A-B.** Lucifer yellow is not thought to be actively transported in the intestine, movement is solely through passive paracellular pathways.

## **6.2 Hypothesis, Aims and Objectives**

### **6.2.1 Hypothesis**

It was hypothesised that conventional and paracrine cultured Caco-2 Transwell models in addition to bioengineered 3D Alvetex co-culture models, will exhibit changes in activity and enhanced function compared to conventional Caco-2 Transwell control layers widely utilised within industry as a gold standard from drug pharmacokinetic analysis.

### **6.2.2 Aims**

The aim of this Chapter is to functionally test the drug transport capabilities of the advanced Transwell paracrine culture and the 3D Alvetex co-culture models. A number of different compounds, specific to a number of different transporter proteins or as passive markers of membrane permeability have been tested to evaluate the functional characteristics of the models.

### **6.2.3 Objectives**

The objectives of this Chapter are summarised below;

- Test the transport capabilities of Transwell and Alvetex co-culture models for the following drug compounds
  - Rhodamine 123 ( ± Verapamil Hydrochloride)
    - P-gp/ MDR1 substrate and competitive inhibitor
  - Atenolol
    - Low permeability paracrine transported compound
  - Propranolol
    - High permeability Paracrine transported compound
  - Etoposide
    - BCRP substrate
  - Lucifer Yellow
    - Low permeability paracrine transported compound

- Methotrexate
  - MRP family substrate
- Calculate Efflux co-efficients for each of the drug compounds tested through analysis of the B-A compared to the A-B transport in order to understand their transport kinetics within the model systems *in vitro*.
- Where possible compare functional data generated here to human tissue data gathered from scientific literature.

## 6.3 Materials and methods

### 6.3.1 Ussing chamber permeability assessment of Transwell and 3D intestinal tissue models.

2D Transwell and 3D Alvetex® models were set up as described in Sections 2.12 and 2.15 respectively. Model permeability assays were achieved utilising the method as previously described (Section 3.2.16). Transport assay drug concentrations were as follows; Etoposide 50µM, Lucifer Yellow 100µM, Methotrexate 10µM, Propranolol 500µM, Atenolol 500µM, Rhodamine 123 5µM, Verapamil Hydrochloride 200µM. All drugs were diluted in DMSO with final DMSO concentrations in assay media of  $\leq 0.1\%$  (v/v).

### 6.3.2 Efflux Co-efficient calculation from Papp permeability values

Efflux co-efficients are a measure of the ratio between B-A (basal to apical) and A-B (apical to basal) drug transport. B-A and A-B transport values were not directly matched as no model was utilised twice for analysis (E.g. Used for both B-A and A-B transport experiments). As such B-A transport was compared to the average of the A-B transport of the same conditions. Efflux co-efficients were calculated utilising the following conventional equation;

$$Efflux = \frac{Transport_{B-A}}{Transport_{Average\ (A-B)}}$$

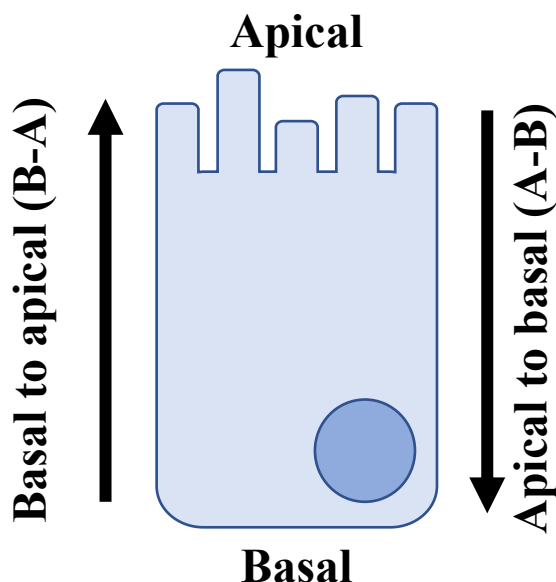


**Figure 6.7: Schematic representation of directional transport within the cells –** Directional transport to give context to directional descriptions used within the text

### **6.3.3 Electrophysiological measurements of Transwell Snapwell and 96 well Alvetex models.**

#### **6.3.3.1 Electrode manufacture**

Firstly, electrodes were created for use within the Ussing chamber devices. Electrode manufacturing procedure was as follows;

2mm diameter silver wire is carefully sanded with fine grit paper to clean the surface of dirt or corrosion. The ends of the wire not to be coated are wrapped in tape to protect the silver surface. Cleaned silver wire is submerged in bleach solution containing sodium hypochlorite over night to create a silver chloride surface coating. Electrode bodies are made from 1ml syringe tips. Current electrodes are trimmed to 3.5cm and voltage electrodes are trimmed to 3cm. A 4% Agar/ 3M KCl solution is heated in the microwave in 15 second bursts until all agar is dissolved into solution. A small hole is made in the rubber plunger of the 1ml syringe and the AgCl electrode is passed through. Pre-cut electrode bodies are filled with hot agar. Whilst the agar is molten, prepared plunger/ AgCl electrodes are pushed into the electrode body. Electrodes are allowed to cool and solidify for a minimum of 30 minutes before first use.

#### **6.3.2.2 Electrophysical measurements**

The process for electrophysiology experiments is as follows:

Carbogen gas cylinder is checked for pressure to ensure sufficient gas volume for one complete experiment (minimum of 50 PSI for a 4 chamber 3 hour experiment when using F size gas cylinders). Turn on the Power lab, Voltage clamp, circulating water bath and PC, allow to boot to desktop. Open Lab chart 8 and ensure Power lab is being correctly recognised in the system. Clean all chambers and reservoirs with appropriate solvents (Transwell Chambers can be cleaned with ethanol. 96 well Alvetex chambers cannot come into contact with ethanol under any circumstances, otherwise the plastic chamber will crack). Ensure all solvent is washed away with transport solution before experimental start.

At the beginning of each day electrode variances must be measured and corrected as follows:

Connect the chambers to the Ussing equipment without the addition of a test membrane. Fill the reservoirs with transport media to the same level as a normal transport assay (Nominally 15ml of glucose (1g/L containing HBSS per reservoir) Start the gas supply and balance the bubble output until they are approximately equal in each reservoir. Bubbles should rise at the rate whereby individual bubbles are moving just quickly enough to be seen. Ensure all transport fluid is at 37°C and that all electrodes are bubble free in the chamber and securely connected to the pre-amp before taking measurements. All electrode variance measurements can be taken on the voltage clamp output. Turn on the pre-amp. Set the voltage clamp to amplify and observe voltage measurement shown. (ensure the system is at the correct temperature before moving forward) Using the offset knob, either add or subtract from the system until the voltage reading shows zero (If the voltage shown is very high, < 2 mV, check for bubbles in the system which block correct circuit completion.)



**Figure 6.8: Representative images of Ag/Cl electrodes used in electrophysiological studies** – electrodes were made from 1ml syringe tips filled with 3M KCl 4% agar solution. Silver wire was coated with silver chloride through submersion in sodium hypochlorite bleach solution.

To correct for fluid resistance, hold down the push to adjust button, notice a new value for voltage shown on the voltage clamp. Whilst holding down the push to adjust button turn the fluid resistance knob until the value shows zero. Switch the measurement on the voltage clamp to measure current. Whilst pressing down the push to adjust button, the measurement should show  $68\mu\text{A}$  ( $\pm 3\mu\text{A}$ ). If  $68\mu\text{A}$  is shown switch back to measure voltage, the chamber is now correctly blanked. If not  $68\mu\text{A}$  check current electrodes for bubbles.

Remove all liquid from the chamber reservoirs. Add the model to the chamber. Carefully, fill the reservoirs with transport media using a 50ml syringe attached to 2mm capillary tubing. Ensure the capillary tubing is as far down the reservoir as possible (close to the test membrane) and slowly fill to avoid model disruption. Make sure bubble lift is moving correctly and no bubbles are lodged in the system that might disrupt drug transport or provide electrical insulation. Check cylinder pressure to ensure sufficient gas pressure remains for full experiment (~2.5 hours). Leave models in the chamber for 30 minutes as a minimum to acclimatise. In order to detect changes in the electrochemical properties of the membranes, models were current clamped to zero volts before being injected with  $10\mu\text{A}$  every 9 seconds for a duration of 1 second (10 second total per cycle). This is achieved by turning the master switch on the voltage clamp from amplify to Int. timer and ensuring the rotary dials are set up for 9 and 1 second durations. Ensure secondary timer is set to current clamp and that the clamp value is set to  $10\mu\text{A}$ . This can be checked by measuring current and waiting for the 1s  $10\mu\text{A}$  spike which can be read and checked on the voltage clamp directly. If doing electrochemical measurements start lab chart at this point. PC must be connected to the internet before lab chart will correctly open. One in the software open a new experimental file. Each pre-amp channel is connected to a corresponding channel on the power lab. Each power lab channel will be shown in the new experimental software. The voltage of each channel from the corrected electrodes will be measured throughout the experiment. Membrane resistance can be calculated by measuring the voltage deflection and dividing by the known injected current. Voltage is recorded throughout the experiment and voltage deflections caused by the injected current were used to calculate the membranes short circuit current and resistance. Drugs are added to reservoirs with time and concentration dependant on the experiment.

At the end of the experimental timecourse stop lab chart recording, save the file, set the voltage clamp to amplify and turn the pre-amp off. Remove reservoir transport media by slowly unscrewing the model chamber. Allow the volume to drip out slowly over the course of a few minutes into a receiving pot. Models cannot be removed and processed as required. Ensure all chambers are washed with hot water followed by an appropriate solvent (ethanol for Transwell, water for Alvetex) immediately.

37°C water baths should be cleaned and water changed regularly with microbe inhibiting products. Reservoirs were unhooked from the entire system once per month for a soak overnight in soapy water to clean any possible biological matter residue.



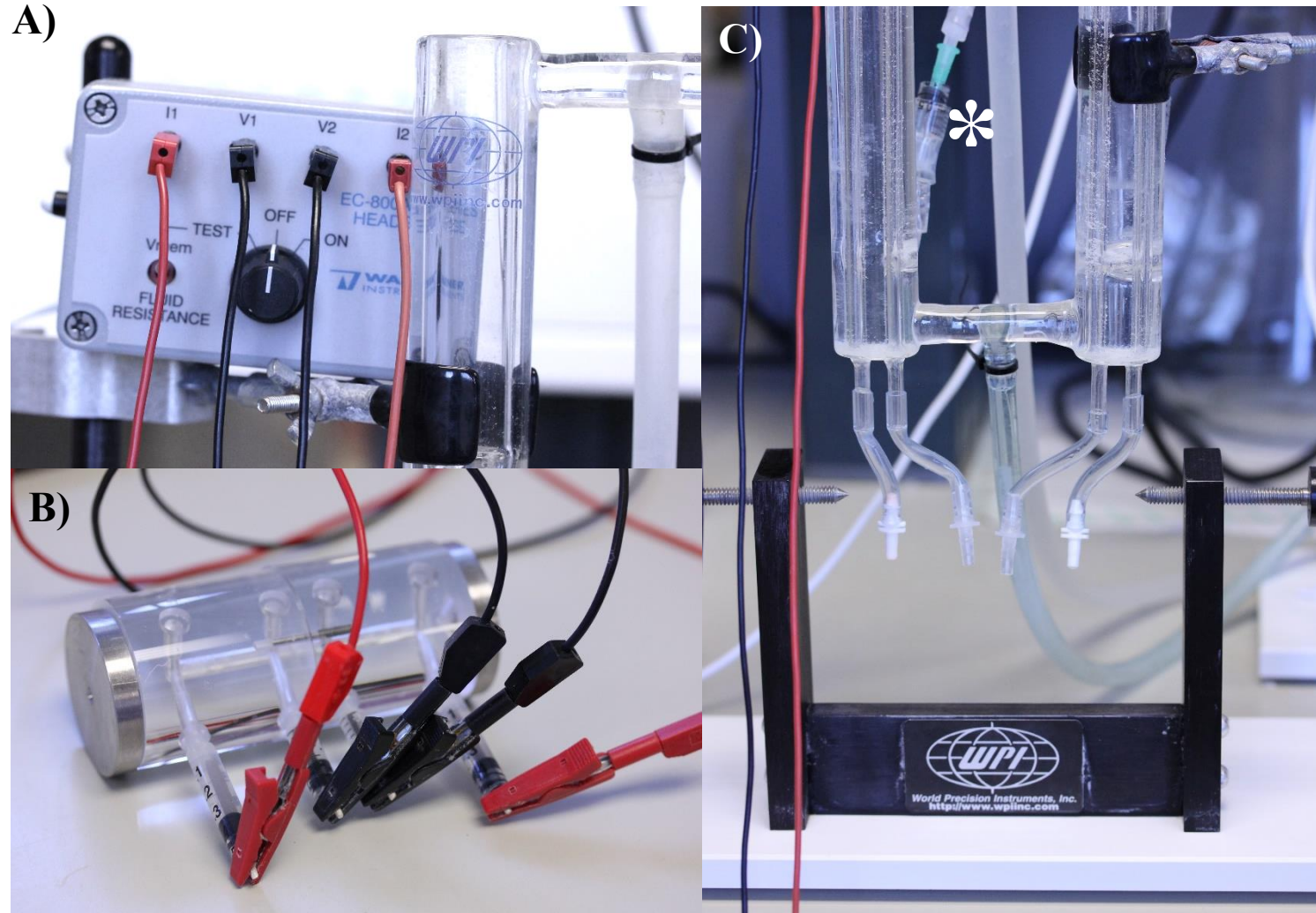


**Figure 6.9: Representative images of Ussing equipment utilised in this study – A) Pre-amp, B) 96 well Ussing chamber set-up, placed together but not within the Ussing chamber, C) Base of the reservoir showing the attachment points of the reservoir to the chamber. Gas input points into the system can also be seen (\*).**

## 6.4 Results

### 6.4.1 Transepithelial resistance measurements of 3D models compared to conventional Caco-2 standards and Human small intestinal sections.

Figure 6.10 shows the relative TEER assessment of 3D Alvetex® Caco-2 fibroblast models compared to the TEER vales of both control and paracrine conditioned media 2D Transwell based Caco-2 systems and typical small intestine resistance data taken from the literature.(338,339) Compared to the 2D control layers the 3D intestinal models all showed a drastic decrease in the overall resistance of the membrane with decreased between 30-40 times lower than seen in controls.

In 3D, intestinal models incorporating either CCD-18co and HIC fibroblast cells had similar effects on effects on overall model trans-membrane resistance with significant decreases in both instances. This is in contrast to the paracrine work shown in Chapter 3 whereby the paracrine effects of both CCD-18co and HIC fibroblasts decrease TEER differentially, with HIC conditioned media only having a small effect on over all model resistance. HDFn 3D models also resulted in a significant reduction in membrane TEER similar to other fibroblast formats albeit at a slightly lesser level than seen in CCD-18co or HIC models. Compared to human tissues however (typical values taken from the literature, (340–342) it is clear that the decrease in overall TEER values seen in 3D models are significantly more similar to that seen *in vivo* with the average small intestinal tissue resistance of around 50 Ohms.cm<sup>2</sup> (dependant on the region of small intestine tested).

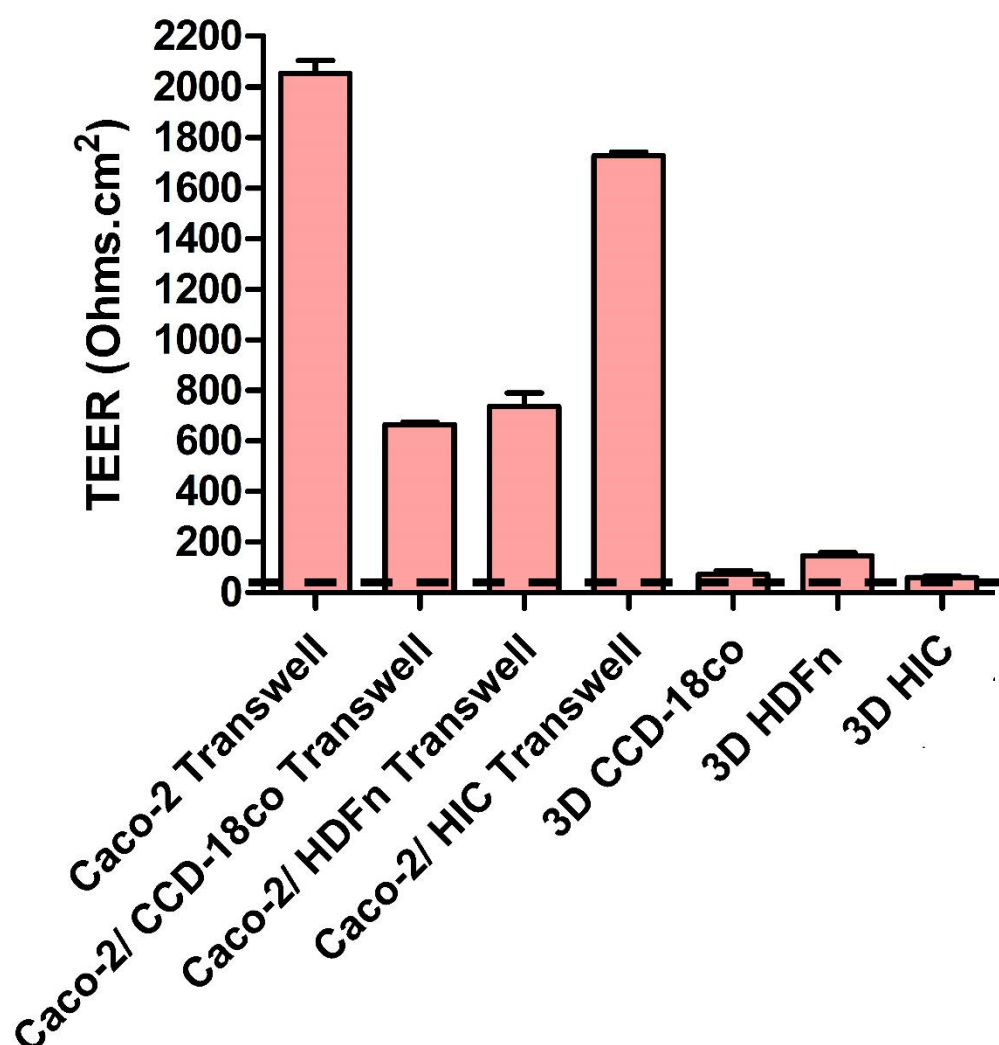


**Figure 6.10: TEER Values of 3D intestinal models shows a significant physiological decrease in TEER compared to conventional 2D Caco-2 Transwell models** – 3D models created using the Alvetex® based 3D culture system show a 30-40 fold decrease in TEER values compared to Caco-2 Transwell culture systems. Ussing chamber analysis of Human tissues derived from the literature show an average tissue resistance of 50-100 ohms.cm<sup>2</sup>. This is represented on the graph with a hashed line. n=4-10 + SEM for test data. N=3-4. n=3 for data found in the literature. Statistical significance is summarised in Table 6.1

3D CCD-18co vs Caco-2 Transwell	***	3D HIC vs Caco-2/ HDFn Transwell	***
3D CCD-18co vs Caco-2/ CCD-18co Transwell	***	Caco-2 Transwell vs Small intestine	***
3D CCD-18co vs Caco-2/ HIC Transwell	***	Caco-2 Transwell vs Caco-2/ CCD-18co Transwell	***
3D CCD-18co vs Caco-2/ HDFn Transwell	***	Caco-2 Transwell vs Caco-2/ HIC Transwell	***
3D HDFn vs Caco-2 Transwell	***	Caco-2 Transwell vs Caco-2/ HDFn Transwell	***
3D HDFn vs Caco-2/ CCD-18co Transwell	***	Small intestine vs Caco-2/ CCD-18co Transwell	***
3D HDFn vs Caco-2/ HIC Transwell	***	Small intestine vs Caco-2/ HIC Transwell	***
3D HDFn vs Caco-2/ HDFn Transwell	***	Small intestine vs Caco-2/ HDFn Transwell	***
3D HIC vs Caco-2 Transwell	***	Caco-2/ CCD-18co Transwell vs Caco-2/ HIC Transwell	***
3D HIC vs Caco-2/ CCD-18co Transwell	***	Caco-2/ HIC Transwell vs Caco-2/ HDFn Transwell	***
3D HIC vs Caco-2/ HIC Transwell	***		

**Table 6.1: TEER expression comparison between Transwell and 3D intestinal models -**  
Individual significances calculated by one way ANOVA with Tukeys post-test analysis 99% confidence rating. \*\*\* = P<0.0001, \*\* = P<0.001, \* = P< 0.01 n=4-10

## 6.4.2 Rhodamine 123 transport and Verapamil Hydrochloride

### MDR1/P-gp inhibition in Caco-2 Snapwell conditioned media models.

Figure 6.12 deals with the Transwell model (control and conditioned) aspect of the full Characterisation only. Figure 6.12 A shows the apparent permeability ( $P_{app}$ ) of Rhodamine 123 in B-A directions for Control Caco-2 Transwell models and paracrine media treated Caco-2 Transwell models. Additionally, the effects of Verapamil Hydrochloride, a known P-gp/ MDR1 inhibitor, added to the system at the beginning of the assay are also shown (Blue bars). Figure 6.12 B shows the same data conditions as A

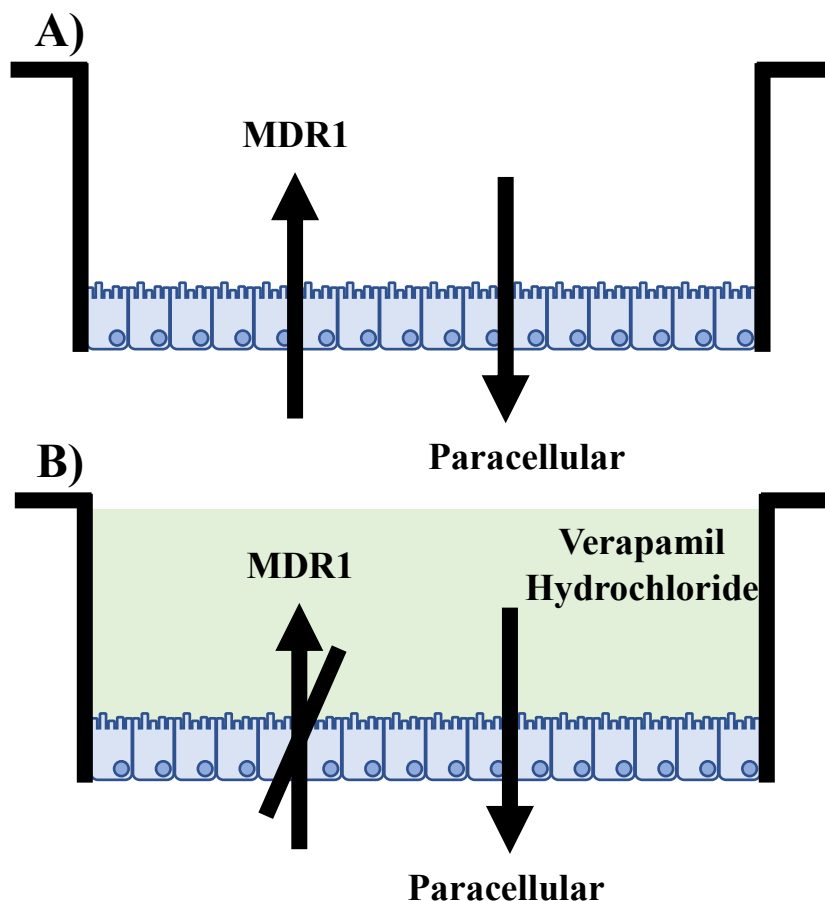


**Figure 6.11: Schematic representation of the transport processes being studied in this experiment** – A) A simple overview of the expected mechanisms involved in Rhodamine 123 transport in systems uninhibited with Verapamil hydrochloride. Main B-A transport is expected to be MDR1 mediated with any A-B transport paracellular in nature. B) shows the effects of the addition of verapamil hydrochloride to the assay system. MDR1 mediated transport is expected to be inhibited.

but in the A-B permeability direction. In control layers Rhodamine 123 is primarily transported B-A with higher B-A Papp compared to the converse. Addition of Verapamil hydrochloride to the assay system decreases Rhodamine 123 apparent permeability when measured in the B-A direction by approximately 60%. Overall, this suggests that Rhodamine 123 transport is primarily through an MDR1/ P-gp directed mechanism, at least in control Transwell models.

Paracrine CCD-18co treated Transwell monolayers show a similar transport phenotype with directional transport biased towards B-A. Importantly, overall Rhodamine 123 permeability between conventionally cultured Transwell controls and CCD-18co conditioned media treated Transwell models is not induced to increase. Similarity as in control models, Rhodamine 123 permeability is efficiently inhibited through treatment with Verapamil Hydrochloride, with a decrease in Rhodamine 123 transport of approximately 75%. Whilst overall Rhodamine permeability is not significantly increased in CCD-18co treated Caco-2 model cultures the increase in inhibitory effect of Verapamil hydrochloride suggests that a higher proportion of transport in CCD18co treated models is MDR1/ P-gp mediated compared to controls.

HDFn paracrine effects on Rhodamine 123 Papp shows a very similar phenotype to both control and CCD-18co treated layers as described above with B-A transport bias. However, B-A transport in HDFn treated monolayers is significantly higher over the control with a Papp of around  $3.5 \times 10^{-6} \text{ cms}^{-1}$  compared to the control values of approximately  $1 \times 10^{-6} \text{ cms}^{-1}$ , SEM however means that this change is not significant. The increased permeability phenotype is almost entirely reversed with the addition of Verapamil hydrochloride providing strong evidence for MDR1/ P-gp again for upregulation in HDFn treated models.

Unlike other model conditions tested, HIC treated models have a slightly lower average Rhodamine 123 Papp level compared to controls and other tested conditions at approximately  $0.3 \times 10^{-6} \text{ cms}^{-1}$ . In spite of this however, the directional polarity of the models is maintained with a clear bias towards B-A transport. Moreover, addition of Verapamil hydrochloride to the assay did not affect Papp Rhodamine 123 rates in HIC models. It was hypothesised that MDR1/P-gp levels are significantly decreased in HIC

conditions models and that the low levels of Rhodamine 123 transport can be attributed to passive paracellular permeability and limited expression of related protein transporters with a degree of cross over substrate specificity with MDR1/P-gp which are not inhibited by verapamil hydrochloride. However, evidence for some small level of MDR1/P-gp function is shown in HIC conditioned media by the slight (non-significant) increase in Rhodamine 123 permeability in inhibited A-B assays. The primary method of A-B directional permeability is through passive paracellular mechanisms. Inhibition of MDR1/P-gp in A-B transport studies would logically increase A-B transport as MDR1/P-gp activity would not work against the passive paracellular transport.

Significance values for both 2D Transwell paracrine models are summarised in Table 6.2.

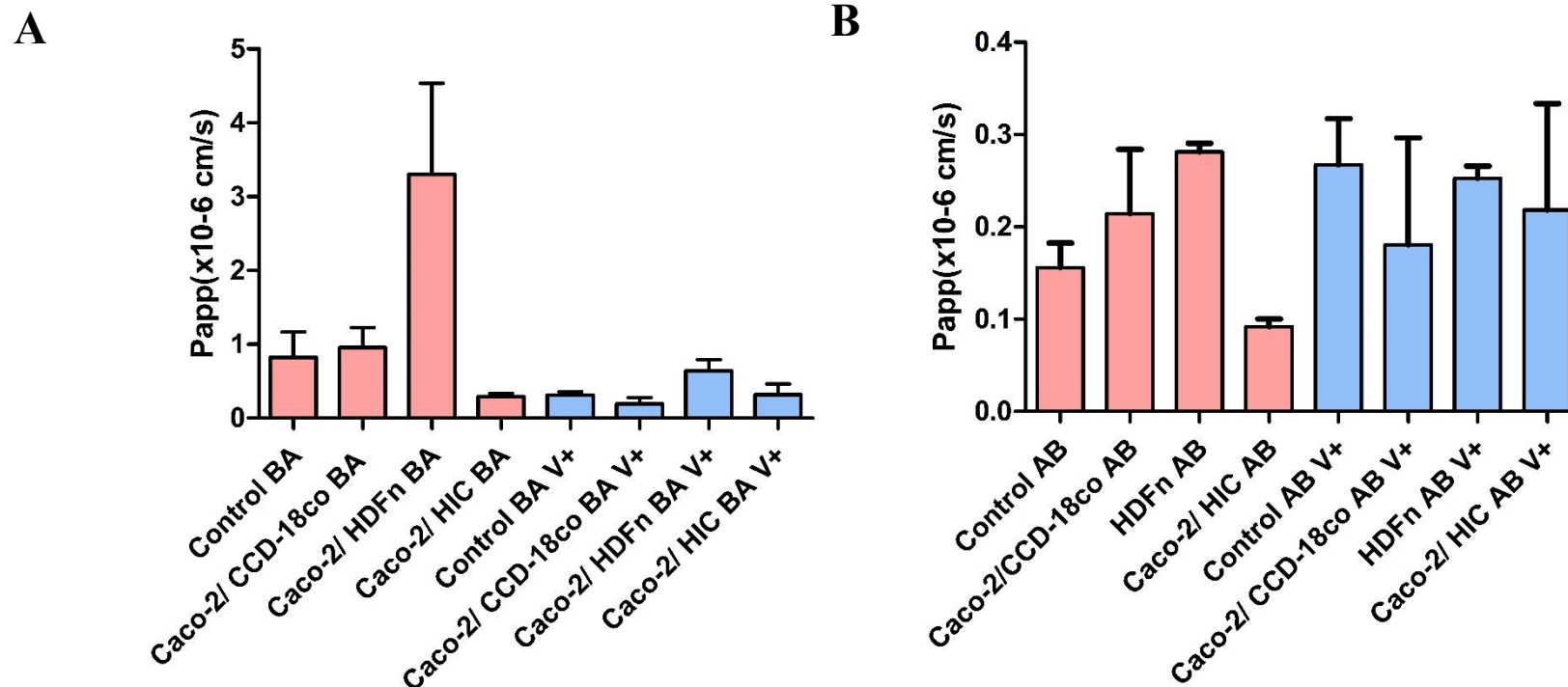


**Figure 6.12: Comparative analysis of Rhodamine 123 transport across Control and paracrine media treated Caco-2 membranes shows a significant increase in Rhodamine 123 transport in HDFn treated Caco-2 layers** – A) Values gained for B-A transport in each culture condition compared to permeability in the presence of Verapamil hydrochloride (V+), B) Values gained for A-B transport in each culture condition compared to permeability in the presence of Verapamil hydrochloride (V+). Verapamil hydrochloride was added to the epithelial layers to test compound specificity to P-gp/ MDR1 mediated transport. n=3 N=3 HDFn V+ n=2 +SEM N=2 Significance is summarised in table 6.2.



Control BA vs Control BA V+	ns	Control AB vs Control AB V+	ns
Control BA vs Caco-2/ CCD-18co BA	ns	Control AB vs Caco-2/CCD-18co AB	ns
Control BA vs Caco-2/ CCD-18co BA V+	ns	Control AB vs Caco-2/ CCD-18co AB V+	ns
Control BA vs Caco-2/ HIC BA	ns	Control AB vs Caco-2/ HIC AB	ns
Control BA vs Caco-2/ HIC BA V+	ns	Control AB vs Caco-2/ HIC AB V+	ns
Control BA vs Caco-2/ HDFn BA	ns	Control AB vs HDFn AB	ns
Control BA vs Caco-2/ HDFn BA V+	ns	Control AB vs HDFn AB V+	ns
Control BA V+ vs Caco-2/ CCD-18co BA	ns	Control AB V+ vs Caco-2/CCD-18co AB	ns
Control BA V+ vs Caco-2/ CCD-18co BA V+	ns	Control AB V+ vs Caco-2/ CCD-18co AB V+	ns
Control BA V+ vs Caco-2/ HIC BA	ns	Control AB V+ vs Caco-2/ HIC AB	ns
Control BA V+ vs Caco-2/ HIC BA V+	ns	Control AB V+ vs Caco-2/ HIC AB V+	ns
Control BA V+ vs Caco-2/ HDFn BA	ns	Control AB V+ vs HDFn AB	ns
Control BA V+ vs Caco-2/ HDFn BA V+	ns	Control AB V+ vs HDFn AB V+	ns
Caco-2/ CCD-18co BA vs Caco-2/ CCD-18co BA V+	ns	Caco-2/CCD-18co AB vs Caco-2/ CCD-18co AB V+	ns
Caco-2/ CCD-18co BA vs Caco-2/ HIC BA	ns	Caco-2/CCD-18co AB vs Caco-2/ HIC AB	ns
Caco-2/ CCD-18co BA vs Caco-2/ HIC BA V+	ns	Caco-2/CCD-18co AB vs Caco-2/ HIC AB V+	ns
Caco-2/ CCD-18co BA vs Caco-2/ HDFn BA	ns	Caco-2/CCD-18co AB vs HDFn AB	ns
Caco-2/ CCD-18co BA vs Caco-2/ HDFn BA V+	ns	Caco-2/CCD-18co AB vs HDFn AB V+	ns
Caco-2/ CCD-18co BA V+ vs Caco-2/ HIC BA	ns	Caco-2/ CCD-18co AB V+ vs Caco-2/ HIC AB	ns
Caco-2/ CCD-18co BA V+ vs Caco-2/ HIC BA V+	ns	Caco-2/ CCD-18co AB V+ vs Caco-2/ HIC AB V+	ns
Caco-2/ CCD-18co BA V+ vs Caco-2/ HDFn BA	*	Caco-2/ CCD-18co AB V+ vs HDFn AB	ns
Caco-2/ CCD-18co BA V+ vs Caco-2/ HDFn BA V+	ns	Caco-2/ CCD-18co AB V+ vs HDFn AB V+	ns
Caco-2/ HIC BA vs Caco-2/ HIC BA V+	ns	Caco-2/ HIC AB vs Caco-2/ HIC AB V+	ns
Caco-2/ HIC BA vs Caco-2/ HDFn BA	*	Caco-2/ HIC AB vs HDFn AB	ns
Caco-2/ HIC BA vs Caco-2/ HDFn BA V+	ns	Caco-2/ HIC AB vs HDFn AB V+	ns
Caco-2/ HIC BA V+ vs Caco-2/ HDFn BA	ns	Caco-2/ HIC AB V+ vs HDFn AB	ns
Caco-2/ HIC BA V+ vs Caco-2/ HDFn BA V+	ns	Caco-2/ HIC AB V+ vs HDFn AB V+	ns
Caco-2/ HDFn BA vs Caco-2/ HDFn BA V+	ns	HDFn AB vs HDFn AB V+	ns

**Table 6.2: Significance values from Rhodamine 123 ±Verapamil Hydrochloride permeability studies of Transwell conditioned media models – B-A and A-B data sets were analysed for significance separately. Individual significances were calculated by one-way ANOVA with Tukeys post-test analysis with 95% confidence rating. \*\*\* = P<0.0005, \*\* = P<0.005, \* = P< 0.05**

### **6.4.3 Rhodamine 123 transport and Verapamil Hydrochloride MDR1/ P-gp inhibition in 3D Caco-2/ Fibroblast bioengineered intestinal equivalents.**

The effects of fibroblast conditioned media on the Rhodamine 123 permeability of Transwell Caco-2 model systems were shown to cause a range of changes in the functional phenotype of the resultant intestinal model. Results in this section focus on the application of the fibroblasts into a 3D cultured stromal epithelial system, designed for the co-culture of multiple cell types into a structurally physiological intestinal model.

Figure 6.14 shows the comparative function of 3D Alvetex intestinal models compared to conventionally cultured control Caco-2 Transwell model function. Figure 6.14 A shows the comparative effects of 3D Alvetex culture compared against control Transwell layers, the gold standard in the B-A permeability direction. Similarly, Figure 6.14 B shows data in the A-B permeability direction. When first considering the B-A direction alone (the primary expected direction of travel for MDR1/ P-gp mediated Rhodamine 123 transport) it was clearly shown that 3D CCD-18co cultures show a much higher permeability than Transwell controls. 3D CCD-18co A-B shows a trend to be lower than B-A values however this change is non-significant due to the large data variation. Furthermore, only a small decrease in overall membrane permeability is seen when models are assayed with the addition of verapamil hydrochloride in B-A and no change at all in the A-B direction. Overall this suggests two things about the function of the epithelium in CCD-18co bioengineered Caco-2 intestinal models compared to conventionally cultured Caco-2 Transwell systems. 1. B-A permeability, whilst increased is not completely due to proportional increases in MDR1/P-gp expression rates because of similar increases in A-B permeability and incomplete inhibition when tested in the presence of Verapamil hydrochloride. 2. Increases in non-inhibitable Rhodamine permeability suggest either increased levels of similar (non-inhibitable) efflux proteins to MDR1 of which Rhodamine 123 shows some degree of substrate specificity or increased passive paracellular permeability. If one compares the TEER values gained from 3D

model systems compared to Transwell Caco-2 models, both conventional and modified, increases in paracellular permeability are not to be unexpected. In either regard increases in both B-A and A-B direction are a welcome change when compared to control Caco-2 Transwell layers. Because Caco-2 Transwell models are known to underestimate MDR1/P-gp and are generally less paracellularly permeable than intestinal tissues. Results shown here suggest that both of these deficiencies may be improved upon with CCD-18co bioengineered 3D Alvetex<sup>®</sup> intestinal models.

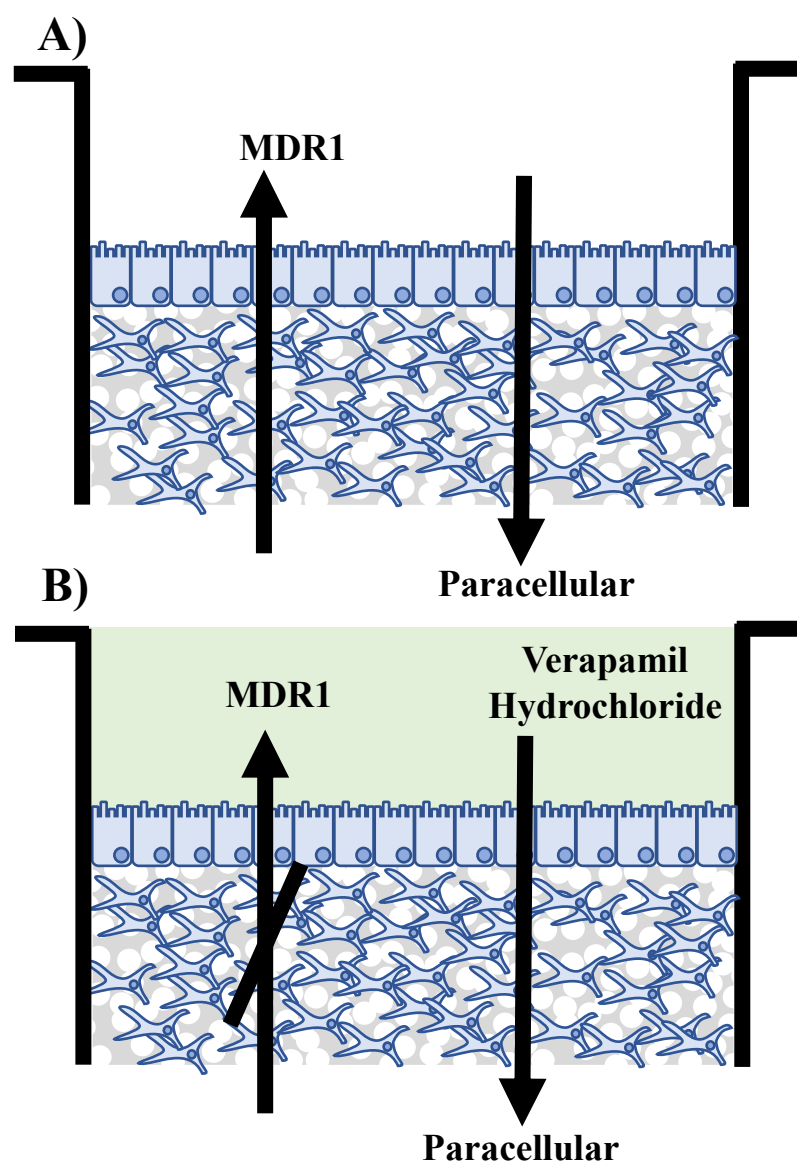


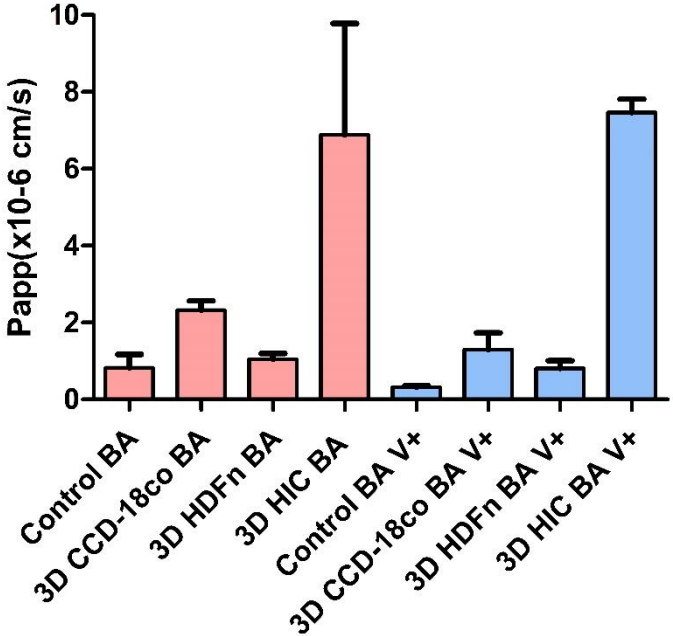
**Figure 6.13: Schematic representation of the transport processes of 3D Alvetex systems being studied in this experiment – A) A simple overview of the expected mechanisms involved in Rhodamine 123 transport in systems uninhibited with Verapamil hydrochloride. Main B-A transport is expected to be MDR1 mediated with any A-B transport paracellular in nature. B) shows the effects of the addition of verapamil hydrochloride to the assay system. MDR1 mediated transport is expected to be inhibited.**

3D HDFn models shows a similar pattern with no significant deviations in permeability between directions of travel or indeed with the addition of Verapamil hydrochloride. One main difference however is in the overall permeability of the membrane. Whereas CCD-18co models showed a significant increase compared to Transwell controls, this improved functional phenotype is attenuated in HDFn cultured models potentially suggesting that

models decrease their active MDR1/ P-gp transporter expression whilst increasing their passive permeability rates.

Similarly to CCD-18co cultured models, HIC models show a trend towards a large increase in B-A membrane permeability compared to conventionally cultured Transwell controls. A-B permeability was also increased when compared to conventionally cultured controls however was lower than HIC 3D model B-A values. Unfortunately, due to model variation this difference is not significant, a seemingly common issue with the use of 3D models, which are inherently more variable than simple 2D counterparts. Again, as seen in other 3D models conditions, addition of verapamil hydrochloride does not appear to have any effect on the rate of B-A membrane permeability suggesting non-MDR1/P-gp mediated Rhodamine 123 Transport. Interestingly, addition of Verapamil Hydrochloride to the A-B direction in HIC 3D models results in a further significant decrease in membrane permeability compared to uninhibited 3D A-B transport to a level similar to that seen in control Transwell models. This is somewhat unexpected as inhibition of MDR1/P-gp should logically increase A-B transfer compared to uninhibited assays. A decrease in A-B transport when inhibited would suggest two hypothesis. 1. Verapamil Hydrochloride inhibits a mechanism involved in actively transporting Rhodamine 123 A-B. 2. Verapamil Hydrochloride rapidly upregulates an active efflux protein able to transport across B-A. Either option would seem unlikely suggesting a different mechanism entirely may be at play.

**A**



**B**

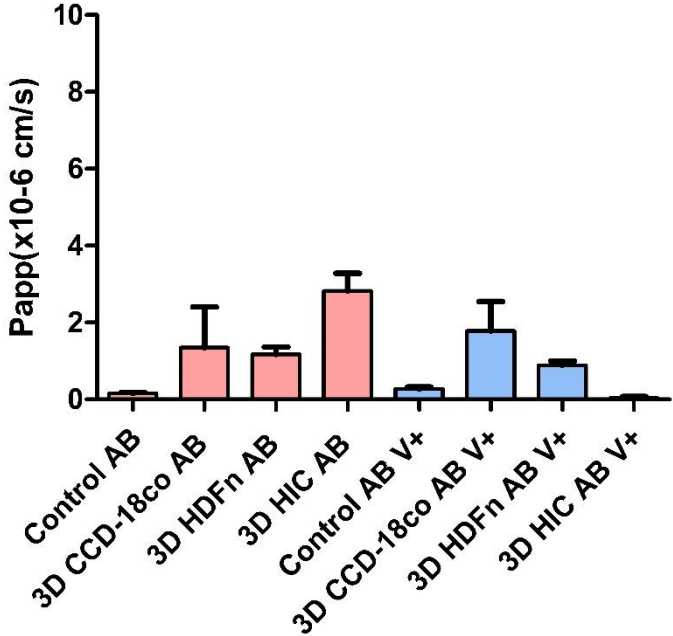


**Figure 6.14: Comparative analysis of Rhodamine 123 transport across Control and 3D Alvetex Caco-2/ Fibroblast intestinal tissue equivalents shows a large increase in Rhodamine 123 membrane permeability in CCD-18co and HIC 3D models –** A) Comparative B-A Papp values between Caco-2 Transwell controls and B-A values from Alvetex<sup>®</sup> based inetstinal models.. B) Comparative A-B Papp values between Caco-2 Transwell controls and A-B values from Alvetex<sup>®</sup> based intestinal models. Generally, 3D models were shown to be more permeable to Rhodamine 123 than Caco-2/ Transwell controls. Addition of Verapamil Hydrochloride did not appear to have any significant effects on reducing membrane Rhodamine 123 permeability. n=3 +SEM. N=3 Significancys are summerised in table 6.3

Control BA vs Control BA V+	ns	Control AB vs Control AB V+	ns
Control BA vs 3D CCD-18co BA	ns	Control AB vs 3D CCD-18co AB	ns
Control BA vs 3D CCD-18co BA V+	ns	Control AB vs 3D CCD-18co AB V+	ns
Control BA vs 3D HDFn BA	ns	Control AB vs 3D HDFn AB	ns
Control BA vs 3D HDFn BA V+	ns	Control AB vs 3D HDFn AB V+	ns
Control BA vs 3D HIC BA	ns	Control AB vs 3D HIC AB	**
Control BA vs 3D HIC BA V+	ns	Control AB vs 3D HIC AB V+	ns
Control BA V+ vs 3D CCD-18co BA	ns	Control AB V+ vs 3D CCD-18co AB	ns
Control BA V+ vs 3D CCD-18co BA V+	ns	Control AB V+ vs 3D CCD-18co AB V+	ns
Control BA V+ vs 3D HDFn BA	ns	Control AB V+ vs 3D HDFn AB	ns
Control BA V+ vs 3D HDFn BA V+	ns	Control AB V+ vs 3D HDFn AB V+	ns
Control BA V+ vs 3D HIC BA	ns	Control AB V+ vs 3D HIC AB	**
Control BA V+ vs 3D HIC BA V+	ns	Control AB V+ vs 3D HIC AB V+	ns
3D CCD-18co BA vs 3D CCD-18co BA V+	ns	3D CCD-18co AB vs 3D CCD-18co AB V+	ns
3D CCD-18co BA vs 3D HDFn BA	ns	3D CCD-18co AB vs 3D HDFn AB	ns
3D CCD-18co BA vs 3D HDFn BA V+	ns	3D CCD-18co AB vs 3D HDFn AB V+	ns
3D CCD-18co BA vs 3D HIC BA	ns	3D CCD-18co AB vs 3D HIC AB	ns
3D CCD-18co BA vs 3D HIC BA V+	ns	3D CCD-18co AB vs 3D HIC AB V+	ns
3D CCD-18co BA V+ vs 3D HDFn BA	ns	3D CCD-18co AB V+ vs 3D HDFn AB	ns
3D CCD-18co BA V+ vs 3D HDFn BA V+	ns	3D CCD-18co AB V+ vs 3D HDFn AB V+	ns
3D CCD-18co BA V+ vs 3D HIC BA	ns	3D CCD-18co AB V+ vs 3D HIC AB	ns
3D CCD-18co BA V+ vs 3D HIC BA V+	ns	3D CCD-18co AB V+ vs 3D HIC AB V+	ns
3D HDFn BA vs 3D HDFn BA V+	ns	3D HDFn AB vs 3D HDFn AB V+	ns
3D HDFn BA vs 3D HIC BA	ns	3D HDFn AB vs 3D HIC AB	ns
3D HDFn BA vs 3D HIC BA V+	ns	3D HDFn AB vs 3D HIC AB V+	ns
3D HDFn BA V+ vs 3D HIC BA	ns	3D HDFn AB V+ vs 3D HIC AB	*
3D HDFn BA V+ vs 3D HIC BA V+	ns	3D HDFn AB V+ vs 3D HIC AB V+	ns
3D HIC BA vs 3D HIC BA V+	ns	3D HIC AB vs 3D HIC AB V+	**

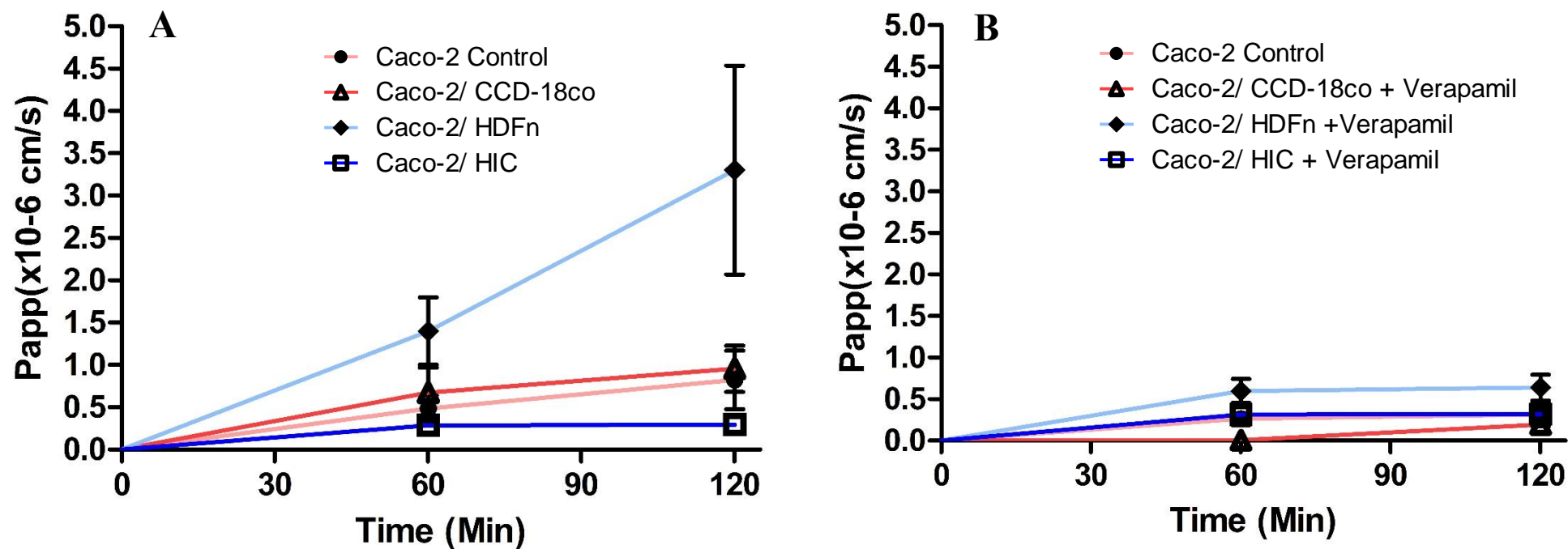
**Table 6.3: Significance values from Rhodamine 123 ±Verapamil Hydrochloride permeability studies of Transwell control compared with Alvetex® based intestinal models** – B-A and A-B data sets were analysed for significance separately. Individual significances were calculated by one-way ANOVA with Tukeys post-test analysis with 95% confidence rating. \*\*\* = P<0.0005, \*\* = P<0.005, \* = P< 0.05

#### **6.4.4 Timecourse analysis of Rhodamine permeability across conventionally and conditioned cultured Transwell models and 3D bioengineered co-culture systems.**

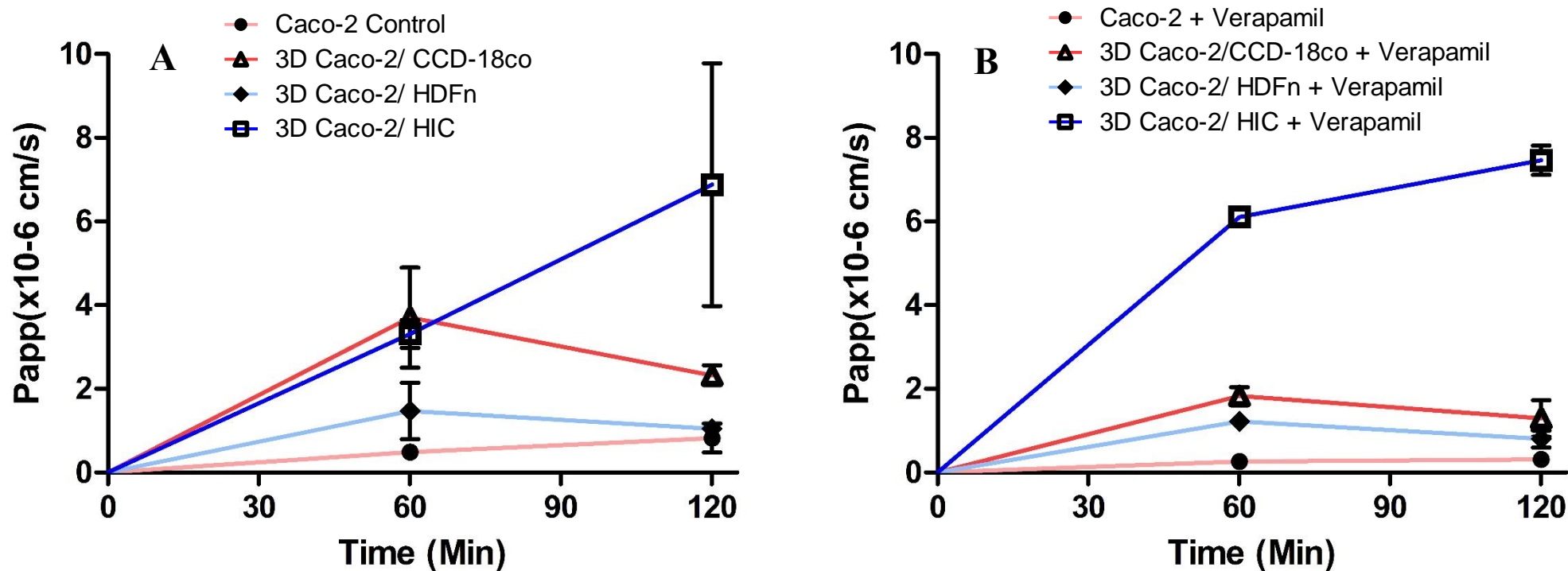
Figure 6.15 shows the permeability of Caco-2 Transwell models to Rhodamine 123 with timepoints taken at 0 (blank), 60 and 120 minutes. Figure 6.15 A shows control timecourse permeability changes, whereas, Figure 6.15 B shows Verapamil Hydrochloride inhibited cell culture layers. The purpose of this analysis is to assess whether permeability over time is linear or as seen here, dependant on time in culture. The main observation is that the rate of Rhodamine 123 transport increases between the 0 and 60 minute timepoints with often, the maximal Papp value for the culture actually occurring at the 60 minute timepoint. Between 60 and 120 minutes in assay, permeability levels plateau with no additional increases in the rate of Rhodamine transport. Caco-2/HDFn the only condition seen to not follow this observable trend.

Figure 6.16 A and B show the same analysis with 3D cultured Alvetex models rather than conditioned media models. A similar overall trend is observed albeit at the higher permeability values of 3D cultures. Where HDFn was the observable anomaly in Transwell cultures, Figure 6.16 A and B clearly shows that in 3D Alvetex conditions, Caco-2/ HIC models show a more linear change in Rhodamine permeability compared to other conditions. It is important to note that a plateau of Papp does not mean that active transport is not occurring, just that the rate of active transport is stable or saturated. A linear change in Papp increase could indicate that Rhodamine Transport is not yet saturated, potentially suggesting high levels of active transporters although variability in 3D models is generally higher than those seen in 2D.





**Figure 6.15: Time course analysis of Rhodamine 123 permeability in paracrine Transwell models throughout the assay period shows a general rapid increase in permeability followed by a plateau phase whereby permeability values stop increasing - A) B-A Conditioned media Transwell models, B) B-A Conditioned media Transwell models with the addition of Verapamil Hydrochloride throughout the assay process. All data is n=3 N=3, HDFn V+ n=2, N=2±SEM**



**Figure 6.16: Time course analysis of Rhodamine 123 permeability in 3D Alvetex tissue equivalent models throughout the assay period shows a general rapid increase in permeability followed by a plateau phase whereby permeability values stop increasing – A) B-A 3D Alvetex models, B) B-A 3D Alvetex models with the addition of Verapamil Hydrochloride throughout the assay process. All data is n=3 N=3, ±SEM**

### **6.4.5 Efflux co-efficient value calculation and analysis to show directional bias in Rhodamine 123 transport within 2D Transwell and 3D Alvetex® intestinal models.**

Figures 6.17 and 6.18 show the efflux co-efficient analysis of both 2D (Figure 6.17) and 3D intestinal cultures (Figure 6.18) Rhodamine 123 Ussing chamber transport. Efflux co-efficients are simply calculated by comparing the Papp values of B-A transport compared to permeability in the A-B direction. For example a co-efficient permeability value of 2 would suggest that the B-A direction of travel was favoured over the A-B direction exactly 2-fold, with twice as much compound transport B-A.

Analysis of Figure 6.17 shows how significant B-A bias is seen in both Control and CCD-18co conditioned media cultures. In both cases this is more pronounced at the 120 minute timepoint rather than at 60 minutes. Addition of Verapamil Hydrochloride to the culture system results in a significant decrease in the efflux co-efficiency to approximately one, suggesting no transport bias of the membranes. This suggests either a significant inhibition of B-A transport or an increase of Rhodamine 123 transport in the A-B direction in verapamil treated model assays. It was known from previous data analysis that changes in efflux co-efficient are likely influenced by both with the former being the largest driver of change.

Efflux co-efficients levels of HDFn and HIC conditioned media layers, whilst still for the most part above a value of 2 (suggesting B-A bias) are lower than their control and CCD-18co counterparts. This suggests that Rhodamine 123 permeability in these models is likely to be MDR1/P-gp mediated to a large extent, due to the comparative ratio between B-A and A-B permeability values, but not to the level as control and CCD-18co fibroblast treated systems which have a higher ratio of B-A/ A-B permeability. Addition of Verapamil Hydrochloride to HDFn and HIC cultures had no significant effects on efflux co-efficient when compared to uninhibited efflux co-efficient values. This suggests that Rhodamine 123 transport in these instances occurred at a similar ratio (B-A/A-B) as in untreated HDFn and HIC model assays. As such, Rhodamine 123 transport in these

instances is more likely through a method not inhibited by Verapamil Hydrochloride, insinuating transport may not be due to MDR1/ P-gp mediated mechanisms alone.

Figure 6.18 shows an analysis of the changing efflux co-efficient seen in 3D co-culture models of the intestinal epithelium. Generally, 3D cultured Alvetex models didn't show a significant bias to any particular direction of molecular movement through the membrane. This is not to say that there was no transport, indeed 3D bioengineered models were regularly shown to have increased Rhodamine 123 permeability across epithelial layers compared to conventionally cultured control Transwell values. As seen previously, addition of Verapamil Hydrochloride didn't have any significant effects on the directional bias of Rhodamine 123 transport except in 3D HIC models whereby a large increase in efflux co-efficient was observed suggesting a high B-A bias in molecular transport. Tables 6.3 specify the significance values of 2D conditioned media and 3D Alvetex models respectively between different model conditions.

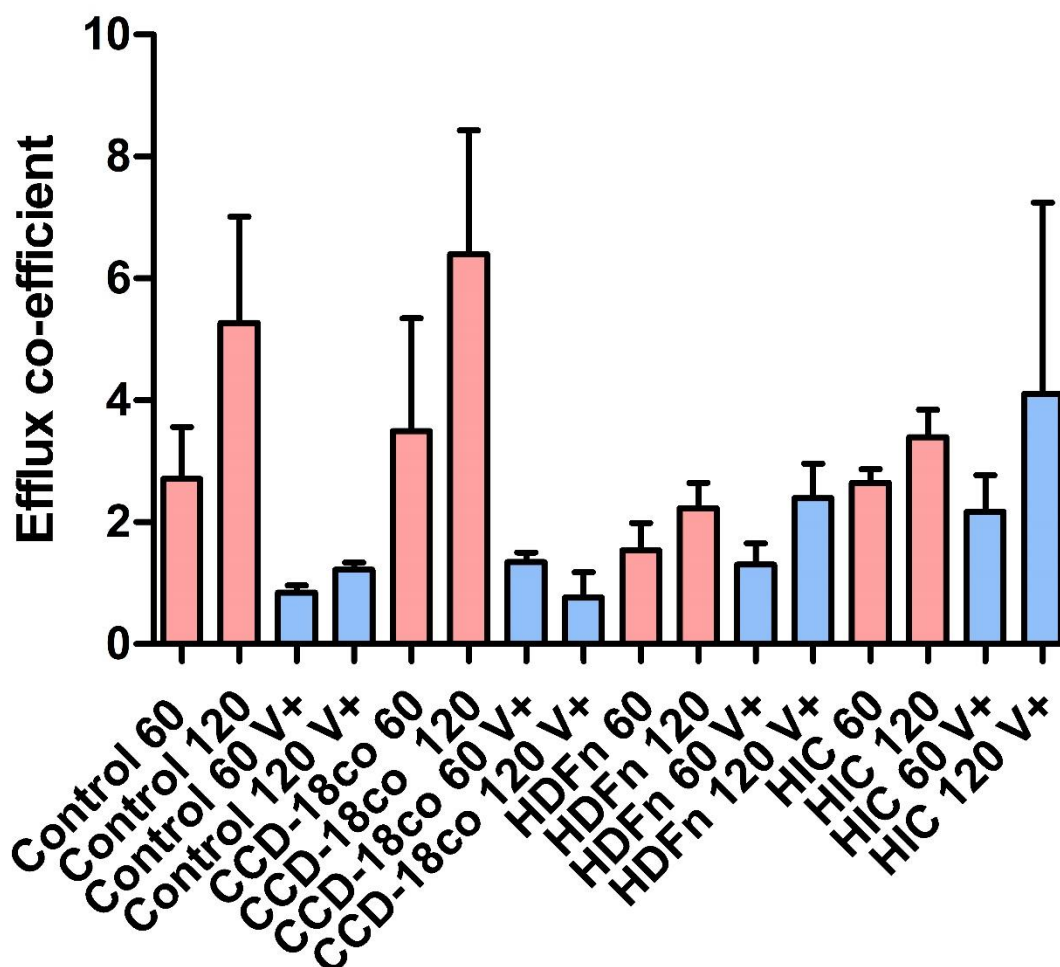


**Figure 6.17: Efflux ratio permeability calculation of 2D Transwell paracrine models for Rhodamine 123** - Efflux ratio is described as a calculation to decide whether bias exist between differential direction of molecular movement in a drug transport assay system. Values over 2 suggest movement in the B-A direction is at least double that of the A-B direction. All uninhibited model layers show significant B-A bias. Addition of Verapamil Hydrochloride in most instances reduces this B-A bias significantly except in the case of HDFn and HIC conditioned layers where no significant change is observed. n = a minimum of 3 independent repeats. HDFn V+ n=2, N=2 +SEM

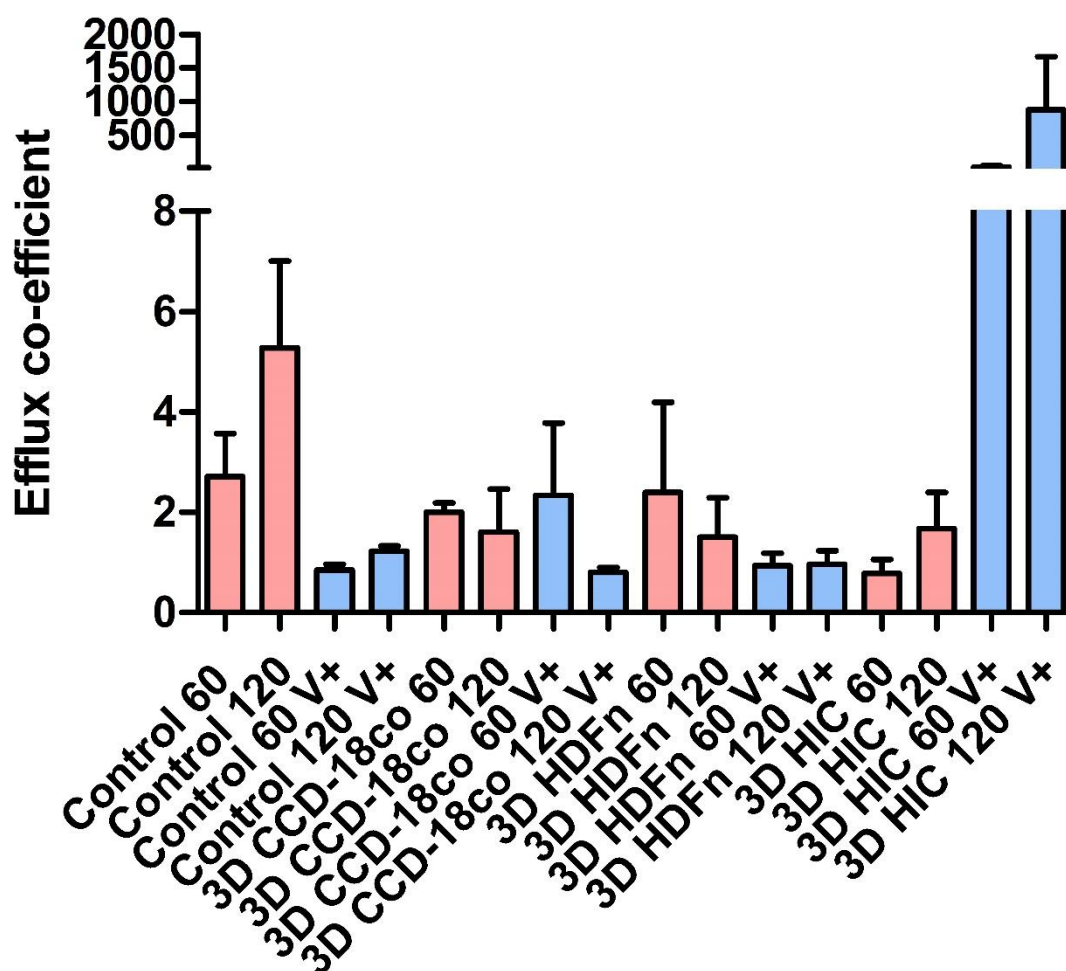


**Figure 6.18: Efflux ratio permeability calculation of 3D Alvetex Caco-2/ Fibroblast models for Rhodamine 123** - Values for 3D Alvetex intestinal models generally speaking are shown to be below 2 in CCD-18co and HDFn instances. HIC models show extremely high Efflux co-efficient values when treated with verapamil hydrochloride, an unusual phenotype not readily explained by data gained in this study. n= a minimum of 3 independent repeats. 3D CCD-18co non-inhibited and 3D HIC models V+ n=2, N=2 +SEM

Chapter 6 –Assessment of 2D and 3D model function

Control 60 vs 3D HIC 120 V+	***	Caco-2/ HIC 60 V+ vs 3D HIC 120 V+	***
Control 120 vs 3D HIC 120 V+	***	Caco-2/ HIC 120 V+ vs 3D HIC 120 V+	***
Control 60 V+ vs 3D HIC 120 V+	***	3D CCD-18co 60 vs 3D HIC 120 V+	***
Control 120 V+ vs 3D HIC 120 V+	***	3D CCD-18co 120 vs 3D HIC 120 V+	***
Caco-2/ CCD-18co 60 vs 3D HIC 120 V+	***	3D CCD-18co 60 V+ vs 3D HIC 120 V+	***
Caco-2/CCD-18co 120 vs 3D HIC 120 V+	***	3D CCD-18co 120 V+ vs 3D HIC 120 V+	***
Caco-2/ CCD-18co 60 V+ vs 3D HIC 120 V+	***	3D HDFn 60 vs 3D HIC 120 V+	***
Caco-2/ CCD-18co V+ vs 3D HIC 120 V+	***	3D HDFn 120 vs 3D HIC 120 V+	***
Caco-2/ HDFn 60 vs 3D HIC 120 V+	***	3D HDFn 60 V+ vs 3D HIC 120 V+	***
Caco-2/ HDFn 120 vs 3D HIC 120 V+	***	3D HDFn 120 V+ vs 3D HIC 120 V+	***
Caco-2/ HDFn 60 V+ vs 3D HIC 120 V+	***	3D HIC 60 vs 3D HIC 120 V+	***
Caco-2/ HDFn 120 V+ vs 3D HIC 120 V+	***	3D HIC 120 vs 3D HIC 120 V+	***
Caco-2/ HIC 60 vs 3D HIC 120 V+	***	3D HIC 60 V+ vs 3D HIC 120 V+	***
Caco-2/ HIC 120 vs 3D HIC 120 V+	***		

**Table 6.4: Efflux co-efficient analysis of Rhodamine 123 in 2D and 3D intestinal models both with and without Verapamil Hydrochloride and at both 60 and 120 minutes assay lengths - Individual significances calculated by one-way ANOVA with Tukeys post-test analysis with 95% confidence rating. \*\*\* = P<0.0005, \*\* = P<0.005, \* = P< 0.05**

### **6.4.6 KGF treatment of Caco-2 Transwell models reduces its models capability to actively transport Rhodamine 123.**

Figure 6.19 shows the Rhodamine 123 transport of dynamics of conventional cultured Caco-2 Transwell layers treated with differential concentration of KGF. Cell layers were cultured for a period of 21 to 25 days prior to assessment of transport kinetics through Ussing chamber design as previously described. Figure 6.19 A shows the transport of Rhodamine 123 across KGF treated layers in the B-A direction of travel. Readings were taken after 120 minutes of transportation. A significant decrease in the levels of Rhodamine transport can be seen when compared with the control Papp values. Levels drop by approximately 50% consistently across all treated layers with no concentration dependent effects.

Figure 6.19 B shows the B-A transfer of Rhodamine 123 in the presence of the MDR1 (P-gp) inhibitor Verapamil Hydrochloride. Untreated Caco-2 layers show a decrease in Rhodamine Papp in the presence of Verapamil Hydrochloride. However, comparison of data levels from Figure 6.19 A and B show that addition of Verapamil hydrochloride caused a significant dose dependant increase in the relative Papp of Rhodamine 123 in KGF treated layers compared to their untreated controls. Additionally, the increase in Rhodamine 123 appears to be concentration dependant on the levels of KGF utilised to treat the Caco-2 layers during culture, with higher KGF levels corresponding with increased Rhodamine 123 transport. This is contrary to what is expected with the know physiological functional of Verapamil hydrochloride and suggests a differential mechanism between KGF treated layers and Rhodamine 123 transport.



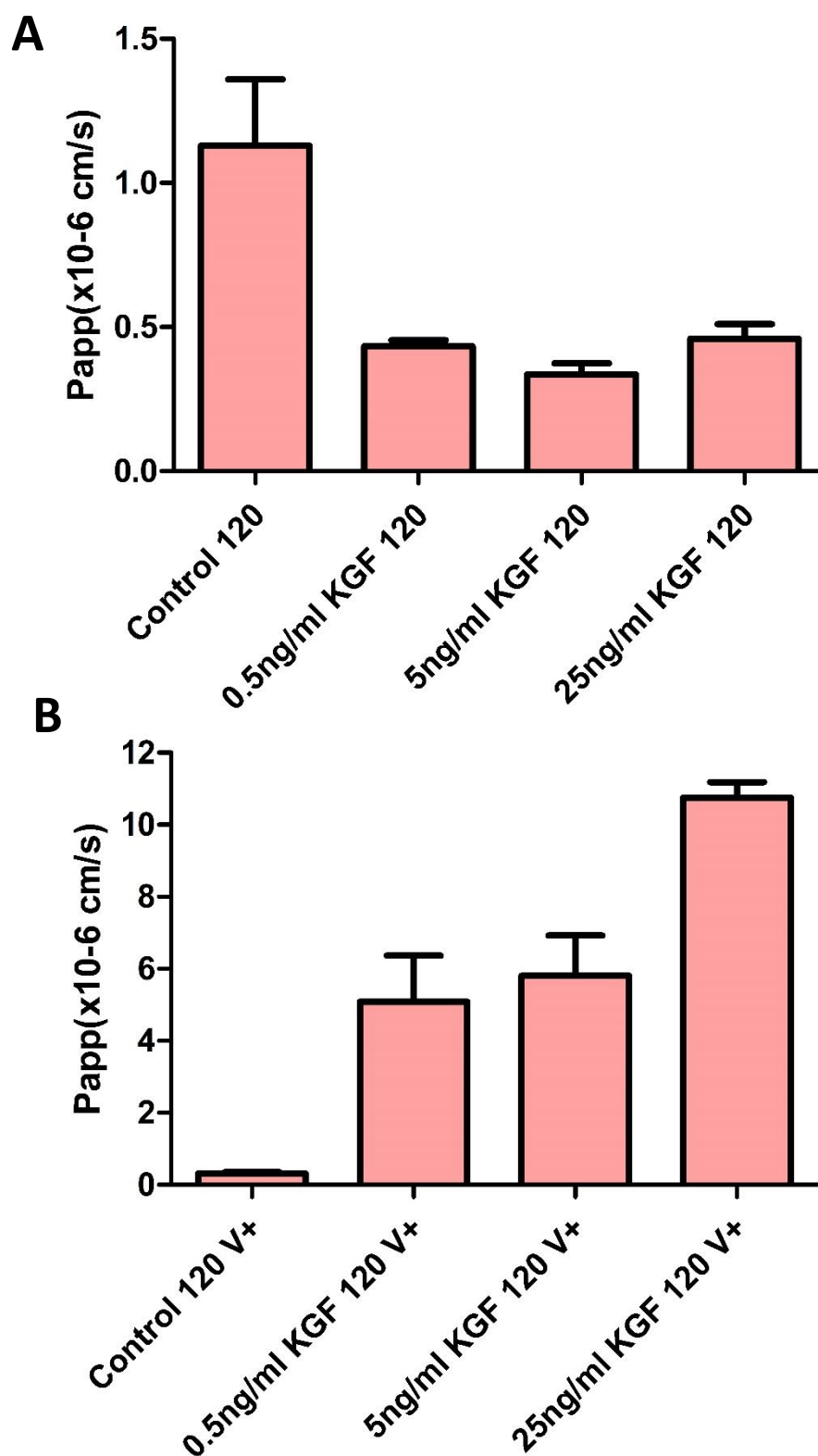


**Figure 6.19: B-A transport of Rhodamine 123 in KGF treated Caco-2 layers shows decreased transport in treated layers versus controls with addition of Verapamil Hydrochloride having a dose dependant increasing effect on membrane permeability – A) B-A transport without the addition of Verapamil Hydrochloride, B) Rhodamine transport with Verapamil hydrochloride. n=3 from a minimum of three independent experiments. +SEM**

Chapter 6 –Assessment of 2D and 3D model function

Control 60 vs 0.5ng/ml KGF 120 V+	***	0.5ng/ml KGF 60 vs 5ng/ml KGF 120 V+	***	5ng/ml KGF 60 vs 5ng/ml KGF 120 V+	***
Control 60 vs 5ng/ml KGF 120 V+	***	0.5ng/ml KGF 60 vs 25ng/ml KGF 60 V+	**	5ng/ml KGF 60 vs 25ng/ml KGF 60 V+	**
Control 60 vs 25ng/ml KGF 60 V+	***	0.5ng/ml KGF 60 vs 25ng/ml KGF 120 V+	***	5ng/ml KGF 60 vs 25ng/ml KGF 120 V+	***
Control 60 vs 25ng/ml KGF 120 V+	***	0.5ng/ml KGF 120 vs 0.5ng/ml KGF 120 V+	***	5ng/ml KGF 120 vs 5ng/ml KGF 120 V+	***
Control 120 vs 0.5ng/ml KGF 120 V+	***	0.5ng/ml KGF 120 vs 5ng/ml KGF 120 V+	***	5ng/ml KGF 120 vs 25ng/ml KGF 60 V+	**
Control 120 vs 5ng/ml KGF 120 V+	***	0.5ng/ml KGF 120 vs 25ng/ml KGF 60 V+	**	5ng/ml KGF 120 vs 25ng/ml KGF 120 V+	***
Control 120 vs 25ng/ml KGF 60 V+	*	0.5ng/ml KGF 120 vs 25ng/ml KGF 120 V+	***	5ng/ml KGF 60 V+ vs 5ng/ml KGF 120 V+	***
Control 120 vs 25ng/ml KGF 120 V+	***	0.5ng/ml KGF 60 V+ vs 0.5ng/ml KGF 120 V+	***	5ng/ml KGF 60 V+ vs 25ng/ml KGF 60 V+	*
Control 60 V+ vs 0.5ng/ml KGF 120 V+	***	0.5ng/ml KGF 60 V+ vs 5ng/ml KGF 120 V+	***	5ng/ml KGF 60 V+ vs 25ng/ml KGF 120 V+	***
Control 60 V+ vs 5ng/ml KGF 120 V+	***	0.5ng/ml KGF 60 V+ vs 25ng/ml KGF 60 V+	*	5ng/ml KGF 120 V+ vs 25ng/ml KGF 60 V+	***
Control 60 V+ vs 25ng/ml KGF 60 V+	***	0.5ng/ml KGF 60 V+ vs 25ng/ml KGF 120 V+	***	5ng/ml KGF 120 V+ vs 25ng/ml KGF 120 V+	***
Control 60 V+ vs 25ng/ml KGF 120 V+	***	0.5ng/ml KGF 120 V+ vs 5ng/ml KGF 60 V+	***	5ng/ml KGF 120 V+ vs 25ng/ml KGF 120 V+	***
Control 120 V+ vs 0.5ng/ml KGF 120 V+	***	0.5ng/ml KGF 120 V+ vs 5ng/ml KGF 120 V+	***	25ng/ml KGF 60 vs 25ng/ml KGF 60 V+	**
Control 120 V+ vs 5ng/ml KGF 120 V+	***	0.5ng/ml KGF 120 V+ vs 5ng/ml KGF 60 V+	***	25ng/ml KGF 60 vs 25ng/ml KGF 120 V+	***
Control 120 V+ vs 25ng/ml KGF 60 V+	**	0.5ng/ml KGF 120 V+ vs 25ng/ml KGF 60 V+	***	25ng/ml KGF 120 vs 25ng/ml KGF 60 V+	**
Control 120 V+ vs 25ng/ml KGF 120 V+	***	0.5ng/ml KGF 120 V+ vs 25ng/ml KGF 120 V+	***	25ng/ml KGF 120 vs 25ng/ml KGF 120 V+	***
0.5ng/ml KGF 60 vs 0.5ng/ml KGF 120 V+	***	0.5ng/ml KGF 120 V+ vs 25ng/ml KGF 120 V+	***	25ng/ml KGF 60 V+ vs 25ng/ml KGF 120 V+	***

**Table 6.5: Significance values for Rhodamine 123 permeability between models of differing KGF concentration both with and without the addition of Verapamil Hydrochloride** - Individual significances calculated by One way ANOVA with Tukeys post-test analysis with 95% confidence rating. \*\*\* = P<0.0005, \*\* = P<0.005, \* = P< 0.05. n=3, N=3

### 6.4.7 Atenolol Transport in Co-culture Transwell model layers.

Figure 6.21 shows the transport kinetics of Atenolol for each of the Transwell paracrine conditions utilised within this study, namely; Control, CCD-18co, HDFn and HIC conditioned medias. Control layers are shown to be relatively impermeable to Atenolol in the B-A direction with an average Papp value of approximately  $0.3\text{--}0.4 \times 10^{-6} \text{ cm/s}$ . Culture of Caco-2 monolayers in paracrine media of CCD-18co cells did not significantly increase permeability in the B-A direction. B-A transport of Atenolol through HDFn and HIC conditioned Transwell layers did have significant effects on the permeability of the resultant model, with increases seen in both conditions. The largest change was seen in HIC conditioned layers. Apical to basal (A-B) transport of Atenolol (Figure 6.21 B) appears be higher (more permeable) that transport measured B-A in most instances, more so in conventionally cultured Caco-2 and CCD-18co conditioned models. In terms of how this relates to membrane physiology, Atenolol has been described as a substrate of OCT1

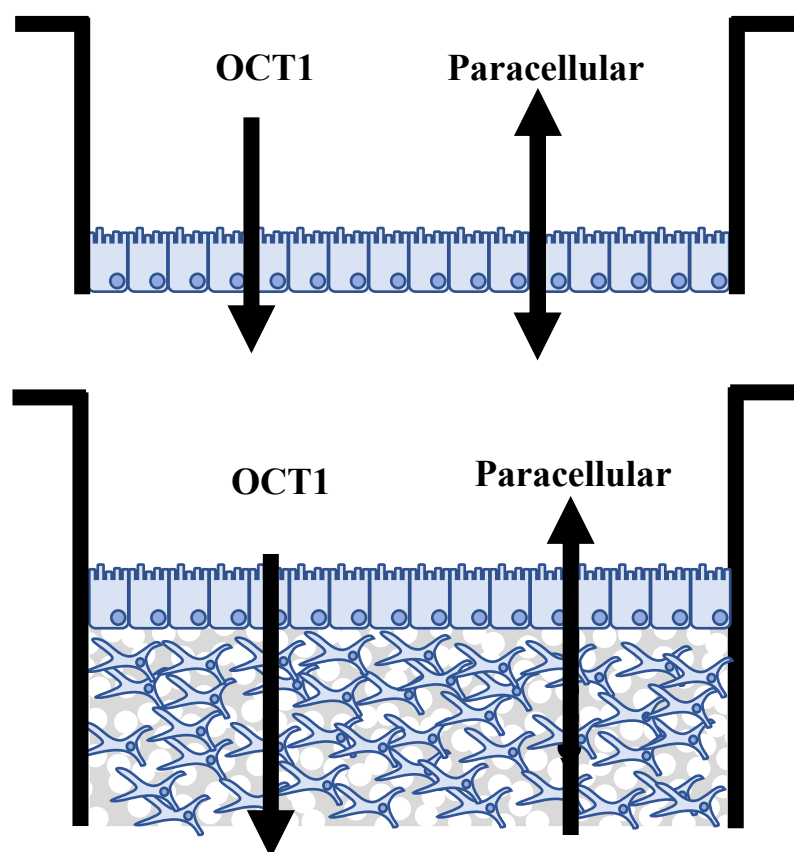


**Figure 6.20: Schematic representation of the expected directional travel mechanisms for Atenolol in Transwell and 3D Alvetex® models – A) Transwell based systems, B) Alvetex® based systems.** Primary expected directional transport is through bi-directional paracellular mechanisms. OCT1 may have some transport capabilities in the A-B directions

within the literature. Unlike some of the other protein functions tested in this study, OCT1 is able to actively transport its substrates into the cell, acting as an uptake transporter rather than an efflux protein. As such one would expect that passive paracellular transport plus the actions of OCT 1 would result in a higher permeability in the A-B directions. Lack of this response in HDFn treated Caco-2 monolayers could be attributed simply to a downregulation of OCT 1 within these samples or an increase in an untested efflux mechanism with substrate homology.

Figure 6.22 shows the differences in Papp between 0, 60 and 120 minutes of transport assay time. Figure 6.22 A shows the B-A transport changes over time. Caco-2 control and Caco-2/ CCD-18co co-cultures can be shown to plateau or decrease in relative Papp after the 60 minute timepoint whereas HIC and HDFn layers continue to rise. A rising Papp indicates an increasing permeability over time, suggesting the system has not yet reached transport equilibrium, assuming passive diffusion across the membrane. Figure 6.22 B shows the same trends but in the A-B direction with Papp values at comparable timepoints generally seen to be higher A-B than B-A.

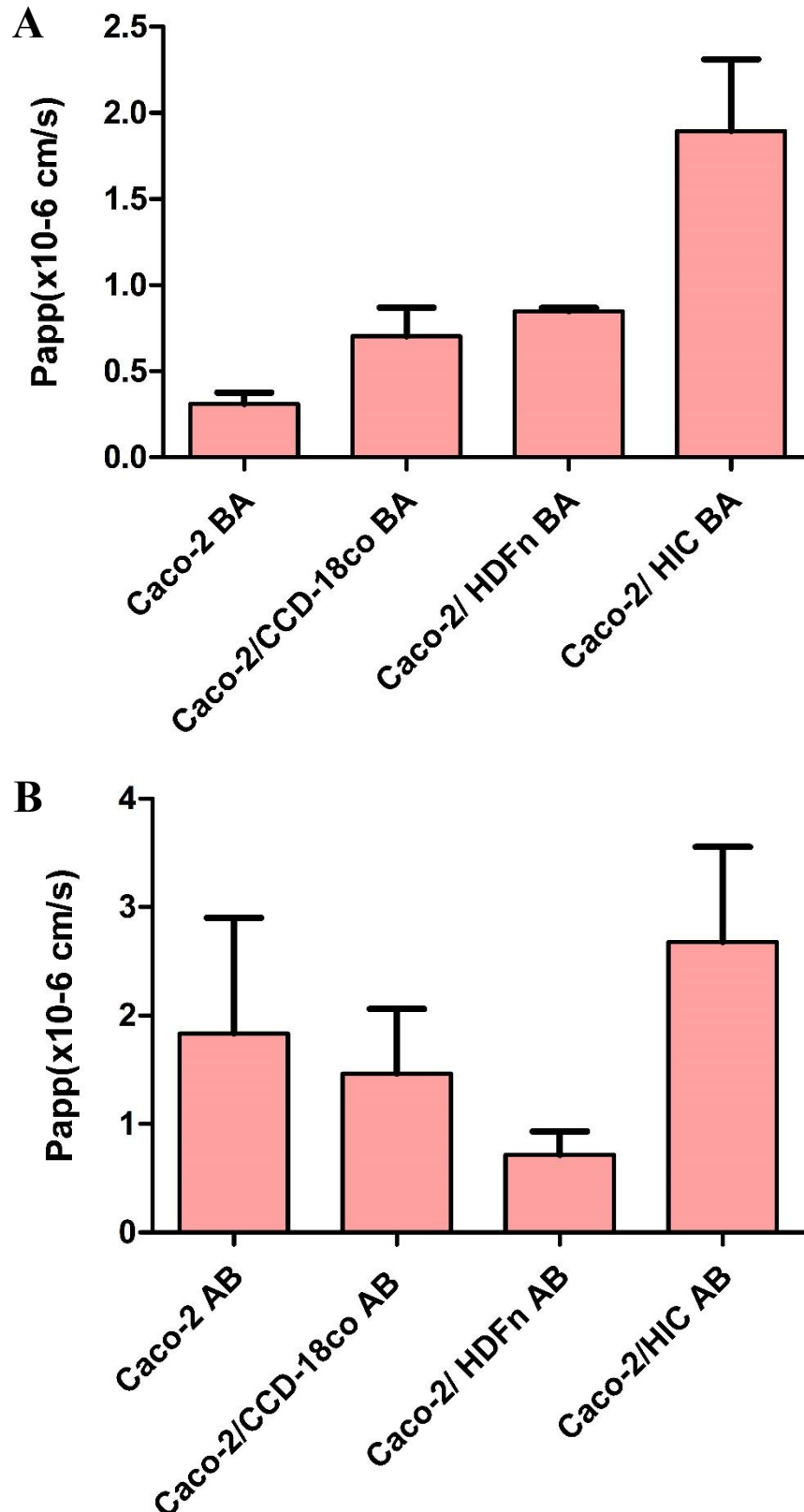


**Figure 6.21: Apparent Caco-2 permeability of Atenolol in Transwell Snapwell model systems –** 21–25 day matured Caco-2 Alvetex co-culture models were tested for their apparent permeability of Atenolol. A) Comparison is of relative Papp values at 120 minutes of transport in the B-A direction of travel. B) relative Papp values at 120 minutes in the A-B direction of travel. n=3-8 +SEM. N=3. Statistical analysis was achieved by one way ANOVA with Tukeys post test analysis. B-A and A-B data sets were analysed for significance separately. Significance values are summarised in table 6.6

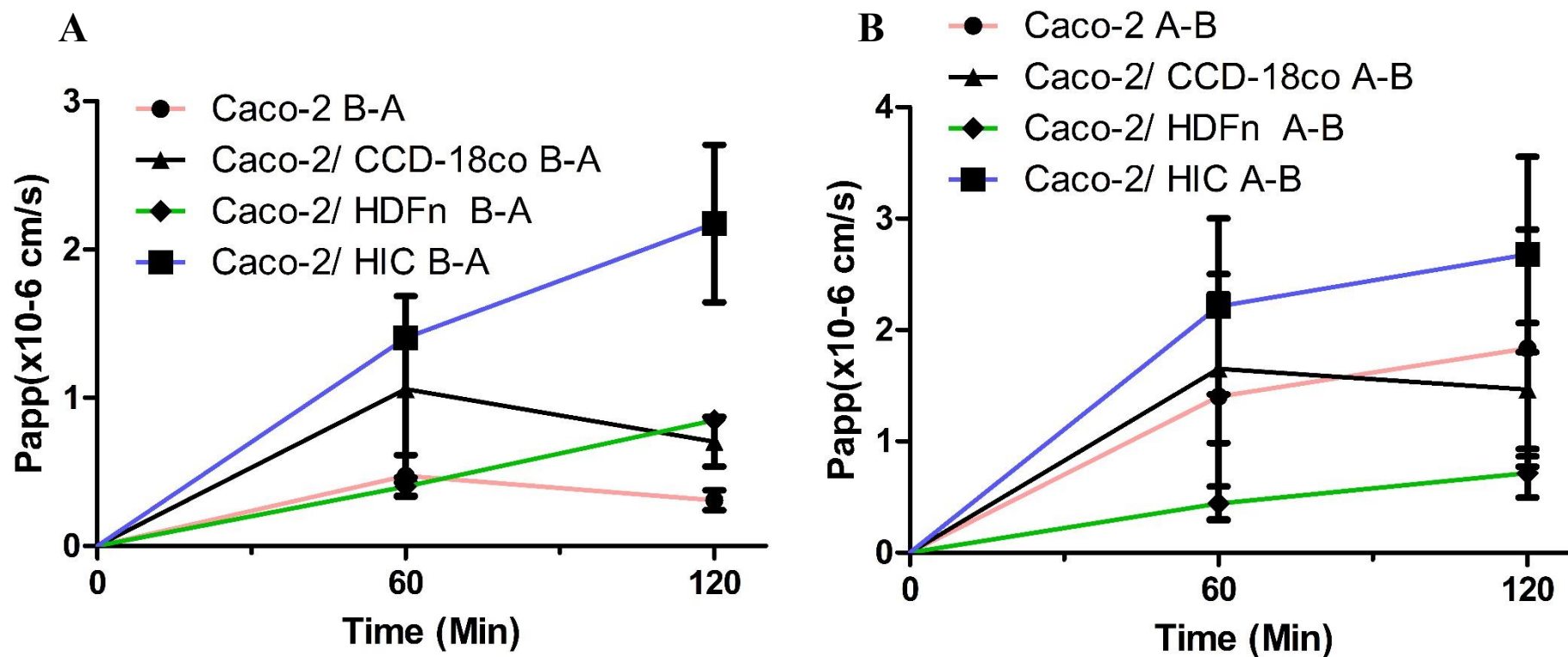


**Figure 6.22: Apparent Caco-2 Transwell permeability of Atenolol in Transwell Co-culture systems** – 21–25 day matured Caco-2 Snapwell monolayers cultured in the conditioned media of either CCD-18co, HDFn or HIC fibroblasts were tested for their apparent permeability of Atenolol. Timepoints were taken at 60 minute intervals. n=2-4 ±SEM, N=2-4

Caco-2 BA vs Caco-2/CCD-18co BA	ns	Caco-2 AB vs Caco-2/CCD-18co AB	ns
Caco-2 BA vs Caco-2/ HDFn BA	ns	Caco-2 AB vs Caco-2/ HDFn AB	ns
Caco-2 BA vs Caco-2/ HIC BA	**	Caco-2 AB vs Caco-2/HIC AB	ns
Caco-2/CCD-18co BA vs Caco-2/ HDFn BA	ns	Caco-2/CCD-18co AB vs Caco-2/ HDFn AB	ns
Caco-2/CCD-18co BA vs Caco-2/ HIC BA	*	Caco-2/CCD-18co AB vs Caco-2/HIC AB	ns
Caco-2/ HDFn BA vs Caco-2/ HIC BA	*	Caco-2/ HDFn AB vs Caco-2/HIC AB	ns

**Table 6.6: Significance values for Atenolol permeability experiments** - Individual significances calculated by One way ANOVA with Tukeys post-test analysis with 95% confidence rating for Atenolol transport. B-A and A-B data sets were analysed for significance separately \*\*\* =  $P < 0.0005$ , \*\* =  $P < 0.005$ , \* =  $P < 0.05$ . n=3, N=3

### 6.4.8 Atenolol Transport in 3D bioengineered Alvetex models.

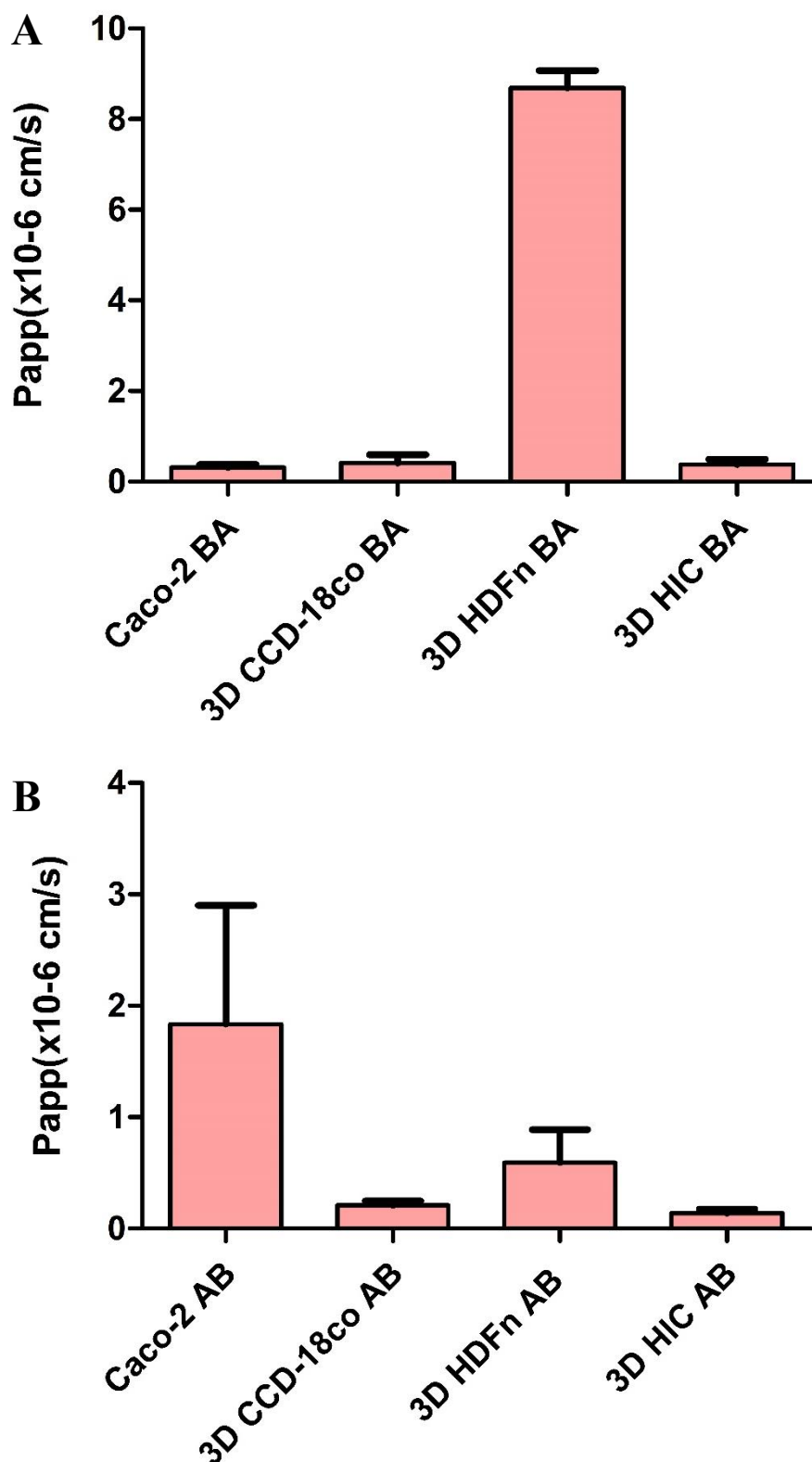
Figure 6.23 shows the apparent permeability of Atenolol through the 3D Alvetex models created within this study, namely; CCD-18co, HDFn and HIC cultured fibroblasts with Caco-2 epithelium cultured on the surface of the fibroblast model. Caco-2 B-A and Caco-2 A-B conditions refer to conventionally cultured Transwell models, used as control comparison layers.

B-A transport (Figure 6.23 A) of Atenolol in 3D cultured CCD-18co and HIC models was shown to be not significantly different from that seen in controls with values ranging around  $0.5 \times 10^{-6} \text{cms}^{-1}$ . B-A transport seen in HDFn layers however was significantly higher than that seen in other conditions at around  $8.5 \times 10^{-6} \text{cms}^{-1}$ . A-B transport (Figure 6.23 B) was higher in control samples as previously described but lower in all 3D cultured conditions than their respective B-A values. These differences between B-A and A-B transport however were insignificant except that of the 3D HDFn transport whereby A-B transport was generally lower. Reasons why A-B transport was so significantly lower than B-A in 3D HDFn models is not readily apparent. Decreased expression of OCT1 would have the effect of simultaneously increasing B-A permeability whilst decreasing relative A-B permeability. However, it could be hypothesised that OCT 1 downregulation could not result in such a large differential effect when compared to other conditions. The OCT family of transporter proteins is known to be expressed within the skin from a number cell types, mainly epithelial. (343)One potential mechanism for the functional

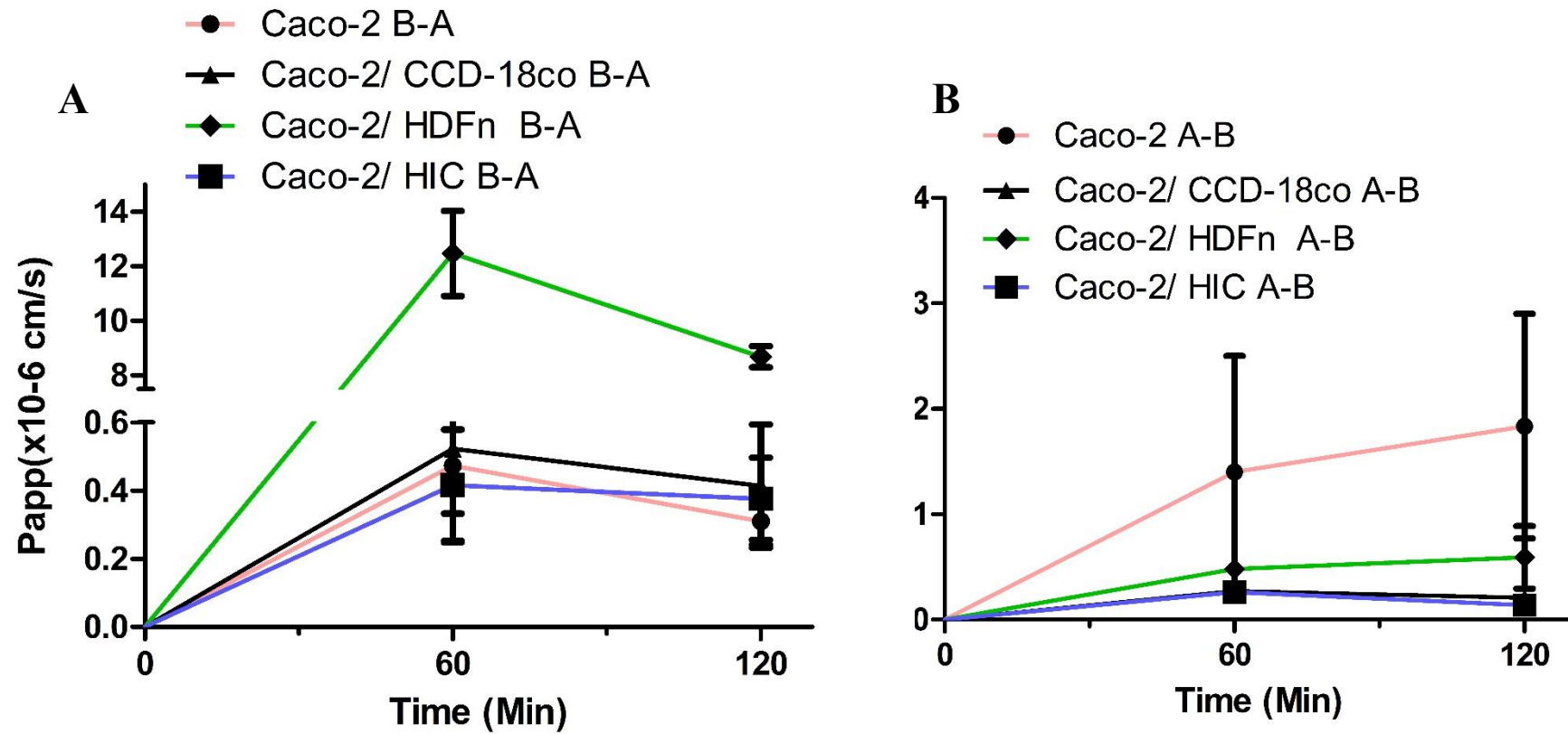
phenotype observed here could be due to OCT 1 upregulation within the HDFn fibroblasts themselves as such limiting the levels of Atenolol able to reach the basal compartment through the HDFn biomimetic intestinal model. Increased B-A transport could be due to a number of mechanisms not tested for in this study such as cross-specificity of atenolol as a substrate for an unknown transporter protein.

Figure 6.24 A, shows the Papp changes over time of 3D cultured CCD-18co, HDFn and HIC 3D Alvetex models. B-A transport comparison shows Caco-2 Transwell, 3D CCD-18co and 3D HIC models are not significantly different from one another. The general shape of the curve shows an increase in Papp values over time within the first 60 minutes followed by a plateau suggesting a constant rate of compound transfer. 3D HDFn models shows a decrease in permeability between 60 and 120 minute timepoints. This suggests permeability is decreasing within the models with later timepoints being less permeable to Atenolol. A-B time course graphs (Figure 6.24 B) show a similar trend with Papp levels plateauing after 60 minutes within the Ussing chamber. No significant deviation was seen up to 120 minutes.





**Figure 6.23: Apparent Caco-2 Transwell permeability of Atenolol in 3D Alvetex Scaffold models systems** – 21–25 day matured Caco-2 Alvetex co-culture models were tested for their apparent permeability of Atenolol. Comparison is of relative Papp values at 120 minutes of transport. A) B-A direction, B) A-B direction n=3-8 +SEM. N=3-4 Significance is shown in Table 6.7.



**Figure 6.24: Apparent Caco-2 Transwell permeability of Atenolol in Alvetex Scaffold co-culture systems** – 21–25 day matured Caco-2 Snapwell monolayers cultured in the conditioned media of either CCD-18co, HDFn or HIC fibroblasts were tested for their apparent permeability of Atenolol. Timepoints were taken at 60 minute intervals. n=2-4, N=2-4 ±SEM

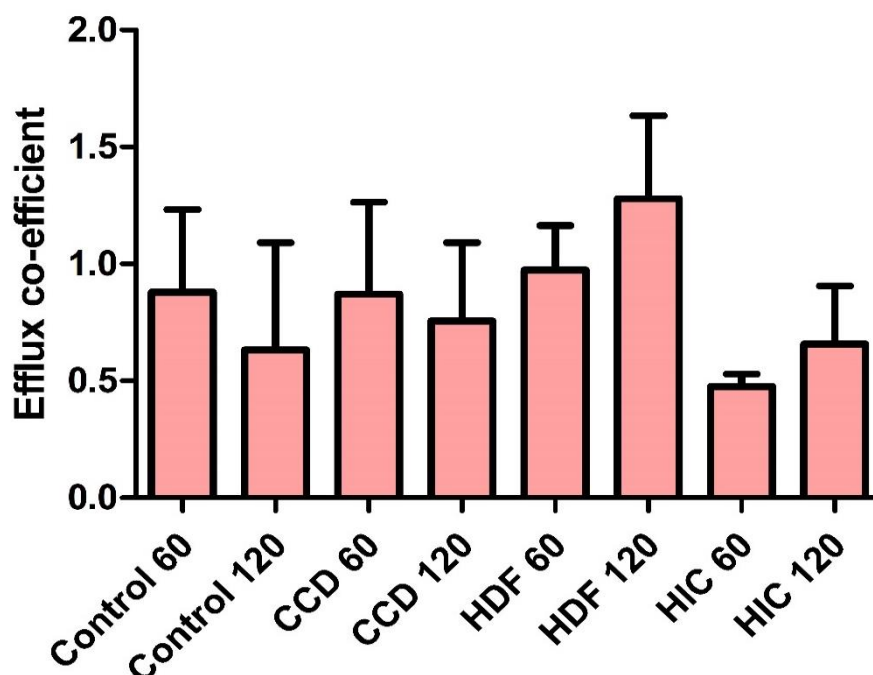
Caco-2 BA vs 3D CCD-18co BA	ns	Caco-2 AB vs 3D CCD-18co AB	*
Caco-2 BA vs 3D HDFn BA	***	Caco-2 AB vs 3D HDFn AB	ns
Caco-2 BA vs 3D HIC BA	ns	Caco-2 AB vs 3D HIC AB	ns
3D CCD-18co BA vs 3D HDFn BA	***	3D CCD-18co AB vs 3D HDFn AB	ns
3D CCD-18co BA vs 3D HIC BA	ns	3D CCD-18co AB vs 3D HIC AB	ns
3D HDFn BA vs 3D HIC BA	***	3D HDFn AB vs 3D HIC AB	ns

**Table 6.7: Significance values for Atenolol permeability in 3D intestinal models -** Individual significances calculated by One way ANOVA with Tukeys post-test analysis with 95% confidence rating. \*\*\* =  $P < 0.0005$ , \*\* =  $P < 0.005$ , \* =  $P < 0.05$ . n=2-8. B-A and A-B data sets were analysed for significance separately

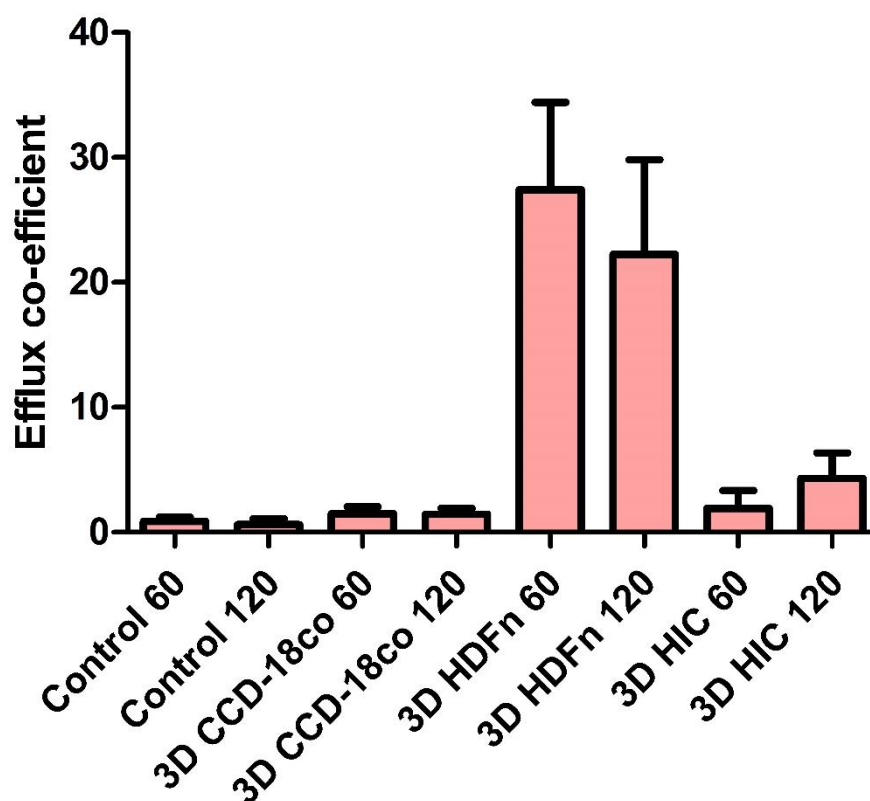
### 6.4.9 Efflux co-efficient of Caco-2 Transwell and 3D bio-engineered Caco-2 Alvetex models for Atenolol.

Figure 6.25 shows the efflux co-efficient values for Atenolol in the 2D paracrine models. In each case there are no significant differences (Table 6.6) between values gained at 60 minutes or at 120 minutes. For the most part, values tend to hover around 1 suggesting there is no particular bias in the direction of travel of this drug in these conditions, especially at the terminal experimental timepoint of 120 minutes.

Figure 6.26 shows the same calculations applied to data gained from the analysis of atenolol transport in 3D intestinal models. 3D CCD-18co models show low efflux co-efficient values suggesting no significant bias in movement. In contrast, 3D HDFn models show a large efflux co-efficient value of between 20-30, suggesting a strong bias in the B-A direction of travel. As discussed earlier the mechanism of action for this increase in B-A transport compared to A-B is unknown. 3D HIC models show a reduced efflux co-efficient compared with 3D HDFn with levels similar to CCD-18co models, suggesting a small bias B-A, potentially through the same mechanism as HDFn models but to a far lesser extent.



**Figure 6.25: Efflux co-efficient calculations shows no significant directional bias in 2D model atenolol transport** – Efflux co-efficients less than or equal to 1 suggest no significant bias in the B-A transport of Atenolol across 2D control and paracrine treated layers. This trend is observed at both 60 and 120 minute timepoints. n=3-8 +SEM. N=3-4 Significance shown in Table 6.6



**Figure 6.26: Efflux co-efficient calculations shows significant differences in the transport bias of HDFn models to other 3D systems and Transwell co-cultures** – The efflux co-efficient calculations of 3D cultured Alvetex models all show significant bias to the B-A transport of Atenolol across models layers. Particularly, HDFn 3D cultured models show a highly significant bias over all other culture conditions. n= 3 +SEM. N=3 Significance shown in Table 6.6

Caco-2 60 vs 3D HDFn 60	***	HIC 60 vs 3D HDFn 60	***
Caco-2 60 vs 3D HDFn 120	***	HIC 60 vs 3D HDFn 120	***
Caco- 120 vs 3D HDFn 60	***	HIC 120 vs 3D HDFn 60	***
Caco- 120 vs 3D HDFn 120	***	HIC 120 vs 3D HDFn 120	***
CCD-18co 60 vs 3D HDFn 60	***	3D CCD-18co 60 vs 3D HDFn 60	***
CCD-18co 60 vs 3D HDFn 120	***	3D CCD-18co 60 vs 3D HDFn 120	***
CCD-18co 120 vs 3D HDFn 60	***	3D CCD-18co 120 vs 3D HDFn 60	***
CCD-18co 120 vs 3D HDFn 120	***	3D CCD-18co 120 vs 3D HDFn 120	***
HDFn 60 vs 3D HDFn 60	***	3D HDFn 60 vs 3D HIC 60	***
HDFn 60 vs 3D HDFn 120	***	3D HDFn 60 vs 3D HIC 120	***
HDFn 120 vs 3D HDFn 60	***	3D HDFn 120 vs 3D HIC 60	***
HDFn 120 vs 3D HDFn 120	**	3D HDFn 120 vs 3D HIC 120	**

**Table 6.8: Significance values for Atenolol Efflux Co-efficient for both 2D and 3D intestinal models** - Individual significances calculated by One way ANOVA with Tukeys post-test analysis with 95% confidence rating. \*\*\* =  $P < 0.0005$ , \*\* =  $P < 0.005$ , \* =  $P < 0.05$ .

### 6.4.10 Propranolol Transport of 2D Transwell co-cultures and 3D Alvetex based intestinal models.

Figure 6.28 shows Propranolol transport data for conventionally cultured control and 2D conditioned media Transwell experiments. Figure 6.28 A demonstrates data in the B-A direction whereas Figure 6.28 B shows permeability in the A-B direction. Generally, Transwell membranes could be considered highly permeable to Propranolol with average Papp values over  $10 \times 10^{-6} \text{cms}^{-1}$  for all conditions.

Control, CCD-18co and HIC conditioned media conditions were all approximately equal with no significant changes in propranolol transport over Control epithelial constructs. In contrast, HDFn paracrine media conditions resulted in an increased permeability trend

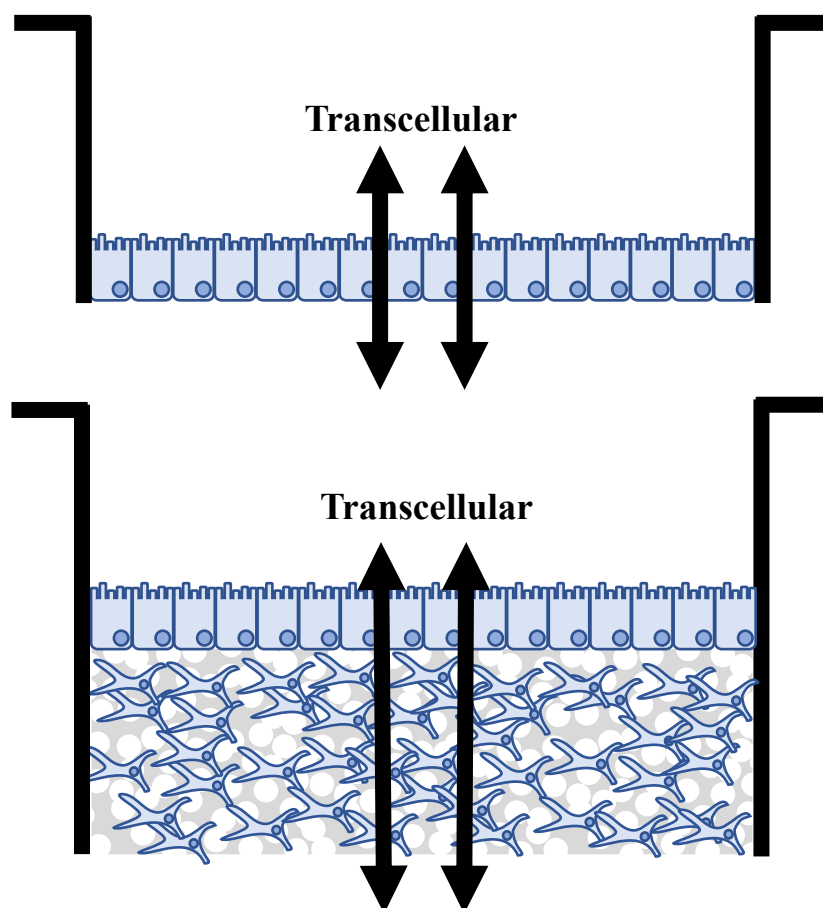


**Figure 6.27: Schematic representation of the expected permeability routes of Propranolol across Transwell and Alvetex models** – Propranolol is a model compound generally utilised as a measurement of passive transcellular transport in vitro across Caco-2 Transwell model membranes.

albeit not significantly different from controls in this study. In all instances B-A and A-B transport appears to be approximately equal between model conditions. Propranolol is thought to cross across the intestinal epithelium purely through a passive transcellular mechanism. Data seen here follows this hypothesis with reasonably similar values seen between conditions and no differences between B-A and A-B directionality.

3D model permeability to Propranolol (Figure 6.29 (A = B-A), (B = A-B)) showed increased variation over their 2D conditioned media counterparts. Generally, all models tested were still reasonably permeable to Propranolol with minimum average Papp values of  $> 5 \times 10^{-6} \text{cms}^{-1}$  in all conditions. 3D CCD-18co Alvetex models exhibited a reduced permeability phenotype compared to control with average Papp values of approximately  $5 \times 10^{-6} \text{cms}^{-1}$ , half of that seen in Control of CCD-18co paracrine 2D Transwell models. This reduced permeability phenotype is also seen in HIC created models albeit non-significant in the latter's case. Additionally, A-B transport appears to be higher than B-A transport in CCD-18co and HIC 3D cultures with A-B transport non-significantly different from Control Papp values in either case. 3D HDFn models show Propranolol permeability non-significantly different from 2D Control epithelial models. Interestingly, the heightened permeability compared to control layers seen in 2D HDFn paracrine media is attenuated when cultured into 3D models. However HDFn 3D models are still significantly higher than its other 3D counterparts.

Decreased permeability values are not completely unexpected in 3D models compared to Transwell systems due to the lipophilic nature of Propranolol. Being lipophilic, propranolol is readily absorbed through the cell membrane and as such sequestered within the cell. The large numbers of fibroblasts within the 3D models will have the effects of buffering the transport capabilities to the extent that they are filled with cells and ECM respectively. For example, the decreased Propranolol permeability seen in 3D CCD-18co and HIC systems is likely due to drug-model sequestration. Analysis of data within the literature shows that Propranolol transportation measurement with tissues are limited due to this factor often making *ex vivo* tissue values non-comparable to Caco-2 Transwell models. (269)

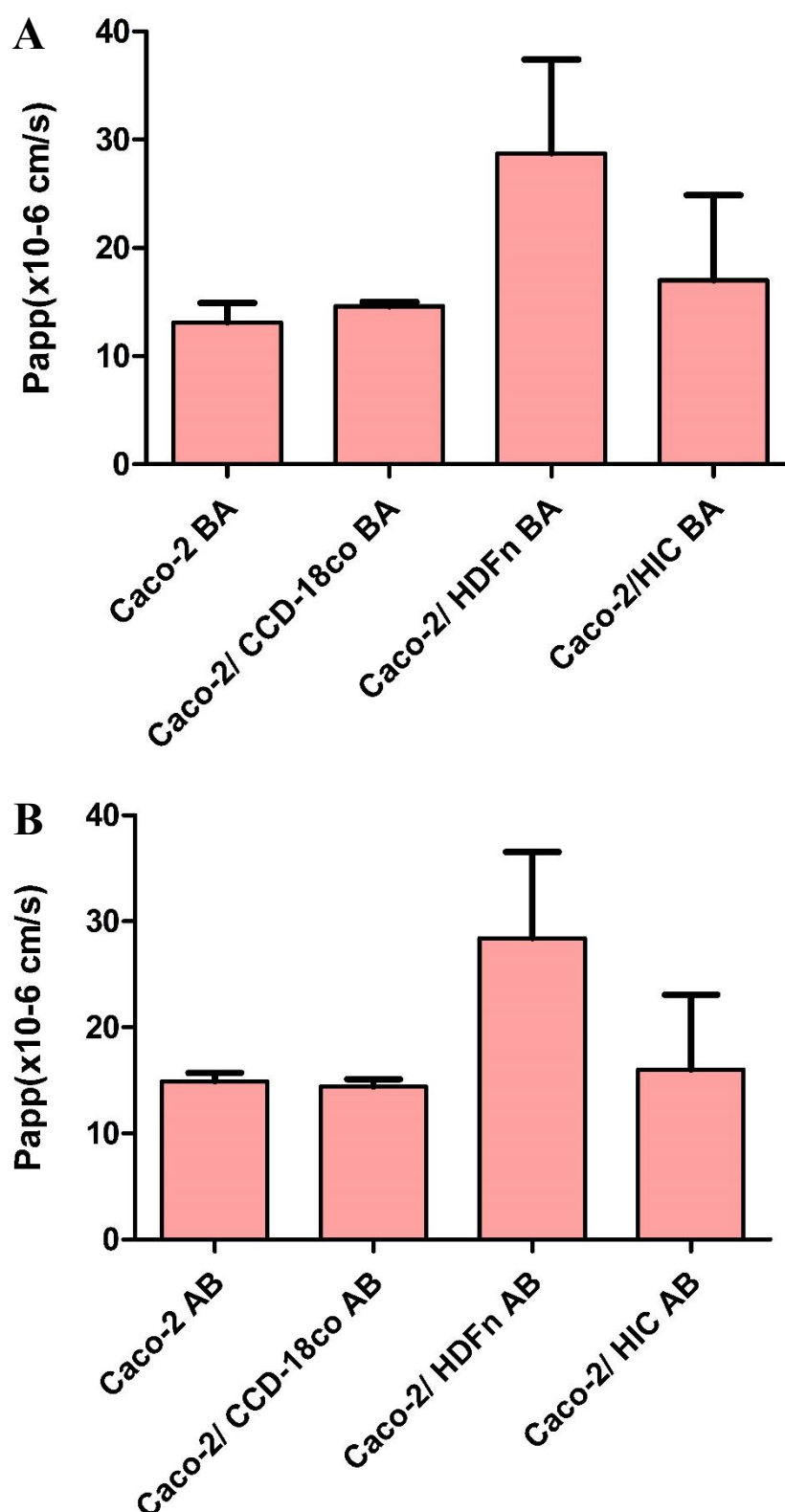


**Figure 6.28: 2D comparison of Propranolol transport across Control and treated Transwell models shows HDFn and HIC treatments increase propranolol permeability.** – All tested conditions show high levels of Propranolol permeability over the 120 minute assay length. A) B-A permeability, B) A-B permeability. HDFn and HIC treated Caco-2 layers appear to show increased permeability over Control and CCD-18oco treated models. n=3 +SEM, N=3. Significance is summarised in table 6.9.



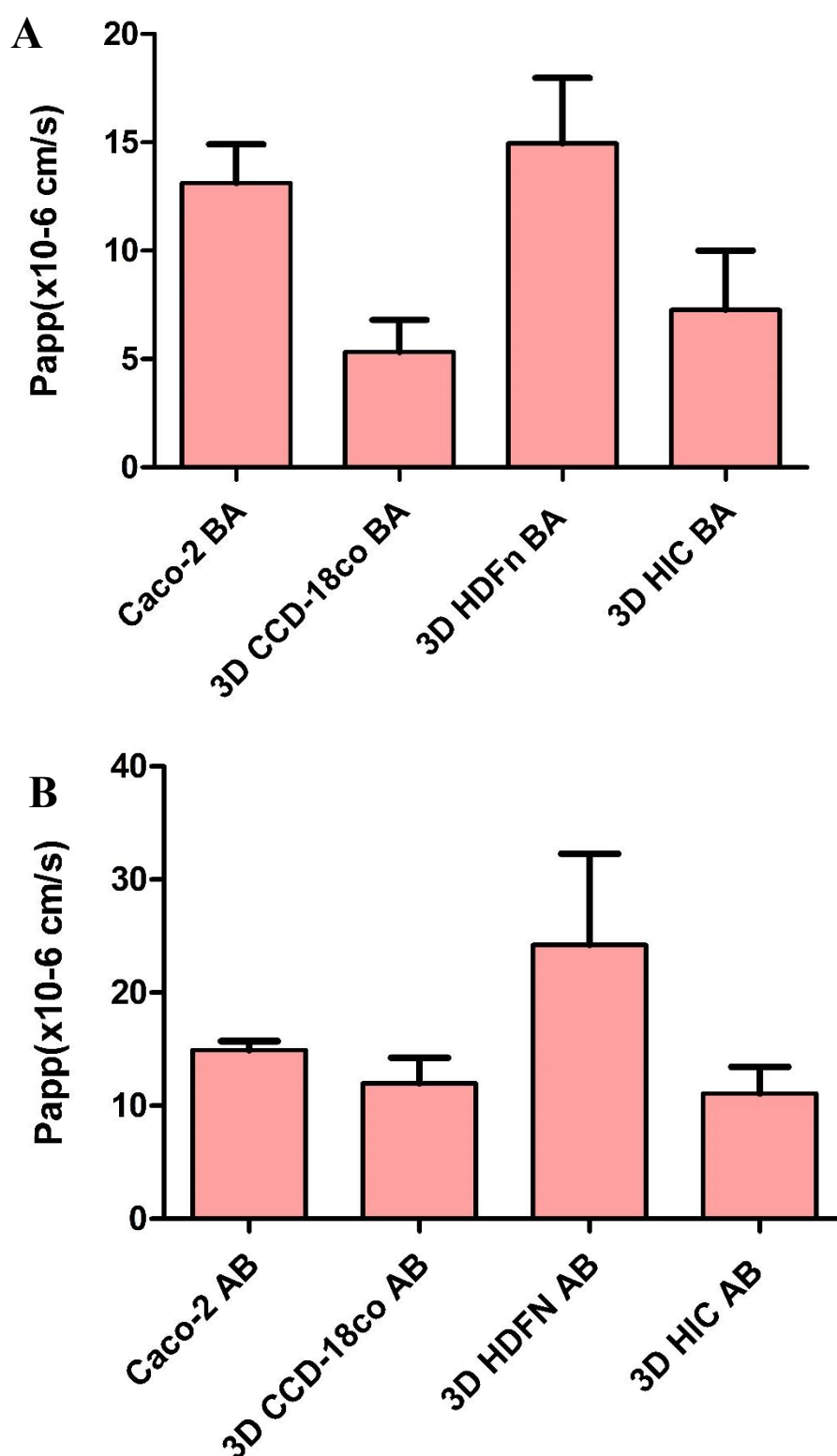


**Figure 6.29: 3D comparison of Propranolol transport across Control and 3D Alvetex models with both CCD-18co and HIC models displaying attenuated propranolol permeability compared to controls** – All tested conditions show high levels of Propranolol permeability over the 120 minute assay length. A) B-A permeability, B) A-B permeability .CCD-18co, HDFn and HIC treated Caco-2 layers appear to show decreased permeability over their 2D paracrine counterparts, with levels similar to control Caco-2 membranes. n=3, N=3, 3D HDFn n=2, N=2 +SEM. Significancy is summerised in table 6.10

Caco-2 BA vs Caco-2/ CCD-18co BA	ns	Caco-2 AB vs Caco-2/ CCD-18co AB	ns
Caco-2 BA vs Caco-2/ HDFn BA	ns	Caco-2 AB vs Caco-2/ HDFn AB	ns
Caco-2 BA vs Caco-2/HIC BA	ns	Caco-2 AB vs Caco-2/ HIC AB	ns
Caco-2/ CCD-18co BA vs Caco-2/ HDFn BA	ns	Caco-2/ CCD-18co AB vs Caco-2/ HDFn AB	ns
Caco-2/ CCD-18co BA vs Caco-2/HIC BA	ns	Caco-2/ CCD-18co AB vs Caco-2/ HIC AB	ns
Caco-2/ HDFn BA vs Caco-2/HIC BA	ns	Caco-2/ HDFn AB vs Caco-2/ HIC AB	ns

**Table 6.9: Significance values for Propranolol in 2D conditioned media Transwell models** - Individual significances calculated by One way ANOVA with Tukeys post-test analysis with 95% confidence rating. \*\*\* =  $P < 0.0005$ , \*\* =  $P < 0.005$ , \* =  $P < 0.05$ . B-A and A\_B permeability data sets were analysed for significance separately

Caco-2 BA vs 3D CCD-18co BA	ns	Caco-2 AB vs 3D CCD-18co AB	ns
Caco-2 BA vs 3D HIC BA	ns	Caco-2 AB vs 3D HIC AB	ns
Caco-2 BA vs 3D HDFn BA	ns	Caco-2 AB vs 3D HDFN AB	ns
3D CCD-18co BA vs 3D HIC BA	ns	3D CCD-18co AB vs 3D HIC AB	ns
3D CCD-18co BA vs 3D HDFn BA	ns	3D CCD-18co AB vs 3D HDFN AB	ns
3D HIC BA vs 3D HDFn BA	ns	3D HIC AB vs 3D HDFN AB	ns

**Table 6.10: Significance values for Propranolol in 3D Alvetex® models** - Individual significances calculated by One way ANOVA with Tukeys post-test analysis with 95% confidence rating. \*\*\* =  $P < 0.0005$ , \*\* =  $P < 0.005$ , \* =  $P < 0.05$ . B-A and A\_B permeability data sets were analysed for significance separately

### 6.4.11 Efflux co-efficient analysis of Propranolol permeability in 2D Transwell Snapwell and 3D Alvetex models.

Figure 6.30 shows the efflux co-efficient values for Propranolol transport in 2D paracrine media Transwell cultures and 3D Alvetex intestinal equivalents. With regards to efflux co-efficient ratios, 2D cultures all show non-significant deviation from the values seen in control Caco-2 Transwell models. Efflux co-efficient values in each case are approximately 1 suggests that there is no bias in the directional movement of Propranolol across Transwell models of the intestine. 3D Alvetex models show a small variation in efflux co-efficient values with a small non-significant decrease compared to control layers. This decrease would suggest that A-B transport is biased in these models over B-A transport. However, as the difference is not significant and the lowest values are still comfortably over 0.5 it is difficult to definitively suggest there is a significant movement bias.

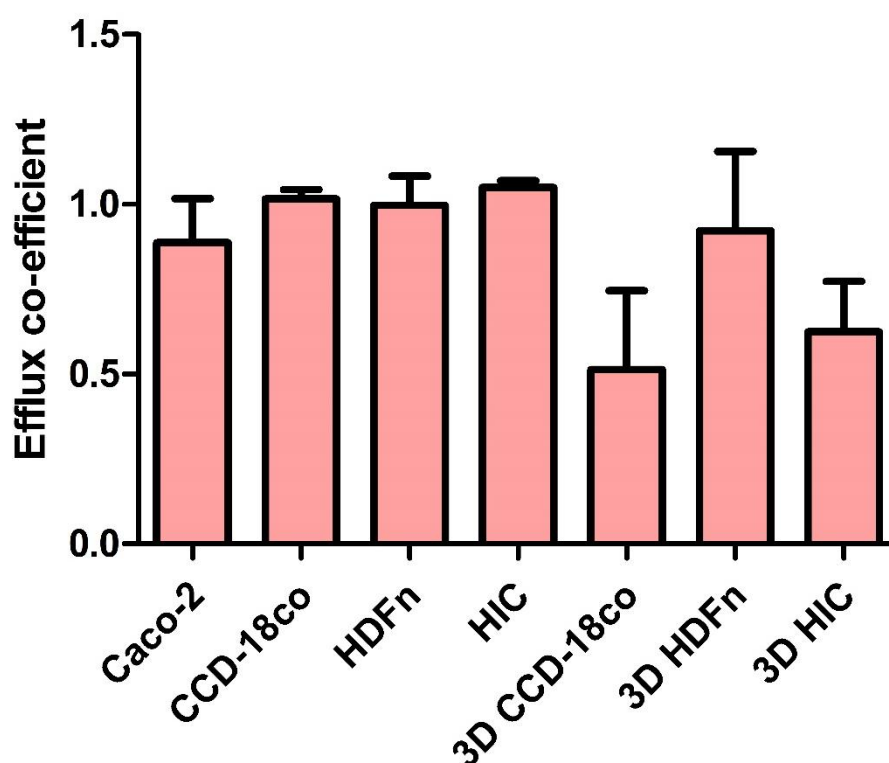


**Figure 6.30: Efflux co-efficient of Propranolol across 2D and 3D intestinal constructs suggests no bias in directional drug transport** – Analysis of 2D Transwell paracrine intestinal constructs suggests no bias in directional movement with efflux co-efficient values of approximately 1. 3D models suggests a level of bias towards A-B movement however efflux co-efficient levels are not sufficiently low to positively rule for A-B directional bias. n=3, N=3, 3D HDFn n=2, N=2 +SEM Significance calculated by one way ANOVA with Tukeys post-test analysis however no significant differences were seen between samples.

### 6.4.12 Etoposide transport of 2D Transwell co-cultures and 3D Alvetex based intestinal models.

Figure 6.32 shows the 2D transport/ permeability of Etoposide through Caco-2 Transwell control and conditioned media constructs. Control B-A transport for Etoposide (Figure 6.32 A) was very low at less than  $0.1 \times 10^{-6} \text{cm}^{-1}$ . Contrastingly, addition of CCD-18co, HIC or HDFn conditioned media to the Caco-2 epithelial constructs resulted in a highly significant increase in the levels of Etoposide transport with approximate Papp values of between  $2\text{-}4 \times 10^{-6} \text{cm}^{-1}$ . These values are significantly more physiologically relevant than the values gained from the control samples. CCD-18co and HIC models were highly

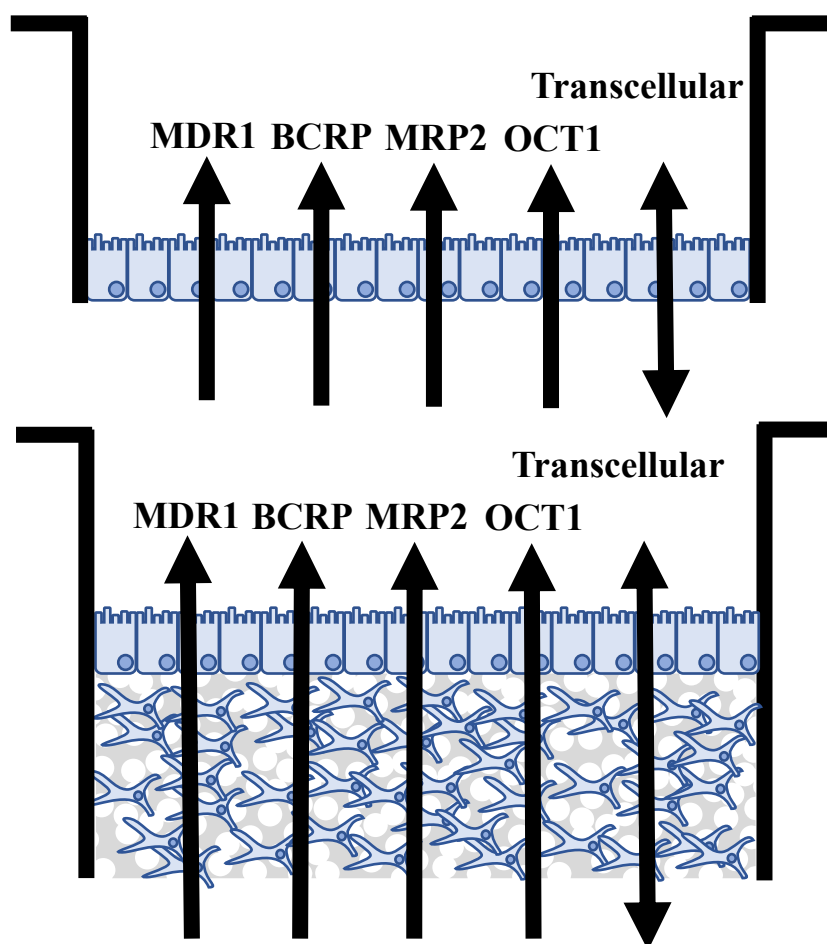


**Figure 6.31: Schematic overview of the expected permeability routes of Etoposide through Caco-2 Transwell and 3D Alvetex intestinal models** – Etoposide is transported by a number of critically important efflux proteins such as MDR1, BCRP, MRP2 and OCT1. In this instance etoposide was chosen primarily as a model drug for MRP2 mediated transport.

variable in their transport capabilities and as such average values are stated with a low degree of certainty. HDFn B-A transport was greatly different than control samples yet not significant. Additionally, all A-B transport experiments (Figure 6.32 B) were far less variable with in each instance, A-B transport was shown to be significantly less than B-A transport. This is to be expected due to the large array of efflux proteins known to be able to transport this compound out of the cells back into the intestinal lumen.

3D transport kinetics exhibit a very similar phenotype (Figure 6.33) with all 3D model cultures having significantly increased Papp values when compared to control conditions. In this instance 3D HIC models showed a markedly higher BA Papp (Figure 6.33 A) than all other conditions with values as high as  $60 \times 10^{-6} \text{cms}^{-1}$ . In this instance it is probable that permeability has been effected by a disruption to the 3D HIC due to mechanical breakage either during culture or through manual handling. Additionally, Caco-2 monolayer which has been demonstrated to form multi-layered sections in parts. Lack of membrane polarity could cause large increases in Papp values which when compared to human and animal tissues are not physiologically relevant in nature. A-B transport (Figure 6.33 B) is significantly lower in 3D HIC conditions, and non-significantly lower in CCD-18co and HDFn models.

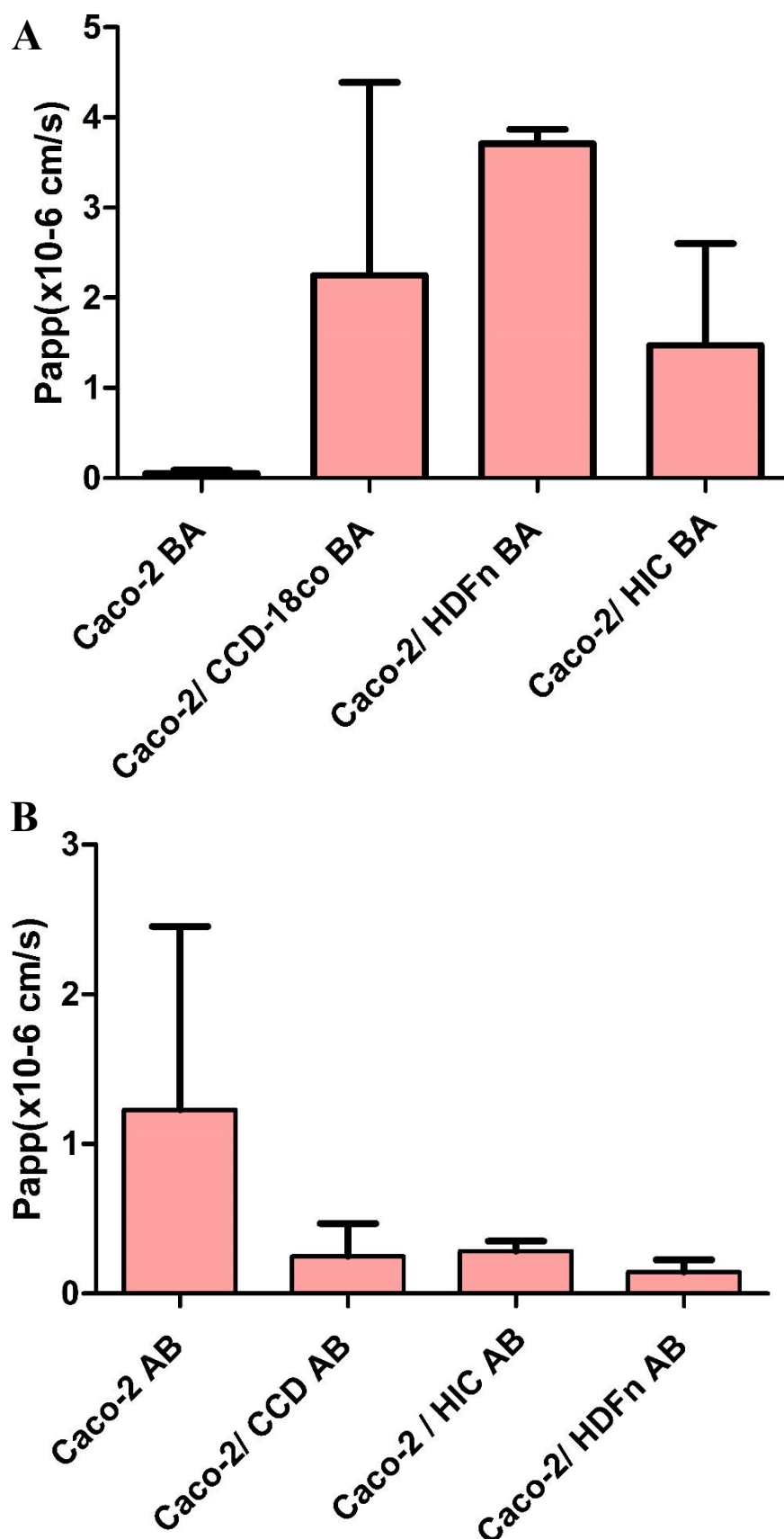


**Figure 6.32: Etoposide 2D paracrine media Transwell comparison shown large significant increases compared to control values in all culture conditions – A) B-A permeability, B) A-B permeability.** CCD-18co, HDFn and HIC conditioned media Transwell layers all show a heightened Etoposide permeability compared to Control layers in both the B-A and A-B directions of travel. n=2-3 +SEM N=2-3. Statistical differences are summarised in table 6.11

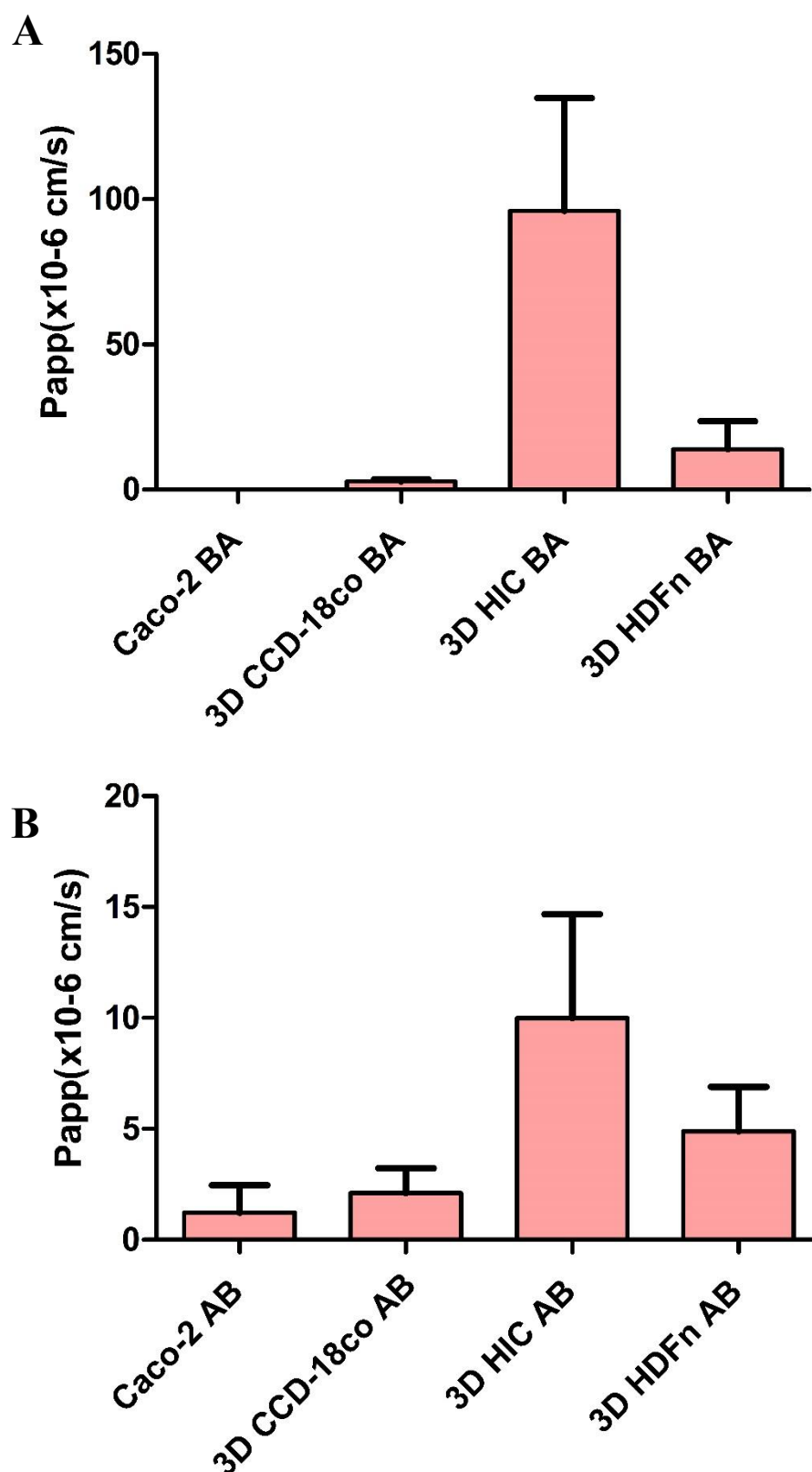


**Figure 6.33: 3D HIC and HDFn Alvetex models show significant Etoposide permeability increases over their 2D paracrine counterparts and 2D Caco-2 Control layers. 3D CCD-18co models similar to CCD-18co conditioned media models – A) B-A permeability, B) A-B permeability. All 3D models tested showed significantly higher Etoposide transport than Caco-2 control layers. HIC B-A transport in particular resulted in Papp values significantly higher than all other conditions tested. n=2-3 +SEM, N=2-3. Statistical differences are summarised in table 6.12**

Caco-2 BA vs Caco-2/ CCD-18co BA	ns	Caco-2 AB vs Caco-2/ CCD-18co AB	ns
Caco-2 BA vs Caco-2/ HDFn BA	ns	Caco-2 AB vs Caco-2/ HDFn AB	ns
Caco-2 BA vs Caco-2/HIC BA	ns	Caco-2 AB vs Caco-2/ HIC AB	ns
Caco-2/ CCD-18co BA vs Caco-2/ HDFn BA	ns	Caco-2/ CCD-18co AB vs Caco-2/ HDFn AB	ns
Caco-2/ CCD-18co BA vs Caco-2/HIC BA	ns	Caco-2/ CCD-18co AB vs Caco-2/ HIC AB	ns
Caco-2/ HDFn BA vs Caco-2/HIC BA	ns	Caco-2/ HDFn AB vs Caco-2/ HIC AB	ns

**Table 6.11: Significance values for Etoposide in 2D conditioned media Transwell models** - Individual significances calculated by One way ANOVA with Tukeys post-test analysis with 95% confidence rating. \*\*\* =  $P < 0.0005$ , \*\* =  $P < 0.005$ , \* =  $P < 0.05$ . B-A and A-B permeability data sets were analysed for significance separately

Caco-2 BA vs 3D CCD-18co BA	ns	Caco-2 AB vs 3D CCD-18co AB	ns
Caco-2 BA vs 3D HIC BA	*	Caco-2 AB vs 3D HIC AB	ns
Caco-2 BA vs 3D HDFn BA	ns	Caco-2 AB vs 3D HDFN AB	ns
3D CCD-18co BA vs 3D HIC BA	**	3D CCD-18co AB vs 3D HIC AB	ns
3D CCD-18co BA vs 3D HDFn BA	ns	3D CCD-18co AB vs 3D HDFN AB	ns
3D HIC BA vs 3D HDFn BA	*	3D HIC AB vs 3D HDFN AB	ns

**Table 6.12: Significance values for Etoposide in 3D Alvetex® models** - Individual significances calculated by One way ANOVA with Tukeys post-test analysis with 95% confidence rating. \*\*\* =  $P < 0.0005$ , \*\* =  $P < 0.005$ , \* =  $P < 0.05$ . B-A and A-B permeability data sets were analysed for significance separately



### **6.4.13 Efflux co-efficient analysis of Etoposide permeability in 2D Transwell Snapwell and 3D Alvetex models demonstrate the differential effects of 3D culture on the permeability of tissue constructs.**

Figure 6.34 shows the efflux co-efficient values for the permeability of Etoposide to 2D conditioned media Transwell models and 3D cultured Alvetex intestinal constructs. What can be clearly seen in that CCD-18co and HIC conditioned media has no significant effects on the efflux co-efficients of the resultant epithelial membrane model. Conversely, HDFn paracrine co-culture seemingly has larger effects on the directional transport bias of the membrane with a large increase in the efflux co-efficient values. This suggests that B-A transport is heavily favoured over A-B and at a significantly higher rate than Control, CCD-18co or HIC models, which whilst lower than HDFn paracrine constructs are still biased to B-A transport in their own right.

Interestingly, the opposite effect is true when analysing the efflux co-efficients of 3D cultured models. CCD-18co and HDFn 3D constructs results in a decrease in the relative efflux co-efficient compared to Control Caco-2 Transwell layers. 3D HIC models are much higher than their CCD-18co and HDFn counterparts yet not significantly different from Caco-2 controls. However, it is important to note that whilst efflux co-efficient values are lower in 3D models when compared to the Control they are still high enough to suggest a B-A transport bias in all conditions.

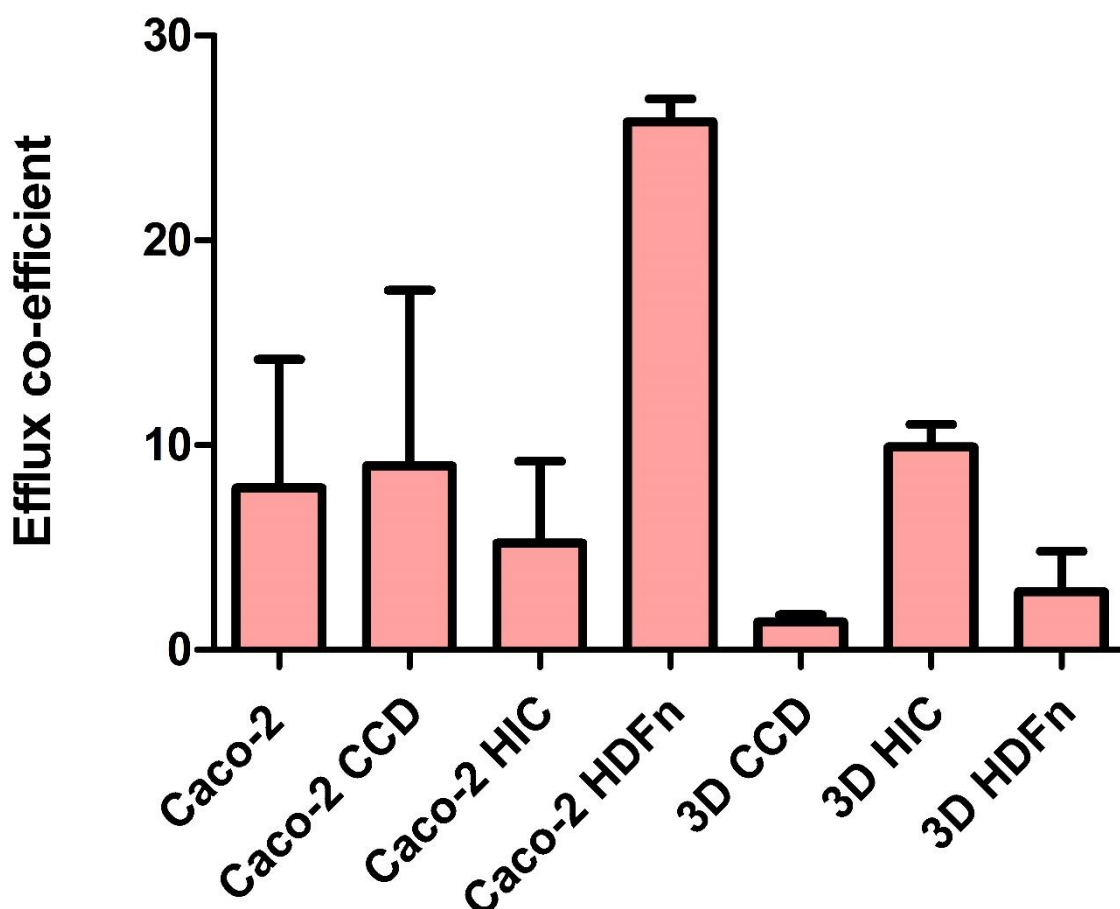


**Figure 6.34: Efflux co-efficient values show significant bias toward B-A transport in all conditions, both 2D and 3D** – Efflux co-efficient values are all above the 1.5 threshold limit for identification of B-A transport bias. In 2D cultures HDFn caused the most significant change in efflux co-efficient with a significant increase. In 3D models variation from control was in the opposite direction with decreases in efflux co-efficient values being observed, with CCD-18co models being the most effected. n=3 +SEM, N=3

Caco-2/ HDFn vs 3D CCD-18co	**
Caco-2/ HDFn vs 3D HDFn	*

**Table 6.13: Significance values for Etoposide efflux co-efficient for both 2D and 3D intestinal models** - Individual significances calculated by One way ANOVA with Tukeys post-test analysis with 95% confidence rating. \*\*\* =  $P < 0.0005$ , \*\* =  $P < 0.005$ , \* =  $P < 0.05$ .

#### 6.4.14 Methotrexate Transport for 2D Transwell paracrine co-cultures.

Methotrexate is a drug first developed in the 1940s as an anticancer drug, effective by reducing the capability of cells in the body to uptake folate, a key component required for the generation of DNA and as such cellular proliferation. Modern medicines have overtaken methotrexate as a chemotherapeutic and as such it is now mostly utilised as a medicine for rheumatoid arthritis. Methotrexate, like most drug compounds is not transported in the gut by a single transporter, with many transporter proteins in the

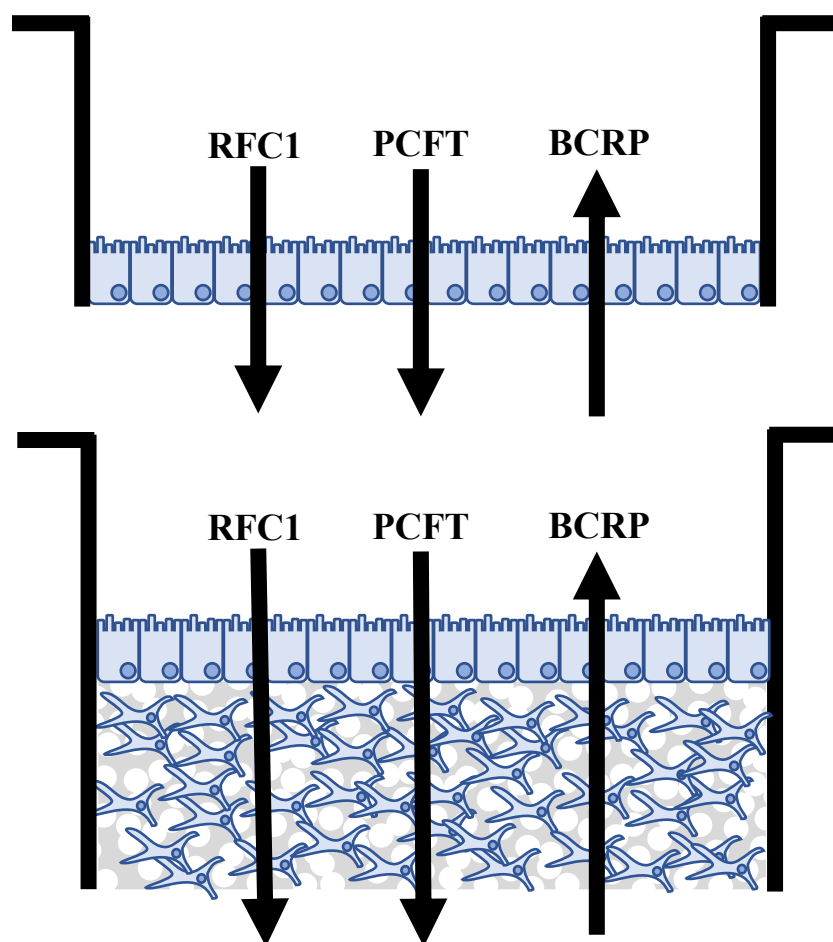


**Figure 6.35: Schematic diagram of the expected permeability routes of Methotrexate in both Transwell and 3D Alvetex intestinal models** – Methotrexate is a folate analogue and as such is up taken by RFC1 and PCFT. In this study methotrexate was primarily utilised as a measure of BCRP activity in the different cellular models.

intestinal enterocytes having largely overlapping functions. However, in this instance methotrexate is being utilised as a marker for BCRP function.

Figure 6.36 shows the relative Papp values of Caco-2 control plus paracrine cultured models. Caco-2 cells in their control format appear to transport methotrexate at a reasonably low rate in the B-A direction (Figure 6.36 A) with an apparent permeability value of around  $0.2 \times 10^{-6} \text{cm/s}$ . Comparatively, paracrine conditioned media of all types was able to increase the permeability of the membrane approximately 3-fold up to a value of  $0.6 \times 10^{-6} \text{cm/s}$ . A-B transport (Figure 6.36 B) shows no particular bias in direction, particularly in control layers but also in HIC and HDFn conditioned media conditions. Some level of directional permeability can be observed in CCD-18co conditions however variation on the levels of transport, particularly in the B-A direction make this difference non-significant in this instance.

### **6.4.15 Methotrexate Transport for 3D Alvetex based intestinal models.**

Figure 6.37 shows the transport capabilities of 3D Alvetex models in the transport of methotrexate in both B-A (Figure 6.37 A) and A-B (Figure 6.37 B) directions of travel. In each instance A-B transport does not appear to be significantly different from B-A transport. 3D models in each case show marginally increased levels of transport in both directions over control values. 3D CCD-18co models show the most modest increase with an average Papp value of around  $0.5 \times 10^{-6} \text{cm/s}$ . 3D HIC models express the highest levels of transport compared to other conditions with an average Papp of approximately  $20 \times 10^{-6} \text{cm/s}$ . However, large levels of data variability suggest that this may be more a flaw in the structural integrity of the model rather than a phenotypic response.

Approximately equal uptake in either direction suggests that uptake and efflux mechanisms are in balance with one another. 3D HIC models show a large increase in B-A and A-B compound transport suggesting two options. 1. The 3D HIC membrane in this instance is allowing the free movement of methotrexate across the epithelium. 2. Influx

and efflux mechanisms are closely related to one another with increases in one correlating with increases in another to maintain B-A/ A-B balance. The first option would seem the most likely if not for the conservation of this observation throughout all the 3D culture systems. Indeed, even though 3D HIC Papp levels are high compared to other conditions tested in this study, they are certainly not high enough to the extent in this case that uncontrolled compound-model passthrough would be likely. What is most likely, as in most of the compounds tested here, is that another as yet unknown mechanism is at play.

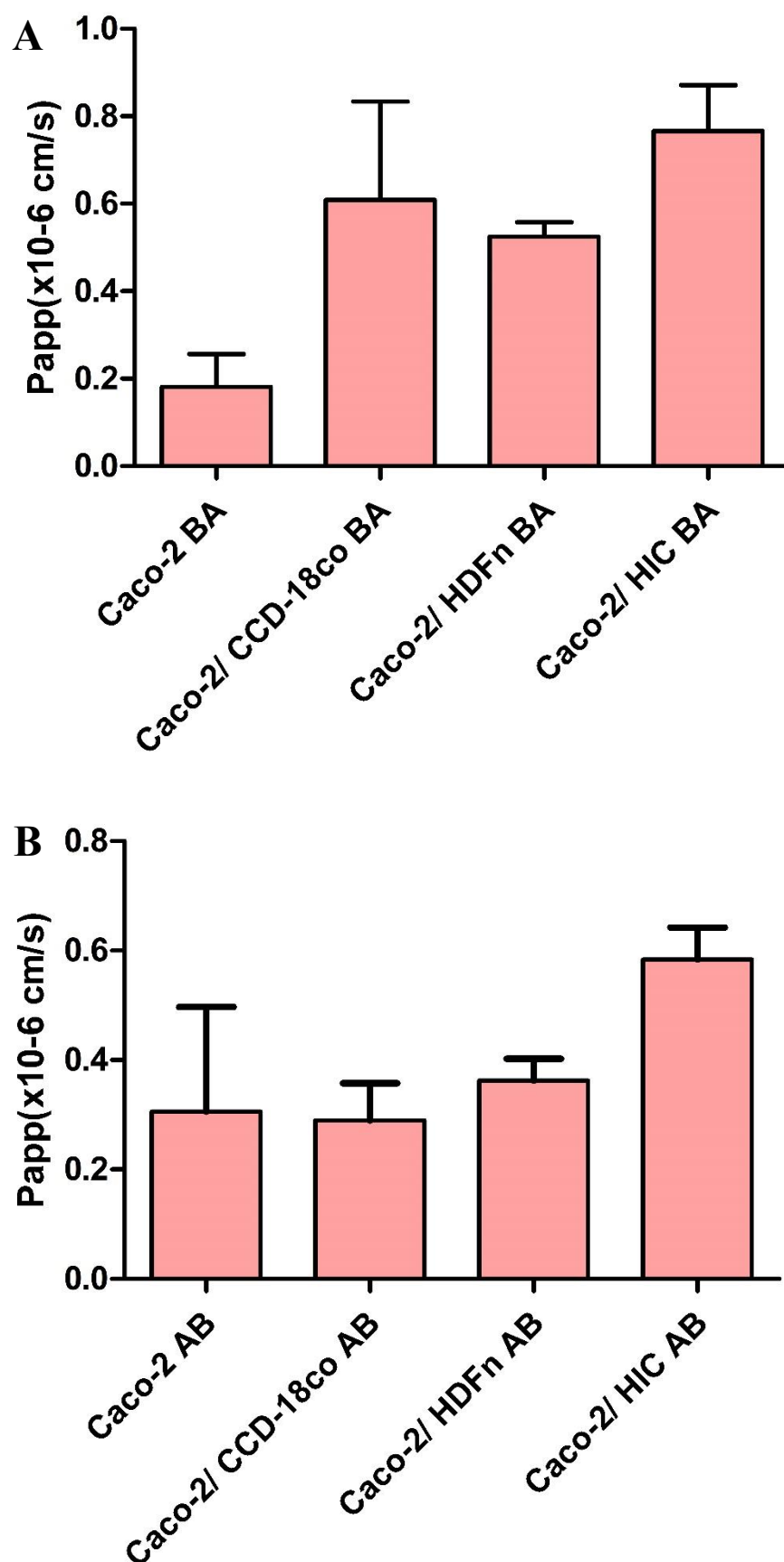


**Figure 6.36: Methotrexate membrane permeability analysis of 2D paracrine Caco-2 co-cultures shows a trending increase in membrane permeability in CCD-18co, HIC and HDFn co-cultures – A) B-A and B) A-B directional transport of methotrexate is utilised as a marker of BCRP mediated active transport. n=3-5 +SEM, N=3-4 Significance is highlighted in Table 6.14**

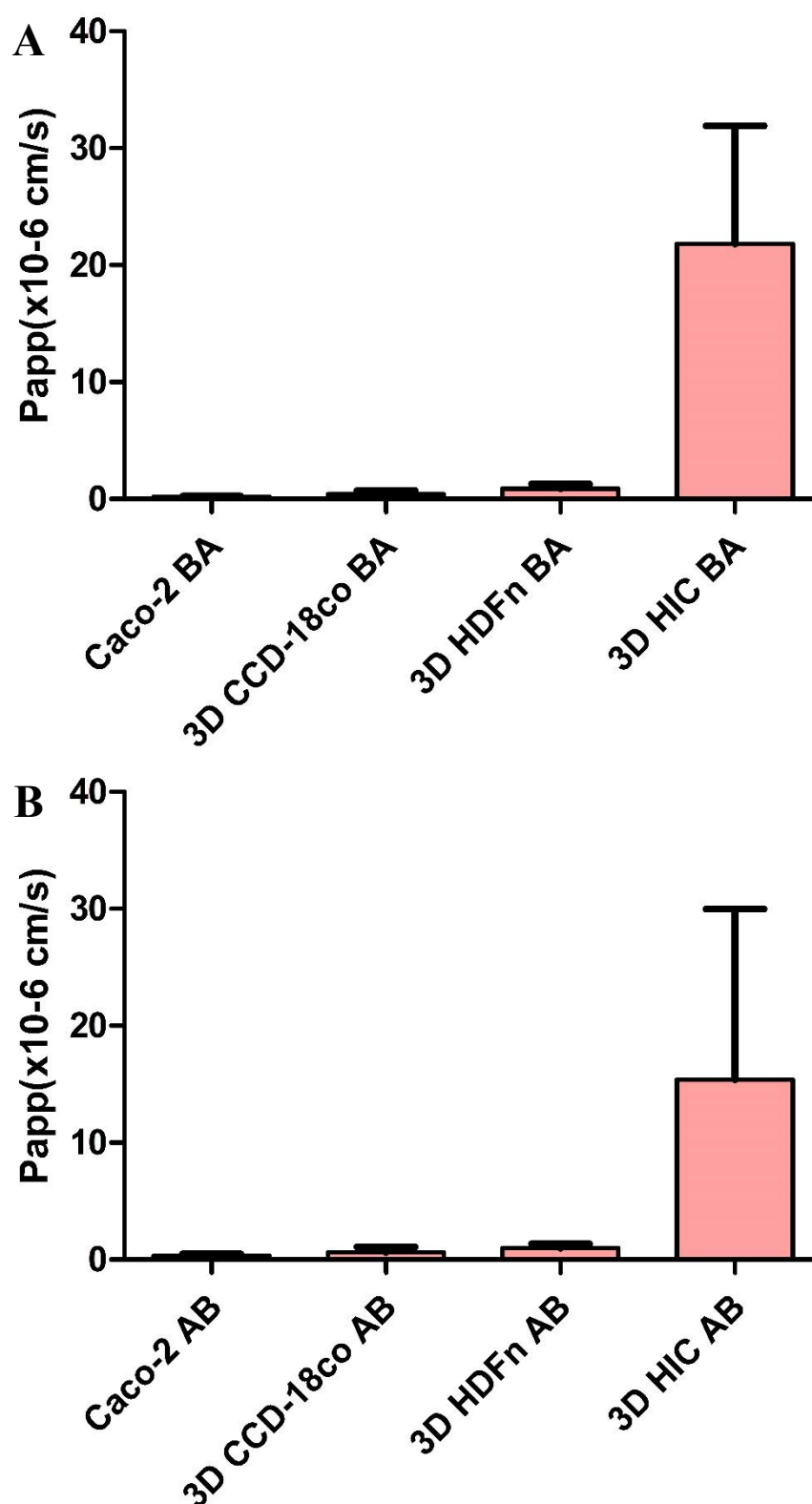


**Figure 6.37: Methotrexate membrane integrity analysis of 3D Alvetex/ Caco-2 co-cultures shows significant increases in membrane permeability in HIC cultures – A) B-A and B) A-B directional transport of methotrexate is utilised as a marker of BCRP mediated active transport. n=3-5 ±SEM, N=3-4. Significance values are highlighted in Table 6.15**

Caco-2 BA vs Caco-2/ CCD-18co BA	ns	Caco-2 AB vs Caco-2/ CCD-18co AB	ns
Caco-2 BA vs Caco-2/ HDFn BA	ns	Caco-2 AB vs Caco-2/ HDFn AB	ns
Caco-2 BA vs Caco-2/HIC BA	ns	Caco-2 AB vs Caco-2/ HIC AB	ns
Caco-2/ CCD-18co BA vs Caco-2/ HDFn BA	ns	Caco-2/ CCD-18co AB vs Caco-2/ HDFn AB	ns
Caco-2/ CCD-18co BA vs Caco-2/HIC BA	ns	Caco-2/ CCD-18co AB vs Caco-2/ HIC AB	ns
Caco-2/ HDFn BA vs Caco-2/HIC BA	ns	Caco-2/ HDFn AB vs Caco-2/ HIC AB	ns

**Table 6.14: Significance values for Methotrexate permeability in 2D Transwell based intestinal models** - Individual significances calculated by One way ANOVA with Tukeys post-test analysis with 95% confidence rating. \*\*\* =  $P < 0.0005$ , \*\* =  $P < 0.005$ , \* =  $P < 0.05$ . B-A and A-B permeability data sets were analysed for significance separately

Caco-2 BA vs 3D CCD-18co BA	ns	Caco-2 AB vs 3D CCD-18co AB	ns
Caco-2 BA vs 3D HDFn BA	ns	Caco-2 AB vs 3D HIC AB	ns
Caco-2 BA vs 3D HIC BA	*	Caco-2 AB vs 3D HDFN AB	ns
3D CCD-18co BA vs 3D HDFn BA	ns	3D CCD-18co AB vs 3D HIC AB	ns
3D CCD-18co BA vs 3D HIC BA	ns	3D CCD-18co AB vs 3D HDFN AB	ns
3D HDFn BA vs 3D HIC BA	ns	3D HIC AB vs 3D HDFN AB	ns

**Table 6.15: Significance values for Methotrexate permeability in 3D Alvetex® based intestinal models** - Individual significances calculated by One way ANOVA with Tukeys post-test analysis with 95% confidence rating. \*\*\* =  $P < 0.0005$ , \*\* =  $P < 0.005$ , \* =  $P < 0.05$ . B-A and A-B permeability data sets were analysed for significance separately



### 6.4.16 Efflux co-efficient values for 2D paracrine Transwell and 3D Alvetex methotrexate model transport.

Figure 6.38 shows the efflux co-efficient transport dynamics of Methotrexate as assessed through the use of 2D paracrine Transwell and 3D Alvetex model systems. When considering the paracrine models alone, little change can be seen when compared to the control models with an average efflux co-efficient of around 1. As described previously this indicates that there is no bias in directional transport of material with approximately equal transport in both B-A and A-B directions. Comparison of this with data gained from 3D transport systems paints a similar picture with, especially HDFn cultures showing no apparent directional bias. 3D CCD-18co and HIC models have a higher efflux coefficient of around 4 and 20 respectively, suggesting significant B-A directional bias. However, large data variation, especially in 3D HIC models may suggest that model integrity is to blame for some of the large transport variations seen here.

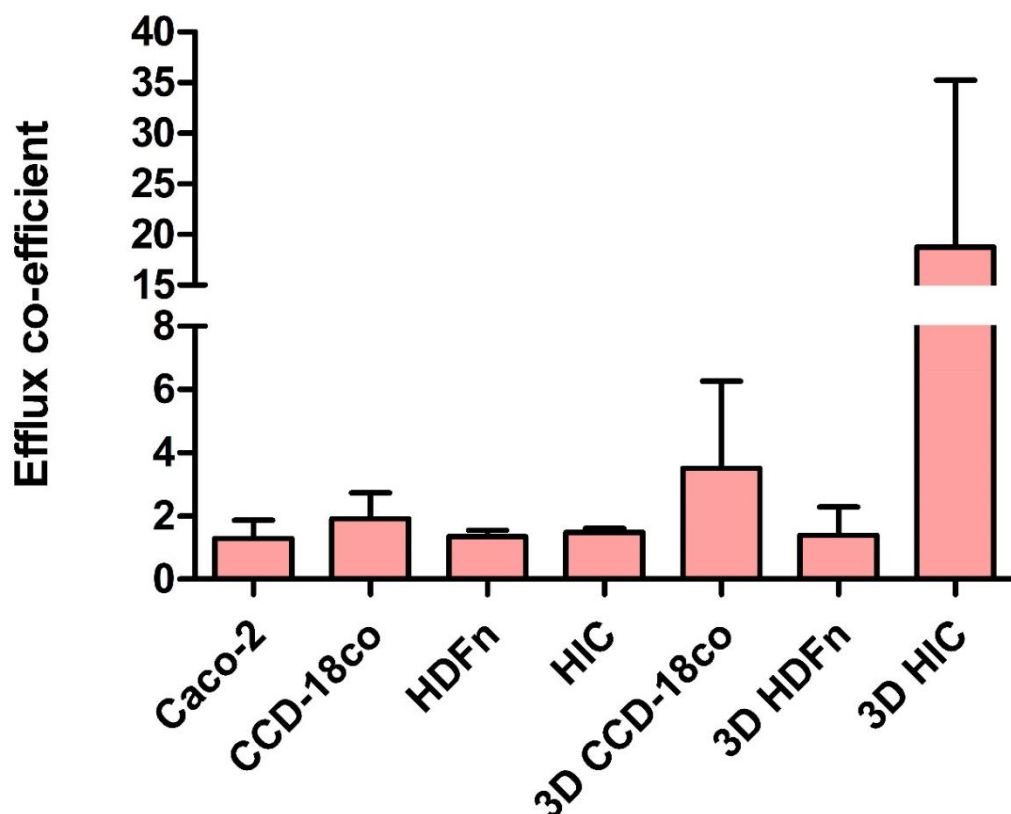


**Figure 6.38: Efflux co-efficient values of Methotrexate comparing controls with paracrine media and 3D Alvetex models** – Data shows no bias toward B-A transport in all 2D paracrine conditions. 3D CCD-18co and HIC models appear to favour B-A transport. n=3 +SEM. N=3 No significance was observed between models

### 6.4.17 Lucifer yellow transport of 2D Transwell co-cultures and 3D Alvetex based intestinal models.

Lucifer yellow is primarily utilised in industry as a marker of paracellular transport, and as such is a proxy for membrane integrity, similar to how TEER values determine a membranes viability for experimentation. Figure 6.40 shows the bidirectional transport of lucifer yellow tested across paracrine media cultured Caco-2 Transwell models. Control layers exhibit B-A (Figure 6.40 A) Papp values of approximately  $1 \times 10^{-6} \text{ cm s}^{-1}$  indicating that lucifer yellow is relatively poorly permeable across control membranes. Addition of CCD-18co paracrine media to the Caco-2 cultures results in a modest, non-significant increase in the apparent permeability of Lucifer yellow. Both HIC and HDFn conditioned media showed a marked and significant decrease in membrane permeability compared to control levels with Papp values approximately half of those seen in untreated control samples. Control and CCD-18co samples showed a bias towards transport in the B-A direction, with significantly reduced Papp values when lucifer yellow is tested A-B

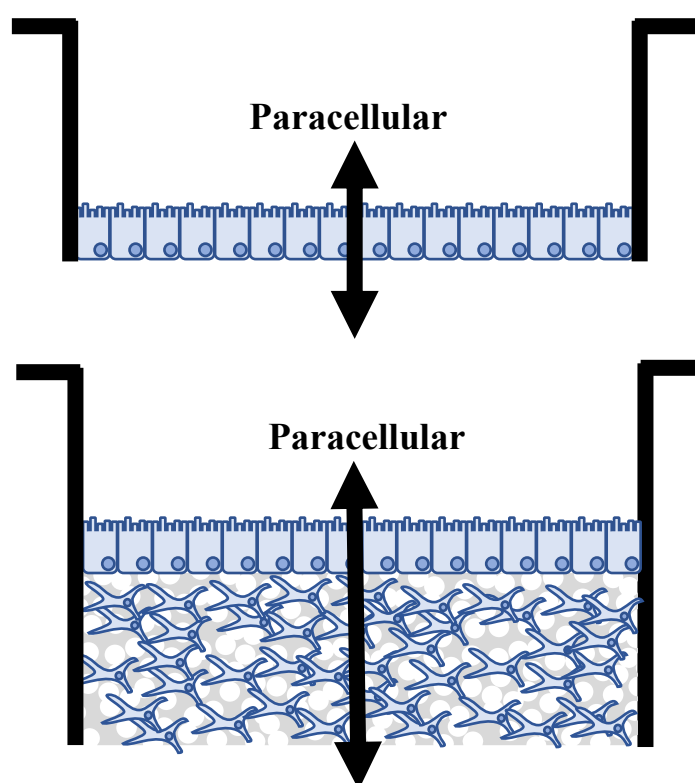


**Figure 6.39: Schematic diagram of expected lucifer yellow transportation routes through both Transwell and Alvetex scaffold intestinal models** – Lucifer yellow is a well-known and characterised compound generally utilised as a marker of paracellular permeability. No known active transport mechanisms are thought to influence lucifer yellow transport.

(Figure 6.40 B). In contrast, HIC and HDFn values were approximately equal bi-directionally with no obvious bias.

Lucifer Yellow membrane integrity analysis of 3D models (Figure 6.41) shows a different phenotype to their 2D counterparts. In all instances (CCD-18co, HIC and HDFn) 3D models showed a moderate increase in B-A permeability to Lucifer yellow with Papp values approximately double those of the control (Figure 6.41 A). Interestingly, the B-A bias seen in CCD-18co paracrine treated 2D models is lost when cultures are grown in 3D. Indeed, all 3D models exhibited approximately equal bi-directional transport, consistent across all 3D models types. A-B values were significantly increased in all 3D conditioned compared to Caco-2 Transwell based controls (Figure 6.41 B). The lucifer yellow values gained for 3D HIC models (along with a similar TEER values) are not significantly different from the other 3D systems with improved histologically analysed structural morphology. As such this lends weight to the idea that whilst HIC cells do not histologically demonstrate the same *in vivo* correlation as other models created here, they do in fact create a confluent layer of Caco-2 cells apically to the fibroblast culture surface, justifying their continued use on this study.

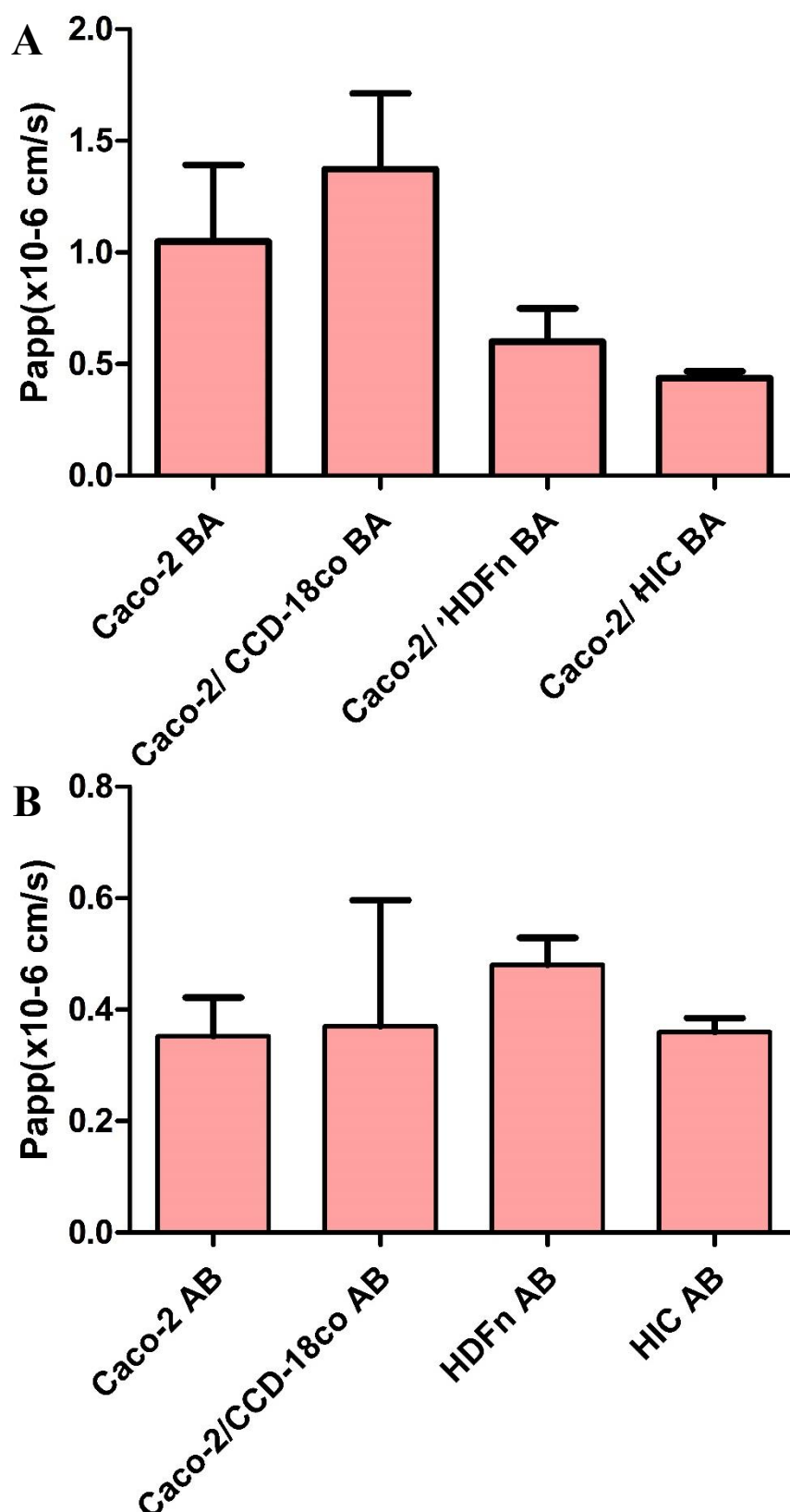


**Figure 6.40: Lucifer yellow membrane integrity analysis of 2D paracrine Caco-2 co-cultures** – A) B-A and B) A-B directional transport of Lucifer Yellow is utilised as a marker of membrane integrity, with lower Papp values suggesting a more tightly bound and impermeable membrane to passive compound transport. n=3-11 +SEM N= a minimum of three independent experiments. Significance is noted in Table 6.16

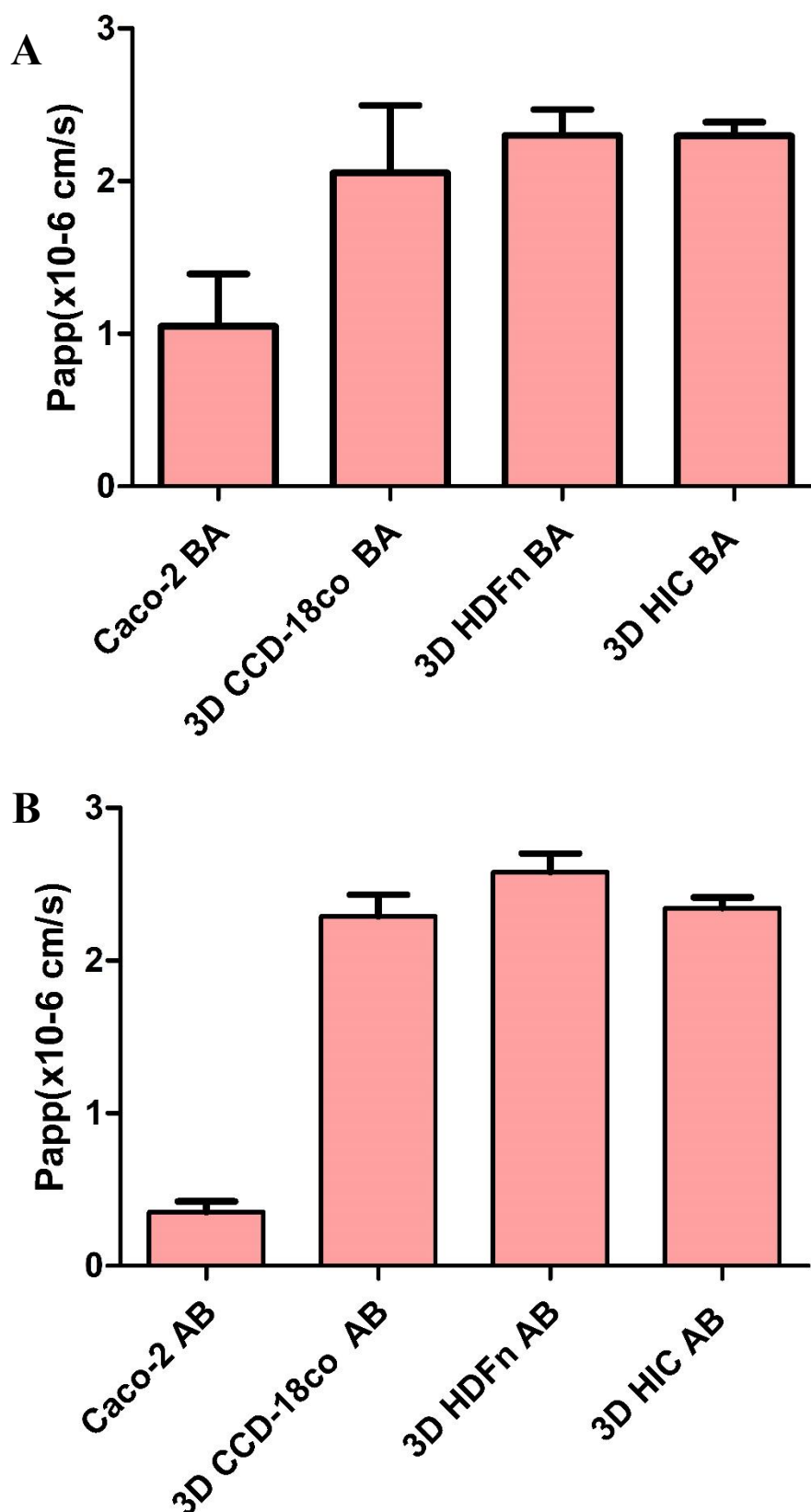


**Figure 6.41: Bi-directional transport of Lucifer Yellow shows significant increase in membrane permeability in 3D Alvetex based intestinal models compared to 2D Transwell alternatives – B-A and A-B transport of lucifer yellow analysed through 3D intestinal model constructs shows a marked increase in permeability compared to control layers. n=3-7 +SEM. N= a minimum of three independent experiments. Significance is noted in Table 6.16**

Caco-2 BA vs Caco-2/ CCD-18co BA	ns	Caco-2 AB vs Caco-2/ CCD-18co AB	ns
Caco-2 BA vs Caco-2/ HDFn BA	ns	Caco-2 AB vs Caco-2/ HDFn AB	ns
Caco-2 BA vs Caco-2/HIC BA	ns	Caco-2 AB vs Caco-2/ HIC AB	ns
Caco-2/ CCD-18co BA vs Caco-2/ HDFn BA	ns	Caco-2/ CCD-18co AB vs Caco-2/ HDFn AB	ns
Caco-2/ CCD-18co BA vs Caco-2/HIC BA	ns	Caco-2/ CCD-18co AB vs Caco-2/ HIC AB	ns
Caco-2/ HDFn BA vs Caco-2/HIC BA	ns	Caco-2/ HDFn AB vs Caco-2/ HIC AB	ns

**Table 6.16: Significance values for Lucifer yellow permeability in 2D intestinal models -** Individual significances calculated by One way ANOVA with Tukeys post-test analysis with 95% confidence rating. \*\*\* =  $P < 0.0005$ , \*\* =  $P < 0.005$ , \* =  $P < 0.05$ . B-A and A-B permeability data sets were analysed for significance separately

Caco-2 BA vs 3D CCD-18co BA	ns	Caco-2 AB vs 3D CCD-18co AB	***
Caco-2 BA vs 3D HDFn BA	ns	Caco-2 AB vs 3D HIC AB	***
Caco-2 BA vs 3D HIC BA	ns	Caco-2 AB vs 3D HDFn AB	***
3D CCD-18co BA vs 3D HDFn BA	ns	3D CCD-18co AB vs 3D HIC AB	ns
3D CCD-18co BA vs 3D HIC BA	ns	3D CCD-18co AB vs 3D HDFn AB	ns
3D HDFn BA vs 3D HIC BA	ns	3D HIC AB vs 3D HDFn AB	ns

**Table 6.17: Significance values for Lucifer yellow permeability in 3D intestinal models -** Individual significances calculated by One way ANOVA with Tukeys post-test analysis with 95% confidence rating. \*\*\* =  $P < 0.0005$ , \*\* =  $P < 0.005$ , \* =  $P < 0.05$ . B-A and A-B permeability data sets were analysed for significance separately

### 6.4.18 Efflux co-efficient of lucifer yellow in 2D and 3D models

Figure 6.42 shows the calculated efflux co-efficient of lucifer yellow permeability across 2D Transwell Snapwell model layers, both control and condition media treated, in addition to 3D Alvetex models. Transwell Caco-2 control and CCD-18co treated layers show a significant trend toward a bias in the B-A direction of compound permeability. In essence, meaning that lucifer yellow in these models is more readily permeable through the B-A direction of travel then the converse A-B. Contrastingly, 2D HIC and HDFn paracrine treated models in addition to all 3D Alvetex models tested show an efflux co-efficient of approximately 1. This suggests that there is no bias in permeability with compound movement approximately equal in any direction of travel.

This differential efflux phenotype can be clearly seen in the original data (Figure 6.40 & 41) whereby A-B directional transport is significantly less than the B-A counterparts.

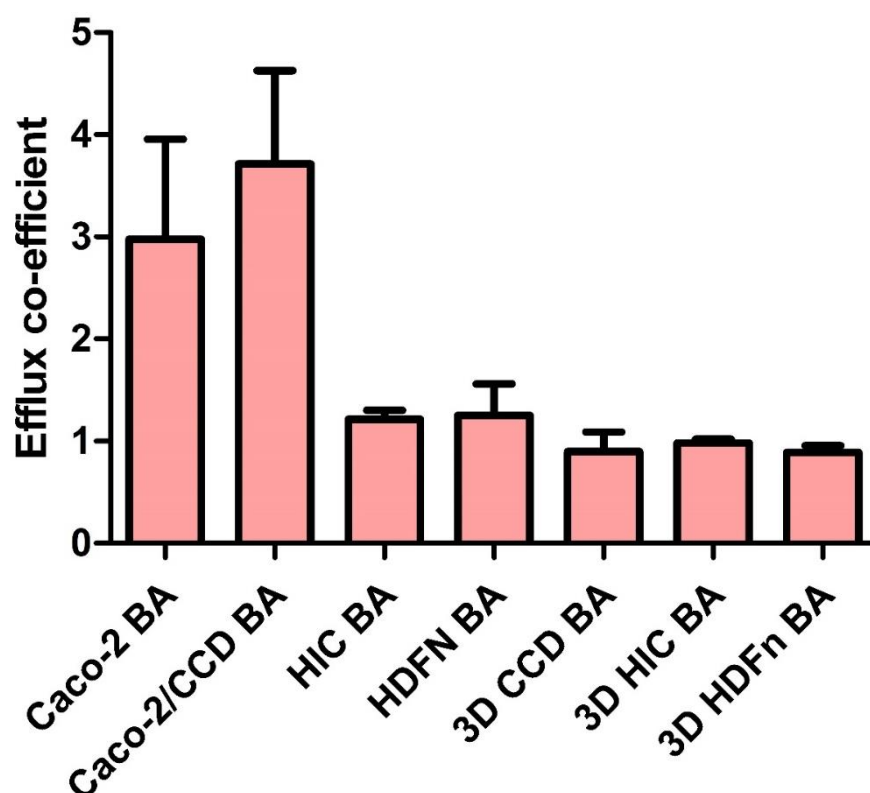


**Figure 6.42: Efflux co-efficient of lucifer yellow analysis suggests Control and 2D CCD-18co layers have a B-A directional bias** – Efflux co-efficient analysis suggests directional bias in control and 2D CCD-18co treated layers. All other conditions indicate equal permeability in either direction. n=3-11 N=3 +SEM. No significance was found between transport models

	<b>Papp BA ± SEM x10<sup>-6</sup></b>								
	<b>Caco-2 control</b>	<b>Caco-2 literature</b>	<b>Caco-2/ CCD-18co</b>	<b>Caco-2/ HDFn</b>	<b>Caco-2/ HIC</b>	<b>3D Caco-2/ CCD-18co</b>	<b>3D Caco-2/ HDFn</b>	<b>3D Caco-2/ HIC</b>	<b>Intestine Tissue</b>
<b>Rhodamine 123</b>	0.82 ± 0.35/	6.84 ± 2.48	0.96 ± 0.27	3.30 ± 1.2	0.29 ± 0.04	2.32 ± 0.24	1.19 ± 0.17	6.88 ± 2.90	1.8 – 3.6 (Porcine)(269)
<b>Atenolol</b>	0.31 ± 0.07	0.66 ± 0.26	0.70 ± 0.17	0.85 ± 0.02	2.18 ± 0.53	0.41 ± 0.18	8.67 ± 0.39	0.38 ± 0.12	11.5 ± 4.09 (Rat Jejunum) (344)  2.82 ± 0.65 (Human)(345)
<b>Propranolol</b>	13.12 ± 1.78	37.51 ± 16.1	14.62 ± 0.40	28.73 ± 8.69	17.03 ± 7.84	5.33 ± 1.49	14.95 ± 3.02	7.27 ± 2.75	6.01 ± 3.41 (Porcine)(346)  1.85–5.50 (Porcine)(269)
<b>Lucifer Yellow</b>	1.05 ± 0.34	2.58 ± 2.34	1.37 ± 0.34	0.60 ± 0.15	0.44 ± 0.03	2.05 ± 0.44	2.30 ± 0.17	2.30 ± 0.09	4.02 ± 2.20 (Human)(345)
<b>Etoposide</b>	0.05 ± 0.04	8.04 ± 1.55	2.25 ± 2.15	3.71 ± 0.16	1.47 ± 1.13	2.88 ± 0.71	13.88 ± 9.72	57.23 ± 6.33	1.13 ± 1.00 (Rabbit) (69) 101 ± 9 (Rat) (67)
<b>Methotrexate</b>	0.18 ± 0.07	0.70 ± 0.50	0.61 ± 0.22	0.52 ± 0.03	0.77 ± 0.10	0.40 ± 0.32	0.89 ± 0.38	21.8 ± 10.11	Unknown

**Table 6.18: Comparative Papp values of models created in this study compared to values gained from the literature for both Caco-2 standards and intestinal tissues (Human and animal)** – All model conditions generally show improvements over internal Caco-2 standards compared to Caco-2 values gained from the literature. Compared to human tissues HDFn 3D models shows the closest similarity of the different models when all test systems are compared.



## **6.5 Discussion**

### **6.5.1 Transport dynamics of model systems and the context for this chapter**

This final chapter is focussed on understanding the influence of fibroblasts of varying origin on the development and differentiation of the Caco-2 epithelium both in terms of the paracrine effects released (Transwell conditioned media experiments) and in the effects of direct co-culture (3D Alvetex<sup>®</sup> based models). The functional characteristics of the differing models were tested for their capabilities to transport a number of model drug compounds; namely, Rhodamine 123, Atenolol, Propranolol, Etoposide, Methotrexate and Lucifer yellow. These drugs were chosen specifically to assess the function of the models in differing ways be they passive absorption (Lucifer yellow, Atenolol and propranolol) (66,90,313) or actively transported (Rhodamine 123 – P-gp, Etoposide – MRP, Methotrexate – BCRP). Understanding the functional characteristics of fibroblast/Myofibroblast conditioned models is key to understanding their relative importance in future research directions as tools for more advanced analysis of NCE compounds, in this instance for their pharmacokinetic properties. The relative transport characteristics of the tested models will be compared to human tissues through thorough examination of available literature.

### **6.5.2 2D paracrine Transwell and 3D intestinal equivalents both show significantly decreased membrane resistance compared to conventionally cultured Caco-2 models.**

Initial investigations into the effects of 3D culture focused on the changing transepithelial electrical resistance of the complete model. Significant decreases in epithelial resistance were seen in 3D when compared to their 2D Snapwell Transwell counterparts whereby in 2D the most significant decrease lowered TEER to approx. 500 Ohms.cm<sup>2</sup> compared to approx. 50 Ohms.cm<sup>2</sup> in 3D systems, a ten-fold difference and a level comparable to measurements in human intestinal tissues.

Understanding the likely causes for this significant decrease can be hypothesised as three fold.

1. Unlike in the Snapwell formats whereby TEER analysis (Chapter 3) uses a standard EVOM-2 TEER device with chopstick electrodes (WPI, UK), a commonly used standard throughout the industry; Alvetex<sup>®</sup> models, due to their novel 96-well format were measured utilising an Ussing chamber as described in section 6.3.2.(347) Both systems rely on the same principle for the measurement of epithelial resistance however it cannot be completely ruled out that differences seen in the overall TEER values gained are due to differences in the equipment being utilised. Human tissue TEER is generally measured through an Ussing chamber device, potentially, explaining the similarity in measurement between models and tissues using this method. TEER measurements in the literature vary widely dependant on the lab culturing and measuring, with differences in equipment/ equipment operator along with variations in Caco-2 origin and passage generally thought to be the main contributors in this inconsistency.
2. Absolute fibroblast numbers was not controlled between 2D paracrine and 3D models. The absolute number of cells/cm<sup>2</sup> seeded into 3D models was far higher when compared to the average density of a 90% confluent 2D culture flask utilised for conditioned media creation. This could lead to an unbalance comparison between model systems with 2D paracrine Transwell models likely stimulated to a lesser extent than in 3D Alvetex<sup>®</sup>. Additionally, due to the vast difference between Snapwell and 96-well Alvetex<sup>®</sup> formats different media volumes were necessarily added to each system, with 3.5ml added to Snapwell and 1.5ml added to Alvetex<sup>®</sup>. In essence this could result in either a dilution or concentration effect depending on the model being analysed. However, data in this thesis clearly shows that absolute seeded number in 3D does not directly correlate with cell numbers growing within the scaffold. Data from chapter 3 on the analysis of KGF levels between system types clearly shows how when normalised to DNA concentration, 3D cultured cells appear to secrete far less KGF than their 2D counterparts.

3. 3D culture allows for direct contact between stromal and epithelial cells in addition to enhancing the paracrine secretome compared to 2D cultured cells. The enhanced secretome could have physiological effects on a number of ways such as: 1. Increasing the levels of small molecules already released in 2D, 2. Changing the ratios of small molecules produced initiating new pathways for differentiation, 3. Producing new signalling molecules not seen in normal 2D conditions. Whilst the actual mechanism is not evidenced here, it is evident that one or a combination of many of these factors allow for enhanced differentiation of epithelial cells, in this case Caco-2, to a level more similar to the *in vivo* tissues. The physiologically relevant changes seen in 2D paracrine cultures lend evidence that changes in TEER within 3D constructs is more likely due to physiological differences in cellular phenotype rather than an artefact of differing culture system.

Due to the differences in the format types between the models tested here the only way to reduce the uncertainty behind the mechanism for change would be to create a custom insert type able to culture both Transwell and Alvetex® systems in the same format. This could be achieved either by modifying Alvetex® to fit the Snapwell format or vice versa. Similar to Patient *et al.* (269)

One of the main contributors to epithelial resistance is the expression and confluency of tight junctional complexes. (206) 3D CCD-18co and HDFn histological analysis shows well defined stromal/ epithelial layers without Caco-2 penetration into the underlying mucosal compartment. HIC intestinal models show a far less organised structure with significant Caco-2 cellular invasion into the underlying mucosae. That isn't to say however that a confluent layer doesn't exist on the surface of the HIC model, just that without structure one would expect function to lag. Changes in Caco-2 surface consistency cannot be ruled out as a potential contributor to the decreases in TEER observed in 3D models. Indeed, the surface topography of Alvetex Scaffold® can be highly irregular due to the largely uncontrolled arrangement of void spaces in the material. Often with areas of significant Caco-2 invasion simply due to Alvetex topography. However, SEM surface topography, histological analysis or immunostaining characterisation of paracrine and 3D models does not appear to show any consistent inconsistencies in Caco-2 epithelial development.

Occludin (a protein component of the tight junctional complex and analogous with tight junction expression) was utilised as a marker for tight junction expression and localisation. All models tested expressed physiological levels of Occludin when immunostained without any noticeable differences in staining intensity. More advanced staining techniques of the epithelial layer as seen in chapter 5 through model clearing and light sheet analysis clearly show a contiguous layer of epithelial cell staining across the surface of the 3D model. More quantitative methods of Occludin measurement were attempted utilising qPCR. Unfortunately, due to the multicellular nature of the 3D models, accurate quantification of relative protein expression cannot be made between different formats due to the dilution effect of fibroblast mRNA. However, analysis of the effects of paracrine media on protein expression showed no significant differences between Controls, CCD-18co, HIC or HDFn. HIC conditions did show a strong, largely decreased trend compared to controls suggesting paracrine HIC influences may have effects on tight junction formation. This hypothesis is unsupported by any significant evidence within this thesis however.

One alternative methodology for the decreases in TEER seen here without any apparent corresponding disruption to tight junctional formation could be the increase in Claudin 2 discussed in chapter 3. Recent evidence has shown that Claudin-2 expression and resultant use within tight junction complexes is increased through the paracrine effects of KGF, a significant component of CCD-18co paracrine media samples.(209,210,221) Claudin-2 has been shown to form “leakier” tight junctions through the creation of small pore structures in the junction complex allowing the movement of ions and other very small compounds through the epithelial layer. Unabridged movement of ions in particular across the membrane could provide one potential reasonable explanation as to why TEER levels would be decreased in these samples as ion movement would naturally result in decreased resistances. As mentioned earlier however, only CCD-18co conditioned media samples showed significant levels of KGF, other fibroblast conditions must therefore either decrease TEER through a different mechanism or other small molecule combinations could work to have the same physiological effects.

### **6.5.3 Analysis of the functional capabilities of epithelial intestinal equivalents through the passive paracellular transport assessment of model drug compounds.**

It is well known that Caco-2 models significantly underestimate the absorption rate of paracellularly transported compounds. (348) This study utilises 3 drugs whose main absorption route is through the paracellular methodology, namely; Lucifer yellow, Atenolol (Low general permeability) and Propranolol (High general permeability).

Lucifer Yellow is a classically utilised molecule used to test barrier integrity within Caco-2 assays, and, along with TEER is the gold standard for determining model viability before more complex uses. (314,349–351) Figure 6.40, 6.41 and 6.42 within this chapter look at the relative Lucifer yellow permeability between both paracrine and 3D models compared to controls. Generally speaking, Lucifer yellow Papp was shown to marginally decrease in HIC and HDFn whilst not changing significantly in CCD-18co paracrine cultures. 3D models on the other hand did see a significant increase in Lucifer yellow Papp suggesting disruption to the epithelial layer compared to Transwell format models. However, the levels to which the 3D models Lucifer Yellow Papp increased to was not significant enough to suggest complete failure of the epithelial membrane. In fact, Culot *et al* note that a Lucifer Yellow Papp  $17 \times 10^{-6}$  is the point at which membrane breakage is likely which is far above the levels seen in even the most permeable of the models tested in this study. (352) In reality, acceptable Papp values for lucifer yellow in industry are far below this outlying level and generally range between  $0.5$  and  $2 \times 10^{-6} \text{ cm s}^{-1}$  dependant on the labs internally chosen cut off points. As such there were no concerns regarding the Papp values of the 3D models in particular which, whilst higher than Caco-2 Transwell controls, were not excessively high enough to suggest membrane malformation.

Atenolol transport was significantly increased in paracrine 2D models up to four fold that of conventionally cultured control layers in Caco-2/ HIC conditioned media samples. Interestingly, some correlations can be drawn between the origin of the fibroblast lineage utilised in each condition and the relative changes on membrane permeability to Atenolol. HIC cells as mentioned previously were isolated from human small intestinal duodenum

samples received from Bioptra, UK, for use in this study. Tissues were cut into small pieces and left in culture until cells began to grow out of the samples. These outgrowths were characterised and utilised in this study with the designation of HIC. As such these are technically the most *in vivo* relevant cells. Dahlgren *et al* conducted a study on the transport kinetics of Atenolol, alongside Metoprolol and Ketoprofen, within human test subject by measurement of drug plasma concentration over time. (353) Drugs were added to variable parts of the intestine through a intraluminal, tube-capsule technique. They found that small intestinal uptake of atenolol was far higher than colonic uptake by a factor of approximately ten-fold. Caco-2 cells are colonic in origin and as such should phenotypically be relatively impermeable to Atenolol, as is shown in the literature. (314,350,354–357) CCD-18co cells are also colonic in origin so physiologically shouldn't increase Atenolol permeability significantly over controls when considering the physiological context. Having said that however, a small increase is seen in the CCD-18co and HDFn conditioned media samples, perhaps suggesting that epithelial development is enhanced through conditioned media over controls levels regardless of the physiological context of the fibroblasts used, improving model sensitivity. Most interesting is the large increase in permeability when cultured with HIC conditioned media. Small intestinal cells therefore can be seen to cause physiologically relevant changes to epithelial cells of colonic origin through the indirect effects of paracrine secretion, in isolation from any other factors.

Analysis of the 3D model's Atenolol transport is less easily reasoned in a physiological context. The beneficial increase on transport seen in paracrine cultures is lost in both CCD-18co and HIC 3D models with no significant changes in transport compared to controls. As mentioned previously it could be hypothesised that this decrease in 3D function is more to do with the absolute number of cells present within the 3D scaffold than a physiological effect of cells cultured in 3D. Whilst efforts were made to seed the same density of Caco-2 cells into 3D models as would exist in the same representative area of 2D cultures, the changing cellular metabolism and proliferative capacity of cells in 3D made this difficult to achieve over long culture periods. 3D HDFn models show a large increase compared to controls which doesn't appear to be supported with literature evidence. Potentially, models were "leaky" as a consequence of model structure however HDFn models were routinely observed to form structurally capable models with little to

no Caco-2 invasion into the underlying stroma. Additionally, 3 independent measurements provide closely matching values with only a small amount of variability. One would expect if increased transport was due to the improper model structural characteristics then permeability values would be far larger and more variable. Indeed, if model structural consistency were an issue then 3D HIC models would be the more likely candidate for excessive permeability due to its inconsistent and poor structural morphology between models. To my knowledge, study of the effects of human dermal fibroblast cells on the morphology and function of Caco-2 cells has not been attempted before. Understanding the exact mechanisms and secretome of HDFn cells is beyond the scope of this work initially and will be revisited in the future direction of this project.

The final passively transported compound utilised in this study is Propranolol. Generally, Propranolol is well known for being readily absorbed by the Caco-2 models and the human intestine. (358,359) Permeability of Propranolol was variable between culture conditions but generally high as expected and comparable for the most part to Caco-2 control transport. Transwell paracrine models in each instance are relatively more permeable than their 3D culture counterparts, with some of the 3D cultures (CCD-18co and HIC) being lower than the Caco-2 Transwell controls. HDFn cultures, as seen in Atenolol transport quantification show the highest increase in membrane permeability compared to controls in Transwell paracrine models and comparatively higher between 3D models. As such this could lend evidence that some unknown mechanism (unlikely to be simple tight junction dysfunction for reasons mentioned above) is inducing HDFn paracrine Caco-2 layers to increase passive permeability. Propranolol is known for being a highly lipophilic (360) compound and as such some levels of compound is likely move into and remain within cellular cytoplasmic spaces. As such, one explanation for the decreases seen in 3D cultures could simply be due to drug retention within the model itself rather than a physiologically relevant change in membrane integrity or function. Indeed, this is a known issue when measuring Propranolol transport in tissues whereby drug sequestration is markedly more pronounced than those seen here due to the sheer number and volume of cellular matter within an active tissue. (269) Considering that the comparative permeability pattern between Transwell models and their 3D counterparts is almost identical in each case albeit lower in 3D models, it is more likely that drug sequestration is responsible for the decrease observed.

### 6.5.4 Actively transported compound analysis

Active transport of compounds was modelled in this study through the transport mechanisms of Rhodamine 123, Etoposide and Methotrexate. Nominally, these model compounds were chosen to study the active transport of MDR1/ P-gp, MRP1/2 and BCRP. However, as mentioned previously, analysis of the function of each drug transporter protein in isolation of the others is difficult, if not impossible, due to the significant levels of overlap which exist between the different transporter substrate specificities. For example, where Etoposide is used here to measure MRP family activity, it is also reasonably well known as a substrate of MDR1/ P-gp.

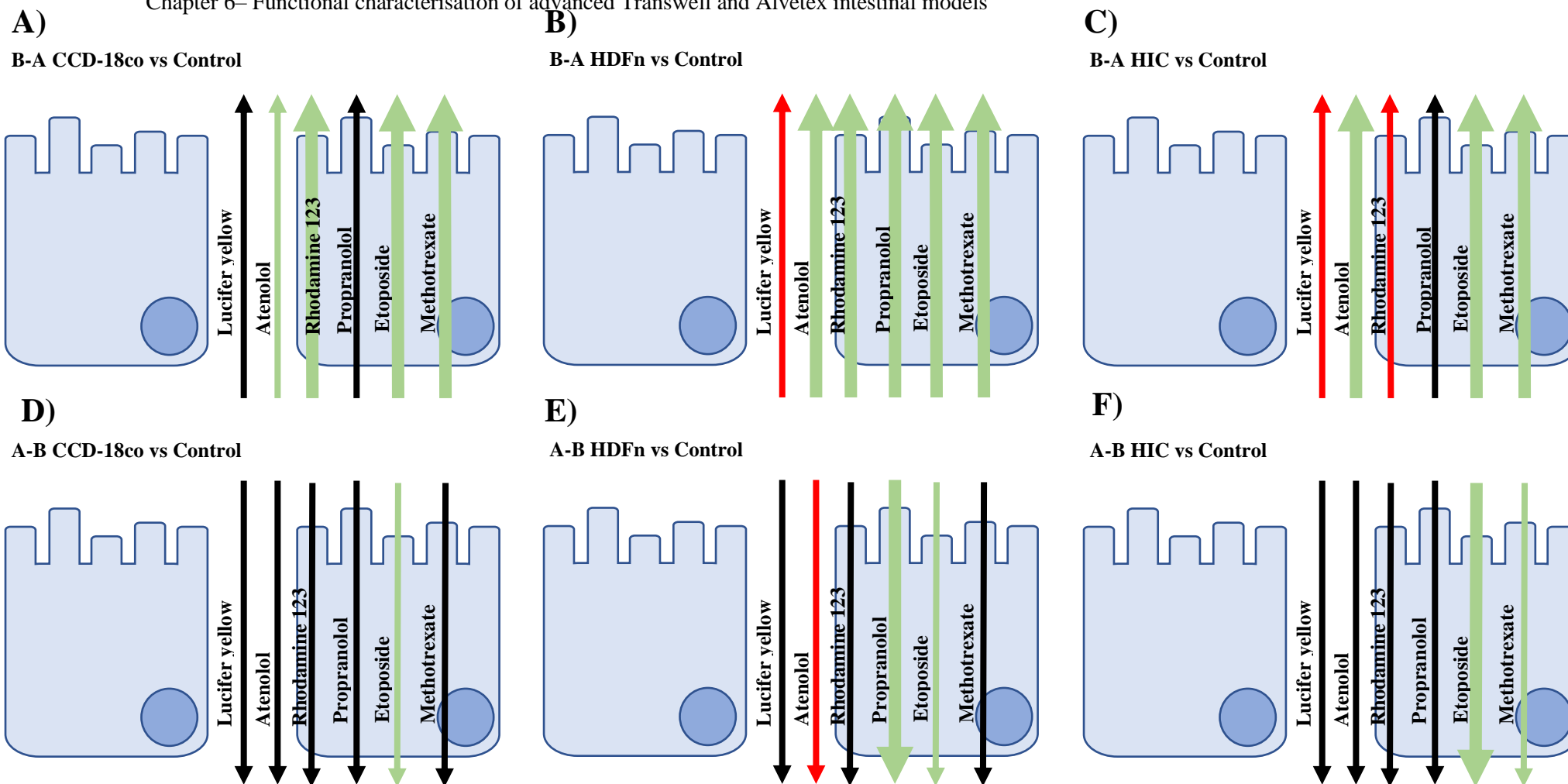
Rhodamine 123 mediated functional analysis of MDR1/ P-gp and the subsequent use of Verapamil Hydrochloride, a competitive inhibitor of MDR1/ P-gp activity can tell a lot about MDR1/ P-gp activity in addition to the levels of overlapping transporter function seen within the models. (361) For example, Caco-2 control layers were shown to be significantly less permeable B-A to Rhodamine 123 after treatment with Verapamil Hydrochloride, as such suggesting that the primary transport mechanism of Rhodamine 123 in control epithelial models is through MDR1/ P-gp. The same is true for CCD-18co and HDFn paracrine treated layers which show a similar pattern (Figure 6.12). Contrastingly, HIC paracrine model Papps are shown to be less effected by the addition of Verapamil Hydrochloride with no significant transport suppression in the case of HIC paracrine and 3D HDFn, as such suggesting Rhodamine 123 transport through some other mechanism, most probably, as mentioned previously, an overlapping ABC transporter protein such as BCRP or MRP1/2. Alternatively, evidence in the literature shows how Verapamil can have effects on the tight junction assembly within the Caco-2 epithelium, potentially increasing rates of paracellular permeability to hydrophilic compounds. (362,363) Sakai *et al* were able to show that the concentration dependant effects of Verapamil were able to increase the membrane permeability to FD-4 (a commonly utilised passive paracellular compound similar to lucifer yellow) approximately 4-6 fold. This could explain some of the anomalous instances in this study whereby application of Verapamil either increased or did no significantly change the membrane permeability to Rhodamine 123 B-A, such as in KGF treated Caco-2 Transwell layers and 3D



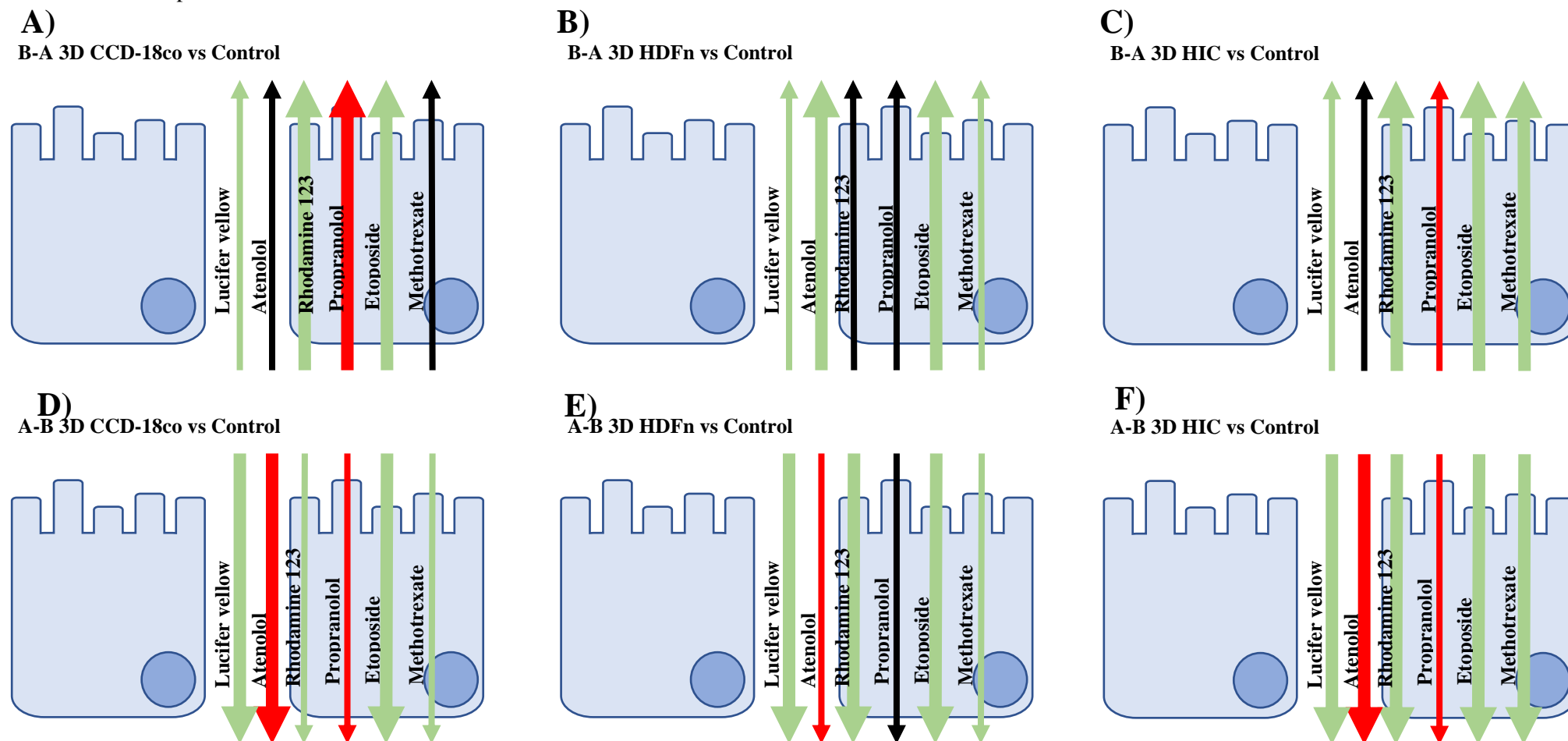
bioengineered models whereby permeability increased and stayed the same respectively in Verapamil treated assays. Indeed, it is the models with the lowest measured TEER values which appear to be most affected by this potential mechanism further supporting evidence that, in some instances, Rhodamine 123 transport is primarily through a paracellular mechanism rather than MDR1/P-gp mediated.

MDR1/ P-gp is thought to be underrepresented in some Caco-2 epithelial models with work in the past by Shirasaka *et al* focussed on increasing MDR1 mediated activity of Caco-2 membranes, They showed the MDR1/ P-gp expression can be induced by co-culture of cells with the drug Vinblastine, normally used as a substrate for MDR1/ P-gp efflux measurements. (364). Additionally, other works have shown that MDR1/ P-gp expression rates can be effected by variables such as Caco-2 passage and culture time with increasing both correlating with increased MDR1/ P-gp expression. (365) Work undertaken in this study has highlighted that HDFn paracrine and all 3D conditions result in significant increase in Rhodamine 123 transport when compared to controls, suggesting, at least partially, an increase in MDR1/ P-gp activity.

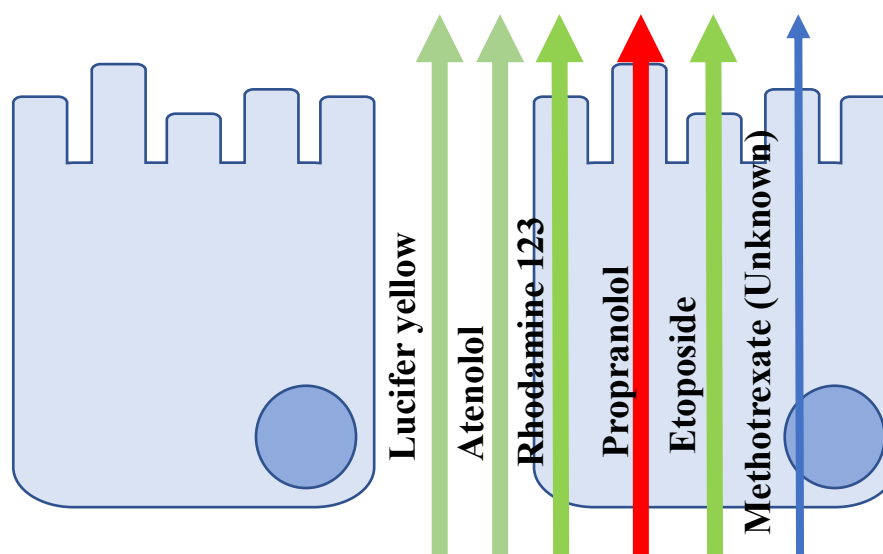
Etoposide and Methotrexate transport (MRP1/2 and BCRP respectively) both show improvements in transport capabilities when Caco-2 layers are cultured with paracrine media from CCD-18co, HDFn and HIC cells. These increases are significant compared to control Caco-2 layers yet small compared to the changes seen in 3D whereby, similar to other conditions, HDFn and HIC 3D models have the greatest increase in permeability. There is some evidence to suggest that BCRP expression in untreated Caco-2 layers is expressed to a lesser level than found in human intestine. (28) Madden *et al* showed that the 3D culture of primary intestinal epithelial cells increased BCRP expression compared to Caco-2 controls, similar to that seen here.



**Figure 6.43: Summary of the complete analysis of 2D Caco-2 Transwell models with the model compounds tested in this study** – Blank lines = No change from control, Thin green line = Small increase in permeability compared to control, Thick green line = Large increase in permeability compared to control, Thin red line = Small decrease in permeability compared to control, Thick red line = Large decrease in permeability compared to control. Generally, in the B-A direction all models tested show some degree of increased functional permeability compared to control layers. Only HIC treated models showed decreases in permeability with regards to both Lucifer yellow and Rhodamine 123. In the A-B (absorptive) direction less change was seen overall with only etoposide shown to consistently increase in permeability. A) B-A CCD-18co vs control, B) B-A HDFn vs Control, C) B-A HIC vs Control, D) A-B CCD-18co vs Control, E) A-B HDFn vs Control, F) A-B HIC vs Control.



**Figure 6.44: Summary of the complete analysis of 3D bioengineered models with the model compounds tested in this study** – Blank lines = No change from control, Thin green line = Small increase in permeability compared to control, Thick green line = Large increase in permeability compared to control, Thin red line = Small decrease in permeability compared to control, Thick red line = Large decrease in permeability compared to control. Generally, in the B-A direction all models tested show some degree of increased functional permeability compared to control layers. Only HIC treated models showed decreases in permeability with regards to both Lucifer yellow and Rhodamine 123. A) 3D B-A CCD-18co vs control, B) 3D B-A HDFn vs Control, C) 3D B-A HIC vs Control, D) 3D A-B CCD-18co vs Control, E) 3D A-B HDFn vs Control, F) 3D A-B HIC vs Control

**B-A Literature tissue values vs Control**

**Figure 6.45: Reported human and animal tissue values compared to Caco-2 Transwell controls**  
 – Blank lines = No change from control, Thin green line = Small increase in permeability compared to control, Thick green line = Large increase in permeability compared to control, Thin red line = Small decrease in permeability compared to control, Thick red line = Large decrease in permeability compared to control. Comparisons of control models to values gained from the literature shows that Caco-2 Transwell systems generally underestimate B-A transfer of model compounds when compared to human and animal intestinal tissues. Decreased Propranolol transport in tissues compared to Transwell models is most likely due to its highly lipophilic nature resulting in high levels of drug acquiescence by cells and ECM. Methotrexate cannot be compared as no human tissue transport values can be found within the literature

## 6.6 Conclusion

It is an important observation to note that in every single instance within this study, Caco-2 transport has been observably lower than the average reported values from the literature. (68,90,313,320,333) In some instances the difference is small such as Lucifer Yellow and Atenolol which, whilst lower, fall within the assays range of error of the reported values. Others such as Etoposide, Rhodamine 123 and Propranolol fall well below reported control values. Encouragingly, often one or more of the co-culture conditions significantly improved the Caco-2 functional phenotype to be more akin to that seen in the literature. In this regard, both co-culture Caco-2 and 3D mucosal models result in a significantly more functionally representative epithelial equivalent compared to the controls in this study. When compared to average values gained from the literature the clear cut benefits to using advanced culture methods is significantly less obvious. The

variation seen in the literature reported values and here speaks volumes as to the suitability of Caco-2 cells as an appropriate tool for NCE development. The cells utilised in this study were obtained from a reputable source and maintained through manufacturers specifications throughout the culture process. Even still, the phenotypic characteristics of these cells were significantly different from other reported values. This really highlights the non-homogenous nature of Caco-2 cells throughout the industry with often seemingly inconsequential details in the operation and maintenance of these cells having large effects on cellular phenotype both in individual experiments and in working culture stocks.

Using the data available at the completion of this study, the “best” model with increased permeability phenotypes compared to both the mean of the internal controls and the mean of the literature reported values is the 3D Caco-2/ HDFn model of the intestinal epithelium. This was simply calculated as the average of the percentage increase in permeability compared to control values, with average values over 100 indicating a general increase in permeability and under 100 generally less permeable. Obviously, this is a very rough technical analysis and doesn’t take into account data variability or even whether an increase in permeability is even a physiologically relevant change. In reality, each model has its own strengths. For example, the largest increase in Rhodamine permeability was seen in HDFn paracrine Transwell cultures whereas 3D HDFn models were most permeable to Atenolol. This data highlights in many respects how a singular test is often insufficient to provide a relevant answer in all conditions. A move to more tailored assays relying on each systems strengths could improve the *in vivo* reliability of NCE research.

## 7. General discussion, project conclusions and future directions

### 7.1 Introduction

In their most general basis, the aims of this project were two-fold. First, to look at the effects of simple modifications to current Transwell models to achieve physiologically relevant changes in Caco-2 epithelial layers assessed by functional pharmacokinetic analysis of drug permeability. These simple modifications involved the paracrine co-culture of Caco-2 Snapwell models with conditioned media from a number of fibroblast cell lines of varying origin, and in direct co-culture experiments with the “goblet cell like” epithelial cell line HT29-MTX. The purpose of these experiments were to understand the importance of a more complete, complex cellular environments on the development of epithelial layers, both in terms of understanding the processes within the models created in this study but more generally as a tool to understand epithelial-mucosal interactions *in vivo*.

Second, to take the understanding formed from the simple co-culture experiments and apply the findings to the creation of a 3D tissue equivalent utilising Alvetex Scaffold<sup>®</sup> and the cell lines studied in the previous aim, namely Caco-2, CCD-18co, HDFn and HIC. These 3D models allowed the study of the effects of direct epithelial-fibroblast co-culture on the pharmacologically relevant drug permeability functions of the resultant models. Additionally, 3D models allow for a study on the effects of substrate morphology and cellular microenvironment on the development of the structural elements of Caco-2 epithelial cells through analysis of cell morphology and junctional marker composition.

The hypothesis was that the Transwell paracrine and 3D co-culture of Caco-2 cells in a more *in vivo* “like” environment would result in a 3D construct more able to model the pharmacokinetic interactions of model drug compounds *in vitro*. This was done in an effort to improve the standard Caco-2 assay currently utilised in industry whilst maintaining as many of the beneficial characteristics of said model (mass producibility, ease of culture, low cost materials and *in vivo* relevancy).

## **7.2 Understanding the needs for an improved *in vitro* model of the intestinal epithelium**

Billions of dollars per year are spent on the development of new drug compounds, many of which are optimised and tested on cellular models *in vitro* of *in vivo* tissues. (366–370) These simple models of intestinal tissues, whilst not perfect, are responsible for the validation of many of the commonly used drugs taken by many people on a daily basis. Through improved understanding of the epithelial interactions by examining the effects of cellular cross talk, either between the indirect effects of underlying, supportive fibroblast populations or through direct co-culture of epithelial cells with said fibroblasts or other components of the intestinal epithelium; this study was able to mimic and understand the function of the *in vivo* intestinal layer. Understanding of the principle biology behind the models being developed has powerful and wide-ranging consequences not only in the production, validation and the reduction of costs associated with NCE development but also as a tool for further research into areas such as; Intestinal disease modelling (371) and mechanism understanding, bacterial-epithelial interactions, (372) development biology, nutrition (373) etc. A sufficiently advanced model is indistinguishable from *in vivo* tissue and as such could be utilised for all the same applications.

## **7.3 Understanding the paracrine microenvironment is key to developing systems with improved *in vivo* mimicry.**

The first chapter of this thesis focussed on three main points. 1. The characterisation of the fibroblasts used within this study through histological and immunological staining techniques. 2. Creation of Caco-2 epithelial models in the paracrine media of each fibroblast cell type. Characteristics such as TEER along with immunological staining of key proteins. 3. Understanding the effects of KGF on the development of the Caco-2 epithelial layer and comparison to the effects of conditioned media samples including quantification of KGF levels in conditioned media.

All fibroblast cell lines tested were observed in a classic spindle like formation. Additional analysis by immunological staining techniques showed cells to be Vimentin positive,  $\alpha$ SMA positive (to a large extent with some mixed populations observed) and Desmin negative, together suggesting fibroblast cells of a myofibroblast origin. Similar in phenotype to intestinal sub-epithelial myofibroblast (ISEMF) populations. The discussion in section 3.5.2 highlighted the importance of good cellular characterisation before the commencement of work with many cell types often miss-identified or used on faith that past observation within the literature were correct. There are a number of phenotypically similar cell types within the sub-epithelial intestinal compartment with mostly overlapping but often distinct niche functions.<sup>(185)</sup> Pericytes are one such cell type which can be easily mixed with myofibroblast cells. Indeed, pericytes are thought to be potentially multipotent in the same way as MSC cells, and as such are potential parent cells to myofibroblast lineages.<sup>(374)</sup> Pericytes absence was confirmed by the absence of Desmin staining. However, this in itself is a fairly poor way to confirm pericyte absence from a culture. More specific pericyte markers such as PDGF-B/PDGFR $\beta$  or Neural glial antigen 2 may be more suited for complete confirmation of absence from a culture. <sup>(183)</sup>

Conditioned media gained from these fibroblast populations was applied to the standard Caco-2 model in an attempt to understand the physiological changes that could be induced by paracrine released small molecules. Significant changes could be observed with improvements in Caco-2 structure from a squamous to cuboidal cellular morphology. Analysis of TEER of the different model systems showed, as expected, a heightened TEER compared to reported intestinal tissue values gained from the literature. However, highly significant decreases of roughly 75% were observed in CCD-18co and HDFn paracrine medias with HIC models showing a more limited, but still significant, decrease. Decreases in TEER could be postulated to be due to changes in tight junction morphology with lower TEER values suggesting either a dysregulation of junction formation or polarity. However, immunostaining of the protein Occludin, a member of the tight junction complex, showed no significant changes in tight junction regularity between the models.

qPCR analysis of the relative expression rates of Occludin mRNA between control, CCD-18co and HDFn treated layers showed no significant differences between mRNA



expression, further confirming an unchanged tight junction phenotype between model conditions. Occludin mRNA levels however, were shown to decrease in HIC conditioned media models. On the surface this would appear to be contradictory, with the two most significant decreases in TEER belonging to conditions which showed no deviation in relative Occludin expression whereas HIC models which do show a decrease in Occludin, only showed a small decrease in overall TEER. Occludin however is only a single component of the tight junctional complex. Analysis of it in isolation of expression of other junctional components cannot be reliably used as a definitive test for tight junctional morphology. As was discussed in chapter 3, other proteins such as claudins are able to modulate the tight junction in terms of function without changing the overall expression rates of the junctional complex as a whole. Indeed, Claudin 2 expression is shown in the literature to be able to increase tight junctional permeability to ions and very small molecules without changing the overall integrity of the epithelial monolayer. (227) Analysis of Claudin 2 expression by qPCR showed a small increase in CCD-18co and HDFn conditions with a decrease in HIC models, similar to that seen in Occludin analysis. It is clear that there are at least two methods in which tight junctions are being modulated between the different conditions, which, if nothing else works to highlight the complex interactions between cells in the epithelium, with often simple looking processes on the surface becoming highly complex on closer analysis. This is a theme that is seen throughout this work, especially when discussing transporter mediated function.

qPCR analysis of functional transporter proteins such as OATP-B, BCRP and MDR1 show a range of changes in treated CCD-18co, HDFn and HIC conditioned media samples. MDR1 or p-gp is a protein well known to be under expressed in Caco-2 compared to intestinal tissues. Interestingly, treatment of Caco-2 models with CCD-18co conditioned media resulted in a decrease in the levels of MDR1 compared to Caco-2 controls. HDFn models on the other hand showed a significant increase, potentially to more physiological levels. Therefore, paracrine constituents of the HDFn conditioned media must be having physiological effects on the development of the Caco-2 model. mRNA qPCR relative expression however is not always the same as relative protein expression and can be influenced in a number of ways which will not affect the functional phenotype of the models. MDR1 expression is a good example of this when analysing the functional transport rates of Rhodamine 123, a specific MDR1/ P-gp substrate. Whilst

mRNA saw a significant decrease in relative expression, functionally, no changes could be seen in membrane transport function in CCD-18co treated conditions. Deregulation between mRNA levels and protein expression can be influenced by a number of factors such as; protein turnover rates, protein function (e.g. secreted proteins will only be translated when required, cell cycle proteins will only be used at certain points of cell cycle etc) and post-transcriptional regulation rates. This was shown in the study by Koussounadis *et al* in their study of mRNA- protein dysregulation, which, although their conclusion was that changes in mRNA generally are physiologically relevant, there are many exceptions which suggest protein quantification should be utilised to confirm mRNA findings. This study was not able to fully characterise protein expression between the different models so qPCR analysis should indicate physiologically deferent changes it cannot be relied upon entirely to explain changes in models functional phenotype.

Initially it was hypothesised that KGF may be the potential paracrine agent responsible for the changes between 2D and 3D models. Indeed, initial investigations into the effects of KGF on the development of Caco-2 layers on Transwell showed promising results in regards to TEER values, with significant dose dependant decreases seen in models treated with 5 and 25 ng/ml of KGF. Interestingly, TEER levels after treatment were very similar to those seen in CCD-18co and HDFn treated cultures with an average TEER value of around 500 ohms, down from over 3000 ohms in control samples.

Histological analysis of KGF treated models shows comparable promising changes, with improved Caco-2 organisation and structural morphology similar to those seen in conditioned media experiments. Immunostaining of KGF treated layers showed no obvious differences between differences in protein expression between KGF concentrations albeit a seemingly dose dependant increase in Villin staining, perhaps suggesting enhanced differentiation over control models with increased development of apical brush border microvilli.

Occludin staining, utilised as before as a marker of tight junction formation, showed no obvious changes in expression between treated samples. Again suggesting changes in TEER values were due to some other mechanism than simple tight junction non-formation or disorganisation. A review of the literature suggests that KGF may also have

a role in the modulation of Claudin 2, another component of the tight junction complex, with upregulation seen in KGF treated cells. Claudin 2 is implicated, as discussed previously, in a morphological change in tight junction structure, allowing an increase in the passive movement of ions and small compounds when compared to other tight junction formulations. This is achieved without significant effects in the rate of tight junction formation or organisation on a macro-cellular basis.

ELISA analysis of conditioned media samples however showed that only CCD-18co cells secreted KGF at any significant rate, with both HDFn and HIC cells secreting significantly lower KGF levels, barely above the minimum assay detection range. HDFn conditioned media showed many of the same phenotypical effects on Caco-2 structure and function as was seen in CCD-18co conditioned media such as decreased TEER and changes to structural and functional morphology. The logical conclusion to this then is that HDFn conditioned media must therefore bring about these similar phenotypes through a different functional mechanism. This highlights the complexity of both epithelial differentiation and the likely composition of paracrine conditioned media. Another possibility is that the major structural and functional changes seen in both HDFn and CCD-18co conditioned medias occur through the same mechanism, just that that mechanism is not mediated by KGF and that the effects of KGF on Caco-2 cells layers, whilst incurring similar structural changes to Caco-2 cells, is entirely co-incidental. Piecing together the exact composition of conditioned media is difficult without any reasonable ways to quickly screen a secretome that don't involve multiple, expensive ELISA based kits. One potential route would be to look at the genome level expression analysis of each cell type in the hope to identify likely upregulated targets. Even then due to the multifaceted ways that secreted compounds interact with one another, understanding the significance of each secreted molecule on the development of the epithelial membrane is difficult, if not impossible, through analysis of each component in isolation of the others.

It is clear that myofibroblasts have significant effects on both the development of Caco-2 epithelial cells and *in vivo*. Placing work achieved here into context with the literature is more difficult than would appear on the surface with some evidence showing enhanced

cellular phenotypes (375–377) in a range of tissues with others stating either no change or a negative effect on cellular phenotype (162)

In terms of suitability for use in an industrial, pharmaceutical setting, it is extremely important that cellular models vary between experiments as little as reasonably possible. Future work in this area, specifically in that associated with myofibroblast effects on epithelial development, should focus on the effects of the paracrine secretome on epithelial differentiation. The use of paracrine media to induce physiologically relevant changes in Caco-2 function and morphology is both a powerful tool to demonstrate the effects of secreted factors, and a poor method for use in industry due to the major deviations in the secretome of cells dependant on origin, age and disease phenotypes. Research should work towards both higher level regulation of the Caco-2 cell model (e.g. validation and use of specific cell banks, reducing inter-lab variability) and in the development of defined medias for the enhanced differentiation of Caco-2 cells to create a more physiologically relevant model systems. There is a growing volume of work which is focussing more on the myofibroblast contribution to cellular phenotypes in models however there is still some distance to go before mastery of myofibroblast secretome. Work focussing on the exact composition of which would be most valuable.

## **7.4 Stromal epithelial interactions result in loss of function of HT29-MTX cells when co-cultured *in vitro*.**

The second results chapter of this thesis focussed on the potential of adding HT29-MTX cells into the Caco-2 model epithelium. This method of modifying Caco-2 membranes is not novel by itself. However, through the addition of CCD-18co paracrine media the study examined the effects of myofibroblast influence on the goblet cell phenotype. This work was seen as a preliminary step towards addition of HT29-MTX cells into the 3D mucosal model, the optimisation of which was ongoing at the same time as this work.

Preliminary investigations into the effects of CCD-18co conditioned media on HT29-MTX cells showed an unfortunate change in the structural and functional phenotype to a significantly less morphologically “goblet-like” cell. This is potentially not unexpected given HT29-MTX parental cell line of HT29, an epithelial cell with some mucous

production capabilities. Unfortunately, work on the co-culture of both HT29-MTX and CCD-18co cells within the literature is sparse. Pereira *et al* to my knowledge are the only people to attempt creating a 3D model with Caco-2, HT29-MTX and CCD-18co. (162) They created their model by culturing CCD-18co cells within a matrigel matrix atop of a Transwell insert. Epithelial cells were then culture on the top of this CCD-18co/ Matrigel scaffold to create the mature model. Analysis of TEER values of the models and Caco-2 Transwell controls did not show the same change membrane resistance as was observed in this study. However, careful review of the images provided within their paper it is clear to see how relatively few CCD-18co cells are present within the matrigel scaffold. Indeed, it was observed in this study that CCD-18co cells when grown in 3D significantly reduced the levels of KGF secretion overall. This suggest that whilst the observations do not match entirely, the differences could be more due to the system used. Conditioned media used by was created by a confluent layer of 2D CCD-18co cells and as such, concentrations of small molecules within the culture models, based on ELISA date gained in this study, are likely to be higher than sparsely 3D cultured CCD-18co cells and could explain the difference in overall phenotype.

Models with HT29-MTX cells added were characterised through qPCR relative expression of key proteins of interest as well as being functionally assessed for Rhodamine 123 permeability. qPCR of MDR1 was essentially absent in HT29-MTX layers as would be expected from a cell with little enterocyte function. Whereas Rhodamine 123 transport in HT29-MTX cell layers was reduced compared to Caco-2 controls, however, not to the extent that would be expected. It was hypothesised that the decreased epithelial resistance observed in HT29-MTX models compared to controls would naturally correlate with a “leaky” epithelium, as such accounting for higher than expected Rhodamine 123 permeability. Nevertheless, CCD-18co treatment of HT29-MTX cell layer did not significantly decrease Rhodamine 123 permeability with increased TEER. However, in this instance Rhodamine 123 permeability could be influenced by the change in cellular phenotype to one more structurally reminiscent of enterocyte lineages. Indeed, if it is assumed that the parental HT29 lineage phenotype is restored upon co-culture with CCD-18co, some small level of MDR1/ P-gp activity was to be expected. (378) Due to the uncertain changes in phenotype is was decided not to optimise HT29-MTX inclusion into the Alvetex 3D model and as such were omitted from

further study. Further experimentation into the nature of the change in structural and functional phenotype of HT29-MTX cells would be required before they could be utilised in a regulated manner where model consistency is important. qv analysis of lineage specific markers such as ATOH1 (379,380), HES1 (379), KLF4(381) or SPDEF (380) could potentially shine some light onto the nature of the structural change.

## **7.5 3D fibroblast culture allows for the development of a complex ECM microenvironment within cell substrates.**

Chapter three focussed on the optimisation of the technology of the 3D model, initially through the culture of the cells within the Alvetex scaffold and ultimately in the generation of further tools, developed to enable the higher throughput generation and analysis of intestinal models. To save time, full quantified optimisation of the models methodology was only done once (with 3 internal repeats) with CCD-18co cells as these were shown to be both the slowest to grow and the most limited in the 3D proliferation capabilities compared to the HDFn cells. Both CCD-18co and HDFn models show good structural morphology and a high level of reproducibility when cultured in the multi-seeded format as optimised in chapter 3.

The HIC cells were first isolated after the model development of both the CCD-18co and HDFn 3D systems. Initially these HIC cells were for conditioned media experiments only as limited cells were available from the cultured explant. These primary cells would quickly lose proliferative capabilities in culture and as such were deemed not suitable for 3D models which at the time first isolation were based on the 12 well format. With the development of the 96 well format, significantly less cells were required per model allowing for the creation of HIC 3D models. In order to keep the 3D models as close to one another as possible the optimised techniques applied to both CCD-18co and HDFn were also applied to HIC model development regardless of their growth phenotype *in vitro*. Unfortunately, HIC mucosal equivalents show significantly poorer structural morphology over both CCD-18co and HDFn models. With significant caco-2 invasion into the underlying stromal tissue. Analysis of their functional properties was continued regardless in chapter 4 as, if nothing else, an example of the importance of model structural morphology on function. In a way, a negative control. Models within this

sections were analysed for their abilities to secrete ECM components into the Alvetex Scaffold structure, creating a cellular niche for differentiation and a support for epithelial cell culture. Differential secretion of ECM protein into the scaffold was highly cellular specific. CCD-18co cells were shown to secrete Collagen I, III and IV into the scaffold, chosen due to being major constituents of the small intestine ECM (Collagen I and III) and an important basement membrane protein (Collagen IV).

## **7.6 Functional analysis of paracrine and 3D models shows significant changes in the function of Caco-2 epithelial layers.**

Results chapter four of this thesis focussed on the functional characterisation of both the advanced Transwell paracrine co-culture models and the 3D models of the intestine, bringing together the work achieved in results chapters one and three of this thesis. A range of compounds was analysed for their apparent permeability (Papp) through the test substrates with each model drug carefully chosen as a substrate for a specific protein under study. Rhodamine 123 for example is a well-known substrate for the efflux protein MDR1/ P-gp. This protein, often under expressed in the Caco-2 epithelium, is key in the development of NCE as P-gp is well known to efflux a range of drug compounds, reducing pharmacokinetic availability to the circulatory system *in vivo*. Verapamil Hydrochloride is a specific P-gp inhibitor and was utilised as such in this study as a mechanism to show substrate specificity.

MDR1/ P-gp is possibly the most extensively studied ABC transporter protein being first isolated in the early 1970s and is important in the resistance of a large variety of compounds. Interestingly, MDR1 and other ABC transporter proteins are known to be inducible, with heightened levels of cellular expression in cells post exposure to MDR1 substrates. In essence this makes for an effective anti-toxicity mechanism *in vivo*, but is an obstructive mechanism when considering drug bioavailability. (382) Other transporters focussed upon in this study which are known as clinically relevant transporter system are MRP1/2 and BCRP. It is important to note that the presence of these drug resistance proteins is not limited to the enterocytes of the intestine. Liver hepatocytes and endothelial cells of the blood brain barrier are also widely known to express high levels

of ABC transporters. Theoretically therefore were a drug to have clinical effects within the brain, there would be a minimum of two barriers through which the drug would have to pass whilst exposed at ABC proteins. In these situations it is imperative that drugs have low ABC substrate specificity in order to ensure bioavailability. (382)

Rhodamine 123 modelling in the models showed a variable change dependant on both the cells utilised (control or paracrine influenced samples) and the dimensional format (Transwell vs Alvetex). Largely speaking, data values gained here were similar to those gained from the literature of other Caco-2 cells models. Generally, 3D models of the intestinal epithelium cultured in Alvetex<sup>®</sup> Scaffold displayed a higher permeability to Rhodamine 123 than their Transwell counterparts. This was true for both B-A and A-B directional travel. Whereas directional polarity was quite clear between Transwell conditioned media and control models, the same is sadly not true for 3D Alvetex<sup>®</sup> tissue equivalents. That is not to say that 3D models lack polarity in general, as that was demonstrated clearly through immunological staining of paraffin embedded sections and TEM imaging of surface Caco-2 layers and is also seen throughout the literature. (162,269,371) A-B directional travel tends to be lower in 3D models just to a far lesser extent than seen in 2D. The loss of permeability polarity alongside increased transport in general would seem to suggest that 3D models passively allow the transfer of Rhodamine 123. This explanation would seem logical until Lucifer yellow transport, a known passively transported compound is considered. Lucifer yellow permeability does not significantly change in 3D compared to 2D Transwell cultures, although in fairness, Lucifer Yellow transport is higher in general in each 3D cultured condition, just not to a significant level. There are of course, a number of ways in which this change in functional physiology could be explained. The first, as mentioned earlier, is the changes in barrier function incurred through modulation of tight junction structure within the epithelial membrane.

Versantwoort et al conducted a similar study whereby they assessed the rate of Rhodamine 123 permeability in both Caco-2 and IEC-18 cells. IEC-18 cells are a non-transformed epithelial cell line derived from rat small intestine. Interestingly, in their study similar to here, polarised Rhodamine 123 transport was only observed in Caco-2 cells, with permeability in either direction approximately equal in IEC-18 cells. (383)One could



make the argument that because IEC-18 cells are non-transformed and of a small intestinal origin they should theoretically be able to mimic *in vivo* physiology *in vitro*. IEC-18 cells are known to be able to create consistent tight junctions whilst differentiating to a lesser extent than Caco-2 cells.(266) Yet rhodamine 123 transport levels were similar in IEC-18 cells as Caco-2 cells in the B-A direction. How then is Rhodamine 123 being transported in IEC-18 cells and is this the same phenotype observe in the 3D intestinal models. P-gp inhibitors such as verapamil hydrochloride as utilised in this study are a good way of elucidating mechanisms of activity. In this study Verapamil hydrochloride addition did show a highly significant decreased in Rhodamine 123 permeability in Transwell samples (Control and CCD-18co). Lack of any change in B-A Rhodamine 123 permeability in the presence of Verapamil Hydrochloride in 3D Alvetex® intestinal equivalent models again lends further evidence that Rhodamine 123 permeability in Alvetex® models is completely not MDR1/ P-gp mediated. The paracrine influences of fibroblasts have been used for decades in stem cell culture as feeder layers to maintain an undifferentiated phenotype.(384) Loss of directional bias in the models could conceivably be due to decreased differentiation compared to conventionally cultured Caco-2 Transwell models As mentioned previously, there is a wide arrangement of highly overlapping functional proteins present in the intestinal epithelium. Upregulation of other transporter proteins within the Caco-2 epithelium could easily explain the change in functional phenotype. Further experimental testing into this phenomenon would be required before models could be utilised as replacements for Caco-2 models in industry.

Regardless of the mechanism at work here, the more important question to ask in the first instance is whether the changes seen here are physiologically relevant. P-gp activity is thought to be underestimated by conventionally cultured Caco-2 models. Table 6.11 shows the Papp summary of all the drugs tested in this study. In regards to Rhodamine 123 all model systems except for Caco-2/ HIC (Transwell) demonstrated an increase in B-A permeability. Whilst Rhodamine 123 is a commonly used marker for Caco-2 transport assays, it is reasonably rare to find comparable Papp values for intestinal tissues of this compound in the literature. However, Patient *et al* (269) utilised porcine intestinal tissues to measure Rhodamine 123 permeability *in vitro*. They found that intestinal tissues were far more permeable to Rhodamine 123 than permeability values seen in the conventionally cultured control Caco-2 layers (Papp; 0.82 (Controls) vs 1.8-3.6 (Porcine

tissues)). In each instance (barring Caco-2 HIC Transwell) each of the models was significantly closer to the *in vitro* tissue permeability values than the conventionally cultured Transwell models. Although, as mentioned earlier, the permeability values gained with the Caco-2 cells used in these systems were significantly lower than is generally seen in the literature (average of 0.82 (this study) vs 6.84 (literature), again highlighting the high degree of variability found within supposedly similar Caco-2 cell populations. MDR1/P-gp is one of the most important considerations when assessing the pharmacokinetic of NCE's. Increased MDR1/P-gp activity in cell culture models will allow for more sensitive assays in to NCE substrate specificity.

As the name would suggest, BCRP was first isolated from breast carcinoma cells in 1997 utilising the MCF-7 breast cancer cell line. (385) Methotrexate transport is facilitated by a number of overlapping protein functions, and as such cannot be utilised to test a single protein transporter in isolation from others with similar functions. Having said this, BCRP is a major clinically relevant efflux transporter of methotrexate and as such has been used in this study as a measurement of BCRP activity on the apical membrane. Unfortunately, BCRP is often co-expressed with MDR1/ P-gp and is highly similar in function, so unravelling the specific actions of both can be challenging as they are known to have a largely overlapping substrate specificity. BCRP is able to efflux a wide variety of xenobiotics from multiple different drug classifications; antibacterial, antivirals, protease inhibitors and statins to name just a few, highlighting the clinical importance of determining BCRP activity on NCE. (382)

In this study Methotrexate was shown to be differentially transported in all conditions tested. In general, transport in the B-A direction was seen to increase with comparative T-test statistical analysis showed that 2D HDFn and 3D HIC models were both significantly higher than control levels with an increase in B-A Papp of 0.34 and 21.62 respectively. 3D HIC transport was an order of magnitude greater than all other conditions tested, with no B-A/ A-B directional bias. This coupled with large levels of variation between tested models suggests that increases in HIC permeability were more due to a lack of epithelial development than a significant change in cellular phenotype. However, loss of B-A/ A-B directional bias is not necessarily an indicator of a loss of membrane

integrity in this instance as other conditions with far lower relative Papp, including controls, also show no significant directional bias.

Methotrexate Papp values in this study are generally in line with those seen within the literature (with exception of 3D HIC/ Caco-2 models) with an average Papp value in the B-A direction of <1. General statistics of oral absorption in humans put methotrexate relatively low at 20%, suggesting that low absorption rates are to be expected for this compound.(386) The biggest question, as is the case for all of the drug transport analysis conducted in this study, is whether the changes seen in the models are physiologically relevant. It is clear that Papp values and % oral absorption rates cannot be directly compared making it difficult to say definitively without *ex vivo* tissue experimentation. Even then, transport assays with *ex vivo* tissues are unlikely to directly reflect the function within the body *in vivo*.

Specifically, in regards to Methotrexate transport within this study, it could be argued that an increase in permeability is more physiologically relevant. A general observation made from the data with comparative analysis of values drawn from the literature (330,387) shows clearly that the Caco-2 in this study were significantly less “functional” in regards to relative permeability in every drug instance tested.

Propranolol is a highly permeable compound in Caco-2 assays and *in vivo* with an average oral bioavailability of 90% and was one of the most consistent throughout all the conditions tested.. Using this knowledge, if data were to be compared and expressed as a percentage the permeability values of each of the drugs to Propranolol, and then compare that percentage to known *in vivo* absorption rates it could give a very basic understanding of how well the system designed is able to model intestinal absorption characteristics. Methotrexate control values result in a 1.24% absorption rate when compared to Propranolol. Taking into account the ~20% methotrexate oral absorption rate, it could be argued that any increase in methotrexate transport seen within the model systems is a physiologically relevant change.

Etoposide is, like many other drugs and as described previously, transported by a range of protein transporters in the gut with overlapping functions such as the aforementioned

MDR1 and BCRP. (388) In this instance MRP family of transporters namely MRP2 function is being assessed through the transport of Etoposide. Multi-drug resistance protein (MRP) transporters are a member of the ATP binding cassette (ABC) superfamily of drug efflux proteins which are well known to be efficient efflux transporters for a number of drug types, anti-viral, anti-bacterial and chemotherapeutic. (389,390) The Caco-2 cells utilised in this study when cultured using conventional Transwell culture techniques (Controls) demonstrated a very low Etoposide permeability of  $0.05 \times 10^{-6}$ , far below the Papp gained from the literature of  $8.04 \times 10^{-6}$  for similarly cultured Caco-2 cells. This follows an observed trend throughout this study when comparing Caco-2 cells used here (ECACC, PHE) to the literature. In each case, addition of paracrine factors or creation of a full mucosal intestinal model resulted in significant increase in the Papp of etoposide compared to conventionally cultured Caco-2 cells.

Again, as with the other compounds described previously, finding human intestinal tissue Papp for this drug is challenging. Animal models for Etoposide transport are also highly variable depending on the system being studied. For example rabbit tissue transport equates to a Papp of roughly  $1.13 \times 10^{-6}$  whereas a similar experiment utilising rat tissue was an order of magnitude higher at  $101 \times 10^{-6}$ . (67,69) In each instance the modified models created in this study fall within the large range seen within animal tissues. Generally, the conserved change seen in all test conditions in this study is an increase in permeability levels to a degree similar to those seen in the Caco-2 conventional literature (Papp values of approximately  $8.04 \times 10^{-6}$ ). As with other drugs tested here, Alvetex® HIC models showed a significantly increased average Papp over other conditions tested in this study, similar in scope to the Rat tissue Papp values seen in the literature. If nothing else this highlights the disadvantages of utilising animal tissues for drug discovery processes, with large variations observed between species.

Takenaka *et al* showed a similar transport rate of Etoposide in their study on the application of primary intestinal cells as an alternative to Caco-2 use. (329) They showed that “primary” human enterocytes derived from intestinal stem (HIEC) cells were able to transport Etoposide at a significantly greater rate than their Caco-2 controls. Indeed, with a Papp of  $1.9 \pm 0.2$ , HIEC cells showed remarkable similarity to values gained in this study when cultured in 3D or in paracrine media. Their conclusion in this study was that a

change in tight junction phenotype alongside junctional “looseness” was one of the main contributors to the increases in model permeability, ideas also explored and described earlier in this thesis as the methodology of action in these models. Etoposide has a fractional absorption rate in humans of approximately 50%. Obviously, intestinal models, even 3D cultured ones, are not expected to replicate this level of permeability due to the large difference in overall model surface area compared to human tissues. However, it was demonstrated here that co-culture of Etoposide in a Transwell system or in a 3D model has the effects of generally increasing model permeability, modelling intestinal tissues.

Lucifer yellow, Atenolol and propranolol were all utilised as passive measurement of membrane integrity of different sized molecules. Lucifer yellow and atenolol were tested for their low Papp values in Caco-2 models whereas conversely Propranolol is known to be able to readily move through Caco-2 epithelial layers with subsequently high Papp values.(66) Passive transport of compounds is a well-known weakness of Caco-2 cell models which generally underestimate the rate at which passive permeability occurs. This is usually due attributes to an increase in tight junction integrity, resulting in a higher TEER values than seen in intestinal tissue, as such decreasing the capability of compounds to move through the membrane in Caco-2 models.

Lucifer yellow permeability in humans has been shown by Rozehnal *et al* (345) to be around  $4.02 \times 10^{-6}$  in human small intestinal samples. Conventionally cultured Caco-2 controls had a permeability of roughly a quarter of that at  $1.05 \times 10^{-6}$  which is low when compared to conventionally cultures Caco-2 values gained from the literature with an average Papp value of  $2.58 \times 10^{-6}$ . Interestingly, paracrine cultured Transwell models in this study resulted in a decrease in apparent Lucifer yellow Papp in both HDFn and HIC conditions with CCD-18co paracrine cultures non-significantly different from controls. Whilst this is good in terms of suggesting that conditioned media does not influence caco-2 ability to form a confluent monolayer in the Transwell system it is contrary to the expected increase in Papp hypothesised to be observed. This is in contrast to 3D cultured Alvetex intestinal equivalent models which do show a modest increase in Lucifer yellow permeability. When one considers the TEER values of 3D models compared to conventionally cultures Caco-2 models and even the significantly lower TEER values of

conditioned media models it becomes apparent that 3D models possess a less tightly joined epithelial layer. Alvetex<sup>®</sup> intestinal model TEER values are significantly closer to the observed TEER of human tissue, with physiologically relevant increases in lucifer yellow Papp potentially making them more accurate models for passive permeability studies.

Atenolol transport in conventionally cultured (control) samples in this study was similar to that seen in the literature for Caco-2 intestinal models with some level of overlap when accounting for data deviation. Analysis of Atenolol permeability through intestinal tissue sections of both human and animals demonstrates a much higher Papp *ex vivo* than in conventionally cultured Caco-2 models. Conditioned media from CCD-18co and HDFn cells did not appreciatively change Atenolol permeability. HIC conditioned media however increased Atenolol Papp significantly to a level much more akin to human intestinal tissue (2.18 Caco-2/ HIC vs 2.82 Human tissue). Conversely, 3D cultured CCD-18co and HIC models were not significantly different from Caco-2 Transwell controls whilst HDFn 3D models were significantly increase. Potentially highlighting the phenotypic effects that 3D culture can have on the secretome of fibroblast cells. Patient *et al* conducted a study similar to that seen here, gaining similar Papp values. The culture of Caco-2 cells on nano-fibre supports did not significantly increase Atenolol permeability over control conditions. Comparison with porcine tissue, Caco-2 models were significantly less permeable as is also suggested in studies of human fractional absorption.(269)

Finally, Propranolol Papp was significantly higher in each case than similar experiments conducted in porcine tissue samples, albeit much lower than reported values seen for permeability in Caco-2 Transwell literature.(269) As mentioned previously however, propranolol is a highly lipophilic compounds and as such is easy uptake through the cellular membrane. As such, Papp values in tissue and 3D models are often artificially decreased due to propranolol sequestration throughout the transport assay into densely packed cells This explains why Transwell monolayer models have such a relatively high Papp value compared to tissue sections but doesn't explain why Caco-2 controls in this study were low compared to literature values. Epithelial resistance was significantly higher in this study than the majority of Caco-2 systems however propranolol is generally

absorbed directly through the plasma membrane. There are some recent, controversial, studies which suggest that P-gp may be able to transport propranolol as such potentially changing permeability values. (391) Alternatively, pH has been shown to critically effects the rate or propranolol transport in an assay system. (320) The use of an Ussing chamber in this study allowed a carefully control the pH of the transport solution through the use of buffers (HBSS) and bubbling of low CO<sub>2</sub> containing carbogen throughout the assay period. Generally however, Transwell based transport assays are conducted “in-well” in a standard culture plate, performed in normal cell culture conditions (high CO<sub>2</sub>). (269,320,392–394)As with most Caco-2 models, most variation seen between studies can be attributed to differences in assay technique. In this instance, no control of CO<sub>2</sub> concentration could have significant effects on buffer pH, changing transport dynamics *in vivo*.

## 7.7 Future work

Future work for the continued development of this model beyond the scope described in this thesis should focus on two parts. 1. Application of intestinal stem cell lines to the model and differentiation of said lines into a functional epithelium incorporating the cellular diversity found *in vivo*. 2. Engineering of the scaffold used to create 3D models to more accurately replicate the *in vivo* morphology of the intestine. For example, micropatterning of the scaffold surface could create villus-like structures for the culture epithelial cells. Application of both of these advances e.g. Addition of the stem cells into the villus structure, could potentially allow for the culture of a crypt niche and formation of an crypt-villus axis *in vitro*.

Were this project to be extended further, additional work could be done to more clearly characterise the model created here to understand the paracrine secretome of the stromal cells utilised in this study. Cross talk between cells within paracrine and 3D models is of utmost importance to their development. For paracrine models specifically, an improved understanding on how co-cultured cells influence epithelial development would allow for the creation of, for example, advanced culture media with the same differentiative effects on Caco-2 cells as paracrine conditioned media without the added difficulty and variability of culturing stromal cell lines. These constituents could be identified in a

number of ways such as through genome sequencing (RNA seq) to identify upregulated genes of interest or through a series of knockdown studies, either genetically based or by incubating cells with target antibodies.

Ultimately, personalised medicine is the future for the pharmacokinetic testing and use of drug compounds. The analysis of the literature throughout this study has demonstrated that in reality, the perfect model doesn't exist, due to large variations in drug availability and overall effectiveness between people, so called perfect models. Bridging this inherent variation will require the development of an array of models able to mimic a large range of human interactions.

## **7.8 Final remarks**

This project has highlighted how 3D models can be powerful tools for the modelling of critical cellular functions within the intestinal epithelium. As has been mentioned throughout this work one of the main difficulties in transferring 3D models into a regulated screening format is their lack of characterisation compared to Caco-2 Transwell models. Indeed, it will take a lot of additional data to get 3D models to the level of characterisation enjoyed by Transwell based systems due to the 30 year head start. Utilising Caco-2 cells within the models developed here is a good start as it allows for direct comparison with Transwell formats, highlighting both the strength and weaknesses of 2D tissue equivalents. Further experimentation with model drugs, is required to really understand the mechanisms of action for drug transport within this studies models. Work done in this thesis shows some good physiologically relevant changes. However, other questions have arisen such as increased non-directional permeability of normally polarised drug compounds in 3D models which would require further work to validate.

The model developed here could be an important first step to industrial acceptance of 3D models on a large scale. Work done in this study alongside the body of evidence described within will provide a basic foundation for the development of future intestinal models. Whose function, ultimately, is in the accurate predictability of NCE within humans and in the limitations of the need for animal models in the future of drug discovery and validation.



## 8. References

1. Merchant JL. Chapter 1 - Transcription and Epigenetic Regulation. In: Johnson LR, Ghishan FK, Kaunitz JD, Merchant JL, Said HM, Wood JD, editors. *Physiology of the Gastrointestinal Tract (Fifth Edition)* [Internet]. Boston: Academic Press; 2012. p. 3–42. Available from: <http://www.sciencedirect.com/science/article/pii/B9780123820266000014>
2. Schwartz M. The life and works of Louis Pasteur. *J Appl Microbiol*. 2001 Oct 1;91(4):597–601.
3. McGonigle P, Ruggeri B. Animal models of human disease: Challenges in enabling translation. *Spec Issue Pharmacol 21st Century Biomed Res*. 2014 Jan 1;87(1):162–71.
4. Williams SM, Haines JL, Moore JH. The use of animal models in the study of complex disease: all else is never equal or why do so many human studies fail to replicate animal findings? *BioEssays*. 2004 Feb 1;26(2):170–9.
5. Lucey BP, Nelson-Rees WA, Hutchins GM. Henrietta Lacks, HeLa Cells, and Cell Culture Contamination. *Arch Pathol Lab Med*. 2009 Sep 1;133(9):1463–7.
6. Ghanemi A. Cell cultures in drug development: Applications, challenges and limitations. *Saudi Pharm J SPJ Off Publ Saudi Pharm Soc*. 2015 Sep;23(4):453–4.
7. Bittermann K, Goss K-U. Predicting apparent passive permeability of Caco-2 and MDCK cell-monolayers: A mechanistic model. *PLOS ONE*. 2017 Dec 27;12(12):e0190319.
8. Fogh J, Trempe G. New Human Tumor Cell Lines. In: Fogh J, editor. *Human Tumor Cells in Vitro* [Internet]. Boston, MA: Springer US; 1975 [cited 2018 Dec 6]. p. 115–59. Available from: [https://doi.org/10.1007/978-1-4757-1647-4\\_5](https://doi.org/10.1007/978-1-4757-1647-4_5)
9. Tsujii M, Kawano S, DuBois RN. Cyclooxygenase-2 expression in human colon cancer cells increases metastatic potential. *Proc Natl Acad Sci*. 1997 Apr 1;94(7):3336.
10. Walker RI, Porvaznik MJ. Disruption of the permeability barrier (zonula occludens) between intestinal epithelial cells by lethal doses of endotoxin. *Infect Immun*. 1978 Aug 1;21(2):655.
11. Coconnier M-H, Bernet M-F, Kernéis S, Chauvière G, Fourniat J, Servin AL. Inhibition of adhesion of enteroinvasive pathogens to human intestinal Caco-2 cells by *Lactobacillus acidophilus* strain LB decreases bacterial invasion. *FEMS Microbiol Lett*. 1993 Jul 1;110(3):299–305.
12. Yu H, Wang Q, Sun Y, Shen M, Li H, Duan Y. A New PAMPA Model Proposed on the Basis of a Synthetic Phospholipid Membrane. *PLOS ONE*. 2015 Feb 3;10(2):e0116502.
13. Brugmann SA, Wells JM. Building additional complexity to in vitro-derived intestinal tissues. *Stem Cell Res Ther*. 2013 Dec 20;4(1):S1.

14. Chen S, Einspanier R, Schoen J. Transepithelial electrical resistance (TEER): a functional parameter to monitor the quality of oviduct epithelial cells cultured on filter supports. *Histochem Cell Biol.* 2015;144(5):509–15.
15. Blume L-F, Denker M, Gieseler F, Kunze T. Temperature corrected transepithelial electrical resistance (TEER) measurement to quantify rapid changes in paracellular permeability. *Pharm.* 2010 Jan;65(1):19–24.
16. Lu S, Gough AW, Bobrowski WF, Stewart BH. Transport properties are not altered across Caco-2 cells with heightened TEER despite underlying physiological and ultrastructural changes. *J Pharm Sci.* 1996 Mar 1;85(3):270–3.
17. Srinivasan B, Kolli AR, Esch MB, Abaci HE, Shuler ML, Hickman JJ. TEER measurement techniques for in vitro barrier model systems. *J Lab Autom.* 2015 Apr;20(2):107–26.
18. Cummins CL, Jacobsen W, Christians U, Benet LZ. CYP3A4-Transfected Caco-2 Cells as a Tool for Understanding Biochemical Absorption Barriers: Studies with Sirolimus and Midazolam. *J Pharmacol Exp Ther.* 2004 Jan 1;308(1):143.
19. Hu M, Li Y, Davitt CM, Huang S-M, Thummel K, Penman BW, et al. Transport and Metabolic Characterization of Caco-2 Cells Expressing CYP3A4 and CYP3A4 Plus Oxidoreductase. *Pharm Res.* 1999 Sep 1;16(9):1352–9.
20. Ren S, Lien EJ. Caco-2 cell permeability vs human gastro-intestinal absorption: QSPR analysis. In: Jucker E, editor. *Progress in Drug Research* [Internet]. Basel: Birkhäuser Basel; 2000. p. 1–23. Available from: [https://doi.org/10.1007/978-3-0348-8391-7\\_1](https://doi.org/10.1007/978-3-0348-8391-7_1)
21. DiMasi JA, Feldman L, Seckler A, Wilson A. Trends in Risks Associated With New Drug Development: Success Rates for Investigational Drugs. *Clin Pharmacol Ther.* 2010 Mar 1;87(3):272–7.
22. DiMasi JA, Grabowski HG, Hansen RW. Innovation in the pharmaceutical industry: New estimates of R&D costs. *J Health Econ.* 2016 May;47:20–33.
23. Kola I, Landis J. Can the pharmaceutical industry reduce attrition rates? *Nat Rev Drug Discov.* 2004 Aug;3(8):711–6.
24. Hirota J, Shimizu S. Chapter 5.2 - Routes of Administration. In: Hedrich HJ, editor. *The Laboratory Mouse (Second Edition)* [Internet]. Boston: Academic Press; 2012. p. 709–25. Available from: <http://www.sciencedirect.com/science/article/pii/B9780123820082000301>
25. Mathias NR, Hussain MA. Non-invasive Systemic Drug Delivery: Developability Considerations for Alternate Routes of Administration. *J Pharm Sci.* 2010 Jan 1;99(1):1–20.
26. Dosh RH, Jordan-Mahy N, Sammon C, Le Maitre CL. Long-term in vitro 3D hydrogel co-culture model of inflammatory bowel disease. *Sci Rep.* 2019 Feb 12;9(1):1812–1812.
27. Li N, Wang D, Sui Z, Qi X, Ji L, Wang X, et al. Development of an Improved Three-Dimensional In Vitro Intestinal Mucosa Model for Drug Absorption Evaluation. *Tissue Eng Part C Methods.* 2013 Jan 25;19(9):708–19.

28. Madden LR, Nguyen TV, Garcia-Mojica S, Shah V, Le AV, Peier A, et al. Bioprinted 3D Primary Human Intestinal Tissues Model Aspects of Native Physiology and ADME/Tox Functions. *iScience*. 2018 Apr 27;2:156–67.
29. Watson CL, Mahe MM, Múnera J, Howell JC, Sundaram N, Poling HM, et al. An in vivo model of human small intestine using pluripotent stem cells. *Nat Med*. 2014 Oct 19;20:1310.
30. Dockray GJ. Topical review. Gastrin and gastric epithelial physiology. *J Physiol*. 1999 Jul 15;518 ( Pt 2)(Pt 2):315–24.
31. Christopher D. Richards GP. *Human Physiology: The basis of medicine*. 3rd ed. Oxford core texts;
32. James Lowe AS. *Human Histology*. 2nd ed.
33. Krause WJ. Brunner's Glands: A Structural, Histochemical and Pathological Profile. *Prog Histochem Cytochem*. 2000 Jan 1;35(4):255–367.
34. Jung C, Hugot J-P, Barreau F. Peyer's Patches: The Immune Sensors of the Intestine. *Int J Inflamm*. 2010 Sep 19;2010:823710–823710.
35. Van Kruiningen HJ, West AB, Freda BJ, Holmes KA. Distribution of Peyer's Patches in the Distal Ileum. *Inflamm Bowel Dis*. 2002 May 1;8(3):180–5.
36. Said HM. Chapter 53 - Intestinal Absorption of Vitamin K: Cellular and Molecular Mechanisms. In: Said HM, editor. *Physiology of the Gastrointestinal Tract (Sixth Edition)* [Internet]. Academic Press; 2018. p. 1197–9. Available from: <http://www.sciencedirect.com/science/article/pii/B9780128099544000530>
37. Silverthorn DE. *Human Physiology - an integrated approach*. 4th ed. Pearson international;
38. Epithelial Cells - an overview | ScienceDirect Topics [Internet]. [cited 2018 Dec 5]. Available from: <https://www.sciencedirect.com/topics/neuroscience/epithelial-cells>
39. Pavelka M, Roth J. Epidermis. In: Pavelka M, Roth J, editors. *Functional Ultrastructure: Atlas of Tissue Biology and Pathology* [Internet]. Vienna: Springer Vienna; 2010 [cited 2018 Dec 11]. p. 240–1. Available from: [https://doi.org/10.1007/978-3-211-99390-3\\_124](https://doi.org/10.1007/978-3-211-99390-3_124)
40. Wilson PA, Hemmati-Brivanlou A. Induction of epidermis and inhibition of neural fate by Bmp-4. *Nature*. 1995 Jul;376(6538):331–3.
41. De Santa Barbara P, Van Den Brink GR, Roberts DJ. Development and differentiation of the intestinal epithelium. *Cell Mol Life Sci*. 2003 Jul;60(7):1322–32.
42. Chapter 25. Germ Layers and Their Derivatives - Review of Medical Embryology Book - LifeMap Discovery [Internet]. [cited 2018 Dec 11]. Available from: <https://discovery.lifemapsc.com/library/review-of-medical-embryology/chapter-25-germ-layers-and-their-derivatives>
43. Sumpio BE, Timothy Riley J, Dardik A. Cells in focus: endothelial cell. *Int J Biochem Cell Biol*. 2002 Dec 1;34(12):1508–12.

44. simple epithelium [Internet]. TheFreeDictionary.com. [cited 2018 Dec 11]. Available from: <https://medical-dictionary.thefreedictionary.com/simple+epithelium>
45. Type I Pneumocyte - an overview | ScienceDirect Topics [Internet]. [cited 2018 Dec 11]. Available from: <https://www.sciencedirect.com/topics/biochemistry-genetics-and-molecular-biology/type-i-pneumocyte>
46. McAteer JA, Evan AP, Gardner KD. Morphogenetic clonal growth of kidney epithelial cell line MDCK. *Anat Rec*. 1987 Mar;217(3):229–39.
47. Sridhar MS. Anatomy of cornea and ocular surface. *Indian J Ophthalmol*. 2018 Feb;66(2):190–4.
48. Enterocyte - an overview | ScienceDirect Topics [Internet]. [cited 2018 Dec 11]. Available from: <https://www.sciencedirect.com/topics/veterinary-science-and-veterinary-medicine/enterocyte>
49. Scully C. 11 - Mucosal, oral and cutaneous disorders. In: Scully C, editor. *Scully's Medical Problems in Dentistry (Seventh Edition)* [Internet]. Oxford: Churchill Livingstone; 2014. p. 323–36. Available from: <http://www.sciencedirect.com/science/article/pii/B9780702054013000114>
50. Tortora GJ, Derrickson B. *Introduction to the human body : the essentials of anatomy and physiology*. Hoboken, N.J.: Wiley; 2015.
51. Gantwerker EA, Hom DB. Skin: Histology and Physiology of Wound Healing. *Clin Plast Surg*. 2012 Jan 1;39(1):85–97.
52. Murakami S, Miki Y. Human skin histology using high-resolution echography. *J Clin Ultrasound*. 1989 Feb 1;17(2):77–82.
53. Roger M, Fullard N, Costello L, Bradbury S, Markiewicz E, O'Reilly S, et al. Bioengineering the microanatomy of human skin. *J Anat*. 2019 Apr 1;234(4):438–55.
54. Schroeder BO. Fight them or feed them: how the intestinal mucus layer manages the gut microbiota. *Gastroenterol Rep*. 2019 Feb 13;7(1):3–12.
55. Park J-H, Kotani T, Konno T, Setiawan J, Kitamura Y, Imada S, et al. Promotion of Intestinal Epithelial Cell Turnover by Commensal Bacteria: Role of Short-Chain Fatty Acids. *PloS One*. 2016 May 27;11(5):e0156334–e0156334.
56. Basivireddy J, Jacob M, Ramamoorthy P, Balasubramanian KA. Alterations in the intestinal glycocalyx and bacterial flora in response to oral indomethacin. *Int J Biochem Cell Biol*. 2005 Nov 1;37(11):2321–32.
57. Jandhyala SM, Talukdar R, Subramanyam C, Vuyyuru H, Sasikala M, Nageshwar Reddy D. Role of the normal gut microbiota. *World J Gastroenterol*. 2015 Aug 7;21(29):8787–803.
58. Guiu J, Hannezo E, Yui S, Demharter S, Ulyanchenko S, Maimets M, et al. Tracing the origin of adult intestinal stem cells. *Nature*. 2019 Jun 1;570(7759):107–11.

59. Hermiston ML, Gordon JI. Organization of the crypt-villus axis and evolution of its stem cell hierarchy during intestinal development. *Am J Physiol-Gastrointest Liver Physiol*. 1995 May 1;268(5):G813–22.
60. Williams JM, Duckworth CA, Burkitt MD, Watson AJM, Campbell BJ, Pritchard DM. Epithelial cell shedding and barrier function: a matter of life and death at the small intestinal villus tip. *Vet Pathol*. 2015 May;52(3):445–55.
61. Kapellos GE, Alexiou TS. Chapter 1 - Modeling Momentum and Mass Transport in Cellular Biological Media: From the Molecular to the Tissue Scale. In: Becker SM, Kuznetsov AV, editors. *Transport in Biological Media* [Internet]. Boston: Elsevier; 2013. p. 1–40. Available from: <http://www.sciencedirect.com/science/article/pii/B9780124158245000011>
62. Benet LZ, Izumi T, Zhang Y, Silverman JA, Wachter VJ. Intestinal MDR transport proteins and P-450 enzymes as barriers to oral drug delivery. *J Controlled Release*. 1999 Nov 1;62(1):25–31.
63. Niessen CM. Tight Junctions/Adherens Junctions: Basic Structure and Function. *J Invest Dermatol*. 2007 Nov 1;127(11):2525–32.
64. Bennett MVL, Barrio LC, Bargiello TA, Spray DC, Hertzberg E, Sáez JC. Gap junctions: New tools, new answers, new questions. *Neuron*. 1991 Mar 1;6(3):305–20.
65. Ramadan Q, Ting FCW. In vitro micro-physiological immune-competent model of the human skin. *Lab Chip*. 2016;16(10):1899–908.
66. Bansal T, Singh M, Mishra G, Talegaonkar S, Khar RK, Jaggi M, et al. Concurrent determination of topotecan and model permeability markers (atenolol, antipyrine, propranolol and furosemide) by reversed phase liquid chromatography: Utility in Caco-2 intestinal absorption studies. *J Chromatogr B*. 2007 Nov 15;859(2):261–6.
67. Parsa A, Saadati R, Abbasian Z, Azad Aramaki S, Dadashzadeh S. Enhanced Permeability of Etoposide across Everted Sacs of Rat Small Intestine by Vitamin E-TPGS. *Iran J Pharm Res IJPR*. 2013;12(Suppl):37–46.
68. Nielsen S, Westerhoff AM, Gé LG, Carlsen KL, Pedersen MDL, Nielsen CU. MRP2-mediated transport of etoposide in MDCKII MRP2 cells is unaffected by commonly used non-ionic surfactants. *Int J Pharm*. 2019 Jun 30;565:306–15.
69. Kunta J, Yan J, Makhey VD, Sinko PJ. Active efflux kinetics of etoposide from rabbit small intestine and colon. *Biopharm Drug Dispos*. 2000 Apr 1;21(3):83–93.
70. Fowler R, Vllasaliu D, Falcone FH, Garnett M, Smith B, Horsley H, et al. Uptake and transport of B12-conjugated nanoparticles in airway epithelium. *J Control Release Off J Control Release Soc*. 2013 Nov 28;172(1):374–81.
71. Schneeberger EE, Lynch RD. The tight junction: a multifunctional complex. *Am J Physiol-Cell Physiol*. 2004 Jun 1;286(6):C1213–28.
72. Lee B, Moon KM, Kim CY. Tight Junction in the Intestinal Epithelium: Its Association with Diseases and Regulation by Phytochemicals. *J Immunol Res*. 2018 Dec 16;2018:2645465–2645465.

73. Feldman GJ, Mullin JM, Ryan MP. Occludin: Structure, function and regulation. *Adhes Proteins Cell Tight Junctions Crit Compon Modul Paracellular Permeability*. 2005 Apr 25;57(6):883–917.
74. Krug SM, Schulzke JD, Fromm M. Tight junction, selective permeability, and related diseases. *Dev Urogenit Syst MTOR Signal Tight Junctions Health Dis*. 2014 Dec 1;36:166–76.
75. Alberts B, Johnson A, Lewis J, Raff M, Roberts K, Walter P. *Cell Junctions*. Mol Biol Cell 4th Ed [Internet]. 2002 [cited 2018 Dec 12]; Available from: <https://www.ncbi.nlm.nih.gov/books/NBK26857/>
76. Hartsock A, Nelson WJ. Adherens and tight junctions: structure, function and connections to the actin cytoskeleton. *Biochim Biophys Acta*. 2008 Mar;1778(3):660–9.
77. Wu C. Focal adhesion: a focal point in current cell biology and molecular medicine. *Cell Adhes Migr*. 2007;1(1):13–8.
78. Borradori L, Sonnenberg A. Structure and Function of Hemidesmosomes: More Than Simple Adhesion Complexes. *J Invest Dermatol*. 1999 Apr 1;112(4):411–8.
79. Niessen CM, Gottardi CJ. Molecular components of the adherens junction. *Apical Junctional Complexes Part I*. 2008 Mar 1;1778(3):562–71.
80. Maître J-L, Heisenberg C-P. Three functions of cadherins in cell adhesion. *Curr Biol CB*. 2013 Jul 22;23(14):R626–33.
81. Pećina-Šlaus N. Tumor suppressor gene E-cadherin and its role in normal and malignant cells. *Cancer Cell Int*. 2003 Oct 14;3:17.
82. van Roy F, Berx G. The cell-cell adhesion molecule E-cadherin. *Cell Mol Life Sci*. 2008 Dec 1;65(23):3756–88.
83. Garrod D, Chidgey M. Desmosome structure, composition and function. *Apical Junctional Complexes Part I*. 2008 Mar 1;1778(3):572–87.
84. Kowalczyk AP, Green KJ. Chapter Five - Structure, Function, and Regulation of Desmosomes. In: van Roy F, editor. *Progress in Molecular Biology and Translational Science* [Internet]. Academic Press; 2013. p. 95–118. Available from: <http://www.sciencedirect.com/science/article/pii/B9780123943118000054>
85. Nielsen MS, Axelsen LN, Sorgen PL, Verma V, Delmar M, Holstein-Rathlou N-H. Gap junctions. *Compr Physiol*. 2012 Jul;2(3):1981–2035.
86. Goodenough DA, Goliger JA, Paul DL. CONNEXINS, CONNEXONS, AND INTERCELLULAR COMMUNICATION. *Annu Rev Biochem*. 1996 Jun 1;65(1):475–502.
87. Rohr S. Role of gap junctions in the propagation of the cardiac action potential. *Cardiovasc Res*. 2004 May 1;62(2):309–22.
88. Meşe G, Richard G, White TW. Gap Junctions: Basic Structure and Function. *J Invest Dermatol*. 2007 Nov 1;127(11):2516–24.

89. Macdonald RS, Thornton WH, Bean TL. Insulin and IGF-1 Receptors in A Human Intestinal Adenocarcinoma Cell Line (Caco-2): Regulation of Na<sup>+</sup> Glucose Transport Across the Brush Border. *J Recept Res.* 1993 Jan 1;13(7):1093–113.
90. Hanani M. Lucifer yellow - an angel rather than the devil. *J Cell Mol Med.* 2012 Jan;16(1):22–31.
91. Johansson MEV, Ambort D, Pelaseyed T, Schütte A, Gustafsson JK, Ermund A, et al. Composition and functional role of the mucus layers in the intestine. *Cell Mol Life Sci.* 2011 Sep 25;68(22):3635.
92. Schneider H, Pelaseyed T, Svensson F, Johansson MEV. Study of mucin turnover in the small intestine by in vivo labeling. *Sci Rep.* 2018 Apr 10;8(1):5760.
93. Kamphuis JBJ, Mercier-Bonin M, Eutamène H, Theodorou V. Mucus organisation is shaped by colonic content; a new view. *Sci Rep.* 2017 Aug 17;7(1):8527.
94. Hooper LV. Chapter 3 - Epithelial Cell Contributions to Intestinal Immunity. In: Alt FW, editor. *Advances in Immunology* [Internet]. Academic Press; 2015. p. 129–72. Available from: <http://www.sciencedirect.com/science/article/pii/S0065277614000091>
95. Pentimikko N, Iqbal S, Mana M, Andersson S, Cognetta AB, Suciú RM, et al. Notum produced by Paneth cells attenuates regeneration of aged intestinal epithelium. *Nature.* 2019 Jul 1;571(7765):398–402.
96. Sato T, van Es JH, Snippert HJ, Stange DE, Vries RG, van den Born M, et al. Paneth cells constitute the niche for Lgr5 stem cells in intestinal crypts. *Nature.* 2010 Nov 28;469:415.
97. Leader M, Collins M, Patel J, Henry K. Desmin: Its value as a marker of muscle derived tumours using a commercial antibody. *Virchows Arch A.* 1987 Jul 1;411(4):345–9.
98. Lewis KJR, Hall JK, Kiyotake EA, Christensen T, Balasubramaniam V, Anseth KS. Epithelial-mesenchymal crosstalk influences cellular behavior in a 3D alveolus-fibroblast model system. *Biomaterials.* 2018 Feb 1;155:124–34.
99. Baulida J. Epithelial-to-mesenchymal transition transcription factors in cancer-associated fibroblasts. *Mol Oncol.* 2017 Jul 1;11(7):847–59.
100. Maas-Szabowski N, Shimotoyodome A, Fusenig NE. Keratinocyte growth regulation in fibroblast cocultures via a double paracrine mechanism. *J Cell Sci.* 1999 Jun 15;112(12):1843.
101. Montesano R, Schaller G, Orci L. Induction of epithelial tubular morphogenesis in vitro by fibroblast-derived soluble factors. *Cell.* 1991 Aug 23;66(4):697–711.
102. Lichtenberger BM, Mastrogiannaki M, Watt FM. Epidermal  $\beta$ -catenin activation remodels the dermis via paracrine signalling to distinct fibroblast lineages. *Nat Commun.* 2016 Feb 3;7(1):10537.
103. Matsusaki M, Hikimoto D, Nishiguchi A, Kadowaki K, Ohura K, Imai T, et al. 3D-fibroblast tissues constructed by a cell-coat technology enhance tight-junction formation of human colon epithelial cells. *Biochem Biophys Res Commun.* 2015 Feb 13;457(3):363–9.

104. Sumigray KD, Terwilliger M, Lechler T. Morphogenesis and Compartmentalization of the Intestinal Crypt. *Dev Cell*. 2018 Apr 23;45(2):183–197.e5.
105. Tran L, Greenwood-Van Meerveld B. Age-associated remodeling of the intestinal epithelial barrier. *J Gerontol A Biol Sci Med Sci*. 2013 Sep;68(9):1045–56.
106. Holt PR. Intestinal Malabsorption in the Elderly. *Dig Dis*. 2007;25(2):144–50.
107. Moorefield EC, Andres SF, Blue RE, Van Landeghem L, Mah AT, Santoro MA, et al. Aging effects on intestinal homeostasis associated with expansion and dysfunction of intestinal epithelial stem cells. *Aging*. 2017 Aug 29;9(8):1898–915.
108. Edwards BK, Noone A-M, Mariotto AB, Simard EP, Boscoe FP, Henley SJ, et al. Annual Report to the Nation on the status of cancer, 1975-2010, featuring prevalence of comorbidity and impact on survival among persons with lung, colorectal, breast, or prostate cancer. *Cancer*. 2014 May 1;120(9):1290–314.
109. Ye L, Sun LX, Wu MH, Wang J, Ding X, Shi H, et al. A Simple System for Differentiation of Functional Intestinal Stem Cell-like Cells from Bone Marrow Mesenchymal Stem Cells. *Mol Ther - Nucleic Acids*. 2018 Dec 7;13:110–20.
110. Paulus U, Loeffler M, Zeidler J, Owen G, Potten CS. The differentiation and lineage development of goblet cells in the murine small intestinal crypt: experimental and modelling studies. *J Cell Sci*. 1993 Oct 1;106(2):473.
111. Clarke LL. A guide to Ussing chamber studies of mouse intestine. *Am J Physiol Gastrointest Liver Physiol*. 2009 Jun;296(6):G1151–66.
112. Fogh J, Wright WC, Loveless JD. Absence of HeLa cell contamination in 169 cell lines derived from human tumors. *J Natl Cancer Inst*. 1977 Feb;58(2):209–14.
113. Enterocyte-like differentiation and polarization of the human colon carcinoma cell line CACO-2 in culture | Request PDF [Internet]. ResearchGate. [cited 2018 Dec 4]. Available from: [https://www.researchgate.net/publication/281082660\\_Enterocyte-like\\_differentiation\\_and\\_polarization\\_of\\_the\\_human\\_colon\\_carcinoma\\_cell\\_line\\_CACO-2\\_in\\_culture](https://www.researchgate.net/publication/281082660_Enterocyte-like_differentiation_and_polarization_of_the_human_colon_carcinoma_cell_line_CACO-2_in_culture)
114. Hidalgo IJ, Raub TJ, Borchardt RT. Characterization of the Human Colon Carcinoma Cell Line (Caco-2) as a Model System for Intestinal Epithelial Permeability. 1989;96(3):14.
115. Sun H, Chow EC, Liu S, Du Y, Pang KS. The Caco-2 cell monolayer: usefulness and limitations. *Expert Opin Drug Metab Toxicol*. 2008 Apr;4(4):395–411.
116. Goto M, Masuda S, Saito H, Inui K. Decreased expression of P-glycoprotein during differentiation in the human intestinal cell line Caco-2. *Biochem Pharmacol*. 2003 Jul 1;66(1):163–70.
117. Kretzschmar K, Clevers H. Organoids: Modeling Development and the Stem Cell Niche in a Dish. *Dev Cell*. 2016 Sep 26;38(6):590–600.
118. Wang X, Yamamoto Y, Wilson LH, Zhang T, Howitt BE, Farrow MA, et al. Cloning and variation of ground state intestinal stem cells. *Nature*. 2015 Jun 11;522(7555):173–8.



119. Dutta D, Heo I, Clevers H. Disease Modeling in Stem Cell-Derived 3D Organoid Systems. *Spec Issue Cancer Org.* 2017 May 1;23(5):393–410.
120. Woo D-H, Chen Q, Yang T-LB, Glineburg MR, Hoge C, Leu NA, et al. Enhancing a Wnt-Telomere Feedback Loop Restores Intestinal Stem Cell Function in a Human Organotypic Model of Dyskeratosis Congenita. *Cell Stem Cell.* 2016 Sep 1;19(3):397–405.
121. Dedhia PH, Bertaux-Skeirik N, Zavros Y, Spence JR. Organoid Models of Human Gastrointestinal Development and Disease. *Gastroenterology.* 2016 May 1;150(5):1098–112.
122. van de Wetering M, Francies HE, Francis JM, Bounova G, Iorio F, Pronk A, et al. Prospective Derivation of a Living Organoid Biobank of Colorectal Cancer Patients. *Cell.* 2015 May 7;161(4):933–45.
123. HT-29 ATCC<sup>®</sup> HTB-38<sup>™</sup> Homo sapiens colon colorectal adenocar [Internet]. [cited 2018 Dec 6]. Available from: [http://www.lgcstandards-atcc.org/products/all/HTB-38.aspx?geo\\_country=gb](http://www.lgcstandards-atcc.org/products/all/HTB-38.aspx?geo_country=gb)
124. Perez-Vilar J, Hill RL. The Structure and Assembly of Secreted Mucins. *J Biol Chem.* 1999 May 11;274(45):31751–4.
125. Hansson GC. Role of mucus layers in gut infection and inflammation. *Curr Opin Microbiol.* 2012 Feb;15(1):57–62.
126. Arike L, Hansson GC. The Densely O-Glycosylated MUC2 Mucin Protects the Intestine and Provides Food for the Commensal Bacteria. *Glycosylation Cell Process Dis.* 2016 Aug 14;428(16):3221–9.
127. Sicard J-F, Le Bihan G, Vogeleer P, Jacques M, Harel J. Interactions of Intestinal Bacteria with Components of the Intestinal Mucus. *Front Cell Infect Microbiol.* 2017;7:387.
128. Corfield AP. Mucins: A biologically relevant glycan barrier in mucosal protection. *Biochim Biophys Acta BBA - Gen Subj.* 2015 Jan 1;1850(1):236–52.
129. Johansson MEV, Sjövall H, Hansson GC. The gastrointestinal mucus system in health and disease. *Nat Rev Gastroenterol Hepatol.* 2013 Jun;10(6):352–61.
130. Bengoa AA, Zavala L, Carasi P, Trejo SA, Bronsoms S, Serradell M de los Á, et al. Simulated gastrointestinal conditions increase adhesion ability of *Lactobacillus paracasei* strains isolated from kefir to Caco-2 cells and mucin. *Food Res Int.* 2018 Jan 1;103:462–7.
131. Lozoya-Agullo I, Araújo F, González-Álvarez I, Merino-Sanjuán M, González-Álvarez M, Bermejo M, et al. Usefulness of Caco-2/HT29-MTX and Caco-2/HT29-MTX/Raji B Coculture Models To Predict Intestinal and Colonic Permeability Compared to Caco-2 Monoculture. *Mol Pharm.* 2017 Apr 3;14(4):1264–70.
132. Akbari A, Lavasanifar A, Wu J. Interaction of cruciferin-based nanoparticles with Caco-2 cells and Caco-2/HT29-MTX co-cultures. *Acta Biomater.* 2017 Dec 1;64:249–58.

133. Li Y, Arranz E, Guri A, Corredig M. Mucus interactions with liposomes encapsulating bioactives: Interfacial tensiometry and cellular uptake on Caco-2 and cocultures of Caco-2/HT29-MTX. *Food Res Int.* 2017 Feb 1;92:128–37.
134. Berger E, Géloën A. Adipocytes as lipid sensors of oleic acid transport through a functional Caco-2/HT29-MTX intestinal barrier. *Adipocyte.* 2019 Jan 2;8(1):83–97.
135. Chen S-X, Xu X-E, Wang X-Q, Cui S-J, Xu L-L, Jiang Y-H, et al. Data from a proteomic analysis of colonic fibroblasts secretomes. *Data Brief.* 2014 Dec 1;1:19–24.
136. Chen S-X, Xu X-E, Wang X-Q, Cui S-J, Xu L-L, Jiang Y-H, et al. Identification of colonic fibroblast secretomes reveals secretory factors regulating colon cancer cell proliferation. *J Proteomics.* 2014 Oct 14;110:155–71.
137. Visco V, Bava FA, d'Alessandro F, Cavallini M, Ziparo V, Torrisi MR. Human colon fibroblasts induce differentiation and proliferation of intestinal epithelial cells through the direct paracrine action of keratinocyte growth factor. *J Cell Physiol.* 2009 Jul;220(1):204–13.
138. Pereira C, Araújo F, Barrias CC, Granja PL, Sarmento B. Dissecting stromal-epithelial interactions in a 3D in vitro cellularized intestinal model for permeability studies. *Biomaterials.* 2015 Jul;56:36–45.
139. Béduneau A, Tempesta C, Fimbel S, Pellequer Y, Jannin V, Demarne F, et al. A tunable Caco-2/HT29-MTX co-culture model mimicking variable permeabilities of the human intestine obtained by an original seeding procedure. *Eur J Pharm Biopharm.* 2014 Jul 1;87(2):290–8.
140. MacAdam A. The effect of gastro-intestinal mucus on drug absorption. *Adv Drug Deliv Rev.* 1993 Sep 1;11(3):201–20.
141. Boegh M, Nielsen HM. Mucus as a Barrier to Drug Delivery – Understanding and Mimicking the Barrier Properties. *Basic Clin Pharmacol Toxicol.* 2015;116(3):179–86.
142. Ferraretto A, Bottani M, Luca PD, Cornaghi L, Arnaboldi F, Maggioni M, et al. Morphofunctional properties of a differentiated Caco2/HT-29 co-culture as an in vitro model of human intestinal epithelium. *Biosci Rep [Internet].* 2018 Apr 27 [cited 2018 Dec 18];38(2). Available from: <https://www.ncbi.nlm.nih.gov/pmc/articles/PMC5920134/>
143. Schweinlin M, Wilhelm S, Schwedhelm I, Hansmann J, Rietscher R, Jurowich C, et al. Development of an Advanced Primary Human In Vitro Model of the Small Intestine. *Tissue Eng Part C Methods.* 2016 Aug 1;22(9):873–83.
144. Nik AM, Reyahi A, Pontén F, Carlsson P. Foxf2 in Intestinal Fibroblasts Reduces Numbers of Lgr5+ Stem Cells and Adenoma Formation by Inhibiting Wnt Signaling. *Gastroenterology.* 2013 May 1;144(5):1001–11.
145. Sneddon JB, Werb Z. Location, Location, Location: The Cancer Stem Cell Niche. *Cell Stem Cell.* 2007 Dec 13;1(6):607–11.
146. Sato T, Clevers H. Growing Self-Organizing Mini-Guts from a Single Intestinal Stem Cell: Mechanism and Applications. *Science.* 2013 Jun 7;340(6137):1190.

147. Drost J, van Jaarsveld RH, Ponsioen B, Zimmerlin C, van Boxtel R, Buijs A, et al. Sequential cancer mutations in cultured human intestinal stem cells. *Nature*. 2015 Apr 29;521:43.
148. Dekkers JF, Wiegerinck CL, de Jonge HR, Bronsveld I, Janssens HM, de Winter-de Groot KM, et al. A functional CFTR assay using primary cystic fibrosis intestinal organoids. *Nat Med*. 2013 Jun 2;19:939.
149. Hoshiba T, Chen G, Endo C, Maruyama H, Wakui M, Nemoto E, et al. Decellularized Extracellular Matrix as an In Vitro Model to Study the Comprehensive Roles of the ECM in Stem Cell Differentiation. *Stem Cells Int*. 2016;2016:6397820–6397820.
150. Sun D, Liu Y, Wang H, Deng F, Zhang Y, Zhao S, et al. Novel decellularized liver matrix-alginate hybrid gel beads for the 3D culture of hepatocellular carcinoma cells. *Int J Biol Macromol*. 2018 Apr 1;109:1154–63.
151. Alabi BR, LaRanger R, Shay JW. Decellularized mice colons as models to study the contribution of the extracellular matrix to cell behavior and colon cancer progression. *Acta Biomater* [Internet]. 2019 Sep 25; Available from: <http://www.sciencedirect.com/science/article/pii/S1742706119306543>
152. Urbani L, Maghsoudlou P, Milan A, Menikou M, Hagen CK, Totonelli G, et al. Long-term cryopreservation of decellularised oesophagi for tissue engineering clinical application. *PLOS ONE*. 2017 Jun 9;12(6):e0179341.
153. Kim M, Perera N, Knight S, Barnett S, Gooi J, Seevanayagam S. P3.16-052 Use of Decellularised Porcine Intestinal Submucosa Extracellular Matrix in Airway Reconstruction to Enable Lung-Sparing Oncological Surgery. *J Thorac Oncol*. 2017 Nov 1;12(11):S2362.
154. Larregieu CA, Benet LZ. Drug discovery and regulatory considerations for improving in silico and in vitro predictions that use Caco-2 as a surrogate for human intestinal permeability measurements. *AAPS J*. 2013 Apr;15(2):483–97.
155. Research C for BE and. Devices Guidances. FDA [Internet]. 2020 Sep 4 [cited 2020 Sep 8]; Available from: <https://www.fda.gov/vaccines-blood-biologics/general-biologics-guidances/devices-guidances>
156. Bauer SR. Stem Cell-based Products in Medicine: FDA Regulatory Considerations. Lanza R, Gearhart J, Hogan B, Melton D, Pedersen R, Thomson J, et al., editors. *Handb Stem Cells*. 2004;805–14.
157. Du P, Paskaranandavadivel N, Angeli TR, Cheng LK, O’Grady G. The virtual intestine: in silico modeling of small intestinal electrophysiology and motility and the applications. *Wiley Interdiscip Rev Syst Biol Med*. 2016;8(1):69–85.
158. Yi Li TJ. Foxp3 expression in A549 cells is regulated by Toll-like receptor 4 through nuclear factor- $\kappa$ B. *Mol Med Rep*. 6:167–72.
159. Maubon N, Le Vee M, Fossati L, Audry M, Le Ferrec E, Bolze S, et al. Analysis of drug transporter expression in human intestinal Caco-2 cells by real-time PCR. *Fundam Clin Pharmacol*. 2007 Dec 1;21(6):659–63.

160. Kyoko O, Kono H, Ishimaru K, Miyake K, Kubota T, Ogawa H, et al. Expressions of tight junction proteins Occludin and Claudin-1 are under the circadian control in the mouse large intestine: implications in intestinal permeability and susceptibility to colitis. *PloS One*. 2014 May 20;9(5):e98016–e98016.
161. Hilgendorf C, Spahn-Langguth H, Regårdh CG, Lipka E, Amidon GL, Langguth P. Caco-2 versus caco-2/HT29-MTX co-cultured cell lines: Permeabilities via diffusion, inside- and outside-directed carrier-mediated transport. *J Pharm Sci*. 2000 Jan 1;89(1):63–75.
162. Pereira C, Araújo F, Barrias CC, Granja PL, Sarmento B. Dissecting stromal-epithelial interactions in a 3D in vitro cellularized intestinal model for permeability studies. *Biomaterials*. 2015 Jul 1;56:36–45.
163. Parrinello S, Coppe J-P, Krtolica A, Campisi J. Stromal-epithelial interactions in aging and cancer: senescent fibroblasts alter epithelial cell differentiation. *J Cell Sci*. 2005 Feb 1;118(3):485.
164. Sengupta N, MacDonald TT. The Role of Matrix Metalloproteinases in Stromal/Epithelial Interactions in the Gut. *Physiology*. 2007 Dec 1;22(6):401–9.
165. Hayward SW. Approaches to Modeling Stromal-Epithelial Interactions. *J Urol*. 2002 Sep 1;168(3):1165–72.
166. Truffi M, Sorrentino L, Monieri M, Fociani P, Mazzucchelli S, Bonzini M, et al. Inhibition of Fibroblast Activation Protein Restores a Balanced Extracellular Matrix and Reduces Fibrosis in Crohn's Disease Strictures Ex Vivo. *Inflamm Bowel Dis*. 2018 Jan 18;24(2):332–45.
167. Lawrance IC, Maxwell L, Doe W. Altered Response of Intestinal Mucosal Fibroblasts to Profibrogenic Cytokines in Inflammatory Bowel Disease. *Inflamm Bowel Dis*. 2001 Aug 1;7(3):226–36.
168. Cannon CL, Neal PJ, Southee JA, Kubilus J, Klausner M. New epidermal model for dermal irritancy testing. *Toxicol In Vitro*. 1994 Aug 1;8(4):889–91.
169. Arnette C, Koetsier JL, Hoover P, Getsios S, Green KJ. In Vitro Model of the Epidermis: Connecting Protein Function to 3D Structure. *Methods Enzymol*. 2016;569:287–308.
170. Bellas E, Seiberg M, Garlick J, Kaplan DL. In vitro 3D Full-Thickness Skin-Equivalent Tissue Model Using Silk and Collagen Biomaterials. *Macromol Biosci*. 2012 Dec 1;12(12):1627–36.
171. Rheinwatd JG, Green H. Serial cultivation of strains of human epidermal keratinocytes: the formation keratinizing colonies from single cell is. *Cell*. 1975 Nov 1;6(3):331–43.
172. Giacomini KM, Krauss RM, Roden DM, Eichelbaum M, Hayden MR, Nakamura Y. When good drugs go bad. *Nature*. 2007 Apr 25;446:975.
173. Lei NY, Jabaji Z, Wang J, Joshi VS, Brinkley GJ, Khalil H, et al. Intestinal Subepithelial Myofibroblasts Support the Growth of Intestinal Epithelial Stem Cells. *PLOS ONE*. 2014 Jan 6;9(1):e84651.

174. Wei SC, Fattet L, Tsai JH, Guo Y, Pai VH, Majeski HE, et al. Matrix stiffness drives epithelial–mesenchymal transition and tumour metastasis through a TWIST1–G3BP2 mechanotransduction pathway. *Nat Cell Biol.* 2015 Apr 20;17:678.
175. Eisenberg JL, Safi A, Wei X, Espinosa HD, Budinger GS, Takawira D, et al. Substrate stiffness regulates extracellular matrix deposition by alveolar epithelial cells. *Res Rep Biol.* 2011 Jan;2011(2):1–12.
176. Elena Martínez AGC. Dynamic photopolymerization produces complex microstructures on hydrogels in a moldless approach to generate a 3D intestinal tissue model. *Biofabrication.* 2019;11(2).
177. Unger BL, McGee DW. Hepatocyte growth factor and keratinocyte growth factor enhance IL-1-induced IL-8 secretion through different mechanisms in Caco-2 epithelial cells. *In Vitro Cell Dev Biol Anim.* 2011 Feb;47(2):173–81.
178. Komuro T. Re-evaluation of fibroblasts and fibroblast-like cells. *Anat Embryol (Berl).* 1990 Aug 1;182(2):103–12.
179. Brittan M, Hunt T, Jeffery R, Poulsom R, Forbes SJ, Hodivala-Dilke K, et al. Bone marrow derivation of pericryptal myofibroblasts in the mouse and human small intestine and colon. *Gut.* 2002 Jun 1;50(6):752.
180. Mifflin RC, Pinchuk IV, Saada JI, Powell DW. Intestinal myofibroblasts: targets for stem cell therapy. *Am J Physiol Gastrointest Liver Physiol.* 2011 May;300(5):G684–696.
181. Kouroumalis A, Nibbs RJ, Aptel H, Wright KL, Kolios G, Ward SG. The Chemokines CXCL9, CXCL10, and CXCL11 Differentially Stimulate Gα<sub>i</sub>-Independent Signaling and Actin Responses in Human Intestinal Myofibroblasts. *J Immunol.* 2005 Oct 15;175(8):5403.
182. Di Sabatino A, Pender SLF, Jackson CL, Prothero JD, Gordon JN, Picariello L, et al. Functional Modulation of Crohn’s Disease Myofibroblasts by Anti-Tumor Necrosis Factor Antibodies. *Gastroenterology.* 2007 Jul 1;133(1):137–49.
183. Yamazaki T, Mukouyama Y-S. Tissue Specific Origin, Development, and Pathological Perspectives of Pericytes. *Front Cardiovasc Med.* 2018 Jun 27;5:78–78.
184. van Dijk CGM, Nieuweboer FE, Pei JY, Xu YJ, Burgisser P, van Mulligen E, et al. The complex mural cell: Pericyte function in health and disease. *Int J Cardiol.* 2015 Jul 1;190:75–89.
185. Ramirez M, Pell N, Mejias M, Fernandez M. Pericytes in the Gut. In: Birbrair A, editor. *Pericyte Biology in Different Organs* [Internet]. Cham: Springer International Publishing; 2019. p. 73–100. Available from: [https://doi.org/10.1007/978-3-030-11093-2\\_5](https://doi.org/10.1007/978-3-030-11093-2_5)
186. Geevarghese A, Herman IM. Pericyte-endothelial crosstalk: implications and opportunities for advanced cellular therapies. *Transl Res J Lab Clin Med.* 2014 Apr;163(4):296–306.
187. Armulik A, Genové G, Betsholtz C. Pericytes: Developmental, Physiological, and Pathological Perspectives, Problems, and Promises. *Dev Cell.* 2011 Aug 16;21(2):193–215.

188. Madison BB, Braunstein K, Kuizon E, Portman K, Qiao XT, Gumucio DL. Epithelial hedgehog signals pattern the intestinal crypt-villus axis. *Development*. 2005 Jan 15;132(2):279.
189. Bergmeier V, Etich J, Pitzler L, Frie C, Koch M, Fischer M, et al. Identification of a myofibroblast-specific expression signature in skin wounds. *Matrix Biol*. 2018 Jan 1;65:59–74.
190. Obniski R, Sieber M, Spradling AC. Dietary Lipids Modulate Notch Signaling and Influence Adult Intestinal Development and Metabolism in *Drosophila*. *Dev Cell*. 2018 Oct 8;47(1):98–111.e5.
191. Simonetta Ferruzza, Carlotta Rossi, Yula Sambuy, Maria Scarino. Serum-reduced and serum-free media for differentiation of Caco-2 cells. *ALTEx - Altern Anim Exp* [Internet]. 2013 May 1 [cited 2019 May 8];30(2). Available from: <https://www.altex.org/index.php/altex/article/view/385>
192. Wahlang B, Pawar YB, Bansal AK. Identification of permeability-related hurdles in oral delivery of curcumin using the Caco-2 cell model. *Eur J Pharm Biopharm*. 2011 Feb 1;77(2):275–82.
193. Sambuy Y, De Angelis I, Ranaldi G, Scarino ML, Stamatii A, Zucco F. The Caco-2 cell line as a model of the intestinal barrier: influence of cell and culture-related factors on Caco-2 cell functional characteristics. *Cell Biol Toxicol*. 2005 Jan 1;21(1):1–26.
194. Beaulieu JF, Quaroni A. Clonal analysis of sucrase-isomaltase expression in the human colon adenocarcinoma Caco-2 cells. *Biochem J*. 1991 Dec 15;280 ( Pt 3)(Pt 3):599–608.
195. Korjamo T, Honkakoski P, Toppinen M-R, Niva S, Reinisalo M, Palmgrén JJ, et al. Absorption properties and P-glycoprotein activity of modified Caco-2 cell lines. *Eur J Pharm Sci*. 2005 Nov 1;26(3):266–79.
196. Sambuy Y, De Angelis I, Ranaldi G, Scarino ML, Stamatii A, Zucco F. The Caco-2 cell line as a model of the intestinal barrier: influence of cell and culture-related factors on Caco-2 cell functional characteristics. *Cell Biol Toxicol*. 2005 Jan 1;21(1):1–26.
197. Woodcock S, Williamson I, Hassan I, Mackay M. Isolation and characterisation of clones from the Caco-2 cell line displaying increased taurocholic acid transport. *J Cell Sci*. 1991 Mar 1;98(3):323.
198. Blume L-F, Denker M, Gieseler F, Kunze T. Temperature corrected transepithelial electrical resistance (TEER) measurement to quantify rapid changes in paracellular permeability. Vol. 65. 2010. 19 p.
199. Helms HC, Waagepetersen HS, Nielsen CU, Brodin B. Paracellular Tightness and Claudin-5 Expression is Increased in the BCEC/Astrocyte Blood–Brain Barrier Model by Increasing Media Buffer Capacity During Growth. *AAPS J*. 2010 Dec 1;12(4):759–70.
200. Briske-Anderson MJ, Finley JW, Newman SM. The Influence of Culture Time and Passage Number on the Morphological and Physiological Development of Caco-2 Cells. *Proc Soc Exp Biol Med*. 1997 Mar 1;214(3):248–57.

201. Kamath AV, Morrison RA, Mathias NR, Dando SA, Marino AM, Chong S. Modulation of tight junctions does not predict oral absorption of hydrophilic compounds: Use of caco-2 and calu-3 cells. *Arch Pharm Res.* 2007 Aug 1;30(8):1002–7.
202. Sabboh-Jourdan H, Valla F, Epriliati I, Gidley MJ. Organic acid bioavailability from banana and sweet potato using an in vitro digestion and Caco-2 cell model. *Eur J Nutr.* 2011 Feb 1;50(1):31–40.
203. Lecluyse EL, Sutton SC, Fix JA. In vitro effects of long-chain acylcarnitines on the permeability, transepithelial electrical resistance and morphology of rat colonic mucosa. *J Pharmacol Exp Ther.* 1993 May 1;265(2):955.
204. Asmar RE, Panigrahi P, Bamford P, Berti I, Not T, Coppa GV, et al. Host-dependent zonulin secretion causes the impairment of the small intestine barrier function after bacterial exposure. *Gastroenterology.* 2002 Nov 1;123(5):1607–15.
205. Johansson PK, Julleson D, Elfving A, Liin SI, Musumeci C, Zeglio E, et al. Electronic polymers in lipid membranes. *Sci Rep.* 2015 Jun 10;5:11242.
206. Anderson JM, Van Itallie CM. Physiology and function of the tight junction. *Cold Spring Harb Perspect Biol.* 2009 Aug;1(2):a002584–a002584.
207. González-Mariscal L, Tapia R, Chamorro D. Crosstalk of tight junction components with signaling pathways. *Apical Junctional Complexes Part I.* 2008 Mar 1;1778(3):729–56.
208. Kim TI, Poulin EJ, Blask E, Bukhalid R, Whitehead RH, Franklin JL, et al. Myofibroblast keratinocyte growth factor reduces tight junctional integrity and increases claudin-2 levels in polarized Caco-2 cells. *Growth Factors Chur Switz.* 2012 Oct;30(5):320–32.
209. Rosenthal R, Milatz S, Krug SM, Oelrich B, Schulzke J-D, Amasheh S, et al. Claudin-2, a component of the tight junction, forms a paracellular water channel. *J Cell Sci.* 2010 Jun 1;123(11):1913.
210. Luettig J, Rosenthal R, Barmeyer C, Schulzke JD. Claudin-2 as a mediator of leaky gut barrier during intestinal inflammation. *Tissue Barriers.* 2015 Jan 14;3(1–2):e977176–e977176.
211. Kim TI. The Role of Barrier Dysfunction and Change of Claudin Expression in Inflammatory Bowel Disease. *Gut Liver.* 2015 Nov;9(6):699–700.
212. Kanaporis G, Brink PR, Valiunas V. Gap junction permeability: selectivity for anionic and cationic probes. *Am J Physiol Cell Physiol.* 2011 Mar;300(3):C600–9.
213. Watanabe M, Ishiwata T, Nishigai K, Moriyama Y, Asano G. Overexpression of keratinocyte growth factor in cancer cells and enterochromaffin cells in human colorectal cancer. *Pathol Int.* 2000 May 1;50(5):363–72.
214. Martín-Saavedra F, Crespo L, Escudero-Duch C, Saldaña L, Gómez-Barrena E, Vilaboa N. Substrate Microarchitecture Shapes the Paracrine Crosstalk of Stem Cells with Endothelial Cells and Osteoblasts. *Sci Rep.* 2017 Nov 9;7(1):15182.

215. Melissaridou S, Wiechec E, Magan M, Jain MV, Chung MK, Farnebo L, et al. The effect of 2D and 3D cell cultures on treatment response, EMT profile and stem cell features in head and neck cancer. *Cancer Cell Int.* 2019 Jan 14;19(1):16.
216. ZANG X-P, LERNER M, BRACKETT D, PENTO JT. Influence of KGF on the Progression of Pancreatic Cancer. *Anticancer Res.* 2009 Aug 1;29(8):3417–20.
217. Riedl A, Schleder M, Pudenko K, Stadler M, Walter S, Unterleuthner D, et al. Comparison of cancer cells in 2D vs 3D culture reveals differences in AKT–mTOR–S6K signaling and drug responses. *J Cell Sci.* 2017 Jan 1;130(1):203.
218. Hassan B, Akcakanat A, Holder AM, Meric-Bernstam F. Targeting the PI3-kinase/Akt/mTOR signaling pathway. *Surg Oncol Clin N Am.* 2013 Oct;22(4):641–64.
219. Drygiannakis I, Valatas V, Sfakianaki O, Bourikas L, Manousou P, Kambas K, et al. Proinflammatory cytokines induce crosstalk between colonic epithelial cells and subepithelial myofibroblasts: Implication in intestinal fibrosis. *J Crohns Colitis.* 2013 May 1;7(4):286–300.
220. Brenmoehl J, Miller S-N, Hofmann C, Vogl D, Falk W, Schölmerich J, et al. Transforming growth factor-beta 1 induces intestinal myofibroblast differentiation and modulates their migration. *World J Gastroenterol.* 2009 Mar 28;15(12):1431–42.
221. Canady J, Arndt S, Karrer S, Bosserhoff AK. Increased KGF Expression Promotes Fibroblast Activation in a Double Paracrine Manner Resulting in Cutaneous Fibrosis. *J Invest Dermatol.* 2013 Mar 1;133(3):647–57.
222. Sorrell JM, Caplan AI. Fibroblast heterogeneity: more than skin deep. *J Cell Sci.* 2004 Feb 15;117(5):667.
223. Han DS, Li F, Holt L, Connolly K, Hubert M, Miceli R, et al. Keratinocyte growth factor-2 (FGF-10) promotes healing of experimental small intestinal ulceration in rats. *Am J Physiol-Gastrointest Liver Physiol.* 2000 Nov 1;279(5):G1011–22.
224. Calabro AR, Konsoula R, Barile FA. Evaluation of in vitro cytotoxicity and paracellular permeability of intact monolayers with mouse embryonic stem cells. *Toxicol Vitro Int J Publ Assoc BIBRA.* 2008 Aug;22(5):1273–84.
225. Suzuki T, Yoshinaga N, Tanabe S. Interleukin-6 (IL-6) regulates claudin-2 expression and tight junction permeability in intestinal epithelium. *J Biol Chem.* 2011 Sep 9;286(36):31263–71.
226. Miyake M, Nakai D. Effect of proinflammatory cytokine IL-6 on efflux transport of rebamipide in Caco-2 cells. *Xenobiotica.* 2017 Sep 2;47(9):821–4.
227. Van Itallie CM, Colegio OR, Anderson JM. The Cytoplasmic Tails of Claudins Can Influence Tight Junction Barrier Properties through Effects on Protein Stability. *J Membr Biol.* 2004 May 1;199(1):29–38.
228. Karlsson J, Wikman A, Artursson P. The mucus layer as a barrier to drug absorption in monolayers of human intestinal epithelial HT29-H goblet cells. *Int J Pharm.* 1993 Oct 15;99(2):209–18.



229. MacAdam A. The effect of gastro-intestinal mucus on drug absorption. *Relev Mucus Adv Drug Deliv.* 1993 Sep 1;11(3):201–20.
230. Boegh M, Nielsen HM. Mucus as a Barrier to Drug Delivery – Understanding and Mimicking the Barrier Properties. *Basic Clin Pharmacol Toxicol.* 2015 Mar 1;116(3):179–86.
231. KISHIMOTO H, MIYAZAKI K, SHIRASAKA Y, INOUE K. Effect of mucus layer on the transcellular absorption of lipophilic drugs in rat small intestine. *FASEB J.* 2018 Apr 1;32(1\_supplement):761.1-761.1.
232. Weiss AA, Babyatsky MW, Ogata S, Chen A, Itzkowitz SH. Expression of MUC2 and MUC3 mRNA in human normal, malignant, and inflammatory intestinal tissues. *J Histochem Cytochem.* 1996 Oct 1;44(10):1161–6.
233. Shurer CR, Kuo JC-H, Roberts LM, Gandhi JG, Colville MJ, Enoki TA, et al. Physical Principles of Membrane Shape Regulation by the Glycocalyx. *Cell.* 2019 Jun 13;177(7):1757–1770.e21.
234. van Putten JPM, Strijbis K. Transmembrane Mucins: Signaling Receptors at the Intersection of Inflammation and Cancer. *J Innate Immun.* 2017 May;9(3):281–99.
235. Johansson MEV, Sjövall H, Hansson GC. The gastrointestinal mucus system in health and disease. *Nat Rev Gastroenterol Hepatol.* 2013 Jun;10(6):352–61.
236. Mack DR, Ahrne S, Hyde L, Wei S, Hollingsworth MA. Extracellular MUC3 mucin secretion follows adherence of *Lactobacillus* strains to intestinal epithelial cells in vitro. *Gut.* 2003 Jun 1;52(6):827.
237. Menon BB, Kaiser-Marko C, Spurr-Michaud S, Tisdale AS, Gipson IK. Suppression of Toll-like receptor-mediated innate immune responses at the ocular surface by the membrane-associated mucins MUC1 and MUC16. *Mucosal Immunol.* 2015 Jan 7;8:1000.
238. Pan F, Han L, Zhang Y, Yu Y, Liu J. Optimization of Caco-2 and HT29 co-culture in vitro cell models for permeability studies. *Int J Food Sci Nutr.* 2015 Aug 18;66(6):680–5.
239. Kim YS, Ho SB. Intestinal goblet cells and mucins in health and disease: recent insights and progress. *Curr Gastroenterol Rep.* 2010 Oct;12(5):319–30.
240. Lesuffleur T, Barbat A, Dussaulx E, Zweibaum A. Growth Adaptation to Methotrexate of HT-29 Human Colon Carcinoma Cells Is Associated with Their Ability to Differentiate into Columnar Absorptive and Mucus-secreting Cells. *Cancer Res.* 1990 Oct 1;50(19):6334.
241. Kitamura H, Cho M, Lee BH, Gum JR, Siddiki BB, Ho SB, et al. Alteration in mucin gene expression and biological properties of HT29 colon cancer cell subpopulations. *Eur J Cancer.* 1996 Sep 1;32(10):1788–96.
242. Liévin-Le Moal V, Huet G, Aubert J-P, Bara J, Forgue-Lafitte M-E, Servin AL, et al. Activation of mucin exocytosis and upregulation of MUC genes in polarized human intestinal mucin-secreting cells by the thiol-activated exotoxin listeriolysin O. *Cell Microbiol.* 2002 Aug 1;4(8):515–29.

243. Béduneau A, Tempesta C, Fimbel S, Pellequer Y, Jannin V, Demarne F, et al. A tunable Caco-2/HT29-MTX co-culture model mimicking variable permeabilities of the human intestine obtained by an original seeding procedure. *Eur J Pharm Biopharm.* 2014 Jul 1;87(2):290–8.
244. Alemka A, Clyne M, Shanahan F, Tompkins T, Corcionivoschi N, Bourke B. Probiotic Colonization of the Adherent Mucus Layer of HT29MTXE12 Cells Attenuates *Campylobacter jejuni* Virulence Properties. *Infect Immun.* 2010 Jun 1;78(6):2812.
245. Haller D, Holt L, Parlesak A, Zanga J, Bäuerlein A, Sartor RB, et al. Differential effect of immune cells on non-pathogenic Gram-negative bacteria-induced nuclear factor-kappaB activation and pro-inflammatory gene expression in intestinal epithelial cells. *Immunology.* 2004 Jun;112(2):310–20.
246. Chen X-M, Elisia I, Kitts DD. Defining conditions for the co-culture of Caco-2 and HT29-MTX cells using Taguchi design. *J Pharmacol Toxicol Methods.* 2010 May 1;61(3):334–42.
247. Kleiveland CR. Co-cultivation of Caco-2 and HT-29MTX. In: Verhoeckx K, Cotter P, López-Expósito I, Kleiveland C, Lea T, Mackie A, et al., editors. *The Impact of Food Bioactives on Health: in vitro and ex vivo models* [Internet]. Cham: Springer International Publishing; 2015. p. 135–40. Available from: [https://doi.org/10.1007/978-3-319-16104-4\\_13](https://doi.org/10.1007/978-3-319-16104-4_13)
248. Ferraretto A, Bottani M, De Luca P, Cornaghi L, Arnaboldi F, Maggioni M, et al. Morphofunctional properties of a differentiated Caco2/HT-29 co-culture as an *in vitro* model of human intestinal epithelium. *Biosci Rep.* 2018 Apr 27;38(2):BSR20171497.
249. Wikman-Larhed A, Artursson P. Co-cultures of human intestinal goblet (HT29-H) and absorptive (Caco-2) cells for studies of drug and peptide absorption. *Eur J Pharm Sci.* 1995 Jun 1;3(3):171–83.
250. Navabi N, McGuckin MA, Lindén SK. Gastrointestinal Cell Lines Form Polarized Epithelia with an Adherent Mucus Layer when Cultured in Semi-Wet Interfaces with Mechanical Stimulation. *PLOS ONE.* 2013 Jul 15;8(7):e68761.
251. Turco L, Catone T, Caloni F, Consiglio ED, Testai E, Stammati A. Caco-2/TC7 cell line characterization for intestinal absorption: How reliable is this *in vitro* model for the prediction of the oral dose fraction absorbed in human? *Toxicol In Vitro.* 2011 Feb 1;25(1):13–20.
252. Xu H, Li Q, Zhao Y, Li J, Ghishan FK. Intestinal NHE8 is highly expressed in goblet cells and its expression is subject to TNF- $\alpha$  regulation. *Am J Physiol Gastrointest Liver Physiol.* 2016 Jan 15;310(2):G64–9.
253. Gahring LC, Carlson NG, Kulmer RA, Rogers SW. Neuronal Expression of Tumor Necrosis Factor Alpha in the OV0UJI fine Brain. *Neuroimmunomodulation.* 1996;3(5):289–303.

254. Artursson P, Karlsson J. Correlation between oral drug absorption in humans and apparent drug permeability coefficients in human intestinal epithelial (Caco-2) cells. *Biochem Biophys Res Commun*. 1991 Mar 29;175(3):880–5.
255. Meaney C, O'Driscoll C. Mucus as a barrier to the permeability of hydrophilic and lipophilic compounds in the absence and presence of sodium taurocholate micellar systems using cell culture models. *Eur J Pharm Sci*. 1999 Jul 1;8(3):167–75.
256. Al-Ghadban S, Kaissi S, Homaidan FR, Naim HY, El-Sabban ME. Cross-talk between intestinal epithelial cells and immune cells in inflammatory bowel disease. *Sci Rep*. 2016 Jul 15;6:29783.
257. Krishna G, Chen K, Lin C, Nomeir AA. Permeability of lipophilic compounds in drug discovery using in-vitro human absorption model, Caco-2. *Int J Pharm*. 2001 Jul 3;222(1):77–89.
258. Yu J, Peng S, Luo D, March JC. In vitro 3D human small intestinal villous model for drug permeability determination. *Biotechnol Bioeng*. 2012 Sep 1;109(9):2173–8.
259. Wang M, Cui C, Ibrahim MM, Han B, Li Q, Pacifici M, et al. Regulating Mechanotransduction in Three Dimensions using Sub-Cellular Scale, Crosslinkable Fibers of Controlled Diameter, Stiffness, and Alignment. *Adv Funct Mater*. 2019 May 1;29(18):1808967.
260. Elbediwy A, Vanyai H, Diaz-de-la-Loza M-C, Frith D, Snijders AP, Thompson BJ. Enigma proteins regulate YAP mechanotransduction. *J Cell Sci*. 2018 Nov 15;131(22):jcs221788.
261. Huch M, Koo B-K. Modeling mouse and human development using organoid cultures. *Development*. 2015 Sep 15;142(18):3113.
262. Derricott H, Luu L, Fong WY, Hartley CS, Johnston LJ, Armstrong SD, et al. Developing a 3D intestinal epithelium model for livestock species. *Cell Tissue Res*. 2019 Feb 1;375(2):409–24.
263. Onozato D, Yamashita M, Nakanishi A, Akagawa T, Kida Y, Ogawa I, et al. Generation of Intestinal Organoids Suitable for Pharmacokinetic Studies from Human Induced Pluripotent Stem Cells. *Drug Metab Dispos*. 2018 Nov 1;46(11):1572.
264. Sodek KL, Brown TJ, Ringuette MJ. Collagen I but not Matrigel matrices provide an MMP-dependent barrier to ovarian cancer cell penetration. *BMC Cancer*. 2008 Aug 5;8(1):223.
265. Fitsanakis VA, Piccola G, Aschner JL, Aschner M. Manganese transport by rat brain endothelial (RBE4) cell-based transwell model in the presence of astrocyte conditioned media. *J Neurosci Res*. 2005 Jul 15;81(2):235–43.
266. Bao Q, Hughes RC. Galectin-3 and polarized growth within collagen gels of wild-type and ricin-resistant MDCK renal epithelial cells. *Glycobiology*. 1999 May 1;9(5):489–95.
267. Vasse GF, Kühn PT, Zhou Q, Bhusari SA, Reker-Smit C, Melgert BN, et al. Collagen morphology influences macrophage shape and marker expression in vitro. *J Immunol Regen Med*. 2018 Mar 1;1:13–20.

268. Kim D, Eom S, Park SM, Hong H, Kim DS. A collagen gel-coated, aligned nanofiber membrane for enhanced endothelial barrier function. *Sci Rep*. 2019 Oct 17;9(1):14915.
269. Patient JD, Hajiali H, Harris K, Abrahamsson B, Tannergren C, White LJ, et al. Nanofibrous Scaffolds Support a 3D in vitro Permeability Model of the Human Intestinal Epithelium. *Front Pharmacol*. 2019;10:456.
270. Renier N, Wu Z, Simon DJ, Yang J, Ariel P, Tessier-Lavigne M. iDISCO: A Simple, Rapid Method to Immunolabel Large Tissue Samples for Volume Imaging. *Cell*. 2014 Nov 6;159(4):896–910.
271. Knight E, Murray B, Carnachan R, Przyborski S. Alvetex®: Polystyrene Scaffold Technology for Routine Three Dimensional Cell Culture. In: Haycock JW, editor. *3D Cell Culture: Methods and Protocols* [Internet]. Totowa, NJ: Humana Press; 2011. p. 323–40. Available from: [https://doi.org/10.1007/978-1-60761-984-0\\_20](https://doi.org/10.1007/978-1-60761-984-0_20)
272. Ugboide CI, Hirst WD, Rattray M. Astrocytes Grown in Alvetex® Three Dimensional Scaffolds Retain a Non-reactive Phenotype. *Neurochem Res*. 2016 Aug 1;41(8):1857–67.
273. Forrest OA, Ingersoll SA, Preininger MK, Laval J, Limoli DH, Brown MR, et al. Frontline Science: Pathological conditioning of human neutrophils recruited to the airway milieu in cystic fibrosis. *J Leukoc Biol*. 2018 Oct 1;104(4):665–75.
274. Costello L, Fullard N, Roger M, Bradbury S, Dicolandrea T, Isfort R, et al. Engineering a Multilayered Skin Equivalent: The Importance of Endogenous Extracellular Matrix Maturation to Provide Robustness and Reproducibility. In: Böttcher-Haberzeth S, Biedermann T, editors. *Skin Tissue Engineering: Methods and Protocols* [Internet]. New York, NY: Springer New York; 2019. p. 107–22. Available from: [https://doi.org/10.1007/978-1-4939-9473-1\\_9](https://doi.org/10.1007/978-1-4939-9473-1_9)
275. Marrazzo P, Maccari S, Taddei A, Bevan L, Telford J, Soriani M, et al. 3D Reconstruction of the Human Airway Mucosa In Vitro as an Experimental Model to Study NTHi Infections. *PLOS ONE*. 2016 Apr 21;11(4):e0153985.
276. Ruminski S, Kalaszczynska I, Dlugosz A, Lewandowska-Szumiel M. Osteogenic differentiation of human adipose-derived stem cells in 3D conditions - comparison of spheroids and polystyrene scaffolds. *Eur Cell Mater*. 2019 May 17;37:382–401.
277. Garreta E, Oria R, Tarantino C, Pla-Roca M, Prado P, Fernández-Avilés F, et al. Tissue engineering by decellularization and 3D bioprinting. *Mater Today*. 2017 May 1;20(4):166–78.
278. Rijal G, Li W. A versatile 3D tissue matrix scaffold system for tumor modeling and drug screening. *Sci Adv*. 2017 Sep 1;3(9):e1700764.
279. Porcelli L, Iacobazzi RM, Di Fonte R, Serrati S, Intini A, Solimando AG, et al. CAFs and TGF- $\beta$  Signaling Activation by Mast Cells Contribute to Resistance to Gemcitabine/Nabpaclitaxel in Pancreatic Cancer. *Cancers*. 2019 Mar 7;11(3):330.
280. Teijeiro-Valiño C, Novoa-Carballal R, Borrajo E, Vidal A, Alonso-Nocelo M, de la Fuente Freire M, et al. A multifunctional drug nanocarrier for efficient anticancer therapy. *J Controlled Release*. 2019 Jan 28;294:154–64.

281. Caragher S, Chalmers AJ, Gomez-Roman N. Glioblastoma's Next Top Model: Novel Culture Systems for Brain Cancer Radiotherapy Research. *Cancers*. 2019 Jan 4;11(1):44.
282. Zepecki JP, Snyder KM, Moreno MM, Fajardo E, Fiser A, Ness J, et al. Regulation of human glioma cell migration, tumor growth, and stemness gene expression using a Lck targeted inhibitor. *Oncogene*. 2019 Mar 1;38(10):1734–50.
283. Kim MH, Wu WH, Choi JH, Kim J, Jun JH, Ko Y, et al. Galectin-1 from conditioned medium of three-dimensional culture of adipose-derived stem cells accelerates migration and proliferation of human keratinocytes and fibroblasts. *Wound Repair Regen*. 2018 Dec 1;26(S1):S9–18.
284. Buchs R, Lehner B, Meuwly P, Schnyder B. Host–Pathogen Interaction Reconstituted in Three-Dimensional Cocultures of Mucosa and *Candida albicans*. *Tissue Eng Part C Methods*. 2018 Jun 14;24(7):412–7.
285. Norman JJ, Desai TA. Methods for Fabrication of Nanoscale Topography for Tissue Engineering Scaffolds. *Ann Biomed Eng*. 2006 Jan 1;34(1):89–101.
286. Salvay DM, Rives CB, Zhang X, Chen F, Kaufman DB, Lowe WL Jr, et al. Extracellular matrix protein-coated scaffolds promote the reversal of diabetes after extrahepatic islet transplantation. *Transplantation*. 2008 May 27;85(10):1456–64.
287. Yildirim ED, Besunder R, Pappas D, Allen F, Güçeri S, Sun W. Accelerated differentiation of osteoblast cells on polycaprolactone scaffolds driven by a combined effect of protein coating and plasma modification. *Biofabrication*. 2010 Mar 1;2(1):014109.
288. Chen Y, Lin Y, Davis KM, Wang Q, Rnjak-Kovacina J, Li C, et al. Robust bioengineered 3D functional human intestinal epithelium. *Sci Rep*. 2015 Sep 16;5:13708.
289. Susewind J, de Souza Carvalho-Wodarz C, Repnik U, Collnot E-M, Schneider-Daum N, Griffiths GW, et al. A 3D co-culture of three human cell lines to model the inflamed intestinal mucosa for safety testing of nanomaterials. *Nanotoxicology*. 2016 Jan 2;10(1):53–62.
290. Elamin E, Jonkers D, Juuti-Uusitalo K, van IJendoorn S, Troost F, Duimel H, et al. Effects of Ethanol and Acetaldehyde on Tight Junction Integrity: In Vitro Study in a Three Dimensional Intestinal Epithelial Cell Culture Model. *PLOS ONE*. 2012 Apr 19;7(4):e35008.
291. Kim SH, Chi M, Yi B, Kim SH, Oh S, Kim Y, et al. Three-dimensional intestinal villi epithelium enhances protection of human intestinal cells from bacterial infection by inducing mucin expression. *Integr Biol*. 2014 Sep 9;6(12):1122–31.
292. Bokhari MA, Akay G, Zhang S, Birch MA. The enhancement of osteoblast growth and differentiation in vitro on a peptide hydrogel—polyHIPE polymer hybrid material. *Biomaterials*. 2005 Sep 1;26(25):5198–208.
293. Audouin F, Heise A. Surface-initiated RAFT polymerization of NIPAM from monolithic macroporous polyHIPE. *Eur Polym J*. 2013 May 1;49(5):1073–9.

294. Hayward AS, Sano N, Przyborski SA, Cameron NR. Acrylic-Acid-Functionalized PolyHIPE Scaffolds for Use in 3D Cell Culture. *Macromol Rapid Commun.* 2013 Dec 1;34(23–24):1844–9.
295. Faralli A, Shekarforoush E, Ajalloueian F, Mendes AC, Chronakis IS. In vitro permeability enhancement of curcumin across Caco-2 cells monolayers using electrospun xanthan-chitosan nanofibers. *Carbohydr Polym.* 2019 Feb 15;206:38–47.
296. McMurtrey RJ. Analytic Models of Oxygen and Nutrient Diffusion, Metabolism Dynamics, and Architecture Optimization in Three-Dimensional Tissue Constructs with Applications and Insights in Cerebral Organoids. *Tissue Eng Part C Methods.* 2016 Mar;22(3):221–49.
297. Wills JW, Hondow N, Thomas AD, Chapman KE, Fish D, Maffei TG, et al. Genetic toxicity assessment of engineered nanoparticles using a 3D in vitro skin model (EpiDerm™). *Part Fibre Toxicol.* 2016 Sep 9;13(1):50–50.
298. Workman MJ, Gleeson JP, Troisi EJ, Estrada HQ, Kerns SJ, Hinojosa CD, et al. Enhanced Utilization of Induced Pluripotent Stem Cell-Derived Human Intestinal Organoids Using Microengineered Chips. *Cell Mol Gastroenterol Hepatol.* 2018 Jan 1;5(4):669–677.e2.
299. Bulut K, Pennartz C, Felderbauer P, Meier JJ, Banasch M, Bulut D, et al. Glucagon like peptide-2 induces intestinal restitution through VEGF release from subepithelial myofibroblasts. *Eur J Pharmacol.* 2008 Jan 14;578(2):279–85.
300. Raymond M, Marchbank T, Moyer MP, Playford RJ, Sanderson IR, Kruidenier L. IL-1 $\beta$  stimulation of CCD-18co myofibroblasts enhances repair of epithelial monolayers through Wnt-5a. *Am J Physiol-Gastrointest Liver Physiol.* 2012 Sep 13;303(11):G1270–8.
301. Sams A, Hastrup S, Andersen M, Thim L. Naturally occurring glucagon-like peptide-2 (GLP-2) receptors in human intestinal cell lines. *Eur J Pharmacol.* 2006 Feb 17;532(1):18–23.
302. Hughes CS, Postovit LM, Lajoie GA. Matrigel: A complex protein mixture required for optimal growth of cell culture. *PROTEOMICS.* 2010 May 1;10(9):1886–90.
303. Nallanthighal S, Heiserman JP, Cheon D-J. The Role of the Extracellular Matrix in Cancer Stemness. *Front Cell Dev Biol.* 2019;7:86.
304. Delon LC, Guo Z, Oszmiana A, Chien C-C, Gibson R, Prestidge C, et al. A systematic investigation of the effect of the fluid shear stress on Caco-2 cells towards the optimization of epithelial organ-on-chip models. *Biomaterials.* 2019 Dec 1;225:119521.
305. Hsieh C-T, Hsu S. Double-Network Polyurethane-Gelatin Hydrogel with Tunable Modulus for High-Resolution 3D Bioprinting. *ACS Appl Mater Interfaces.* 2019 Sep 11;11(36):32746–57.
306. Patuzzo S, Goracci G, Gasperini L, Ciliberti R. 3D Bioprinting Technology: Scientific Aspects and Ethical Issues. *Sci Eng Ethics.* 2018 Apr 1;24(2):335–48.

307. Sato T, Stange DE, Ferrante M, Vries RGJ, van Es JH, van den Brink S, et al. Long-term Expansion of Epithelial Organoids From Human Colon, Adenoma, Adenocarcinoma, and Barrett's Epithelium. *Gastroenterology*. 2011 Nov 1;141(5):1762–72.
308. Wang Y, Kim R, Gunasekara DB, Reed MI, DiSalvo M, Nguyen DL, et al. Formation of Human Colonic Crypt Array by Application of Chemical Gradients Across a Shaped Epithelial Monolayer. *Cell Mol Gastroenterol Hepatol*. 2018 Jan 1;5(2):113–30.
309. Troutman MD, Thakker DR. Rhodamine 123 Requires Carrier-Mediated Influx for Its Activity as a P-Glycoprotein Substrate in Caco-2 Cells. *Pharm Res*. 2003 Aug 1;20(8):1192–9.
310. Hirsch-Ernst KI, Ziemann C, Rustenbeck I, Kahl GF. Inhibitors of mdr1-dependent transport activity delay accumulation of the mdr1 substrate rhodamine 123 in primary rat hepatocyte cultures. *Toxicology*. 2001 Oct 5;167(1):47–57.
311. Yumoto R, Murakami T, Nakamoto Y, Hasegawa R, Nagai J, Takano M. Transport of Rhodamine 123, a P-Glycoprotein Substrate, across Rat Intestine and Caco-2 Cell Monolayers in the Presence of Cytochrome P-450 3A-Related Compounds. *J Pharmacol Exp Ther*. 1999 Apr 1;289(1):149–55.
312. Tan H-Y, Trier S, Rahbek UL, Dufva M, Kutter JP, Andresen TL. A multi-chamber microfluidic intestinal barrier model using Caco-2 cells for drug transport studies. *PLOS ONE*. 2018 May 10;13(5):e0197101.
313. Chen X, Slättengren T, de Lange ECM, Smith DE, Hammarlund-Udenaes M. Revisiting atenolol as a low passive permeability marker. *Fluids Barriers CNS*. 2017 Oct 31;14(1):30.
314. Teksin ZS, Seo PR, Polli JE. Comparison of drug permeabilities and BCS classification: three lipid-component PAMPA system method versus Caco-2 monolayers. *AAPS J*. 2010 Jun;12(2):238–41.
315. Mimura Y, Yasujima T, Ohta K, Inoue K, Yuasa H. Functional identification of organic cation transporter 1 as an atenolol transporter sensitive to flavonoids. *Biochem Biophys Rep*. 2015 Jul 1;2:166–71.
316. The International Transporter Consortium, Giacomini KM, Huang S-M, Tweedie DJ, Benet LZ, Brouwer KLR, et al. Membrane transporters in drug development. *Nat Rev Drug Discov*. 2010 Mar 1;9:215.
317. Kong L, Song C, Ye L, Xu J, Guo D, Shi Q. The effect of lycopene on cytochrome P450 isoenzymes and P-glycoprotein by using human liver microsomes and Caco-2 cell monolayer model. *Int J Food Sci Nutr*. 2018 Oct 3;69(7):835–41.
318. Lu C, Fu K, Cao K, Wei J, Zhou J, Zhao D, et al. Permeability and transport mechanism of trihexyphenidyl hydrochloride in Caco-2 cell monolayer model with a validated UPLC-MS/MS method. *J Pharm Biomed Anal*. 2019 Oct 21;112924.
319. Katneni K, Pham T, Saunders J, Chen G, Patil R, White KL, et al. Using Human Plasma as an Assay Medium in Caco-2 Studies Improves Mass Balance for Lipophilic Compounds. *Pharm Res*. 2018 Sep 17;35(11):210.

320. Zheng Y, Benet LZ, Okochi H, Chen X. pH Dependent but not P-gp Dependent Bidirectional Transport Study of S-propranolol: The Importance of Passive Diffusion. *Pharm Res.* 2015 Aug;32(8):2516–26.
321. Thomae AV, Wunderli-Allenspach H, Krämer SD. Permeation of Aromatic Carboxylic Acids across Lipid Bilayers: The pH-Partition Hypothesis Revisited. *Biophys J.* 2005 Sep 1;89(3):1802–11.
322. Avdeef A, Kansy M, Bendels S, Tsinman K. Absorption-excipient-pH classification gradient maps: Sparingly soluble drugs and the pH partition hypothesis. *Eur J Pharm Sci.* 2008 Jan 1;33(1):29–41.
323. Shore PA, Brodie BB, Hogben CAM. THE GASTRIC SECRETION OF DRUGS: A pH PARTITION HYPOTHESIS. *J Pharmacol Exp Ther.* 1957 Mar 1;119(3):361.
324. Hickman RJS, Neill J. Influence of pH on Drug Absorption from the Gastrointestinal Tract: A Simple Chemical Model. *J Chem Educ.* 1997 Jul 1;74(7):855.
325. Jedlitschky G, Hoffmann U, Kroemer HK. Structure and function of the MRP2 (ABCC2) protein and its role in drug disposition. *Expert Opin Drug Metab Toxicol.* 2006 Jun 1;2(3):351–66.
326. S G Creemers, P M van Koetsveld, W W De Herder, F Dogan, G J H Franssen, R A Feelders, et al. MDR1 inhibition increases sensitivity to doxorubicin and etoposide in adrenocortical cancer. *Endocr Relat Cancer.* 2019;26(3):367–78.
327. Obuchi W, Ohtsuki S, Uchida Y, Ohmine K, Yamori T, Terasaki T. Identification of Transporters Associated with Etoposide Sensitivity of Stomach Cancer Cell Lines and Methotrexate Sensitivity of Breast Cancer Cell Lines by Quantitative Targeted Absolute Proteomics. *Mol Pharmacol.* 2013 Feb 1;83(2):490.
328. Liang Y, Li S, Chen L. The physiological role of drug transporters. *Protein Cell.* 2015 May 1;6(5):334–50.
329. Takenaka T, Harada N, Kuze J, Chiba M, Iwao T, Matsunaga T. Application of a Human Intestinal Epithelial Cell Monolayer to the Prediction of Oral Drug Absorption in Humans as a Superior Alternative to the Caco-2 Cell Monolayer. *J Pharm Sci.* 2016 Feb 1;105(2):915–24.
330. Khan ZA, Tripathi R, Mishra B. Methotrexate: a detailed review on drug delivery and clinical aspects. *Expert Opin Drug Deliv.* 2012 Feb 1;9(2):151–69.
331. Yee SW, Gong L, Badagnani I, Giacomini KM, Klein TE, Altman RB. SLC19A1 pharmacogenomics summary. *Pharmacogenet Genomics.* 2010 Nov;20(11):708–15.
332. Visentin M, Diop-Bove N, Zhao R, Goldman ID. The intestinal absorption of folates. *Annu Rev Physiol.* 2014;76:251–74.
333. Breedveld P, Zelcer N, Pluim D, Sönmezer Ö, Tibben MM, Beijnen JH, et al. Mechanism of the Pharmacokinetic Interaction between Methotrexate and Benzimidazoles. *Cancer Res.* 2004 Aug 15;64(16):5804.



334. Maeda T, Miyazono Y, Ito K, Hamada K, Sekine S, Horie T. Oxidative stress and enhanced paracellular permeability in the small intestine of methotrexate-treated rats. *Cancer Chemother Pharmacol*. 2010 May 1;65(6):1117–23.
335. Beutheu Youmba S, Belmonte L, Galas L, Boukhettala N, Bôle-Feysot C, Déchelotte P, et al. Methotrexate Modulates Tight Junctions Through NF- $\kappa$ B, MEK, and JNK Pathways. *J Pediatr Gastroenterol Nutr* [Internet]. 2012;54(4). Available from: [https://journals.lww.com/jpgn/Fulltext/2012/04000/Methotrexate\\_Modulates\\_Tight\\_Junctions\\_Through.6.aspx](https://journals.lww.com/jpgn/Fulltext/2012/04000/Methotrexate_Modulates_Tight_Junctions_Through.6.aspx)
336. Antonescu IE, Rasmussen KF, Neuhoﬀ S, Fretté X, Karlgren M, Bergström CAS, et al. The Permeation of Acamprosate Is Predominantly Caused by Paracellular Diffusion across Caco-2 Cell Monolayers: A Paracellular Modeling Approach. *Mol Pharm*. 2019 Nov 4;16(11):4636–50.
337. Saez-Tenorio M, Domenech J, García-Rodríguez A, Velázquez A, Hernández A, Marcos R, et al. Assessing the relevance of exposure time in differentiated Caco-2/HT29 cocultures. Effects of silver nanoparticles. *Food Chem Toxicol*. 2019 Jan 1;123:258–67.
338. Altay G, Larrañaga E, Tosi S, Barriga FM, Batlle E, Fernández-Majada V, et al. Self-organized intestinal epithelial monolayers in crypt and villus-like domains show effective barrier function. *Sci Rep*. 2019 Jul 12;9(1):10140.
339. Noben M, Vanhove W, Arnauts K, Santo Ramalho A, Van Assche G, Vermeire S, et al. Human intestinal epithelium in a dish: Current models for research into gastrointestinal pathophysiology. *United Eur Gastroenterol J*. 2017 Jul 21;5(8):1073–81.
340. Sjöberg Å, Lutz M, Tannergren C, Wingolf C, Borde A, Ungell A-L. Comprehensive study on regional human intestinal permeability and prediction of fraction absorbed of drugs using the Ussing chamber technique. *Eur J Pharm Sci*. 2013 Jan 23;48(1):166–80.
341. Takenaka T, Harada N, Kuze J, Chiba M, Iwao T, Matsunaga T. Human Small Intestinal Epithelial Cells Differentiated from Adult Intestinal Stem Cells as a Novel System for Predicting Oral Drug Absorption in Humans. *Drug Metab Dispos*. 2014 Nov 1;42(11):1947.
342. Balimane PV, Chong S. Cell culture-based models for intestinal permeability: A critique. *Drug Discov Today*. 2005 Mar 1;10(5):335–43.
343. Roberts DW, Newton RA, Beaumont KA, Helen Leonard J, Sturm RA. Quantitative analysis of MC1R gene expression in human skin cell cultures. *Pigment Cell Res*. 2006 Feb 1;19(1):76–89.
344. Roos C, Dahlgren D, Sjögren E, Tannergren C, Abrahamsson B, Lennernäs H. Regional Intestinal Permeability in Rats: A Comparison of Methods. *Mol Pharm*. 2017 Dec 4;14(12):4252–61.
345. Rozehnal V, Nakai D, Hoepner U, Fischer T, Kamiyama E, Takahashi M, et al. Human small intestinal and colonic tissue mounted in the Ussing chamber as a tool for characterizing the intestinal absorption of drugs. *Eur J Pharm Sci*. 2012 Aug 15;46(5):367–73.

346. Arnold YE, Thorens J, Bernard S, Kalia YN. Drug Transport across Porcine Intestine Using an Ussing Chamber System: Regional Differences and the Effect of P-Glycoprotein and CYP3A4 Activity on Drug Absorption. *Pharmaceutics*. 2019 Mar 21;11(3):139.
347. Blackburn JG, Hazen-Martin DJ, Detrisac CJ, Sens DA. Electrophysiology and ultrastructure of cultured human proximal tubule cells. *Kidney Int*. 1988 Feb 1;33(2):508–16.
348. DiMarco RL, Hunt DR, Dewi RE, Heilshorn SC. Improvement of paracellular transport in the Caco-2 drug screening model using protein-engineered substrates. *Biomaterials*. 2017 Jun;129:152–62.
349. Torreele E, Bourdin Trunz B, Tweats D, Kaiser M, Brun R, Mazué G, et al. Fexinidazole – A New Oral Nitroimidazole Drug Candidate Entering Clinical Development for the Treatment of Sleeping Sickness. *PLoS Negl Trop Dis*. 2010 Dec 21;4(12):e923.
350. Aungst BJ, Nguyen NH, Bulgarelli JP, Oates-Lenz K. The Influence of Donor and Reservoir Additives on Caco-2 Permeability and Secretory Transport of HIV Protease Inhibitors and Other Lipophilic Compounds. *Pharm Res*. 2000 Oct 1;17(10):1175–80.
351. Sumsakul W, Na-Bangchang K. Permeability of plumbagin across human intestinal cell in vitro. *Arch Pharm Res*. 2016 Mar 1;39(3):380–9.
352. Culot M, Lundquist S, Vanuxeem D, Nion S, Landry C, Delplace Y, et al. An in vitro blood-brain barrier model for high throughput (HTS) toxicological screening. *Toxicol In Vitro*. 2008 Apr 1;22(3):799–811.
353. Dahlgren D, Roos C, Lundqvist A, Abrahamsson B, Tannergren C, Hellström PM, et al. Regional Intestinal Permeability of Three Model Drugs in Human. *Mol Pharm*. 2016 Sep 6;13(9):3013–21.
354. Da Silva LC, Da Silva TL, Antunes AH, Rezende KR. A Sensitive Medium-Throughput Method to Predict Intestinal Absorption in Humans Using Rat Intestinal Tissue Segments. *J Pharm Sci*. 2015 Sep 1;104(9):2807–12.
355. Yu J, Li N, Lin P, Li Y, Mao X, Bao G, et al. Intestinal transportations of main chemical compositions of *polygoni multiflori radix* in caco-2 cell model. *Evid-Based Complement Altern Med ECAM*. 2014;2014:483641–483641.
356. Volpe DA. Application of method suitability for drug permeability classification. *AAPS J*. 2010 Dec;12(4):670–8.
357. Hou TJ, Zhang W, Xia K, Qiao XB, Xu XJ. ADME Evaluation in Drug Discovery. 5. Correlation of Caco-2 Permeation with Simple Molecular Properties. *J Chem Inf Comput Sci*. 2004 Sep 1;44(5):1585–600.
358. Yee S. In Vitro Permeability Across Caco-2 Cells (Colonic) Can Predict In Vivo (Small Intestinal) Absorption in Man—Fact or Myth. *Pharm Res*. 1997 Jun 1;14(6):763–6.
359. Stockdale TP, Challinor VL, Lehmann RP, De Voss JJ, Blanchfield JT. Caco-2 Monolayer Permeability and Stability of Chamaelirium luteum (False Unicorn) Open-Chain Steroidal Saponins. *ACS Omega*. 2019 Apr 30;4(4):7658–66.

360. McAinsh J, Cruickshank JM. Beta-blockers and central nervous system side effects. *Pharmacol Ther.* 1990 Jan 1;46(2):163–97.
361. Balimane PV, Patel K, Marino A, Chong S. Utility of 96 well Caco-2 cell system for increased throughput of P-gp screening in drug discovery. *Eur J Pharm Biopharm.* 2004 Jul 1;58(1):99–105.
362. Sakai M, Noach ABJ, Blom-Roosemalen MCM, De Boer AG, Breimer DD. Absorption enhancement of hydrophilic compounds by verapamil in Caco-2 cell monolayers. *Biochem Pharmacol.* 1994 Sep 15;48(6):1199–210.
363. Yao H, Wang C, Lu W, Li W, Jing W, Zhang J, et al. Comparative pharmacokinetics of verapamil and norverapamil in normal and ulcerative colitis rats after oral administration of low and high dose verapamil by UPLC-MS/MS. *Xenobiotica.* 2019 Oct 21;1–9.
364. Shirasaka Y, Kawasaki M, Sakane T, Omatsu H, Moriya Y, Nakamura T, et al. Induction of Human P-Glycoprotein in Caco-2 cells: Development of a Highly Sensitive Assay System for P-Glycoprotein-Mediated Drug Transport. *Drug Metab Pharmacokinet.* 2006 Jan 1;21(5):414–23.
365. Anderle P, Niederer E, Rubas W, Hilgendorf C, Spahn-Langguth H, Wunderli-Allenspach H, et al. P-Glycoprotein (P-gp) Mediated Efflux in Caco-2 Cell Monolayers: The Influence of Culturing Conditions and Drug Exposure on P-gp Expression Levels. *J Pharm Sci.* 1998 Jun 1;87(6):757–62.
366. Awad A, Trenfield SJ, Goyanes A, Gaisford S, Basit AW. Reshaping drug development using 3D printing. *Drug Discov Today.* 2018 Aug 1;23(8):1547–55.
367. Gouglas D, Thanh Le T, Henderson K, Kaloudis A, Danielsen T, Hammersland NC, et al. Estimating the cost of vaccine development against epidemic infectious diseases: a cost minimisation study. *Lancet Glob Health.* 2018 Dec 1;6(12):e1386–96.
368. Ronaldson-Bouchard K, Vunjak-Novakovic G. Organs-on-a-Chip: A Fast Track for Engineered Human Tissues in Drug Development. *Cell Stem Cell.* 2018 Mar 1;22(3):310–24.
369. Trenfield SJ, Awad A, Goyanes A, Gaisford S, Basit AW. 3D Printing Pharmaceuticals: Drug Development to Frontline Care. *Trends Pharmacol Sci.* 2018 May 1;39(5):440–51.
370. Cummings J, Reiber C, Kumar P. The price of progress: Funding and financing Alzheimer's disease drug development. *Alzheimers Dement Transl Res Clin Interv.* 2018 Jan 1;4:330–43.
371. Roh TT, Chen Y, Paul HT, Guo C, Kaplan DL. 3D bioengineered tissue model of the large intestine to study inflammatory bowel disease. *Biomaterials.* 2019 Dec 1;225:119517.
372. Shaban L, Chen Y, Fasciano AC, Lin Y, Kaplan DL, Kumamoto CA, et al. A 3D intestinal tissue model supports *Clostridioides difficile* germination, colonization, toxin production and epithelial damage. *Anaerobe.* 2018 Apr 1;50:85–92.
373. Yin Y-B, de Jonge HR, Wu X, Yin Y-L. Enteroids for Nutritional Studies. *Mol Nutr Food Res.* 2019 Aug 1;63(16):1801143.

374. Hsia L, Ashley N, Ouaret D, Wang LM, Wilding J, Bodmer WF. Myofibroblasts are distinguished from activated skin fibroblasts by the expression of AOC3 and other associated markers. *Proc Natl Acad Sci*. 2016 Apr 12;113(15):E2162.
375. Cui T, Theuns S, Desmarests LMB, Xie J, De Gryse GMA, Yang B, et al. Establishment of porcine enterocyte/myofibroblast co-cultures for the growth of porcine rota- and coronaviruses. *Sci Rep*. 2018 Oct 12;8(1):15195.
376. Venter C, Niesler C. A triple co-culture method to investigate the effect of macrophages and fibroblasts on myoblast proliferation and migration. *BioTechniques*. 2018 Feb 1;64(2):52–8.
377. Ishikawa S, Ishimori K, Ito S. A 3D epithelial–mesenchymal co-culture model of human bronchial tissue recapitulates multiple features of airway tissue remodeling by TGF- $\beta$ 1 treatment. *Respir Res*. 2017 Nov 22;18(1):195.
378. Lorke DE, Krüger M, Buchert R, Bohuslavizki KH, Clausen M, Schumacher U. In Vitro and In Vivo Tracer Characteristics of an Established Multidrug-Resistant Human Colon Cancer Cell Line. *J Nucl Med*. 2001 Apr 1;42(4):646–54.
379. Akiyama J, Okamoto R, Iwasaki M, Zheng X, Yui S, Tsuchiya K, et al. Delta-like 1 expression promotes goblet cell differentiation in Notch-inactivated human colonic epithelial cells. *Biochem Biophys Res Commun*. 2010 Mar 19;393(4):662–7.
380. Lo Y-H, Chung E, Li Z, Wan Y-W, Mahe MM, Chen M-S, et al. Transcriptional Regulation by ATOH1 and its Target SPDEF in the Intestine. *Cell Mol Gastroenterol Hepatol*. 2016 Oct 21;3(1):51–71.
381. Katz JP, Perreault N, Goldstein BG, Lee CS, Labosky PA, Yang VW, et al. The zinc-finger transcription factor Klf4 is required for terminal differentiation of goblet cells in the colon. *Development*. 2002 Jun 1;129(11):2619.
382. Jani M, Ambrus C, Magnan R, Jakab KT, Beéry E, Zolnerciks JK, et al. Structure and function of BCRP, a broad specificity transporter of xenobiotics and endobiotics. *Arch Toxicol*. 2014 Jun 1;88(6):1205–48.
383. Versantvoort CH., Ondrewater RC., Duizer E, Van de Sandt JJ., Gilde AJ, Groten JP. Monolayers of IEC-18 cells as an in vitro model for screening the passive transcellular and paracellular transport across the intestinal barrier: comparison of active and passive transport with the human colon carcinoma Caco-2 cell line. *Environ Toxicol Pharmacol*. 2002 Jul 1;11(3):335–44.
384. Llamas S, García-Pérez E, Meana Á, Larcher F, del Río M. Feeder Layer Cell Actions and Applications. *Tissue Eng Part B Rev*. 2015 Aug;21(4):345–53.
385. Doyle LA, Yang W, Abruzzo LV, Krogmann T, Gao Y, Rishi AK, et al. A multidrug resistance transporter from human MCF-7 breast cancer cells. *Proc Natl Acad Sci U S A*. 1998 Dec 22;95(26):15665–70.
386. Teresi ME, Crom WR, Choi KE, Mirro J, Evans WE. Methotrexate bioavailability after oral and intramuscular administration in children. *J Pediatr*. 1987 May 1;110(5):788–92.

387. Yokooji T, Yumoto R, Nagai J, Takano M, Yokooji T, Murakami T. Role of intestinal efflux transporters in the intestinal absorption of methotrexate in rats. *J Pharm Pharmacol*. 2007 Sep 1;59(9):1263–70.
388. Akhtar N, Talegaonkar S, Ahad A, Khar RK, Jaggi M. Potential of a novel self nanoemulsifying carrier system to overcome P-glycoprotein mediated efflux of etoposide: In vitro and ex vivo investigations. *J Drug Deliv Sci Technol*. 2015 Aug 1;28:18–27.
389. Borst P, Evers R, Kool M, Wijnholds J. A Family of Drug Transporters: the Multidrug Resistance-Associated Proteins. *JNCI J Natl Cancer Inst*. 2000 Aug 16;92(16):1295–302.
390. Roy U, Barber P, Tse Dinh Y ching, Batrakova E, Mondal D, Nair M. Role of MRP transporters in regulating antimicrobial drug inefficacy and oxidative stress-induced pathogenesis during HIV-1 and TB infections. *Front Microbiol*. 2015;6:948.
391. Kell DB, Dobson PD, Oliver SG. Pharmaceutical drug transport: the issues and the implications that it is essentially carrier-mediated only. *Drug Discov Today*. 2011 Aug 1;16(15):704–14.
392. Hilgers AR, Conradi RA, Burton PS. Caco-2 Cell Monolayers as a Model for Drug Transport Across the Intestinal Mucosa. *Pharm Res*. 1990 Sep 1;7(9):902–10.
393. Kaldas MI, Walle UK, Walle T. Resveratrol transport and metabolism by human intestinal Caco-2 cells. *J Pharm Pharmacol*. 2003 Mar 1;55(3):307–12.
394. Dugardin C, Briand O, Touche V, Schonewille M, Moreau F, Le May C, et al. Retrograde cholesterol transport in the human Caco-2/TC7 cell line: a model to study trans-intestinal cholesterol excretion in atherogenic and diabetic dyslipidemia. *Acta Diabetol*. 2017 Feb 1;54(2):191–9.

## 9. Appendix and supplementary information.

### 9.1 Negative control images

#### 9.1.1 Fibroblast negative controls for 2D immunostained samples

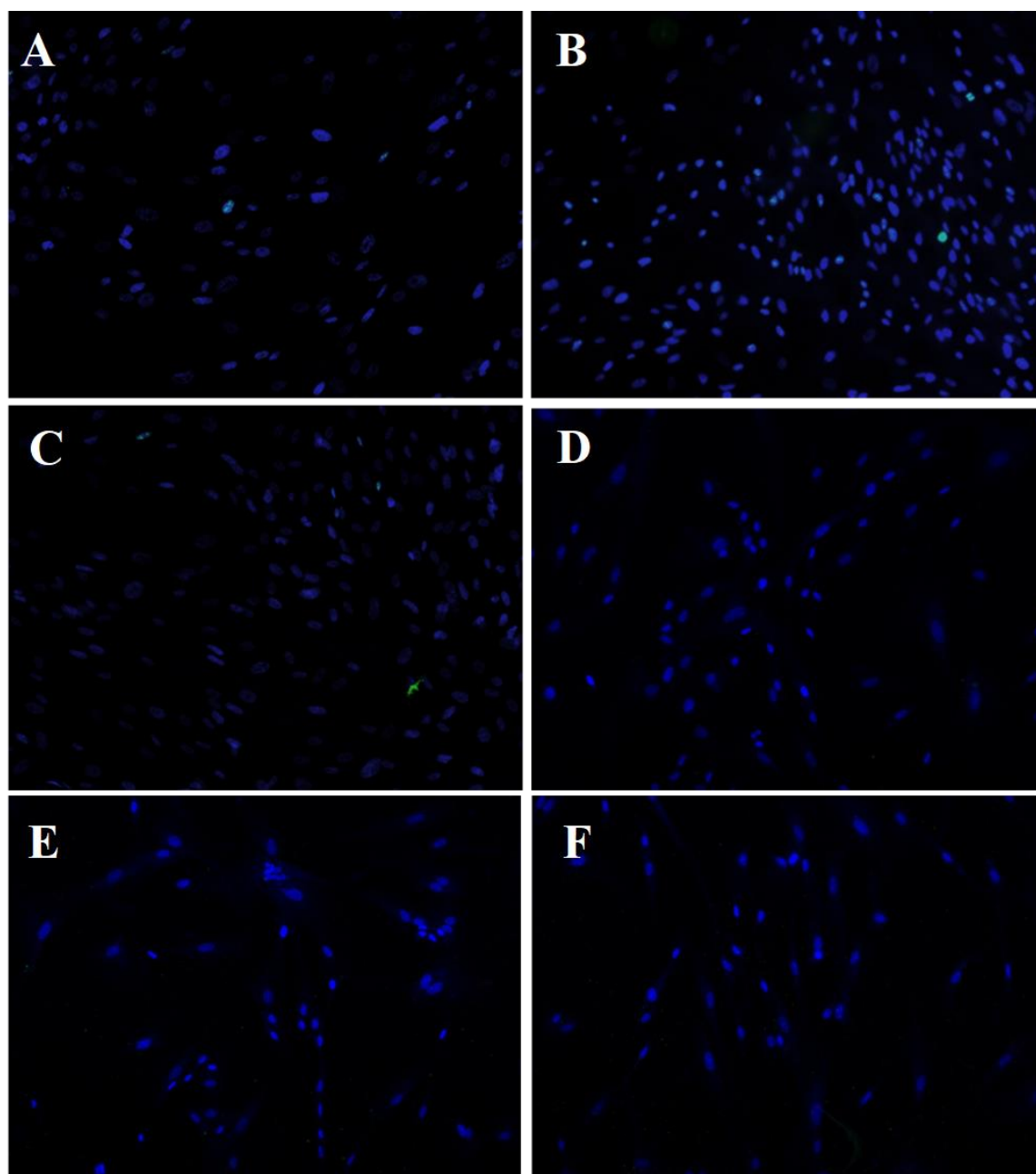


**Figure S1: Negative control images for 2D fibroblast cell lines – A-B) CCD-18co, mouse and rabbit respectively C-D) HDFn, mouse and rabbit respectively E-F) HIC, mouse and rabbit respectively. 2D fibroblast negative controls relate to Figure 3.3. Images representative of multiple observations**

### 9.1.2 Epithelial lineage negative controls for 2D immunostained samples.

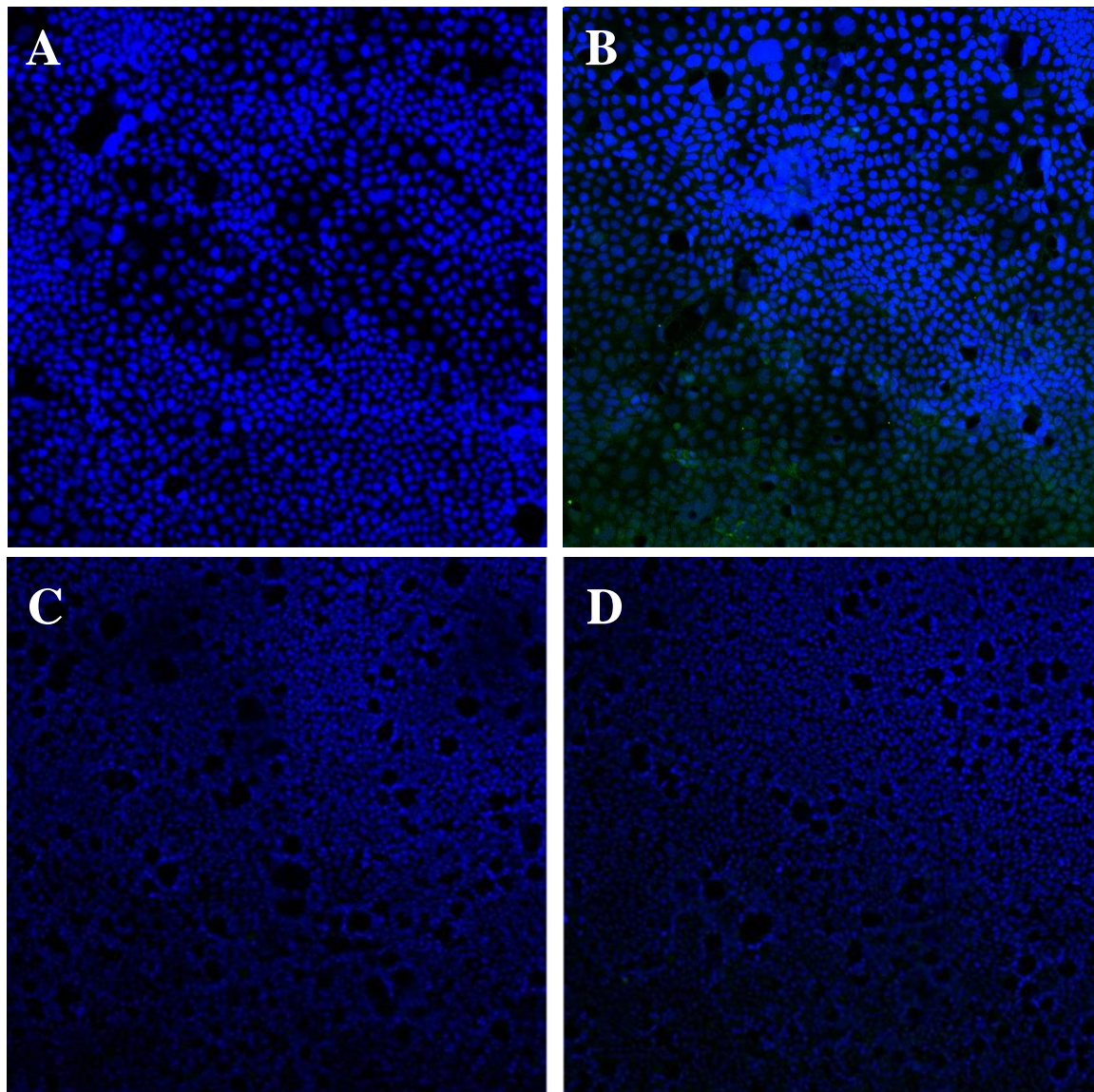


**Figure S2: Negative control images for 2D Epithelial** – A-B) Caco-2 mouse and rabbit negative control respectively. C-D) HT29-MTX mouse and rabbit negative control respectively. Images represent negative controls for Figures 3.4-7, 3.12 & 3.26. Staining and imaging seen in aforementioned figures was all done concurrently.



### 9.1.3 Caco-2 Transwell negative controls

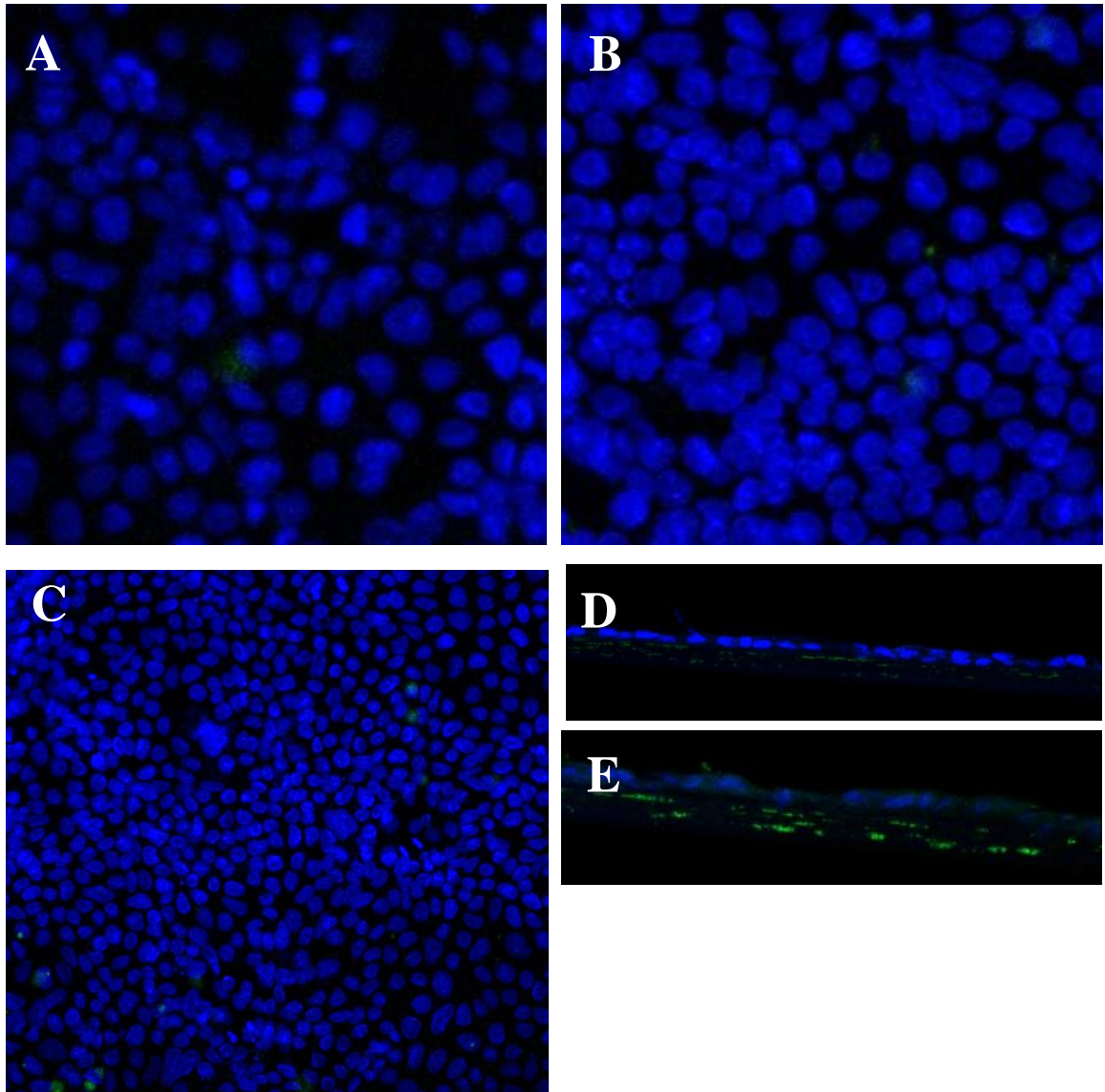


**Figure S3: Negative control images for wholemount and transverse Caco-2 Transwell models** – A) Caco-2 control, relating to Figures 3.13. B) Caco-2/ CCD-18co treated, relating to figure 3.14, C) Caco-2/ KGF (25ng/ml) treated relating to figures 3.20-23, D) Transverse Caco-2 Transwell section relating to Figure 3.13. E) Transverse Caco-2/ CCD-18co Transwell section relating to Figure 3.14. All staining in these figures utilised primary antibodies of mouse origin and were processed concurrently.



### 9.1.4 Caco-2 and HT29-MTX Transwell controls

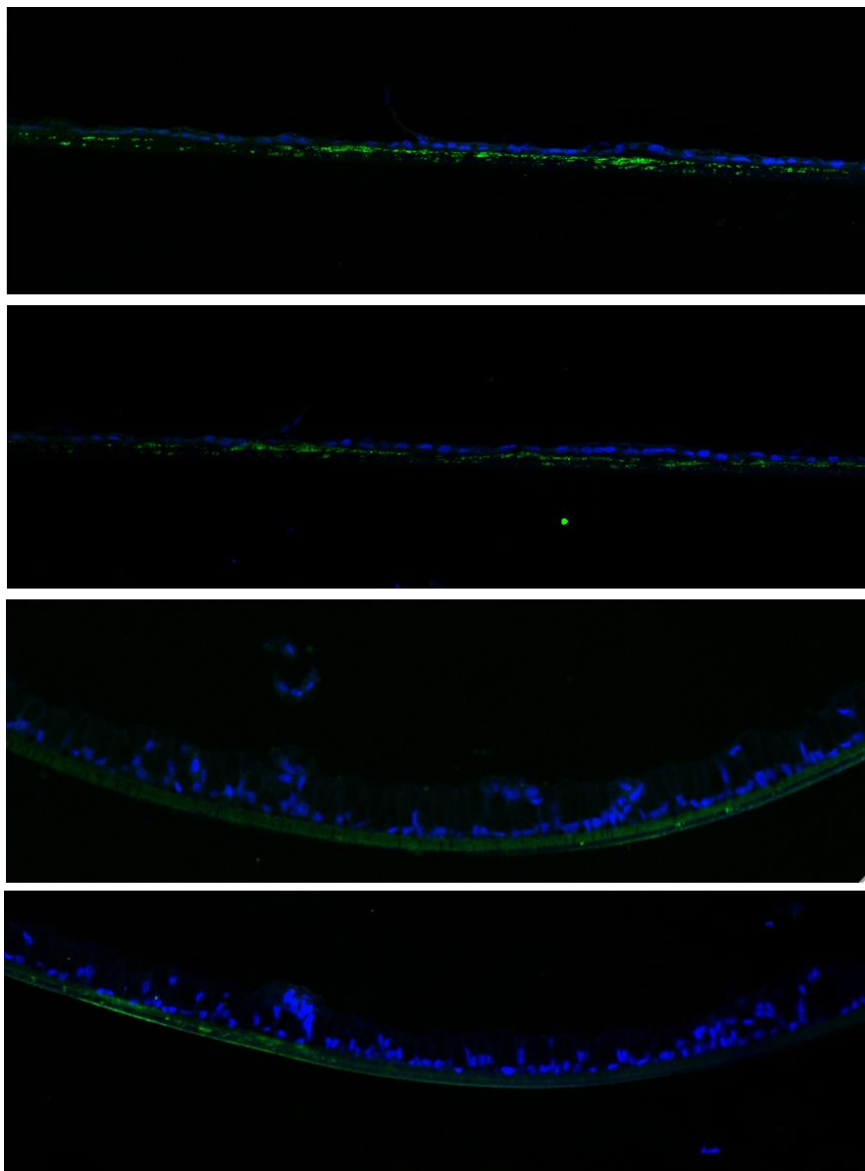


**Figure S4: Negative control images for Sectioned Transwell models containing Caco-2 and HT29-MTX – A,B) Caco-2 Transwell models, Control and CCD-18co treated respectively C,D) HT29-MTX Transwell models, Control and CCD-18co treated respectively. Images representative of multiple observations. Controls relate to Figure 4.11. E-cadherin antibody was of mouse origin.**

### 9.1.5 3D model negative controls

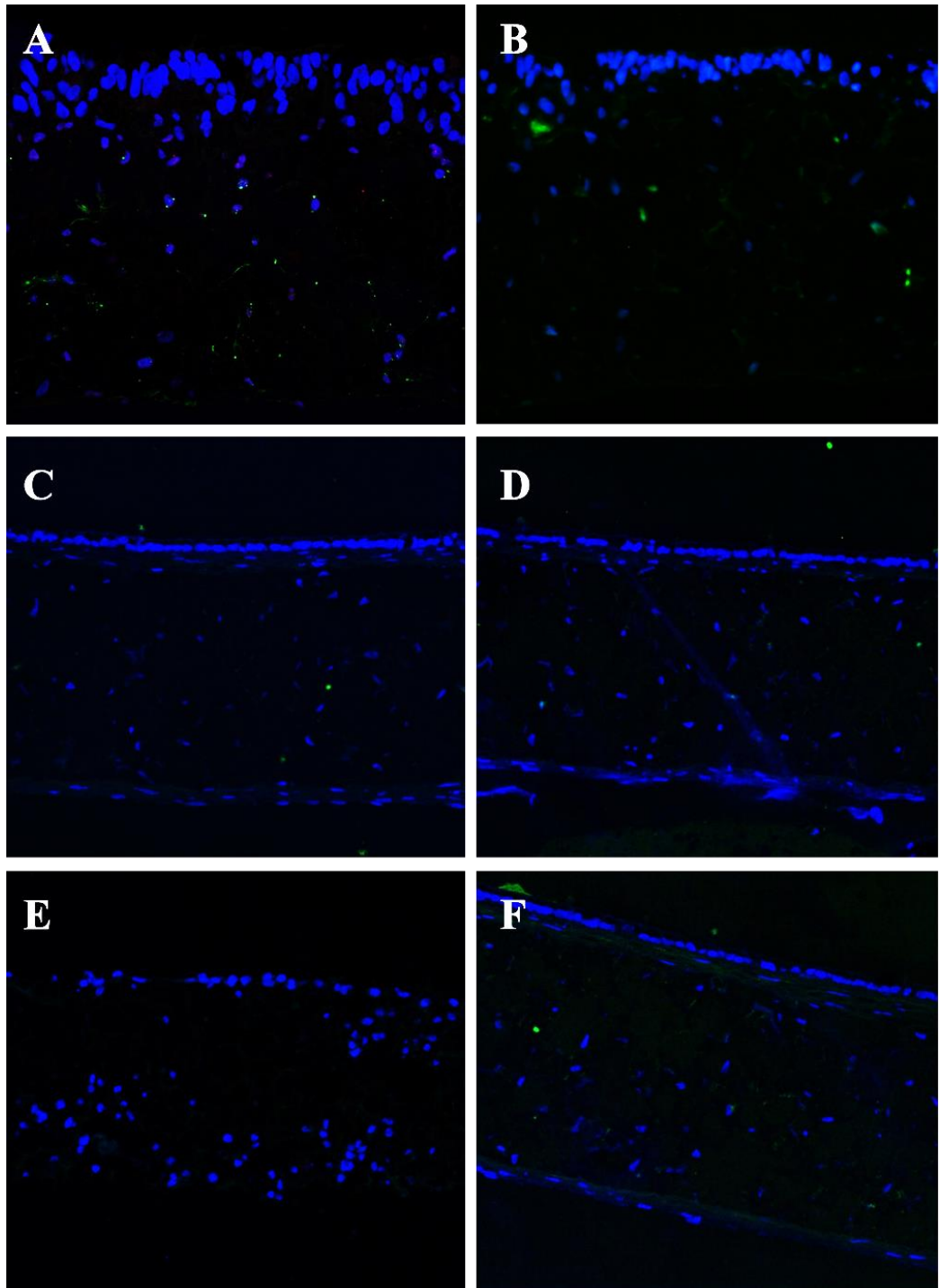


**Figure S5: Negative control images for Sectioned 3D models** – A,B) CCD-18co 3D models, mouse and rabbit secondary antibody respectively C,D) HDFn 3D models, mouse and rabbit secondary antibody respectively E,F) HIC 3D models, mouse and rabbit secondary antibody respectively. Images representative of multiple observations

### 9.1.6 Human tissue negative controls

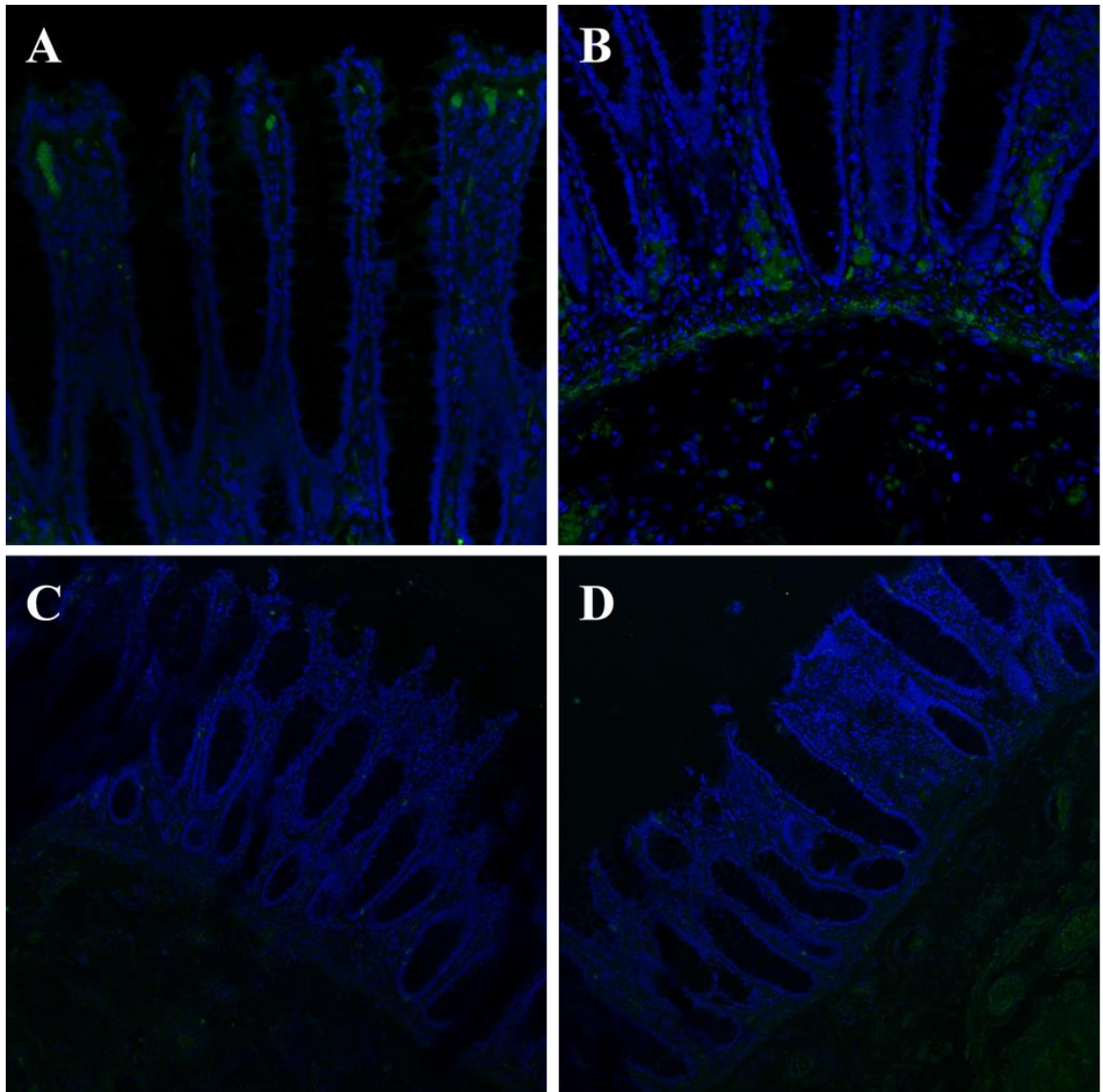


**Figure S6: Negative control images for human tissues** – A,B) Small intestine mouse and rabbit secondary antibody respectively, C,D) Colon mouse and rabbit secondary antibody respectively Relating to Figures 5.22-27. Images are representative of multiple observations.

## 9.2 Intrinsic permeability of different Alvetex formats

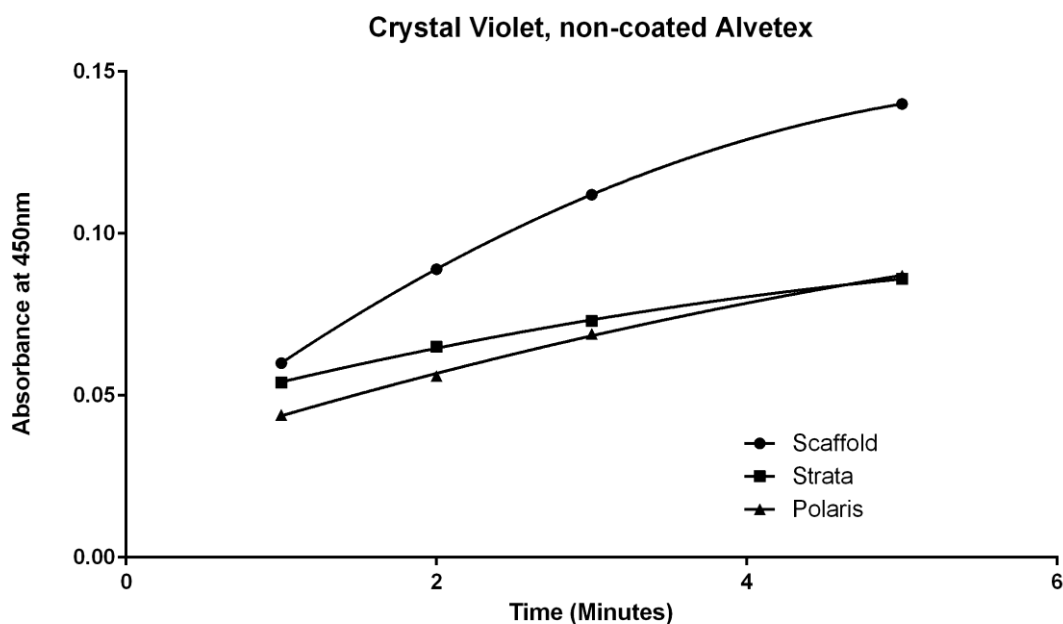


**Figure S7: Preliminary data for the intrinsic permeability of different Alvetex formats to Crystal Violet dye** – Crystal Violet was added to the apical compartment of a permeability chamber. Samples were taken at 30 second intervals and absorbance was measured at 450nm. N=1, n=1

## 9.3 PCR Primer optimisation

All primers utilised in the quantitative RT-PCR seen in this study were taken from pre-established, published peer-reviewed materials. Therefore, all primer utilised here should have high degrees of target specificity efficiency. In order to check the validity of the sources from which primers were gained a select number of primers were chosen for further analysis.

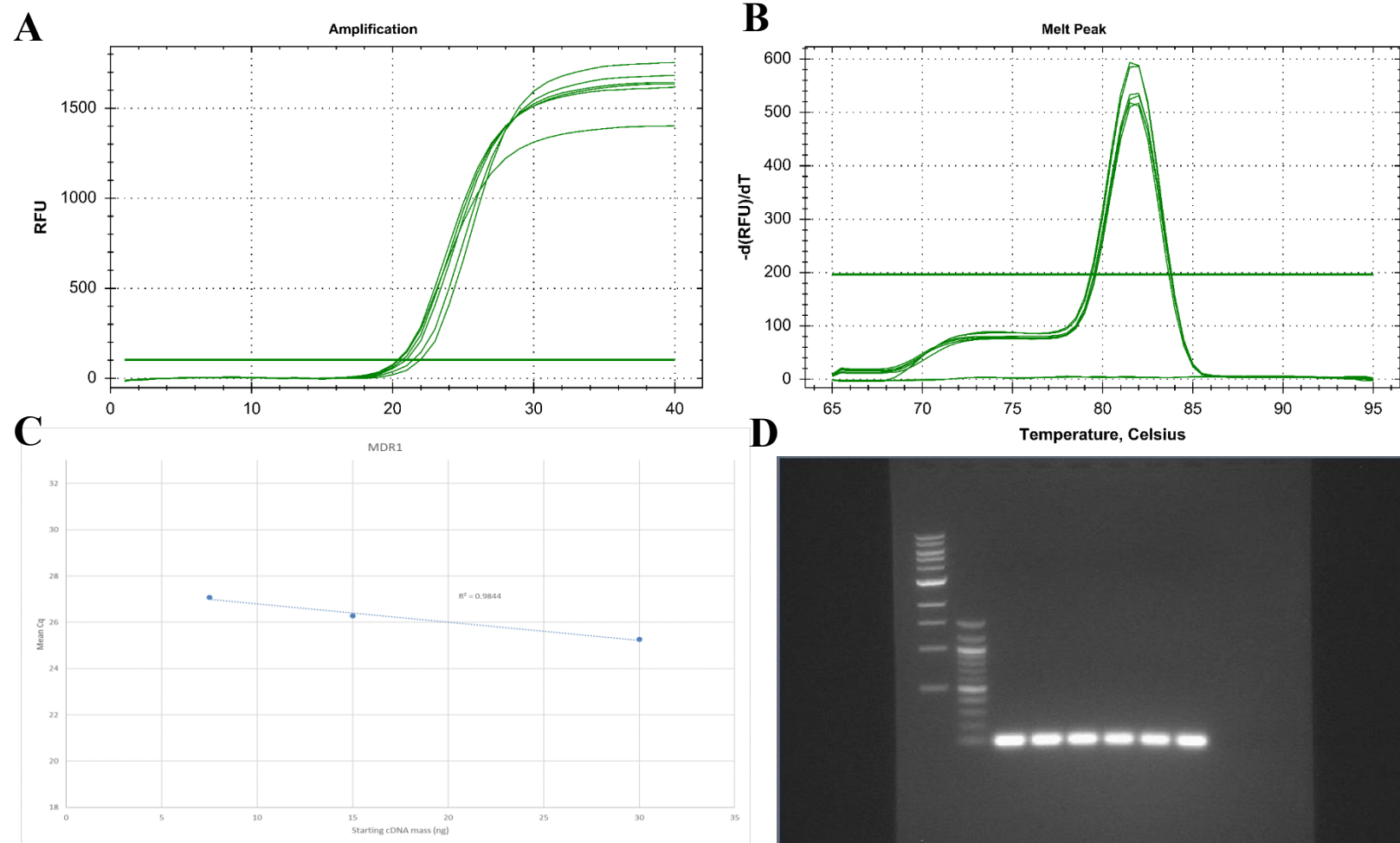


**Figure S8: MDR1 primer optimisation and efficiency check** – A) Normal amplification curves utilised for calculation of  $R^2$ . B) Melt peak to show primer specificity, C)  $R^2$  plotted diagram,  $R^2 = 0.9844$ , D) Product gel run, single band at correct weight suggests primer specificity for sequence of interest.

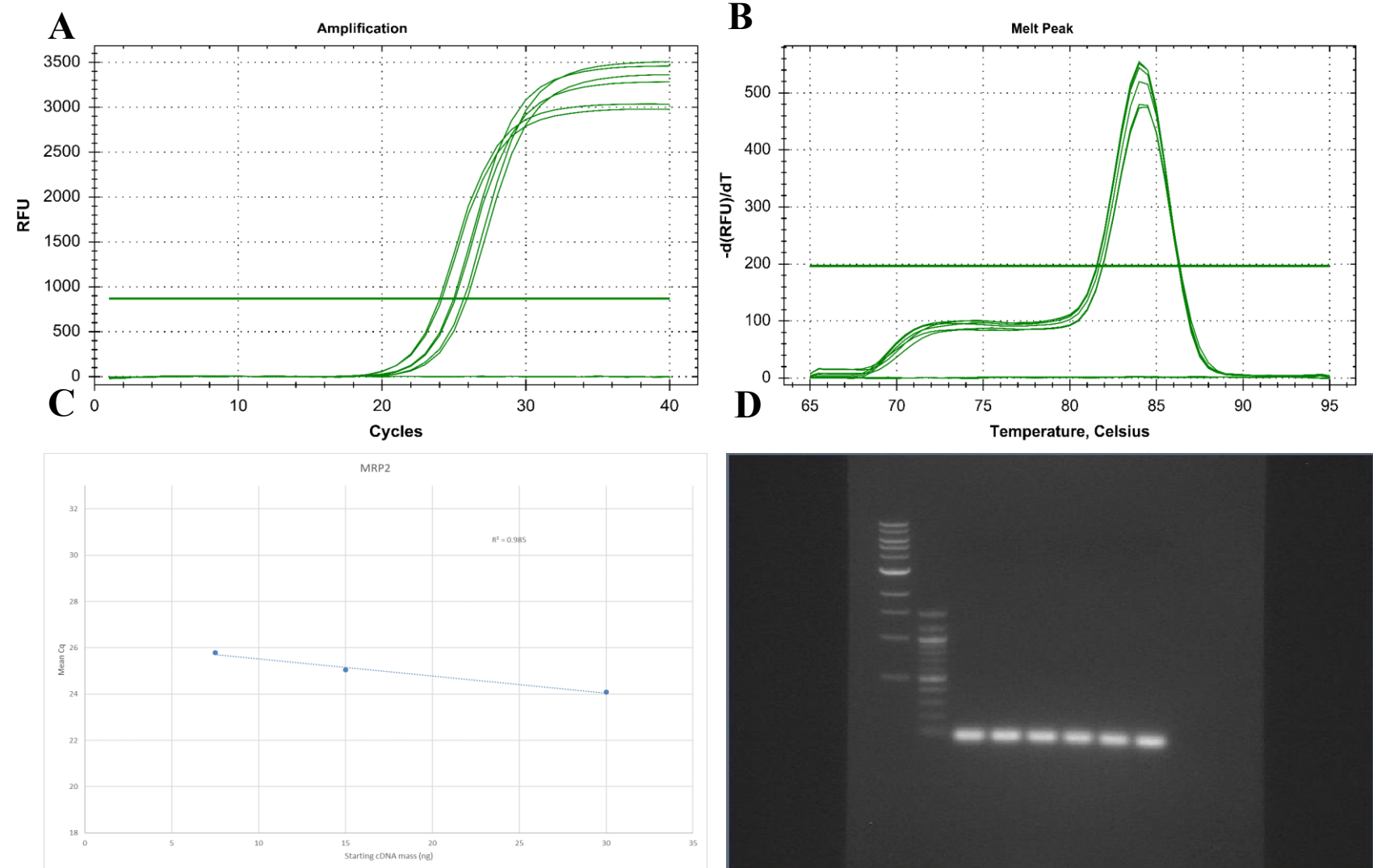


**Figure S9: MRP2 primer optimisation and efficiency check** – A) Normal amplification curves utilised for calculation of  $R^2$ . B) Melt peak to show primer specificity, C)  $R^2$  plotted diagram,  $R^2 = 0.985$ , D) Product gel run, single band at correct weight suggests primer specificity for sequence of interest.

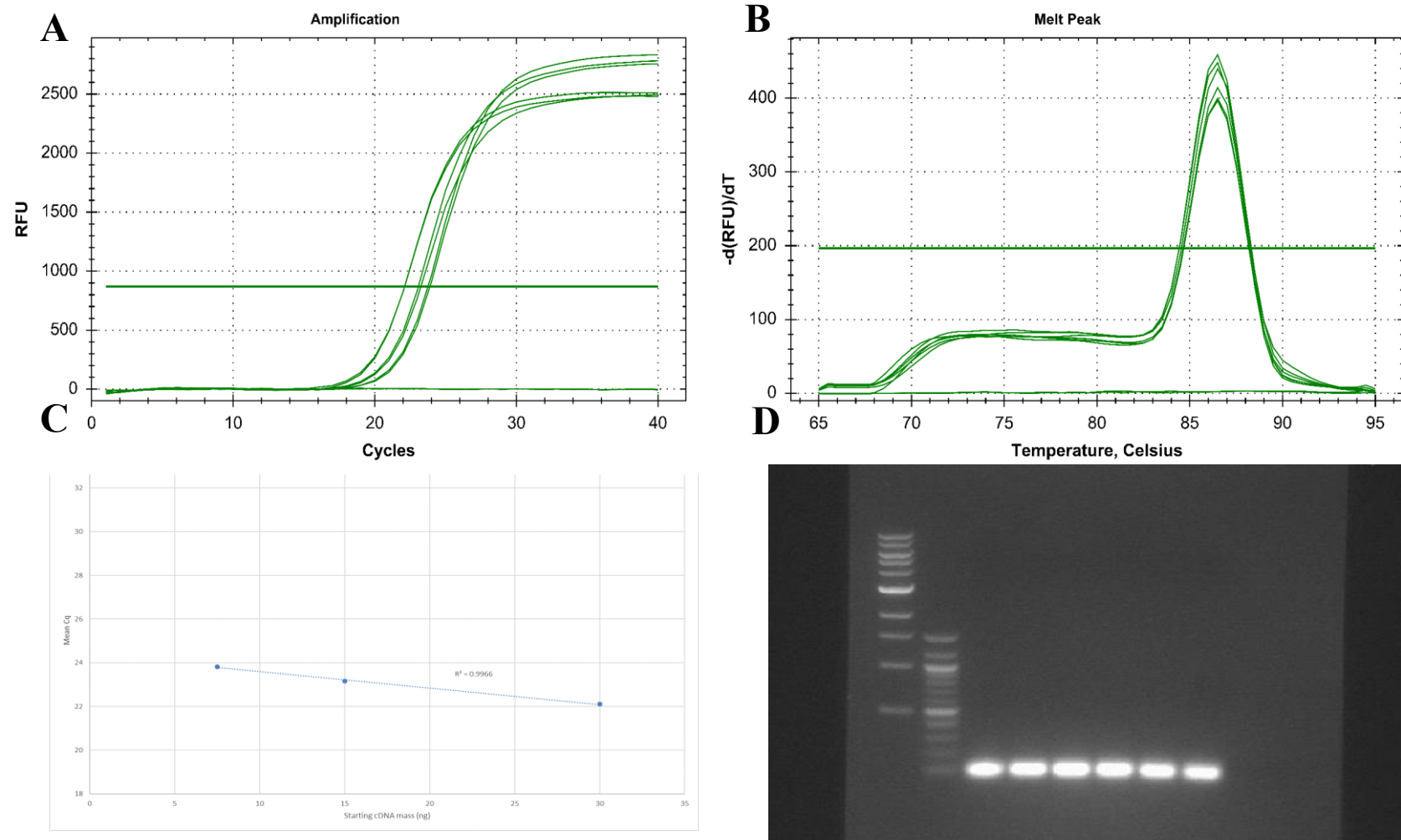


**Figure S10: OATP-B primer optimisation and efficiency check** – A) Normal amplification curves utilised for calculation of  $R^2$ . B) Melt peak to show primer specificity, C)  $R^2$  plotted diagram,  $R^2 = 0.9966$ , D) Product gel run, single band at correct weight suggests primer specificity for sequence of interest.



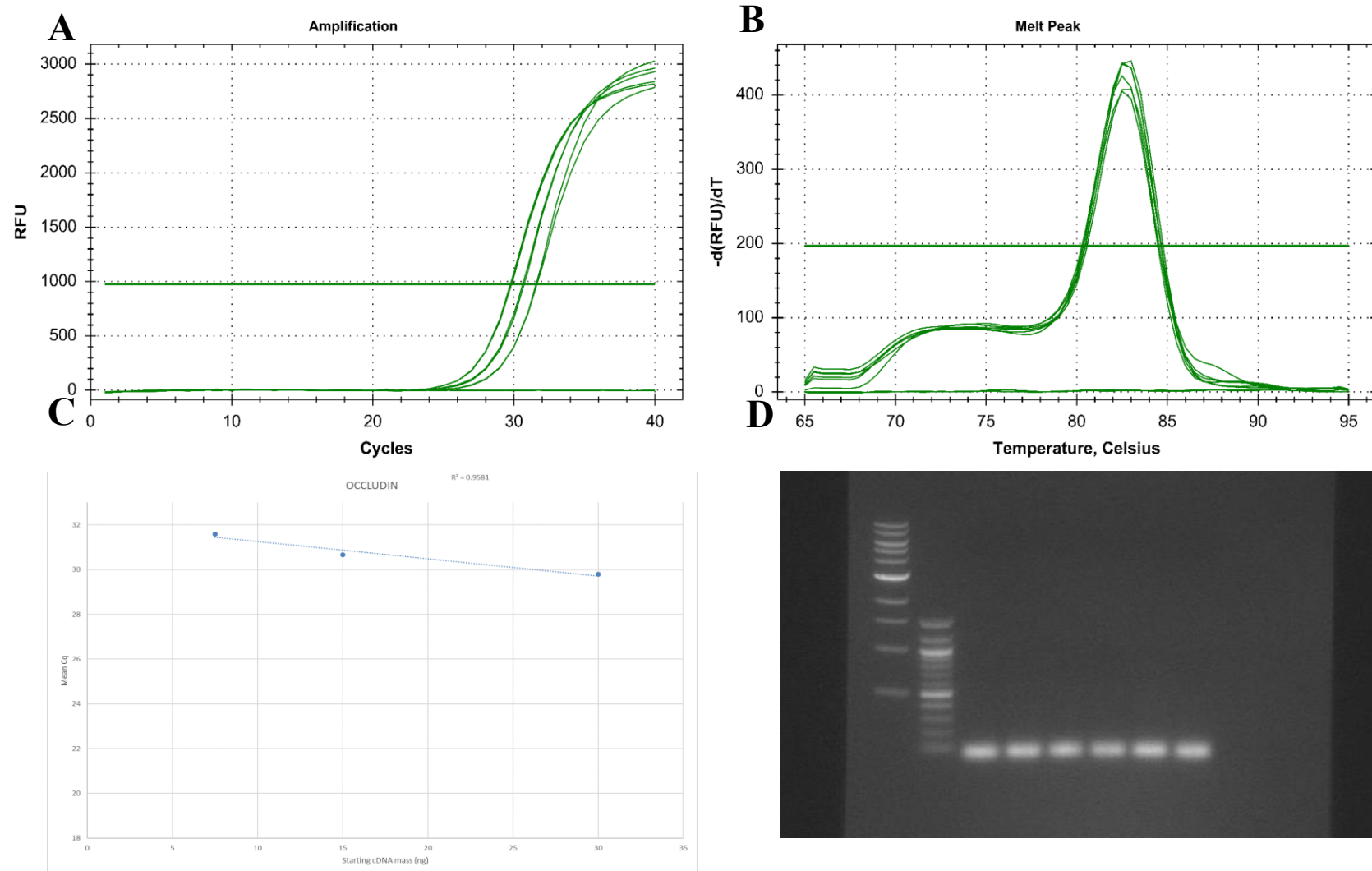


**Figure S11: Occludin primer optimisation and efficiency check** – A) Normal amplification curves utilised for calculation of  $R^2$ . B) Melt peak to show primer specificity, C)  $R^2$  plotted diagram,  $R^2 = 0.9581$ , D) Product gel run, single band at correct weight suggests primer specificity for sequence of interest.



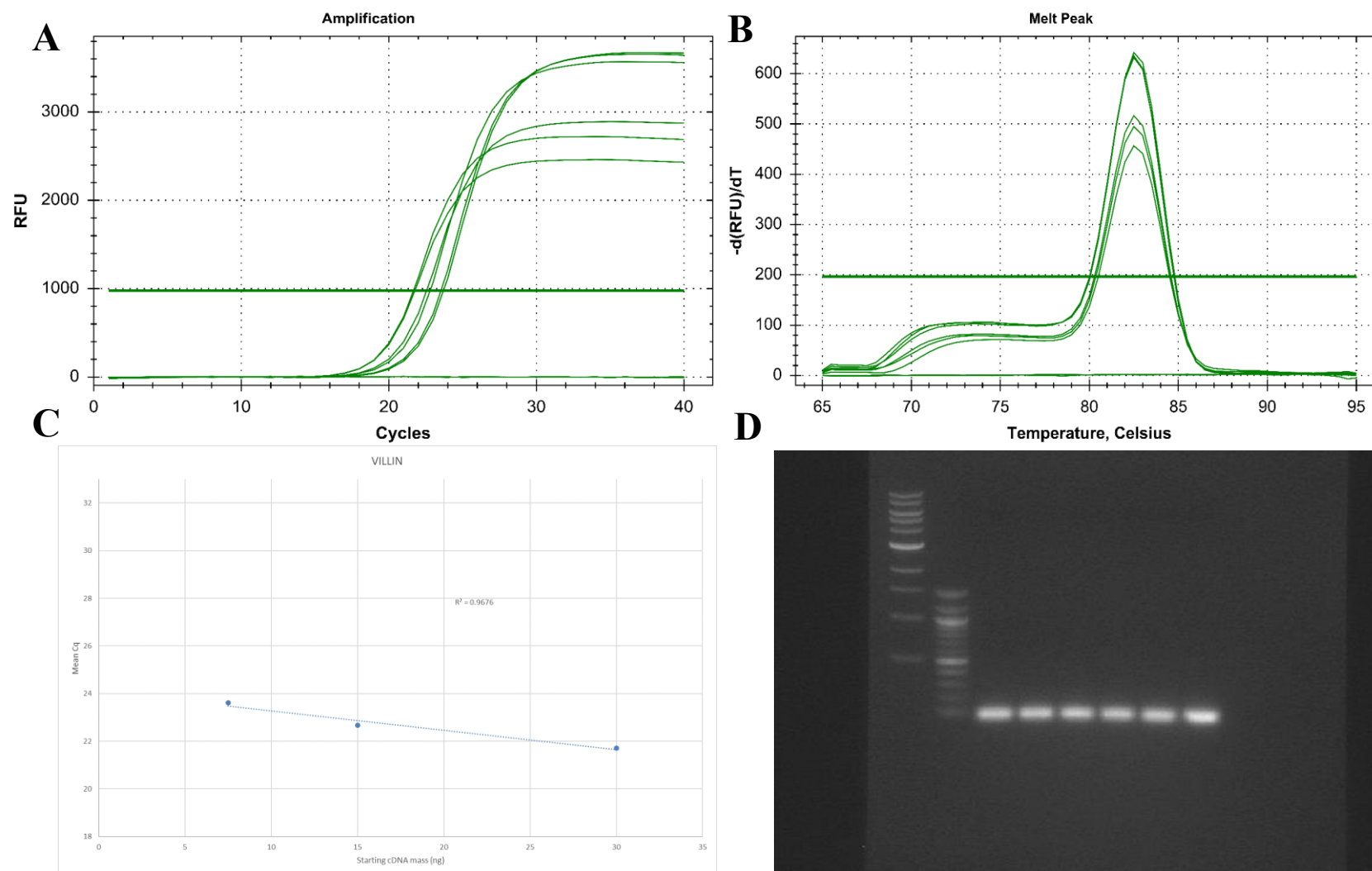


**Figure S12: Villin primer optimisation and efficiency check** – A) Normal amplification curves utilised for calculation of  $R^2$ . B) Melt peak to show primer specificity, C)  $R^2$  plotted diagram,  $R^2 = 0.9676$ , D) Product gel run, single band at correct weight suggests primer specificity for sequence of interest.

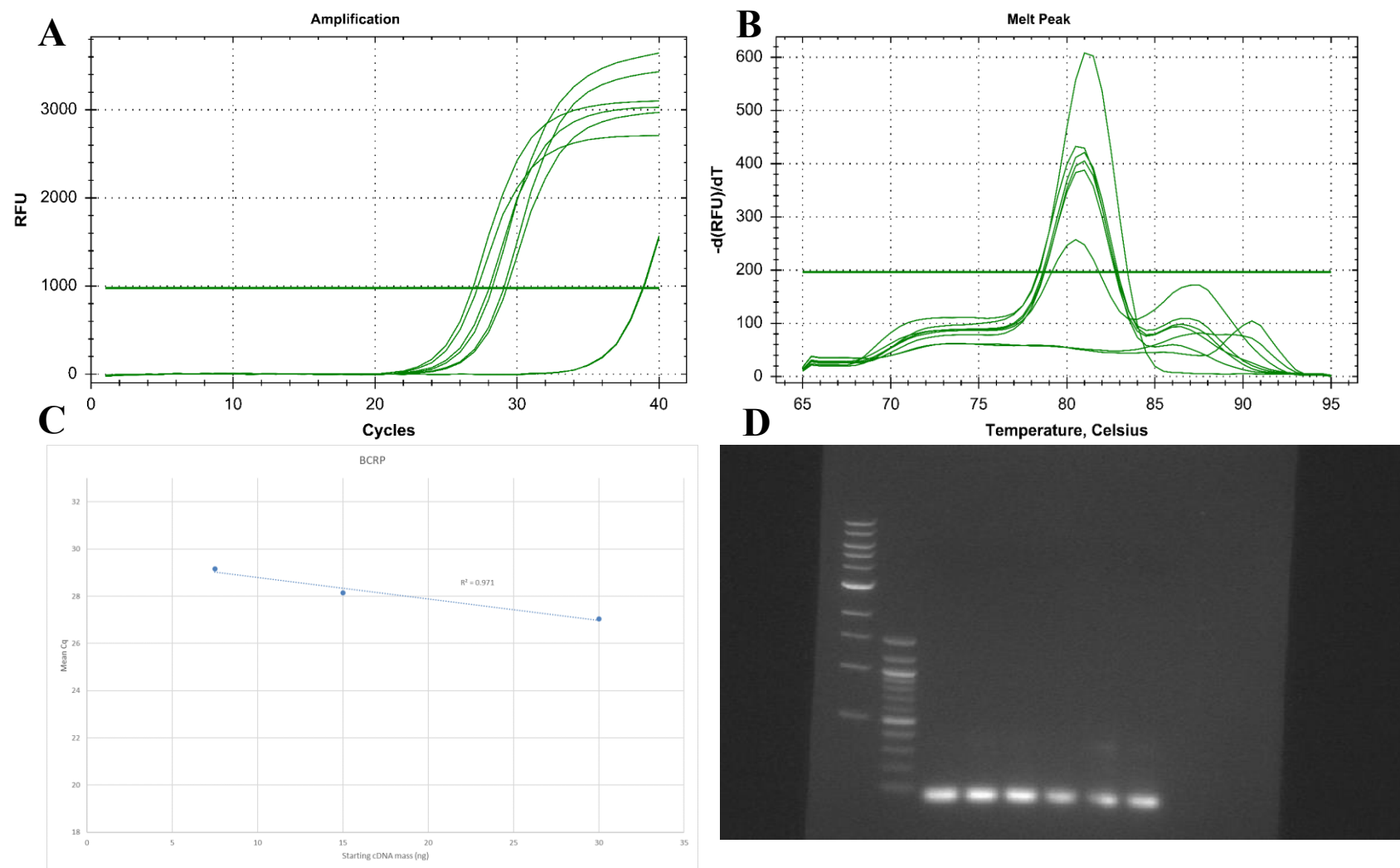


**Figure S13: BCRP primer optimisation and efficiency check** – A) Normal amplification curves utilised for calculation of  $R^2$ . B) Melt peak to show primer specificity, C)  $R^2$  plotted diagram,  $R^2 = 0.971$ , D) Product gel run, single band at correct weight suggests primer specificity for sequence of interest.

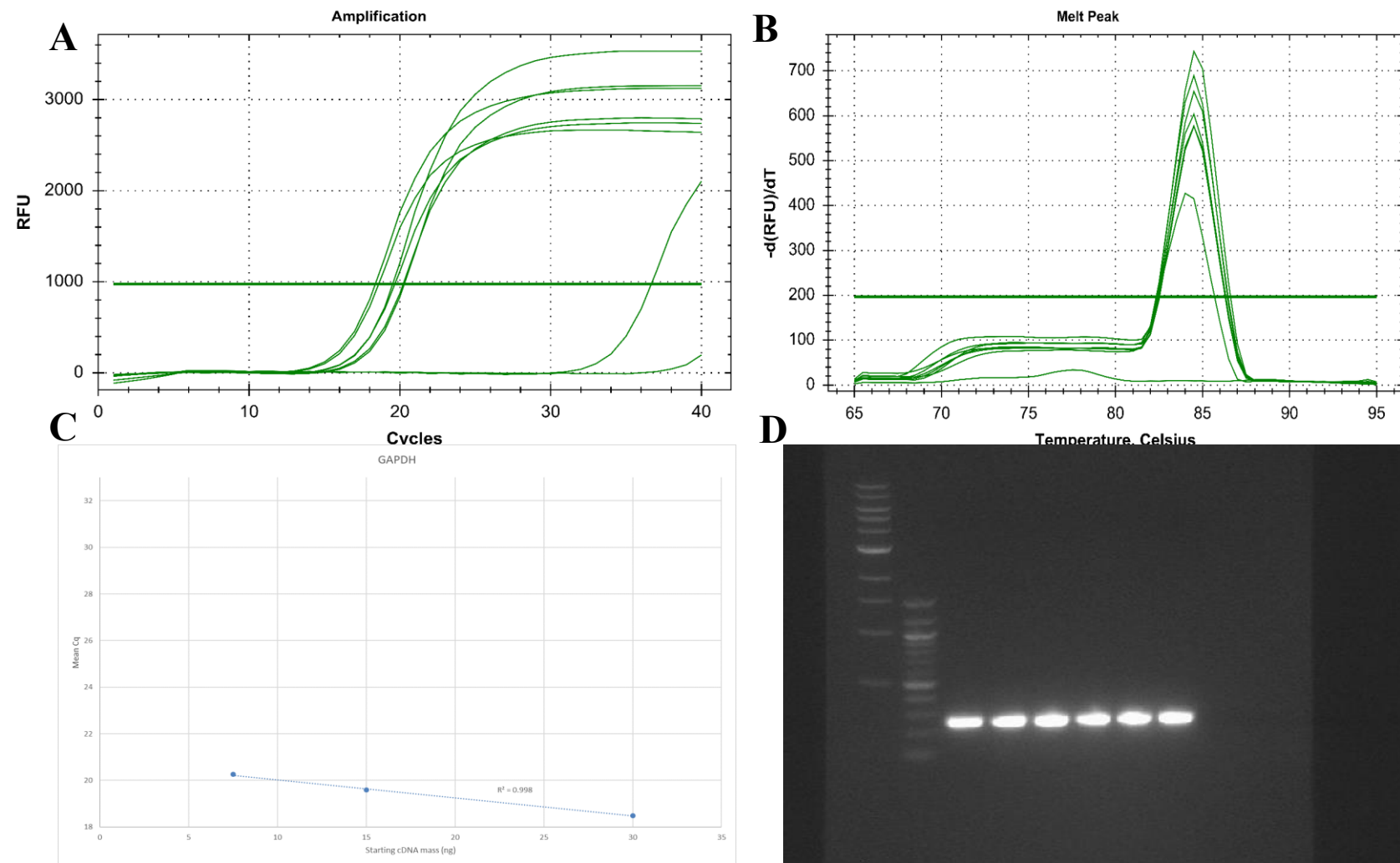


**Figure S14: GAPDH primer optimisation and efficiency check** – A) Normal amplification curves utilised for calculation of  $R^2$ . B) Melt peak to show primer specificity, C)  $R^2$  plotted diagram,  $R^2 = 0.998$ , D) Product gel run, single band at correct weight suggests primer specificity for sequence of interest.

9.4 Project poster presentations

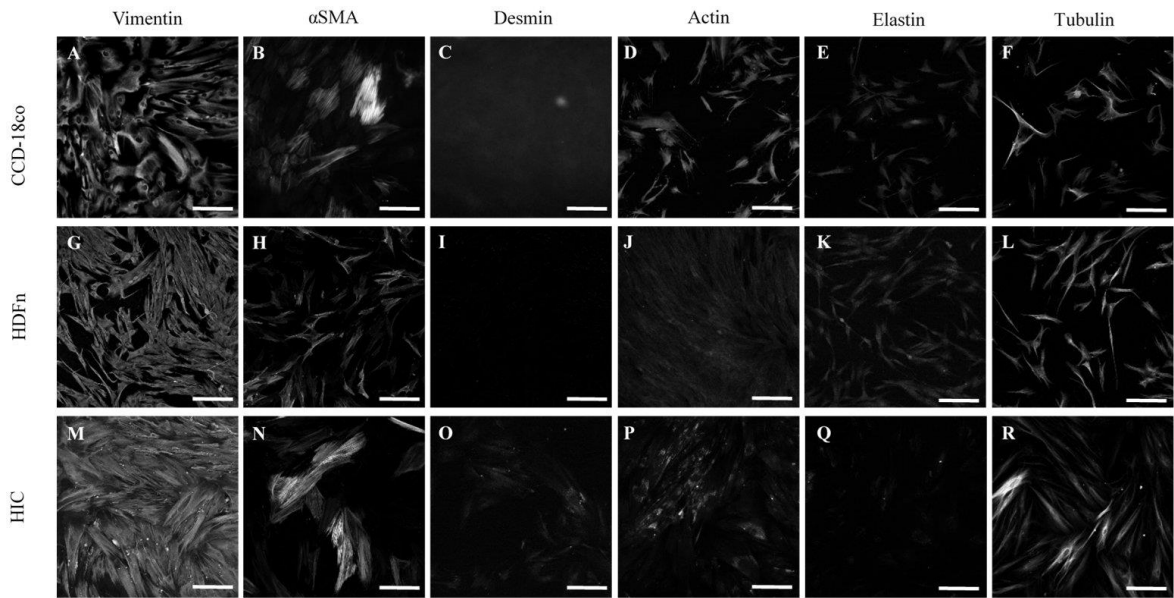


**Figure S15: Green channel for Figure 3.3** - Positive staining (Green channel) of 2D fibroblast cells. Mixed staining of Figure 3.3

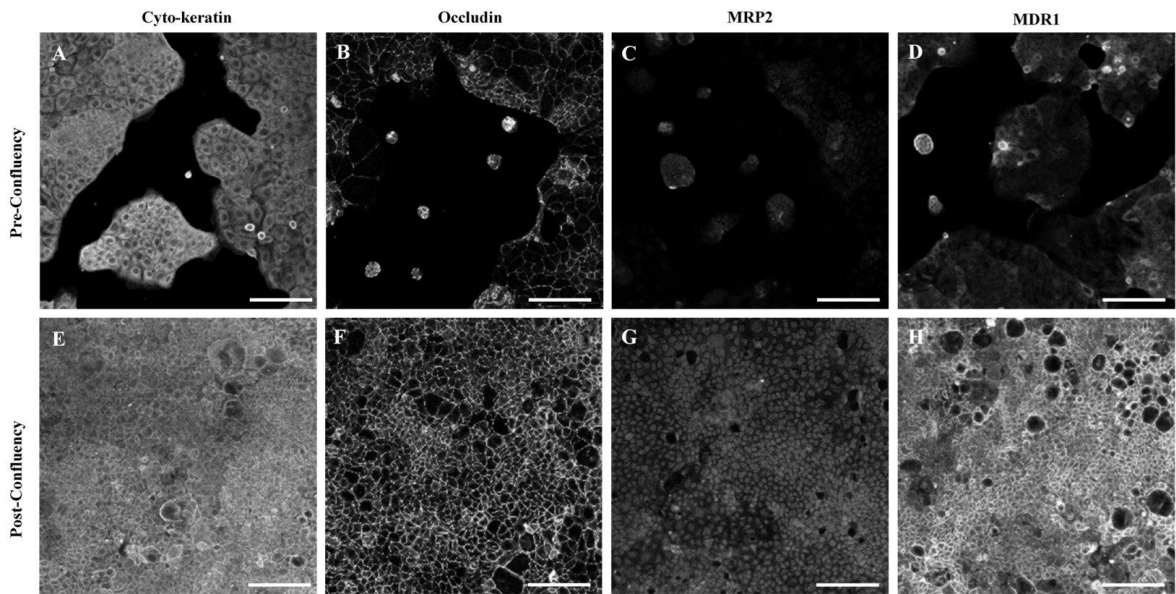


**Figure S16: Green channel for Figure 3.4** - Positive staining (Green channel) of 2D Caco-2 cells. Mixed staining of Figure 3.4

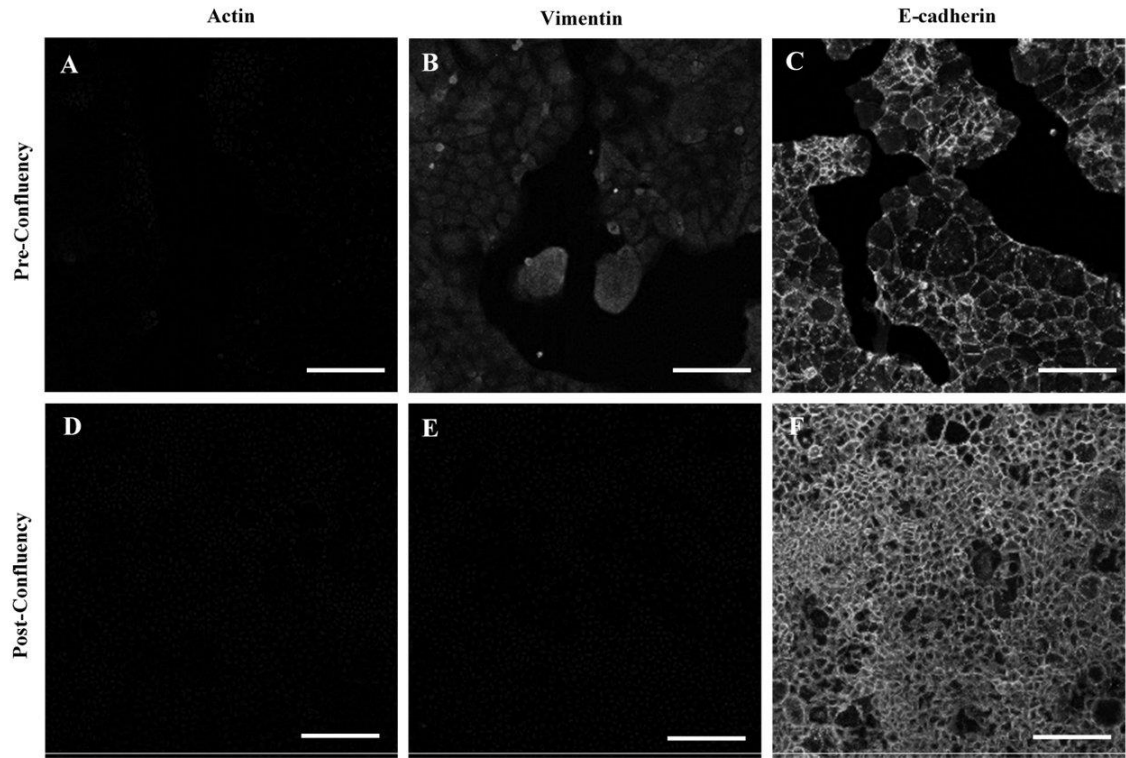


**Figure S17: Green channel for Figure 3.5** - Positive staining (Green channel) of 2D Caco-2 cells. Mixed staining of Figure 3.5

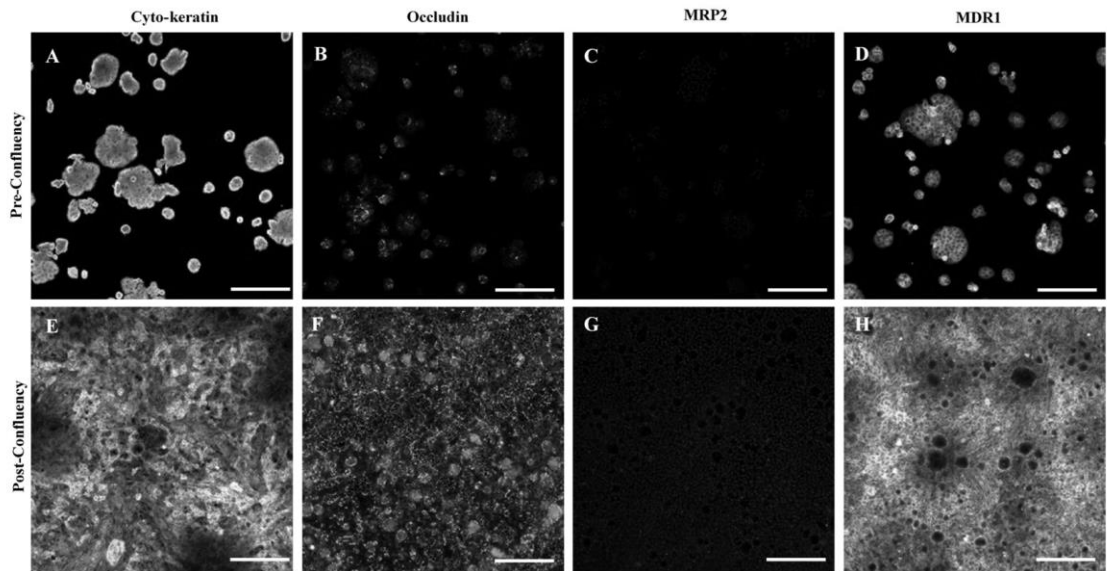


**Figure S18: Green channel for Figure 3.6** - Positive staining (Green channel) of 2D HT29-MTX cells. Mixed staining of Figure 3.6

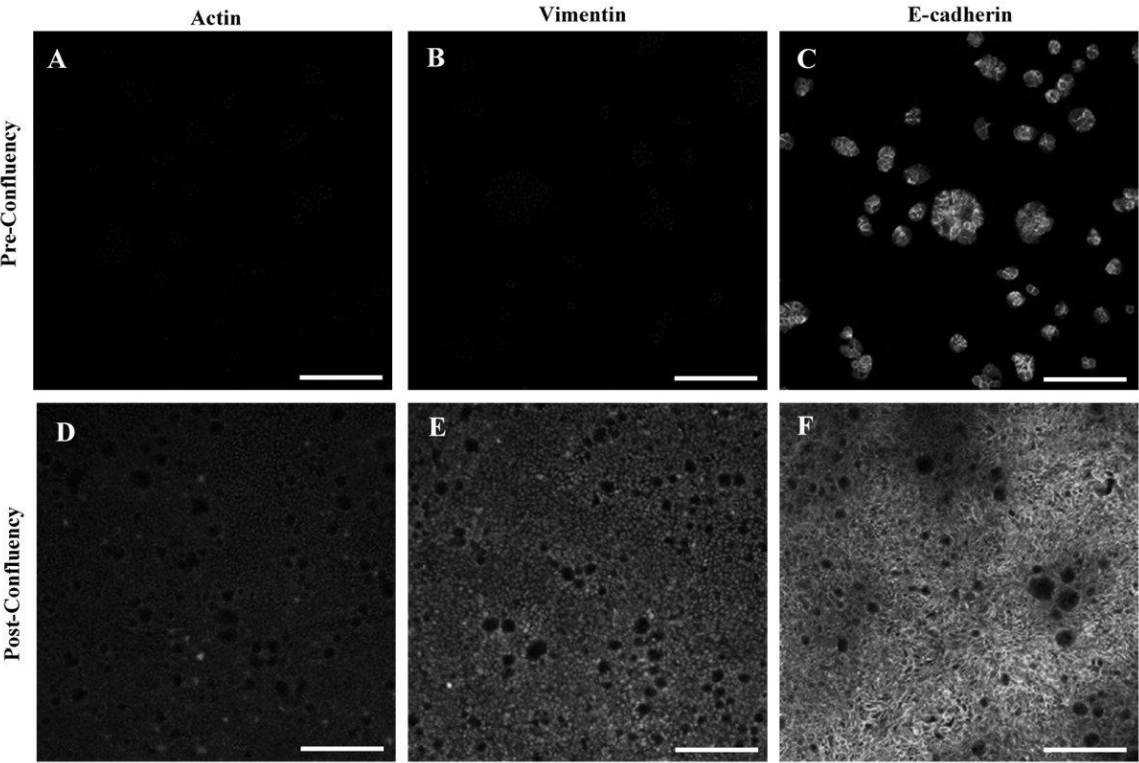


**Figure S19: Green channel for Figure 3.7** - Positive staining (Green channel) of 2D HT29-MTX cells. Mixed staining of Figure 3.7

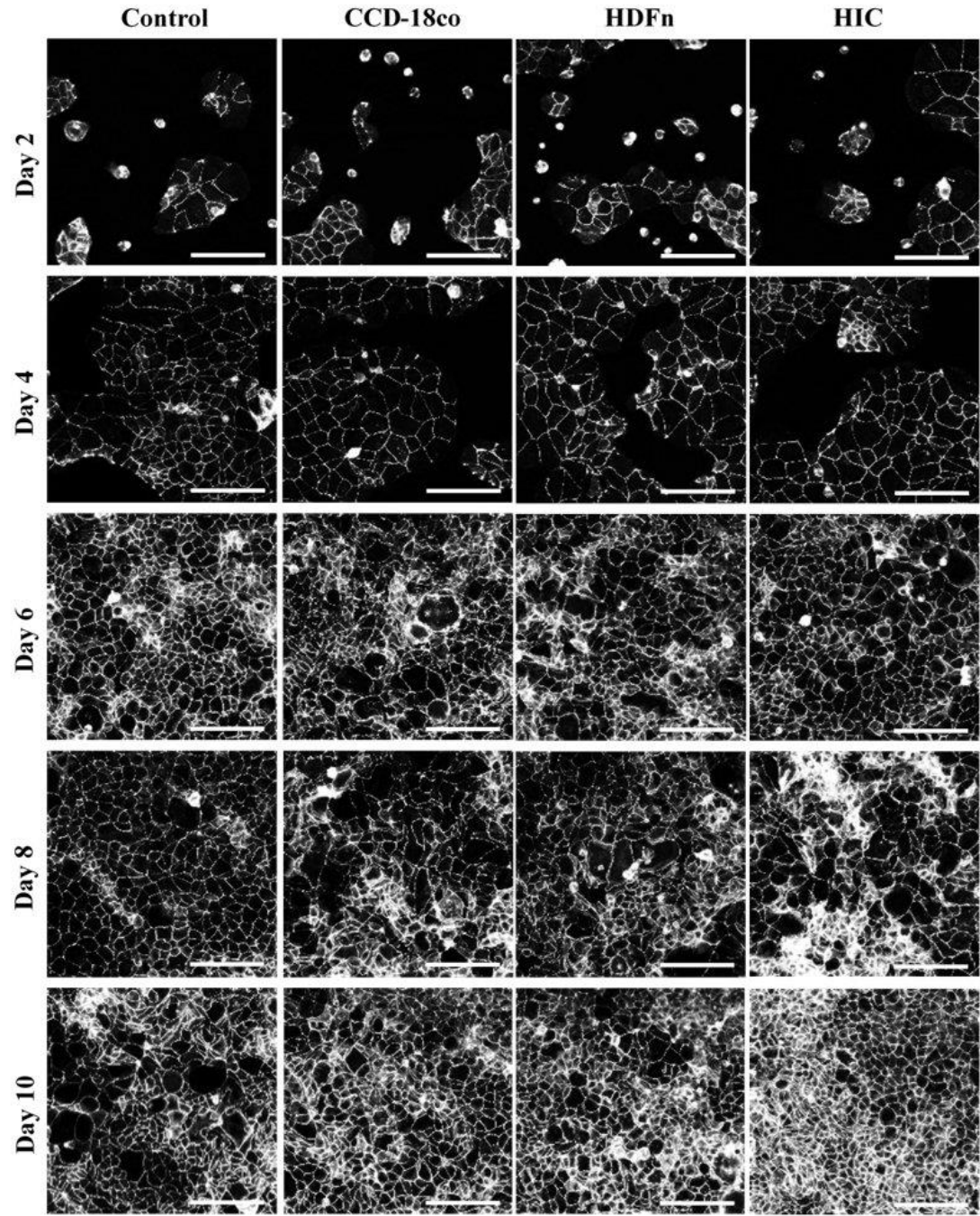


**Figure S20: Green channel for Figure 3.12** - Positive staining (Green channel) of 2D Caco-2 cells stained for Occludin, Figure 3.12



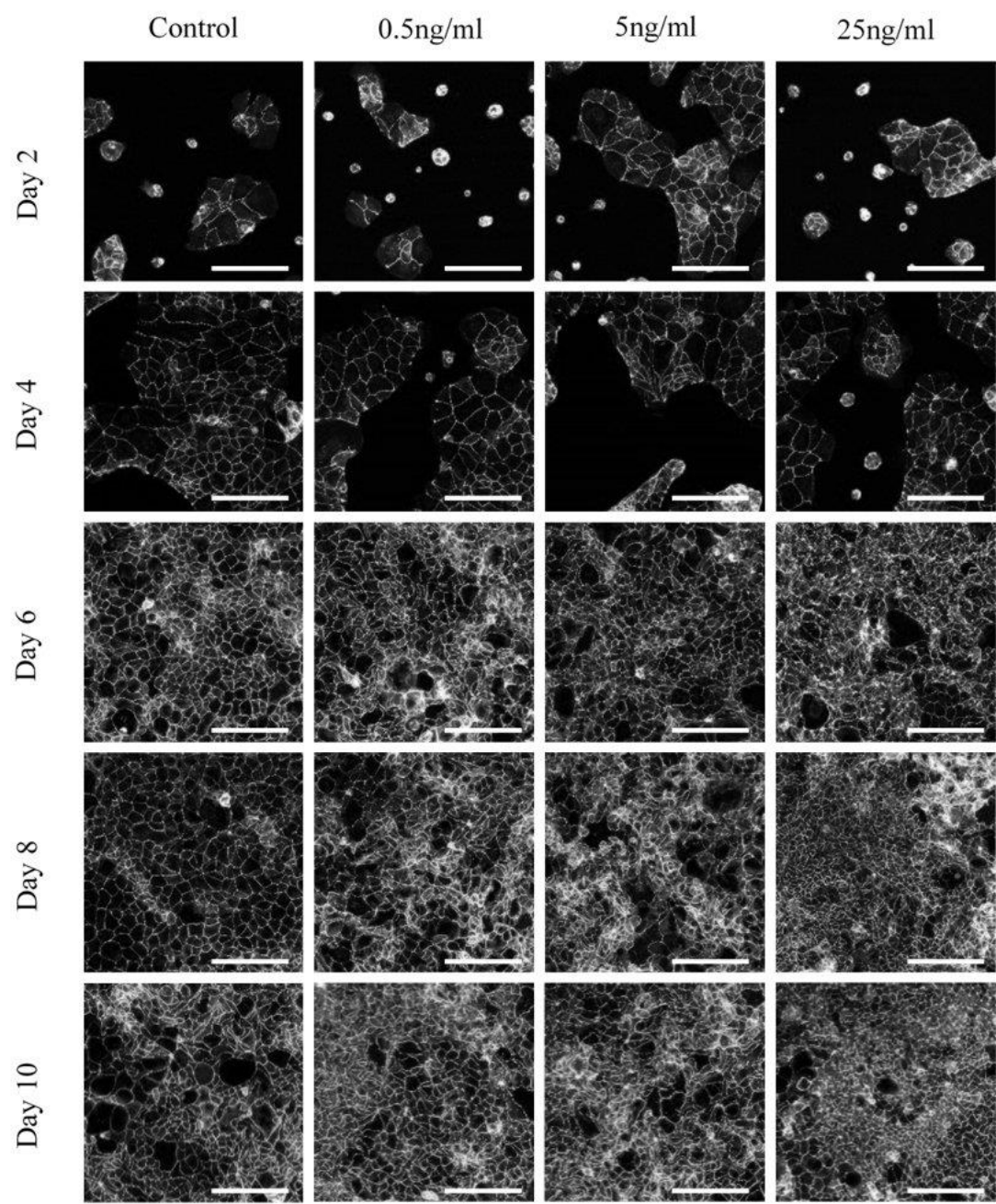


**Figure S21: Green channel for Figure 3.26** - Positive staining (Green channel) of 2D Caco-2 cells stained for Occludin, Figure 3.26



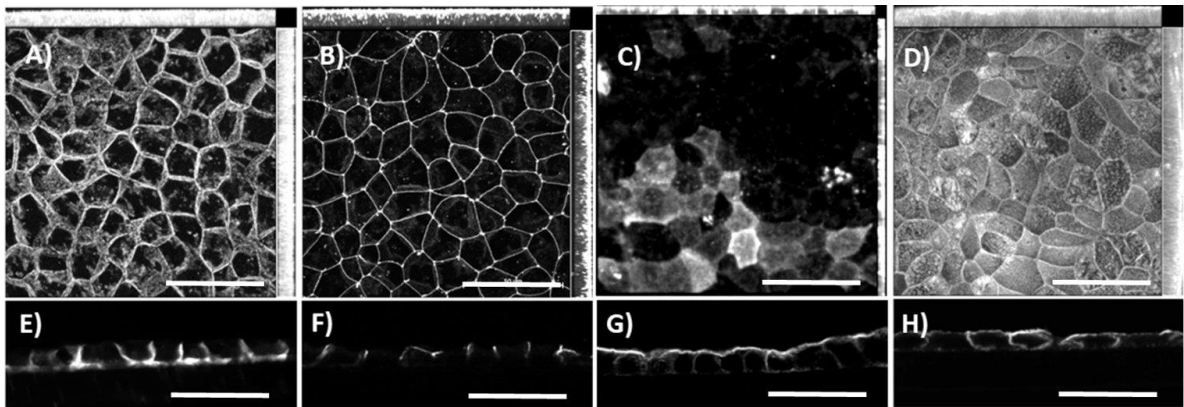


**Figure S22: Green channel for Figure 3.13** - Positive staining (Green channel) of Caco-2 cells grown on Transwell, Figure 3.13

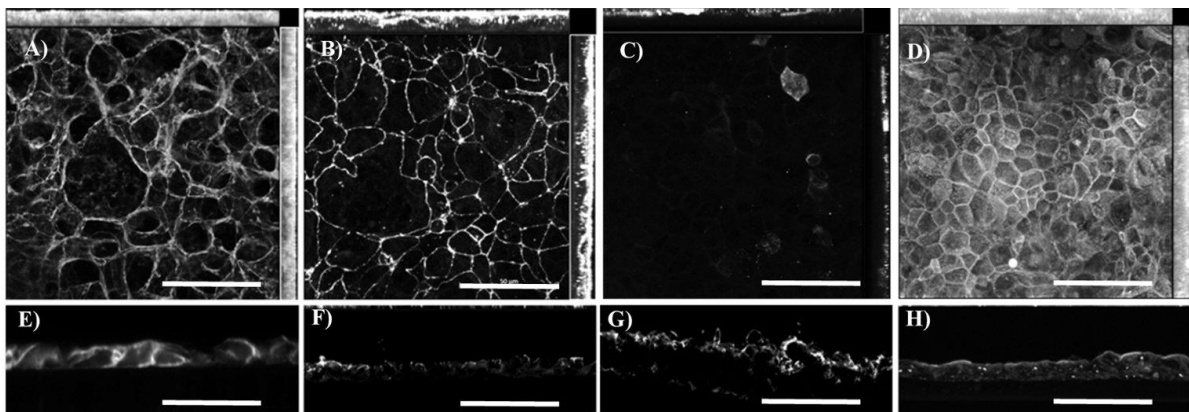


**Figure S23: Green channel for Figure 3.14** - Positive staining (Green channel) of Caco-2 cells grown on Transwell, Figure 3.14

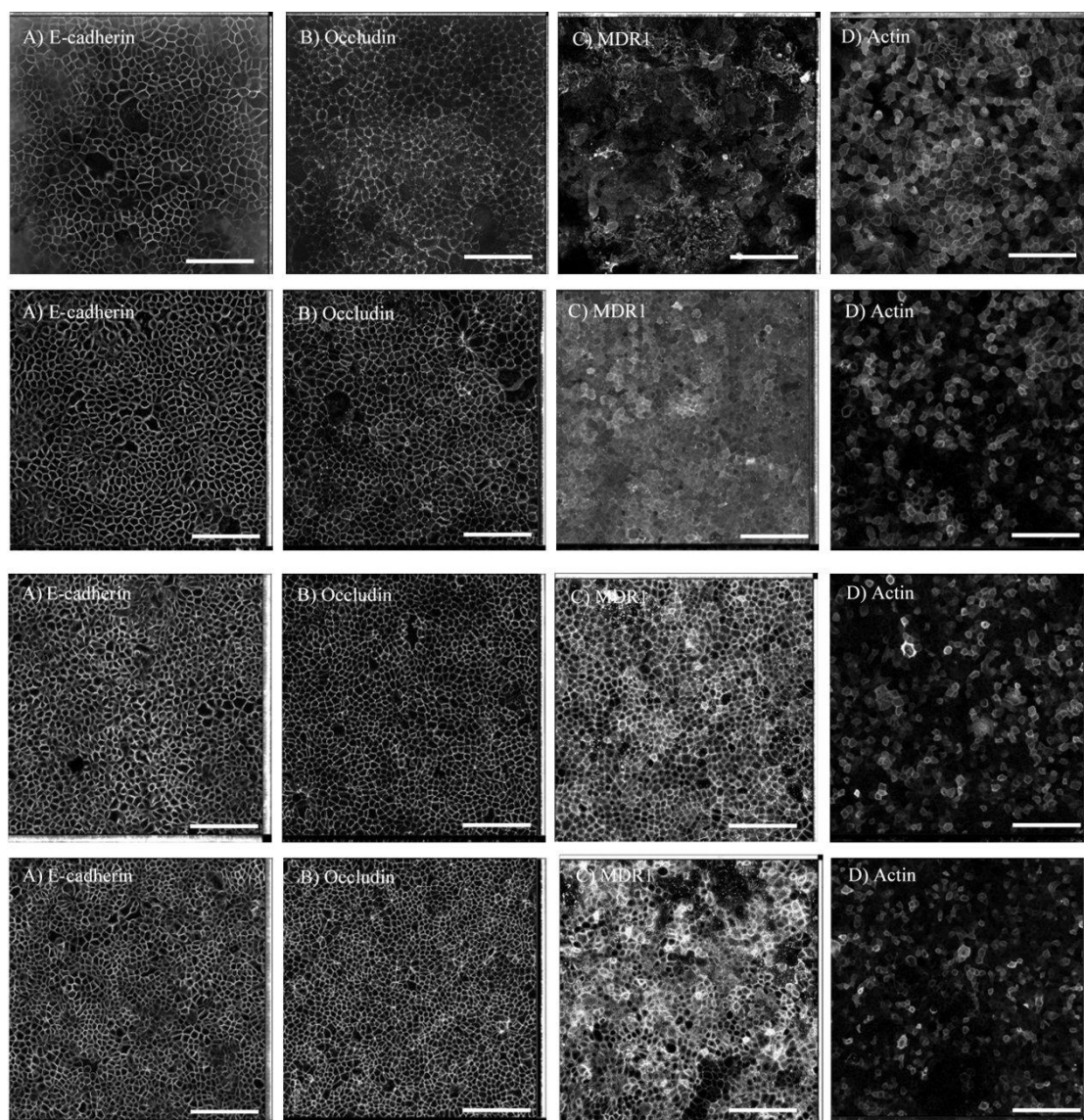


**Figure S24: Green channel for Figure 3.20-23** - Positive staining (Green channel) of Caco-2 cells grown on Transwell in the presence of KGF, Figure 3.20-23 respectively.

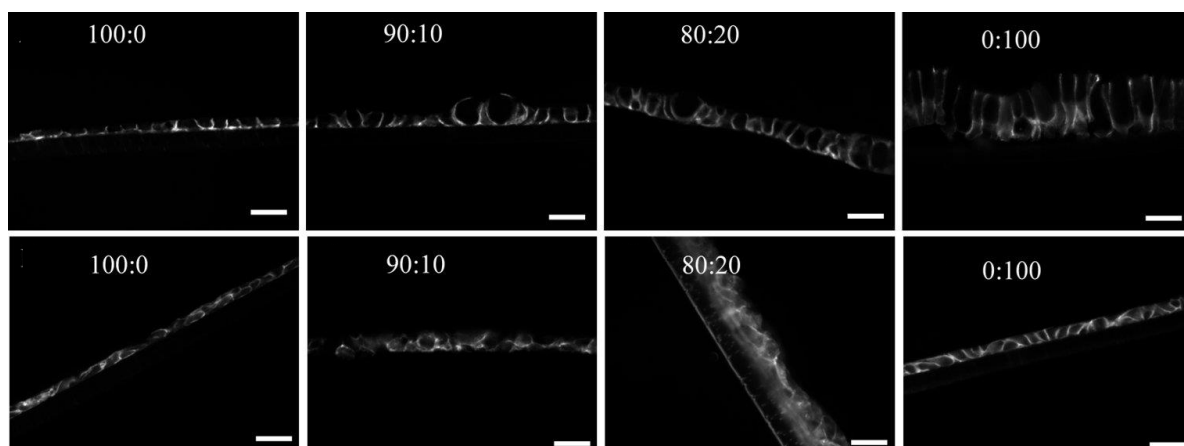


**Figure S25: Green channel for Figure 4.11** - Positive staining (Green channel) of E-cadherin in Caco-2/ HT29-MTX co-cultures, Figure 4.11

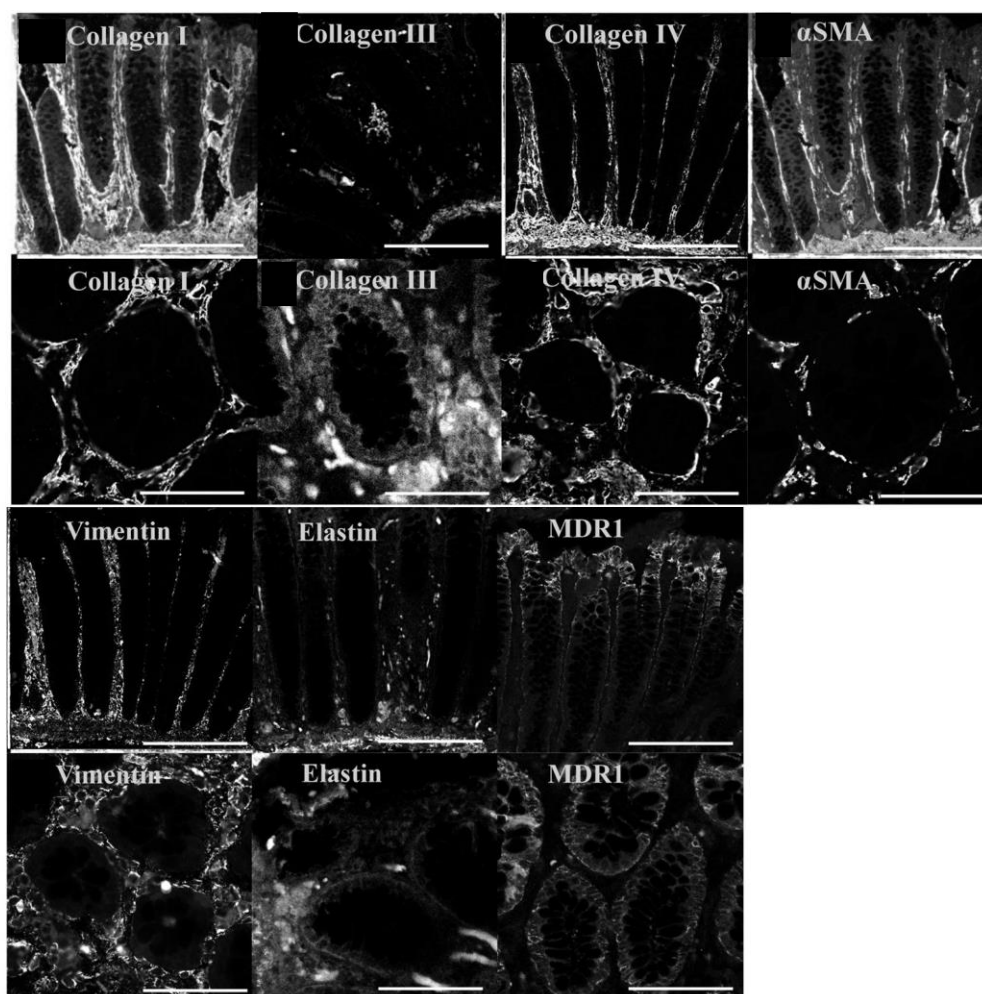


**Figure S26: Green channel for Figure 5.22/23** - Positive staining (Green channel) of Colonic human tissues, Figures 5.22 and 5.23.

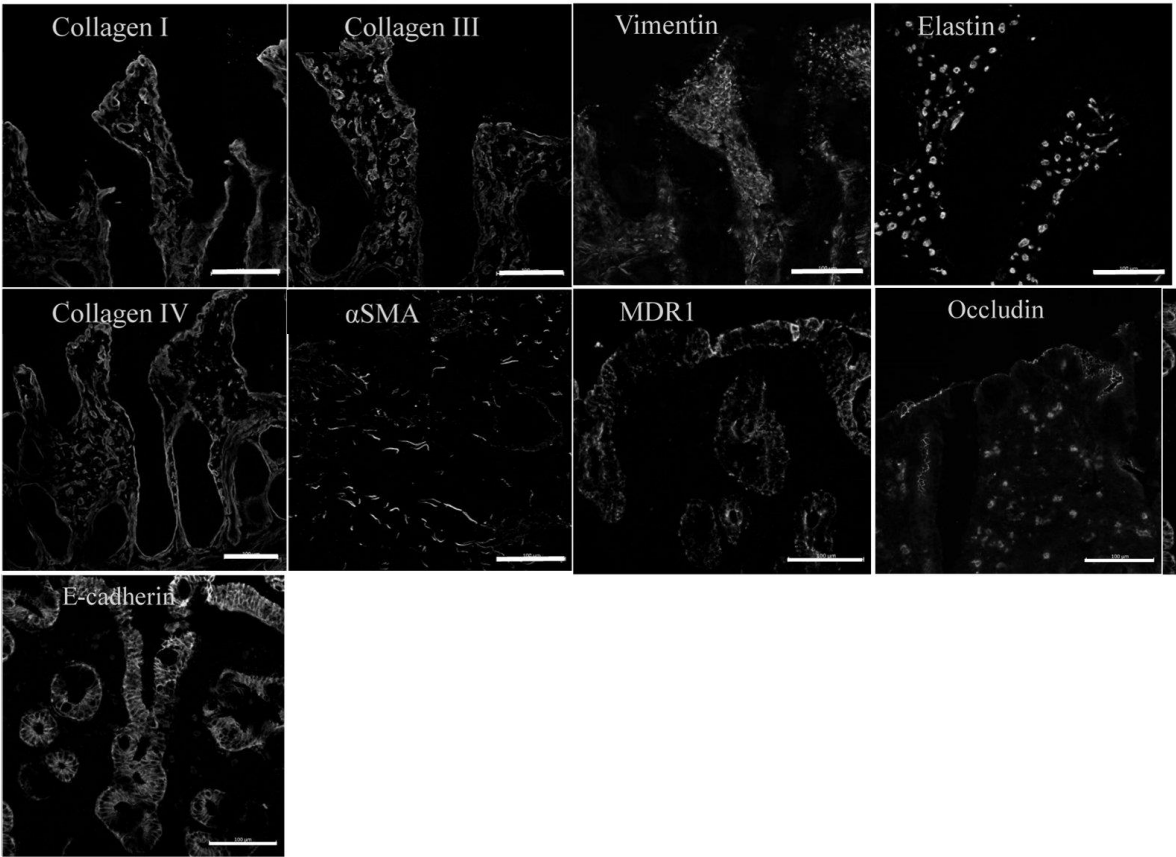


**Figure S27: Green channel for Figure 5.25-27** - Positive staining (Green channel) of Small intestine human tissues, Figures 5.25, 5.26 and 5.27.

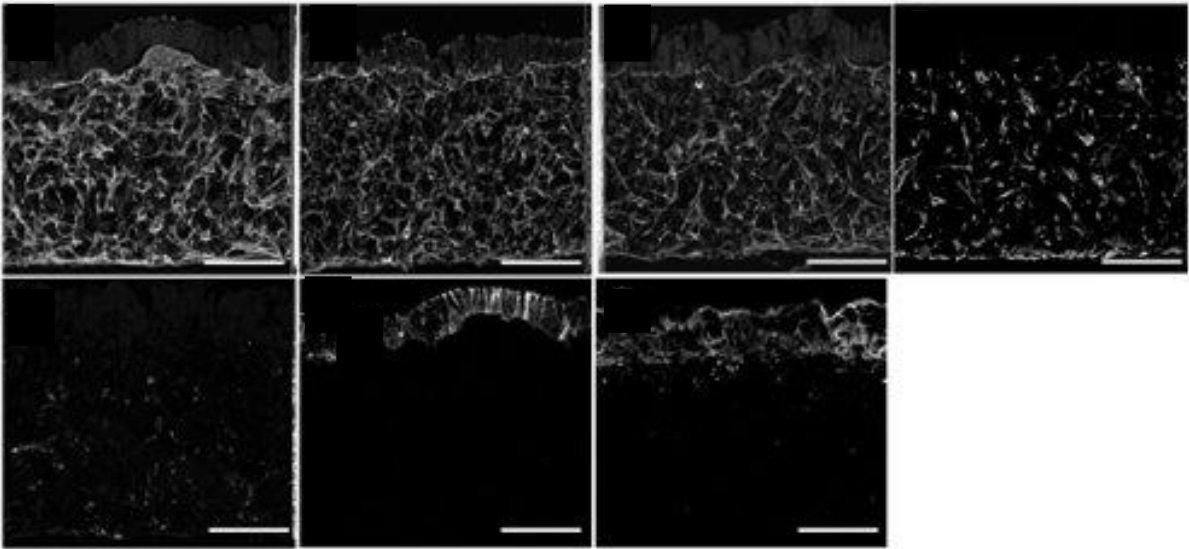


**Figure S28: Green channel for Figure 5.28** - Positive staining (Green channel) of 3D alvetex cultures created with CCD-18co fibroblast cells, Figure 5.28

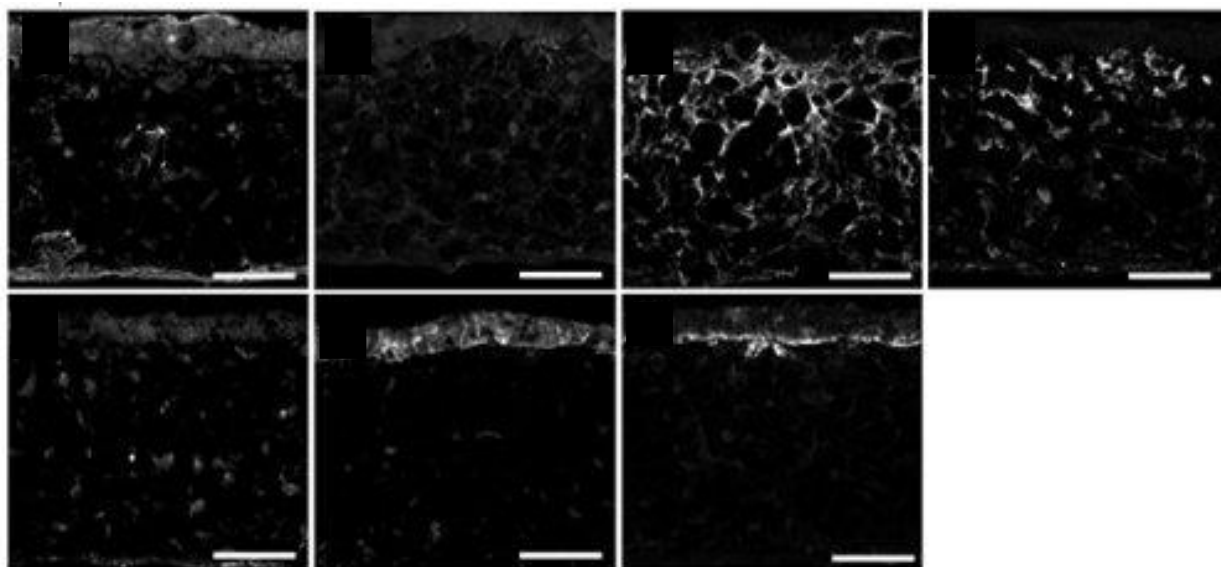


**Figure S29: Green channel for Figure 5.29** - Positive staining (Green channel) of 3D alvetex cultures created with HDFn fibroblast cells, Figure 5.29

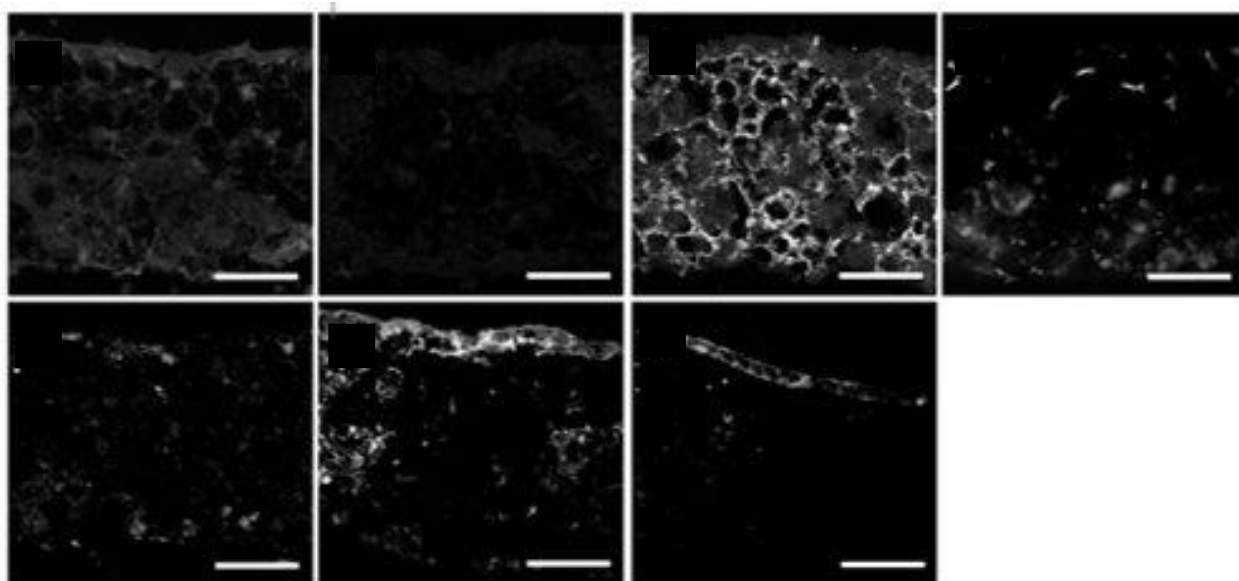


**Figure S30: Green channel for Figure 5.30** - Positive staining (Green channel) of 3D alvetex cultures created with HIC fibroblast cells, Figure 5.30



## 9.5 Project poster presentations

